CIP-DATA LIBRARY TECHNISCHE UNIVERSITEIT EINDHOVEN

Duits, Remco

Perceptual Organization in Image Analysis :a mathematical approach based on scale, orientation and curvature / by Remco Duits - Eindhoven : Technische Universiteit Eindhoven, 2005.
Proefschrift. - ISBN 90-386-2747-5
NUR 919
Subject headings: image Analysis / α scale space theory / group theory / evolution equations / wavelet theory / functional Hilbert spaces / robust orientation estimation

This research is/was supported by the Technology Foundation STW, applied science division of NWO and the technology programme of the Ministry of Economic Affairs

Front cover image: “ The horse called Perceptual Grouping” (2003) (fragment of) oil-painting by the author of this PhD-thesis.

Copyright © 2005 by Remco Duits

Printed by Printservice Technische Universiteit Eindhoven, Eindhoven, the Netherlands

Perceptual Organization in Image Analysis

A mathematical approach based on scale, orientation and curvature.

PROEFSCHRIFT

ter verkrijging van de graad van doctor aan de
Technische Universiteit Eindhoven, op gezag van de
Rector Magnificus, prof.dr.ir. C.J. van Duijn, voor een
commissie aangewezen door het College voor Promoties
in het openbaar te verdedigen
op woensdag 14 september 2005 om 16.00 uur

door

Remco Duits

geboren te Weert

Dit proefschrift is goedgekeurd door de promotoren:

prof.dr.ir. B.M. ter Haar Romeny
en
prof.dr.ir. J. de Graaf

Copromotor:
dr. L.M.J. Florack

Contents

Foreword **1**

Introduction **2**

Outline of the Thesis **6**

Preliminaries **11**

I Scale **15**

1 α Scale Spaces on the Unbounded Domain. **16**

1.1 Introduction 16

1.2 Axioms 18

1.3 Strongly Continuous Semi-groups 23

1.3.1 Strong Continuity of Poisson and Gaussian Semigroup. 26

1.3.2 Infinitesimal Generators of Strongly Continuous Semigroups and their Resolvents 27

1.3.3 Holomorphic Semigroups 28

1.4 Evolution Equations Corresponding to α Scale Spaces. 29

1.4.1 The Diffusion Equation 30

1.4.2 The Poisson Equation 31

1.4.3 Clifford Analytic Extension of Poisson Scale Space 38

1.5 Fractional Powers of Closed Operators 42

1.5.1 Fractional Powers of the Minus Laplace Operator: $(-\Delta)^{\alpha}$, $0 < \alpha \leq 1$ 47

1.5.2 Derivation of the Poisson Semigroup from the Gaussian Semigroup . . . 47

1.5.3 Verification of the Axioms with respect to the α Scale Spaces 48

1.6 Gaussian Filtering and Poisson Filtering 49

1.6.1 Using one dimensional kernels in multi-dimensional implementation . . 50

1.6.2 Derivatives of the 1D Poisson and Gaussian Kernel 52

1.6.3 Gaussian and Poisson Scale Space from Energy Minimization 56

1.7 Defocussing of an Idealized Optical System and the Cauchy Kernel 56

1.8 Conclusion and Discussion 59

2 α Scale Spaces on the Bounded Domain with Neumann Boundary Conditions 60

2.1 Introduction 60

2.2 The Rectangle Case 64

2.2.1 The Unbounded Domain Case as a Limit of the Rectangular Case. . . . 65

2.3 The Disc Case 66

2.4 The Monogenic Scale Space on a Bounded Domain and its Application in Phase-Based Image processing 69

2.4.1 Construction and Implementation of Monogenic Scale Space on a Bounded Domain 72

2.5 Truncation of the Fourier Series Expansions 74

2.6 Conclusion 76

3 Deep Structure 78

3.1 Introduction 78

3.2 Grey-Value Flow 79

3.3 A Comparison of the Topology within α Scale Spaces 80

3.3.1 Local Morse Theory for Gaussian Scale Space and Poisson Scale Space 81

3.3.2 A Partition of Equivalence Classes of $\tilde{G}$-stable Gaussian Deformations . 84

3.3.3 A partition of $\mathcal{G}$-stable Poisson Deformations 85

3.4 Linear Image Reconstruction from a Sparse Set of α Scale Space Features by means of Inner Products of Sobolev Type 88

3.4.1 Generalization of the Standard Linear Image Reconstruction Scheme . . 89

3.4.2 Gelfand Triples 92

3.4.3 A Linear Image Reconstruction Based on Inner Products of Sobolev Type 94

3.4.4 Linear Reconstruction Algorithms 97

3.4.5 Experiments 100

3.4.6 Flux-features 100

3.5 Conclusion 106

II Orientation **107**

4 Invertible Orientation Scores as an Application of Generalized Wavelet Theory **108**

4.1 Introduction 108

4.2 Preliminaries and Notation 111

4.3 Wavelet Theory 113

4.3.1 Continuous Wavelet Theory on 1D-Signals 113

4.3.2 Wavelet Transformations constructed by Unitary Irreducible Representations of Locally Compact Groups 115

4.4 A Functional Hilbert Space Approach to Wavelet Theory 118

4.4.1 The Construction of a Unitary Map from H to $\mathbb{C}_K^{\mathbb{I}}$ 120

4.4.2 Generalization of Wavelet Reconstruction Theorem for Affine Groups . 122

4.5 Stability reconstruction of image f from its orientation score U_f 126

4.6 Classes of Wavelets that allow Wellposed Reconstruction 128

4.6.1 A Simple Approach to Parameterization of Proper Wavelet classes . . . 130

4.6.2 A General Approach to Parameterization of Proper Wavelet Classes . . 137

4.7 Orientation Scores on 3D images 143

4.7.1 A Simple Approach for Constructing 3D Proper Wavelets 144

4.7.2 General Approach of Constructing 3D proper wavelets 146

4.8 Image Enhancement by means of Left-Invariant Operations on Orientation Scores 152

4.8.1 Geometry of the Euclidean Motion Group 154

4.8.2 Basic Left Invariant Operations on Orientation Scores 158

4.8.3 Evolution Equations Corresponding to Left Invariant Stochastic Processes on the 2D Euclidean Motion Group 160

4.9 Analytic Approximations of (the Green's functions of) the Left-invariant Evolutions on the Euclidean Motion Group 163

4.9.1 A Heisenberg Approximation of The Euclidean Motion Group 164

4.9.2 Better Analytic Approximations of The Green's function by means of Cylindrical Coordinates 171

4.9.3 Using Slope rather than Orientation 172

4.9.4 Evolution Equations Corresponding to Left Invariant Stochastic Processes on the 3D Euclidean Motion Group 175

4.10 Evolution Equations Corresponding to Left Invariant Stochastic Processes on the Similitude Group 177

4.10.1 Green's Functions for the Cases $D_{44} = 0$ 180

4.10.2 Green's functions for the cases $\kappa_0 = 0$, $D_{11} = 0$. 180

4.11 Conclusion 187

5 Robust Orientation Estimation **188**

5.1 Introduction 188

5.2 Channel Representations 189

5.2.1 Channel Smoothing for Robust Orientation Estimation 192

5.3 Tensor Voting 196

5.3.1 The cases $d = 2$ and $N \leq 2$ 197

5.3.2 The Case $d = 3$ and $N = 2$. 201

5.4 Explicit Relation between 2D-Tensor Voting and G-Convolutions on Orientation Scores 205

5.5 Gauge Coordinates along Robust Orientation Fields and its Application to Curvature Estimation 206

5.5.1 Curvature in 2D-images 206

5.6 Conclusion 211

III Appendix **213**

6 Appendix Scale **214**

6.1 The Reproducing kernels $R^2_{k,\gamma}$ of the Sobolev spaces $\mathbb{H}^{k,2}_{\gamma}(\mathbb{R}^2)$, $k > 1$. 214

6.2 Holomorphic Semigroups and Generalized Functions 217

6.2.1 Example: The Test Space Corresponding to Poisson Filtering 218

7 Appendix Orientation **220**

7.1 The Bochner-Hecke Theorem and the Spectral Decomposition of the Hankel Transform 220

7.2 Proof of Theorem 18 221

7.3 Asymptotic behavior of the wavelet $\psi^0\big|_{\phi=0}$ 222

7.4 Examples of Proper Wavelets in General Approach 223

7.4.1 The cases $\alpha_m^n = \delta_m^{nl}$, $l \in \mathbb{N} \cup \{0\}$ fixed 223

7.5 Minimal Uncertainty States 225

7.6 Derivation of the exponent mapping $\exp : T_e(G) \to G$ 228

7.7 Numerical Scheme and Analysis for Computing Resolvent of Evolutions on Orientation Scores 229

7.7.1 Explicit Finite Difference Scheme 231

7.8 Numerical scheme of G-Convolutions, $G = \mathbb{R}^2 \rtimes \mathbb{T}$. 233

7.9 Steerability 234

7.9.1 Steerable Tensor fields 235

Foreword

Image analysis is a field of endeavour to which many scientific disciplines have contributed. As a field of engineering it aims to solve societal problems related to imaging, such as in biomedical imaging, robot vision, and remote sensing. As a science proper it tries to answer fundamental questions of how visual information may be represented and processed, either on a computer or in the visual cortex. Not surprisingly, the attendants of a typical conference in the field will invariably form a mixed company of biomedical and electrical engineers, physicists, computer scientists, and mathematicians, with various backgrounds.

I have heard people remark that image analysis is plain anarchy. Precisely because so many methodologies and application areas are involved the aspect of communication should not be underestimated. The only way to improve this is to agree on an unambiguous description language, and the only candidate language that has a chance of fulfilling this role is mathematics in its widest sense. A mathematical foundation of an image analysis algorithm enables verifiability and facilitates further development by exposing strengths and weaknesses in a transparent and objective way. Therefore in this thesis we put high emphasis on the mathematical underpinning of our new theory and resulting algorithms.

Remco Duits
Eindhoven, May 3, 2012.

Introduction

The aim of this thesis is to develop new mathematical models for perceptual organization in (medical) images, as a tool for segmentation and image understanding. Perceptual organization is the organization of *local* image features/fragments into the *global* structure of an image. The term has its origin in psycho-physics and is also known as perceptual grouping. It is well-known that the human visual system does an excellent job of combining local image fragments into a comprehensive scene description. In psycho-physics experiments are done to understand how the human visual system puts all the local receptive field responses measured in the retina into a consistent non-local description of an image. These experiments resulted in a well-known number of general laws, the so-called *Gestalt Principles of Perceptual Organization*, cf.[129]:

- **Proximity:**
  Similar parts that are close together in time or space appear to belong together and tend to be perceived together.
- **Similarity:**
  Similar parts tend to be seen together as forming a group.
- **Continuity of Direction:**
  There is a tendency in our perception to follow a direction, to connect elements in a way that makes them seem contiguous or flowing in a particular direction.
- **Closure:**
  There is a tendency in our perception to complete incomplete figures, to fill in gaps and units forming a closed figure tend to be perceived together.
- **Common Fate:**
  Units moving in the same direction at the same speed tend to form a group.

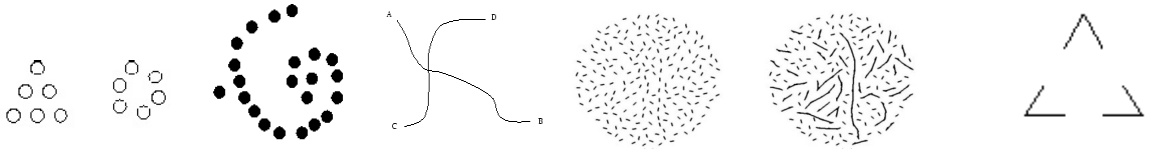

Figure 1: Examples of Gestalt laws. From left to right: proximity grouping of dots in 2 clusters, grouping by dots by good continuation, grouping by continuation of direction (it is perceived as line AB crossing line CD), closure of the three corners into a triangular figure.

In this thesis we do not consider time-dependent images/video sequences. Therefore we only consider the Gestalt laws proximity, continuity of direction, similarity and closure as guiding principles for our mathematical models for perceptual organization, see figure 1. In the second part of this thesis we construct orientation scores of images. These orientation scores are inspired by orientation columns in the primary cortex of our own visual system. To get a first impression we refer to figure 4.1 and figure 4.2.

Our orientation scores are constructed by an oriented/directed wavelet from which, in contrast to the usual approaches in image analysis, the original image can be reconstructed from each fixed scale orientation score. To achieve this result it was necessary to construct a new generalization of the standard wavelet theory, well-known in theoretical physics, image analysis and signal processing. This result allows us to do perceptual organization in the orientation scores where besides position, local orientation is explicitly represented. We make a clear mathematical classification of allowable perceptual grouping operations on the orientation scores. As an example we consider left invariant evolution equations on these orientation scores in full detail in order to enhance elongated structures in images and to automatically close the gaps in between, see figure 4.30 and figure 4.24.

In the first part of thesis, however, we consider another highly relevant issue in the understanding of images: The notion of scale. The scale of observation is very important for the understanding of images, see figure 2. Besides scale selection, it is also very relevant how

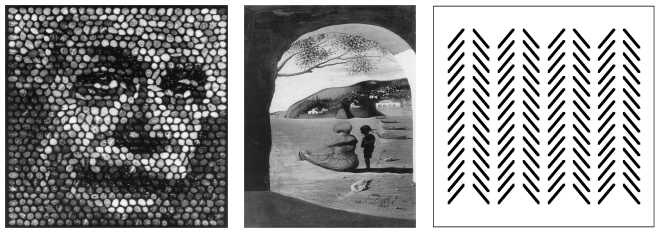

Figure 2: Some examples to stress the role of scale in our visual perception.

structures are nested as scale increases. Given an image we construct so-called α scale space representations that follow from a list of axioms, beyond the well-established Gaussian scale space. The topological structure within theses scale space representations is called the deep structure of an image, cf.[83], [85]. By increasing the scale of observation extrema (and thereby structures) disappear. The points where the spatial topology changes in scale space, i.e. the points where an extremum annihilates with a saddle or the points where an extrema and a saddle arise are called top-points, see figure 3. We will compare and analyze the deep structure within the α scale space representations and show that it is possible to get good approximative reconstructions of the image, given the second order structure at these top-points.

Before statistical and neural network-based implementations can be developed, we need to understand the differential deep structure of images. Therefore this thesis deals with the basics in low-level rather than high-level computer vision, where we focus on differential geometric and group-theoretical methods. In our opinion it is important to follow a generic approach with not too many priors and unknown parameters, since this replaces the problem rather than it solves the problem. Moreover we put high emphasis on the stability of the operations involved. For example, in contrast to the usual approaches in image analysis, we do not apply thresholds

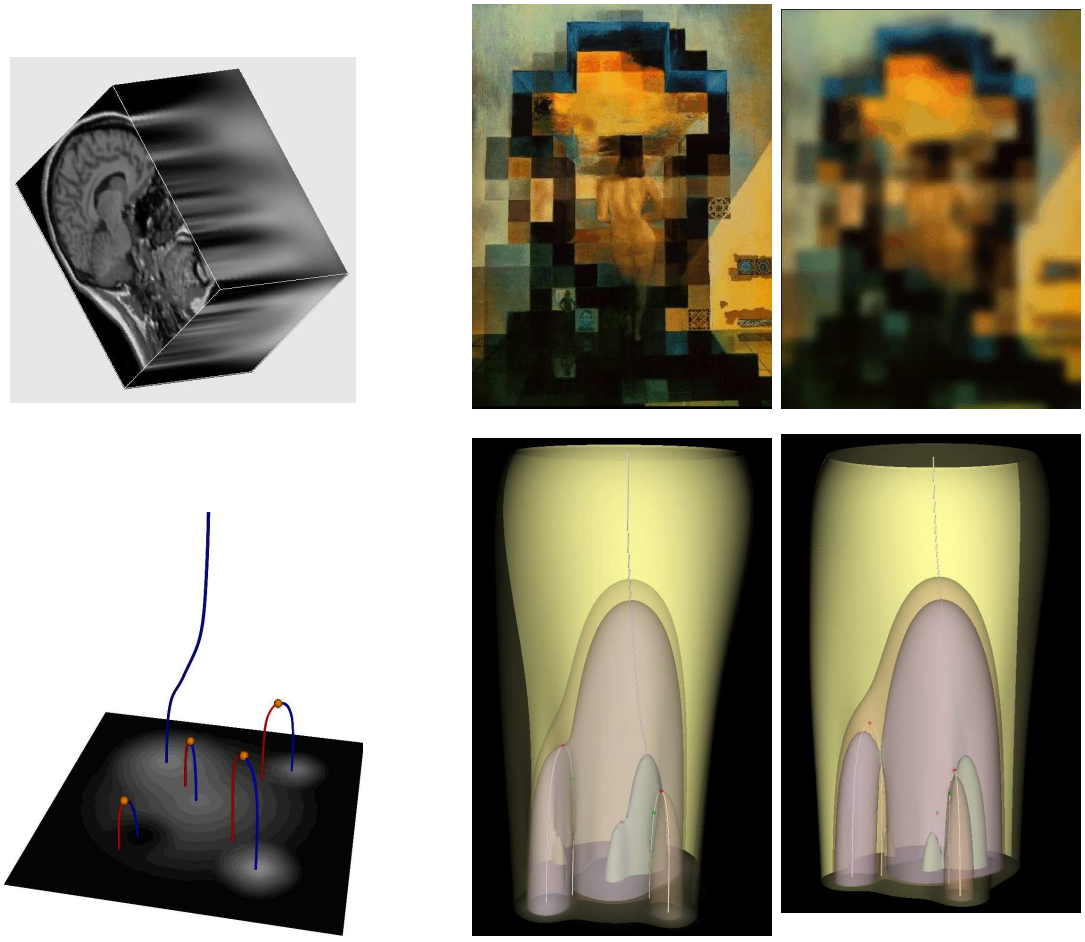

Figure 3: Illustrations of the hierarchical nesting within the deep structure of a scale space representation. Top row; left: illustration of a scale space representation of an image, right: two slices (small scale and large scale) in a scale space representation of a painting of Salvador Dali. Bottom row; left: the critical paths and their top points of a simple image consisting of only a few blobs, right: the nesting of isophotes (i.e. iso-intensity surfaces) through top-points and the nesting of critical curves through saddle points in scale space. For further details on multi-scale segmentation we refer to [106].

on our data as they are by definition ill-posed operations.

In the development of our algorithms and the corresponding theory we are inspired by biological measurements on receptive fields in the human visual system. Since both *scale* analysis and *orientation* (and curvature) analysis seem to play a dominant role in our human visual system, we focus on these two aspects in our theory and algorithm development for perceptual organization.

Outline of the Thesis

This thesis consists of two parts, dealing with scale and orientation. Furthermore there is an appendix, which is also separated in a scale and orientation part. The line of thought in these two parts is similar and in both cases the role of evolution equations, group theory and reproducing kernel Hilbert spaces is dominant. Nevertheless these parts are disjoint and can be considered as separate parts. With this respect we notice that section 4.10 provides a first step of combining these two parts.

Although the appendix contains somewhat detailed and technical issues, we stress that some important mathematical results in this thesis are actually inside the appendix. The most important results in the appendix are inside section 6.1, section 7.2, section 7.1, section 7.4, section 7.7 and section 7.8. We did not include these chapters in the scale and orientation part, as they interrupt the main line of this thesis from an image analysis point of view.

Part I : Scale

In the first chapter we consider the axioms of scale space theory on the unbounded domain. We show that (in contrast to previous belief) there exists a parameterized $\alpha \in (0, 1]$ class beyond the well-established Gaussian case ($\alpha = 1$) of scale space representations that is uniquely determined by these axioms. We call these scale space representations of images α *scale spaces*.[1] Some observations with this respect were already made by Pauwels et al.[104] with respect to scale space representations of 1D-signals. Our main contributions in [28], new to the image analysis literature, with this respect are:

- The generators of the α scale spaces are given by fractional powers of the minus Laplacian: $-(-\Delta)^{\alpha}$, the exact meaning of which is explained in Section 1.5, where we applied (and summarized) some more general results of Yosida[132] to our specific case.
- We show that the case $\alpha = \frac{1}{2}$ corresponds to Poisson scale space, obtained by harmonic

[1] In this thesis we mostly omit the word representation and write α scale space (or in particular Gaussian scale space) rather than α-scale space representation (or in particular Gaussian scale space representation). Although this is improper from the mathematical point of view, as one should clearly make a distinction between a function and its domain, we follow the usual convention in image analysis at this point for the sake of simplicity.

extension on the upper plane $s > 0$, by means of the factorization

$$u_{ss} + \Delta u = (\partial_s - \sqrt{-\Delta})(\partial_s + \sqrt{-\Delta})u = 0.$$

Furthermore we explain how the Monogenic scale space (first introduced for multi-scale phased based image processing by Felsberg and Sommer[47]) obtained by Clifford analytic extension of Poisson scale space is related to the first order jet in a Gaussian scale space by including the grey-value flow of a scale space.

- We put an overcomplete set of axioms, listed in section 1.2, that we raised from various literature on scale space theory and show that α scale spaces satisfy *all* these additional demands (except for causality, where strong causality must be replaced by weak causality).
- We show how several other non-axiomatic properties of Gaussian scale space (such as energy minimization and the structure of the derivatives of the α-convolution kernel) are translated to the Poisson case $\alpha = \frac{1}{2}$.
- We analyze the topological differences in α scale spaces.

In the second chapter we consider scale spaces on a bounded domain Ω with no-flux Neumann boundary condition, cf.[26],[44]. In this case the generator of an α scale space extends to a compact self-adjoint operator on $\mathbb{L}_2(\Omega)$ and thereby it has a complete orthogonal set of eigen functions. From this observation we deduce that the α scale spaces on a bounded domain have the same eigen images. Taking the fractional power of the generator now becomes fairly easy, by taking the fractional power of the eigenvalues. So the only difference is the relative damping of the eigen modes over scale $s > 0$. As an example we consider both the case where Ω equals a rectangle and the case where Ω equals a disk.

In the third chapter we first focus in section 3.3 on the topological structure of the α scale spaces, the so-called deep structure of images, cf.[32]. Here we apply the singularity theory of Damon, cf. [18],[17], to both Poisson and Gaussian scale space and deduce that scale space creations are stable events in Poisson scale space of a 1 dimensional signal, whereas they can not occur in a Gaussian scale space of a 1 dimensional signal. Further we give some examples on non-artificial images where the topological structure differs drastically between Gaussian and Poisson scale space. This makes sense from the physical point of view as potential physics clearly differs from heat physics. After appropriate re-scaling the critical curves depend continuously on α, but there do exist transitions of creations into annihilations over α. Moreover it happens quite often that different pairs of extrema and saddles annihilate in the α scale spaces.[2]

Then in section 3.4, cf.[31] we focus on the issue of reconstruction from toppoints and deal with the question: Is it possible to give a good approximation of an image given a sparse set of linear scale space features ? There are several reasons for this consideration. First of all we want to know what features actually tell about images.[3] If the image can be reconstructed in approximation by this limited set of features, this reduces the data and moreover we may as well manipulate the features rather than manipulating the whole image. Secondly, we want to

[2]Typically, there is a large difference between α scale spaces of images including high frequency-components. With this respect we notice that the tails of the Poisson kernel are stronger than the tails of the Gaussian kernels.

[3]Before applying ad-hoc cluster-algorithms in feature spaces (where each axis has a different physical dimension) as is usually the case in more applied image analysis.

investigate whether the up to second order differential structure in the top-points of a scale space of a daily-life image is sufficient to get a good reconstruction of that image at bottom scale. Finally, we notice that a good reconstruction scheme is needed for applications such as content-based image retrieval and image editing (retrieving sub-scenes from images).

It turns out that inner products of Sobolev type (and the corresponding Gelfand triple structure) are extremely useful for image reconstruction of images from a sparse set of linear α scale space features. The common (non)-linear reconstruction frameworks follow an Euler Lagrange minimization. However, if the Lagrangian is a norm induced by an inner product of a Hilbert space, then by the Pythagoras theorem this Euler Lagrange minimization boils down to a simple orthogonal projection within the corresponding Hilbert space. This basic observation has been overlooked in image analysis, cf.[100] and [89], for the cases where the Lagrangian equals a norm of Sobolev type, resulting in iterative non-linear numerical methods, where already an exact solution with a non-iterative linear algorithm is at hand. Therefore we provide a general theory on linear image reconstructions and metameric classes of images. By applying this theory we obtain visually more attractive reconstructions than the previously proposed linear methods and we find connected curves in the metameric class of images, determined by a fixed set of linear features, with a monotonic increase of smoothness. Although the idea can be applied to any linear feature reconstruction or principle component analysis, we mainly focus on reconstructions from so-called topological features such as top-points and grey-value flux in scale space, obtained from geometrical observations in the deep structure of a scale space.

Part II : Orientation

The orientation part consists of two chapters. Chapter 4 deals with invertible orientation scores as an application of generalized wavelet theory, cf.[33], [24], [23], [27], [21]. It is the most important chapter of the thesis. Although we put emphasis on the mathematical theory, it is a somewhat unconventional mixture of abstract mathematics on the one hand and a new wavelet application in image analysis on the other hand. It is mainly inspired by the earlier works of Kalitzin et al.[79], August et al.[9], Zweck et al.[133] and Mumford[97] and puts them (at least part of their works) in a unified mathematical framework. We provide new insights, combine the techniques proposed by these authors and answer many open questions that inevitably arise from their (in our opinion highly interesting) work. The second part (more precisely, sections) of chapter 4 has been achieved with a close cooperation with Markus van Almsick, who is preparing his dissertation[4] on contextual operations, cf.[122].

In chapter 5 there is a relatively strong focus on typical application issues in image analysis. Here we analyse two well-established techniques for robust orientation estimation in image analysis, tensor voting and channel representations. We give a mathematical summary of these methods, generalize some of the results, put the connection to the unified framework in chapter 4, cf.[123], and use them to obtain a much more robust and practical local Gauge-coordinate system than the usual Gauge-coordinate system tangential to and orthogonal to

[4] In his work, there is a stronger focus on the physics (rather than the mathematics) involved and is particularly recommended for physicists in image analysis.

isophotes as proposed in[5] [68] and [51]. The latter statement is briefly illustrated by the computation/estimation of curvature of elongated structures.

Outline of Chapter 4

First we consider the construction of and reconstruction from an orientation score of an image. We show that the transformation that maps an image to an orientation score is in fact a wavelet transformation obtained by a representation of the Euclidean motion group onto $\mathbb{L}_2(\mathbb{R}^2)$ and a line detecting wavelet $\psi \in \mathbb{L}_1(\mathbb{R}^2) \cap \mathbb{L}_2(\mathbb{R}^2)$. Since this representation is reducible the general wavelet reconstruction theorem does not apply. Therefore we had to develop a new and more general wavelet theory, based on reproducing kernel theory, which is explained in section 4.4. Here the main result is Theorem 19 whose proof is given in the appendix section 7.2. This fundamental theorem has several other consequences in both image and signal processing. For example, many (difficult) sampling theorems in signal/image processing directly follow from this theorem, see Corollary 3.

By means of Theorem 19 we get Corollary 5 which gives us full control over the stability of the wavelet transform and it inverse between image and orientation score. As a result, by proper choice of the wavelet ψ, the image f can be reconstructed from a single scale orientation score U_f in a robust way, which is not possible in the usual wavelet theory frameworks based on a irreducible representation of the similitude group!

We develop and implement several approaches to obtain proper wavelets (which are also good line detectors in practice) in the 2 dimensional case, $d = 2$. In section 4.7 we generalize these results (with implementation) to the 3 dimensional case, $d = 3$. These proper wavelets give rise to a stable transformation from image to orientation score and vice versa, and thereby they allows us to relate operations Φ on orientation scores to operations Υ on images in a robust way.

Then in section 4.8 we show that operations Φ must be left invariant in order to obtain a Euclidean invariant transformation Υ on images. As an example we observe the probability of collision of particles from two left invariant stochastic processes (including curvature) on the Euclidean motion group, which is used to automatically detect elongated structures and to automatically close gaps between them.

This bring us to the framework of resolvents of linear left invariant second order evolution equations on the 2D Euclidean motion group $G = \mathbb{R}^2 \rtimes \mathbb{T}$, the solution of which is a convolution with the Green's function on G. In section 4.9 we construct analytic approximations for these Green's functions (which are simple and very useful for practical applications), and their modes, by replacing (both in cartesian and cylindrical coordinates) the generators of the Euclidean

[5] Using local Gauge-coordinate systems adapted to the image structure is of course a very good idea from the mathematical point of view. Nevertheless, in practice people have poor experiences (especially with respect to noise) with geometrical methods in computing higher order structure such as for example curvature. We think that the main reason for this practical shortcoming is the fact that the local coordinate system is aligned with isophotes, which usually do not lie along elongated structures and which very easily break apart if scale increases.

motion group by generators of a Lie-group of Heisenberg type.

Finally, in section 4.10, we make a first step in combining the frameworks of scale and orientation in this thesis by considering multiple scale orientation scores on which we apply the resolvents of linear left invariant second order evolution equations on the similitude group. In a special case we are able to derive the exact analytic Green's functions of these resolvents.

Outline of Chapter 5

Orientation scores are a nice tool for *well-posed image enhancement* by means of left-invariant processing on the orientation scores. However, for many practical applications where detection of oriented structures is required it is more relevant to obtain a fast robust estimation for a *single* orientation per position, rather than image enhancement via orientation scores where the columns $U_f(\mathbf{x}, \cdot)$ represent a *distribution of the local orientation* per position $\mathbf{x}$. In chapter 5 we discuss to 2 methods (robust orientation estimation by means of channel representations as explained in section 5.2 and steerable tensor voting as explained in section 5.3) for computation of a robust vector field (encoding orientation and the confidence of the orientation) from a non-robust orientation field computed from the image f.

The intuitive idea behind these methods is strongly inspired by the Gestalt laws proximity and good continuation. In both methods the main idea is that each single orientation vector is compared to its surrounding/context by means of a model of continuation. If the vector is nicely aligned with the vectors in its surroundings according to the model of continuation it is maintained, otherwise the orientations in the context adapt this direction according to our model of good continuation.

In section 5.4 we show that tensor voting is in fact a G-convolution[6] on an orientation score, which puts the connection of section 5.3 with the more general framework of section 4. This again shows the generality (and strength) of the concept of G-convolution in image analysis. For a numerical scheme of steerable G-convolutions we refer to section 7.8 in the Appendix.

Finally, in section 5.5 we use the robust vector fields to obtain local Gauge coordinate systems, that are much more practical than the local Gauge coordinates based on the (Gaussian) gradient of an image as these fields are much better aligned with the local structures in the image. As a practical example we consider the computation of curvature of elongated structures in images.

[6] Where G stands for the Euclidean motion group, the domain of the orientation scores.

Preliminaries

Function Spaces.

- $C(\Omega)$: The vector space of continuous functions from Ω to $\mathbb{R}$.
- $C^k(\Omega)$, $k \in \mathbb{N} \cup \{0\}$: The vector space of k-fold continuously differentiable functions on Ω, with $C^0(\Omega) = C(\Omega)$.
- $C^\infty(\Omega)$: The vector space of smooth, i.e. infinitely differentiable functions on Ω.
- $\mathbb{L}_p(\Omega, \mu)$: The quotient space consisting of functions with finite L_p norm $(p > 0)$, i.e. $\left(\int\limits_\Omega |f|^p \, \mathrm{d}\mu \right)^{1/p} < \infty$ on Ω with respect to the nil space of the L_2-norm, which consists of all functions f on Ω with zero measure support, i.e. $f = 0$ almost everywhere. Mostly μ equals the usual Lebesgue measure $\mathrm{m_d}$ and then we write $\mathbb{L}_p(\Omega)$ for short.
- $\mathbb{L}_\infty(\Omega)$: The vector space of functions f for which $\sup_{x \in \Omega} |f(x)|$ exists.
- $\mathcal{D}(\Omega)$: The vector space consisting of all infinitely differentiable functions with compact support within Ω. This space is equipped with the local convex topology generated by the semi-norms $q_N : \mathcal{D}(\Omega) \to \mathbb{R}$ $(N \in \mathbb{N})$ given by

$$q_N(f) = \sup_{|\boldsymbol{\alpha}| < N} \sup_{\mathbf{x} \in \Omega} |(D^\alpha f)(\mathbf{x})|$$

- Define the semi-norms $p_N : C^\infty(\mathbb{R}^d) \to \mathbb{R}$ $(N \in \mathbb{N})$ by

$$p_N(f) = \sup_{|\boldsymbol{\alpha}| < N} \sup_{\mathbf{x} \in \mathbb{R}^d} (1 + \|\mathbf{x}\|^2)^N |(D^\alpha f)(\mathbf{x})| \; .$$

- $\mathcal{S}_d$: The vector space consisting of all infinitely differentiable functions f such that $p_N(f) < \infty$ for all $N \in \mathbb{N}$. This space is equipped with the local convex topology generated by the semi-norms p_N. The elements in the dual space $\mathcal{S}'_d$ are often called tempered distributions. The Fourier transform of a tempered distribution Λ is defined[7] by $\hat{\Lambda}(\phi) = \Lambda(\hat{\phi})$.

[7] To every $f \in \mathbb{L}_1(\mathbb{R}^d)$ corresponds a distribution Λ_f. Note that the definitions of Fourier transform of resp. f and Λ_f coincide (as they should): $(\hat{\Lambda_f})(\phi) = \Lambda_f(\hat{\phi}) = \int f\hat{\phi} = \int \hat{f}\phi = (\Lambda_{\hat{f}})(\phi)$. Moreover, the same argument is valid if $f \in \mathbb{L}_2(\mathbb{R}^d)$.

- Associate to each $s > 0$ a positive measure μ_s, by setting

$$\mathrm{d}\mu_{\mathrm{s}}(\mathbf{y}) = (1 + \|\mathbf{y}\|^2)^{\mathrm{s}}\, \mathrm{dm}_{\mathrm{d}}(\mathbf{y}) \qquad \mathrm{s} > 0. \tag{1}$$

  $\mathbb{H}_s(\mathbb{R}^d)$: The Sobolev space of order $s > 0$ on $\mathbb{R}^d$, which equals the vector space consisting of all tempered distributions Λ with Fourier transform in $\mathbb{L}_2(\mathbb{R}^d; \mu_s)$.

- The dual of a vector space X is the vector space consisting of all continuous linear functionals on X and will be denoted by X'.

- A Hilbert space is a vector space equipped with an inner product such that every Cauchy sequence converges (with respect to the norm induced by the inner product).

- A functional Hilbert space[8] is a Hilbert space consisting of complex valued functions on an index set $\mathbb{I}$ on which the point evaluation $\delta_{\mathbf{a}}$, is a continuous/bounded linear functional for all $\mathbf{a} \in \mathbb{I}$. Consequently, it has a Riesz representant $K_{\mathbf{a}} \in H$

$$f(\mathbf{a}) = \langle \delta_{\mathbf{a}}, f \rangle = (K_{\mathbf{a}}, f)_H.$$

  The function $K : \mathbb{I} \times \mathbb{I} \to \mathbb{C}$ given by $K(\mathbf{a}, \mathbf{b}) = (K_{\mathbf{a}}, K_{\mathbf{b}})_H = K_{\mathbf{b}}(\mathbf{a})$ is called reproducing kernel. Notice that the spaces $\mathbb{L}_2(\mathbb{R}^d)$ are *not* functional Hilbert spaces.

General Convention: Images/signals are assumed to be within $\mathbb{L}_2(\mathbb{R}^d)$. For signals $d = 1$. For images $d = 2$, unless explicitly stated otherwise.

Special Functions.

- The d-dimensional Gaussian kernel G_s at scale s is given by

$$G_s(\mathbf{x}) = \frac{1}{(4\pi s)^{d/2}} e^{-\frac{\|\mathbf{x}\|^2}{4s}}. \tag{2}$$

  Occasionally, we will parameterize the Gaussian kernel by its standard deviation σ and write $\mathcal{G}_\sigma = G_s$, where we notice that $s = \frac{\sigma^2}{2}$.

- The d-dimensional Cauchy kernel is given by

$$H_s(\mathbf{x}) = \frac{2}{\sigma_{d+1}} \frac{s}{(s^2 + \|\mathbf{x}\|^2)^{\frac{d+1}{2}}}, \tag{3}$$

  where $\sigma_{d+1} = \frac{2(\pi)^{d+1}}{\Gamma\left(\frac{d+1}{2}\right)}$ In image analysis the Cauchy kernel is mostly known as the Poisson kernel, therefore in this thesis both names refer to the same probability density function.

Operators.

- $\mathcal{L}(X, Y)$: The vector space consisting of linear operators from X into Y. If $X = Y$ we write $\mathcal{L}(X)$ for short.

[8] Also known as reproducing kernel Hilbert space.

- $\mathcal{B}(X,Y)$: The vector space consisting of continuous (i.e. bounded) linear operators from X into Y. If $X = Y$ we write $\mathcal{B}(X)$ for short.
- The range of a linear operator A will be denoted by $\mathcal{R}(A)$ and its nilspace will be denoted by $\mathcal{N}(A)$.
- If $\mathcal{A} \in \mathcal{B}(X)$, with spectrum $\sigma(\mathcal{A})$, then its resolvent is defined by

$$R(\lambda;\mathcal{A}) = (\lambda I - \mathcal{A})^{-1} \ .$$

  for all $\lambda \in \rho(\mathcal{A}) = \mathbb{C} \setminus \sigma(\mathcal{A})$.
- The Fourier transform $\mathcal{F} : \mathbb{L}_2(\mathbb{R}^d) \to \mathbb{L}_2(\mathbb{R}^d)$, is almost everywhere defined by

$$[\mathcal{F}(f)](\boldsymbol{\omega}) = \hat{f}(\boldsymbol{\omega}) = \frac{1}{(2\pi)^{d/2}} \int\limits_{\mathbb{R}^d} f(\mathbf{x})\, e^{-i\boldsymbol{\omega}\cdot\mathbf{x}}\, \mathrm{d}\mathbf{x} \ .$$

  Notice that $\|\mathcal{F}[f]\|^2 = \|f\|^2$ for all $f \in \mathbb{L}_2(\mathbb{R}^d)$ and that $\mathcal{F}[f * g] = (2\pi)^{d/2}\mathcal{F}[f]\mathcal{F}[g]$, for all $f, g \in \mathbb{L}_2(\mathbb{R}^d)$.
- We use the following notation for Euclidean/polar coordinates in the spatial and the Fourier domain, respectively: $\mathbf{x} = (x,y) = (r\cos\phi, r\sin\phi)$, $\boldsymbol{\omega} = (\omega_x, \omega_y) = (\rho\cos\varphi, \rho\sin\varphi)$, with $\phi, \varphi \in [0, 2\pi), r, \rho > 0$. The corresponding complex variables, will be denoted by $z = x + iy = re^{i\phi}$ and $w = \omega_x + i\omega_y = \rho e^{i\varphi}$.
- The Laplace transform[9] $\mathcal{L}(f)$ of a function $f \in \mathbb{L}_2(\mathbb{R}^+)$ is defined by

$$[\mathcal{L}(f)](\lambda) = \int\limits_0^\infty f(x)\, e^{-\lambda x}\, dx, \text{for } \Re(\lambda) > 0.$$

- A so-called Gaussian derivative operator $D_s^{\mathbf{n}} \in \mathcal{B}(\mathbb{L}_2(\mathbb{R}^2))$ is given by

$$D_s^{\mathbf{n}} f = D^{\mathbf{n}}(G_s * f) = (D^{\mathbf{n}} G_s) * f \ , s > 0, \mathbf{n} = (n^1, \ldots, n^d) \in \mathbb{N}^d, \tag{4}$$

  $D_s^{\mathbf{n}} f$ is called the $\mathbf{n}$-th order Gaussian derivative of image $f \in \mathbb{L}_2(\mathbb{R}^d)$ at scale $s > 0$.

Groups and Representations.

- $\mathrm{Aut}(\mathbb{R}^d) = \{A : \mathbb{R}^d \to \mathbb{R}^d \mid A \text{ linear and } A^{-1} \text{ exists}\}$
- dilation group $D(d) = \{A \in \mathrm{Aut}(\mathbb{R}^d) \mid A = aI, a > 0\}$.
- orthogonal group $O(d) = \{X \in \mathrm{Aut}(\mathbb{R}^d) \mid X^T = X^{-1}\}$
- rotation group $SO(d) = \{R \in O(d) \mid \det(R) = 1\}$.

[9] Formally, the Laplace Transform maps the space $\mathbb{L}_2(\mathbb{R}^+)$ onto the Hardy Lebesgue class $H^2(0)$, cf. [132] p.163.

- circle group $\mathbb{T} = \{z \in \mathbb{C} \mid |z| = 1\}$, $z = e^{i\theta}$, $\theta = \arg z$ with group homomorphism $\tau : \mathbb{T} \to SO(2) \subset \mathrm{Aut}(\mathbb{R}^2)$:

$$\tau(z) = R_\theta = \begin{pmatrix} \cos\theta & -\sin\theta \\ \sin\theta & \cos\theta \end{pmatrix} . \tag{5}$$

- Let T and S be locally compact groups and let $\tau : T \to \mathrm{Aut}(S)$ be a group homomorphism. The **semi-direct product** $S \rtimes_\tau T$ is defined to be the group (which is again locally compact) with underlying set $\{(s,t) \mid s \in S,\ t \in T\}$ and group operation

$$(s,t)(s',t') = (s\tau(t)s', tt') . \tag{6}$$

  In this thesis we will often consider the semi-direct products $\mathbb{R}^d \rtimes D(1)$ and the Euclidean Motion group $\mathbb{R}^d \rtimes \mathrm{SO}(d)$, with in particular the 2D-Euclidean motion group $\mathbb{R}^2 \rtimes \mathrm{SO}(2) \equiv \mathbb{R}^2 \rtimes \mathbb{T}$ where τ is given by (5).The group product (6) is now given by

$$g\,g' = (\mathbf{b}, e^{i\theta})(\mathbf{b}', e^{i\theta'}) = (\mathbf{b} + R_\theta \mathbf{b}', e^{i(\theta+\theta')}) \ , g = (\mathbf{b}, e^{i\theta}), g' = (\mathbf{b}', e^{i\theta'}) \in \mathbb{R}^2 \rtimes \mathbb{T}.$$

- A representation $\mathcal{R}$ of a group G into a Hilbert space H is a homomorphism $\mathcal{R}$ between G and $\mathcal{B}(H)$, the space of bounded linear operators on H. It satisfies $\mathcal{R}_{gh} = \mathcal{R}_g \mathcal{R}_h$ for all $g \in G, h \in G$ and $\mathcal{R}_e = I$. A representation $\mathcal{R}$ is irreducible if the only invariant closed subspaces of H are H and $\{\mathbf{0}\}$ and otherwise reducible. We mainly consider unitary representations (i.e. $\|\mathcal{U}_g\psi\|_H = \|\psi\|_H$ for all $g \in G$ and $\psi \in H$), which will be denoted by $\mathcal{U}$ rather than $\mathcal{R}$. Within the class of unitary representations we mainly consider the representations of $\mathbb{R}^d \rtimes T$ into $\mathbb{L}_2(\mathbb{R}^d)$ which are given by

$$(\mathcal{U}_g\psi)(\mathbf{x}) = \frac{1}{\sqrt{\det(\tau(t))}} \psi((\tau^{-1}(t))(\mathbf{x} - \mathbf{b})), \text{ with } g = (\mathbf{b}, \tau(t)) \in \mathbb{R}^d \rtimes T. \tag{7}$$

  We will call these representations **left-regular actions** of $G = \mathbb{R}^d \rtimes T$ in $\mathbb{L}_2(\mathbb{R}^d)$.

- Let $\mathbf{b} \in \mathbb{R}^d$, $a > 0$ and $g \in G$ with corresponding $\tau(g) \in \mathrm{Aut}(\mathbb{R}^d)$. Then the unitary operators $f \mapsto \check{f}$, $\mathcal{T}_\mathbf{b}$, $\mathcal{D}_a$ and $\mathcal{R}_g$ on $\mathbb{L}_2(\mathbb{R}^d)$ are defined by

$$\begin{array}{ll} \check{f}(\mathbf{x}) = f(-\mathbf{x}) & \mathcal{T}_\mathbf{b}\psi(\mathbf{x}) = \psi(\mathbf{x} - \mathbf{b}) \\ \mathcal{D}_a\psi(\mathbf{x}) = \frac{1}{a^{\frac{d}{2}}}\psi(\frac{\mathbf{x}}{a}) & \mathcal{R}_g\psi(\mathbf{x}) = \frac{1}{\sqrt{\det\tau(g)}}\psi((\tau(g))^{-1}\mathbf{x}) . \end{array} \tag{8}$$

  The mappings $\mathbf{b} \mapsto \mathcal{T}_\mathbf{b}$, $g \mapsto \mathcal{R}_g$, $a \mapsto \mathcal{D}_a$ are respectively left regular actions of $\mathbb{R}^d, D(d), G$ into $\mathbb{L}_2(\mathbb{R}^d)$.

Sets.

- Let Ω be a subset of $\mathbb{R}^d$, then $\overline{\Omega}$ denotes the closure of Ω. The boundary of Ω which equals $\overline{\Omega} \setminus \Omega$, is denoted by $\partial\Omega$. The outward normal to the boundary is denoted by $\mathbf{n}$.

- The d-dimensional ball in $\mathbb{R}^d$ with respect to the Euclidean metric, with center $\mathbf{a}$ and radius $R > 0$, will be denoted by $B_{\mathbf{a},R}$. The total surface measure of $\partial B_{\mathbf{a},R}$ equals $\sigma_d R^{d-1}$. From $\int_{\mathbb{R}^d} e^{-\|\mathbf{x}\|^2} d\mathbf{x} = \pi^{d/2}$, it easily follows that

$$\sigma_d = \frac{2\,(\pi)^{\frac{d}{2}}}{\Gamma(d/2)}. \tag{9}$$

Part I

Scale

Chapter 1

α Scale Spaces on the Unbounded Domain.

1.1 Introduction

Constructions of linear scale space representations based on rigorous axiomatics date back to the 1960's with the publications by Iijima [75, 76] in the context of pattern recognition. This early work was followed by numerous publications [102, 83, 90, 5, 91, 51, 69, 82, 99, 104, 116]. The pivot in all derivations is some set of axioms expressing desirable group and/or semigroup properties. For an overview see Weickert [128].

It is commonly taken for granted that the Gaussian scale space paradigm is the unique solution to a set of reasonable axioms if one disregards minor modifications, such as spatial inhomogeneities [53], diffeomorphisms [57, 56], and anisotropies [127], which can be easily accounted for. That this is in fact not true has been pointed out by Pauwels [104], who proposed a one-parameter class of scale space filters in Fourier space, which are compatible with some basic axioms. Following Pauwels we dismiss separability as a viable basic axiom, since it is a coordinate dependent notion. It is a straightforward that any C^1, normalised filter which is both separable and isotropic must be a Gaussian, see (1.70). Under the assumption of positivity the corresponding parameter domain is a finite interval $\alpha \in (0, 1]$, where $\alpha = 1/2$ and $\alpha = 1$ the correspond to Poisson, respectively Gaussian scale space.

In this chapter we scrutinize properties of these α scale spaces (and in particular Poisson scale space) in the spatial domain, and show that they indeed obey *all* basic axioms initially believed to hold only for the Gaussian case.[1] To demonstrate this we adopt an overcomplete set of axioms that capture the various subsets that have been employed in the derivation of the Gaussian scale space paradigm. In addition, some of the conjectures raised by Pauwels [104] are verified by rigorous proofs, whereas some intuitive expectations are disproved. For example, it turns out that, contrary to previous belief, the Fourier filters for *all* parameter values, including the Poisson filter, do possess infinitesimal generators in the spatial domain in

[1] The usual causality principle must be relaxed, but the main result remains.

the sense of linear derivative operators.

The most natural case of all α scale spaces is the Poisson scale space since it is the only one where the scale parameter has the same physical dimension as the spatial variables x_i, allowing Euclidean geometry *within scale space*. Moreover, its Clifford analytic extension, which is first introduced in a computer vision context by Felsberg and Sommer[47] has several practical benefits. Initially, Felsberg and Duits worked independently on the subject of Poisson scale space following a different approach, but later a cooperation had been started on the subject of finite domain scale spaces, cf. [26], [44] which will not be considered in this chapter, but which is extensively discussed in the next chapter.

In this chapter Poisson scale space is shown to be associated with the *first order linear scale space pseudo p.d.e.*

$$\frac{\partial u}{\partial s} = -\sqrt{-\Delta}\, u\,,$$

which at the same time illustrates the cause of previous failure, viz. the fact that the possibility of a generator in the form of a *fractional power of a derivative operator*—the precise definition of which will be outlined in this chapter–has been overlooked. The solution of this equation for initial condition f is nevertheless a perfectly viable, smooth scale space image, which is essentially different from its Gaussian counterpart. The solution can in fact be written as a straightforward convolution in closed-form using Poisson filters. Just like convolving images with Gaussian kernels is equivalent to solving the diffusion equation on the upper half space, convolving images with Poisson kernels is equivalent to solving the Dirichlet problem on the upper half space. Finally, we establish an explicit connection between the various scale space representations, in particular Poisson and Gaussian scale spaces. The α scale spaces correspond to α-stable Lévy motions in the field of stochastic[2] processes, for further details we refer to [114]. For the application of α-stable Lévy processes as a model for natural image statistics we refer to our earlier work [105]. In this thesis we will not consider the α-scale spaces from the probabilistic point if view. Nevertheless, at this point we do stress that these processes arise at the generalization of the central limit theorem, by Feller[41]chapter IX.8. This generalization states that if a weighted sum of independent identically distributed[3] (say by p) random variables converges, the limit is distributed according to an α-kernel. By considering asymptotics on $\int_{-x}^{x} y^2 p(y)\mathrm{dy}$ it is even possible to characterize the unique limiting distribution.[4]

The mapping from original image f and scale s onto the scale space representation u of the image f will be denoted by $\Phi : \mathbb{L}_2(\mathbb{R}^d) \times \mathbb{R}^+ \to \mathbb{L}_2(\mathbb{R}^d)$. The filtered image at a fixed scale $s > 0$ will be denoted by $u(\cdot, s)$ and is given by

$$u(\mathbf{x}, s) = \Phi[f, s](\mathbf{x}) \ , \mathbf{x} \in \mathbb{R}^d$$

In order to stress that $s > 0$ is fixed, we sometimes write $\Phi_s f$ in stead of $\Phi[f, s]$.

[2]Scale space theory can be approached in three ways: as semigroups, as evolution equations (partial differential equations) and as stochastic processes (probability theory).

[3]For example a sum of independent Cauchy distributed variables, is again Cauchy distributed as we have $H_{s_1} * H_{s_2} = H_{s_1+s_2}$ for all $s_1, s_2 > 0$, see Axiom 6 !

[4]If the distribution p has finite variance, then the limiting distribution is Gaussian and we arrive in the usual central limit theorem. Imposing finite variance however is often an unnecessary constraint. In general (except for the Gaussian case), variance of the convolution kernel is not an appropriate measure of resolution inside a scale space.

1.2 Axioms

First we will summarize some basic observations with respect to blurring:

- If the scale s tends to zero, the blurred image must tend to the original image. For continuous images this convergence must be pointwise.
- If two images f_1, f_2 satisfy $f_1(\mathbf{x}) \leq f_2(\mathbf{x})$ almost everywhere on $\mathbb{R}^d$, then the corresponding filtered images u_1, u_2 must satisfy $u_1(\mathbf{x}) \leq u_2(\mathbf{x})$ almost everywhere on $\mathbb{R}^d$.
- Successive blurring at scale $s_1 > 0$ and $s_2 > 0$ must correspond to a single, effective blurring with an aperture $s > 0$ uniquely determined by s_1 and s_2. In this chapter we focus on the case
$$s = s_1 + s_2 \tag{1.1}$$
Note that the cases $s = (s_1^p + s_2^p)^{1/p}$, with $0 < p < \infty$ can be brought to (1.1) after re-parameterizing according to $s' = s^p$.
- There are two ways of imposing causality constraints:
  - weak causality:
    Local extrema with respect to both scale ($s > 0$) and space ($\mathbf{x} \in \mathbb{R}^d$) within scale space are not allowed: Closed isophotes within scale space are not allowed.
  - strong causality:
    Blurring an image must lead to less extreme grey values. Local extrema with respect to space (not scale) should not enhance.
- Blurring an image should be an isotropic process, since a priori we do not know the internal structure of an image.
- Filtering a translated image is the same as translating the filtered image.
- The operator which maps an original image onto its blurred image on a fixed scale, will be assumed to be linear.
- During the blurring process information will be lost. So, from an information theoretical point of view entropy should increase during the blurring process.

These requirements will be formalized as follows:

1. An arbitrary original image f is assumed to be a member of $\mathbb{L}_2(\mathbb{R}^d)$ with compact support.
2. For all $f \in \mathbb{L}_2(\mathbb{R}^d)$ we must have
$$\Phi[\mathcal{T}_{\mathbf{b}} f, s] = \mathcal{T}_{\mathbf{b}} \Phi[f, s]$$
(i.e. translation invariance) for all $\mathbf{b} \in \mathbb{R}^d$. For definition of $\mathcal{T}_{\mathbf{b}}$, recall (4.7).

3. For all $a > 0$ and $s \geq 0$ there exists a unique s' such that for all $f \in \mathbb{L}_2(\mathbb{R}^d)$

$$\Phi[\mathcal{D}_a f, s] = \mathcal{D}_a \Phi[f, s'],$$

where we recall (4.7) for definition of $\mathcal{D}_a$. We will assume that the corresponding rescaling function Ψ which maps s onto s' is a strictly increasing continuous function such that $\Psi(0) = 0$ and $\Psi(s) \to \infty$ as $s \to \infty$.

4. Preservation of positivity:

$$f > 0 \Rightarrow \Phi[f, s] > 0.$$

5. The blurring operator $f \mapsto \Phi[f, s]$ ($s > 0$ fixed) can be regarded in two different ways

I assume that operator $f \mapsto \Phi[f, s] \in \mathcal{B}(\mathbb{L}_2(\mathbb{R}^d), \mathbb{L}_2(\mathbb{R}^d))$, i.e.

$$\begin{aligned} \Phi[f + g, s] &= \Phi[f, s] + \Phi[g, s] \\ \Phi[\lambda f, s] &= \lambda \Phi[f, s] \end{aligned}$$

for all $s > 0, f, g \in \mathbb{L}_2(\mathbb{R}^d)$, $\lambda \in \mathbb{R}$ and there exists a $C > 0$ such that

$$\|\Phi[f, s]\|_{\mathbb{L}_2(\mathbb{R}^d)} \leq C \|f\|_{\mathbb{L}_2(\mathbb{R}^d)} .$$

for all $f \in \mathbb{L}_2(\mathbb{R}^d)$ and $s > 0$ (fixed).

II assume that operator $f \mapsto \Phi[f, s] \in \mathcal{B}(\mathbb{L}_2(\mathbb{R}^d), \mathbb{L}_\infty(\mathbb{R}^d))$,

$$\begin{aligned} \Phi[f + g, s] &= \Phi[f, s] + \Phi[g, s] \\ \Phi[\lambda f, s] &= \lambda \Phi[f, s] \end{aligned}$$

for all $s > 0, f, g \in \mathbb{L}_2(\mathbb{R}^d), \lambda \in \mathbb{R}$ and there exists a $C > 0$ such that

$$\|\Phi[f, s]\|_{\mathbb{L}_\infty(\mathbb{R}^d)} \leq C \|f\|_{\mathbb{L}_2(\mathbb{R}^d)} .$$

6. For all $s_1, s_2 > 0$ we must have

$$\Phi[\Phi[\cdot, s_1], s_2] = \Phi[\cdot, s_1 + s_2] .$$

7. Causality constraints:

a) *Weak Causality Constraint*
Any scale space isophote $u(\mathbf{x}, s) = \lambda$ is connected to the ground plane $s = 0$

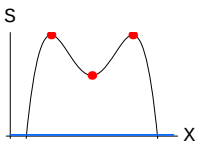

Figure 1.1: Weak causality

b) *Strong Causality Constraint*
For every $s_1 \geq 0$ and $s_2 > 0$ with $s_2 > s_1$ the intersection of any connected component of an isophote within the domain $\{(\mathbf{x}, s) \in \mathbb{R}^d \times \mathbb{R}^+ \mid \mathbf{x} \in \mathbb{R}^d, s_1 \leq s < s_2\}$ with the plane $s = s_1$ is not empty.

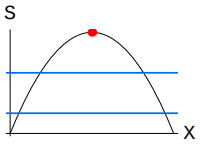

Figure 1.2: Strong causality

8. For all $f \in \mathbb{L}_2(\mathbb{R}^d)$ we must have

$$\lim_{s \downarrow 0} \Phi[f, s] = f \text{ in } \mathbb{L}_2 \text{ sense.}$$

Moreover if f is continuous, then the above limit also holds pointwise. If we restrict Φ to subspace $\mathcal{D}(\mathbb{R}^d) \times \mathbb{R}^+$ then we can write

$$\lim_{s \downarrow 0} \Phi[\cdot, s](\mathbf{x}) = \delta_{\mathbf{x}}$$

according to the weak star topology on $\mathcal{D}'(\mathbb{R}^n)$.

9. Rotation invariance, i.e. Let $R \in SO(d)$. Define $\mathcal{R}_R : \mathbb{L}_2(\mathbb{R}^d) \to \mathbb{L}_2(\mathbb{R}^d)$ by

$$[\mathcal{R}_R \psi](\mathbf{x}) = \Psi(R\mathbf{x}) \qquad \mathbf{x} \in \mathbb{R}^d \ .$$

Then we must have

$$\mathcal{R}_R \Phi_s[f] = \Phi_s[\mathcal{R}_R f],$$

for all $f \in \mathbb{L}_2(\mathbb{R}^d), s > 0$.

10. Average grey-value invariance, i.e.

$$\|\Phi_s[f]\|_{\mathbb{L}_1(\mathbb{R}^d)} = \|f\|_{\mathbb{L}_1(\mathbb{R}^d)}, \tag{1.2}$$

for all $s > 0, f \geq 0 \in \mathbb{L}_1(\mathbb{R}^d)$.

11. Increase of Entropy.
Consider a scale space u of a positive image f, i.e. $u(\cdot, s) = \Phi[f, s]$ and $f > 0$ (and thereby by Axiom 4 we have $u > 0$) almost everywhere such that

$$[\mathcal{E}(u)](s) = -\int_{\mathbb{R}^d} u(\mathbf{x}, s) \ln u(\mathbf{x}, s) \, \mathrm{d}\mathbf{x} \qquad (\mathrm{s} > 0) \ , \tag{1.3}$$

is finite. The mapping $\mathcal{E}(u) : \mathbb{R}^+ \to \mathbb{R}$ is called the entropy of u. Ignoring constants, the entropy is invariant under scaling: $\mathcal{E}(\lambda u)(s) = \lambda \mathcal{E}(u)(s) - (\lambda \log \lambda) \, u_{av}$, where $\lambda > 0$, u_{av} is the average grey value of u. Using this scaling it is always possible to ensure that (1.3) is positive, since $u \log u < 0 \Leftrightarrow 0 < u < 1$. The entropy is a measure of missing information and therefore the entropy should be a monotonically increasing function on[5] $\mathbb{R}^+$, i.e. $\frac{\partial}{\partial s}[\mathcal{E}(u)](s) > 0$ for all source images f. Moreover, we want $\frac{\partial}{\partial s}[\mathcal{E}(u)](s) \to 0$ if $s \to \infty$.

[5] Using Cauchy Schwarz and the fact that $u \to f$ for $s \downarrow 0$ in $\mathbb{L}_2$ sense one obtains that $\mathcal{E}(u)$ is also continuous in 0.

Next we summarize the direct consequences of these axioms. For instance by the following theorem it follows that $f \to \Phi[f,s]$, ($s>0$ fixed) is an integral operator.

Theorem 1 *(Dunford-Pettis) Let X be a measurable space, according to measure $\mu : X \to \mathbb{R}^+$. Let $1 \leq p < \infty$. Let $\mathcal{A}$ be a bounded operator from $\mathbb{L}_p(X)$ into $\mathbb{L}_\infty(X)$, then there exists a $K \in \mathbb{L}_1(X \times X)$ such that*

$$\sup_{\boldsymbol{x}} \left(\int_X |K(x,y)|^q \, d\mu(y) \right)^{1/q} = \|A\| \ ,$$

with $q>0$ such that $\frac{1}{p}+\frac{1}{q}=1$ and for all $f \in \mathbb{L}_p(X)$ we have that:

$$(\mathcal{A}\, f)(x) = \int_X K(x,y) f(y) d\mu(y)$$

for almost every $x \in X$.

For a proof see [14]p.113-114. If we take $X=\mathbb{R}^d$ equipped with the Lebesgue measure and $p=2$, then[6] $q=2$ and by Axiom 5(II) we have that the mapping $f \mapsto \Phi[f,s]$, with $s>0$ fixed, is an integral operator. By Axiom 2 (translation invariance) it follows that operator Φ is given by

$$\Phi[f,s](\mathbf{x}) = \int_{\mathbb{R}^d} K_s(\mathbf{x}-\mathbf{y}) f(\mathbf{y}) \, \mathrm{d}\mathbf{y} \tag{1.4}$$

for a certain $K_s \in \mathbb{L}_2(\mathbb{R}^d)$. By Axiom 4 we have $K_s > 0$ for all $s>0$ and therefore by means of Axiom 10, Fubini's theorem and again Axiom 4 we have that $K_s \in \mathbb{L}_1(\mathbb{R}^d)$, with $\|K_s\|_{\mathbb{L}_1(\mathbb{R}^d)} = 1$ for all $s>0$, since

$$\|f\|_{\mathbb{L}_1(\mathbb{R}^d)} = \int_{\mathbb{R}^d} \Phi(f,s)(\mathbf{x}) \mathrm{d}\mathbf{x} = \int_{\mathbb{R}^d} \int_{\mathbb{R}^d} K_s(\mathbf{x}-\mathbf{y}) \mathrm{d}\mathbf{x} f(\mathbf{y}) \mathrm{d}\mathbf{y} = \|K_s\|_{\mathbb{L}_1(\mathbb{R}^d)} \|f\|_{\mathbb{L}_1(\mathbb{R}^d)} < \infty$$

for some $f \in \mathbb{L}_1(\mathbb{R}^d)$ with $f>0$.

Lemma 1 *If $f \in \mathbb{L}_1(\mathbb{R}^d)$, then $\hat{f} \in C_0(\mathbb{R}^d)$, and $\|\hat{f}\|_{\mathbb{L}_\infty(\mathbb{R}^d)} \leq (2\pi)^{-d/2} \|f\|_{\mathbb{L}_1(\mathbb{R}^d)}$*

For proof see [112]p.169.
Notice that the mapping $f \mapsto K * f$ is also a continuous mapping from $\mathbb{L}_2(\mathbb{R}^d)$ into itself: By the Plancherel theorem Fourier Transform is a unitary operator on $\mathbb{L}_2(\mathbb{R}^d)$ and by the above lemma the Fourier Transform of K is continuous on $\mathbb{R}^d$ with $\|\hat{K}\|_{\mathbb{L}_\infty(\mathbb{R}^d)} < \infty$. So it follows that the mapping $f \mapsto \mathcal{F}(K*f) = \hat{K}\hat{f}$ is bounded on $\mathbb{L}_2(\mathbb{R}^d)$.

Next, we will use (1.4) in order to adjust the other axioms. Axiom 6 can now be written

$$K_{s_2} * (K_{s_1} * f) = K_{s_1+s_2} * f \qquad \text{, for all } f \in \mathbb{L}_2(\mathbb{R}^d) \ . \tag{1.5}$$

[6] In a Hilbert space the Riesz identification identifies the original space with its dual.

Due to Axiom 9 the kernel K_s only depends on $\|\mathbf{x}\|$, since only then we have $\mathcal{R}_R K_s = K_s$ and

$$\begin{aligned}\mathcal{R}_R\Phi_s[f](\mathbf{x}) &= \int_{\mathbb{R}^d} K_s(R\mathbf{x}-\mathbf{y})f(\mathbf{y})\,\mathrm{d}\mathbf{y}\\ &= \int_{\mathbb{R}^d} K_s(R(\mathbf{x}-\mathbf{u})f(R\mathbf{u})\,\mathrm{dR}\mathbf{u}\\ &= \int_{\mathbb{R}^d} K_s(\mathbf{x}-\mathbf{u})[\mathcal{R}_R f](\mathbf{u})\,\mathrm{d}\mathbf{u}\\ &= \Phi_s[\mathcal{R}_R f](\mathbf{x}) \qquad \text{for all } \mathbf{x}\in\mathbb{R}^d.\end{aligned}$$

It is shown by Pauwels [104] (for $d=1$, but the generalization to arbitrary $d\in\mathbb{N}$ is straightforward) that if Axioms 1-3,5,6,9,10 are satisfied, the Fourier Transform of the convolution kernel *must* be equal to

$$K_s(x) = \frac{1}{\Psi(s)}\phi\left(\frac{x}{\Psi(s)}\right) \tag{1.6}$$

where the Fourier Transform of ϕ has the form:

$$\hat{\phi}(\omega) = e^{-a|\omega|^{2\alpha}} \qquad \alpha>0, a\geq 0 \tag{1.7}$$

and the corresponding re-scaling function is given by $\Psi(s)=s^{1/(2\alpha)}$. This result is not surprising as we will see in Section 1.4. Notice that the constant a is not relevant for practice; it disappears after re-scaling $s\mapsto a\,s$. The trivial case $a=0$ leads to the non interesting case of the identity operator $\Phi[f,s]=f$ (for all $s>0$). So Axioms 1-3,5,6,9,10 impose that the only possible convolution kernels are given by:

$$K_s^{(\alpha)}(\mathbf{x}) = [\mathcal{F}^{-1}(\boldsymbol{\omega}\mapsto e^{-\|\boldsymbol{\omega}\|^{2\alpha}s})](\mathbf{x}). \tag{1.8}$$

These kernels were already briefly mentioned (with $\alpha\in\mathbb{R}$) as possible scale space kernels by Florack [50]p.25 where they were discarded because of their non-separability for $\alpha\neq 1$.

Axiom 4 is only satisfied[7] if $\alpha\leq 1$. This easily follows by

$$\begin{aligned}(-i)^n\int_{\mathbb{R}} x^n\phi(x)\,\mathrm{dx} &= \int_{\mathbb{R}}\phi(x)\left(\tfrac{\partial^n}{\partial\omega^n}e^{-i\,\omega\,x}\right)\big|_{\omega=0}\,\mathrm{dx}\\ &= \sqrt{2\pi}\left(\tfrac{\partial^n}{\partial\omega^n}\hat{\phi}\right)(0) \qquad n\in\mathbb{N}\,.\end{aligned} \tag{1.9}$$

Take $n=2$ and notice that $|\omega|^\beta$ is at least twice differentiable and $\hat{\phi}''(0)=0$ for $\beta>2$.

Now we have (uniquely) obtained the α class of scale spaces, we will have a closer look at the non-trivial causality principles. Let's start with Axiom 7b, the strong causality principle. It is shown by Hummel[74] that this principle is equivalent to the following maximum principle:

Definition 1 *(Special Cylinder Maximum Principle.) Let Ω be a (arbitrary) bounded subset of $\mathbb{R}^d$ and $s_1>0$ such that u is continuous on $\overline{\Omega}\times[0,s_1]$, then u attains its maximum or minimum in say $(\boldsymbol{x},s)\in\overline{\Omega}\times[0,s_1]$. Either we must have $s=0$ or $\boldsymbol{x}\in\partial\Omega$.*

Notice that there are quite some maximum principles in analysis, for instance the more famous one for harmonic functions see Theorem 7, therefore we will not speak of *the* maximum principle. Another well known causality constraint in image analysis is Koenderink's principle:

[7] This coincides for the case $\alpha=1/2$(Poisson semigroup) with a general result on strongly elliptic forms. See Robinson[111] Proposition 3.6

Definition 2 *(Koenderink's principle of non-enhancement of local spatial extrema.)*
Let $u(\boldsymbol{x}, s)$ be a scale space representation then $u_s(\boldsymbol{x}, s)\,\Delta u(\boldsymbol{x}, s) > 0$ at spatial extremal points $(\boldsymbol{x}, s)$, i.e. at points $(\boldsymbol{x}, s)$ where the spatial gradient $(\nabla_{\boldsymbol{x}} u)(\boldsymbol{x}, s) = \boldsymbol{0}$ and the spatial Hessian $(\nabla^2_{\boldsymbol{x}} u)(\boldsymbol{x}, s)$ is positive or negative definite.

Both Koenderink's principle, the strong causality principle and the special cylinder maximum principle exclude the α scale spaces with $\alpha \neq 1$, while they are all satisfied by the Gaussian case $\alpha = 1$. See [109] for validation of the special cylinder maximum principle in the Gaussian case.

Felsberg[48] has given an example in which he shows that the Koenderink's principle in Poisson scale space($\alpha = 1/2$) is not satisfied. We have verified, see Figure 1.4, that the same holds for the scale spaces $\alpha \in (0.5, 1)$ and that (critical)isophotes in the α scale spaces depend continuously on the α parameter. Moreover, the maximum principle follows from the Koenderink's principle: Since Koenderink's principle ensures that local spatial extrema are not enhanced (which follows by a simple Taylor expansion and the fact that $\Delta u = \mathrm{trace}(\nabla^2 u)$), so obviously the extrema will not be in the interior of the cylinder. They can also not lie on top of the cylinder: Suppose there would be say a maximum on top of the cylinder, then from $u \in C^2(\mathbb{R}^d, \mathbb{R}^+)$ it follows that in a small environment within the cylinder around this maximum both $u_s(\mathbf{x}, s)\Delta u(\mathbf{x}, s) > 0$ and $\Delta u(\mathbf{x}, s) < 0$, so in this small environment we have $u_s(\mathbf{x}, s) < 0$, i.e. grey-values decrease towards the the top of the cylinder and therefore the image cannot assume a maximum on the top.

The weak causality principle is satisfied by all α scale spaces. The fact that Poisson scale space ($\alpha = 1/2$) satisfies the weak causality principle is already shown by Felsberg cf. [48]. A small modification of his proof makes it possible to generalize his result to the α scale spaces. In stead of using the maximum principle (Theorem 7) for harmonic functions in order to exclude the possibility of closed isophotes we use the fact that (see (1.23))

$$\begin{cases} u_s = -(-\Delta)^{\alpha} u & \mathbf{x} \in \Omega \\ u|_{\partial\Omega} = c & c \in \mathbb{R} \end{cases}$$

has a unique solution which is given by $u(\mathbf{x}, s) = c, \mathbf{x} \in \Omega$ and by Taylor expansion $u(\mathbf{x}, s) = c$ for all $\mathbf{x} \in \mathbb{R}^d$ and $s > 0$, which would imply $f(\mathbf{x}) = c$, contradicting the first axiom.

1.3 Strongly Continuous Semi-groups

In this section we first examine some (non trivial) general theory of strongly continuous semi-groups. Afterwards we will focus on the strongly continuous semigroups corresponding to our one parameter class of filters given by (1.6). The concept of strongly continuous semigroups is important as a neat theoretical approach to Axiom 6 and in particular Axiom 8. The general attitude in image analysis with respect to this is much more sloppy and from a practical and pragmatic point of view this is understandable.

As noticed in Axiom 1 the domain of an original image is assumed to be the whole $\mathbb{R}^d$. In practice images are given on a bounded domain and thereby they must be extended in some

way and thereby external information will be included as scale increases.[8] Of course there are other possibilities which we will not discuss in this chapter (we return to this in Chapter 2) like working on a bounded domain and imposing $\frac{\partial u}{\partial n} = 0$ at its boundary[9], cf. [26], [44] or working with a torus (periodic extensions). In view of all these alternatives (each having their own advantages and disadvantages) we will first discuss a more general concept of strongly continuous (semi-)groups, namely continuous representations of Lie-groups G, with identity I, into a Banach space X. For the sake of clarity some proofs of theorems within this section are omitted. They can be found in [20] and [29].

Definition 3 *Γ is a bounded continuous representation of G into a Banach space X if*

1. *$\Gamma(g) \in \mathcal{L}(X)$ and $\sup_{g\in G} \|\Gamma(g)\|_{\mathcal{L}(X)} < \infty$ for all $g \in G$.*
2. *the mapping $g \mapsto \Gamma(g)$ from G into $\mathcal{L}(X)$ is a homomorphism.*
3. *$\lim_{g\to I}[\Gamma(g)]x = x$ for all $x \in X$.*

Examples:

- The left regular representation L: $X = \mathbb{L}_p(G)$, $(L_g\phi)(h) = \phi(g^{-1}h)$.
  In particular:
  $G = (\mathbb{R}^d, +)$, $X = \mathbb{L}_p(\mathbb{R})$, $[L_{\mathbf{t}}\phi](\mathbf{x}) = \phi(\mathbf{x} - \mathbf{t})$.
- $G = (SO(d), \cdot)$, $X = \mathbb{L}_2(\mathbb{R}^d)$, $[\mathcal{P}_R\phi](\mathbf{x}) = \phi(R^{-1}\mathbf{x})$

The specific case if $G = (\mathbb{R}^+, +)$ with the extra restriction $s > 0$ leads to following definition.

Definition 4 *(Strongly continuous Semi-group) Let X be a Banach Space, and suppose that to every $s > 0$ is associated an operator $Q_s \in B(X)$, in such way that*

- *$Q_{s_1+s_2} = Q_{s_1}Q_{s_2}$ for all $s_1, s_2 > 0$*
- *$\lim_{s\to 0} \|Q_s x - x\| = 0$ for every $x \in X$.*

Then $s \mapsto Q_s$ will be called a strongly continuous semigroup.

It can be shown, cf.[29], that a semigroup is strongly continuous if and only if it is weak-weak continuous and $\lim_{s\downarrow 0}\langle f, Q_s x\rangle = \langle f, x\rangle$ for all $x \in X$ and $f \in X'$.

[8] Even if the bounded image is extended with zeros , i.e. assuming that f is compactly supported on the given domain, these zeros from outside the image spoil the evolution process as scale increases.

[9] This boundary condition ensures that the average grey value is maintained. Analogue to thermic isolation in heat physics.

Definition 5 *Let G be a Lie-group. A sequence $\{e_n\} \subset \mathbb{L}_1(G)$ is a bounded approximation of unity if*

1. $\sup_{n\in\mathbb{N}} \|e_n\|_{\mathbb{L}_1(G)} < \infty$
2. $\lim_{n\to\infty} \int_G e_n \, \mathrm{dg} = 1$
3. *The following equality must hold for every neighborhood V of $\mathbf{0}$:*

$$\lim_{n\to\infty} \int_{G\setminus V} |e_n| \, \mathrm{dg} = 0 \tag{1.10}$$

Notice that if G is a finite d-dimensional Lie-group with global parametrization $\phi : G \to \mathbb{R}^d$, an integration over G is given by

$$\int_G f(g) \, \mathrm{dg} = \int_{\mathrm{W}\subset\mathbb{R}^{\mathrm{d}}} \mathrm{f}(\mathrm{g}(\varphi_1, \ldots, \varphi_{\mathrm{d}})) \, \mathrm{d}\varphi_1 \ldots \mathrm{d}\varphi_{\mathrm{d}},$$

Definition 6 *Let X be a reflexive Banach space and let Q be a continuous representation of some Lie-group G into X. Let $\psi \in \mathbb{L}_1(G)$, then we define the operator $\mathcal{Q}(\psi) : X \to X$, by*

$$[\mathcal{Q}(\psi)]x = \int_G \psi(g) Q_g x \, \mathrm{dg} \tag{1.11}$$

i.e.

$$\langle f, \mathcal{Q}(\psi)x\rangle = \int_G \psi(g)\langle f, Q_g x\rangle \, \mathrm{dg} \text{ for all } \mathrm{f} \in \mathrm{X}' \, . \tag{1.12}$$

Note that (1.12) indeed defines $\mathcal{Q}$, since in a reflexive Banach space $\hat{x}(f) = f(x)$ defines an isomorphism between X'' and X. Further note that $\langle f, Q_g x\rangle$ is uniformly bounded in g ;

$$|\langle f, Q_g x\rangle| \leq \|f\|\|Q_g\|\|x\| \leq C\|f\|\|x\| \tag{1.13}$$

for a certain $C > 0$ and $\psi \in \mathbb{L}(G)$, so the integral in the right-hand side of (1.12) is convergent. Moreover, it follows by (1.13) that $\mathcal{Q}$ is a bounded operator on X.

If we take $Q = L$ the left regular representation, then we obtain

$$\mathcal{L}(\psi)\,\phi = \psi *_G \phi \text{ i.e. } [\mathcal{L}(\psi)\,\phi](h) = \int_G \psi(g)\phi(g^{-1}h) \, \mathrm{dg},$$

the concept of G-convolution, which will also return in the second part of this thesis.

Theorem 2 *Let X be a reflexive Banach space. Let Q be a continuous representation of some Lie-Group G into X. Let $\{e_n\}$ be a bounded approximation of unity, then*

$$\lim_{n\to\infty} \mathcal{Q}(e_n)x = x \text{ in } X \text{ , for all } x \in X \ .$$

Proof
Let $x \in X$ and let $\epsilon > 0$. From the third condition of Definition 3 it follows that there exists a neighborhood $V \subset G$ of the unity I in G such that $\|Q_g x - x\| < \frac{\epsilon}{3 \sup \|e_n\|_{\mathbb{L}_1(\mathbb{R}^d)}}$ for all $g \in V$. But then we have

$$\begin{aligned}
\|\mathcal{Q}(e_n)x - x\| &= \| \int_G e_n(g) Q_g x \, \mathrm{dg} - \mathrm{x}\| = \leq \| \int_G \mathrm{e_n(g) Q_g x \, dg} - \int_G \mathrm{e_n(g)\, x \, dg}\| + \| \left(\int_G \mathrm{e_n(g) \, dg} - 1 \right) \mathrm{x}\| \\
&\leq \int_V |e_n(g)| \|Q_g x - x\| \, \mathrm{dg} + \int_{G\setminus V} \mathrm{|e_n(g)| \|Q_g x - x\| \, dg} + |\int_G \mathrm{e_n(g) \, dg} - 1| \, \|\mathrm{x}\| \\
&\leq \tfrac{\epsilon}{3} + \left(\int_{G\setminus V} |e_n(g)| \, \mathrm{dg} \right) \|x\| (1 + \sup_{g\in G} \|Q_g\|) + |\int_G e_n(g) \, \mathrm{dg} - 1| \, \|\mathrm{x}\|
\end{aligned}$$

Now by the second and third condition of Definition 5 it follows that there exists a $N \in \mathbb{N}$ such that

$$\|\mathcal{Q}(e_n)x - x\| < \frac{\epsilon}{3} + \frac{\epsilon}{3} + \frac{\epsilon}{3} = \epsilon$$

for all $n > N$ $\square$.

1.3.1 Strong Continuity of Poisson and Gaussian Semigroup.

Now we focus onto the special case of the Poisson and Gaussian scale spaces:
Take $G = (\mathbb{R}^d, +)$, $X = \mathbb{L}_p(\mathbb{R}^d)$ $(p \geq 1)$, $Q = L$ and let $\{t_n\}$ be a sequence in $\mathbb{R}^+$ such that $t_n \downarrow 0$.
Let K_s $(s > 0)$ be a kernel such that

$$\int_{\mathbb{R}^d} K_s(\mathbf{x}) \, \mathrm{d}\mathbf{x} = 1 \ , \ \mathrm{K_s} \geq 0 \ , \ \lim_{\mathrm{s}\downarrow 0} \int_{\mathbb{R}^\mathrm{d}\setminus \mathrm{V}} |\mathrm{K_s(x)}| \, \mathrm{d}\mathbf{x} = 0 \ .$$

For instance the Gaussian kernel $K_s(\mathbf{x}) = G_s(\mathbf{x})$ or the Poisson kernel $K_s(\mathbf{x}) = H_s(\mathbf{x})$. Then $e_n = K_{t_n}$ is bounded approximation of the unity and by the above theorem we obtain:

$$\lim_{n\to\infty} K_{t_n} * \phi = \phi \text{ in } \mathbb{L}_2(\mathbb{R}^d)$$

Since this is valid for all $t_n \to 0$, we obtain

$$\lim_{t\downarrow 0} K_t * \phi = \phi \text{ in } \mathbb{L}_2(\mathbb{R}^d) \ . \tag{1.14}$$

Applying Fourier Transform with respect to $\mathbf{x}$ to the Dirichlet problem, see (1.25), respectively Diffusion problem, see (1.24), defined on the half space $\mathbb{R}^d \times \mathbb{R}^+$ one obtains respectively $\hat{u}(\omega, s) = e^{-|\omega| s} \hat{f}(\omega)$ and $\hat{u}(\omega, s) = e^{-|\omega|^2 s} \hat{f}(\omega)$. Using this together with $\widehat{f * g} = \hat{f}\hat{g}$ and $e^{a+b} = e^a e^b$ leads to (1.5). To this end we remark that we used that

$$K_{s_1} * (K_{s_2} * f) = (K_{s_1} * K_{s_2}) * f \ . \tag{1.15}$$

This equality holds for $f \in \mathbb{L}_2(\mathbb{R}^d)$, since the direct product in the Fourier domain is associative. (If f is a distribution, then things become more complicated). Therefore both the *Gaussian semigroup* $s \mapsto (\phi \mapsto G_s * \phi)$ and the *Poisson semigroup* $s \mapsto (\phi \mapsto H_s * \phi)$ are strongly continuous semigroups on $\mathbb{L}_2(\mathbb{R}^d)$. Finally, we notice that the semigroups corresponding to the α scale spaces are also strongly continuous which will be shown in Theorem 10.

1.3.2 Infinitesimal Generators of Strongly Continuous Semigroups and their Resolvents

Given a strongly continuous semigroup Q on a Banach space X, we define the operators $\mathcal{A}_\epsilon$, for $\epsilon > 0$ by

$$A_\epsilon = \tfrac{Q_\epsilon - I}{\epsilon} \tag{1.16}$$

Define

$$\mathcal{A}x = \lim_{\epsilon \downarrow 0} \mathcal{A}_\epsilon x \tag{1.17}$$

for all $x \in \mathcal{D}(\mathcal{A})$, that is , for all $x \in X$ for which the limit (1.17) exists in the norm topology of X. It is clear that $\mathcal{D}(\mathcal{A})$ is a subspace of X and $\mathcal{A}$ is thus a linear operator in X. This operator, which is essentially $Q'(0)$, is called the *infinitesimal generator* of the semigroup Q.

A bounded operator $\mathcal{A}$ on a Banach space X, which is prescribed on a dense subset has a unique extension on X, i.e. $\mathcal{A}$ is densely defined. For if $x_n \to x$, then $\mathcal{A}x_n \to \mathcal{A}x$. An unbounded operator must be closed to have this property. This means that for all sequences in X, which converge to say $x \in X$ and whose images $\{\mathcal{A}x_n\}$ happen to converge, the limit should be equal to $\mathcal{A}x$. The next theorem shows that an infinitesimal generator of a strongly continuous semi-group, which might be unbounded, is indeed densely defined.

Theorem 3 *Let Q be a strongly continuous semigroup on Banach Space X. Let $\mathcal{A}$ be its infinitesimal generator, then the domain of the infinitesimal generator is dense in X, i.e. $\overline{\mathcal{D}(A)} = X$. Moreover, since $\mathcal{A}$ is a closed operator, it is thereby densely defined.*

The next theorem, which will be frequently used in this thesis, gives an explicit expression for the resolvent of a strongly continuous semigroup.

Theorem 4 *Consider a semi group Q with infinitesimal generator $\mathcal{A}$. Put*[10]

$$\omega = \lim_{s \to \infty} \frac{\log \|Q_s\|}{s} \ . \tag{1.18}$$

Then for $\lambda \in \mathbb{C}$, with $\Re(\lambda) > \omega$, one has $\lambda \in \rho(A)$ and

$$(\lambda I - \mathcal{A})^{-1} x = R(\lambda; \mathcal{A})x = \int_0^\infty e^{-\lambda s} Q_s x \, \mathrm{ds} \tag{1.19}$$

[10] One can show that such a limit always exist.

Remarks:

- Take $X = \mathbb{L}_2(\mathbb{R}^d)$. Let $f \in \mathbb{L}_2(\mathbb{R}^d)$. Let $\mathbf{x} \in \mathbb{R}^d$. Then equation (1.19) states that $[R(\lambda;\mathcal{A})f](\mathbf{x})$ is in fact the Laplace transform of $s \mapsto Q_s f(\mathbf{x})$ evaluated at λ. This is not surprising, since application of Laplace transform onto the evolution equation

$$\begin{cases} \frac{\partial}{\partial s} u = \mathcal{A}u \\ u(\mathbf{x},0) = f(\mathbf{x}) \qquad \mathbf{x} \in \mathbb{R}^d \end{cases}$$

gives

$$\begin{array}{ll} \lambda\,\mathcal{L}(u(\mathbf{x},\cdot))(\lambda) - u(\mathbf{x},0) & = \\ \lambda\mathcal{L}(u(\mathbf{x},\cdot))(\lambda) - f(\mathbf{x}) & = \mathcal{A}\,\mathcal{L}(u(\mathbf{x},\cdot))(\lambda)\ , \end{array}$$

so therefore

$$\begin{aligned} \mathcal{L}(u(\mathbf{x},\cdot))(\lambda) &= \int_0^\infty u(\mathbf{x},s)e^{-\lambda s}\,\mathrm{ds} \\ &= [R(\lambda;\mathcal{A})f](\mathbf{x})\ . \end{aligned}$$

Thereby the resolvent of the generator of the α scale space, $\mathcal{A} = -(-\Delta)^\alpha$, which is studied in detail in Section 1.5, is a convolution with the Laplace transform of the α convolution kernel *with respect to* s:

$$[R(\lambda;-(-\Delta)^\alpha)f](\mathbf{x}) = [\mathcal{L}(s \mapsto K_s^{(\alpha)}) * f](\mathbf{x}).$$

The Laplace transform of the 1D respectively 2D Gaussian kernel is given by $\frac{e^{-\sqrt{a}x}}{2\sqrt{a}}$ respectively $\frac{K_0(\sqrt{a}r)}{2\pi}$, where K_0 is the zeroth order modified Bessel function of the second kind, relating Gaussian scale space theory to Tikhonov regularisation, see [54] who worked out this idea. In this thesis we return to this observation in more detail in section 3.4.

- For *uniformly* continuous semigroups, i.e. semigroups for which $s \to Q_s$ is continuous as a mapping $[0,\infty) \to \mathcal{B}(X)$ we even have

$$R(\lambda;\mathcal{A}) = \int_0^\infty e^{-\lambda s} Q_s\,\mathrm{ds} \quad , \text{ for } \Re(\lambda) > \|\mathcal{A}\|. \tag{1.20}$$

For these semigroups we have $\mathcal{Q}_s = e^{s\mathcal{A}}$, so (1.20) is a generalization of the well-known formula

$$\mathcal{L}(s \mapsto e^{as})(\lambda) = \int_0^\infty e^{(a-\lambda)s}\,\mathrm{ds} = \frac{1}{\lambda - \mathrm{a}}\ , \text{for all a} \in \mathbb{C}\ :\ \Re(\lambda) > |\mathrm{a}|.$$

1.3.3 Holomorphic Semigroups

In Theorem 10 we will show that all α semigroups and in particular the Poisson and the Gaussian semi-group on $\mathbb{L}_2(\mathbb{R})$ are holomorphic[11]. For these filtering processes this means that

[11] For the constant α in part 2. of (1.21) in the Poisson case, see proof of Theorem 10.

as soon as a source image f is filtered with a finite scale $s > 0$ it can be expanded in a Taylor series with respect to $s > 0$.

A holomorphic semigroup on a Banach space X is a semigroup Q, such that Q has a holomorphic extension into a cone $\{\lambda \in \mathbb{C} \ : \ |\arg \lambda| < \arctan \frac{1}{\alpha e}\}$, $\alpha > 0$ in the complex plane, locally given by $Q_\lambda x = \sum_{n=0}^{\infty} \frac{(\lambda - s)^n}{n!} Q_s^{(n)} x$, $x \in X$.

Yosida[132]p.255, has shown that holomorphic semigroups are exactly those semigroups which satisfy

$$\begin{array}{ll} 1. & Q_s x \in \mathcal{D}(\mathcal{A}) \text{ , for all } s > 0, x \in X \\ 2. & \|s\, Q'_s\| = \|s\, \mathcal{A} Q_s\| \leq \alpha \text{ for all } s \in (0, 1] \ . \end{array} \tag{1.21}$$

We will mention some regularity results, that played an important role in the proof of the above statement. For their proofs, see [20].

Lemma 2 *Let Q be a strongly continuous semigroup, with infinitesimal generator $\mathcal{A}$ in a Banach space X. Let $n \in \mathbb{N}$ and $x \in \mathcal{D}(\mathcal{A}^n)$. Then*

1. *$Q_s x \in \mathcal{D}(\mathcal{A}^n)$ for all $s > 0$, $x \in X$.*
2. *$Q_s x$ is n times continuously differentiable with respect to s*
3. *$Q_s^{(n)}(x) = \mathcal{A}^n Q_s x = Q_s \mathcal{A}^n x \ s > 0, x \in X$.*

Theorem 5 *Let Q be a strongly continuous semi-group, with infinitesimal generator $\mathcal{A}$ in a Banach space X. Suppose $Q_s x \in \mathcal{D}(\mathcal{A})$ for all $x \in X$ and $s > 0$. Then*

$$\left\{ \begin{array}{l} Q_s x \in \mathcal{D}(\mathcal{A}^n) \text{ for all } s > 0, x \in X \\ Q_s x \text{ is } n \text{ times differentiable with respect to } s \\ Q_s^{(n)}(x) = \mathcal{A}^n Q_s x = \left(Q'_{\frac{s}{n}}\right)^n x = \left(\mathcal{A} Q_{\frac{s}{n}}\right)^n x \ , \\ s > 0, x \in X \end{array} \right. \tag{1.22}$$

for all $n \in \mathbb{N}$.

1.4 Evolution Equations Corresponding to α Scale Spaces.

The infinitesimal generator of the α semigroup given by $s \mapsto (f \mapsto K_s^{(\alpha)} * f)$ corresponding to the α scale space is given by $-(-\Delta)^\alpha$, which will be explained in Section 1.5 (Theorem 10) in detail.
In other words the α scale spaces given by $u(\mathbf{x}, s) = (K_s^{(\alpha)} * f)(\mathbf{x})$ satisfy the pseudo differential evolution system

$$\left\{ \begin{array}{l} u_s = -(-\Delta)^\alpha u \\ \lim\limits_{s \downarrow 0} u(\cdot, s) = f(\cdot) \ . \end{array} \right. \tag{1.23}$$

A semi-group and in particular corresponding to the α scale spaces is completely determined by (the spectral decomposition of) its generator. It is not difficult to give a *heuristical* impression of how Axioms 1-3,5,6,(first part of)8, 9,10 lead to the generators $\mathcal{A} = -(-\Delta)^\alpha$:

1. By Axiom 5 and 8 it follows that are indeed strongly semigroups with infinitesimal generator $\mathcal{A}$ which correspond to the possible scale spaces.
2. By rotational invariance, the fact that $\mathcal{F}\mathcal{R}_R = \mathcal{R}_R\mathcal{F}$ and by Plancherels theorem which states that $\mathcal{F}$ is an isometry from $\mathbb{L}_2(\mathbb{R}^d)$ into itself it follows that the corresponding operator in the Fourier domain is functionally dependent on $\|\boldsymbol{\omega}\|^2$.
3. By $[\mathcal{F}(\partial_x f)](\omega) = i\omega\mathcal{F}(\omega)$ this means that the generator must be functionally dependent on Δ: $\mathcal{A} = f(\Delta)$.
4. Since scale space solutions are not allowed to explode as $s \to \infty$ (Axiom 10) we have $f(\Delta) < 0$.
5. By Axiom 3 (dilation invariance) and $\frac{1}{\lambda^2}\Sigma_\lambda\Delta = \Delta\Sigma_\lambda$ it follows that f must be a homogeneous polynomial of one variable, i.e. a monomial $\mathcal{A} = -(-\Delta)^\alpha$ and by the positivity axiom $\alpha < 1$. The cases $\alpha < 0$ are not allowed since their corresponding scale spaces explode and the case $\alpha = 0 \Rightarrow \mathcal{A} = \mathcal{I}$ is not allowed by the average grey-value axiom.

In this section we will mainly focus to the case $\alpha = \frac{1}{2}$, which corresponds to Poisson scale space. But first we will have a short look to the familiar Gaussian case ($\alpha = 1$).

1.4.1 The Diffusion Equation

Definition 7 *The Diffusion problem on the half space $\mathbb{R}^d \times \mathbb{R}^+$ is defined by:*

$$\begin{array}{ll} [\partial_s - \Delta]u = u_s - \Delta u = 0 & \boldsymbol{x} \in \mathbb{R}^d, s > 0 \\ \lim\limits_{s\downarrow 0} u(\boldsymbol{x}, s) = f(\boldsymbol{x}) & \boldsymbol{x} \in \mathbb{R}^d \end{array} \tag{1.24}$$

If we apply Fourier Transform we obtain the unique solution of this problem, namely $u(\mathbf{x}, s) = \mathcal{F}^{-1}(\boldsymbol{\omega} \mapsto e^{-|\boldsymbol{\omega}|^2 s}\hat{f}(\boldsymbol{\omega}))(\mathbf{x}) = (G_s * f)(\mathbf{x})$. So filtering with Gaussian kernels corresponds to solving the diffusion system 1.24.
It is well known in the scale space community that filtering with Gaussian kernels satisfies all axioms mentioned in Section 1.2. See for instance (Sporring-Nielsen-Florack-Johansen[115] Section 4). Therefore we will only mention some details.
In Section 1.3 it is shown that the mapping from $\mathbb{R}^+ \to B(\mathbb{L}_2(\mathbb{R}))$ given by $s \mapsto (f \mapsto (G_s * f))$ is a *strongly continuous* semi-group. Further on one can show in exactly the same matter as was done in Theorem 6 that $\lim\limits_{s\downarrow 0} |(G_s * f)(\mathbf{x}) - f(\mathbf{x})| = 0$ for all $\mathbf{x} \in \mathbb{R}^d$, whenever f is bounded and continuous on $\mathbb{R}$.
J.Weickert has shown a general theorem from which it follows the axiom on increase of entropy is satisfied in a Gaussian scale space. See Weickert [127]p.67 Theorem 3. Nevertheless, the result easily follows by substituting $u_s = \Delta u$ in equality (1.28) and use Green's second identity (i.e. the fact that Δ is self-adjoint).

1.4.2 The Poisson Equation

Definition 8 *The Dirichlet problem on the half space $\mathbb{R}^d \times \mathbb{R}^+$ is defined by*

$$\begin{array}{ll} \Delta_{\boldsymbol{x},s} u = \Delta u + u_{ss} = 0 & \boldsymbol{x} \in \mathbb{R}^d, s > 0 \\ \lim\limits_{s \downarrow 0} u(\boldsymbol{x}, s) = f(\boldsymbol{x}) & \boldsymbol{x} \in \mathbb{R}^d \end{array} \tag{1.25}$$

If we apply Fourier Transform we obtain the solution of this problem, namely $\mathcal{F}^{-1}(\boldsymbol{\omega} \mapsto e^{-\|\boldsymbol{\omega}\|^s} \hat{f}(\boldsymbol{\omega})) = \mathcal{F}^{-1}(\boldsymbol{\omega} \mapsto e^{-\|\boldsymbol{\omega}\|^s}) * f = H_s * f$. See subsection 1.4.2.3 for an alternative derivation, using the Green's function.

1.4.2.1 Explicit Verification of all Axioms

In this paragraph we will show that the mapping $\Phi : \mathbb{L}_2(\mathbb{R}^d) \times \mathbb{R}^+ \to \mathbb{L}_2(\mathbb{R}^d)$ given by $\Phi[f, s] = H_s * f$ satisfies *all* axioms. It is trivial that Axiom 1-3 are satisfied. Axiom 4 is satisfied since the kernel H_s is positive.
Let $s > 0$ be fixed. Note that $f \mapsto H_s * f$ is a bounded operator, since the kernel is an element of $\mathbb{L}_1(\mathbb{R}^d)$, see Theorem 1, and thereby Axiom 5(I) is satisfied. We even have $H_s \in \mathbb{L}_2(\mathbb{R}^d)$ so it is also a bounded operator from $\mathbb{L}_2(\mathbb{R}^d)$ into $\mathbb{L}_\infty(\mathbb{R}^d)$, since by Cauchy-Schwarz

$$\sup_{\mathbf{x} \in \mathbb{R}^d} |(H_s * f)(\mathbf{x})| \leq \|H_s\|_{\mathbb{L}_2(\mathbb{R}^d)} \|f\|_{\mathbb{L}_2(\mathbb{R}^d)} \ . \tag{1.26}$$

So Axiom 5(II) is also satisfied. Axiom 6 and the first part of Axiom 8 are already proven in Section 1.3. The rest will be proven in Theorem 6. We have already noticed in section 1.2 that all α scale spaces and in particular $\alpha = 1/2$ obey the weak causality principle, Axiom 7a. Although harmonic functions satisfy the mean value principle[12] and the main maximum principle , see Theorem 7, they do not satisfy the special cylinder maximum principle, cf. Definition 1, since extrema can lie on top of the cylinder. This coincides with the fact that the strong causality axiom and Koenderink's principle are not satisfied when $\alpha = 1/2$. An easy example of a harmonic function which doesn't satisfy Koenderink's principle is given by[13] $h(x, y, s) = \cos(s\sqrt{2}) \cosh x \cosh y$.

Axiom 9 is obviously satisfied since the kernel only depends on $\|\mathbf{x}\|$ and for the verification of Axiom 10 we only need to show that the $\mathbb{L}_1$-norm of the Poisson kernel equals 1:

$$\|H_s\|_{\mathbb{L}_1(\mathbb{R}^d)} = \frac{2}{\sigma_{d+1}} \int\limits_{\mathbb{R}^d} \frac{s}{(s^2 + \|\mathbf{x}\|^2)^{\frac{d}{2}}} \, \mathrm{d}\mathbf{x} = \frac{2\sigma_{\mathrm{d}}}{\sigma_{\mathrm{d+1}}} \int\limits_0^\infty \frac{\mathrm{s\,r^{d-1}}}{(\mathrm{s^2 + r^2})^{\frac{\mathrm{d}}{2}}} \, \mathrm{dr} = \frac{2\sigma_{\mathrm{d}}}{\sigma_{\mathrm{d+1}}} \frac{\sqrt{\pi}\Gamma(\mathrm{d}/2)}{2\Gamma((\mathrm{d}+1)/2)} = 1. \tag{1.27}$$

For the verification of the entropy axiom, Axiom 11, see Theorem 8 which is a new result.

[12] Moreover if a function satisfies the mean value principle, then it must be harmonic!
[13] Notice that this function cannot be a scale space function.

Theorem 6 *Let $f \in \mathbb{L}_2(\mathbb{R}^d)$ and suppose f is continuous on $\mathbb{R}^d$ and bounded on $\mathbb{R}^d$ i.e. $\sup_{\boldsymbol{x}\in\mathbb{R}^d} |f(\boldsymbol{x})| = M < \infty$, then*

$$\lim_{s\downarrow 0} |(H_s * f)(\boldsymbol{x}) - f(\boldsymbol{x})| = 0 \quad \textit{for all } \boldsymbol{x} \in \mathbb{R}^d \ .$$

Proof
Let $\mathbf{x} \in \mathbb{R}^n$ and let $\epsilon > 0$. Since f is continu, there exists a $\delta > 0$ such that

$$|f(\mathbf{x}) - f(\mathbf{y})| < \frac{\epsilon}{2} \quad \text{for all } \mathbf{y} \in B_{\mathbf{x},\delta} \ .$$

As a result

$$\begin{aligned} |(H_s * f)(\mathbf{x}) - f(\mathbf{x})| \ &= \tfrac{2s}{\sigma_{d+1}} \left| \int\limits_{\mathbb{R}^2} \tfrac{f(\mathbf{y})-f(\mathbf{x})}{(\|\mathbf{x}-\mathbf{y}\|^2+s^2)^{\frac{d+1}{2}}} \, \mathrm{d}\mathbf{y} \right| \\ &\leq \tfrac{2s}{\sigma_{d+1}} \int\limits_{B_{\mathbf{x},\delta}} + \int\limits_{\mathbb{R}^2\setminus B_{\mathbf{x},\delta}} \tfrac{|f(\mathbf{y})-f(\mathbf{x})|}{(\|\mathbf{x}-\mathbf{y}\|^2+s^2)^{\frac{d+1}{2}}} \, \mathrm{d}\mathbf{y} \\ &\leq \tfrac{\epsilon}{2} + \tfrac{4M\, s\, \sigma_d}{\sigma_{d+1}} \int\limits_{\delta}^{\infty} r^{-2} \, \mathrm{d}r \end{aligned}$$

So there exists an $S > 0$ small enough such that

$$|(H_s * f)(\mathbf{x}) - f(\mathbf{x})| < \epsilon \text{ for all } s < S \ . \qquad \square$$

In particular we have

$$\langle \delta_{\mathbf{x}}, f \rangle = f(\mathbf{x}) = \lim_{s\downarrow 0} (H_s * f)(\mathbf{x})$$

for all $f \in \mathcal{D}(\mathbb{R}^d)$, $\mathbf{x} \in \mathbb{R}^d$.
So, if we denote the mapping $f \mapsto (H_s * f)(\mathbf{x})$ by $Q_s^{\mathbf{x}}$ then

$$D^\alpha Q_s^{\mathbf{x}} \to D^\alpha \delta_{\mathbf{x}} \text{ in } \mathcal{D}'(\mathbb{R}^d) \text{ for every multi-index } \alpha \ .$$

Theorem 7 *(The main maximum principle for harmonic functions)*
Let Ω be a connected open subset of $\mathbb{R}^n$, $n \in \mathbb{N}$. Let f be a harmonic function on Ω. If f attains its maximum at $\boldsymbol{a} \in \Omega$, then f is a constant.

Proof
Let M denote the set of maximum points of f in Ω. Then M is closed in Ω since f is continuous. The set M is also open, because of the mean value theorem for harmonic functions.[14] But since Ω is connected, the only open and closed subsets of Ω are Ω and the empty set. $\square$

If Ω is bounded and if f is continuous on $\overline{\Omega}$, then f attains a maximum and minimum on $\overline{\Omega}$. From Theorem 7 it follows that this extreme points lie on $\partial\Omega$.

[14] $f(\mathbf{a}) = \frac{1}{\tau_n R^n} \int\limits_{B_{\mathbf{a},R}} f(\mathbf{x}) \, d\mathbf{x}$, $\mathbf{a} \in \Omega$, $R > 0$.

Theorem 8 *Let u be the Poisson scale space of a positive image, i.e. $u(\boldsymbol{x}, s) = (H_s * f)(\boldsymbol{x})$, $\boldsymbol{x} \in \mathbb{R}^d, s > 0$, for a certain $f \in \mathbb{L}_2(\mathbb{R}^d)$ such that $0 < f < 1$ almost every where. Let $\mathcal{E}(u) : \mathbb{R}^+ \to \mathbb{R}$ be defined by (1.3). Then $s \mapsto [\mathcal{E}(u)](s)$ is monotonically increasing. Moreover, $\frac{\partial}{\partial s}\mathcal{E}_s(u) \to 0$ for $s \to \infty$.*

Proof
First, we will show that the second order partial derivative to s is negative. We use $u_{ss} = -\Delta u$ and at the end Green's first identity (partial integration).

$$\begin{aligned}
\tfrac{\partial^2[\mathcal{E}(u)](s)}{\partial s^2} &= -\textstyle\int_{\mathbb{R}^d} \frac{\partial^2}{\partial s^2}(u(\mathbf{x}, s)\, \ln u(\mathbf{x}, s))\, \mathrm{d}\mathbf{x} \\
&= -\int\limits_{\mathbb{R}^d} \tfrac{(u_s(\mathbf{x},s))^2}{u(\mathbf{x},s)}\, \mathrm{d}\mathbf{x} \\
&\quad -\int\limits_{\mathbb{R}^d} (\ln u(\mathbf{x}, s) + 1) u_{ss}(\mathbf{x}, s)\, \mathrm{d}\mathbf{x} \\
&< \int\limits_{\mathbb{R}^d} (\ln u(\mathbf{x}, s) + 1) \Delta u(\mathbf{x}, s)\, \mathrm{d}\mathbf{x} \\
&= \int\limits_{\mathbb{R}^d} \ln u(\mathbf{x}, s)\, \Delta u(\mathbf{x}, s)\, \mathrm{d}\mathbf{x} \\
&= -\int\limits_{\mathbb{R}^d} \tfrac{\|\nabla u(\mathbf{x},s)\|^2}{u(\mathbf{x},s)}\, \mathrm{d}\mathbf{x} \leq 0
\end{aligned}$$

Notice with respect to the first inequality that the positivity axiom and $0 < f$ imply that $0 < u(\cdot, s)$ for all $s > 0$. Next, we note that $\lim_{s\to\infty} \frac{\partial}{\partial s}[\mathcal{E}(u)](s) = 0$. This follows from

$$\frac{\partial}{\partial s}[\mathcal{E}(u)](s) = -\int\limits_{\mathbb{R}^d} (\ln u + 1) \frac{\partial u}{\partial s}\, \mathrm{d}\mathbf{x} \tag{1.28}$$

and the fact that $\lim_{s\to\infty} \frac{\partial}{\partial s} u(\mathbf{x}, s) = 0$. Finally, we will show that $s \mapsto \frac{\partial[\mathcal{E}(u)](s)}{\partial s}$, is continuous on $(0, \infty)$:
Let $t > 0$. Let $\{t_n\}_{n\in\mathbb{N}}$ be a sequence in $\mathbb{R}^+$, such that $t_n \to t \;\; (n \to \infty)$.
By Lebesgue's dominated convergence principle and the fact that u is continuously differentiable with respect to s.

$$\begin{aligned}
\lim_{t_n\to t}[\mathcal{E}(u)](t_n) &= \lim_{t_n\to t} \int\limits_{\mathbb{R}^d} (1 + \ln u(\mathbf{x}, t_n)) u_s(\mathbf{x}, t_n)\, \mathrm{d}\mathbf{x} \\
&= \int\limits_{\mathbb{R}^d} \lim_{t_n\to t} (1 + \ln u(\mathbf{x}, t_n)) u_s(\mathbf{x}, t_n)\, \mathrm{d}\mathbf{x} = [\mathcal{E}(\mathrm{u})](\mathrm{t})
\end{aligned}$$

As a result we have $\frac{\partial[\mathcal{E}(u)](s)}{\partial s} > 0$ for all $s > 0$. □

1.4.2.2 The Infinitesimal Generator of the Poisson Semigroup

First we will examine the case $d = 1$ and later we generalize to the case $d > 1$.

By applying Fourier Transform with respect to $\mathbf{x}$ onto the Dirichlet problem one obtains the ordinary differential equation

$$\begin{cases} \frac{\partial^2}{\partial s^2}\hat{u}(\omega,s) & = \omega^2\,\hat{u}(\omega,s) \\ \hat{u}(\omega,0) & = \hat{f}(\omega). \end{cases}$$

Normally, one would find $\hat{u}(\omega,s) = Ae^{-|\omega|s}\hat{f}(\omega) + Be^{|\omega|s}\hat{f}(\omega)$, but by Plancherel's theorem and the fact that $Q_s \in B(\mathbb{L}_2(\mathbb{R}^1))$, for all $s > 0$, it follows that $B = 0$. So, in the Fourier domain the infinitesimal generator becomes $-|\omega|$. Since operator $\frac{\partial^2}{\partial x^2}$ is negative definite and self-adjoint (Δ in the general case $d \in \mathbb{N}$) we have that the infinitesimal generator of Q equals $-\sqrt{-\frac{\partial^2}{\partial x^2}}$. For more information on fractional powers, see Section 1.5.
To this end we remark that

$$\left(\frac{\partial^2}{\partial s^2} + \frac{\partial^2}{\partial x^2}\right) = \left(\frac{\partial}{\partial s} - \sqrt{-\frac{\partial^2}{\partial x^2}}\right)\left(\frac{\partial}{\partial s} + \sqrt{-\frac{\partial^2}{\partial x^2}}\right) \ .$$

Operator $\frac{\partial^2}{\partial x^2}$ is a continuous operator from $\mathbb{H}_k(\mathbb{R})$ $(k > 0)$ into $\mathbb{H}_{k-2}(\mathbb{R})$ and $-\sqrt{-\frac{\partial^2}{\partial x^2}}$ is a continuous operator from $\mathbb{H}_k(\mathbb{R})$ $(k > 0)$ into $\mathbb{H}_{k-1}(\mathbb{R})$. The domain of an infinitesimal operator is always dense in X, see Theorem 3. In our case, we have $X = \mathbb{L}_2(\mathbb{R}) = \mathbb{H}_0(\mathbb{R})$. From Hille[35] (Theorem 21.4.2 p.576) it follows that

$$\mathcal{D}(\sqrt{-\tfrac{\partial^2}{\partial x^2}}) = \{f \in S' \,:\, \omega \mapsto -|\omega|\hat{f}(\omega) \in \mathcal{F}(\mathbb{L}_2(\mathbb{R}))\}.$$

Since Fourier Transformation is a unitary operation on $\mathbb{L}_2(\mathbb{R})$ and since $\mathbb{H}_1(\mathbb{R}) \subset \mathbb{L}_2(\mathbb{R})$ we thus obtain that

$$\mathcal{D}(\sqrt{-\frac{\partial^2}{\partial x^2}}) = \mathbb{H}_1(\mathbb{R}) \ ,$$

which is indeed dense in $\mathbb{L}_2(\mathbb{R})$. Next we will show some properties of the infinitesimal generator of Q.

Theorem 9 *The infinitesimal generator $\mathcal{A} = -\sqrt{-\frac{\partial^2}{\partial x^2}}$ of the Poisson semi-group Q on $\mathbb{L}_2(\mathbb{R})$ given by*

$$[Q_s f](x) = (H_s * f)(x) \qquad x \in \mathbb{R}, f \in \mathbb{L}$$

is symmetric, negative definite and satisfies

$$\mathcal{A}f = -Hf' \text{ for all } f \in \mathbb{H}_1(\mathbb{R}) \ , \tag{1.29}$$

with $H : \mathbb{L}_2(\mathbb{R}) \to \mathbb{L}_2(\mathbb{R})$ the Hilbert Transform, which can be given by an integral in principal value sense:

$$(Hf)(x) = \frac{1}{\pi} \int_{-\infty}^{\infty} \frac{f(t)}{x-t}\,\mathrm{dt} \ , \tag{1.30}$$

existing for almost every x.

Proof
First we will show that the Hilbert transform is properly defined by (1.30):
Let $f \in \mathbb{L}_2(\mathbb{R})$. Define $g_j : \mathbb{R} \to \mathbb{R}$, $j \in \mathbb{N}$ by

$$g_j(x) = \begin{cases} \sqrt{\frac{2}{\pi}}\frac{1}{x} & \text{if } \frac{1}{j} < |x| < j \\ 0 & \text{else} \end{cases}$$

Using contour integration in the complex plane (Jordan's lemma) one easily finds the pointwise limit

$$\begin{aligned} \lim_{j\to\infty} \hat{g}_j(\omega)\hat{f}(\omega) &= \sqrt{\tfrac{1}{2\pi}}\sqrt{\tfrac{2}{\pi}}\hat{f}(\omega) \int\limits_{-\infty,PV}^{\infty} \frac{e^{-i\omega x}}{x}\,\mathrm{dx} \\ &= -\tfrac{2i}{\pi}\hat{f}(\omega) \lim_{j\to\infty} \int\limits_{1/j}^{j} \frac{\sin(\omega x)}{x}\,\mathrm{dx} \\ &= -i\,\mathrm{sgn}(\omega)\hat{f}(\omega) \qquad (\omega \in \mathbb{R}) \end{aligned} \tag{1.31}$$

and obviously $(\omega \to -i\,\mathrm{sgn}(\omega) f(\omega)) \in \mathbb{L}_2(\mathbb{R})$. Therefore by Lebesgue's dominated convergence principle, $(\omega \to \hat{g}_j(\omega)\hat{f}(\omega))$ converges to $(\omega \to -i\,\mathrm{sgn}(\omega)\hat{f}(\omega))$ in $\mathbb{L}_2$ sense. So, by Plancherel we conclude that $f * g_j$ converges in $\mathbb{L}_2(\mathbb{R})$. This limit is called the Hilbert transform of f and is given by (1.30).
We have for $f \in \mathcal{D}(\mathcal{A}) = \mathbb{H}_1(\mathbb{R})$

$$\begin{aligned} -\mathcal{F}(Hf')(\omega) &= -\lim_{j\to\infty} \mathcal{F}(f' * g_j)(\omega) = -i\omega \left(\lim_{j\to\infty} \hat{g}_j(\omega) \right) \hat{f}(\omega) \\ &= i\omega\, i\,\mathrm{sgn}(w)\hat{f}(\omega) = -|\omega|\hat{f}(\omega) = \mathcal{F}(\mathcal{A}f)(\omega)\ . \end{aligned} \tag{1.32}$$

Note that $f' \in \mathbb{L}_2(\mathbb{R})$ for all $f \in \mathbb{H}_1(\mathbb{R})$.
By Plancherel's theorem we now conclude

$$\mathcal{A}f = -Hf' \text{ for all } f \in \mathbb{H}_1(\mathbb{R})\ .$$

Next, we will use this equality in order to show that $\mathcal{A}^* = \mathcal{A}$ and $\mathcal{A} < 0$. As this can only be the case if

$$\begin{cases} 1.\ (Hf', g) = (f, Hg') \\ 2.\ (Hf', f) > 0 \quad \text{for all } f, g \in \mathbb{H}_1(\mathbb{R})\ . \end{cases}$$

From (1.31) it follows that

$$\widehat{Hf}(\omega) = -i\,\mathrm{sgn}(\omega)\hat{f}(\omega) \text{ for every } f \in \mathbb{L}_2(\mathbb{R}) \tag{1.33}$$

Using (1.33), it is easy to show 1. and 2. :

1. $(Hf', g) = (\widehat{Hf'}, \hat{g}) = (i\,\omega(-i)\,\mathrm{sgn}(w)\,\hat{f}, \hat{g}) = (\hat{f}, |\omega|\hat{g}) = (\hat{f}, \widehat{Hg'}) = (f, Hg')$
2. $(Hf', f) = (\widehat{Hf'}, \hat{f}) = |\omega|\,(\hat{f}, \hat{f}) = (\hat{f}, |\omega|\hat{f}) > 0$ □

Remarks:

- One can show similarly to the 1D case above, that the Poisson scale space generator in the d-dimensional case is given by

$$-\sqrt{-\Delta} = -\mathbf{R}\cdot\nabla = -\nabla\cdot\mathbf{R} = -\sum_{j=1}^{d} R_j\,\partial_j, \tag{1.34}$$

where ∂_j is short notation for $\frac{\partial}{\partial x_j}$ and $\mathbf{R} = \sum_{j=1}^{d} \mathbf{e}_j R_j$, where $\{\mathbf{e}_j\}_{j=1}^{d+1}$ are an orthogonal base for $\mathbb{R}^{d+1}$, denotes the Riesz Transform, which is given by the *principal value* integral

$$R_j f(\mathbf{x}) = \frac{2}{\omega_{d+1}} \int_{\mathbb{R}^d} \frac{x_j - y_j}{\|\mathbf{x} - \mathbf{y}\|^{d+1}} f(\mathbf{y}) \, \mathrm{d}\mathbf{y} \tag{1.35}$$

Notice that if $d = 1$ the Riesz Transform equals the Hilbert Transform. Notice that the Gaussian equivalent of (1.34) is given by $\Delta = \nabla \cdot \nabla$. Consequently, the $(d+1)D$ vector scale space consisting of Gaussian scale space and its first order spatial derivatives corresponds to the Poisson scale space and its Riesz transform components, which is first put in the context of image analysis by Felsberg[47] and which will be further examined in subsection 1.4.3:

$$\begin{array}{c} \mathbf{e}_{d+1}(G_s * f)(\mathbf{x}) + \sum_{j=1}^{d} \mathbf{e}_j (\partial_j G_s * f)(\mathbf{x}) \\ \leftrightarrow \\ \mathbf{e}_{d+1}(H_s * f)(\mathbf{x}) + \sum_{j=1}^{d} \mathbf{e}_j (R_j H_s * f)(\mathbf{x}) \ , \end{array} \tag{1.36}$$

with respect to image analysis this means that analogue to the fact that $-\nabla(G_s * f)(\mathbf{x})$ equals the *grey-value flow* in a Gaussian scale space $\mathbf{R}(H_s * f)(\mathbf{x})$ describes the *grey-value flow* in a Poisson scale space. Since by Gauss' divergence theorem we have for all $\Omega' \subset \Omega$:

$$\frac{\partial}{\partial s} \int_{\Omega'} u_\alpha(\mathbf{x}, s) \, \mathrm{d}\mathbf{x} = \begin{cases} \int_{\partial\Omega'} \nabla u \cdot \mathbf{n} \, \mathrm{d}\sigma & \alpha = 1 \\ -\int_{\partial\Omega'} \mathbf{R} u \cdot \mathbf{n} \, \mathrm{d}\sigma & \alpha = 1/2 \end{cases} . \tag{1.37}$$

- In the general d dimensional case the Laplace operator (with respect to both s and $\mathbf{x}$) can be factorized in an analogous matter:

  $$u_{ss} + \Delta u = (\partial_s - \sqrt{-\Delta})(\partial_s + \sqrt{-\Delta})u = 0$$

  and since the nill-space of the linear operator in the left factor of the factorization is zero, this equation is equivalent to

  $$(\partial_s + \sqrt{-\Delta})u = 0 \Leftrightarrow u_s = -\sqrt{-\Delta}\, u \ ,$$

  which indeed corresponds to the pseudo differential equation in (1.23) when $\alpha = 1/2$.

- Both property 1. and 2. can also be shown by applying partial integration onto the principal value integral representation for the Hilbert Transform given by (1.30).

- From (1.33), it follows that H is an $\mathbb{L}_2(\mathbb{R})$-isometry , of period 4. (Fourier Transform also has this property) Since,

  $$\begin{cases} H^2 f = -f \\ \|Hf\|_{\mathbb{L}_2(\mathbb{R})} = \|f\|_{\mathbb{L}_2(\mathbb{R})} \text{ for all } f \in \mathbb{L}_2(\mathbb{R}) \end{cases} \tag{1.38}$$

  Another consequence of the above together with Theorem is that

  $$\partial^{2k} = (-1)^k \mathcal{A}^{2k}, k \in \mathbb{N} \tag{1.39}$$

  By the second equality of (1.38) it follows that $\|H\| = 1$ and therefore by (1.29) it follows that $\|\mathcal{A}\| = 1$, i.e. the according semigroup Q is a contraction semigroup.

- The operators $\mathcal{A} = -\sqrt{-\frac{\partial^2}{\partial x^2}}$, $\partial = \frac{\partial}{\partial x}$ and $\partial^2 = \frac{\partial^2}{\partial x^2}$ respectively the infinitesimal generators of the Poisson, translation and Gaussian semigroup, have all the same smooth elements since

$$\mathcal{D}(\mathcal{A}^\infty) = \bigcap_{n=1}^{\infty} \mathcal{D}(\mathcal{A}^n) = \bigcap_{n=1}^{\infty} \mathbb{H}_n = \bigcap_{n=1}^{\infty} \mathbb{H}_{2n} = \mathbb{H}_\infty$$

and the same analytic elements since the Hilbert transform, which equals the (operator) product of $\mathcal{A}^{-1}\partial$ is unitary on $\mathbb{L}_2(\mathbb{R})$. For a definition of these items see Appendix 6.2. In case we regard the Poisson semigroup on $\mathbb{L}_\infty(\mathbb{R})$ equipped with the sup-norm $\|f\|_{\mathbb{L}_\infty(\mathbb{R})} = \sup_{x\in\mathbb{R}} |f(x)|$ then these operators still have the same smooth and analytic elements as we will show next, but operator $\mathcal{A}$ is no longer linearly[15] bounded by ∂. Since the Poisson semigroup is a contraction semigroup, we have by equality (1.19) that the (operator) norm of $R(\epsilon, \mathcal{A}) = (\epsilon\, I - \mathcal{A})^{-1}$ is at most 1. So $\|(I - \epsilon\mathcal{A})f\| \geq \|f\|$ for all $\epsilon > 0$ and $f \in \mathcal{D}(\mathcal{A}) = \mathbb{H}_1$. Therefore

$$\begin{aligned}
\epsilon\|\mathcal{A}f\|_{\mathbb{L}_\infty(\mathbb{R})} &\leq \|(I + \epsilon\mathcal{A})f\|_{\mathbb{L}_\infty(\mathbb{R})} + \|f\|_{\mathbb{L}_\infty(\mathbb{R})} \\
&\leq \|(I - \epsilon^2\mathcal{A}^2)f\|_{\mathbb{L}_\infty(\mathbb{R})} + \|f\|_{\mathbb{L}_\infty(\mathbb{R})} \\
&\leq \epsilon^2\|\mathcal{A}^2 f\|_{\mathbb{L}_\infty(\mathbb{R})} + 2\|f\|_{\mathbb{L}_\infty(\mathbb{R})}
\end{aligned}$$

Obviously, $\partial : \mathbb{H}_1 \to \mathbb{L}_2$, satisfies $\|\partial\| \leq 1$ and therefore we can apply the same reasoning on ∂ and obtain a similar estimate. By taking $\mathcal{A}^{2m} f$ respectively $\partial^{2m} f$ instead of f and $\epsilon = 1$ in these estimates and using (1.39), we obtain

$$\|\partial^{2m} f\|_{\mathbb{L}_\infty(\mathbb{R})} = \|\mathcal{A}^{2m} f\|_{\mathbb{L}_\infty(\mathbb{R})}$$

for $f \in \mathbb{H}_{2m}$ and

$$\begin{aligned}
\|\partial^{2m+1} f\|_{\mathbb{L}_\infty(\mathbb{R})} &\leq \|\mathcal{A}^{2m+2} f\|_{\mathbb{L}_\infty(\mathbb{R})} + 2\|\mathcal{A}^{2m} f\|_{\mathbb{L}_\infty(\mathbb{R})} \\
\|\mathcal{A}^{2m+1} f\|_{\mathbb{L}_\infty(\mathbb{R})} &\leq \|\partial^{2m+2} f\|_{\mathbb{L}_\infty(\mathbb{R})} + 2\|\partial^{2m} f\|_{\mathbb{L}_\infty(\mathbb{R})} \text{ for } f \in \mathbb{H}_{2m+2}
\end{aligned}$$

1.4.2.3 Green's Function on the Half Space $s > 0$

Another way to obtain the solution of the Laplace problem is by using the fundamental solution $S : \left(\mathbb{R}^d \times \mathbb{R}\right) \times \left(\mathbb{R}^d \times \mathbb{R}\right) \to \mathbb{R}$ given by

$$\begin{cases} S(\hat{\mathbf{x}}, \hat{\mathbf{y}}) = \frac{1}{(d-1)\,\sigma_{d+1}} \|\hat{\mathbf{x}} - \hat{\mathbf{y}}\|^{1-d} & \text{for } d \geq 2, \\ S(\hat{\mathbf{x}}, \hat{\mathbf{y}}) = \frac{1}{2\pi} \log \frac{1}{\|\hat{\mathbf{x}} - \hat{\mathbf{y}}\|} & \text{for } d = 1, \end{cases} \tag{1.40}$$

for $\hat{\mathbf{x}} = (\mathbf{x}, s) \neq (\mathbf{y}, t) = \hat{\mathbf{y}}$. This pointwise notation of the fundamental solution might be deceptive, since in strict sense S is a distribution in $\mathcal{D}'(\mathbb{R}^n)$ with non-compact support. However, since Δ is an elliptic operator with constant coefficients the fundamental solution can be regarded as an infinitely differentiable function outside the origin. See, Rudin [112] Theorem 8.12 p.201.

[15] It is shown in Robinson[111]p.49 that the Hilbert transform is unbounded as an operator from $\mathbb{L}_\infty(\mathbb{R})$.

Define $\hat{\mathbf{y}}* = (\mathbf{y}, -t)$. This point is the result of mirroring $\hat{\mathbf{y}}$ in the plane $s = 0$. Then one can easily verify that Green's function on a half plane is given by[16]

$$G(\hat{\mathbf{x}}, \hat{\mathbf{y}}) = S(\hat{\mathbf{x}}, \hat{\mathbf{y}}) - S(\hat{\mathbf{x}}, \hat{\mathbf{y}}*) \tag{1.41}$$

Recall Green's second identity on a bounded region Ω with boundary $\partial\Omega$ and outward normal $\mathbf{n}$.

$$\int_{\Omega} u\Delta v - v\Delta u \, \mathrm{d}\mathbf{x} = \int_{\partial\Omega} \mathrm{u}\frac{\partial \mathrm{v}}{\partial \mathrm{n}} - \mathrm{v}\frac{\partial \mathrm{u}}{\partial \mathrm{n}} \, \mathrm{d}\sigma$$

Take[17] $v = G$ and $\Omega = (\mathbb{R}^d \times \mathbb{R}^+) \cap (B_{\mathbf{0},R} \setminus B_{\mathbf{y},\delta})$, with $\delta > 0$ sufficiently small and $R > 0$ sufficiently large. Then one can verify that $\int_{\partial B_{\mathbf{y},\delta}, s>0} \left(u\frac{\partial v}{\partial n} - v\frac{\partial u}{\partial n}\right) \, d\sigma \to u(\mathbf{x}, s)$ and

$$\int_{\partial B_{\mathbf{0},R}} \left(u\frac{\partial v}{\partial n} - v\frac{\partial u}{\partial n}\right) \, d\sigma \to 0$$

if respectively $\delta \downarrow 0$ and $R \to \infty$. Moreover, Green's function G is harmonic on Ω. As a result we obtain

$$u(\mathbf{x}, s) = \int_{\mathbb{R}^d} f(\mathbf{y}) \left.\frac{\partial G(\hat{\mathbf{x}}, \hat{\mathbf{y}})}{\partial t}\right|_{t=0} \mathrm{d}\sigma_{\mathbf{y}} \ . \tag{1.42}$$

Now by equation (1.40) we find

$$\begin{aligned} \left.\tfrac{\partial G(\hat{\mathbf{x}},\hat{\mathbf{y}})}{\partial t}\right|_{t=0} &= \left.\tfrac{\partial S(\hat{\mathbf{x}},\hat{\mathbf{y}})}{\partial t}\right|_{t=0} - \left.\tfrac{\partial S(\hat{\mathbf{x}},\hat{\mathbf{y}}*)}{\partial t}\right|_{t=0} \\ = 2\left.\tfrac{\partial S(\hat{\mathbf{x}},\hat{\mathbf{y}})}{\partial t}\right|_{t=0} &= \tfrac{2}{\sigma_{d+1}} \tfrac{s}{(s^2+\|\mathbf{x}-\mathbf{y}\|^2)^{\frac{d+1}{2}}} = H_s(\mathbf{x}-\mathbf{y}) \end{aligned}$$

and substituting this result into equation (1.42) we indeed find: $u(\mathbf{x}, s) = (H_s * f)(\mathbf{x})$.

1.4.3 Clifford Analytic Extension of Poisson Scale Space

In this subsection we give a theoretic background to a highly interesting new approach to scale space theory which was first introduced by Felsberg and Sommer[47].

In case of 1D-signals ($d = 1$) it is possible to extend the Poisson scale space to an analytic scale space $\tilde{u}(x + is) = u_A(x, s) = u(x, s) + iv(x, s)$, simply by adding i times the harmonic conjugate v which is determined (up to a constant) by the Cauchy-Riemann equations $u_x = v_s$ and $u_s = -v_x$. The harmonic conjugate is given by $v(x, s) = (Q_s * f)(x, s)$, where Q_s denotes the conjugate Poisson kernel which is given by the Hilbert transform of the Poisson kernel:

$$Q_s(\mathbf{x}) = (HH_s)(x) = \frac{1}{\pi}\frac{x}{s^2 + x^2} \ .$$

This follows directly by Cauchy's integral formula for analytic functions:

$$\tilde{u}(z) = \frac{1}{2\pi i}\oint_C \frac{\tilde{u}(w)}{w - z} \, dw \qquad z = x + is \ , \tag{1.43}$$

[16] Physically, one could say that the potential field of a positive charge and that of a mirrored negative charge cancel out along $s = 0$.

[17] It is sloppy to use $\Delta S(\hat{\mathbf{x}}, \hat{\mathbf{y}}) = -\delta(\hat{\mathbf{x}} - \hat{\mathbf{y}})$ and apply Green's second identity on $\Omega = \mathbb{R}^d \times \mathbb{R}^+$, but interesting enough the result is the same.

where C is any positively oriented simple curve around z, since

$$H_s(x) = \frac{1}{\pi}\frac{s}{s^2+x^2} = -\Re\left(\frac{1}{(2\pi i)(z)}\right) \qquad Q_s(x) = \frac{1}{\pi}\frac{x}{s^2+x^2} = -\Im\left(\frac{1}{(2\pi i)(z)}\right) . \quad (1.44)$$

In particular by taking $C = C_0 \cup C_R \cup C_\delta$, with $C_0 = [-R,-\delta]\cup[\delta,R]$ and $C_R = \{z \in \mathbb{C}_+ \mid |z| = R\}$, $C_\delta = \{z \in \mathbb{C}_+ \mid |z| = \delta\}$ in (1.43) and letting $\delta \to 0$, $R \to \infty$ we obtain the Cauchy operator $C : \mathbb{L}_2(\mathbb{R}) \to H^2(\mathbb{C}_+)$ which is given by

$$\begin{aligned}(Cf)(x,s) &= \tfrac{1}{2\pi i}\int_{\mathbb{R}} \tfrac{f(t)}{t-z}\mathrm{dt} \\ &= \tfrac{1}{2}((H_s * f)(x) + i\,(Q_s * f)(x)) \ , z = x+is \in \mathbb{C}_+ \ ,\end{aligned}$$

where the space $H^2(\mathbb{C}_+)$ consists of all analytic functions F on $\mathbb{C}_+$ such that $\sup_{t>0}\int_{-\infty}^{\infty} |F(x+it)|^2\,\mathrm{dx} < \infty$. Any signal can be split uniquely and orthogonally into an analytic and a non-analytic part:

$$\begin{aligned}\mathbb{L}_2(\mathbb{R}) &= H^2(\partial\mathbb{C}_+)\bigoplus(H^2(\partial\mathbb{C}_+))^\perp \ , \\ f &= f_{AN} + f_{NAN} = \tfrac{f+iHf}{2} + \tfrac{f-iHf}{2}.\end{aligned}$$

where the subspace of analytic signals is given by

$$H^2(\partial\mathbb{C}_+) = \{f \in \mathbb{L}_2(\mathbb{R}) \mid \mathrm{supp}(\mathcal{F}[f]) \subset [0,\infty)\}.$$

To this end we recall (1.33) so indeed $\mathcal{F}[f_{AN}](\omega) = 0$ for $\omega < 0$. Further we notice[18]

$$\begin{aligned}Cf &= C(f_{AN}) + C(f_{NAN}) = C(f_{AN}) + 0 \\ \lim_{s\downarrow 0} Cf(\cdot,s) &= f_{AN} \ .\end{aligned}$$

In practice f is real valued, so then $f = 2\Re(f_{AN})$ and consequently

$$u(x,s) = \Re\tilde{u}(x,s) = 2\Re(Cf_{AN})(x,s) = (H_s * f)(x).$$

Remarks:

- Physically, the Poisson scale space should be regarded as a potential system rather than a heat system. The isophotes within the Poisson scale space correspond to equi-potential curves and the isophotes within the conjugate Poisson scale space correspond to the flow-lines. By the Cauchy-Riemann equations these lines intersect each other orthogonally through each point (x,s):

  $$(\partial_x,\partial_s)u \cdot (\partial_x,\partial_s)v = u_x v_s + u_s v_x = 0 \ .$$

  For instance the isophotes of the Poisson kernel $K^{(1/2)}$ are the semi-circles $x^2+(s-a)^2 = a^2$, $a,s>0, x \in \mathbb{R}$ which intersect the flow lines $(x+a)^2+s^2 = a^2$, $a,x \in \mathbb{R}, s>0$ orthogonal, see Figure 1.3. It might be tempting to regard f as charge density distribution, but this is not correct:[19] f is the potential at the boundary, due to some charge-distribution in the plane $s<0$.

[18] If restricted to the subspace of analytic signals the Cauchy operator is an isometric isomorphism such that the non tangential limit $\lim_{s\downarrow 0} Cg(\cdot,s) = g(\cdot)$ for all $g \in H^2(\partial\mathbb{C}_+)$, cf.[63]p.113

[19] By writing $u = f + \mathcal{D}(\Delta f)$, where $\mathcal{D}$ denotes the Dirichlet operator (i.e. $\Delta_{\mathbf{x},s}\mathcal{D}f = -f$ and $\mathcal{D}(f)(\mathbf{x},0) = 0$) it is possible to regard Δf as a charge density function (independent of $s>0$).

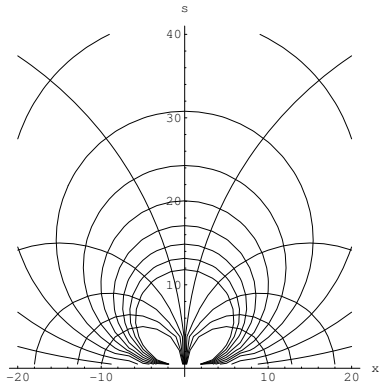

Figure 1.3: The Poisson scale space of the δ-distribution $\delta_{\mathbf{0}}$: The isolines of the Poisson kernel (isophotes) and the isolines of its harmonic conjugate (streamlines) intersect each other orthogonally.

- The 2D Laplace operator can be split into two different ways:

$$\begin{aligned} \Delta_2 &= (\partial_s + i\partial_x)(\partial_s - i\partial_x) = 4\partial_{\bar{z}}\partial_z \\ \Delta_2 &= (\partial_s - \sqrt{-\partial_{xx}})(\partial_s + \sqrt{-\partial_{xx}}) \ . \end{aligned} \tag{1.45}$$

  The space of analytic signals $H_2(\partial\mathbb{C}^+)$ is very special since its elements are treated similarly by the operators $-\sqrt{-\Delta}$ and $i\partial_x$:

$$-\sqrt{-\partial_{xx}} f = i\partial_x f \qquad \text{for } f \in H_2(\partial\mathbb{C}^+),$$

  which can easily be verified in the Fourier domain. Consequently for sufficiently smooth[20] f ($f \in \mathbb{H}_\infty$):

$$\begin{aligned} u(x,s) &= (H_s * f)(x) = (e^{-s\sqrt{-\partial_{xx}}} f)(x) \\ &= (e^{s\, i\partial_x} f)(x) = \tilde{u}(x+is) \ . \end{aligned}$$

- The extension of the Gaussian semigroup restricted to the positive imaginary axis corresponds to the Schrödinger semigroup of the free particle. Let P be the restriction of the extension of the Poisson semigroup Q to the positive imaginary axis, i.e. $P_t = Q_{it}, t > 0$, then the restriction of P to the analytic signal subspace $H^2(\partial\mathbb{C}^+)$ equals the positive wavefront semigroup restricted to $H^2(\partial\mathbb{C}^+)$ and the restriction of P to $(H^2(\partial\mathbb{C}^+))^\perp$ equals the negative wavefront semigroup restricted to $(H^2(\partial\mathbb{C}^+))^\perp$. Since analogue to (1.45) we have:

$$\begin{aligned} u_{tt} - u_{xx} &= (\partial_t - \partial_x)\,(\partial_t + \partial_x)\, u \\ &= \left(\partial_t - i\sqrt{-\partial_{xx}}\right)\left(\partial_t + i\sqrt{-\partial_{xx}}\right) u \ . \end{aligned}$$

Complex analytic extension can only be done in the signal case ($d = 1$). For images $d \geq 2$ an analogue recipe can be followed, using the more general notion of Clifford analytic functions. To this end some knowledge of Clifford algebra is necessary, cf.[42], [63] . Let

$$\{\mathbf{e}_i\}_{i=1}^n = \{\mathbf{e}_i\}_{i=1}^d \cup \{\mathbf{e}_{d+1}\}, n = d+1,$$

be an orthonormal base in $\mathbb{R}^n$ and let $\mathbb{R}_n$ and $\mathbb{R}_n^+$ be the Clifford algebra and its even subalgebra of $\mathbb{R}^n$. Let Ω be an open set in $\mathbb{R}^n$.

[20] Actually, sufficiently smooth should be replaced by analytic vectors, see Appendix 6.2, but in order to avoid confusion with analytic functions this term is avoided.

Definition 9 *A function $\tilde{u} \in C^\infty(\Omega, \mathbb{R}_n^+)$ is Clifford analytic on Ω if*

$$\nabla_n \tilde{u} = \sum_{j=1}^{n} \boldsymbol{e}_j \frac{\partial \tilde{u}}{\partial x^j} = 0 \ .$$

There again exists a (generalized) Cauchy integral theorem for these functions, cf.[63]p.103. Analogue to the $d = 1$ case we define the closed subspace of $\mathbb{L}_2(\mathbb{R}^d)$:

$$H^2(\partial\mathbb{R}_n^+) = \{f \in \mathbb{L}_2(\mathbb{R}^d) \mid (I - \mathbf{Re}_{d+1})f = 0\}.$$

Notice that $(\mathbf{R}f, \mathbf{R}f)_{\mathbf{L}_2(\mathbb{R}^d)} = (f, f)_{\mathbb{L}_2(\mathbb{R}^d)}$ and $(\mathbf{R})^2 = \sum R_j^2 = -I$ and again we can split complex valued signals into a Clifford analytic and orthogonal to Clifford analytic part:

$$\mathbb{L}_2(\mathbb{R}^d) = H^2(\partial\mathbb{R}_n^+) \bigoplus (H^2(\partial\mathbb{R}_n^+))^\perp$$
$$f = \tfrac{f+\mathbf{Re}_{d+1}f}{2} + \tfrac{f-\mathbf{Re}_{d+1}f}{2} = f_{AN} + f_{NAN} \ ,$$

Notice that these two subspaces of $\mathbb{L}_2(\mathbb{R}^d)$ are precisely the irreducible subspaces of the semi-direct product of the dilation and translation group on $\mathbb{R}^d$ and that $\frac{I+\mathbf{Re}_{d+1}}{2}$ and $\frac{I-\mathbf{Re}_{d+1}}{2}$ are the orthogonal projections on them.

We define the Cauchy operator $C : \mathbb{L}_2(\mathbb{R}^d) \to H^2(\mathbb{R}_n^+)$ by

$$(Cf)(\mathbf{x}, s) = \frac{1}{\sigma_{d+1}} \int\limits_{\mathbb{R}^d} \frac{\mathbf{z} - \mathbf{u}}{\|\mathbf{z} - \mathbf{u}\|^{d+1}} \mathbf{e}_{d+1} f(\mathbf{u}) \, \mathrm{d}\mathbf{u} \ ,$$

$\mathbf{z} = \sum\limits_{j=1}^{d} x^j \mathbf{e}_j + s\mathbf{e}_{d+1}$, which can again be expressed in the Poisson kernel and its harmonic conjugate:

$$\mathbf{Q}_s(\mathbf{x}) = \mathbf{R}H_s(\mathbf{x}) = \sum_{j=1}^{d} \mathbf{e}_j R_j H_s(\mathbf{x}) = \sum_{j=1}^{d} \mathbf{e}_j Q_s^{(j)}(\mathbf{x}) = \sum_{j=1}^{d} \frac{2}{\sigma_{d+1}} \frac{x^j \mathbf{e}_j}{(s^2 + \|\mathbf{x}\|^2)^{\frac{d+1}{2}}} \ ,$$

by

$$(Cf)(\mathbf{x}, s) = \frac{1}{2}(H_s * f)(\mathbf{x}) + \frac{1}{2} \sum_{j=1}^{d} \mathbf{e}_j \mathbf{e}_{d+1} (Q_s^{(j)} * f)(\mathbf{x}) = (H_s * (\frac{1}{2}(I + \mathbf{Re}_{d+1}))f)(\mathbf{x}) = (H_s * f_{AN})(\mathbf{x}).$$

Remarks:

- The nil-space of C equals $(H^2(\partial\mathbb{R}_n^+))^\perp$, so $Cf = C(f_{AN} + f_{NAN}) = C(f_{AN})$.
- Let $n = 3$, $d = 2$ and $\tilde{u}$ be Clifford analytic, then $\nabla_n \tilde{u} = 0$ and therefore

$$\nabla_3 \tilde{u} = \nabla_3 \cdot (\tilde{u}\mathbf{e}_3) + \nabla_3 \wedge (\tilde{u}\mathbf{e}_3) = 0 + \mathbf{0} \tag{1.46}$$

  so if we put $\mathbf{u}_M = \tilde{u}\mathbf{e}_3$ we have $\operatorname{rot} \mathbf{u}_M = \mathbf{0}$ and $\operatorname{div} \mathbf{u}_M = 0$ from which it follows that $\mathbf{u}_M$ has a harmonic potential $\mathbf{u}_M = \nabla_3 p$, with $\Delta_3 p = 0$.

- The monogenic scale space $\mathbf{u}_M$ which is introduced by Felsberg and Sommer, cf.[42] (for $d = 2$) is given by

$$\begin{aligned}\mathbf{u}_M(\mathbf{x}, s) &= \tilde{u}(\mathbf{x}, s)\mathbf{e}_{d+1} = 2(Cf)(\mathbf{x}, s)\mathbf{e}_{d+1} \\ &= (H_s + \sum_{j=1}^{d} \mathbf{e}_j \mathbf{e}_{d+1} R_j H_s) * \mathbf{f}) \\ &= \mathbf{e}_{d+1}(H_s * f)(\mathbf{x}) \\ &+ \sum_{j=1}^{d} \mathbf{e}_j (Q_s^{(j)} * f)(\mathbf{x}) \ ,\end{aligned}$$

  where $\mathbf{f} = f\mathbf{e}_{d+1}$. By equation (1.34) and (1.36) it follows that the other components in the monogenic scale space besides the Poisson scale space describe the Poisson image flow analogue to the fact that $-\nabla u$ describes the Gaussian image flow.

Some interesting local features can easily be obtained from the Monogenic/Clifford analytic scale spaces, such as the local phase $\mathbf{r}$, vector field, local attenuation A (amplitude e^A), local orientation ($\frac{\mathbf{r}}{\|\mathbf{r}\|}$). These concepts are again generalizations of the local phase analysis in signal analysis and are related by the logarithm of the Monogenic scale space, cf. [44], [48]. We return to this in a more practical perspective for the case $d = 2$ in Section 2.4.

1.5 Fractional Powers of Closed Operators

This section gives a short introduction into the theory of fractional powers of positive, closed and self adjoint operators. First, we deal with some general theory and then we apply it to the special case $\mathcal{A} = \Delta$. For more details the reader is referred to Yosida[132], Rudin[112] and Balakrishnan[10].

For every positive, closed self-adjoint operator (not necessarily bounded) $-\mathcal{A} > 0$ on a Hilbert space H there exists a unique self-adjoint operator $\mathcal{B}$, such that $\mathcal{B}^2 = -\mathcal{A}$. This can be shown by using a resolution of the identity E on the Borel subsets of the real line such that $(\mathcal{A}x, y) = \int_0^\infty s \ dE_{x,y}(s)$, which exists since $-\mathcal{A}$ is self adjoint. Operator $\mathcal{B}$ is then uniquely defined by

$$(\mathcal{B}x, y) = \int_0^\infty \sqrt{s} \ \mathrm{dE_{x,y}(s)}. \tag{1.47}$$

See, Rudin[112] Theorem 13.31 and 13.30.
In this report we write $\sqrt{-A}$ or $-\mathcal{A}^{\frac{1}{2}}$ in stead of $\mathcal{B}$. Notice that *if* $-\mathcal{A}$ is also compact, $\sigma(-\mathcal{A})$ is discrete and $-\mathcal{A}$ has a complete set of eigenfunctions. Then operator $\sqrt{-\mathcal{A}}$ is uniquely determined by taking square roots of the eigenvalues. This is exactly what happens if one deals with α scale spaces on a finite domain, with Neumann boundary conditions! Then the α scale spaces are directly related to the Gaussian scale space simply by taking α powers of the minus eigenvalues of the diffusion generator, i.e. the solution of the α scale space on a finite domain with Neumann boundary conditions takes the simple form $u_\alpha = \sum_n (f_n, f) f_n e^{-(-\lambda_n)^\alpha s}$,

see Chapter 2 or [26]. However in this chapter we focus on the infinite $\mathbb{R}^d$ case in which it takes more effort to derive the direct relation between the α scale spaces as we will see.

Given a strongly continuous semigroup Q with infinitesimal generator $\mathcal{A}$ one can construct a *holomorphic* semigroup $\hat{Q}_\alpha \quad (0 < \alpha < 1)$, such that the corresponding infinitesimal generator $\hat{\mathcal{A}}_\alpha$ equals $-(-\mathcal{A})^\alpha$, which is defined by (1.61), see Theorem 10. In Theorem 10 we will show that these operators indeed satisfy $(-\mathcal{A})^\alpha(-\mathcal{A})^\beta = (-\mathcal{A})^{\alpha+\beta}$ for $\alpha + \beta < 1$ and $\alpha = \beta = \frac{1}{2}$. From this we conclude that the square root of $-\mathcal{A}$ is indeed *explicitly* given by (1.61) setting $\alpha = \frac{1}{2}$. We will apply this fundamental theory to the case $\mathcal{A} = \Delta$ and thereby construct the α scale spaces from their "mother" scale space; the Gaussian scale space, which at the same time gives the strong connection between all α scale spaces. First we will do some preparation before we obtain this fundamental result.

For $s, \sigma > 0$, $0 < \alpha < 1$ we define $q_{s,\alpha} : \mathbb{R} \to \mathbb{R}$ by [21]

$$q_{s,\alpha}(\lambda) = \begin{cases} \frac{1}{2\pi i} \int_{\sigma-i\infty}^{\sigma+i\infty} e^{z\lambda - sz^\alpha} \, \mathrm{dz} & \text{if } \lambda \geq 0 \\ 0 & \text{else} \end{cases} \tag{1.48}$$

where the branch of $z^\alpha = e^{\alpha \ln z} = |z|^\alpha e^{i\alpha \arg(z)}$ is the one valued function in the z-plane cut along the negative real axis. By Cauchy's integration theorem it immediately follows that (1.48) is independent of the choice of $\sigma = \Re(z) > 0$. By deforming the path of integration in (1.48) to the union of two paths $re^{i\theta}$, $re^{-i\theta}$, for *any* fixed $\theta \in \frac{\pi}{2}$ and r running from 0 to infinity we obtain by some straightforward computations

$$q_{s,\alpha}(\lambda) = \frac{1}{\pi} \int_0^\infty \sin\left(\lambda r \, \sin\theta - s\, r^\alpha \, \sin(\alpha\theta) + \theta\right) * e^{\lambda r \, \cos\theta - s\, r^\alpha \, \cos(\alpha\theta)} \, \mathrm{dr} \tag{1.49}$$

Yosida[132] uses this formula, in particular the case $\theta = \theta_\alpha = \frac{\pi}{1+\alpha}$, frequently in the proofs in paragraph $IX - 11$ of his book. In order to avoid these nasty calculations we will use Laplace transform properties of $q_{t,\alpha}$ instead. The Laplace Transform $\mathcal{L}(q_{s,\alpha})$ of $q_{s,\alpha}$ is given by

$$\mathcal{L}(q_{s,\alpha})(\mu) = e^{-s\mu^\alpha} \qquad \mu > 0 \; , \tag{1.50}$$

since by Cauchy's theorem of residue after choosing $\sigma < s$ we have

$$\int_0^\infty e^{-\lambda\mu} q_{s,\alpha}(\lambda) \, \mathrm{d}\lambda \;\; = \frac{-1}{2\pi i} \int_{\sigma-i\infty}^{\sigma+i\infty} \frac{1}{z-\mu} e^{-z^\alpha s} \, \mathrm{dz} = \mathrm{e}^{-\mathrm{s}\mu^\alpha} \; .$$

As a result we have

$$q_{s+t,\alpha} = q_{s,\alpha} \star q_{t,\alpha} \qquad s, t > 0 \; , \tag{1.51}$$

where $\star$ represents the convolution product with respect to Laplace transform. Moreover, by (1.50) it follows that:

$$\mathcal{L}(q_{1,\alpha})(s^{1/\alpha}\mu) = \mathcal{L}(q_{s,\alpha})(\mu) \qquad s, \mu > 0$$

[21] In general inverse Laplace transformation can be done by using the inversion formula

$$f(\lambda) = \frac{1}{2\pi i} \int_{\sigma-i\infty}^{\sigma+i\infty} e^{\lambda z} [\mathcal{L}(f)](z) \, \mathrm{dz}$$

with σ such that $\mathcal{L}(f)(z)$ is analytic on $\Re(z) \geq \sigma$. So, $q_{s,\alpha}$ is in fact the inverse Laplace transform of $\mu \mapsto e^{-s\mu^\alpha}$.

and therefore[22]

$$s^{-\frac{1}{\alpha}}\, q_{1,\alpha}(s^{-1/\alpha}\lambda) = q_{s,\alpha}(\lambda) \quad s > 0 \tag{1.52}$$

By differentiating (1.50) with respect to s we have

$$\mathcal{L}(q'_{s,\alpha})(\mu) = -\mu^{\alpha} e^{-s\mu^{\alpha}} \tag{1.53}$$

Consequently,

- $\mathcal{L}(q'_{1,\alpha})(\mu\, s^{1/\alpha}) = s\, \mathcal{L}(q'_{s,\alpha})(\mu)$, $s > 0$, which gives us the following equation

$$s^{-1-1/\alpha} q'_{1,\alpha}(s^{-1/\alpha}\lambda) = q'_{s,\alpha}(\lambda) \qquad \lambda, s > 0\ . \tag{1.54}$$

- Let $s \downarrow 0$ in (1.53) we easily obtain

$$\lim_{s\downarrow 0} q'_{s,\alpha}(\lambda) = -\frac{\lambda^{-\alpha-1}}{\Gamma(-\alpha)}. \tag{1.55}$$

  Since,

$$\begin{aligned} \mathcal{L}(\lambda^{-1-\alpha})(\mu) &= \mu^{\alpha}\left(\mu^{-\alpha}\textstyle\int_0^{\infty} \lambda^{-\alpha-1} e^{-\mu\lambda}\, \mathrm{d}\lambda\right) \\ &= \mu^{\alpha}\Gamma(-\alpha)\ . \end{aligned} \tag{1.56}$$

  Note that $0 < \alpha < 1$, the Gamma function can be extended analytically to $\mathbb{C} \setminus \mathbb{Z}^-$ by $\Gamma(z) = \frac{\Gamma(z+n)}{(z+n-1)(z+n-2)\cdots z}$, $-n \le \Re(z) \le 0$.

It can be shown (see Yosida[132]p.261) that

$$q_{s,\alpha}(\lambda) = \lim_{n\to\infty} \frac{(-1)^n}{n} \left(\frac{n}{\lambda}\right)^{n+1} \mathcal{L}^{(n)}(q_{s,\alpha})(\frac{n}{\lambda}) \quad , \lambda > 0\ .$$

Thereby,

$$q_{s,\alpha}(\lambda) \ge 0 \qquad \text{for all } \lambda > 0\ . \tag{1.57}$$

Obviously we have $\int_0^{\infty} q_{s,\alpha}(\lambda)\ d\lambda < \infty$, for instance by (1.49). Further we have $|q_{s,\alpha}(\lambda)e^{-\mu\lambda}| \le |q_{s,\alpha}(\lambda)| = q_{s,\alpha}(\lambda)$, so by Lebesgue's dominated convergence principle and (1.50) we have

$$\begin{aligned} \int_0^{\infty} q_{s,\alpha}(\lambda)\ \mathrm{d}\lambda &= \int_0^{\infty} \lim_{\mu\downarrow 0} q_{s,\alpha}(\lambda) e^{-\mu s}\ \mathrm{d}\lambda \\ &= \lim_{\mu\downarrow 0} \mathcal{L}(q_{s,\alpha})(\mu) = 1 \end{aligned} \tag{1.58}$$

As a result, since $q_{s,\alpha}$ is differentiable with respect to s, we have

$$\int_0^{\infty} \frac{\partial q_{s,\alpha}(\lambda)}{\partial s}\ d\lambda = 0, \qquad s > 0. \tag{1.59}$$

Let Q be a semigroup on a Banach space X, with infinitesimal generator $\mathcal{A}$. Define for $1 > \alpha > 0$ the operator $\hat{Q}_{s,\alpha} : X \to X$ by

$$\hat{Q}_{s,\alpha} x = \int_0^{\infty} q_{s,\alpha}(\eta)\, Q_\eta x\ \mathrm{d}\eta \qquad (\mathrm{s} > 0)\ . \tag{1.60}$$

[22]Equation (1.52) corresponds to the scale invariance axiom, Axiom 3.

Theorem 10 *Let Q be a strongly continuous semigroup, with infinitesimal generator $\mathcal{A}$ on a Banach space X such that $\mathcal{A}$ has a resolvent $R(\lambda;\mathcal{A}) = (\lambda I - \mathcal{A})^{-1}$ for all $\lambda > 0$. Let $\hat{Q}_{s,\alpha} : X \to X$ be given by (1.60).*
Then, the mapping $s \to \hat{Q}_{s,\alpha}$ is a holomorphic semigroup on X, which infinitesimal generator $-\hat{\mathcal{A}}_\alpha$ satisfies

$$\hat{\mathcal{A}}_\alpha = (-\mathcal{A})^\alpha \ ,$$

where $(-\mathcal{A})^\alpha$ is the operator on X given by

$$(-\mathcal{A})^\alpha x = \frac{\sin \alpha\pi}{\pi} \int_0^\infty \lambda^{\alpha-1} \, (\lambda I - \mathcal{A})^{-1} \, (-\mathcal{A}x) \, \mathrm{d}\lambda \ , \tag{1.61}$$

for $x \in \mathcal{D}(\mathcal{A})$. Moreover, if $\sup_{\Re(\lambda)>0} |\Re(\lambda)| \cdot \|R(\lambda;\mathcal{A})\| < \infty$, then

$$\begin{aligned} &(-\mathcal{A})^\alpha(-\mathcal{A})^\beta = (-\mathcal{A})^{\alpha+\beta} \qquad 0 < \alpha + \beta < 1 \\ &\lim_{\alpha\uparrow 1}(-\mathcal{A})^\alpha x = (-\mathcal{A})x \qquad \textit{if} \quad x \in \mathcal{D}(\mathcal{A}) \\ &\lim_{\alpha\downarrow 0}(-\mathcal{A})^\alpha x = x \qquad \textit{if} \quad \lim_{\lambda\downarrow 0} \lambda \, R(\lambda;\mathcal{A})x = 0 \ . \end{aligned} \tag{1.62}$$

Proof
First we will show that $s \to \hat{Q}_{s,\alpha}$ is a strongly continuous semigroup for every $\alpha > 0$. Let $\alpha \in (0,1)$, $x \in X$ and $s, t > 0$. Then, by (1.60) and (1.51) we have

$$\begin{aligned} \hat{Q}_{s,\alpha}\left(\hat{Q}_{t,\alpha}x\right) &= \int_0^\infty \int_0^\infty q_{s,\alpha}(\eta) q_{t,\alpha}(\xi) \, Q_{\xi+\eta}x \, \mathrm{d}\xi \, \mathrm{d}\eta \\ &= \int_0^\infty \left(q_{s,\alpha} \star q_{t,\alpha}\right)(\sigma) \, Q_\sigma x \, \mathrm{d}\sigma \\ &= \int_0^\infty \left(q_{s+t,\alpha}\right)(\sigma) \, Q_\sigma x \, \mathrm{d}\sigma \\ &= \hat{Q}_{s+t,\alpha}x \ . \end{aligned}$$

So, $\hat{Q}_{s+t,\alpha} = \hat{Q}_{s,\alpha}\hat{Q}_{t,\alpha}$. Further, by (1.52) and by substitution $\xi = s^{-1/\alpha}\,\eta$ we obtain

$$\begin{aligned} \hat{Q}_{s,\alpha}x &= \int_0^\infty s^{-1/\alpha} \, q_{1,\alpha}(s^{-1/\alpha}\,\eta) \, Q_\eta x \, \mathrm{d}\eta \\ &= \int_0^\infty q_{1,\alpha}(\xi) \, Q_{\xi s^{1/\alpha}} x \, \mathrm{d}\xi \ . \end{aligned} \tag{1.63}$$

Now from Lebesgue's dominated convergence principle it follows that

$$\lim_{s\downarrow 0} \|\hat{Q}_{s,\alpha}x - x\|_X = \int_0^\infty q_{1,\alpha}(\xi) \left\{ \lim_{s\downarrow 0} \|Q_{\xi s^{1/\alpha}}x - x\| \right\} \, \mathrm{d}\xi$$

which tends to 0 as $s \downarrow 0$. Secondly, we will show that this semigroup is holomorphic. By (1.54) and by substitution $\xi = s^{-1/\alpha}\lambda$ it follows that

$$\hat{Q}'_s x = \int_0^\infty q'_{s,\alpha}(\lambda) Q_\lambda x \, \mathrm{d}\lambda = \frac{1}{\mathrm{s}} \int_0^\infty \mathrm{q}'_{1,\alpha}(\xi) \, \mathrm{Q}_{\mathrm{s}^{1/\alpha}\,\xi}\mathrm{x} \, \mathrm{d}\xi \ .$$

Due to the uniform boundedness principle (See Theorem 2.5.2 [66]) there exists a $M > 0$ such that $\|Q_s\| \leq M$ for all $s \leq 1$. Therefore,

$$\|sQ'_s\| \leq M \int_0^\infty |q'_{1,\alpha}(\xi)| \, \mathrm{d}\xi < \infty \ .$$

So by (1.21) we have that $\hat{Q}$ is indeed a holomorphic semigroup.

Thirdly, we show that the infinitesimal generator of this semigroup indeed equals $-\mathcal{A}^\alpha$. Using (1.55) and (1.59) we obtain

$$\begin{aligned} \hat{\mathcal{A}}_\alpha x = \hat{Q}'_0 x &= \lim_{s\downarrow 0} \int_0^\infty q'_{s,\alpha}(\lambda) \, Q_\lambda x \, \mathrm{d}\lambda \\ &= \lim_{s\downarrow 0} \int_0^\infty q'_{s,\alpha}(\lambda) \, \left(Q_\lambda - I\right) x \, \mathrm{d}\lambda \\ &= -\tfrac{1}{\Gamma(-\alpha)} \int_0^\infty \lambda^{-\alpha-1}(Q_\lambda - I)x \, \mathrm{d}\lambda \ , \end{aligned} \tag{1.64}$$

for $x \in \mathcal{D}(\mathcal{A})$. We will rewrite this expression by using (1.56) with $1+\alpha$ in stead of $-\alpha$, Theorem 4 and the formula $\Gamma(z)\Gamma(1-z) = \pi/\sin \pi z$:

$$\begin{aligned} \hat{A}_\alpha x &= \tfrac{1}{\Gamma(-\alpha)\Gamma(1+\alpha)} \int_0^\infty \left\{ \int_0^\infty e^{-\lambda t} t^\alpha \, \mathrm{d}t \right\} (I - Q_\lambda) \, x \, d\lambda \\ &= \tfrac{\sin \alpha\pi}{\pi} \int_0^\infty t^\alpha \left((tI - \mathcal{A})^{-1} - t^{-1} I \right) x \, \mathrm{d}t \\ &= \tfrac{\sin \alpha\pi}{\pi} \int_0^\infty t^{\alpha-1} (tI - \mathcal{A})^{-1} \mathcal{A} x \, \mathrm{d}t \end{aligned}$$

for $x \in \mathcal{D}(\mathcal{A})$. Since a formal proof of (1.62) yields much computation we will skip the proof. For a proof see Yosida[132] p.267.
Nevertheless, we will show this for the special case that $\mathcal{A}$ is self-adjoint. Notice that by assumption $\mathcal{A}$ must be negative definite. From (1.61) it follows that $\hat{\mathcal{A}}_\alpha$ is also self adjoint, commuting with $\mathcal{A}$. So with the eye on the spectral resolution (1.47) and the fact that $\mathcal{A}$ and $\hat{\mathcal{A}}_\alpha$ are commuting self-adjoint operators on a Banach space, it follows that we only need to show (1.62) for the case that x equals an eigenfunction with eigenvalue $-\mu$, $\mu > 0$ (with respect to $\mathcal{A}$). We shall use the formula

$$\begin{aligned} \int_0^\infty \tfrac{v^{p-1}}{1+v} \, \mathrm{dv} &= \mathrm{Beta}(p, 1-p) = \tfrac{\Gamma(p)\Gamma(1-p)}{\Gamma(1)} \\ &= \tfrac{\pi}{\sin \pi p} \quad , 0 < \Re(p) < 1. \end{aligned} \tag{1.65}$$

This integral is convergent and analytic (as a function of p) and can be calculated by a "Pac-Man" contour around the real axis in the complex plane or by substitution of $t = \frac{x}{1+x}$ in Euler's beta function.
By straightforward computation and (1.65) we have

$$\begin{aligned} -(-\mathcal{A})^\alpha x &= -\tfrac{\sin \alpha\pi}{\pi} \int_0^\infty \tfrac{t^{\alpha-1}}{t+\mu} \mu x \, \mathrm{d}t \\ &\quad -\mu^\alpha \tfrac{\sin \alpha\pi}{\pi} \int_0^\infty \tfrac{v^{p-1}}{1+v} x \, \mathrm{dv} = -\mu^\alpha \mathrm{x}, \end{aligned}$$

$x \in E_\mu(\mathcal{A})$,$(v = \frac{t}{\mu})$. So, $(-\mathcal{A})^\alpha(-\mathcal{A})^\beta = \mathcal{A}^{\alpha+\beta}$, for $\alpha + \beta < 1$. Moreover, we have $\lim_{\alpha\uparrow 1}(-\mathcal{A})^\alpha x = \lim_{\alpha\uparrow 1} -\mu^\alpha x = -\mu x = -\mathcal{A}x$ and $\lim_{\alpha\downarrow 0} -(-\mathcal{A})^\alpha x = x$. □

Remark:
In the special case where $\mathcal{A}$ is self-adjoint and negative definite we also have $\left(-(-\mathcal{A})^{1/2}\right)^2 = -\mathcal{A}$. Take $\alpha = \beta = 1/2 - 1/n$,$n \in \mathbb{N}$ in (1.62) and let $n \to \infty$.
Although in the general case the eigenvalues need not be real-valued (1.62) remains valid, if $\alpha+\beta < 1$. If x is an eigenfunction of $-\mathcal{A}$ with eigenvalue μ. One may think that this condition is due to the convergence of (1.65), but probably this is not true! To this end we notice that the infinity of the integral is due to the representation of $-(-\mathcal{A})^\gamma x$ by (1.61), which is valid for $0 < \gamma < 1$.
The true essence of the restriction $\alpha + \beta < 1$ is that the formula

$$z^{\alpha+\beta} = z^\alpha z^\beta \qquad \text{with } z \in \mathbb{C} \text{ such that } \Re(z) > 0$$

is only valid for $(0 <)\alpha + \beta < 1$, since the argument of $z^{\alpha+\beta}$ may not exceed the negative axis cut in the complex plane. Note that by the assumptions of Theorem 10 the real part of eigenvalues of the operator $-\mathcal{A}$ in this theorem must be positive. This problem doesn't arise in the self adjoint case where all eigenvalues are real valued.

1.5.1 Fractional Powers of the Minus Laplace Operator: $(-\Delta)^\alpha$, $0 < \alpha \leq 1$

By Green's first respectively second identity it follows that Δ is a negative definite respectively self adjoint operator on the vector space of twice continuously differentiable functions. This vector space is dense in $\mathbb{H}_2(\mathbb{R}^d)$ and since Δ is a closed operator Δ is also self adjoint and positive on the Banach space $\mathbb{H}_2(\mathbb{R}^d)$. Therefore we can apply Theorem 10 to the Gaussian semigroup $Q : \mathbb{R}^+ \to \mathcal{B}(\mathbb{H}_2(\mathbb{R}^d))$ and obtain a new holomorphic semigroup $\hat{Q} : \mathbb{R}^+ \to \mathcal{B}(\mathbb{H}_{2\alpha}(\mathbb{R}^d))$ with infinitesimal generator $-(-\Delta)^\alpha$ which satisfies

$$\begin{aligned} \hat{Q}_s f &= \int_0^\infty q_{t,\alpha}(\xi) Q_\xi f \, \mathrm{d}\xi \qquad \mathrm{f} \in \mathbb{L}_2(\mathbb{R}^\mathrm{d}), \\ -(-\Delta)^\alpha f &= \tfrac{\alpha\pi}{\pi} \int_0^\infty t^{\alpha-1} R(t;\Delta)\, \Delta f \, \mathrm{dt} \qquad \mathrm{f} \in \mathbb{H}_2(\mathbb{R}^\mathrm{d}). \end{aligned}$$

1.5.2 Derivation of the Poisson Semigroup from the Gaussian Semigroup

The special case $\alpha = \frac{1}{2}$ leads to the Poisson semigroup. Since by equality (1.49), for the special case $\theta = \pi$, we have

$$q_{s,1/2}(\xi) = \frac{1}{\pi} \int_0^\infty e^{-\xi r} \sin(s\sqrt{r}) \, \mathrm{dr} = \frac{8\mathrm{s}}{\xi\sqrt{\pi\xi}} \, \mathrm{e}^{-\mathrm{s}^2/4\xi} \, .$$

So the Poisson semigroup is given by:

$$\begin{aligned}\left(\hat{Q}_s f\right)(\mathbf{u}) &= \int_0^\infty q_{s,1/2}(\eta) Q_\eta f \,\mathrm{d}\eta = \int_0^\infty \frac{8\mathrm{s}}{\eta\sqrt{\pi\eta}} \mathrm{e}^{-\frac{\mathrm{s}^2}{4\eta}} \int_{\mathbb{R}^\mathrm{d}} \frac{\mathrm{e}^{-\frac{\|\mathbf{u}-\mathbf{v}\|^2}{4\eta}}}{(4\pi\eta)^{\mathrm{d}/2}} \,\mathrm{f}(\mathbf{v})\,\mathrm{d}\mathbf{v}\,\mathrm{d}\eta \\ &= \frac{2^{(3-d)}}{\pi^{\frac{d+1}{2}}} \int_{\mathbb{R}^d} \left(\int_0^\infty \frac{e^{-\frac{\|\mathbf{u}-\mathbf{v}\|^2}{4\eta}}}{\eta^{(d+1)/2}} \,\mathrm{d}\eta \right) f(\mathbf{v})\mathrm{d}\mathbf{v} = \frac{2}{\sigma_{\mathrm{d}+1}} \int_{\mathbb{R}^\mathrm{d}} \frac{\mathrm{s}}{(\mathrm{s}^2+\|\mathbf{u}-\mathbf{v}\|^2)^{\frac{\mathrm{d}+1}{2}}} \mathrm{f}(\mathbf{v})\,\mathrm{d}\mathbf{v} = (\mathrm{H_s} * \mathrm{f})(\mathbf{u})\end{aligned} \tag{1.66}$$

for all $\mathbf{u} \in \mathbb{R}^d$ and $s > 0$, which is indeed a convolution with the Poisson kernel. Notice that (1.66) relates Poisson and Gaussian scale space in a very explicit way. This is somewhat similar to the relation between Gaussian scale space and Tikhonov-regularization, where a Tikhonov scale space representation is obtained by means of a Laplace transform with respect to scale.

1.5.3 Verification of the Axioms with respect to the α Scale Spaces

Let us consider the scale evolution system

$$\begin{cases} \dfrac{\partial u}{\partial s} &= -(-\Delta)^\alpha \, u \quad (0 < \alpha < 1)\,, \\ \lim\limits_{s \downarrow 0} u(\mathbf{x}, s) &= f(\mathbf{x}) \qquad (\mathbf{x} \in \mathbb{R}^d)\,. \end{cases} \tag{1.67}$$

Since we already verified the axioms in the Poisson case ($\alpha = 1/2$), we will only highlight the axioms for which a generalization to the case $\alpha \in (0, 1)$ is not trivial. Notice that we have already shown in section 1.2 that all α scale spaces obey the weak causality principle. They do not satisfy the Koenderink's principle nor the special cylinder maximum principle nor the strong causality principle. Felsberg[48] used a signal consisting of three delta spikes to show that Koenderink's principle is sometimes not satisfied in Poisson scale space. We use the same example to illustrate the evolution of isophotes as α increases, see Figure 1.4. Next we derive a formal expression for the α convolution kernel in the spatial domain:

$$\begin{aligned} u(\mathbf{x}, s) &= \left[\hat{Q}_s f\right](\mathbf{x}) = \int_0^\infty q_{s,\alpha}(t)(G_t * f)(\mathbf{x})\,\mathrm{dt} \\ &= \left(\left[\int_0^\infty q_{s,\alpha}(t) G_t \,\mathrm{dt} \right] * f \right)(\mathbf{x})\ , \alpha \in (0,1). \end{aligned} \tag{1.68}$$

So the convolution kernel equals $\int_0^\infty \frac{q_{s,\alpha}(t)}{\sqrt{4\pi t}} e^{\frac{-\|\mathbf{x}\|^2}{4t}}\,\mathrm{dt}$. Since $q_{s,\alpha}$ is positive cf. (1.57) and $\|q_{s,\alpha}\|_{\mathbb{L}_1(\mathbb{R}^d)} = 1$ we have by Lebesgue's dominated convergence principle:

$$\| \int_0^\infty q_{t,s} K_t \,\mathrm{dt} \|_{\mathbb{L}_1(\mathbb{R}^\mathrm{d})} = \int_0^\infty \mathrm{q_{t,s}} \|\mathrm{K_t}\|_{\mathbb{L}_1(\mathbb{R}^\mathrm{d})} \,\mathrm{dt} = \int_0^\infty \mathrm{q_{t,s}}\,\mathrm{dt} = 1.$$

So indeed average grey value is preserved, when using this filter. It also follows from (1.68) and the positivity of $q_{s,\alpha}$ that Axiom 4 is satisfied. See also (1.9). It follows directly from (1.52) and (1.68) that Axiom 3 is satisfied. It follows from (1.68) and the rotation invariance of the Gaussian kernel that the rotation invariance property is also satisfied. In a analogue matter we have that the convolution kernel has a finite $\mathbb{L}_2$-norm, therefore by Cauchy Schwarz it follows that Q_s is a bounded operator from $\mathbb{L}_2(\mathbb{R}^d)$ into $\mathbb{L}_\infty(\mathbb{R}^d)$.

With regard to Axiom 11 we remark that until now a generalization of Theorem 8 has not been found. Notice that the evolution parameter of the α scale spaces have different physical dimension, namely $[\text{LENGTH}]^{2\alpha}$. Moreover, the α scale spaces for $\alpha < 1$ do not have finite variance, which directly follows from (1.9). Variance is *not* a good general measure for kernel width. This is only true for the Gaussian case.

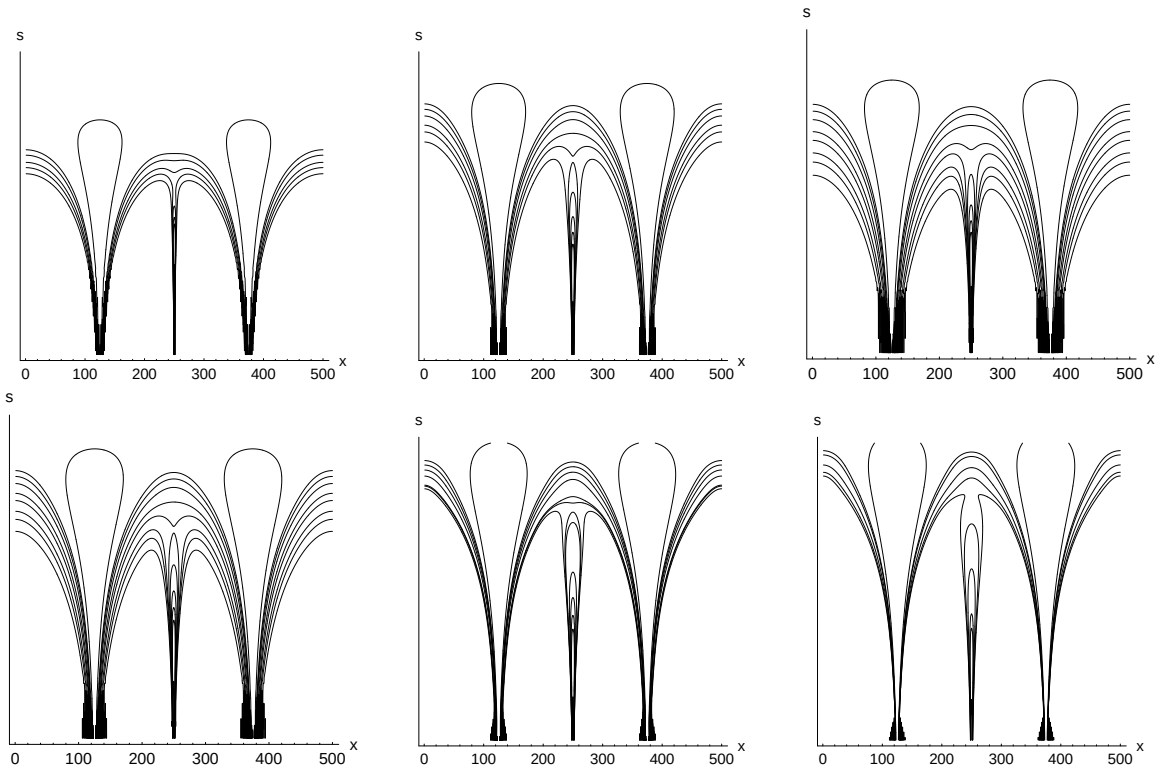

Figure 1.4: Isophotes of various scale space representations of a signal consisting of 1 small delta spike between two larger delta spikes. Top row: $\alpha = 0.5$ (Poisson scale space), $\alpha = 0.6$, $\alpha = 0.7$, bottom row: $\alpha = 0.8$, $\alpha = 0.9$ and $\alpha = 1$ (Gaussian scale space). The parameter α denotes the fractional power, cf. Eq. (1.67) . The α scale spaces are sampled according to $s_\alpha = e^{\alpha\tau_n}$, with equidistant τ_n. To this end we notice that both $(s_\alpha)^{\frac{1}{2\alpha}}$ and $\sqrt{s_1} = \sigma$ have dimension [Length], so comparison between scale spaces should always be $(s_\alpha)^{\frac{1}{2\alpha}} \leftrightarrow \lambda\sqrt{s_1} = \lambda\sigma$, where $\lambda > 0$ is some dimensionless constant. Therefore, the stretching of the isophotes as α increases is of no importance. The above figure shows that for each $\alpha \in (0.5, 1)$ there exist locally concave critical isophotes (at the center of the figures at the middle extremum) and the fact that isophotes seem to evolve in a smooth manner as α increases.

1.6 Gaussian Filtering and Poisson Filtering

In this section we mainly focus on special properties (besides the mentioned axioms) of Gaussian filtering and investigate whether similar results can be obtained using Poisson filtering. It will turn out that the derivatives of the Poisson kernels have at least as nice properties as the derivatives of the Gaussian kernels. At the end of this section we will present some practical results using different members of the unique class of filters, satisfying all Axioms. The following

figure shows the similarity between the Gaussian and Poisson kernel:

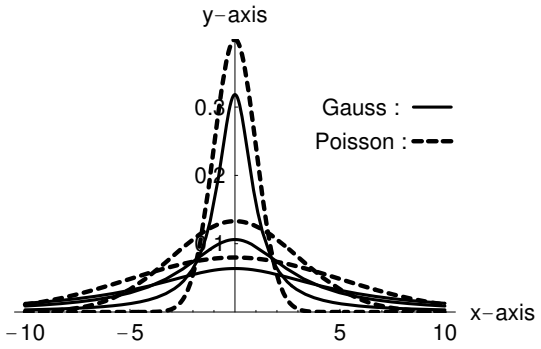

Figure 1.5: The graphs of Gaussian kernels $\sigma = 1, 3, 5$ and Poisson for $s = 1, 3, 5$.

1.6.1 Using one dimensional kernels in multi-dimensional implementation

The Gaussian kernel G_s is separable and even satisfies

$$G(x_1, \ldots, x_d) = \prod_{i=1}^{d} G_s^{(1)}(x_i) \ , \tag{1.69}$$

with $G^{(1)}$ the 1D Gauss kernel. Of course this is a very nice property with respect to multi-dimensional implementation in the spatial domain, since computation becomes order $O(dn)$ in stead of $O(n^d)$. It is easy to see that the Poisson kernel H_s does not have this property. Namely, suppose $H_s(x_1, \ldots, x_d) = \prod_{j=1}^{d} f_s^j(x_j)$, then we would have

$$\frac{\frac{\partial}{\partial x_i} H_s(x_1, \ldots, x_d)}{H_s(x_1, \ldots, x_d)} = \frac{[f_s^i]'(x_i)}{f_s^i(x_i)} \qquad \text{for all } i = 1 \ldots d \ ,$$

with the righthand side depending only on x_i, but clearly the left hand side depends on $x_1, \ldots, x_d$. The only C^1 filter Φ which is both separable $\Phi(x, y) = \phi(x)\psi(y)$ and isotropic must be Gaussian, since

$$\begin{array}{l} \mathcal{R}_R \Phi = \Phi \text{ for all } R \in SO(d) \Leftrightarrow \\ (y\partial_x - x\partial_y)\, \Phi(x, y) = 0 \Leftrightarrow \\ \frac{y\psi(y)}{\psi'(y)} = \frac{x\phi(x)}{\phi'(x)} = C \ . \end{array} \tag{1.70}$$

The separability of Gaussian kernels coincides with the fact that the 1D infinitesimal generators (∂_i^2) commute and satisfy

$$\Delta = \sum_{i=1}^{d} \partial_i^2 \ .$$

Although the 1D infinitesimal generators of 1D Poisson semigroups commute they do not satisfy the last property:

$$-\sqrt{-\Delta} \neq \sum_{i=1}^{d} -\sqrt{-\partial_i^2} \ ,$$

but they do satisfy

$$(-\sqrt{-\Delta})^2 = -\Delta = -\sum_{i=1}^{d} \partial_i^2 = \sum_{i=1}^{d} (-\sqrt{-\partial_i^2})^2 \ . \tag{1.71}$$

Suppose we would write in case $d = 3$:

$$-\sqrt{-\Delta} = \sum_{i=1}^{3} -\mathbf{e}_i \sqrt{-\partial_i^2} \ ,$$

with $\{\mathbf{e}_i\}$ a righthanded orthonormal base in a 3D euclidian space. Then it follows by (1.71) that the $\mathbf{e}_i$ must satisfy

$$\frac{1}{2}(\mathbf{e}_i \mathbf{e}_j + \mathbf{e}_j \mathbf{e}_i) = \delta_{ij} \qquad\qquad i, j = 1 \ldots 3 \ .$$

But this means that our 3-space is thus extended to the real 3DClifford/Pauli algebra

$$P = \{1, \mathbf{e}_1, \mathbf{e}_2, \mathbf{e}_3, \mathbf{e}_1\mathbf{e}_2, \mathbf{e}_2\mathbf{e}_3, \mathbf{e}_3\mathbf{e}_1, \mathbf{e}_1\mathbf{e}_2\mathbf{e}_3 = i\},$$

equipped with product $ab = (a, b) + a \wedge b$. Therefore the commutator with respect to this Clifford product equals $2\ a \wedge b$. Therefore, in general[23]

$$\prod_{i=1}^{d} e^{\ -\mathbf{e}_i \sqrt{-\partial_i^2}} \neq e^{-\sqrt{-\Delta}}.$$

The primitive of the Poisson kernel can be explicitly derived. In the one dimensional case it is given by $P_s(x) = \arctan\left(\frac{x}{s}\right)$, $x > 0$. In d-dimensions it is given by

$$P_s(\mathbf{x}) = 2\frac{\sigma_d}{d\,\sigma_{d+1}} \left(\frac{r}{s}\right)^d F_{2,1}[\frac{d}{2}, \frac{d+1}{2}, \frac{2+d}{2}, -\frac{r^2}{s^2}],$$

where we recall that σ_d is given by (9) and where the hypergeometric function $F_{2,1}$ is given by

$$F_{2,1}[a; b; c; z] = \sum_{k=0}^{\infty} \left(\frac{(a)_k (b)_k}{(c)_k}\right) \frac{z^k}{k!} \tag{1.72}$$

and $(a)_k = \frac{\Gamma[a+k]}{\Gamma[a]}$.

For $d = 2m$ (1.72) can be simplified into

$$\frac{\sigma_{2m}}{\sigma_{2m+1}} (-1)^m B_{-\left(\frac{r}{s}\right)^2}(m, \frac{1}{2} - m) \ ,$$

where $B_z(a; b)$ denotes the incomplete beta function.

For $d = 1$ and $d = 2$ we obtain $P_s(x) = \frac{1}{\pi} \arctan\left(\frac{|x|}{s}\right)$ and $P_s(\mathbf{x}) = 1 - \frac{1}{\sqrt{1+\left(\frac{\|\mathbf{x}\|}{s}\right)^2}}$.

[23] One may think of using the Campbell-Baker-Hausdorff formula, since the Clifford product commutator is known.

1.6.2 Derivatives of the 1D Poisson and Gaussian Kernel

It is well known that the derivatives of the Gaussian kernel are given by

$$G_s^{(n)}(x) = \frac{(-1)^n}{\sigma} H_n(\frac{x}{\sigma})\, G_s(x) \quad , x \in \mathbb{R}, n \in \mathbb{N},$$

where H_n is the Hermite polynomial of order n. These are orthogonal polynomials, with respect to the weight function $w(x) = e^{-x^2}$ and satisfy:

$$\begin{aligned}
&H_n''(x) - 2xH_n'(x) + 2nH_n(x) = 0\\
&H_n(x) = (-1)^n e^{x^2} D^{(n)} e^{-x^2}\\
&e^{2xt-t^2} = \sum_{n=0}^{\infty} \tfrac{H_n(x)}{n!} t^n\\
&H_n(x) = n! \sum_{k=0}^{\lfloor \frac{n}{2} \rfloor} \tfrac{(-1)^k (2x)^{n-2k}}{k!(n-2k)!}\\
&H_n(x) = \tfrac{H_{n+1}'}{2(n+1)}\\
&H_{n+2}(x) = 2xH_{n+1}(x) - 2(n+1)H_n(x)\ .
\end{aligned}$$

A Hermite polynomial H_n is even (odd) if and only if the order n is even (odd) and it has n distinct real nil-points, which lie between the $n+1$ distinct real nil-points of H_{n+1}. The functions $\Psi_n : \mathbb{R} \to \mathbb{R}$ given by $\Psi_n(x) = e^{-\frac{x^2}{2}} H_n(x)$ form a complete orthogonal set in $\mathbb{L}_2(\mathbb{R})$ and they form a base of eigenfunctions with respect to Fourier transform, $\widehat{\Psi_n}(\omega) = i^n \Psi(\omega)$.

The above results are quite useful in practice, therefore we investigate if some kind of similar results also appear in differentiating the Poisson kernel. Before we give a (partially) affirmative answer to this question we note that, surprisingly enough, we did not find a study on the derivatives of the Cauchy kernel in both mathematics (special functions and stochactic processes) and image analysis literature.

First we will consider the 1D-Poisson kernel ($d = 1$) and then we consider the more difficult case of the multivariate Poisson kernel, where $d > 1$. n-fold differentiation of the 1D-Poisson kernel leads to:

$$H_s^{(n)}(x) = \frac{P_{n,s}(x)}{(x^2 + s^2)^{n+1}}\ , \tag{1.73}$$

where $P_{n,s}$ is a polynomial of n-th order in x.
By differentiating both sides of (1.73) one easily obtains the recursion formula:

$$P_{n+1,s}(x) = P_{n,s}'(x)(s^2 + x^2) - 2(n+1)xP_{n,s}(x)\ n = 0, 1, \dots\ . \tag{1.74}$$

Next we derive a formula for the polynomials $P_{n,s}$. Write $H_s(x) = \frac{1}{2\pi i}\left(\frac{1}{x-is} - \frac{1}{x+is}\right)$, then

$$H_s^{(n)}(x) = \frac{1}{2\pi i}\left[\frac{(-1)^n n!}{(x-is)^{n+1}} - \frac{(-1)^n n!}{(x+is)^{n+1}}\right]\ ,$$

so,

$$P_{n,s}(x) = \frac{(-1)^n n!}{2i\pi}\left[(x+is)^{n+1} - (x-is)^{n+1}\right]. \tag{1.75}$$

Using Newton's binomium we obtain

$$P_{n,s}(x) = \frac{(-1)^n n!}{\pi} \sum_{k=0}^{\lfloor \frac{n}{2} \rfloor} \binom{n+1}{2k+1} x^{n-2k} s^{2k+1} (-1)^k \ . \tag{1.76}$$

From this it directly follows that:

$$P'_{n,s}(x) = -(n+1)n \ P_{n-1,s}(x) \ , \tag{1.77}$$

$n = 1, 2 \ldots$. It now follows by (1.74) and (1.77) that

$$P_{n+1,s}(x) + 2(n+1)xP_{n,s}(x) + n(n+1)(x^2+s^2) \, P_{n-1,s}(x) = 0 \ .$$

Moreover, from (1.76) it follows that the polynomials $P_{n,s}$ satisfy the second order differential equation:

$$(s^2+x^2)P''_{n,s}(x) - 2nxP'_{n,s}(x) + n(n+1)P_{n,s}(x) = 0 \ .$$

If we write $z = x + is = re^{i\theta}$, $(z \in \mathbb{C}, r > 0, 0 < \theta < \pi)$, then (1.75) and (1.73) can be written

$$\left\{ \begin{array}{ll} H_s^{(n)}(x) & = \frac{(-1)^n}{\pi r^{n+1}} \sin((n+1)\theta) = \Im \left\{ \frac{z^{n+1}}{|z|^{2n+2}} \right\} \\ & = \frac{(-1)^n}{2\pi i} \left[\overline{z}^{-(n+1)} - z^{-(n+1)} \right] \ , \\ P_{n,s}(x) & = \frac{(-1)^n n!}{2\pi i} \left[z^{n+1} - \overline{z}^{n+1} \right] \end{array} \right. \tag{1.78}$$

So for all $n \in \mathbb{N} \cup \{0\}$ the mapping $(\mathbf{x}, s) \mapsto P_{n,s}(\mathbf{x})$ is a homogeneous harmonic polynomial. In the sequel we will denote this mapping with Ψ_n. It satisfies[24]

$$(\Psi_n, \Psi_m)_{\mathbb{L}_2(\partial B_{\mathbf{0},R})} = 2 * \frac{(-1)^{n+m} n! m! R^{n+m+3}}{\pi^2} \int_0^\pi \sin((n+1)\theta) \sin((m+1)\theta) \mathrm{d}\theta = \delta_{\mathrm{nm}} \frac{(\mathrm{n!})^2 \mathrm{R}^{2\mathrm{n}+3}}{\pi} \tag{1.79}$$

Note that the set consisting of the mappings $(x, s) \mapsto H_s^{(n)}(x)$ $n = 0, 1 \ldots$ is also orthogonal on the (upper half of the) unit circle.
Define $\chi_n : \mathbb{C} \to \mathbb{C}$ by

$$\chi_n(z) = \frac{(-1)^n}{2\pi i} \left[\overline{z}^{-(n+1)} - z^{-(n+1)} \right],$$

then by (1.79) we have $H_s^n(x) = \chi_n(x + is)$. Since $\overline{z} = \frac{1}{z}$ on the unit disk, we have

$$\int_{\partial B_{\mathbf{0},1}} \chi_n(z) \chi_m(z) \, \frac{\mathrm{d}z}{iz} = \frac{(-1)^{n+m+1} n! m!}{2\pi} \operatorname*{Res}_{z=0} (z^n - z^{-n})(z^{(m+1)} - z^{-(m+1)}) = \delta_{nm} \frac{(n!)^2}{\pi} \ .$$

One might hope that there exists a smooth isotropic weight function $w \geq 0$, such that the set $\{H_s^{(n)}\}_{n \in \mathbb{N} \cup \{0\}}$ is orthogonal with respect to $\int_{-\infty}^{\infty} f(x)g(x)w(x) \, \mathrm{dx}$, but this can not be the case as we will next show by contour-integration in the complex plane:

[24] Formally, we have $s > 0$ so Ψ_n is only defined for $s > 0$. Therefore, use Schwarz reflection principle if necessary.

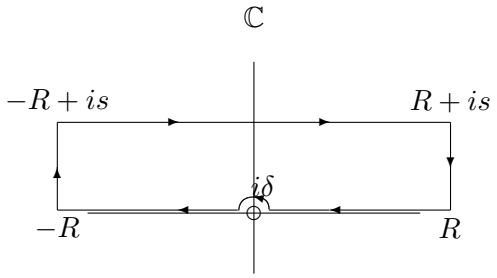

So, by letting $R \to \infty$ and $\delta \downarrow 0$ we have

$$\int_{-\infty}^{\infty} H_s^{(n)} H_s^{(m)}(x) w(x^2+s^2)\,\mathrm{dx} = \int_{\mathrm{is}+\mathbb{R}} \chi_{\mathrm{n}}(\mathrm{z})\chi_{\mathrm{m}}(\mathrm{z})\mathrm{w}(|\mathrm{z}|^2)\,\mathrm{dz} =$$
$$= \tfrac{1}{2} \operatorname*{Res}_{z=0} \left[\{z^{-n-m-2} - z^{-(n+1)}(z-2is)^{-(m+1)} - z^{-(m+1)}(z-2is)^{-(n+1)}\} g(z)\right] ,$$

with $g(z)$ analytic on $\{z \in \mathbb{C} : 0 \leq \Im(z) \leq s\} \setminus \{0\}$ such that $g(z) = w(z)$ on C_1.[25] From the fact that $\operatorname*{Res}_{z=0} z^{-n} = \delta_{n1}$ it follows that either z^n, z^m, or z^{n+m+1} must appear in the expansion of $g(z)$ in order to obtain δ_{mn}. But this means that w will depend on n or m.

For each $n \in \mathbb{N} \setminus \{1\}$ the polynomial $P_{n,s}$, $s > 0$, has n real-valued zero's which lie around the zero's of $P_{n-1,s}$, see figure 1.6.
We will show this by induction:

Since $P_{1,s}(x) = \frac{-2s}{\pi} x$ and $P_{2,s}(x) = \frac{s}{\pi}(-2s^2 + 6x^2)$, it is obvious that the above statement holds for $n = 2$.
Let $n \in \mathbb{N}$ and suppose that the above statement holds for this n. Then because $(x^2+s^2) > 0$ and the fact that $P_{n+1,s}(x) = (x^2+s^2)^{n+2} H_s^{n+1}(x) = (x^2+s^2)^{n+2} \left(\frac{d}{dx}\right) H_s^n(x)$ it follows by Rolle's Theorem that H_s^{n+1} has $n-1+2 = n+1$ real-valued zero's that lay around the n real valued zero's of $H_s^n(x)$.
Note that the zeros of the n-th order Poisson kernel derivative coincide with the zeros of $P_{n,s}$

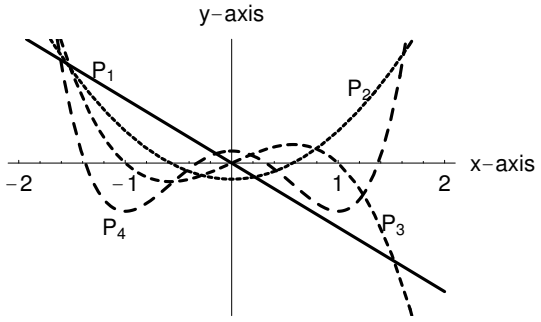

Figure 1.6: The graphs of $P_{n,1}$ for $n = 1, \ldots, 4$

and that the graphs show familiar behaviour as the Gaussian derivatives.

[25] Substitute $(z-2is)$ for $\overline{z}$ in the expansion of $w(|z|^2)$ with respect to $|z|^2 = z\overline{z}$.

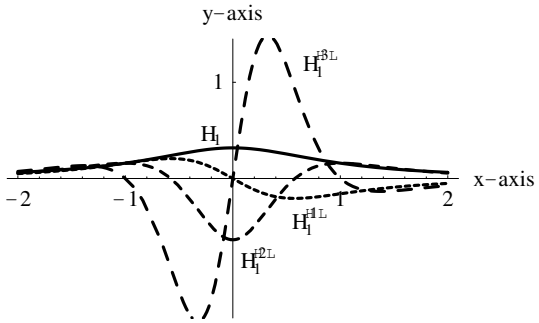

Figure 1.7: The graphs of $H_1^{(n)}$ for $n = 1, \ldots, 4$

1.6.2.1 Radial derivatives of the multivariate Poisson/Cauchy kernel

It follows by induction that the n-fold radial derivative of the multivariate Poisson kernel is of the form

$$\left(\frac{\partial}{\partial r}\right)^n H_s(\mathbf{x}) = \frac{P_{n,s}^d(r)}{(r^2+s^2)^{\frac{d+1}{2}+n}}\ , r = \|\mathbf{x}\|,$$

where $P_{n,s}^d(r)$ is a polynomial of degree n in r, which satisfies the recursion relation

$$(r^2+s^2)(P_{n,s}^d)'(r) - (d+1+2n)rP_{n,s}^d(r) = P_{n+1,s}^d(r).$$

The multivariate Poisson kernel in d-variables relates to the 1D-Poisson kernel by means of

$$H_{s,d}(\mathbf{x}) = \frac{\Gamma\left(\frac{d+1}{2}\right)}{s^{\frac{d-1}{2}}} \left(H_{s,d=1}(\|\mathbf{x}\|)\right)^{\frac{d+1}{2}}.$$

From this equality it follows that

$$\left(\frac{\partial}{\partial r}\right)^n H_s(\mathbf{x}) = \frac{\Gamma\left(\frac{d+1}{2}\right)}{s^{\frac{d-1}{2}}} \left(H_s(\|\mathbf{x}\|)\right)^{\frac{d+1}{2}-n} \sum_{\substack{i_1+\ldots i_n = n \\ i_1 \geq \ldots \geq i_n}} p_{i_1,\ldots,i_n}(\frac{d+1}{2}) H_s^{(i_1)}(r)\cdots H_s^{(i_n)}(r), \quad (1.80)$$

where $p_{i_1,\ldots,i_n}$ are known polynomials of degree less or equal to n. For example, $p_1(t) = t$, $p_{11}(t) = t(t-1)$, $p_{20}(t) = t$, $p_{111}(t) = (t-2)(t-1)t$, $p_{300}(t) = t$, $p_{210}(t) = 3(t-1)t$. Notice that $p_{i_1,\ldots,i_n}(1) = \delta_{n\,i_1}$, so indeed the left hand side and right hand side coincide in case $d = 1$.

We deduce from (1.80) that

$$P_{n,s}^d(r) = \Gamma\left(\frac{d+1}{2}\right) \pi^{n-\frac{d+1}{2}} s^{1-n} \sum_{\substack{i_1+\ldots i_n = n \\ i_1 \geq \ldots \geq i_n}} p_{i_1,\ldots,i_n}(\frac{d+1}{2})\ P_{i_1,s}(r)\cdots P_{i_n,s}(r).$$

Now we deduce from (1.78) that

$$P_{n,s}^d(r) = (-1)^n \pi^{-\frac{d+1}{2}} s^{-n+1} \Gamma\left(\frac{d+1}{2}\right) r^{2n} \sum_{\substack{i_1+\ldots i_n = n \\ i_1 \geq \ldots \geq i_n}} \sin\{(i_1+1)\theta\}\sin\{(i_2+1)\theta\}\cdots\sin\{(i_n+1)\theta\}\ ,$$

with $z = r + is = \sqrt{r^2+s^2}e^{i\theta}$. We notice that $(r,s) \mapsto P_{n,s}^d(r)$ is a homogeneous: $P_{n,\lambda s}^d(\lambda r) = \lambda^{n+1} P_{n,s}^d(r)$. It is a harmonic polynomial if $d = 1$, which is not the case for general $d > 1$.

1.6.3 Gaussian and Poisson Scale Space from Energy Minimization

Let f be an entire analytic vector with respect to the Gaussian respectively Poisson filtering, i.e. $f \in \mathcal{D}(\mathcal{A}^\infty) = \bigcap_{n\in\mathbb{N}} \mathcal{D}(\mathcal{A}^n) = \mathbb{H}_\infty$ such that $\sum_{k=1}^{\infty} \frac{s^n}{n!}\|\mathcal{A}^k f\|_{\mathbb{L}_2} < \infty$ for all $s > 0$. See appendix for definition and properties of analytic vectors.

In section 1.4.2.2 we have shown that the analytic vectors of the first order operators $\mathcal{A} = -\sqrt{-\Delta}$ and $\mathcal{A} = \partial$ are the same. The solution of the diffusion problem on the upper half space ($s > 0$) can now be written $u = e^{s\Delta} f$ and the solution of the Dirichlet problem on the upper half space ($s > 0$) can be written $u = e^{-s\sqrt{-\Delta}} f$. These solutions are (respectively) the solutions of the following minimization problems:

$$\begin{aligned}
\min_u \mathcal{E}_{\text{Gauss}}[u](s) &= \int_{\mathbb{R}^d} (f-u)^2 + \sum_{|\alpha|=1}^{\infty} \tfrac{s^{|\alpha|}}{\alpha!}(D^\alpha u)^2 \,\mathrm{d}\mathbf{x} \;, \\
\min_u \mathcal{E}_{\text{Poisson}}[u](s) &= \int_{\mathbb{R}^d} (f-u)^2 + \sum_{k=1}^{\infty} \tfrac{s^k}{k!}\|(-\Delta)^{k/4} u\|^2 \,\mathrm{d}\mathbf{x} \qquad s > 0.
\end{aligned}$$

with $s > 0$ and $\alpha = \alpha_1 \ldots \alpha_d$ are multi-indices. For the Gaussian case this was already mentioned by Nielsen et al.[98]. Before we verify this statement, we remark that by using respectively partial integration and multinomial coefficients we have

$$\begin{aligned}
&\sum_{|\alpha|=1}^{\infty} \tfrac{s^{|\alpha|}}{\alpha!}\|D^\alpha u\|^2 = \sum_{k=1}^{\infty} s^k \sum_{|\alpha|=k} \tfrac{1}{\alpha_1!\alpha_2!\ldots\alpha_d!} \left(\tfrac{\partial^{\alpha_1}}{\partial x_1^{\alpha_1}} \cdots \tfrac{\partial^{\alpha_d}}{\partial x_d^{\alpha_d}} u, \tfrac{\partial^{\alpha_1}}{\partial x_1^{\alpha_1}} \cdots \tfrac{\partial^{\alpha_d}}{\partial x_d^{\alpha_d}} u \right)_{\mathbb{L}_2(\mathbb{R}^d)} \\
&= \sum_{k=1}^{\infty} \tfrac{s^k (-1)^k}{k!} \left(\sum_{|\alpha|=k} \binom{k}{\alpha_1 \ldots \alpha_d} \tfrac{\partial^{2\,\alpha_1}}{\partial x_1^{2\,\alpha_1}} \cdots \tfrac{\partial^{2\,\alpha_d}}{\partial x_d^{2\,\alpha_d}} u, u \right)_{\mathbb{L}_2(\mathbb{R}^d)} = \sum_{k=1}^{\infty} \tfrac{s^k}{k!} (\,(-\Delta)^k u, u\,)_{\mathbb{L}_2(\mathbb{R}^d)} \;.
\end{aligned}$$

With regard to the Poisson minimization we remark that $(-\Delta)^{k/4}$ is self adjoint. So we have

$$\begin{aligned}
\mathcal{E}_{\text{Gauss}}[u](s) &= \|f-u\|^2_{\mathbb{L}_2(\mathbb{R}^d)} + (u, e^{-s\Delta}u)_{\mathbb{L}_2(\mathbb{R}^d)} - (u,u)_{\mathbb{L}_2(\mathbb{R}^d)} \\
\mathcal{E}_{\text{Poisson}}[u](s) &= \|f-u\|^2_{\mathbb{L}_2(\mathbb{R}^d)} + (u, e^{s\sqrt{-\Delta}}u)_{\mathbb{L}_2(\mathbb{R}^d)} - (u,u)_{\mathbb{L}_2(\mathbb{R}^d)} \;,
\end{aligned}$$

and therefore by means of the Euler Lagrange principle:

$$\begin{aligned}
2(u-f) + 2\sum_{k=1}^{\infty} \tfrac{s^k}{k!}(-\Delta)^k u = 0 \qquad &\Leftrightarrow u = e^{s\Delta} f \\
2(u-f) + 2\sum_{k=1}^{\infty} \tfrac{s^k}{k!}(\sqrt{-\Delta})^k u = 0 \quad &\Leftrightarrow u = e^{-s\sqrt{-\Delta}} f \;.
\end{aligned}$$

Note that because of Sobolev's lemma (see Yosida[132] p.174-175), the extra term added to the $\mathbb{L}_2$ (mean squared) part ensures that on every bounded open subset Ω of $\mathbb{R}^d$ there exists a $\tilde{u} \in C^\infty(\Omega)$ such that $u(\mathbf{x}) = \tilde{u}(\mathbf{x})$ almost everywhere on Ω.

1.7 Defocussing of an Idealized Optical System and the Cauchy Kernel

The relation between an idealized optical system and the Cauchy-kernel is first mentioned by Felsberg[42]. Surprisingly enough this has been completely ignored by the image analysis

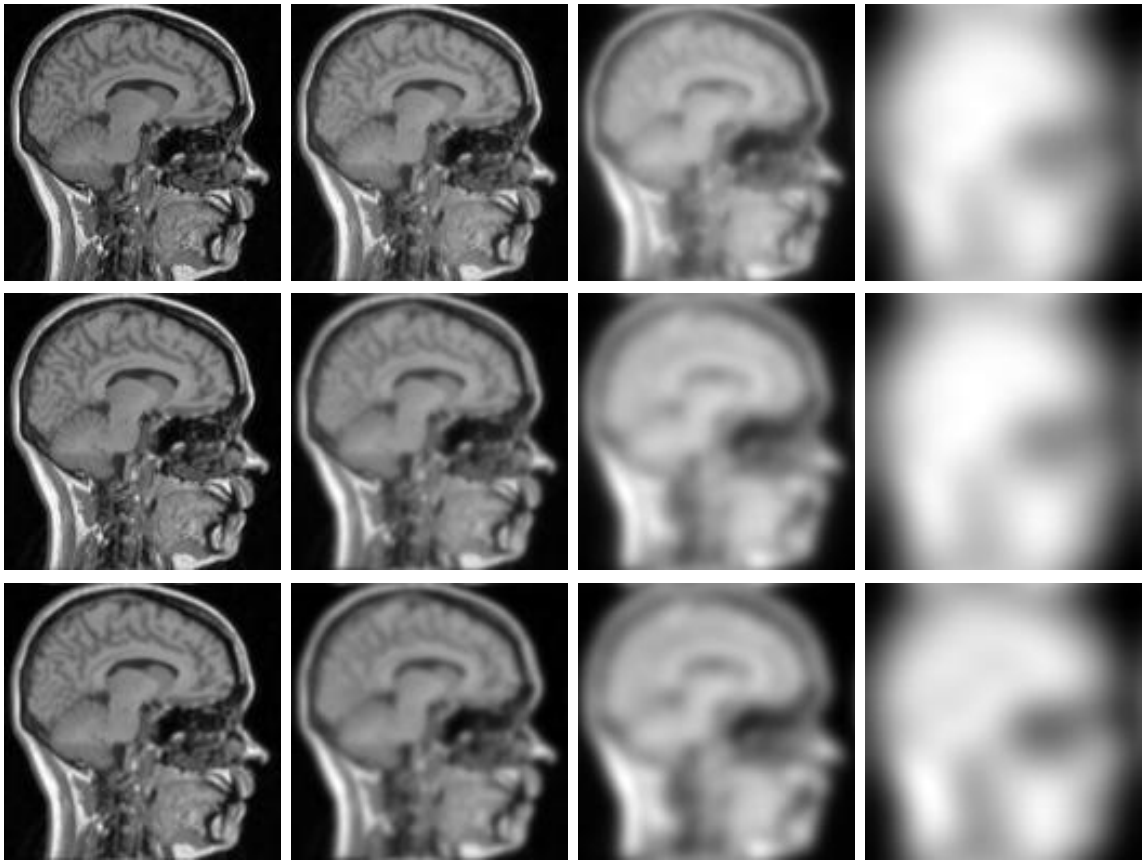

Figure 1.8: Various scale space representations of a 128×128 MR brain slice. Top row: $\alpha = \frac{1}{2}$ (Poisson scale space), middle row: $\alpha = \frac{3}{4}$, bottom row: $\alpha = 1$ (Gaussian scale space). The parameter α denotes the fractional power, cf. Eq. (1.67). Grey-values have been mapped to full range for the sake of clarity.

community. Here we give a short mathematical derivation yielding the same result.

Let C be a point source before an infinitely high ideal lens and assume the photon intensity around P is uniformly distributed (i.e. spherical wave-fronts), see figure 1.9. Then the probability density of finding a photon P on position $\mathbf{x}$ on a sphere S with radius R around P is given by $\frac{1}{4\pi R^2}1_S$. This also holds for its image around P'' behind the lens. we now have

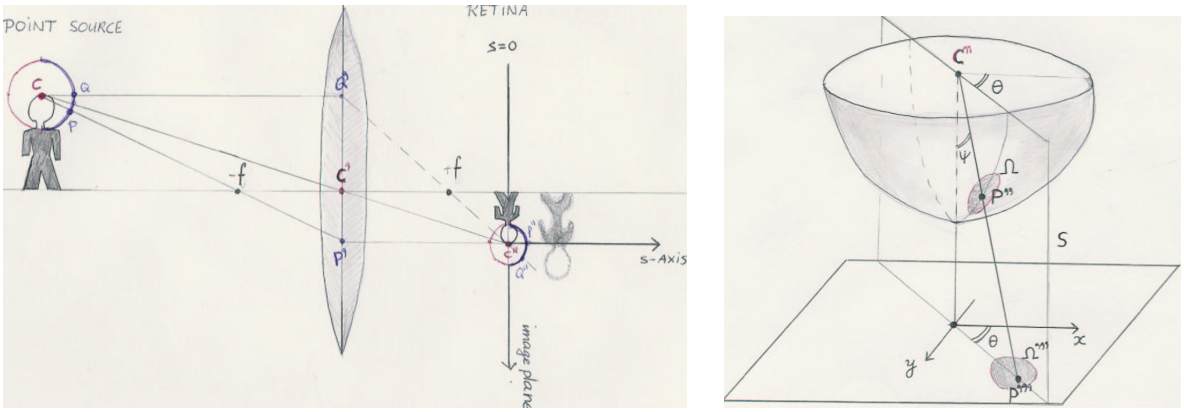

Figure 1.9: Left: A point source P in front of an idealized optical system. Right: Enlarged section around P'' in left figure and its stereographic projection on the screen (or image plane)

$$\begin{aligned}
\mathcal{P}(P'' \in \Omega) &= \tfrac{\mu(\Omega)}{2\pi} = \int\limits_{\Omega} \tfrac{1}{2\pi}\, \mathrm{d}\sigma(\mathbf{v}) = \int\limits_{\gamma^{-1}(\Omega)} \tfrac{\sin\psi}{2\pi}\, \mathrm{d}\psi\mathrm{d}\theta \\
&= \tfrac{1}{2\pi} \int\limits_{(\phi\circ\gamma^{-1})(\Omega)} \tfrac{r}{\sqrt{r^2+s^2}} \left|\det \begin{pmatrix} 1 & 0 \\ 0 & \frac{s}{r^2+s^2} \end{pmatrix}\right| \mathrm{d}r\mathrm{d}\theta \\
&= \int\limits_{(\phi\circ\gamma^{-1})(\Omega)} \tfrac{s}{\sqrt{(r^2+s^2)^{3/2}}}\, r\mathrm{d}r\mathrm{d}\theta \\
&= \tfrac{1}{2\pi} \int\limits_{\Omega'''} \tfrac{s}{(\|\mathbf{x}\|^2+s^2)^{3/2}}\, \mathrm{d}\mathbf{x} = \int\limits_{\Omega'''} \mathrm{K}_{\mathrm{s}}^{(1/2)}(\mathbf{x})\, \mathrm{d}\mathbf{x} \\
&= \mathcal{P}(P''' \in \Omega''')
\end{aligned}$$

for all sets Ω'' on the sphere and all corresponding stereographic projections Ω''' on the xy-plane, where we notice that $r = \sqrt{x^2+y^2}$, $s > 0$, $\psi = \arctan\left(\frac{r}{s}\right)$, $\sin\psi = \frac{r}{\sqrt{r^2+s^2}}$, $\|\mathbf{v}\| = R$ and

$$\begin{aligned}
&\mathbf{v} = \gamma(\psi,\theta) = (R\cos\psi, R\sin\psi\cos\theta, R\sin\psi\sin\theta) \\
&(r,\theta) = \phi(\psi,\theta) = (s\tan\psi,\theta), \\
&\mathbf{x} = (r\cos\theta, r\sin\theta),
\end{aligned}$$

see figure 1.9. The plane $s = 0$ lies at b from the optical center where b follows by focal length f and the distance v of the object to lens, by means of the lens formula $\frac{1}{f} = \frac{1}{v} + \frac{1}{b}$. The screen is located at $s + b$ from the optical center. The higher $s > 0$ the less the resolution of of the projection on the screen. At $s = 0$ all light beams cross at the spatial origin, yielding a Dirac-distribution, as $s > 0$ increases the point-spread function of this (highly idealized) optical system is given by a Cauchy kernel.

Remark: This experiment coincides with the fact that if the initial condition (i.e. the original image) f equals a Dirac-distribution at the origin, its scale space will be given by

	Poisson Scale Space	Gaussian Scale Space
Physics:	Potential Theory	Heat Physics
Generator:	$-\sqrt{-\Delta} = -\nabla \cdot \mathbf{R}$	$\Delta = \nabla \cdot \nabla$
Flow:	$\mathbf{R}(K_s^{\frac{1}{2}} * f)(\mathbf{x}) = (\mathbf{Q}_s * f)(\mathbf{x})$	$-\nabla(K_s^1 * f)(\mathbf{x})$
Extension	Monogenic S.S.	1st order jet
Derivatives:	Spherical Harmonics	Hermite-polynomials

Figure 1.10: A short overview of the correspondence between Gaussian scale space and Poisson scale space.

$u(\mathbf{x}, s) = H_s(\mathbf{x})$, $s > 0$ and thereby the isophotes in a Poisson scale space lie spherical around the origin $(\mathbf{0}, 0)$.

1.8 Conclusion and Discussion

A unified framework to scale space theory on d-dimensional images on the unbounded domain is presented. An overcomplete set of scale space axioms leads uniquely to a parameterized class of scale spaces, the so-called α scale spaces, with corresponding filters of which the Fourier Transform is given by $e^{-s\|\omega\|^{2\alpha}}$. The special cases $\alpha = 1$ and $\alpha = 1/2$ lead to respectively Gaussian and Poisson scale space, with corresponding Gaussian and Poisson kernel. For implementation in the spatial domain Poisson filtering is a good alternative to Gaussian scale space in the sense that typical properties are maintained, besides the fact that all scale space axioms are satisfied. For implementation in the Fourier domain (which implicitly boils down to boundary conditions), cf.[26], all α scale spaces are relevant for practice.

The general theory of constructing a holomorphic semigroup with infinitesimal generator $-(-\mathcal{A})^\alpha$, $0 < \alpha < 1$ out of a strongly continuous semigroup with infinitesimal generator $\mathcal{A}$ that is a fractional power $0 < \alpha < 1$ of $-\mathcal{A}$ applied to the Laplace operator, reveals the *strong connection* between this whole family. Therefore it seems reasonable that Gaussian and Poisson scale space show similar results. Nevertheless, there are two main differences. First, the physical dimension of the Poisson evolution parameter is [LENGTH], while the physical dimension of the Gaussian evolution parameter equals [LENGTH^2]. Second, from an analytic point of view there is an essential difference: In Poisson scale space one solves the Dirichlet problem instead of the Diffusion problem on the upper half space, which means that the kernels and the filtered images are *harmonic functions*. This is a very nice property indeed, e.g. with regard to singularity analysis. The filtered images are then locally approximated by polynomials satisfying the PDE. In Poisson scale space this approximation will be a series of spherical harmonics converging uniformly on compact sets, with the useful property that the spherical harmonics form a complete orthogonal set on a ball or sphere. Further advantages over Gaussian scale space are: The mean value principle and its (Clifford) analytic extension, which corresponds $(d = 2)$ to the monogenic scale space which is first introduced by Felsberg[47]. Although in the sense of grey-value flow, this $(d+1)$-dimensional vector scale space is analogue to the $(d+1)$-dimensional vector space consisting of the Gaussian scale space and its first order derivatives, it yields several local features which cannot be obtained in the latter.

Chapter 2

α Scale Spaces on the Bounded Domain with Neumann Boundary Conditions

2.1 Introduction

In scale space theory the domain is usually taken $\{(\mathbf{x}, s) \mid s > 0, \mathbf{x} \in \mathbb{R}^d\}$, but this introduces some drawbacks. Real images are not defined on the whole $\mathbb{R}^d$ and we have to extend them somehow to the whole $\mathbb{R}^d$. Thereby, besides the original image f, external information will affect the scale space and its topological structure, especially at large scales. Moreover, since grey-values are allowed to flow out of the image, the average grey value is not maintained. To compensate this effect the image is often re-normalized at different scales with different normalization factors (depending on the external information and scale). As a result scale spaces in practice are quite different from the scale spaces in theory.

Another consequence of the unbounded domain is a continuous Fourier-spectrum, where a discrete Fourier spectrum and the corresponding Fourier series are easier to understand with respect to $\mathbb{L}_2$-considerations ($\mathbb{L}_2$ error estimation) rather than point-wise considerations. In practice Fourier transforms are always implemented by discrete Fourier transforms, which implicitly boils down to periodic extension of the image (so boundary conditions are used after all). A priori the behavior of an image at the boundary is not known and therefore it is impossible to solve *all* these problems perfectly. We choose an approach were this damage is reduced. Moreover, the connection between the α scale spaces will become almost trivial.

The α scale space u_α on a bounded oriented domain Ω, with boundary $\partial\Omega$ and outward normal $\mathbf{n}$ with Neumann boundary conditions is defined as the solution of the following boundary value

problem :

$$\begin{cases} \frac{\partial u}{\partial s} & = -(-\Delta)^{\alpha} u \qquad \mathbf{x} \in \Omega, s > 0 \quad \text{Evolution Equation} \\ \frac{\partial u}{\partial n}\big|_{\partial\Omega} & = 0 \qquad\qquad\qquad\qquad\qquad\quad \text{Neumann Boundary Condition} \\ \lim_{s \downarrow 0} u(\cdot, s) & = f(\cdot) \qquad\qquad\qquad\qquad\quad \text{Initial Condition .} \end{cases} \tag{2.1}$$

By working on a finite domain two scale space axioms must be adapted:

- Translation invariance ($\Phi[T_{\mathbf{a}} f, s] = T_{\mathbf{a}} \Phi[f, s]$) does not make sense unless the Neumann boundary condition is translated together with f. As a result the solution of (2.1) is no longer a convolution.
- Monotonic increase of entropy on $\mathbb{R}^d$ must be replaced by increase of entropy on the bounded domain Ω, i.e. the entropy function now becomes

  $$[\mathcal{E}(u)](s) = -\int_{\Omega} u(\mathbf{x}, s) \, \ln u(\mathbf{x}, s) \, \mathrm{d}\mathbf{x} \qquad (\mathrm{s} > 0) \ , \tag{2.2}$$

  where we again note that $0 < f < 1 \Rightarrow 0 < u < 1$ and therefore $\mathcal{E}(u) > 0$.
- Rotation invariance ($\Phi[\mathcal{R}_R f, s] = \mathcal{R}_R \Phi[f, s]$) is only satisfied if Ω is a ball in $\mathbb{R}^d$. For 2D images this means that one must work on a disc to obtain rotational invariance.

With respect to the causality axiom we remark that similar to the unbounded case the α ($0 < \alpha < 1$) evolutions with the Neumann boundary condition do not satisfy Koenderink's principle of non-enhancement of local extrema: $(u_s \Delta u)(x, y, s) \geq 0$ in (spatial) extrema $((x, y, s), u(x, y, s))$, but they do satisfy the weak causality constraint in the sense that every isophote is connected to the ground plane, following exactly the same argument as for the unbounded case, cf. [30] .

There are quite some fundamental reasons to impose the Neumann boundary condition. Before mentioning them we would like to remark that the right-hand side of Green's first and second identity vanishes

$$\int_{\Omega} g \Delta f + \nabla g \cdot \nabla f \, \mathrm{d}\mathbf{x} = \int_{\partial\Omega} \mathrm{g} \frac{\partial \mathrm{f}}{\partial \mathrm{n}} \, \mathrm{d}\sigma = 0 \tag{2.3}$$

$$\int_{\Omega} g \Delta f - f \Delta g \, \mathrm{d}\mathbf{x} = \int_{\partial\Omega} \mathrm{g} \frac{\partial \mathrm{f}}{\partial \mathrm{n}} - \mathrm{f} \frac{\partial \mathrm{g}}{\partial \mathrm{n}} \, \mathrm{d}\sigma = 0 \tag{2.4}$$

for functions $f, g \in C^2(\Omega) \cap C^1(\overline{\Omega})$, such that $\frac{\partial f}{\partial n} = \frac{\partial g}{\partial n} = 0$.

1. Average grey-value is maintained over scale, which immediately follows for the Gaussian case ($u_s = \Delta u$) by the no-flux Neumann boundary condition:

   $$\frac{\partial}{\partial s}(1, u)_{\mathbb{L}_2(\Omega)} = \frac{\partial}{\partial s} \int_{\Omega} u(\mathbf{x}, s) \, \mathrm{d}\mathbf{x} = \int_{\Omega} \Delta \mathrm{u}(\mathbf{x}, \mathrm{s}) \, \mathrm{d}\mathbf{x} = \int_{\partial\Omega} \frac{\partial \mathrm{u}}{\partial \mathrm{n}} \, \mathrm{d}\sigma = 0 \ . \tag{2.5}$$

   As a result average grey-value is maintained for all α scale spaces, since all α scale spaces have a common complete orthonormal base of eigenfunctions including the constant function with corresponding eigenvalue $0 = -(0)^{\alpha}$, see the third item of this list.

2. The Neumann boundary condition is essential for monotonic increase of entropy, which can be shown for the Poisson $\alpha = 1/2$ and Gaussian case $\alpha = 1$.

   - For Gaussian scale space, we have for $f > 0$, by Green's second identity(2.4):

   $$\begin{aligned}\tfrac{\partial}{\partial s}[\mathcal{E}(u)](s) &= -\int_\Omega \Delta u(\log u + 1)\ \mathrm{d}\mathbf{x} = -\int_\Omega \Delta \mathrm{u}(\log \mathrm{u})\ \mathrm{d}\mathbf{x} \\ &= -\int_\Omega u \operatorname{div}\left(\tfrac{\nabla u}{u}\right)\ \mathrm{d}\mathbf{x} = \int_\Omega \left(\tfrac{\|\nabla \mathrm{u}\|^2}{\mathrm{u}}\right)\ \mathrm{d}\mathbf{x} \geq 0\ .\end{aligned}$$

   - For Poisson scale space: Follow the proof of Theorem 5.3 in [30] use Ω in stead of $\mathbb{R}^d$ and notice that the right hand side of Green's first identity vanishes because of the Neumann boundary condition.

3. The eigenvalue problem

   $$\begin{cases} \Delta f = \lambda f \\ \frac{\partial f}{\partial n} = 0 \end{cases} \qquad f \in C^2(\Omega) \cap C^1(\overline{\Omega}) \tag{2.6}$$

   is equivalent to the eigenvalue problem:

   $$\mathcal{K}f = -\frac{1}{\lambda} f, \quad f \in \mathbb{L}_2(\mathbb{R}^d), \tag{2.7}$$

   where the kernel operator $\mathcal{K} : \mathbb{L}_2(\Omega) \to \mathbb{L}_2(\Omega)$ is given by

   $$\mathcal{K}(f)(\mathbf{x}) = (N_{\mathbf{x}}(\cdot), f(\cdot))_{\mathbb{L}_2(\Omega)} = \int_\Omega N(\mathbf{x}, \mathbf{y}) f(\mathbf{y})\ \mathrm{d}\mathbf{y} \qquad \text{for almost every } \mathbf{x} \in \mathbb{R}^{\mathrm{d}}\ ,$$

   where N is the function of Neumann on Ω, i.e. the sum $N(\mathbf{x}, \mathbf{y}) = S(\mathbf{x}, \mathbf{y}) + h(\mathbf{x}, \mathbf{y})$, of the fundamental solution S and a function h, which is the unique solution (up to a constant) of:

   $$\begin{aligned} \Delta_{\mathbf{x}} h(\mathbf{x}, \mathbf{y}) &= 0 && \mathbf{y} \in \Omega \\ \tfrac{\partial h}{\partial n} &= -\tfrac{\partial S}{\partial n} - 1/\mu(\partial\Omega) && \mathbf{y} \in \Omega\ . \end{aligned}$$

   If we would have worked with Dirichlet boundary conditions, such equivalence can be obtained using Green's function in stead of Neumanns function as a kernel for the kernel operator $\mathcal{K}$. Analogue to the Dirichlet problem, where the solution can be represented by $f(\mathbf{y}) = -\int_\Omega G(\mathbf{x}, \mathbf{y}) \Delta f\ \mathrm{d}\mathbf{x}$, where G denotes Green's function, the solution of the Neumann problem is given by

   $$f(\mathbf{y}) = -\int_\Omega N(\mathbf{x}, \mathbf{y})(\Delta f)(\mathbf{x})\ \mathrm{d}\mathbf{x} + \frac{1}{\mu(\partial\Omega)} \int_{\partial\Omega} \mathrm{f}(\mathbf{x})\ \mathrm{d}\sigma\ ,\ \mathbf{y} \in \Omega$$

   see [71]p.232-235 for a formal treatment.[1] Further we notice that the Neumann problem has a unique solution up to a constant, therefore the second term in the right hand side is not essential. By this result and the uniqueness of the Neumann problem (up to constants) we indeed find that system (2.7) follows from system (2.6). The reverse (in particular the twice continuously differentiable property of f) is more difficult to

[1] These results can be obtained in a heuristic way by substituting Green's and Neumann's function in Green's second identity and using $\Delta S(\cdot, \mathbf{y}) = -\delta_{\mathbf{y}}$.

show since it is due to Weyl's lemma, cf. [71] p.225-226, p.200. Operator $\mathcal{K}$ is positive and self-adjoint $\mathcal{K}^* = \mathcal{K}$ since $N(\mathbf{y},\mathbf{x}) = N(\mathbf{x},\mathbf{y})$, which is due to the symmetry of the fundamental solution $S(\mathbf{x},\mathbf{y}) = S(\mathbf{y},\mathbf{x})$:

$$\begin{aligned}(\mathcal{K}f, g)_{\mathbb{L}_2(\Omega)} &= \int_\Omega \overline{(\mathcal{K}f)(\mathbf{x})} g(\mathbf{x})\, \mathrm{d}\mathbf{x} \\ &= \int_{\Omega\times\Omega} N(\mathbf{y},\mathbf{x})\overline{f(\mathbf{x})} g(\mathbf{y})\, \mathrm{d}\mathbf{x}\, \mathrm{d}\mathbf{y} \\ &= \int_\Omega \overline{f(\mathbf{x})} \int_\Omega N(\mathbf{y},\mathbf{x}) g(\mathbf{y})\, \mathrm{d}\mathbf{x}\, \mathrm{d}\mathbf{y} \\ &= \int_\Omega \overline{f(\mathbf{x})} \int_\Omega N(\mathbf{x},\mathbf{y}) g(\mathbf{y})\, \mathrm{d}\mathbf{x}\, \mathrm{d}\mathbf{y} = (\mathrm{f}, \mathcal{K}\mathrm{g})_{\mathbb{L}_2(\Omega)}\ ,\end{aligned}$$

for all $f, g \in \mathbb{L}_2(\Omega)$.

Moreover, operator $\mathcal{K}$ is compact since every Hilbert-Schmidt operator[2] is compact, [3] p.190, 202. We will now show that $\mathcal{K}$ is indeed a Hilbert-Schmidt operator, i.e. an operator with finite double-norm,

$$\begin{aligned}|||\mathcal{K}||| &= \left[\sum_{i=1}^{\infty} \|\mathcal{K}\phi_i\|_{\mathbb{L}_2(\Omega)}\right]^{1/2} \\ &= \left[\sum_{i=1}^{\infty} \int_\Omega |(\mathcal{K}\phi_i)(\mathbf{x})|^2\, \mathrm{d}\mathbf{x}\right]^{1/2} \\ &= \left[\int_\Omega \sum_{i=1}^{\infty} |(N(\mathbf{x},\cdot), \phi_i)_{\mathbb{L}_2(\Omega)}|^2\, \mathrm{d}\mathbf{x}\right]^{1/2} \\ &= \left[\int_{\Omega\times\Omega} |N(\mathbf{x},\mathbf{y})|^2\, \mathrm{d}\mathbf{x}\, \mathrm{d}\mathbf{y}\right]^{1/2} \\ &\leq \left[\int_{\Omega\times\Omega} |S(\mathbf{x},\mathbf{y})|^2\, \mathrm{d}\mathbf{x}\, \mathrm{d}\mathbf{y}\right]^{1/2} + \left[\int_{\Omega\times\Omega} |h(\mathbf{x},\mathbf{y})|^2\, \mathrm{d}\mathbf{x}\, \mathrm{d}\mathbf{y}\right]^{1/2} < \infty \text{ if } d \leq 3\end{aligned} \tag{2.8}$$

for any complete orthonormal base $\{\phi_i\}_{i\in\mathbb{N}}$ in $\mathbb{L}_2(\Omega)$. Some remarks with respect to (2.8):

- The last equality is Bessel's equality which is valid for every complete orthonormal base.
- The first inequality is the triangle equality and is due to Minkowski's inequality.
- The second integral in the last expression is finite since Ω is bounded and h is continuous on Ω. If one uses spherical coordinates around the singularity to express the first integral within the first integral one obtains $O(\frac{1}{r^{2(d-2)}})O(r^{d-1}) = O(r^{-d+3})$, which is finite if $d \leq 3$.

From a fundamental result from functional analysis it now follows that there exists a complete (countable) set of eigen functions $\{f_n\}_{n\in\mathbb{N}}$, with positive eigenvalues μ_n which tend to zero as $n \to \infty$, cf. [131]p.167. By the equivalence between eigenvalue problems (2.6) and (2.7) these eigen functions are also the eigen functions of the generator of the Gaussian semi-group with corresponding eigenvalues $\lambda_n = -\frac{1}{\mu_n} < 0$ (tending to minus infinity as $n \to \infty$) and thereby these functions f_n are the eigen images of the Gaussian

[2]Operator $\mathcal{K}$ is also compact for the cases $d \leq 3$, but it is no longer a Hilbert Schmidt operator.

evolution operator $\Phi_1 : \mathbb{L}_2(\Omega) \times \mathbb{R}^+ \to \mathbb{L}_2(\Omega)$ with Neumann boundary conditions with eigenvalues $e^{\lambda_n s}$ (tending to 0 as $n \to \infty$):

$$u_1(\cdot, s) = \Phi_1[f, s] = \sum_{n \in \mathbb{N}} \Phi_1[f_n](f_n, f) = \sum_{n \in \mathbb{N}} f_n (f_n, f) e^{\lambda_n s} \ .$$

Taking the α-th power of the Gaussian generator now becomes fairly easy by taking the α-th power of the eigenvalues. As a result the α scale space operator on a bounded domain with Neumann boundary conditions is given by:

$$u_\alpha(\cdot, s) = \Phi_\alpha[f, s] = \sum_{n \in \mathbb{N}} \Phi_\alpha f_n (f_n, f) = \sum_{n \in \mathbb{N}} f_n (f_n, f) e^{-(-\lambda_n)^\alpha s} \ . \tag{2.9}$$

In contrast to the unbounded domain case, it is now relatively easy to compare the α scale spaces. To this end we notice that the scale s in the α scale space has a physical dimension that depends on α: $[s] = [\text{Length}]^{2\alpha}$. In the bounded domain we can define a dimensionless scale parameter which we will call relative scale $s_\alpha = \frac{s}{\rho^{2\alpha}}$, where ρ equals the radius of the smallest sphere around Ω.

In the next two subsections we will focus on the special cases where Ω is a rectangle respectively a disc. The first case is interesting purely from a pragmatic point of view, since in computer vision images are mostly rectangles and Euclidean coordinates are relatively easy to handle. Although the disc case is less pragmatic, it is still operational and from the theoretical point of view it is a better approach in the sense that rotational invariance axiom is satisfied. Moreover, with respect to human vision a disc seems more natural than the rectangle.

2.2 The Rectangle Case

By the method of separation $u_\alpha(x, y, s) = X(x)Y(y)G(s)$ we can find the orthonormal base of eigen images of all α scale spaces on a rectangle with Neumann boundary conditions, whose existence for the general domain case has been shown earlier in this section. First we will focus on the Gaussian case and then take the α powers of the eigenvalues to obtain the other cases.

$$\frac{X''(x)}{X(x)} + \frac{Y''(y)}{Y(y)} = \frac{G'(s)}{G(s)} = \lambda \qquad \lambda < 0,\ s > 0,\ x \in (0, a),\ y \in (0, b) \tag{2.10}$$

and by the initial condition it again follows that $G(s) = e^{\lambda s}$.

$$-\frac{X''(x)}{X(x)} + \lambda = \frac{Y''(y)}{Y(y)} = \mu \qquad \mu \in \mathbb{R}. \tag{2.11}$$

To satisfy the Neumann boundary condition we must have:

$$\begin{aligned} Y'(b) = Y'(0) = 0 \\ X'(a) = X'(0) = 0 \end{aligned} \tag{2.12}$$

From the Sturm-Liouville theory it follows that $\mu \leq 0$. The case $\mu = 0$ gives $Y_0(y) = 1$. The case $\mu < 0$ leads to $Y_n(y) = \cos\left(\frac{n\pi y}{b}\right)$ with $n \in \mathbb{N}$, with eigenvalues $\mu_n = -\left(\frac{n\pi}{b}\right)^2$. Substituting

these eigenvalues into (2.11) one also obtains a standard Sturm-Liouville problem for X, which leads to the eigenvalues of the generator of the Gaussian (α=1) evolution problem

$$\lambda_{mn} = -\left\{ \left(\frac{n\pi}{b}\right)^2 + \left(\frac{m\pi}{a}\right)^2 \right\} \qquad n, m = 0, 1, 2, \ldots \tag{2.13}$$

with corresponding eigenfunctions $(x, y) \mapsto \cos\left(\frac{n\pi x}{a}\right)\cos\left(\frac{n\pi y}{b}\right)$, $n, m = 1, 2, \ldots$. So again u_α can be written

$$u_\alpha(x, y, s) = A_{00} + \sum_{n,m=1}^{\infty} A_{nm} \cos\left(\frac{m\pi x}{a}\right)\cos\left(\frac{n\pi y}{b}\right) \; e^{-\left\{\left(\frac{n\pi}{b}\right)^2+\left(\frac{m\pi}{a}\right)^2\right\}^\alpha s} \qquad \alpha \in (0, 1]. \tag{2.14}$$

Although this point wise notation might seem a bit deceptive, but under Dirichlet conditions on f this series converges point wise and uniformly in $\mathbf{x}$ on $[0, a] \times [0, b]$. The constants are uniquely determined and can be found by expanding f in a double Fourier cosine series.

Theorem 11 *The general solution of the α evolution problem with Neumann boundary condition on a rectangle $[0, a] \times [0, b]$ is given by:*

$$\begin{aligned} &u_\alpha^{(a,b)}(x, y, s) = \sum_{m=0}^{\infty}\sum_{n=0}^{\infty} \left(\int_0^a \int_0^b f(x', y')\, l_{mn}(x', y')\, \mathrm{dx'}\, \mathrm{dy'} \right) l_{mn}(x, y)\; e^{-\left\{\left(\frac{n\pi}{b}\right)^2+\left(\frac{m\pi}{a}\right)^2\right\}^\alpha s} \\ &\alpha \in (0, 1], a > 0, b > 0, \end{aligned} \tag{2.15}$$

where $l_{mn} : \mathbb{R}^2 \to \mathbb{R}$ is given by

$$l_{mn}(x, y) = \frac{2\cos\left(\frac{m\pi x}{a}\right)\cos\left(\frac{n\pi y}{b}\right)}{\sqrt{ab(1+\delta_{m0})(1+\delta_{n0})}} \; .$$

Notice that $\{l_{mn}\}_{\mathbb{L}_2(\Omega)}$ indeed is a complete orthonormal base for $\mathbb{L}_2([0, a] \times [0, b])$. Therefore the series in (2.15) converges in $\mathbb{L}_2$-sense. Under weak (Dirichlet) conditions it also converges pointwise and uniformly. The separation constants $\left\{ \left(\frac{n\pi}{b}\right)^2 + \left(\frac{m\pi}{a}\right)^2 \right\}$ are the eigenvalues of the Gaussian generator. The relative scale is given by $s_\alpha = \frac{2^{2\alpha}s}{(a^2+b^2)^\alpha}$. It indeed follows by (2.15) that the only difference between the α scale spaces on a square is the relative contribution of each eigen mode to the evolution proces.

2.2.1 The Unbounded Domain Case as a Limit of the Rectangular Case.

We will show that if $a, b \to \infty$ the discrete solution $u_\alpha^{(a,b)}(x, y, s)$ converges to the convolution $u^{(\alpha)}(x, y, s) = (K_s^{(\alpha)} * f^{ev})(x, y)$, where $f^{ev} : \mathbb{R}^2 \to \mathbb{R}$ is the even extension of $f : [0, a]\times[0, b] \to \mathbb{R}$ with support on $[-a, a] \times [-b, b]$. This convolution can be rewritten

$$\begin{aligned} &(f^{ev} * K_s^{(\alpha)})(x, y) = \mathcal{F}^{-1}[\mathcal{F}(f^{ev} * K_s^{(\alpha)})](x, y) = \mathcal{F}^{-1}\left[\boldsymbol{\omega} \mapsto e^{-\|\boldsymbol{\omega}\|^{2\alpha}s}[\mathcal{F}(f^{ev})](\omega_1, \omega_2)\right](x, y) \\ &\tfrac{1}{4\pi^2}\int_{\mathbb{R}}\int_{\mathbb{R}} e^{-\|\boldsymbol{\omega}\|^{2\alpha}s} \left(\int_{\mathbb{R}}\int_{\mathbb{R}} f^{ev}(x', y')\, e^{-i\omega_1 x' - i\omega_2 y'}\, \mathrm{dx'}\, \mathrm{dy'} \right) e^{i\omega_1 x + i\omega_2 y}\, \mathrm{d}\omega_1\, \mathrm{d}\omega_2 \end{aligned} \tag{2.16}$$

Since $(f^{ev} * K_s^{(\alpha)})$ is both even in x and y the last e-power can be replaced by a cosine. The first e-power is even in ω, but this means that the second e-power can also be replaced by a cosine, i.e. (2.16) can be written

$$\frac{1}{4\pi^2}\int\limits_{\mathbb{R}^2} e^{-\|\boldsymbol{\omega}\|^{2\alpha}s}\left(\int\limits_{\mathbb{R}^2} f^{ev}(x',y')\,\cos(\omega_1 x')\cos(\omega_2 y')\,\mathrm{dx}'\,\mathrm{dy}'\right)\cos(\omega_1 x)\cos(\omega_2 y)\,\mathrm{d}\omega_1\,\mathrm{d}\omega_2 \quad (2.17)$$

This integral equals the following Riemann sum, sampled equidistantly in $\boldsymbol{\omega}_{nm} = (\omega_{1m}, \omega_{2n}) = (\frac{m\pi}{a}, \frac{n\pi}{b})$, $m, n\mathbb{Z}$ and using the fact that $\mathrm{supp}(f^{ev}) \subseteq [-a,a]\times[-b,b]$ we indeed obtain

$$\lim_{a\to\infty}\lim_{b\to\infty}\sum_{m=0}^{\infty}\sum_{n=0}^{\infty}(f, l_{mn})_{\mathbb{L}_2([0,a]\times[0,b])} l_{mn}(x,y)\; e^{-\left\{\left(\frac{n\pi}{b}\right)^2+\left(\frac{m\pi}{a}\right)^2\right\}^{\alpha}s}. \quad (2.18)$$

2.3 The Disc Case

The α evolution equation with Neumann boundary condition described in cylindrical coordinates on the disc is given by:

$$\begin{cases} \frac{\partial u}{\partial s} & = -(-\Delta)^{\alpha}u \qquad r = \|\mathbf{x}\| \le a, s > 0 & \text{Evolution Equation} \\ \frac{\partial u}{\partial r}\big|_{r=a} & = 0 & \text{Boundary Condition} \\ u(r,\phi,0) & = f(r,\phi) & \text{Initial Condition} \end{cases} \quad (2.19)$$

Obviously, we do not want u to explode to infinity if s tends to infinity and therefore we impose the additional constraint that u is finite at $r = 0$ or at least locally in $\mathbb{L}_2$. In the sequel we will denote these additional constraints with (AC). Again we first solve (2.19) for the particular case $\alpha = 1$ (diffusion equation) and obtain the general case simply by taking a fractional power of the eigenvalues. In polar coordinates we have

$$\frac{\partial u}{\partial s} = \frac{\partial^2 u}{\partial r^2} + \frac{1}{r}\frac{\partial u}{\partial r} + \frac{1}{r^2}\frac{\partial^2 u}{\partial \phi^2}\ . \quad (2.20)$$

Note that the homogeneous part of (2.19) is given by evolution equation, the Neumann boundary condition and (AC). Therefore we first construct a complete set of orthogonal eigen functions of the linear solution space of this part of our evolution system and then take care of the non-homogeneous part, i.e. the initial condition.

Separating $u(r,\phi,s) = R(r)S(s)\Phi(\phi)$, gives us

$$\frac{R''(r)}{R(r)} + \frac{1}{r}\frac{R'(r)}{R(r)} + \frac{\Phi''(\phi)}{r^2\Phi(\phi)} = \frac{S'(s)}{S(s)} = \lambda \in \mathbb{R}\ . \quad (2.21)$$

So $S(s) = e^{\lambda s}$ and

$$\frac{r^2\,R''(r)}{R(r)} + \frac{r\,R'(r)}{R(r)} - \lambda r^2 = -\frac{\Phi''(\phi)}{\Phi(\phi)} = \mu \in \mathbb{R}\ , \quad (2.22)$$

Since we have $\Phi(0) = \Phi(2\pi)$ it now follows that $\mu = m^2$, $m \in \mathbb{Z}$ and we find the two independent solutions

$$\begin{aligned} \Phi_m^{(1)}(\phi) &= e^{i\,m\,\phi} \\ \Phi_m^{(2)}(\phi) &= e^{-i\,m\,\phi} \end{aligned} \quad (2.23)$$

Since we are interested in linearly independent solutions we may as well work with one function $\eta_m : (-\pi, \pi] \to \mathbb{C}$ defined by $\eta_m(\phi) = e^{i\,m\,\phi}$, with $m \in \mathbb{Z}$.

With respect to λ we must observe the following cases:

- $\lambda = 0$.
  - and $m = 0$: The solution of the Euler ordinary differential equation reads $R(r) = A + B \log r$, but due to the boundary condition B must be zero so we find the single independent solution $R_0^0(r) = 1$.
  - and $m \neq 0$: This leads to the Euler ordinary differential equation $r^2\,R''(r) + r\,R'(r) - m^2 R(r) = 0$, with independent solutions $R_m^{0,(1)}(r) = r^m$, $R_m^{0,(2)}(r) = r^{-m}$. The latter doesn't contribute to the solution space since we imposed (A.C.) and the first doesn't satisfy the boundary condition.
- $\lambda = -p^2 \neq 0$. Set $q = pr$, then $\frac{\partial}{\partial q} = \frac{1}{p}\frac{\partial}{\partial r}$, so if we define $\tilde{R} : \mathbb{R} \to \mathbb{R}$, by $\tilde{R}(q) = R(r)$ we arrive at Bessel's ordinary differential equation:

$$q^2\,\tilde{R}''(q) + q\,\tilde{R}'(q) + (q^2 - m^2)\tilde{R}(q) = 0\ . \tag{2.24}$$

As every linear second order differential equation this equation has two linear independent solutions, $J_m(q)$ and $Y_m(q)$. The latter doesn't satisfy (A.C.) so we will only need the Bessel functions of the first kind: $R_m^{-p^2} = J_m(pr)$, with $m = 0, 1, 2, \ldots$. The Bessel functions of the first kind are given by

$$J_m(z) = \sum_{k=0}^{\infty} \frac{(-1)^k}{k!\Gamma(m+k+1)} \left(\frac{z}{2}\right)^{2k-m} \qquad m \in \mathbb{Z}\ z \in \mathbb{C}. \tag{2.25}$$

One might think that the cases $m = -1, -2, \ldots$ must be excluded because of (A.C.), but this is not true, since $\Gamma(-m + w + 1)$ has poles in $w = 0, 1, \ldots, m-1$:

$$\frac{1}{\Gamma(-m+k+1)} = \begin{cases} 0 & ,k = 0, 1, 2, \ldots, m-1, \\ \frac{1}{(k-m)!} & ,k = m, m+1, \ldots\ , \end{cases}$$

so,

$$\begin{aligned} J_{-m}(z) \ &= \sum_{k=m}^{\infty} \tfrac{(-1)^k}{k!(k-m)!} \left(\tfrac{z}{2}\right)^{2k-m} = \\ &\sum_{k=0}^{\infty} \tfrac{(-1)^{k+m}}{k!(k+m)!} \left(\tfrac{z}{2}\right)^{m+2k} = (-1)^m J_m(z) \end{aligned} \tag{2.26}$$

and thereby J_m and J_{-m} are linearly dependent.

The boundary condition (B.C.) gives us the discrete possibilities

$$p_{m,n} = \frac{j'_{m,n}}{a} \Leftrightarrow \lambda_{m,n} = -\left(\frac{j'_{m,n}}{a}\right)^2, \tag{2.27}$$

where $j'_{m,n}$ equals the nth positive zero of $J'_m(r)$. These simple zeros lie around the ones of $J_m(r)$ and the distance between $j'_{m,n+1}$ and $j'_{m,n}$ tends quickly to π. There is no need to regard negative zero's since by $J_m(-z) = (-1)^m\,J_m(z)$ we have $j_{m,-n} = -j_{m,n}$, so that no new independent solutions would be obtained.

Therefore the solutions of the homogeneous part of the $\alpha = 1$(diffusion) evolution problem can now be written:

$$u_1(r,\phi,s) = f_{AV} + \sum_{m\in\mathbb{Z}}\sum_{n\in\mathbb{N}} C_{mn}\, J_m(j'_{m,n}\frac{r}{a})\, e^{i\,m\,\phi}\, e^{-\left(\frac{j'_{m,n}}{a}\right)^2 s}. \tag{2.28}$$

where $C_{ij} \in \mathbb{C}$ are constants, which will turn out to be uniquely determined by the non-homogeneous initial condition.

Define $h_{mn} : (0,a)\times(\pi,\pi] \to \mathbb{C}$, $m \in \mathbb{Z}, n \in \mathbb{N}$ by

$$h_{mn}(r,\phi) = \frac{1}{a\sqrt{\pi\left(1-\left(\frac{m}{j'_{m,n}}\right)^2\right)}}\, \frac{J_m(j'_{m,n}r/a)}{J_m(j'_{m,n})}\, e^{i\,m\,\phi}\ , \tag{2.29}$$

where the Bessel functions of the first kind are given by (2.25). Note that $h_{mn} = \overline{h_{-mn}}$. Define $h_{00} : (0,a)\times(\pi,\pi] \to \mathbb{C}$, by $h_{00}(r,\phi) = \frac{1}{\sqrt{\pi}a}$.

Theorem 12 *The set* $\{h_{mn}\}_{m\in\mathbb{Z},n\in\mathbb{N}\cup\{0\}}$ *is a complete orthonormal base of* $\mathbb{L}_2(B_{\mathbf{0},a}) = \mathbb{L}_2(S_1)\otimes \mathbb{L}_2((0,a),rdr)$ *and they are eigen functions of the infinitesimal generator of evolution system (2.19) with corresponding eigenvalue* 0 *respectively* $-(\frac{j_{m,n}}{a})^{2\alpha}$.
The general solution of (2.19) is given by:

$$\begin{aligned} u_\alpha(r,\phi,s) &= \sum_{m=-\infty}^{\infty}\sum_{n=0}^{\infty}(f,h_{mn})_{\mathbb{L}_2(B_{\mathbf{0},a})}h_{mn}(r,\phi)\, e^{-\left(\frac{j'_{m,n}}{a}\right)^{2\alpha}s} = \\ f_{AV} &+ \sum_{m\in\mathbb{Z}}\sum_{n\in\mathbb{N}} \frac{\left[\int_0^a\int_{-\pi}^{\pi} f(\rho,\theta)\, J_m(j'_{m,n}\frac{\rho}{a})\, e^{i\,m\,\theta}\, \rho\,\mathrm{d}\rho\,\mathrm{d}\theta\right]}{a^2 J_m^2(j'_{m,n})\pi\left(1-(\frac{m}{j'_{m,n}})^2\right)}\, J_m(j'_{m,n}\tfrac{r}{a})\, e^{i\,m\,\phi}\, e^{-\left(\frac{j'_{m,n}}{a}\right)^{2\alpha}s}. \end{aligned} \tag{2.30}$$

Proof
The proof follows from the method of separation (see above) since the separation constants are the eigenvalues of the generator and the corresponding functions the eigen functions of the generator. We have already shown for the general case Ω open bounded subset of $\mathbb{R}^d$ that these eigenfunctions form a complete orthonormal base of $\mathbb{L}_2(\Omega)$. So this completes the proof. □

For explicit verification of the fact that the eigenfunctions h_{mn} form a complete orthonormal base, we refer to [25].
Remarks:

- We have shown in general, cf. (2.5), that average grey-value f_{AV} is maintained. If s tends to infinity u indeed tends to $\frac{h_{00}(r,\phi)}{\sqrt{\pi}a}(f,h_{00})_{\mathbb{L}_2(B_{\mathbf{0},a})} = f_{AV}$.
- Under minor conditions the series also converges point-wise and uniformly, cf. [126] pp.591 sec 18-24.

- The physical dimension of the evolution parameter within the αth scale space s equals $[\text{Length}]^{2\alpha}$, so the exponent in (2.30) has no physical dimension. The *relative scale* in the disc case is given by $s_\alpha = \frac{s}{a^{2\alpha}}$.
- By $j'_{-m,n} = j'_{m,-n} = -j'_{-m,-n} = -j'_{m,n}$ we have $\overline{h_{mn}} = h_{-mn}$. From this it follows that $\overline{c_{mn}} = c_{-mn}$ if f is real valued. Moreover we have $j'_{m,0} = 0 \Leftrightarrow m \neq 0$. So then we have

$$u_\alpha(r,\phi,s) = f_{AV} + 2\sum_{m=1}^{\infty}\sum_{n=1}^{\infty} \text{Re}\left[(h_{mn}, f)_{\mathbb{L}_2(B_{\mathbf{0},a})} h_{mn}(r,\phi)\right]\ e^{-\left(\frac{j'_{m,n}}{a}\right)^{2\alpha} s}.$$

- It is shown in [25] that if the radius a of the disc tend to infinity one obtains the usual α scale spaces and corresponding convolution kernels given by (1.8).

2.4 The Monogenic Scale Space on a Bounded Domain and its Application in Phase-Based Image processing

The main conceptual advantage of Poisson scale space over Gaussian scale space is that there exists a Clifford analytic extension of this scale space, consisting of $d+1$-components. The first component of this Clifford analytic scale space equals the Poisson scale space and the vector function consisting of the remaining d components is the grey-value flow (obtained by the Riesz transform $\mathbf{R}$) within this Poisson scale space. This corresponds to the first order yet of a Gaussian scale space, simply because of the Gauss divergence theorem and $\Delta = \nabla \cdot \nabla$ and $-\sqrt{-\Delta} = \nabla \cdot \mathbf{R}$, recall Subsection 1.4.2.2 and in particular (1.36). Therefore many practical methods in Gaussian scale spaces directly relate to methods in Poisson scale simply by replacing the role of $\nabla \leftrightarrow \mathbf{R}$.

However, the advantage of a Clifford analytic extension lies within the Cauchy-Riemann equations that hold for Clifford analytic extension, see (2.35) and the fact the logarithm of an analytic function is again analytic.

The logarithm of the monogenic scale space representation of an image f yields a smooth multi-scale representation of the local attenuation A (local amplitude e^A) and local phase vector field $\mathbf{r}$

$$\begin{array}{ll} (A,\mathbf{r}) & = \log(u,\mathbf{R}u) = \left(\log\sqrt{|u|^2+\|\mathbf{R}u\|^2}, \frac{\mathbf{R}u}{\|\mathbf{R}u\|}\arctan\frac{\|\mathbf{R}u\|}{u}\right) \Leftrightarrow \\ (u,\mathbf{R}u) & = e^{A\mathbf{r}} = e^A\left(\cos\|\mathbf{r}\|, \frac{\mathbf{r}}{\|\mathbf{r}\|}\sin\|\mathbf{r}\|\right). \end{array} \tag{2.31}$$

In case of signals ($d=1$), we have $\log(w) = \int_1^w \frac{1}{w}\text{dw} = |\log w| + i\arg w$, where we made a cut along the negative real axis to obtain the main value of the log, and where $w = f(z) = |w|e^{i\arg w}$. In practical signal processing the local phase and local amplitude are often obtained by taking the logarithm of a windowed Fourier transform of a signal evaluated at the frequency that fits within the window. The drawback here is that the window size introduces an inappropriate measure of scale, resulting in an ill-posed multi-scale local phase. With this respect (2.31) after computing the analytic scale space with the 1D-Poisson kernel and its conjugate (1.44) is highly preferable. In this case the logarithm of the analytic scale space $u_A(x,s) = (H_s *$

$f)(x) + i(Q_s * f)(x)$, yields a decomposition in local phase and local amplitude: $\log u_A(x,s) = A(x,s) + i\, r(x,s) = \log|u_A(x,s)| + i \arg u_A(x,s)$. Since the logarithm of an analytic function is again analytic, it satisfies the Cauchy-Riemann equations:

$$\begin{aligned} A_x &= r_s, \\ A_s &= -r_x. \end{aligned} \tag{2.32}$$

From these equations we deduce that the scale derivative A_s of the local attenuation equals the local frequency r_x. Moreover, local amplitude maxima are points of phase congruency, i.e.

$$A_x(x,s) = 0 \Leftrightarrow r_s(x,s) = 0. \tag{2.33}$$

From the physical point of view this makes sense, as on an edge the phase is typically maintained over scale.

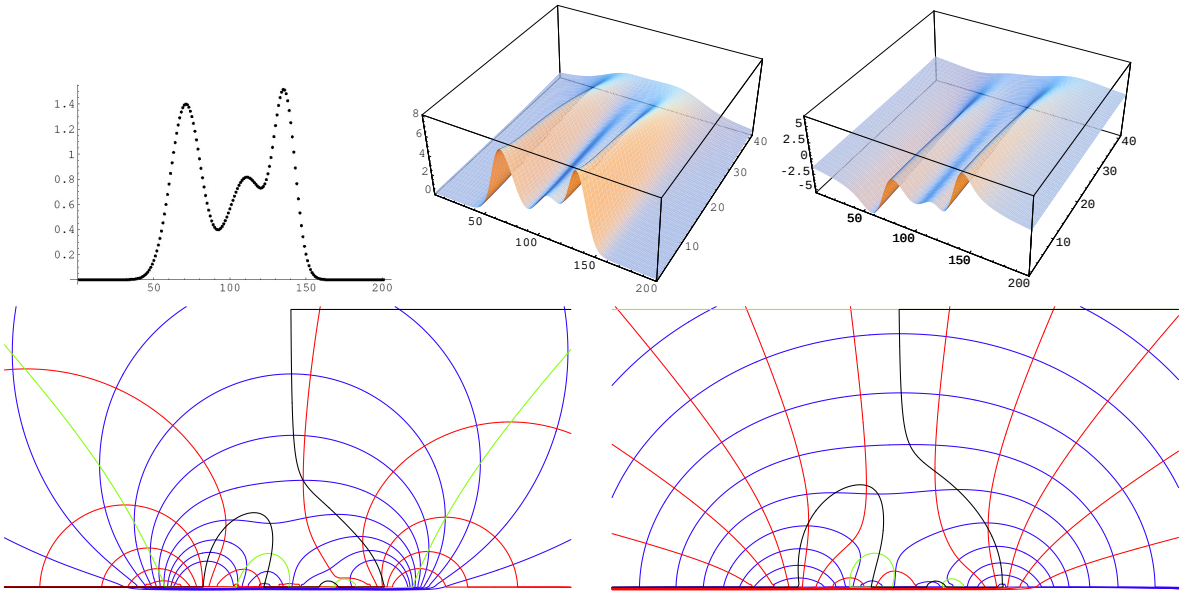

Figure 2.1: Top row, from left to right, original signal, Poisson scale space of original signal, Conjugate Poisson scale space of original signal. Bottom row, from left to right: Deep-structure (critical curves and isophotes) in respectively analytic scale space and in logarithm of analytic scale space.

In image analysis $d > 1$ the local phase is a vector-field. If the image (or rather the blurred image $u(\cdot,s) = H_s * f$) is *locally 1D* at $\mathbf{x}$, i.e. there exists a smooth $g : [-\epsilon, \epsilon] \to \mathbb{R}$ such that $f(\mathbf{x}) = g(\mathbf{n} \cdot \mathbf{x})$, the length of the phase vectors gives the phase of the blurred image along the local orientation $\mathbf{n}(\mathbf{x}) \in \mathbb{R}^d$, with $\|\mathbf{n}(\mathbf{x})\| = 1$.

We shall now consider only the case $d = 2$, where we recall that in the unbounded domain the monogenic scale space is given by 3D vector space

$$\mathbf{u}_M(\mathbf{x},s) = (\mathbf{q}(\mathbf{x},s), p(\mathbf{x},s)) = \sum_{j=1}^{2} \mathbf{e}_j (Q^{(j)} * f)(\mathbf{x}) + \mathbf{e}_3 (H_s * f)(\mathbf{x}) \ ,$$

where we use short notation $p(\mathbf{x}, s) = u_f^{\alpha=\frac{1}{2}}(\mathbf{x}, s) = (H_s * f)(\mathbf{x})$ and $\mathbf{q}(\mathbf{x}, s) = [\mathbf{R}u(\cdot, s)](\mathbf{x})$.

The logarithm of a Clifford analytic function is in general not Clifford analytic. Nevertheless, if we again assume our image to be locally 1D, then the local phase vector field and the local attenuation form a Riesz triplet[42] and the generalized Cauchy-Riemann equations hold for $\tilde{v} = A + r^1\mathbf{e}_1\mathbf{e}_3 + r^2\mathbf{e}_2\mathbf{e}_3 \leftrightarrow \mathbf{v} = A\mathbf{e}_3 + r^1\mathbf{e}_1 + r^2\mathbf{e}_2$:

$$\begin{aligned} \nabla_3\tilde{v} = 0 \quad &\Leftrightarrow \nabla_3 \cdot (\tilde{v}\mathbf{e}_3) + \nabla_3 \wedge (\tilde{v}\mathbf{e}_3) = 0 + \mathbf{0} \\ &\Leftrightarrow \operatorname{rot}\mathbf{v} = \mathbf{0} \text{ and } \operatorname{div}\mathbf{v} = 0 \\ &\Leftrightarrow \begin{cases} \partial_x r_2 - \partial_y r_1 = \partial_x A - \partial_s r_1 = \partial_y A - \partial_s r_2 = 0 \\ \nabla_2 \cdot \mathbf{r} + \partial_s A = 0, \end{cases} \end{aligned} \tag{2.34}$$

which clearly is the 2D equivalent of (2.32).

Practical Consequences/Advantages:

- The main practical advantage of a phase vector field over for example the gradient field is that it is approximatively invariant under grey-value transformations of the type $\tilde{f}(\mathbf{x}) = \mu(\mathbf{x})f(\mathbf{x})$, $\mu : \mathbb{R}^2 \to \mathbb{R}$. To this end we notice that such a transformation leads to

  $$\tilde{u}_A(\mathbf{x}, s) = (H_s * \tilde{f} + \mathbf{R}H_s * \tilde{f})(\mathbf{x}) \approx \tilde{\mu}(\mathbf{x})\, u_A(\mathbf{x}, s),$$

  for some smooth $\tilde{\mu} : \mathbb{R}^2 \to \mathbb{R}$ and $s > 0$ sufficiently small, and obviously $\arg\{\tilde{\mu}(\mathbf{x})u_A(\mathbf{x}, s)\} = 0 + \arg(u_A(\mathbf{x}, s))$. This is in contrast to the gradient field where a locally constant μ gives $\nabla(\tilde{f}) = \mu\nabla f + f\nabla\mu \approx \mu\nabla f$. This makes phase-based image processing to a large extend invariant to changes of lighting conditions. For explicit practical examples, where this turns out to be beneficial we refer to Felsberg[43].

- Furthermore, phase-based image by means of the Monogenic scale space is claimed to be much more robust to noise than Gaussian derivative operators, cf. [42]. This makes also sense from the mathematical point of view: The Riesz-transform is a bounded operator from $\mathbb{L}_2(\mathbb{R}^d)$ to $\mathbf{L}_2(\mathbb{R}^d)$, where the Gradient is an unbounded operator[3] from $\mathbb{L}_2(\mathbb{R}^d)$ to $\mathbf{L}_2(\mathbb{R}^d)$.

- The local frequency is $\nabla_2 \cdot \mathbf{r}$ and is opposite to the scale derivative of local attenuation.

- Local amplitude maxima are points of phase congruency, recall (2.33). This can be used for example for multi-scale edge detection, see figure 2.2.

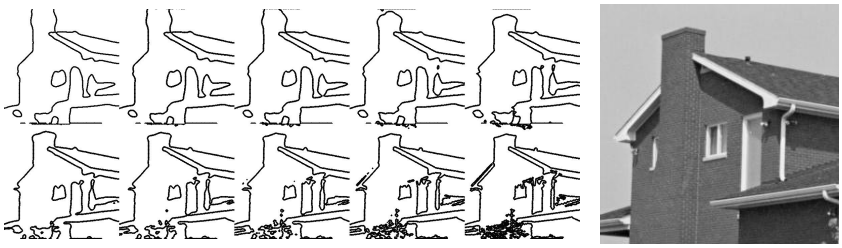

Figure 2.2: The phase congruency surface $\{(\mathbf{x}, s) \in \mathbb{R}^2 \times \mathbb{R}^+ \mid \frac{\partial \mathbf{r}}{\partial s}(\mathbf{x}, s) = 0\}$ in Poisson scale space describes the edge evolution through scale space.

[3] A Gaussian gradient is bounded, but the operator-norm of this operator is rather large at small scales.

2.4.1 Construction and Implementation of Monogenic Scale Space on a Bounded Domain

Just like the third component of the monogenic scale space which is the Poisson scale space will take the form of a scale dependent Fourier series on the bounded domain case, the first two components which describe the image flow within Poisson scale space will also become scale dependent Fourier series solutions. By the generalized Cauchy-Riemann equations, recall (1.46), for $\tilde{u} = \mathbf{u}_M \mathbf{e}_3 = p + \sum_{j=1}^{2} q_j \mathbf{e}_j \mathbf{e}_3$, where $\mathbf{u}_M = \tilde{u}\mathbf{e}_3 = p\mathbf{e}_3 + \sum_{j=1}^{2} q_j \mathbf{e}_j$ equals the monogenic scale space, we have that

$$\begin{aligned} \nabla_3 \tilde{u} = 0 \quad &\Leftrightarrow \nabla_3 \cdot (\tilde{u}\mathbf{e}_3) + \nabla_3 \wedge (\tilde{u}\mathbf{e}_3) = 0 + \mathbf{0}, \\ &\Leftrightarrow \operatorname{rot} \mathbf{u} = \mathbf{0} \text{ and } \operatorname{div} \mathbf{u} = 0 \\ &\Leftrightarrow \begin{cases} \partial_x q_2 - \partial_y q_1 = \partial_x p - \partial_s q_1 = \partial_y p - \partial_s q_2 = 0 \\ \nabla_2 \cdot \mathbf{q} + \partial_s p = 0 \end{cases} \end{aligned} \tag{2.35}$$

these q_j components will not satisfy the NBC condition at the boundary, which is easily understood since they describe the Poisson image flow and is illustrated in the next figure:

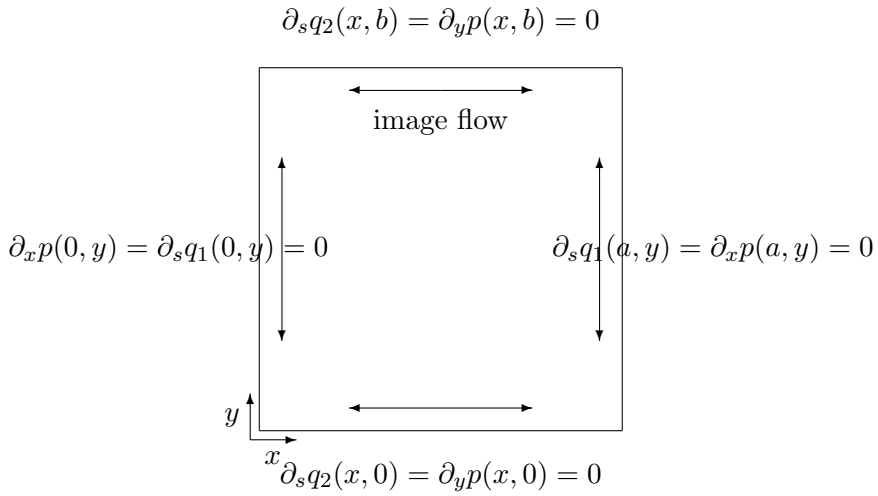

Boundary conditions monogenic scale space on rectangle $[0,a] \times [0,b]$

The field/flow-lines will become vertical when approaching the boundary $x = 0$ and $x = a$ in the upper plane $\{(x,s) : s > 0\}$. So by the generalized Cauchy Riemann equations it is not well posed to impose additional conditions on q_i at the boundary, in fact the monogenic scale space $u_M^{(a,b)}$ on a bounded domain Ω and in particular for the rectangle $\Omega = [0,a] \times [0,b]$ with no-flux boundary conditions is uniquely determined by the PDE system:

$$\begin{cases} \operatorname{rot} \mathbf{u}_M = \mathbf{0} \text{ and } \operatorname{div} \mathbf{u}_M = 0 \\ \lim_{s \downarrow 0} p(\cdot, s) = f(\cdot) \text{ in } \mathbb{L}_2(\Omega)\text{-sense} \\ \left. \frac{\partial p}{\partial n} \right|_{\partial\Omega} = 0 \ . \end{cases} \tag{2.36}$$

Here we will consider the rectangular case only, since the construction of monogenic scale space on a disc obtained by Clifford Analytic extension of the Poisson scale space on a disc, is not

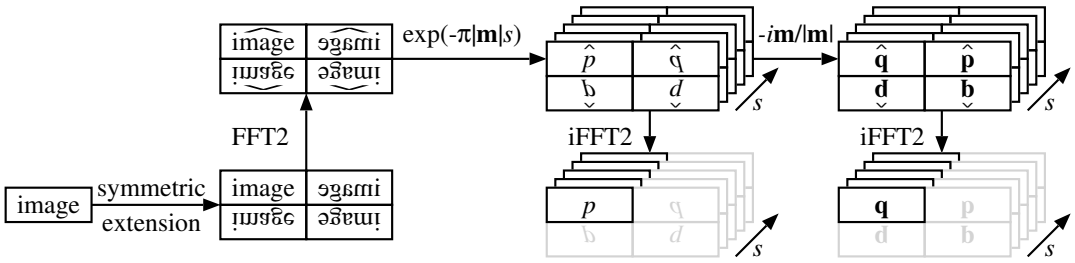

Figure 2.3: Algorithm for computing the monogenic scale space. The image is symmetrically extended. Applying FFT, multiplying the appropriate frequency responses, and applying the inverse FFT yields the Poisson scale space p and its image flow $\mathbf{q}$. Notice that $\mathbf{m} = \left(\frac{m}{a}, \frac{n}{b}\right)$.

that simple/practical as in the rectangular case, for details see Duits[25]ch:3.3.

Since we already determined the Poisson scale space on a rectangle, see (2.15), it is easy do determine the harmonic potential ψ by integration with respect to scale s, since $p = \partial_s \psi$,

$$\psi(\mathbf{x}, s) = \sum_{m=0}^{\infty} \sum_{n=0}^{\infty} \frac{(l_{mn}, f)_{\mathbb{L}_2([0,a]\times[0,b])}}{\pi \sqrt{\left(\frac{n}{b}\right)^2 + \left(\frac{m}{a}\right)^2}} l_{mn}(x, y)\, e^{-\pi \sqrt{\left(\frac{n}{b}\right)^2 + \left(\frac{m}{a}\right)^2} s} + C \ . \tag{2.37}$$

and the harmonic conjugates/image flow $\mathbf{q}$ are then obtained by:

$$\mathbf{q}(\mathbf{x}, s) = \nabla \psi(\mathbf{x}, s) = \sum_{m=0}^{\infty} \sum_{n=0}^{\infty} \frac{2(l_{mn}, f)_{\mathbb{L}_2([0,a]\times[0,b])}}{\sqrt{ab}\sqrt{\left(\frac{n}{b}\right)^2 + \left(\frac{m}{a}\right)^2}} \begin{pmatrix} \frac{m}{a} \sin\left(\frac{m\pi x}{a}\right) \cos\left(\frac{n\pi y}{b}\right) \\ \frac{n}{b} \cos\left(\frac{m\pi x}{a}\right) \sin\left(\frac{n\pi y}{b}\right) \end{pmatrix} e^{-\pi \sqrt{\left(\frac{n}{b}\right)^2 + \left(\frac{m}{a}\right)^2} s} , \tag{2.38}$$

where we notice that the summations over m and n in (2.37) and (2.38) should exclude the case $m = n = 0$ in which case the corresponding term does not exist.

Implementation:

If we extend the image symmetrically according to figure 2.3, then applying periodic boundary conditions to the original image yields the solution in the left upper part. The simple mathematical reason for this is that the extended image is even with respect to x and y which implies that the discrete Fourier transform of the symmetrically extended image is just the discrete cosine transform needed. The extended image is 4 times as large which costs more computation time, but this is more than compensated by the advantage of using the *fast* fourier transform. If $a, b \to \infty$ the discrete spectrum $\boldsymbol{\omega}_{mn} = \pi \mathbf{m}$ fills $\mathbb{R}^2$ and the continuous case is obtained. Notice that the Riesz transform $\mathbf{R}$ which maps p onto $\mathbf{q}$ in the continuous case boils down to a multiplication with $-i\frac{\boldsymbol{\omega}}{\|\boldsymbol{\omega}\|}$ in the Fourier domain, so the multiplication with $-i\frac{\mathbf{m}}{\|\mathbf{m}\|} = -i\frac{\boldsymbol{\omega}_{mn}}{\|\boldsymbol{\omega}_{mn}\|}$ can be regarded as the discrete Riesz transform. Notice that this indeed corresponds to(2.38), since for instance the first component of $-i\frac{\mathbf{m}}{\|\mathbf{m}\|}$, i.e. $-\frac{im}{a}\frac{1}{\|\mathbf{m}\|}$ is odd with respect m and even with respect to n which indeed leads to a sine in x-direction and cosine in y-direction.

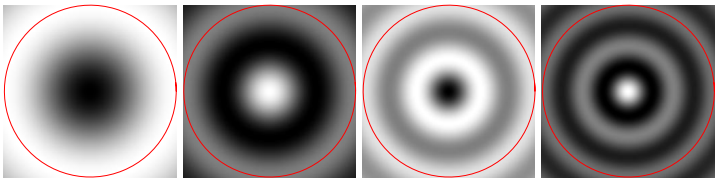

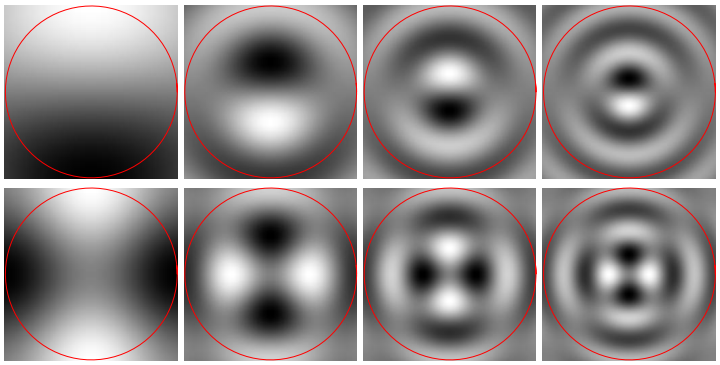

Figure 2.4: The real part of various evolution eigen modes h_{mn}, cf. (2.29), of the α scale spaces on a disc. Top row $m = 0$ and $n = 1, \dots 4$, middle row $m = 1$ for $n = 1 \dots 4$, bottom row $m = 2$ and $n = 1, \dots 4$. The circle denotes the boundary of the disc.

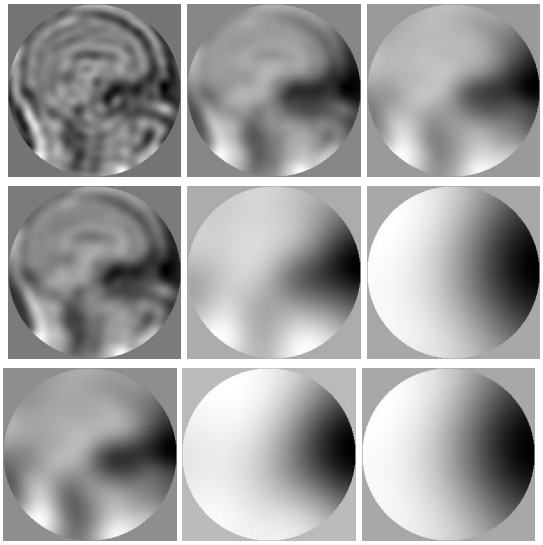

Figure 2.5: Various scale space representations of a 128×128 MR brain slice. Top row: $\alpha = \frac{1}{2}$ (Poisson scale space), middle row: $\alpha = \frac{3}{4}$, bottom row: $\alpha = 1$ (Gaussian scale space). On respective relative scales $s_\alpha = \frac{s}{a^{2\alpha}} = 0.01, 0.1, 0.2$. Notice that the higher frequency components are longest maintained in the Poisson scale.

2.5 Truncation of the Fourier Series Expansions

In practice f can not be expanded in the infinite (countable) base $\{f_{mn}\}$ of common eigen functions of the α scale space operators; the Fourier series must be truncated at say $m = M$ and $n = N$. The most natural norm for error estimation is the $\mathbb{L}_2(B_{\mathbf{0},a})$-norm:

$$\begin{aligned}(\varepsilon^{(\alpha)}_{MN}(s))^2 &= \|u_\alpha(\cdot, s) - \sum_{m=0}^{M}\sum_{n=0}^{N}(f_{mn}, f) f_{mn} e^{-(-\lambda_{mn})^\alpha s}\|^2_{\mathbb{L}_2(B_{\mathbf{0},a})} \\ &= \left(\sum_{m=0}^{\infty}\sum_{n=N+1}^{\infty} + \sum_{n=0}^{N}\sum_{m=M+1}^{\infty}\right) \left|(f_{mn}, f)_{\mathbb{L}_2(\Omega)}\right|^2 e^{-2(-\lambda_{mn})^\alpha s} \,.\end{aligned} \tag{2.39}$$

The α scale spaces on a bounded domain have the same eigen functions and can thereby be implemented simultaneously. For such an implementation it is important to have a sharp error estimation which depends explicitly on M, N, s and α, since as α increases the series can be chopped sooner to maintain the same amount of accuracy. Moreover, as the relative scale $s_\alpha > 0$ increases, the higher frequency components vanish so the series can also be chopped sooner as s_α increases. Notice that in practice for sampled images frequencies above the Nyquist-frequencies M' and N' are omitted, so one can replace the infinite upper limits by these frequencies. In the disc case we found $f_{mn} = h_{mn}$, $\lambda_{mn} = -\frac{j'_{m,n}}{a}$ and in the square case we found $f_{mn} = l_{mn}$ and $\lambda_{mn} = -\left(\frac{n\pi}{b}\right)^2 - \left(\frac{m\pi}{a}\right)^2$. Here we will only estimate the error in the square case. For details with regard to disk case, see [25]. In order to have a sharp estimation we assume that

$$|(l_{mn}, f)|^2 \leq C(\frac{1}{m^v n^w}) \text{ for } m > M \text{ and } n > N, \tag{2.40}$$

where $v, w > 1, C > 0$ are fixed and not difficult to estimate in practice. Due to Cauchy-Schwarz one can estmimate *roughly* with $C = \|f\|^2_{\mathbb{L}_2([0,a]\times[0,b])}$, $v = w = 0$. In estimating the $\mathbb{L}_2$ error (below) we use the Hölder inequality $(\mathbf{x}, \mathbf{y})_2 \leq \|\mathbf{x}\|_p \|\mathbf{y}\|_q$, for $1/p + 1/q = 1$, applied with $p = 1/\alpha$, $\mathbf{x} = (\left|\frac{m\pi}{a}\right|^{2\alpha}, \left|\frac{n\pi}{b}\right|^{2\alpha})^T$ and $\mathbf{y} = (1,1)^T$, yielding

$$\left(\left(\frac{n\pi}{b}\right)^2 + \left(\frac{m\pi}{a}\right)^2\right)^\alpha \geq 2^{\alpha-1}\left(\left(\frac{m\pi}{a}\right)^{2\alpha} + \left(\frac{n\pi}{b}\right)^{2\alpha}\right) \quad \text{and therefore,}$$

$$\begin{aligned}
(\varepsilon^{(\alpha)}_{MN}(s))^2 &= \left(\sum_{m=0}^{\infty}\sum_{n=N+1}^{\infty} + \sum_{n=0}^{N}\sum_{m=M+1}^{\infty}\right) \left|(l_{mn}, f)_{\mathbb{L}_2([0,a]\times[0,b])}\right|^2 e^{-2\left(\left(\frac{n\pi}{b}\right)^2 + \left(\frac{m\pi}{a}\right)^2\right)^\alpha s} \\
&\leq \left(\sum_{m=0}^{\infty}\sum_{n=N+1}^{\infty} + \sum_{n=0}^{N}\sum_{m=M+1}^{\infty}\right) C\, e^{-2^\alpha\left(\left(\frac{n\pi}{b}\right)^{2\alpha} + \left(\frac{m\pi}{a}\right)^2\right)^{2\alpha} s} \frac{1}{m^v n^w} \\
&= C\left(\sum_{m=0}^{\infty}\sum_{n=N+1}^{\infty} + \sum_{n=0}^{N}\sum_{m=M+1}^{\infty}\right) \frac{(\eta(a,\alpha,s))^{m^{2\alpha}}}{m^v} \frac{(\eta(b,\alpha,s))^{n^{2\alpha}}}{n^w} \\
&= C\left(\sum_{m=0}^{\infty} \frac{(\eta(a,\alpha,s))^{m^{2\alpha}}}{m^v}\right)\left(\sum_{n=N+1}^{\infty} \frac{(\eta(b,\alpha,s))^{n^{2\alpha}}}{n^w}\right) \\
&+ C\left(\sum_{n=0}^{N} \frac{(\eta(b,\alpha,s))^{m^{2\alpha}}}{m^v}\right)\left(\sum_{m=M+1}^{\infty} \frac{(\eta(a,\alpha,s))^{n^{2\alpha}}}{n^w}\right) \quad ,
\end{aligned} \tag{2.41}$$

where $\eta(a,\alpha,s) = e^{-2^\alpha\left(\frac{\pi}{a}\right)^{2\alpha}s} << 1$. The Poisson case $\alpha = 1/2$ is easiest to estimate, since standard series expansions can be used, cf. [25]. For instance estimate (2.41) in case $v = w = 0$ becomes:

$$(\varepsilon^{(1/2)}_{MN}(s))^2 \leq \|f\|^2 \left(\frac{1}{1-\eta(a,1/2,s)} \frac{(\eta(b,1/2,s))^{N+1}}{1-\eta(b,1/2,s)} + \frac{1-(\eta(b,1/2,s))^{N+1}}{1-\eta(b,1/2,s)} \frac{(\eta(a,1/2,s))^{M+1}}{1-\eta(a,1/2,s)}\right).$$

But also in the general α case one can find a sharp estimation, using the following inequality

$$\sum_{m=M+1}^{\infty} \frac{r^{-m^{2\alpha}}}{m^v} \leq \int_M^{\infty} \frac{r^{-x^{2\alpha}}}{x^v}\,\mathrm{dx} = \frac{(\log \mathrm{r})^{\frac{\mathrm{m}-1}{2\alpha}}\Gamma[-\frac{\mathrm{m}-1}{2\alpha}, \mathrm{M}^{2\alpha}\log \mathrm{r}]}{2\alpha} \qquad \mathrm{r} = \frac{1}{\eta} > 1,$$

which follows by monotonic decrease of the function $x \mapsto \frac{r^{-x^{2\alpha}}}{x^v}$ on $\mathbb{R}$ and where $\Gamma[a,z] = \int_z^{\infty} t^{a-1}e^{-t}\mathrm{dt}$ denotes the incomplete Gamma function.

2.6 Conclusion

Since images are given on a bounded domain in practice and because it is not desirable that grey-vales from outside the image[4] affect the scale space, we observed the α scale spaces on a bounded domain with Neumann-boundary conditions. Moreover, the mathematical description and connection between the α scale spaces become relatively easy. First some general results are proven and then the explicit solutions expanded in a *common* complete orthonormal base of eigenfunctions are given for the (pragmatic) case of the rectangle and the (more difficult) case of the disc. Further we have shown that the α scale spaces on the unbounded domain are limits of these bounded domain cases. A sharp estimate of the $\mathbb{L}_2$-error as a function of α and scale, which is caused by cutting of the Fourier series of the α scale space representation, is given, which can be used for simultaneous implementation. Finally, we focus on the construction of the monogenic scale space on a bounded domain. Here by imposing a Neumann boundary condition on the first component of this vector scale space, the generalized Cauchy-Riemann equations take care of the boundary conditions of the flow components. From the monogenic scale space on a bounded domain we obtain a vector scale space representation of the local phase and local amplitude of an image, by taking the logarithm. If the original image is locally 1D, this vector scale space again satisfies generalized Cauchy-Riemann equations. Consequently, local frequency (divergence of phase vector field) equals the scale derivative of local attenuation and local amplitude maxima are points of phase congruency (which is useful for multi-scale edge detection).

[4]Introduced by zero padding in the usual convolution framework.

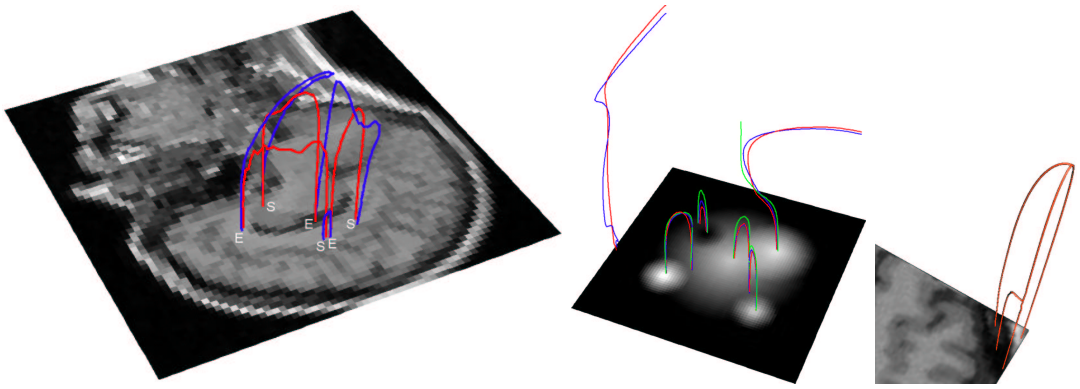

Figure 2.6: Left and middle: Critical curves through scale space. Critical curves in respectively Poisson (red) and Gaussian (blue) in finite domain scale space of square MRI-image and in green critical curves unbounded Gaussian scale space. The left picture shows that the topological hierarchy in Poisson and Gaussian scale space can be *different*. The middle picture shows that away from the boundary the unbounded domain and bounded domain critical paths are quite similar. Notice that in the unbounded domain one extremum survives in the center of mass (as it should according to [92]) of the image (and one at infinity), whereas in the bounded domain case a maximum and minimum survive on the boundary. Right: typical illustration of how critical paths meet at the boundary. On the boundary (because of Neumann-boundary condition) the critical curves behave as in scale spaces of signals; minimum and maximum annihilate. The critical paths that come from inside the image are saddle paths annihilating with the extrema (maximum and minimum) on the boundary.

Chapter 3

Deep Structure

3.1 Introduction

The topological structure (or so-called deep structure) in an α scale space and in particular the change of topological structure of $u(\cdot, s)$ over $s > 0$, reflects the hierarchical structure of objects (like blobs) in an image. As the resolution increases extrema disappear until at finite scale $S > 0$ (under some weak conditions) only one extremum is left, cf.[92]. Points in scale space where a saddle and extremum annihilate or points where an extremum and a saddle are created are called top-points. The set of top-points is given by

$$\{(\mathbf{x}, s) \mid (\det H_{\mathbf{x}} u(\cdot, s))(\mathbf{x}) = 0 \text{ and } (\nabla_{\mathbf{x}} u(\cdot, s))(\mathbf{x}) = \mathbf{0}\}.$$

At these points the topological structure changes. Other interesting points in scale space are scale space saddles[1], these are exactly those points were $\nabla_{\mathbf{x},s} u(\mathbf{x}, s) = (\mathbf{0}, 0)$. Although it is possible to construct a hierarchical tree-structure by means of these points, cf. [87], they do not seem to be as natural as the top-points. For investigation on the stability of top-points we refer to Balmachnova et al. [11].

The tangent vector $\partial_\beta(\mathbf{x}(\beta), s(\beta))$, with $s = \beta \det H_{\mathbf{x}} u$ of a critical path (moving with infinite speed through a top-point) in an α scale space is given by

$$\partial_\beta(\mathbf{x}(\beta), s(\beta)) = (-\tilde{H}_{\mathbf{x}} u \nabla_{\mathbf{x}} \partial_s u, \det H_{\mathbf{x}}(u)\beta),$$

where $\frac{1}{\det(H_{\mathbf{x}} u)} \tilde{H}_{\mathbf{x}} u = (H_{\mathbf{x}} u)^{-1}$. This directly follows by application of the chain rule:

$$\partial_\beta(\nabla_{\mathbf{x}} u(\mathbf{x}(\beta), s(\beta))) = H_{\mathbf{x}} u(\mathbf{x}(\beta), s(\beta))\dot{\mathbf{x}}(\beta) + \nabla_{\mathbf{x}} u_s(\mathbf{x}(\beta), s(\beta))\frac{ds}{d\beta} = \mathbf{0}.$$

The curvature at a top-point (or catastrophe point) $(\mathbf{x}*, s*)$ along a critical curve is given by $\kappa(\mathbf{x}*, s*) = \frac{1}{\|\overline{\mathbf{w}}(\mathbf{x}*, s*)\|^2} \det M(\mathbf{x}*, s*)$, where

$$M(\mathbf{x}*, s*) = \left(\begin{array}{cc} H_{\mathbf{x}} u & \partial_s(\nabla_{\mathbf{x}} u)^T \\ \nabla_{\mathbf{x}} \det H_{\mathbf{x}} u & \partial_s \det H_{\mathbf{x}} u \end{array} \right) \Bigg|_{(\mathbf{x},s)=(\mathbf{x}*,s*)}, \tag{3.1}$$

[1] As is shown in [30], there do not exist interior extrema (with respect to scale and position) in α scale spaces.

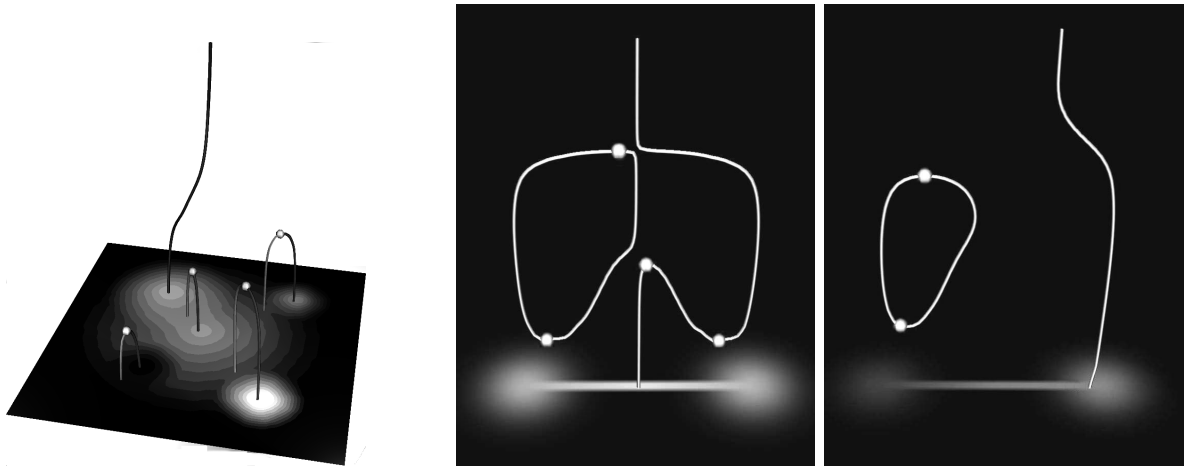

Figure 3.1: Left: Illustration of annihilations in Gaussian scale space of simple 2D image. Right: Illustration of creations in Gaussian scale space of simple 2D image.

In case the curvature at a catastrophe point is negative, the catastrophe is an annihilation and if the curvature is positive, the catastrophe is a creation. For proof and definition of $\overline{\mathbf{w}}(\mathbf{x}*, s*)$ we refer to[2] Florack[49]. See figure 3.1 for illustrations of annihilations and creations in simple images, recall Figure 2.6 for the typical difference on bounded domain and unbounded domain scale spaces, and see figure 3.3 for the somewhat surprising differences between the deep structure of α scale spaces.

3.2 Grey-Value Flow

Another important geometrical quantity in the deep-structure of images is the *grey-value flow* within an α scale space u_f^α of image f. This multi-scale vector field is given by

$$\mathbf{F}_\alpha[u_f^\alpha](\mathbf{x}, s) = (\mathbf{f}_s^\alpha * f)(\mathbf{x}), \tag{3.2}$$

where $\mathbf{f}_s^\alpha(\mathbf{x}) = \mathcal{F}^{-1}[\boldsymbol{\omega} \mapsto i\frac{1}{\|\boldsymbol{\omega}\|^{2(1-\alpha)}}\boldsymbol{\omega}\, e^{-s\|\boldsymbol{\omega}\|^{2\alpha}}](\mathbf{x})$. To this end we notice that

$$\frac{\partial}{\partial s}[u_f^\alpha] = -(-\Delta)^\alpha u_f^\alpha = \operatorname{div}\mathbf{F}_\alpha[u_f],$$

which is easily verified in the Fourier domain: $-\|\boldsymbol{\omega}\|^{2\alpha} = i\boldsymbol{\omega} \cdot i\frac{1}{\|\boldsymbol{\omega}\|^{2(1-\alpha)}}\boldsymbol{\omega}$. The grey-value flow tells us how the grey-value particles flow within the scale space representation and reveals the interaction between extremal paths in scale space. We will use this flux vector field to compute so-called flux features. For the special case of a Gaussian scale space $\alpha = 1$ the grey-value flow is obtained by means of the gradient as we have $\mathbf{F}_{\alpha=1}[u_f](\mathbf{x}, s) = \nabla_{\mathbf{x}} u_f(\mathbf{x}, s)$ and $\mathbf{f}_s^{\alpha=1} = \nabla_{\mathbf{x}} K_s^1(\mathbf{x})$. For the special case of a Poisson scale space $\alpha = \frac{1}{2}$ the grey value flow is obtained by means of the Riesz transform $\mathbf{F}_{\alpha=\frac{1}{2}}[u_f](\mathbf{x}, s) = \mathbf{R}_{\mathbf{x}} u_f(\mathbf{x}, s)$ and $\mathbf{f}_s^{\alpha=\frac{1}{2}}$ equals

[2] In the work of Florack[49], the case $\alpha = 1$ is considered only, but as long as the scale derivatives in his work are not replaced by Laplace operators, the results also hold for $\alpha \in (0, 1]$.

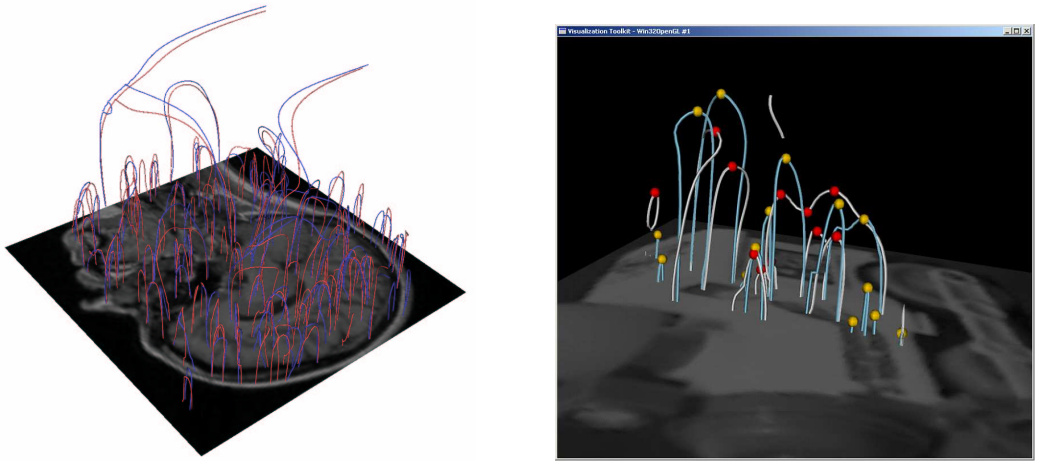

Figure 3.2: Left: Illustration of critical paths within Gaussian (in blue) and Poisson scale space (in red) of MRI-image of the brain. Right: Illustration of differences between the deep structure of α scale spaces in a fixed box $[s_1, s_2] \times [x_1, x_2] \times [y_1, y_2]$, $s_1 < s_2$, $x_1 < x_2$, $y_1 < y_2$ in scale space.

the vector-valued conjugate Poisson kernel: $\mathbf{f}_s^{\alpha=\frac{1}{2}}(\mathbf{x}) = \mathbf{R}_{\mathbf{x}} K_s^{1/2}(\mathbf{x}) = \frac{2}{\sigma_{d+1}} \frac{\mathbf{x}}{(s^2+\|\mathbf{x}\|^2)^{\frac{d+1}{2}}}$. By extending a scale space with its flow, one obtains a vector scale space which equals the first order jet of a Gaussian scale space if $\alpha = 1$ and which equals the monogenic scale space if $\alpha = \frac{1}{2}$, recall Figure 1.10.

3.3 A Comparison of the Topology within α Scale Spaces

In the previous chapters of this thesis, we explained the strong connection that exists between α scale spaces. On the one hand the strong connection between α scale spaces is interesting as it smoothly relates methods using a Gaussian scale space, to methods using a Poisson scale space and visa versa. On the other hand the strong connection/similarity on (both the unbounded domain and bounded domain) α scale spaces raises the question whether there is a relevant difference between them.

In this section we approach this issue only from a topological point of view, i.e. we investigate the differences (and analogies) between the deep structure of α scale spaces. As we will show **there exist strong differences in the deep structure of α-scale spaces**.

In chapter 1, we already mentioned a strong difference between α scale spaces with respect to the behavior of *isophotes*, by means of causality (and the related max principles and Koenderink's principle), recall figures 1.1, 1.2 and figure 1.4.

Here we will consider differences of the behavior of *critical curves* in α scale spaces. The critical curves through α scale spaces continuously depend on α, if scale is re-parameterized by $s \mapsto C * s^{1/(2\alpha)}$. Here the dimensionless constant $C > 0$ is still arbitrary and in our evaluations

it is chosen to scale the last annihilation at a fixed scale. Furthermore we notice that the physical dimension of the re-parameterized scale equals length for all $\alpha \in (0, 1]$. It is not surprising that the critical curves (under this re-parametrization) evolve continuously as the α scale spaces (on both bounded and unbounded domain) continuously depend on α, recall (1.6) and (2.9). However, in practice, it quite often happens that different extrema and saddles annihilate in α scale spaces, because of bifurcations with respect to the deformation of the scale space parameterized by α. Top-points are created and annihilated with increasing α, see figure 3.3. Although, not considered here, this may be a point for further investigation from a Morse-theoretical point of view.

3.3.1 Local Morse Theory for Gaussian Scale Space and Poisson Scale Space

In this subsection we give a short summary of the local Morse theory developed initially by James Damon[16], for the diffusion equation and investigate how they translate to the case of the Poisson equation. It turns out that the generic topological changes in Poisson scale space correspond to the generic topological changes in Gaussian scale space. However, a fundamental difference between the frameworks is that a Poisson scale space allows creations in scale spaces of 1D signals ($d = 1$), whereas in the Gaussian scale space the diffusion equation does not allow creations in a scale space of a 1D signal. Although these creations in a 1D Poisson scale space are stable/generic in the mathematical sense, they do not seem to occur frequently in practical situations[3]. Nevertheless, we will show both analytic and representative numerical examples of 1D-Poisson scale spaces including creation events.

Damon[16] introduces the groups $G = \mathcal{H}$, with $\mathcal{H}$ the group of pairs (ϕ, c), with $\phi : \mathbb{R}^{d+1} \to \mathbb{R}$ and $c : \mathbb{R} \to \mathbb{R}$ diffeomorphisms, acting on the space of solutions of smooth functions $\mathcal{S}_\alpha$ satisfying the evolution equation $\frac{\partial u}{\partial s} = -(-\Delta)^\alpha u$, $\alpha \in (0, 1]$, (in particular α scale spaces) the group action

$$g \cdot u(x, s) = u(\phi_1(\mathbf{x}, s), \phi_2(s)) + c(s) \ ,$$

where $g \in \mathcal{H}$, the group of pairs $(\mathbf{x}, s) \mapsto (\phi_1(\mathbf{x}, s), \phi_2(s), c(s))$, where $c : \mathbb{R} \to \mathbb{R}$, $\phi_1 : \mathbb{R}^{d+1} \to \mathbb{R}^d$ and $\phi_2 : \mathbb{R}^+ \to \mathbb{R}^+$ are diffeomorphisms and where $\phi_2'(0) > 0$. Furthermore, Damon[16] introduces the group $G = \mathcal{IS}$, with $\mathcal{IS}$ the group of pairs (ϕ, ψ, c), with $c \in \mathbb{R}$ constant and $\phi : \mathbb{R}^{d+1} \to \mathbb{R}$, $\psi : \mathbb{R}^2 \to \mathbb{R}$ diffeomorphisms of the form $\phi(\mathbf{x}, s) = (\phi_1(x, s), \phi_2(s))$ and $\psi(y, t) = (\psi_1(y, t), t)$ with $\phi_2'(0) > 0$ and $\frac{\partial}{\partial y}\psi(0, 0) > 0$ and $\psi(0, t) = 0$, acting on $\mathcal{S}_\alpha$ by

$$g \cdot u(x, s) = \psi_1(u \circ \phi(\mathbf{x}, s), s) + c = \psi_1(u(\phi_1(\mathbf{x}, s), \phi_2(s)), s) + c \ .$$

By introducing these groups, he defines equivalence relations by means of

$$u \sim v \text{ iff there exists a } g \in G \text{ such that } u = g \cdot v, \tag{3.3}$$

i.e. two elements within $\mathcal{S}_\alpha$ are equivalent iff they lie on the same orbit, which yields $\mathcal{H}$ and $\mathcal{IS}$-equivalence depending on the choice of group (action).[4] However, here we follow an

[3] They do seem to occur more frequently in the conjugate Poisson scale space

[4] Notice that with respect to $\mathcal{IS}$-equivalence, that the $\mathcal{IS}$-group action is rather similar to the $\mathcal{H}$-group, but the intensity may change over scale as well (by ψ_1) and the role of $s > 0$ is no longer distinguished, so that by the equivalence relation one keeps track of local changes of an iso-intensity surface as it undergoes a transition and the intensity level of that critical point.

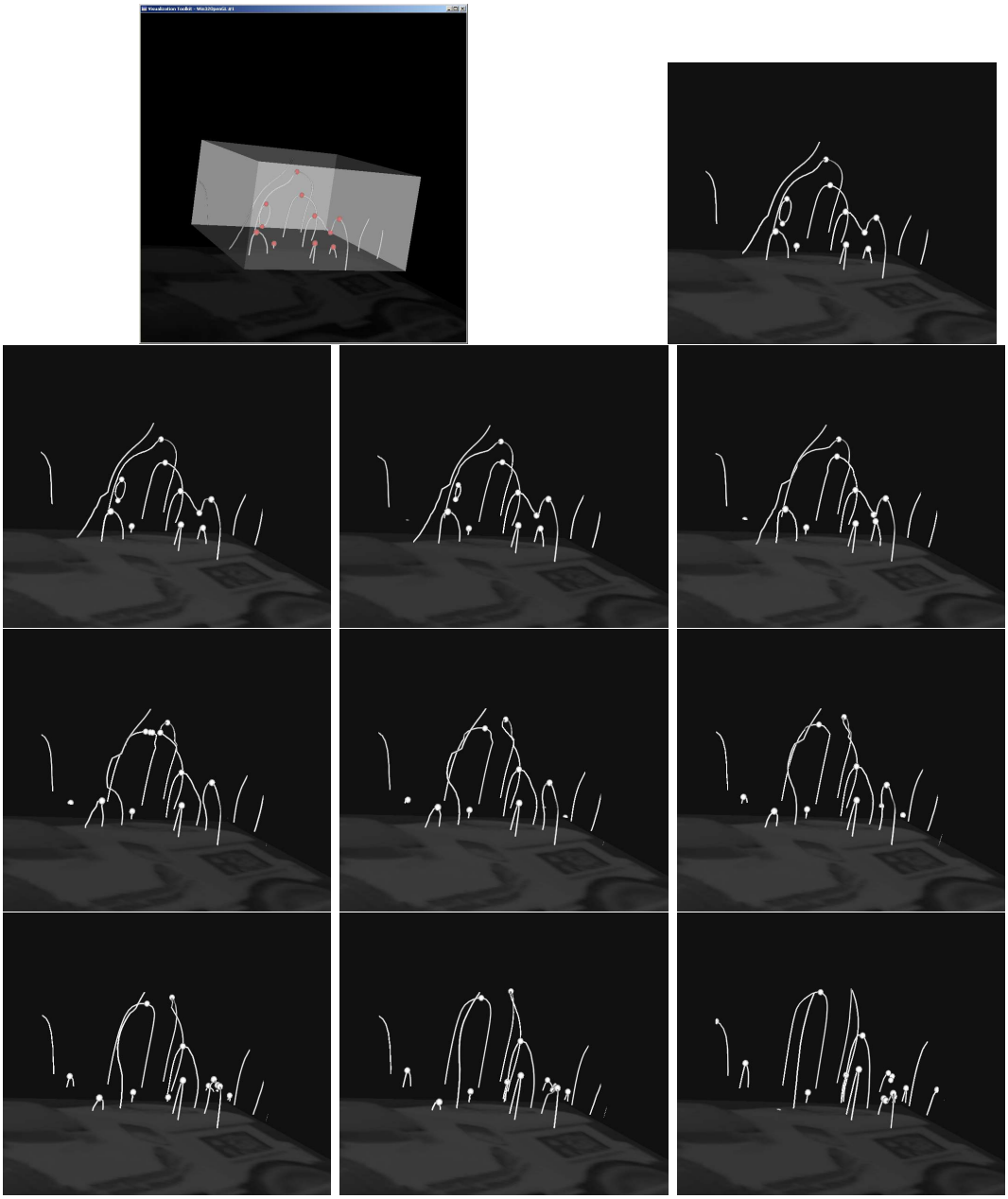

Figure 3.3: The critical curves through α scale spaces of some arbitrary 2D-grey-value image only plotted within a box $[s_1, s_2] \times [x_1, x_2] \times [y_1, y_2]$, $s_1 < s_2$, $x_1 < x_2, y_1 < y_2$. Top down, bottom row, from $\alpha = 1$ (Gaussian scale space) down to $\alpha = 1/2$ Poisson scale space, $\alpha = 0.1, 0.95, 0.9, \ldots, 0.5$. Notice that in the case $\alpha = 1$ there are two creations (two crtical curves are bending below). In one of these cases (the closed loop) this creation is immediately followed by a annihilation of the same extremum and saddle. The critical curves continuously depend on α, but still for example at $\alpha \approx 0.75$ a (besides the bifurcation where the closed creation-annihilation-loop disappears) bifurcation arises where a scale space creation and annihilation meet eachother.

approach first formulated by J.C.van der Meer to singularity theory for the diffusion equation, which is similar to the case $G = \mathcal{IS}$ similar cf. [124]. In this approach the action of the group $G = \mathrm{Diff}_d \times \mathrm{Diff}_1$, with Diff_n the group of diffeomorphisms from $\mathbb{R}^d$ to itself, on images $f : \mathbb{R}^d \to \mathbb{R}$ is given by

$$(g \cdot f)(\mathbf{x}) = \psi \cdot f \cdot \phi^{-1}(\mathbf{x}), \qquad g = (\phi, \psi).$$

Notice that this group rather acts on the set of images, rather than on the space of double sided ($\tilde{u}_f = e^{-(-\sqrt{-\Delta})s} f, s \in \mathbb{R}$) scale spaces, which are to be considered as 1-parameter deformations on images.

Definition 10 *Let $f : \mathbb{R}^d \to \mathbb{R}$. A 1-parameter deformation(or unfolding[5]) of f is a continuous map $u : \mathbb{R}^d \times \mathbb{R}^1 \to \mathbb{R}$ such that $u(\boldsymbol{x}, \boldsymbol{0}) = f(\boldsymbol{x})$.*

By considering 1-parameter deformations of the identity of the group G we obtain the group G_{un}, which acts on 1-parameter deformations of images (in particular scale spaces) by means of

$$(\tilde{g} \cdot u)(\mathbf{x}, s) = \tilde{\psi}(u(\tilde{\phi}^{-1}(\mathbf{x}, s)), s) \ ,$$

where $\tilde{\psi}(y, 0) = \psi(y)$ and $\tilde{\phi}^{-1}(\mathbf{x}, 0) = (\phi^{-1}(\mathbf{x}), 0)$. Notice that $(\tilde{g} \cdot \tilde{u}_f)(\mathbf{x}, 0) = (g \cdot f)(\mathbf{x})$, for all $\tilde{g} \in G_{un}$ corresponding to a certain $g \in G$ for every $f \in \mathbb{L}_2(\mathbb{R}^2)$.

Definition 11 *Two deformations u, v are called $\tilde{G}$-equivalent if u lies within the obit of v, or more precisely, there exists a $\tilde{g} \in \tilde{G}$ such that $u \sim v \Leftrightarrow u = \tilde{g} \cdot v$.*

Definition 12 *A function $f : \mathbb{R}^d \to \mathbb{R}$ is G-stable if any deformation is G-equivalent to the constant deformation. A deformation u is $\tilde{G}$-stable[6] if any deformation of u is $\tilde{G}$ equivalent to the constant deformation.*

A function $f : \mathbb{R}^d \to \mathbb{R}$ is G-stable (or generic) iff the tangent space at f, $T_G(f)$ equals $\mathcal{E}_0$, the space of all smooth germs of functions at zero.

Lemma 3 *A double-sided scale space representation $\tilde{u}_f$ is $\tilde{G}$-stable iff either f is stable or the co-dimension of f in $\mathcal{E}_0$ equals 1, dim$(\mathcal{E}_0/T_G(f)) = 1$, and $\frac{\partial}{\partial s}\tilde{u}_f\big|_{\tau=0}$ generates the complement.*

However, we are merely interested in single sided scale spaces where scale is a strictly positive parameter, $s > 0$, as we do not want to include de-blurring, as this is ill-posed.

This means that in the co-dimension one case we can only generate half [7] of the remainder in the tangent space.

[5] With unfolding one usually means the map $(\mathbf{x}, s) \mapsto (u(\mathbf{x}, s), s)$.

[6] The notion of stability can be rephrased as follows: A function u is stable if all functions that are close to u (in an appropriate topology) are $\tilde{G}$-equivalent to u.

[7] The sign of $\frac{\partial u}{\partial s}\big|_{s=0}$ relative $T_G(f)$ to inside $\mathcal{E}_0$ becomes relevant in the definition of $\tilde{G}$-equivalence.

This is the reason for a distinction between one-sided and two sided stability. In the case of two sided stability the function (or rather germ) f was already stable, whereas in the second case the co-dimension of f in $\mathcal{E}_0$ equals 1. For further details, see Van der Meer[124].

3.3.2 A Partition of Equivalence Classes of $\tilde{G}$-stable Gaussian Deformations

The space of $\tilde{G}$-stable Gaussian Deformations $\mathcal{S}_{\alpha=1}$ can be partitioned into equivalence classes due to the equivalence relation defined in Definition 11. First we consider the case $d \geq 2$. Then the equivalence classes (germs) are represented by one of the following functions:

1. Two sided stable germs:
   (a) $u(\mathbf{x}, s) = x_1$, (submersion)
   (b) $2ds + \sum_{i=1}^{d} x_i^2$,
   (c) $\sum_{i=1}^{d} a_i x_i^2$, with $\sum_{i=1}^{d} a_i = 0$ all $a_i \neq 0$. (classified by the signs of a_i)
2. One sided stable germs:
   (a) $x_1^3 - 6\,x_1(x_2^2 + s) + Q(x_2, \ldots, x_d, s)$, (creations of critical points),
   (b) $x_1^3 + 6s\,x_1 + Q(x_2, \ldots, x_d, s)$, (annihilations of critical points),

   with $Q(\mathbf{x}, s) = \sum_{k=2}^{d} \epsilon_k(x_k^2 + 2s)$, with $\epsilon_k = \pm 1$ for $k = 2, \ldots, n$.

The two-sided stable germs are of less interest since in all of these cases $T_{\mathcal{G}}(f) = \mathcal{E}_0$ and thereby $T_{\mathcal{G}}(f) + \mathbb{R}^+ \frac{\partial u}{\partial s}\big|_{s=0} = T_{\mathcal{G}}(f) = \mathcal{E}_0$. So here we have no bifurcations of the critical paths in scale space.

It follows from Lemma 3 that the only bifurcations the image f can undergo as a consequence of Gaussian blurring are given by singularities of co-dimension 1. The standard form of a co-dimension one function is given by

$$C_1(\mathbf{x}) = x_1^3 + \sum_{i=2}^{d} a_i x_i^2, a_i \neq 0, \tag{3.4}$$

with universal deformation $x_1^3 + t\,x_1 + \sum_{i=2}^{d} a_i x_i^2$. For $t > 0$ there are no critical points while for $t < 0$ there are two critical points, a saddle and an extremum. This is known as the cusp catastrophe [108].

The Gaussian deformation of C_1 is given by $(G_s * C_1)(\mathbf{x}) = x_1^3 + 6s\,x_1 - 2(\sum_{i=2}^{d} a_i)s + \sum_{i=2}^{d} a_i x_i^2$. This yields the germs describing the annihilation of critical points in a Gaussian scale space. Notice that the complement to the tangent space is spanned by the vector $\Delta C_1(\mathbf{x}) = 6\,x_1 \equiv x_1$.

Consider $C_2(\mathbf{x}) = x_1^3 - 6x_2^2x_1 + \sum_{i=2}^d a_i x_i^2$. Although C_2 is equivalent to C_1 their Gaussian deformations are not one-sided equivalent: The Gaussian deformation of C_2 equals $G_s * C_2(\mathbf{x}) = x_1^3 - 6x_2^2x_1 - 6x_1 s - 2(\sum_{i=2}^d a_i)s + \sum_{i=2}^d a_i x_i^2$, so now the complement to the tangent space is spanned by the vector $\Delta C_2(\mathbf{x}) = -6\, x_1 \equiv -x_1$.

The case $d = 1$ can be treated in an analogue matter, *except for the annihilation germ*, where no such x_2 is at hand. Creations can not occur in a Gaussian scale space. Recall, to this end that the curvature at a catastrophe point $(\mathbf{x}*, s*)$ (u_{xx} and u_x vanish) equals $\kappa = \frac{1}{\|\overline{\mathbf{w}}\|^2} \det M$, see (3.1). In $1D$ the matrix M is given by

$$M(\mathbf{x}*, s*) = \begin{pmatrix} u_{xx}(\mathbf{x}*, s*) & u_{xs}(\mathbf{x}*, s*) \\ u_{xxx}(\mathbf{x}*, s*) & u_{xxs}(\mathbf{x}*, s*) \end{pmatrix},$$

and since $u_{xx}(\mathbf{x}*, s*) = 0$ it directly follows from

$$\det M(\mathbf{x}*, s*) = -u_{xs}(\mathbf{x}*, s*)u_{xxx}(\mathbf{x}*, s*) = -(u_{xxx}(\mathbf{x}*, s*))^2$$

that the curvature is always negative, allowing only annihilations and no creations. Notice that this argument does not hold in a Poisson scale space, where

$$\det M(\mathbf{x}*, s*) = u_{xs}(\mathbf{x}*, s*)u_{xxx}(\mathbf{x}*, s*) = -\frac{1}{2}[\frac{d}{ds}u_{xs}]^2(\mathbf{x}*, s*) = -\frac{1}{2}[\frac{d}{ds}v_{xx}]^2(\mathbf{x}*, s*),$$

where v denotes the conjugate Poisson scale space and is not a priori negative.

3.3.3 A partition of $\mathcal{G}$-stable Poisson Deformations

Following the same line as for the Gaussian case we obtain the following partition of $\tilde{G}$-stable Poisson deformations:

1. Two sided stable germs:
   (a) $u(\mathbf{x}, s) = x_1$, (submersion)
   (b) $-2ds^2 + \sum_{i=1}^d x_i^2$
   (c) $\sum_{i=1}^d a_i x_i^2$, with $\sum_{i=1}^d a_i = 0$ all $a_i \neq 0$. (classified by the signs of a_i)
2. One sided stable germs:
   (a) $x_1^3 - 3s^2\, x_1 - s\, x_1 + Q(x_2, \ldots, x_d, s)$, (creations of critical points),
   (b) $x_1^3 - 3s^2\, x_1 + s\, x_1 + Q(x_2, \ldots, x_d, s)$, (annihilations of critical points),

   with $Q(\mathbf{x}, s) = \sum_{k=2}^d \epsilon_k(x_k^2 - s^2)$, where $\epsilon_k = \pm 1$ for $k = 2, \ldots, d$.

The annihilation and creation germ are obtained by means of harmonic extension of the cusp catastrophe C_1 given by (3.4). To this end we notice that $\Re((x_1^3 \pm is)^3) = x_1^3 - 3s^2x_1$. At this point it should be noticed that the Laplace operator factorizes in 2 different ways

$$\Delta_{d+1} = \frac{\partial^2}{\partial s^2} + \frac{\partial^2}{\partial x_1^2} + \Delta_{d-1} = \left(\frac{\partial}{\partial s} - \sqrt{-\Delta_d}\right)\left(\frac{\partial}{\partial s} + \sqrt{-\Delta_d}\right) = \left(\frac{\partial}{\partial s} + i\frac{\partial}{\partial s}\right)\left(\frac{\partial}{\partial s} - i\frac{\partial}{\partial s}\right) + \Delta_{d-1},$$

As we already noticed, the first factorization tells us that upward harmonic extension of an image $f \in \mathbb{L}_2(\mathbb{R}^d)$ under the additional requirement that the harmonic extension should uniformly vanish as $s \to \infty$ is equivalent to solving the first order pseudo differential evolution system (1.23) for $\alpha = 1/2$, leading to Poisson scale space. Here we only consider local behavior and do not have the additional requirement at hand. Therefore harmonic extension of the 1 cusp catastrophe (with co-dimension 1) is not sufficient. For example, a creation by harmonic extension could be due to a Poisson de-blurring.[8] More precisely, the Poisson deformation could in principle be obtained by means of the evolution generated by $+\sqrt{-\Delta}$ rather than $-\sqrt{-\Delta}$). At this point, in comparison to the Gaussian case, there arises a technical problem as the convolution of the cusp catastrophe with the Poisson kernel does not exist.

Therefore (as we are interested in local behavior only) we compute $(H_s^d * g_{b,\varepsilon}^d)(\mathbf{x})$, where H_s^d denotes the d dimensional Poisson/Cauchy kernel and

$$g_{b,\varepsilon}^d(\mathbf{x}) = g_{b,\varepsilon}^1(x_1) = (x_1^3 + \varepsilon x_1)1_{[-b,b]}(x_1), \mathbf{x} = (x_1, \ldots, x_d),$$

where $\varepsilon = \pm 1$ and $1_{[-b,b]}(x_1) = 1$ if $|x_1| < b$ and 0 elsewhere. Some computation yields

$$\begin{aligned}(H_s^d * g_{b,\varepsilon}^d)(\mathbf{x}) &= (H_s^1 * g_{b,\varepsilon}^1)(x_1) \\ &= \tfrac{1}{2\pi}\left\{8\,x_1\,b\,s - 2(x_1^3 - 3x_1s^2 + \varepsilon x_1)\left[\arctan\left(\tfrac{x_1-b}{s}\right) - \arctan\left(\tfrac{x_1+b}{s}\right)\right]\right. \\ &\qquad \left. -s(s^2 - 3x_1^2 + 2)\log\tfrac{(x_1-b)^2+s^2}{(x_1+b)^2+s^2}\right\}.\end{aligned}$$

If we now omit the order $O(b)$-term and take the limit $b \to \infty$ we indeed obtain the annihilation ($\varepsilon = 1$) and creation ($\varepsilon = -1$) germs $x_1^3 - 3\,x_1s^2 + \varepsilon x_1$, $\varepsilon = \pm 1$.

Further we notice that in contrast to the Gaussian case creations are $\mathcal{G}$-stable in the 1D-case $d = 1$. Notice that in the 1D-creation case the critical paths of the above germ are given by $x(s) = \pm\sqrt{s^2 + \frac{1}{3}s}$, $s > 0$, whereas the critical paths of the annihilation germ are given by $x(s) = \pm\sqrt{s^2 - \frac{1}{3}s}$, $s < 0$.

For a simple analytic example of a 1D-creation (at scale $s = 0$) in Poisson scale space, where the initial condition only consists of 3-delta spikes, see figure 3.4. To this end we notice that in stead of δ-spikes (which are distributions, not functions) one may as well take the step function $f = -1_{(-d,d)} + 1_{(a-d,a+d)} + C * 1_{(-b-d,-b+d)}$, with $a, b > 2 * d$ as initial condition. In this case the Poisson scale space can also be computed analytically and the scale space is given by

$$\begin{aligned}u_f^\alpha(x,s) &= \tfrac{1}{\pi}\left(\arctan\left(\tfrac{x-a+d}{s}\right) - \arctan\left(\tfrac{x-a-d}{s}\right)\right. \\ &\quad \left. - \arctan\left(\tfrac{x+d}{s}\right) + \arctan\left(\tfrac{x+d}{s}\right) + C\arctan\left(\tfrac{x+b+d}{s}\right) - C\arctan\left(\tfrac{x+b-d}{s}\right)\right),\end{aligned}$$

which also has five extrema at $s = 1/4$, for example at $\approx -1.50, 0.128, 0.304, 2.96$ and 4.00, if $a = 4$, $b = 1.5$, $d = 0.1$, $C = 25$. For a numerical example of a 1D-creation *within* (at a scale $s > 0$) Poisson scale space see figure 3.5.

[8] Annihilations become creations if $s \mapsto -s$.

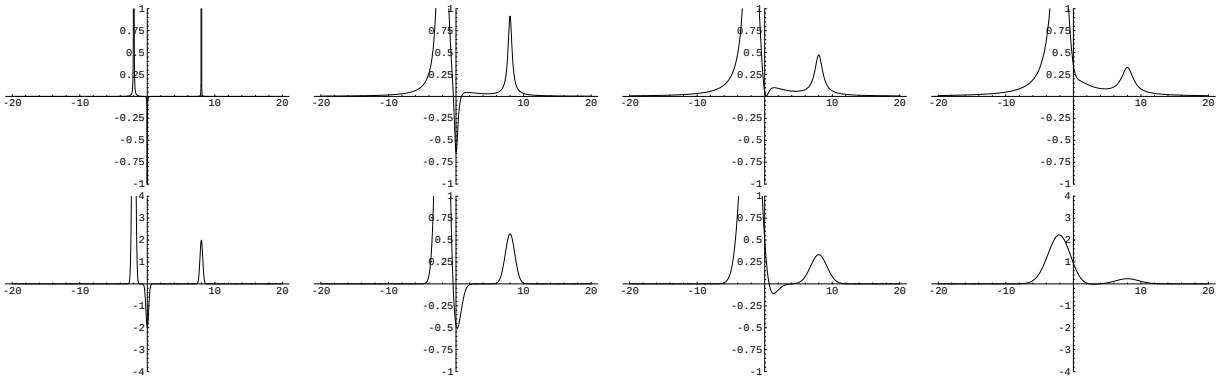

Figure 3.4: Top Row: From left to right, slices of the Poisson scale space, $u_f^\alpha(\cdot, s)$, of a signal f consisting of only 3 δ-spikes, with analytic solution $u_s^{\alpha=1/2}(x) = K_s^{\alpha=1/2}(x-a) + K_s^{\alpha=1/2}(x) + c * K_s^{\alpha=1/2}(x+b)$, $a = 8, b = 2, c = 10$ at $s = 0.001$, $s = 0.05, s = 0.1, s = 0.15$. Bottom Row: Corresponding Gaussian scale space $u_s^{\alpha=1}(x) = K_s^{\alpha=1}(x-a) + K_s^{\alpha=1}(x) + c * K_s^{\alpha=1}(x+b)$, $s = (1/2)\sigma^2$ at $\sigma = 0.2$, $\sigma = 0.7, \sigma = 0.12, \sigma = 0.17$. This simple analytical example gives a clear illustration of a creation (3 singular points at $s = 0$ become 5 singular points at $s > 0$) in Poisson scale space at $s = 0$, whereas in the Gaussian scale space the number of extrema remains 3 as it should as creations can not occur in a 1D-Gaussian scale space. Notice that the extremum at $x \approx 1.5$ increases in value in the Poisson scale space, this is not possible in a Gaussian scale space, due to the Koenderink's principle, which is related to the difference in causality (and maximum principle) between Gaussian and Poisson scale space.

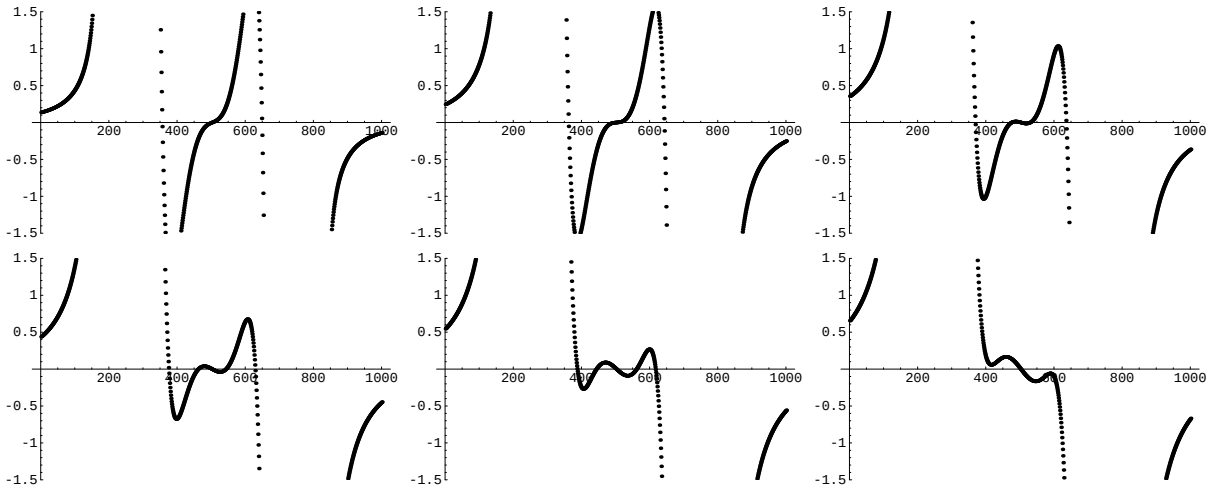

Figure 3.5: Top down, left to right, slices of a numerical implementation of a 1D-Poisson scale space, $u_f^\alpha(\cdot, s)$, of a numerical signal f, with $s = 0, 0.4, 0.8, 1.2, 1.6., 2.0$. It is clearly seen that a creation event takes place at $(x, s) \approx (500, 0.5)$.

3.4 Linear Image Reconstruction from a Sparse Set of α Scale Space Features by means of Inner Products of Sobolev Type

In α scale space one can use all kinds of differential invariants to detect local structure such as corners and lines. These differential invariants $\Phi : C^\infty(\mathbb{R}^d) \to C^\infty(\mathbb{R}^d)$ are algebraic (not necessarily linear) combinations of so-called α derivatives of $f \in \mathbb{L}_2(\mathbb{R}^d)$, given by

$$D_s^{\mathbf{n}} f := D^{\mathbf{n}}(K_s^\alpha * f) = (D^{\mathbf{n}} K_s^\alpha) * f \ , \qquad s > 0, \alpha \in (0,1], \mathbf{n} = (n^1, \ldots, n^d) \in \mathbb{N}^d, \tag{3.5}$$

such that they are Euclidean invariant, i.e. $\Phi \circ \mathcal{U}_g = \mathcal{U}_g \circ \Phi$, for all g within the Euclidean motion group $G = \mathbb{R}^d \rtimes SO(d)$, where $\mathcal{U} : G \mapsto \mathcal{B}(\mathbb{L}_2(\mathbb{R}^d))$ is given by $\mathcal{U}_g \psi(\mathbf{x}) = \psi(R^{-1}(\mathbf{x} - \mathbf{b})), g = (\mathbf{b}, R) \in G$.

Notice that the α derivatives given by (3.5) are *bounded* (and thereby well-posed) operators on $\mathbb{L}_2(\mathbb{R}^d)$, which is clearly not the case for the usual derivative operators. This statement directly follows from the Plancherel Theorem and the fact that $\omega \mapsto \omega^p e^{-s|\omega|^{2\alpha}}$ is uniformly bounded on $\mathbb{R}$ for all $p \in \mathbb{N}$. In case $d = 2$ a complete set of functionally independent differential invariants up to second order is given by

$$\{u, u_x^2 + u_y^2, u_{xx} + u_{yy}, u_{xx} u_y^2 - 2u_{xy} u_x u_y + u_{yy} u_x^2, u_{xx} u_x u_y - u_x^2 u_{xy} + u_y^2 u_{xy} - u_x u_y u_{yy}\}. \tag{3.6}$$

By introducing Gauge coordinates w, v, where w is along the gradient of $u = u_f^\alpha$ and v orthogonal to it, i.e.

$$\mathbf{e}_w(\mathbf{x}) = \frac{\nabla_{\mathbf{x}} u}{\|\nabla_{\mathbf{x}} u\|} \text{ and } \mathbf{e}_v(\mathbf{x}) = R_{\frac{\pi}{2}} \mathbf{e}_w, \tag{3.7}$$

these differential invariants are simply expressed as

$$\{u, (u_w)^2, u_{ww} + u_{vv}, (u_w)^2 u_{vv}, (u_w)^2 u_{vw}\}. \tag{3.8}$$

Beyond Euclidean invariance, there is affine invariance. A differential invariant $\Phi : C^\infty(\mathbb{R}^d) \to C^\infty(\mathbb{R}^d)$ is called affine invariant if $\mathcal{U}_g \, \Phi = \Phi \, \mathcal{U}_g$, for all $g \in \mathbb{R}^d \rtimes A(d)$, where $A(d) = \{M \in GL(d) : \det M = 1\}$. In the case $d = 2$, we have that every element in $A(2)$ is a composite of a rotation, shearing and an axis-rescaling. The respective matrix representations of these linear mappings are given by

$$R_\theta = \begin{pmatrix} \cos\theta & -\sin\theta \\ \sin\theta & \cos\theta \end{pmatrix}, \qquad S_c = \begin{pmatrix} 1 & c \\ 0 & 1 \end{pmatrix}, \qquad L_\lambda = \begin{pmatrix} \lambda & 0 \\ 0 & \lambda^{-1} \end{pmatrix}, \tag{3.9}$$

$\theta \in [0, 2\pi), c \in \mathbb{R}$ and $\lambda \in \mathbb{R} \setminus \{0\}$. Consequently, a differential invariant which is also invariant under (the left regular actions of) the subgroups $\{S_c \mid c \in \mathbb{R}\}$ and $\{L_\lambda \mid \lambda \in \mathbb{R} \setminus \{0\}\}$ is affine invariant. The affine invariants up to second order are given by $\{u, \det H_{\mathbf{x}}(u), (R_{\pi/2} \nabla_{\mathbf{x}} u)^T H_{\mathbf{x}}(u) R_{\pi/2} \nabla u\}$ or equivalently in Gauge-coordinates

$$\{u, u_{vv} u_{ww} - u_{vw}^2, u_w^2 u_{vv}\}.$$

Notice that in a top point all these affine differential invariants vanish.[9]

[9] The other way around need not be true: $u_{vv} u_w = 0$ and $\det Hu(\cdot, s) = 0$ is equivalent to $u_w = \det Hu(\cdot, s) = 0$ or $u_{vv} = u_{vw} = 0$. In the latter case the isophote curvature and the flowline curvature vanish, i.e. the isophotes and flowlines are locally straight lines.

With respect to affine invariants on $u_f^\alpha(\cdot, s)$ it should be noticed (as this is sometimes overlooked in image analysis) that they do not correspond to affine features on the original image f, since in general for $g = (A, \mathbf{b})$ and $u^\alpha_{\mathcal{U}_g f}(\cdot, s) = \mathcal{U}_g\, u_f^\alpha(\cdot, s)$ holds for all $f \in \mathbb{L}_2(\mathbb{R}^2)$ if and only if A is orthogonal.

For example top-points are the unique points on a critical path were the affine invariant $u \mapsto u_{vv}u_{ww} - u_{vw}^2$ vanishes. Nevertheless, the scale space locations of a top-point are *not* affine invariant. More precisely, suppose $\{(\mathbf{x}_i^*, s_i^*) \mid i = 1, \dots N\}$ is the set of top-point locations of original image f, then the set of top-point locations of $\mathcal{U}_g f$, with $g = (A, \mathbf{b})$ and $\det A = 1$, $A^T \neq A^{-1}$ does *not* necessarily coincide with $\{(A\mathbf{x}_i^* + \mathbf{b}, \phi(s_i^*)) \mid i = 1, \dots N\}$, for some (monotonic) $\phi : \mathbb{R}^+ \to \mathbb{R}^+$. For an example, see Figure 3.6.

3.4.1 Generalization of the Standard Linear Image Reconstruction Scheme

In this section we will generalize the standard linear reconstruction scheme from the usual case where the space of images is modelled as $\mathbb{L}_2(\mathbb{R}^2)$ to the more general case of an arbitrary Hilbert space H. Later we consider the case where H is a Hilbert space of Sobolev-type.

Let $\{\tilde{\psi}_k\}_{k=1}^n$ be a set of n continuous linear functionals (features) on a Hilbert space H, which are linearly independent. Then by the Riesz representation theorem there exist unique $\{\psi_k\}_{k=1}^n$ in H such that $\langle \tilde{\psi}_k, f\rangle = (\psi_k, f)_H$, for all $f \in H$. The values $(\psi_k, f)_H$, $k = 1, \dots, n$ are called features. Let V be the span of $\{\psi_k\}_{k=1}^n$. Two images $f, g \in H$ have the same features iff $f - g \in V^\perp$. This defines an equivalence relation on H and the equivalence classes are given by

$$[f] = \{g \in H \mid g \sim f\} = f + V^\perp \ .$$

Theorem 13 *Inside the metameric class of images, the unique element with minimal H-norm equals the orthogonal projection of f onto V:*

$$\mathcal{P}_V f = \sum_{k=1}^{n} (\psi^k, f)\psi_k, \tag{3.10}$$

where the reciprocal base vectors are given by $\psi^k = \sum_{l=1}^{n} G^{kl}\psi_l$, where $\sum_{k=1}^{n} G^{ik}G_{kj} = \delta_j^i$, with Gramm-matrix: $G = [G_{kj}] = [(\psi_k, \psi_j)_H]$.

Proof By the Pythagoras theorem we have

$$\min_{g\in[f]} \|g\|^2 = \min_{g\in[f]} \|g - \mathcal{P}_V f + \mathcal{P}_V f\|^2 = \min_{g\in[f]} \|g - \mathcal{P}_V f\|^2 + \|\mathcal{P}_V f\|^2 \tag{3.11}$$

and this equals $\|\mathcal{P}_V f\|^2$ only in the case $g = \mathcal{P}_V f$. Finally we notice that a closed[10] linear subspace of a Hilbert space is again a Hilbert space and thereby the orthogonal projection is

[10] A finite dimensional subspace is always closed, but this statement reveals how to deal with the case $n \to \infty$.

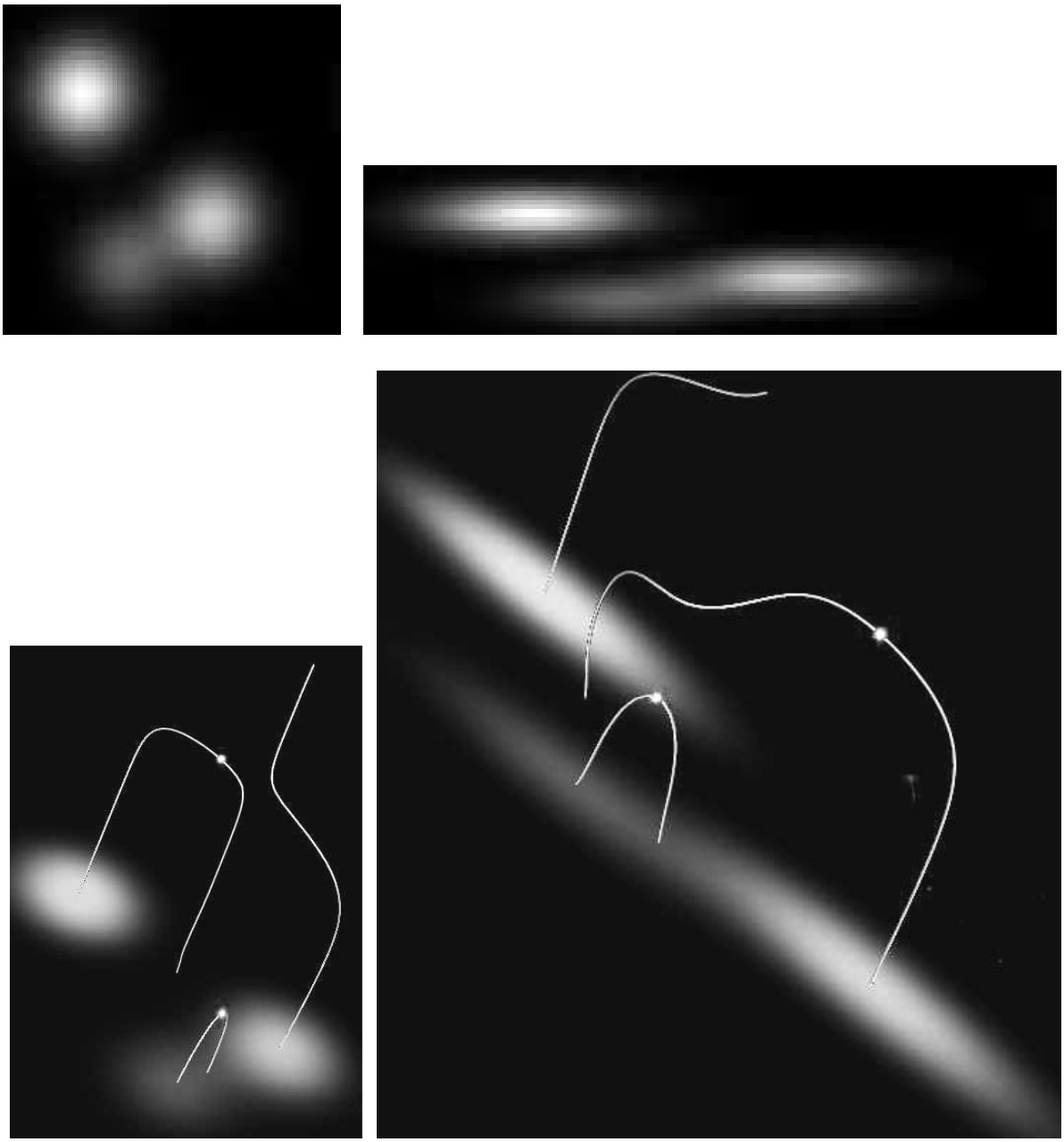

Figure 3.6: The positions of top-points is not affine invariant. Upper row: left original image, right affinely transformed image $(x, y) \mapsto (2x, \frac{1}{2}y)$. Bottom row critical paths and top-points in corresponding scale spaces.

unique. □

The special case $H = \mathbb{L}_2(\mathbb{R}^2)$ in Theorem 13, is a standard linear reconstruction scheme in image analysis, see for example [100] and later [88], [81]. In image analysis this reconstruction theory is usually put in a more indirect Euler-Lagrange framework. For example in the work of Nielsen and Lillholm, cf. [100], [88], where it is already mentioned that the prior need not be an $\mathbb{L}_2$-norm and that there exist much better priors (in the sense that one clearly obtains visually more appealing image reconstructions), such as minimal entropy and a first order Sobolev-norm. But the authors used iterative non-linear schemes to approximate the global minimum. In case of a minimum entropy based prior, which is not[11] a norm induced by an inner product, this is a sensible approach. However, in the case where the prior equals a norm of Sobolev type the exact minimum is given by $P_V f$ according to Theorem 13. Lemma 4 shows that if the prior is a norm on a Hilbert space this boils down to the same result as in Theorem 13 (*as it should*).

Lemma 4 *In the Euler Lagrange framework, the unique solution of the minimization of the convex positive energy $E(g) = \frac{1}{2}(g,g)_H$, under the conditions $(\psi_i, g)_H = c_i \in \mathbb{C}$ (fixed) for $i = 1, \ldots, n$, where $\{\psi_i\}$ are linearly independent in H,satisfies*

$$< DE(g), f >= (g,f) = \sum_{i=1}^{n} \lambda^i (\psi_i, f)_H, \quad \text{for all } f \in H \tag{3.12}$$

and is given by the orthogonal projection $g = \mathcal{P}_V f$, given by (3.10), of the original image f on the linear span V of the filters ψ_i.

Proof
The uniqueness and last part of the proof is already given by Theorem 13. With respect to the first part we only mention that the Gateaux variation of the energy at g in the direction of f is given by

$$< DE(g), f >= \lim_{\lambda \to 0} \frac{E(g + \lambda f) - E(f)}{\lambda} = (g,f), \text{ for all } f \in H$$

and the Lagrange multipliers must be equal to $\lambda^i = (\psi^i, g)$, where $\{\psi^i\}_{i=1}^n$ denotes the reciprocal basis. □

Instead of iterative schemes we can directly compute the exact solution $P_V f$, for the cases (recall the example in section 3.4.2.1) where the Hilbert space H equals a space of Sobolev-type, for example $\mathbb{H}_\gamma^{k,2}(\mathbb{R}^2) = \{f \in \mathbb{L}_2(\mathbb{R}^2) \mid (Rf, Rf) = (R^2 f, f) < \infty\}$, where $R = (I + \gamma^{2k} |\Delta|^k)^{\frac{1}{2}}$, $k = 1, 2, \ldots$, $\gamma > 0$, as explained in Corollary 1. In the next chapter we will deal with some important theoretical issues that inevitably arise when working with spaces of Sobolev type, but it is not necessary to understand all details to understand the algorithm from a practical point of view. At this point, if the reader is not interested in these more theoretical aspects, he/she is directly referred to Figures 3.8 and 3.7 and Corollaries 1 and 2.

[11] A norm on a vector space V is induced by an inner product iff the parallelogram law $\|\mathbf{x} + \mathbf{y}\|^2 + \|\mathbf{x} - \mathbf{y}\|^2 = 2(\|\mathbf{x}\|^2 + \|\mathbf{y}\|^2)$ holds for all $\mathbf{x}, \mathbf{y} \in V$. In this case the inner product is given by $(\mathbf{x}, \mathbf{y}) = \frac{1}{4}\{\|\mathbf{x} + \mathbf{y}\|^2 - \|\mathbf{x} - \mathbf{y}\|^2 + i\|\mathbf{x} - i\mathbf{y}\|^2 - i\|\mathbf{x} + i\mathbf{y}\|^2\}$.

3.4.2 Gelfand Triples

Let H be a complex Hilbert space and $\mathcal{R}$ an unbounded, positive and selfadjoint operator on H, for which the inverse $\mathcal{R}^{-1}$ is bounded. Note that the boundedness of $\mathcal{R}^{-1}$ implies that the domain $D(\mathcal{R}) = \{f \in H \mid \mathcal{R}f \in H\}$ equals $D(\mathcal{R}) = \mathcal{R}^{-1}(H)$.

Definition 13 *Define the space H^I as the linear space $D(\mathcal{R})$ equipped with the inner product $(f,g)_I = (\mathcal{R}f, \mathcal{R}g)_H$ for all $f, g \in H$.*

Notice that H^I is again a Hilbert space: Let f_n be a Cauchy sequence in H^I. Then $\mathcal{R}f_n$ is a Cauchy sequence in H. H is a Hilbert space, so $\mathcal{R}f_n \to g$ in H, for some $g \in H$. But then, since $\mathcal{R}^{-1}$ is bounded, it follows that f_n is also a Cauchy sequence in H: $\|f_n - f_m\| \leq \|\mathcal{R}^{-1}\|\|\mathcal{R}f_n - \mathcal{R}f_m\|$. So $f_n \to f$ in H, for some $f \in H$. Now $\mathcal{R}$ is self adjoint and therefore closed, so $f \in \mathcal{D}(\mathcal{R})$ and $\mathcal{R}f = g$. Now we have $\mathcal{R}f_n \to \mathcal{R}f$ in H, so $f_n \to f$ in H^I and $f \in H^I$.

Definition 14 *Define the Hilbert space H^{-I} as the completion of H equipped with the inner product $(f,g)_{-I} = (\mathcal{R}^{-1}f, \mathcal{R}^{-1}g)_H$.*

The operator $\mathcal{R}$ on H induces the map $\tilde{\mathcal{R}} : H^I \to H$ by $\tilde{\mathcal{R}}f = \mathcal{R}f$ for all $f \in H^I = D(\mathcal{R})$. Since $\|\tilde{\mathcal{R}}f\|_H = \|f\|_I$ for all $f \in H^I$, the map $\tilde{\mathcal{R}}$ is an isometry. By boundedness of R^{-1}, it follows that $\tilde{R}$ is also surjective and hence a unitary map.

Define $\check{\mathcal{R}} : D(\mathcal{R}) \to H^{-I}$ by $\check{\mathcal{R}}f = \mathcal{R}f$ for all $f \in D(\mathcal{R})$. Since $\|\check{\mathcal{R}}f\|_{-I} = \|f\|_H$ for all $f \in D(\mathcal{R})$, the map $\check{\mathcal{R}}$ is closable and its extension is an isometry. Since $\mathcal{R}(D(\mathcal{R})) = H$ and H is dense in H^{-I} the closure is also surjective, hence a unitary map. Write $\tilde{\check{\mathcal{R}}}$ for the closure of $\check{\mathcal{R}}$. Hence the following triple (known as Gelfand Triple) is obtained

$$H^I \overset{\tilde{\mathcal{R}}}{\hookrightarrow} H \overset{\tilde{\check{\mathcal{R}}}}{\hookrightarrow} H^{-I}. \tag{3.13}$$

It follows by the Riesz representation theorem and the unitarity of $\tilde{\mathcal{R}}$ and $\tilde{\check{\mathcal{R}}}$ that the space H^{-I} is naturally isomorphic to the anti-dual space of H^I under the pairing $\langle F, f\rangle = (\tilde{\check{\mathcal{R}}}^{-1}F, \tilde{\mathcal{R}}f)_H$ for all $F \in H^{-I}$ and $f \in H^I$. Note that by the selfadjoint-ness of $\mathcal{R}$

$$\langle F, f\rangle = (F, f)_H \tag{3.14}$$

if $F \in H$ for all $f \in H^I$. In this paper $\mathcal{R}$, $\tilde{\mathcal{R}}$ and $\tilde{\check{\mathcal{R}}}$ are all denoted by the same symbol $\mathcal{R}$. From the context it is clear which operator is meant by this symbol.

3.4.2.1 Spaces of Sobolev Type

By a Theorem of John von Neumann, [132]p.200, we have that for every closed densely defined operator $\mathcal{A}$ in a Hilbert space H the operator $\mathcal{A}^*\mathcal{A}$ is self adjoint and $(I + \mathcal{A}^*\mathcal{A})$ has a bounded

inverse. So a particular case of a Gelfand triple is obtained by setting $\mathcal{R} = (I + \mathcal{A}^*\mathcal{A})^{1/2}$, where $\mathcal{A}$ is a closed densely defined operator. In that case we have

$$(f, g)_I = (\mathcal{R}f, \mathcal{R}g)_H = (f, g)_H + (\mathcal{A}f, \mathcal{A}g)_H \ . \tag{3.15}$$

Example 1: Let $k \in \mathbb{N}$. Then it is well-known that the operator $D_k = (1 + \gamma^{2k}|\triangle|^k)^{\frac{1}{2}}$ with domain $\mathbb{H}^{k,2}_\gamma(\mathbb{R}^2)$ is an unbounded, positive and self-adjoint operator on $\mathbb{L}_2(\mathbb{R}^2)$ with bounded inverse. So $\mathcal{A} = \gamma(\sqrt{-\Delta})^k$ and $\mathcal{R} = D_k$ and we obtain the Gelfand triple

$$\mathbb{H}^{k,2}_\gamma(\mathbb{R}^2) \hookrightarrow \mathbb{L}_2(\mathbb{R}^2) \hookrightarrow \mathbb{H}^{-k,2}_\gamma(\mathbb{R}^2). \tag{3.16}$$

For a detailed discussion on these spaces, in particular $\gamma = 1$, we refer to [132]I.10, pp.56.
Remark: The Gelfand triple structure is interesting for the case that $\mathcal{A}$ is unbounded, since if $\mathcal{A}$ is bounded (and thereby $\mathcal{R}$ is bounded) we have by (3.15) that :

$$\|f\|^2_H \leq \|f\|^2_I \leq (1 + \|\mathcal{A}\|^2)\|f\|^2_H,$$

so the norms (and the thereby induced topologies) are equivalent. Moreover, if $\mathcal{A}$ is bounded the set $\mathcal{D}(\mathcal{R})$ equals H and the Riesz representant of $f \mapsto (\phi, f)$ in H^I is given by $\mathcal{R}^{-2}\phi = (I + \mathcal{A}^*\mathcal{A})^{-1}\phi$:

$$(\mathcal{R}^{-2}\phi, f)_I = (\mathcal{R}^{-1}\phi, \mathcal{R}f)_H = (\mathcal{R}\mathcal{R}^{-1}\phi, f)_H = (\phi, f)_H.$$

Summarizing, if $\mathcal{A}$ is bounded the sets H^I and H are equal and by the Riesz representation theorem H is unitary equivalent with its dual H', so operator $\mathcal{A}$ only tells us how H is identified with H'.

3.4.2.2 Trajectory Spaces

In a Hilbert Space H we consider the general evolution equation $\frac{du}{ds} = \mathcal{A}u$, with $\mathcal{A}$ a negative unbounded self-adjoint operator. $\mathcal{A}$ is the infinitesimal generator of a holomorphic semi-group. Solutions $u(\cdot) : (0, \infty) \to H$ of this equation are called trajectories. Such a trajectory may or may not correspond to an "initial condition at $s = 0$" in H. The set of trajectories is considered as a space of generalized functions. The test function space is defined to be $\mathcal{S}_{H,\mathcal{A}} = \bigcup_{s>0} e^{s\mathcal{A}}(H)$.

Theorem 14 *Let H be a Hilbert space. Let Q be a strongly continuous, holomorphic semi-group, with infinitesimal generator $\mathcal{A} < 0$. Then $\mathcal{S}_{H,\mathcal{A}}$ consists exactly of those $f \in \mathcal{D}(\mathcal{A}^\infty)$ such that*

$$\sum_{k=1}^{\infty} \frac{s^k}{k!}\|\mathcal{A}^k f\| < \infty \qquad \textit{for a certain } s > 0 \ . \tag{3.17}$$

This is a well-known result in functional analysis and its proof can for example be found in [111] or in the Appendix of this thesis, section 6.2, Theorem 25.Now by taking $\mathcal{R} = e^{-s\mathcal{A}}$ on H, with bounded inverse $e^{s\mathcal{A}}$ we obtain the following Gelfand triples:

$$\mathcal{S}_{H,\mathcal{A}} \overset{\mathcal{R}}{\hookrightarrow} H \overset{\mathcal{R}}{\hookrightarrow} \mathcal{S}'_{H,\mathcal{A}}. \tag{3.18}$$

Example: $H = \mathbb{L}_2(\mathbb{R}^d)$, $\mathcal{A} = \Delta$, then $(\mathcal{R}^{-1}f) = K_s^1 * f$, where $K_s^1 = G_s$ is the Gaussian kernel, and we obtain the Gelfand triple

$$\mathcal{S} \overset{\mathcal{R}}{\hookrightarrow} \mathbb{L}_2(\mathbb{R}^d) \overset{\mathcal{R}}{\hookrightarrow} \mathcal{S}'. \tag{3.19}$$

where $\mathcal{S}_{\mathbb{L}_2(\mathbb{R}^d),\Delta} = \mathcal{S} = \{\phi \in C^\infty(\mathbb{R}^d) \mid \forall_{\mathbf{k},\mathbf{q}} \sup_{\mathbf{x}\in\mathbb{R}^d} |\mathbf{x}^{\mathbf{k}}\phi^{(\mathbf{q})}| < \infty\}$ is the usual Schwarz space.[12]

3.4.3 A Linear Image Reconstruction Based on Inner Products of Sobolev Type

By taking the space of images H^I (for example $H^I = \mathbb{H}_\gamma^{2k,2}(\mathbb{R}^d)$ or $H^I = \mathcal{S}_{\mathbb{L}_2(\mathbb{R}^(d)),-(-\Delta)^\alpha}$) in Theorem 13 we obtain the metameric class

$$[f] = \{g \in H^I \mid (\kappa_k, f)_I = (\kappa_k, g)_I, \text{ for } k = 1, \ldots, n\}\ , \quad \text{with } \kappa_k = \mathcal{R}^{-2}\psi_k, k = 1, \ldots n,$$

and the optimal solution within this metameric class $\arg\min_{g\in[f]} \|g\|_{H^I}^2$, is given by $g = P_V f$. Notice that $(\kappa_k, g)_I = (\psi_k, g)_{\mathbb{L}_2(\mathbb{R}^2)}$, so the metameric classes still consist of images (within H^I) with the same features. But initially, the space of images was the modeled by $H = \mathbb{L}_2(\mathbb{R}^2)$ space (and not the smooth space H^I), so we want our metameric classes within $\mathbb{L}_2(\mathbb{R}^2)$ rather than H^I. Theorem 15, takes care of this.

Theorem 15 *Let $f \in H$. Let $[f]$ denote the metameric class of all elements $g \in H$ such that*

$$g \sim f \Leftrightarrow (\mathcal{R}^{-1}f, \mathcal{R}\kappa_k)_I = (\mathcal{R}^{-1}g, \mathcal{R}\kappa_k)_I\ ,\ \textit{for all } k = 1, \ldots, n.$$

with $\kappa_k \in H^{II} := (H^I)^I$, i.e. $\mathcal{R}\kappa_k \in H^I$. Then the unique solution of the minimization problem $\min_{g\in H^I, g\sim f} \|g\|_I$ is given by $g = P_V^{ext} f := \sum_{i=1}^n (\mathcal{R}\kappa^i, \mathcal{R}^{-1}f)_I \kappa_i$, with $\kappa^i = \sum_{j=1}^n G^{ij}\kappa_j$, where $\sum_{k=1}^n G^{ik}G_{kj} = \delta_j^i$, with $G_{kj} = (\kappa_k, \kappa_j)_I$.

Proof
First notice that P_V^{ext} is the natural extension of P_V, i.e. the restriction of P_V^{ext} to H^I equals P_V: $P_V^{ext}\big|_{H^I} = P_V$, which directly follows by the fact that $\mathcal{R}$ is self adjoint and therefore

$$(\mathcal{R}\psi, \mathcal{R}^{-1}f)_I = (\psi, f)_I \text{ for all } f \in H^I \text{ and } \psi \in H^{II}. \tag{3.20}$$

Without loss of generality we may assume that $\{\kappa_k\}$ is an orthonormal base in H_I. Then we have $g - P_V^{ext} f \perp P_V^{ext}$, since by $f \sim g$ and (3.20) it follows that

$$(g - P_V^{ext} f, P_V^{ext})_I = \sum_{j=1}^n (\mathcal{R}\kappa^j, \mathcal{R}^{-1}f)(g, \kappa_j) - \sum_{j=1}^n \overline{(\mathcal{R}\kappa^j, \mathcal{R}^{-1}f)}(\mathcal{R}\kappa^j, \mathcal{R}^{-1}f) = 0\ .$$

So again Pythagoras: $\min_{g\sim f, g\in H_I} \|g\|_I^2 = \min_{g\sim f, g\in H_I} \|g - \mathcal{P}_V^{ext} f + \mathcal{P}_V^{ext} f\|_I^2 = \min_{g\sim f, g\in H_I} \|g - \mathcal{P}_V^{ext} f\|_I^2 + \|\mathcal{P}_V^{ext} f\|_I^2$ we conclude that this equals $\min_{g\sim f, g\in H_I} \|g\|_I^2 = \|\mathcal{P}_V^{ext} f\|_I^2$ iff $g = \mathcal{P}_V^{ext} f$ □

[12] In case of the Poisson semigroup ($\mathcal{A} = -\sqrt{-\Delta}$) leads to the Gelfand-Shilov space $\mathcal{S}_1$ rather than the Schwarz space, see [30].

By taking the respective pairs $H = \mathbb{L}_2(\mathbb{R}^d)$, $\mathcal{R} = (I + \gamma^{2k}|\Delta|^k)^{\frac{1}{2}}$ and $H = \mathbb{L}_2(\mathbb{R}^d)$, $\mathcal{R} = e^{\frac{s}{2}|\Delta|^\alpha}$ in Theorem 15 we obtain the following corollaries:

Corollary 1 *Let $f \in \mathbb{L}_2(\mathbb{R}^d)$. Let $[f]$ denote the equivalence class of all elements $g \in \mathbb{L}_2(\mathbb{R}^d)$ such that*

$$g \sim f \Leftrightarrow (\psi_i, f)_{\mathbb{L}_2(\mathbb{R}^2)} = (\psi_i, g)_{\mathbb{L}_2(\mathbb{R}^2)}, \text{ for all } i = 1, \ldots, n.$$

Then the unique solution of the minimization problem

$$\min_{g \in \mathbb{H}^{k,2}_\gamma(\mathbb{R}^2), g \sim f} \|g\|^2_{\mathbb{H}^{k,2}_\gamma(\mathbb{R}^2)} = \min_{g \in \mathbb{H}^{k,2}_\gamma(\mathbb{R}^2), g \sim f} (g,g)_{\mathbb{L}_2(\mathbb{R}^2)} + (g, \gamma^{2k}|\Delta|^k g)_{\mathbb{L}_2(\mathbb{R}^2)}$$

is given by $g = P^{ext}_V f$, where $P^{ext}_V f = \sum_{i=1}^n ((I + \gamma^{2k}|\Delta|^k)^{\frac{1}{2}}\kappa^i, (I + \gamma^{2k}|\Delta|^k)^{-\frac{1}{2}} f)_{\mathbb{H}^{k,2}_\gamma(\mathbb{R}^2)} \kappa_i$, where κ^i are the reciproke vectors of $\kappa_i = (I + \gamma^{2k}|\Delta|^k)^{-1}\psi_i$.

Important: Notice that $\kappa_i = \mathcal{R}^{-2}\psi_i = R^{d=2}_{k,\gamma} * \psi_i$, where

$$R^{k,\gamma}_{d=2}(\mathbf{x}) = \mathcal{F}^{-1}(\boldsymbol{\omega} \mapsto \frac{1}{2\pi}(1 + \gamma^{2k}|\boldsymbol{\omega}|^{2k})^{-1})(\mathbf{x}) \tag{3.21}$$

is the reproducing kernel (at $\mathbf{0}$) of $\mathbb{H}^{k,2}_\gamma(\mathbb{R}^2)$, for $k > 1$, see Appendix 6.1. The reproducing kernels are needed to project $\mathbb{L}_2$-linear onto linear Sobolev-features, which is the basic reason for the succes of our approach to feature reconstruction: The features themselves do not change, but the projection basis is subject to a Tikhonov regularization. In this way " the reconstructed Lena gets rid of her smallpox ", in Fig 3.8.

Corollary 2 *Let $f \in \mathbb{L}_2(\mathbb{R}^d)$. Let $[f]$ denote the equivalence class of all elements $g \in \mathbb{L}_2(\mathbb{R}^d)$ such that*

$$g \sim f \Leftrightarrow (\psi_k, f)_{\mathbb{L}_2(\mathbb{R}^2)} = (\psi_k, g)_{\mathbb{L}_2(\mathbb{R}^2)}, \text{ for all } k = 1, \ldots, n.$$

Then the unique solution of the minimization problem

$$\min_{g \in \mathcal{S}_{\mathbb{L}_2(\mathbb{R}^2), -|\Delta|^\alpha}, g \sim f} (g,g)_{\mathbb{L}_2(\mathbb{R}^2)} + \sum_{k=1}^\infty \frac{1}{k!}(g, s^{2k}|\Delta|^{\alpha k} g)_{\mathbb{L}_2(\mathbb{R}^2)} \tag{3.22}$$

is given by $g = P^{ext}_V f$, where $P^{ext}_V f = \sum_{i=1}^n (e^{\frac{s}{2}|\Delta|^\alpha}\kappa^i, e^{-\frac{s}{2}|\Delta|^\alpha} f)_{\mathcal{S}_{\mathbb{L}_2(\mathbb{R}^2), -|\Delta|^\alpha}} \kappa_i$, where κ^i are the reciproke vectors of $\kappa_i = \left(e^{\frac{s}{2}|\Delta|^{2\alpha}}\right)^{-2} \psi_i = K^\alpha_{s/2} * K^\alpha_{s/2} * \psi_i = K^\alpha_s * \psi_i$.

We are mainly interested in the case where the features are obtained by α derivatives within the scale space image u of the original image f, i.e. $\psi_k(\mathbf{x}) = (\tau_{\mathbf{b}_k} D^{\mathbf{n}_k} K_{s_k})^\alpha(\mathbf{x}) = D^{\mathbf{n}_k} K^\alpha_{s_k}(\mathbf{x} - \mathbf{b}_k)$ for some multi-index $\mathbf{n}_k$, some position $\mathbf{b}_k \in \mathbb{R}^d$ and some scale s_k. In this case we can analytically compute the Grammian matrix (and thereby analytically compute the solution $g = P^{ext}_V f$):

$$\begin{aligned} G_{kj} &= (\kappa_k, \kappa_j)_{\mathcal{S}_{\mathbb{L}_2(\mathbb{R}^2), -|\Delta|^\alpha}} = (\mathcal{R}^{-2}\psi_k, \mathcal{R}^{-2}\psi_j)_{\mathcal{S}_{\mathbb{L}_2(\mathbb{R}^2), -|\Delta|^\alpha}} = (\mathcal{R}^{-1}\psi_k, \mathcal{R}^{-1}\psi_j)_{\mathbb{L}_2(\mathbb{R}^2)} \\ &= (\tau_{\mathbf{b}_k} D^{\mathbf{n}_k} K^\alpha_{s_k + (s/2)}, \tau_{\mathbf{b}_j} D^{\mathbf{n}_j} K^\alpha_{s_j + (s/2)})_{\mathbb{L}_2(\mathbb{R}^2)} = \left(K^\alpha_{s_j + s_k + s}\right)^{(\mathbf{n}_k + \mathbf{n}_j)} (\mathbf{b}_k - \mathbf{b}_j) \ . \end{aligned} \tag{3.23}$$

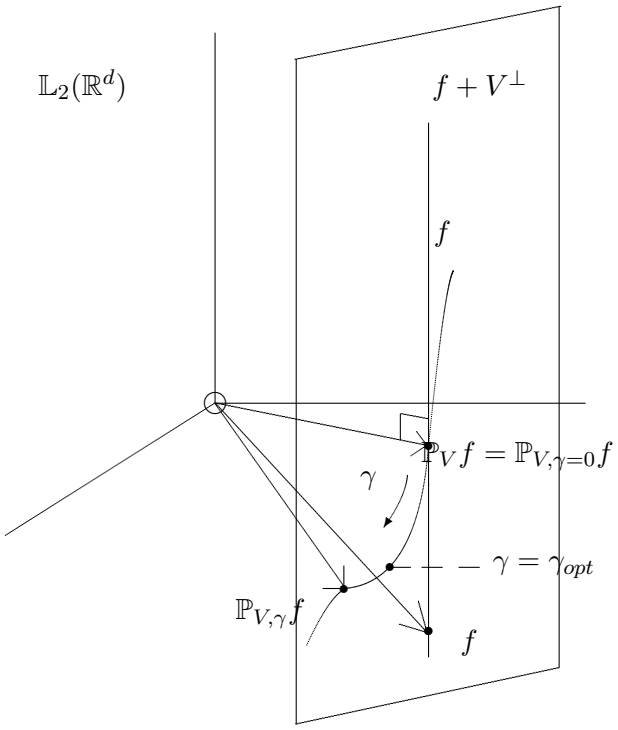

Figure 3.7: Illustration of metameric class V of images with equal features. For $\gamma = 0$ we have a orthogonal projection. For $\gamma > 0$ this projection is orthogonal in $\mathbb{H}_\gamma^{k,2}(\mathbb{R}^2)$ and thereby it (its extension) is a skew projection in $\mathbb{L}_2(\mathbb{R}^2)$. We obtain a connected curve parametized by γ where the smoothness of the projection increases with $\gamma > 0$.

Important: Here again the features are preserved and the base functions are smoothed. But now the smoothing kernels are given by the α-kernels themselves rather than the reproducing kernels of the isotropic Sobolev-spaces in the previous corollary. So instead of Tikhonov-regularization we smooth according to ordinary α-scale spaces. The relation between these qualitatively different ways of smoothing is given by the Laplace transform with respect to the scale parameter

$$\boxed{\mathcal{L}[s \mapsto K_s^\alpha](\gamma^{-2k}) = \gamma^{2k} R^{d=2}_{k,\gamma,\mathbf{0}} \quad \text{for all } \gamma > 0, \text{ where } \alpha = k.} \tag{3.24}$$

By interchanging the order of Laplace transformation and integration, it is not difficult to obtain an analytic formula for the Grammian matrix in Corollary 1 (and thereby analytic formulas for the orthogonal projection) for the cases where $\alpha = k$ as we will show in the next subsection.

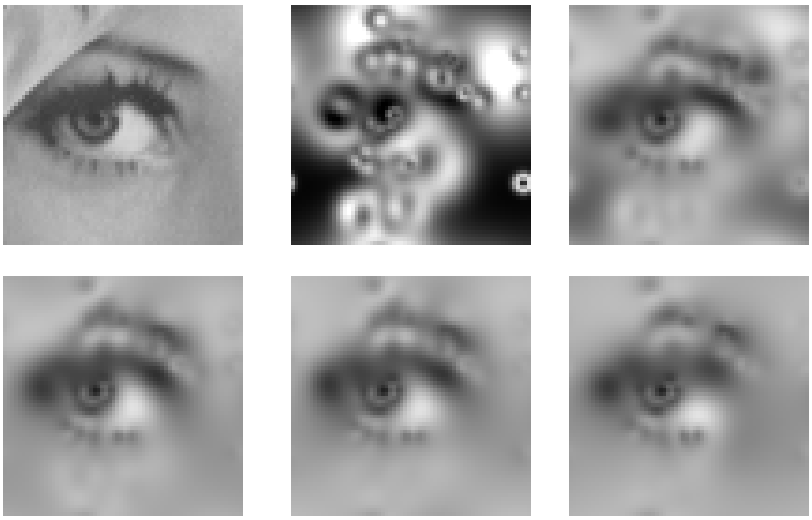

Figure 3.8: Reconstruction from 31 top-points of "Lena's eye" with up to second order features only. The upper row shows the original image and reconstructions with $\gamma = 0$ and $\gamma = 5$. The second row shows reconstructions with $\gamma = 22$, $\gamma = 50$ and $\gamma = 250$. The first image in the second row shows the reconstruction with the lowest relative $\mathbb{L}_2$-error. For more details on evaluation we refer to our earlier work,[78],[80].

3.4.4 Linear Reconstruction Algorithms

Next we explicitly describe the reconstruction algorithm, for the case $H = \mathbb{L}_2(\mathbb{R}^2)$ and $\mathcal{R} = (I + \gamma^{2k}|\Delta|^k)^{\frac{1}{2}}$, but we notice that the algorithm is easily translated to other pairs $(H, \mathcal{R})$.

1. Suppose a set of scale space positions is given $\{\mathbf{x}_i, s_i\}$, for example top-points. Suppose at the i-th point we want to include the N_i-th jet.
2. Compute the normalization factors

$$(\lambda_{\mathbf{x}_i,\mathbf{n}_i,s_i})^2 \quad = \frac{e^{\gamma^{-2k}\, s}}{2\pi\gamma^{2k}} \int_{2\,s_i}^{\infty} (K_t^\alpha)^{(2\,\mathbf{n}_i)}(\mathbf{0})\; e^{-t\gamma^{-2k}} \mathrm{d}t. \tag{3.25}$$

where $\mathbf{n}_i$ is any multi-index such that $|\mathbf{n}_i| \leq N_i$. In case $k = \alpha = 1$ they are equal to

$$\frac{e^{2\gamma^{-2}s_i}}{(2\pi)^3\gamma^2}(-s)^{-|\mathbf{n}_i|}\,\Gamma[n_i^1+\frac{1}{2}]\,\Gamma[n_i^2+\frac{1}{2}]\,E_{1+|\mathbf{n}_i|}(2\gamma^{-2}s_i)\ , \tag{3.26}$$

where $E_n(z) = \int_1^\infty t^{-n}e^{-zt}\,\mathrm{d}t$ denotes the well-known exponential integral function.

3. Compute the feature vector $\mathbf{f} = (\mathbf{f}_{\mathbf{n}_1}, \ldots, \mathbf{f}_{\mathbf{n}_n})$, with

$$\mathbf{f}_{\mathbf{n}_j} = (\lambda_{\mathbf{x}_i,\mathbf{n}_i,s_i})^{-1}\ D_{s_j}^{\mathbf{n}_j} f(\mathbf{x}_j) = (\lambda_{\mathbf{x}_i,\mathbf{n}_i,s_i})^{-1}\ (K_{s_j}^{(\mathbf{n}_j)} * f)(\mathbf{x}_j),\ \text{for all } |\mathbf{n}_j| \leq N_j.$$

4. Compute the basis vectors $\{\kappa_j\}_{j=1}^n$:

$$\kappa_j(\mathbf{x}) = (\lambda_{\mathbf{x}_i,\mathbf{n}_i,s_i})^{-1}(R^d_{\gamma,k,\mathbf{0}} * K_{s_j}^{(\mathbf{n}_j)})(\mathbf{x}), \mathbf{x} \in \mathbb{R}^d.$$

5. Compute the Grammian Matrix

$$\begin{aligned} G^{2k,\gamma}_{\mathbf{x}_i,\mathbf{n}_i,s_i\,;\,\mathbf{x}_j,\mathbf{n}_j,s_j} &= (\kappa_i,\kappa_j)_I = (\lambda_{\mathbf{x}_i,\mathbf{n}_i,s_i})^{-1}(\lambda_{\mathbf{x}_j,\mathbf{n}_j,s_j})^{-1} \\ &\quad \tfrac{1}{2\pi}\int_{\mathbb{R}^2} \tfrac{1}{1+\gamma^{2k}\|\boldsymbol{\omega}\|^{2k}}(i\boldsymbol{\omega})^{\mathbf{n}_i+\mathbf{n}_j}\,\tfrac{e^{-(s_i+s_j)\|\boldsymbol{\omega}\|^{2\alpha}}}{4\pi^2}e^{i\boldsymbol{\omega}\cdot(\mathbf{x}_i-\mathbf{x}_j)}\,\mathrm{d}\boldsymbol{\omega}, \end{aligned} \tag{3.27}$$

organized in $N_i \times N_j$- matrices G_{ij} organized as block-matrices in an $N_n \times N_n$-square matrix G, where $N_n = \sum_{j=1}^n N_j$.

6. Compute $\mathbf{h} = G^{-1}\mathbf{f}$ by means of a singular value decomposition: Let $V = (\mathbf{v}_1|\cdots|\mathbf{v}_n)$ be the matrix, where $\mathbf{v}_i$ are the orthonormal eigenvectors of G^TG, with positive eigenvalues σ_i^2, then $G = U\,D\,V^T$, where $D = \mathrm{diag}(\sigma_i)$ and the orthogonal matrix U is given by $U = A\,V\,D^{-1}$. So compute

$$\mathbf{h} = V\,D^{-1}\,U^T\,\mathbf{f} = \sum_{i=1}^n \frac{\mathbf{u}_i\cdot\mathbf{f}}{\sigma_i}\mathbf{v}_i, \tag{3.28}$$

where σ_i is put to zero if it is smaller than a given tolerance. Notice to this end that the condition number of the matrix G equals $\|G\|\|G^{-1}\| = \frac{\sigma_1}{\sigma_n}$, where σ_1 and σ_n equal respectively the largest and smallest singular value.

7. Compute the reconstruction image $\sum_{i=1}^n h^i\kappa_i(\mathbf{x})$ for all $\mathbf{x} \in \mathbb{R}^2$.

The two key-points in this algorithm is the computation of the Grammian matrix (3.27) and the computation of $\mathbf{h}$ where this Grammian matrix has to be inverted. Furthermore, we notice that the normalization step (3.25) is important concerning the condition number of the Grammian matrix as it ensures that all diagonal elements are equal to 1.

3.4.4.1 Computation of the Grammian Matrix

In the trajectory space case, where $\mathcal{R} = e^{s|\Delta|^\alpha}$ we can compute the Grammian matrix symbolically, which makes the algorithm much faster. Next we will derive a similar (but slightly less elegant) formula for the cases $H = \mathbb{L}_2(\mathbb{R}^2)$ and $\mathcal{R} = (I + \gamma^{2k}|\Delta|^k)^{\frac{1}{2}}$ and $k = 2^p$, $p \in \mathbb{N} \cup \{0\}$. With this respect we notice that by means of the recursion relation 6.4 derived in section 4.4 of the Appendix it follows that

$$G^{2k,\gamma}_{\mathbf{x}_i,\mathbf{n}_i,s_i\,;\,\mathbf{x}_j,\mathbf{n}_j,s_j} = \frac{1}{2}\left[G^{k,\gamma\,e^{\frac{+i\pi}{4k}}}_{\mathbf{x}_i,\mathbf{n}_i,s_i\,;\,\mathbf{x}_j,\mathbf{n}_j,s_j} + G^{k,\gamma\,e^{\frac{-i\pi}{4k}}}_{\mathbf{x}_i,\mathbf{n}_i,s_i\,;\,\mathbf{x}_j,\mathbf{n}_j,s_j}\right], \tag{3.29}$$

so the cases $p = 1, 2, 3$ easily follow by the cases $p = 0$, i.e. $k = 1$.

We now consider the case $k = \alpha$ and compute the other cases by means of the recursion (3.29). In case $k = \alpha$, it directly follows from (3.27) that $s = s_i + s_j \mapsto G^{k=\alpha,\gamma}_{\mathbf{x}_i,\mathbf{n}_i,s_i\,;\,\mathbf{x}_j,\mathbf{n}_j,s_j}$ satisfies the following differential equation

$$G^{k=\alpha,\gamma}_{\mathbf{x}_i,\mathbf{n}_i,s_i\,;\,\mathbf{x}_j,\mathbf{n}_j,s_j} - \gamma^{2k}\,\frac{\partial}{\partial s}G^{k=\alpha,\gamma}_{\mathbf{x}_i,\mathbf{n}_i,s_i\,;\,\mathbf{x}_j,\mathbf{n}_j,s_j} = (\lambda_{\mathbf{x}_i,\mathbf{n}_i,s_i})^{-1}(\lambda_{\mathbf{x}_j,\mathbf{n}_j,s_j})^{-1}\frac{1}{2\pi}(K^\alpha_s)^{(\mathbf{n}_i+\mathbf{n}_j)}(\mathbf{x}_i - \mathbf{x}_j),$$

where we notice that this first order differential equation must be solved under the side condition $G^{k=\alpha,\gamma}_{\mathbf{x}_i,\mathbf{n}_i,s_i\,;\,\mathbf{x}_j,\mathbf{n}_j,s_j} \to 0$ as $s = s_i + s_j \to \infty$. By the method of variation of constants one directly finds

$$G^{k=\alpha,\gamma}_{\mathbf{x}_i,\mathbf{n}_i,s_i\,;\,\mathbf{x}_j,\mathbf{n}_j,s_j} = (\lambda_{\mathbf{x}_i,\mathbf{n}_i,s_i})^{-1}(\lambda_{\mathbf{x}_j,\mathbf{n}_j,s_j})^{-1}\frac{e^{\gamma^{-2k}\,s}}{2\pi\gamma^{2k}}\int_s^\infty (K^\alpha_t)^{(\mathbf{n}_i+\mathbf{n}_j)}(\mathbf{x}_i - \mathbf{x}_j)\,e^{-t\gamma^{-2k}}\mathrm{dt}, \quad s = s_i + s_j. \tag{3.30}$$

This result can also be obtained by application of Laplace transform with respect to scale, recall (3.24), on (3.23), as we have

$$G^{k=\alpha,\gamma}_{\mathbf{x}_i,\mathbf{n}_i,s_i\,;\,\mathbf{x}_j,\mathbf{n}_j,s_j} = (\lambda_{\mathbf{x}_i,\mathbf{n}_i,s_i})^{-1}(\lambda_{\mathbf{x}_j,\mathbf{n}_j,s_j})^{-1}\frac{1}{2\pi\gamma^{2k}}\mathcal{L}[t \mapsto K^{(\mathbf{n}_i+\mathbf{n}_j)}_{t+s_i+s_j}(\mathbf{x}_i - \mathbf{x}_j)](\gamma^{-2k}).$$

Further we notice that in the cases $\mathbf{x}_i \neq \mathbf{x}_j$ the domain of integration in (3.30) can be split:

$$\begin{aligned} G^{k=\alpha,\gamma}_{\mathbf{x}_i,\mathbf{n}_i,s_i\,;\,\mathbf{x}_j,\mathbf{n}_j,s_j} &= (\lambda_{\mathbf{x}_i,\mathbf{n}_i,s_i})^{-1}(\lambda_{\mathbf{x}_j,\mathbf{n}_j,s_j})^{-1}\tfrac{e^{\gamma^{-2k}\,s}}{2\pi\gamma^{2k}}\left(\int_0^\infty - \int_0^s\right)(K^\alpha_t)^{(\mathbf{n}_i+\mathbf{n}_j)}(\mathbf{x}_i - \mathbf{x}_j)e^{-t\gamma^{-2k}}\mathrm{dt} \\ &= (\lambda_{\mathbf{x}_i,\mathbf{n}_i,s_i})^{-1}(\lambda_{\mathbf{x}_j,\mathbf{n}_j,s_j})^{-1}\tfrac{e^{\gamma^{-2k}\,s}}{2\pi\gamma^{2k}}\left[\gamma^{2k}(R^{d=2}_{k,\gamma})^{(\mathbf{n}j+\mathbf{n}_i)}(\mathbf{x}_i - \mathbf{x}_j) - \int_0^s (K^\alpha_t)^{(\mathbf{n}_i+\mathbf{n}_j)}(\mathbf{x}_i - \mathbf{x}_j)\,\mathrm{dt}.\right] \end{aligned}$$

In the cases $\mathbf{x}_i = \mathbf{x}_j$ (that often arise in the top-point reconstruction) the Gramm-matrix elements are easily computed. For example in case $\alpha = 1$ (Gaussian scale space) they are given by

$$G^{k=\alpha=1,\gamma,s}_{\mathbf{x}_i,\mathbf{n}_i,s_i\,;\,\mathbf{x}_j,\mathbf{n}_j,s_j} = (\lambda_{\mathbf{x}_i,\mathbf{n}_i,s_i})^{-1}(\lambda_{\mathbf{x}_j,\mathbf{n}_j,s_j})^{-1}\frac{e^{\gamma^{-2}s}}{(2\pi)^3\gamma^2}(-s)^{-\frac{\nu_1+\nu_2}{2}}\Gamma[\frac{\nu_1+1}{2}]\Gamma[\frac{\nu_2+1}{2}]E_{1+\frac{\nu_1+\nu_2}{2}}(\gamma^{-2}s)\,,$$

with $\nu_q = n^q_i + n^q_j$ *even* positive integers (if either ν_1 or ν_2 is odd the Grammian-matrix element is zero), $q = 1, 2$, and where $E_n(z) = \int_1^\infty t^{-n}e^{-zt}\,\mathrm{dt}$ denotes the well-known exponential integral function.

3.4.5 Experiments

In our top-point reconstructions we first selected a fixed number of stable top-points. We used two methods of quantifying the stability of top-points, the simplest is by means of the differential total variation

$$\sigma^4 \text{Trace}(H^2 u)(\mathbf{x}*, s*), \text{ at top point } (\mathbf{x}*, s*)$$

proposed by Platel et al.[107] and the more sophisticated method developed by Balmachnova et al., for details see [11]. To get an idea how the top-point reconstructions work out for different orders k of the underlying Sobolev space we refer to figure 3.9 and figure 3.10. The reconstructions are typically most visually appealing for $k \in (1, 2]$. To this end we notice that the kernels $R^{d=2}_{k,\gamma,\mathbf{c}}$ have a singularity at $\mathbf{x} = \mathbf{c}$ iff $k \leq 1$, the closer k approximates 0 the stronger this singularity becomes, the worse the discretization artifacts (with symmetrically sampling around the singularity) become. On the other hand if $k >> 1$, the kernels get start to oscillate yielding nasty negative sidelobes in the base functions, yielding practical problems (sampling).[13] Further we notice that minimization of the k-th order isotropic Sobolev norm,

$$\|g\|^2_{\mathbb{H}^{k,2}_\gamma} = \|g\|^2_{\mathbb{L}_2(\mathbb{R}^2)} + \gamma^2 \||\Delta|^{\frac{k}{2}} g\|^2_{\mathbb{L}_2(\mathbb{R}^2)},$$

also implies that the $\mathbb{L}_2$-norms of the generalized derivatives (up to order k) of f are minimized. Minimization of the k-th order isotropic Sobolev norm implies minimization of all Sobolev norms of order $l \leq k$. Notice to this end that

$$\|g\|^2_{\mathbb{H}^{l,2}_\gamma} \leq C(k,l) \|g\|^2_{\mathbb{H}^{k,2}_\gamma} \text{ for all } 0 \leq l \leq k, \text{ and all } g \in \mathbb{H}^{k,2}_\gamma,$$

where $C(k,l)$ equals the unique maximum value of the function $\rho \mapsto \frac{1+\rho^{2l}}{1+\rho^{2k}}$ on $\mathbb{R}^+$. Finally, we notice that the trajectory case (which is easier to implement, recall (3.23)) boils down to a minimization of an isotropic Sobolev norm of infinite order (3.22), where the coefficient of

$$\| |\Delta|^{\frac{\alpha * k}{2}} f \|^2$$

equals $\frac{s^k}{k!}$. The role of the reproducing kernel $R^{d=2}_{k,\gamma,\mathbf{c}}$ is now replaced by the α-convolution kernel (or in particularly Gaussian kernel if $\alpha = 1$), although these convolution kernels are smooth the results are not as well as in the low order Sobolev cases, see Figure 3.9 and Figure 3.10. Finally, we notice that the more details the original image has, the more top-points in scale space, the better the reconstruction, see Figure 3.11.

3.4.6 Flux-features

Besides the regularizing effect of minimizing Sobolev norms there is another advantage of using Sobolev inner products: There exist several interesting features (such as grey-value fluxes) of images which can be constructed by means of Sobolev inner products, but which cannot be constructed in the usual framework of $\mathbb{L}_2$-inner products. For example point evaluation

[13] By (3.24) the reproducing kernels $R^{d=2}_{k=\alpha,\gamma,\mathbf{c}}$ Laplace transform of the α-convolution kernels which also have these negative side-lobes for $\alpha > 1$.

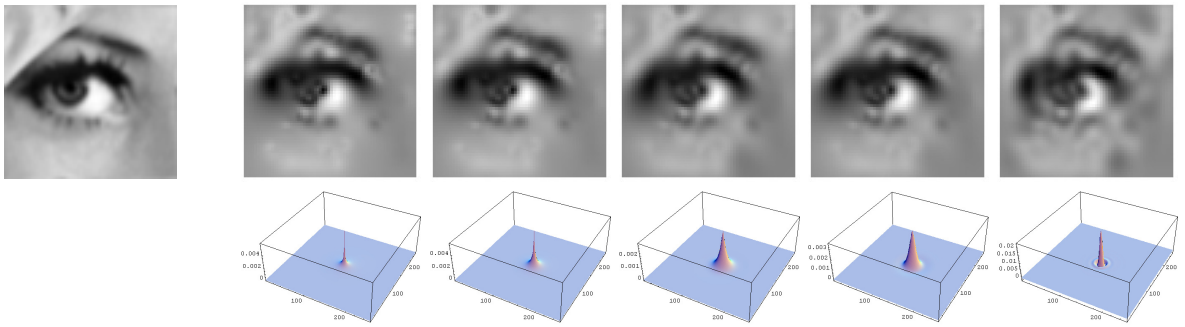

Figure 3.9: Reconstruction from 40 top-points of "Lena's eye" with up to 2nd order features only. Upper row, left: original image. Upper row, right: top-point reconstructions with respectively $(k,\gamma) = (0.75,20),(1,10),(1.5,8),(2,6),(4,2)$. The bottom row shows the involved reproducing kernels $R^{d=2}_{k,\gamma,\mathbf{c}}$, where $\mathbf{c} \in \mathbb{R}^2$ is the center of the image domain. The reconstructions are typically most visually appealing for $k \in (1,2]$. For $0 < k \leq 1$ the reproducing kernels are singular at $\mathbf{c}$, in these cases the results are usually also visually appealing if the kernels are truncated and symmetrically sampled around the singularity, but the closer k gets to 0, the stronger the discretization artifacts for small $\gamma > 0$.

Figure 3.10: Reconstruction from 40 top-points of "Lena's eye" with up to 4th order features, using Singular Value Decomposition with a fixed tolerance, for respectively $(k,\gamma) = (0.75,20),(1,10),(1.5,8),(2,6),(3,4),(4,2)$. For a comparison to the second order reconstruction with the same values of (k,γ), see figure 3.9. For the sake of comparison we took exactly the same values (k,γ), but at this point we notice that increasing the order of the linear features, the base functions become more oscillatory, so larger values of γ would yield more appealing results.

$\delta_{\mathbf{a}}(f) = f(\mathbf{a})$ is a continuous linear functional on $\mathbb{H}^{k,2}_{\gamma}(\mathbb{R}^2)$, $k > 1$. As a result (by the Riesz representation Theorem) there exists reproducing kernels, see Appendix 6.1, $R^2_{k,\gamma} \in \mathbb{H}^{k,2}_{\gamma}(\mathbb{R}^2)$, $k > 1$ such that $\delta_{\mathbf{a}}(f) = f(\mathbf{a}) = (\tau_{\mathbf{a}} R^2_{k,\gamma}, f)$, which makes point evaluations linear features. This cannot be done within the more familiar $\mathbb{L}_2(\mathbb{R}^2)$ space. Another example of possible linear features are so-called flux-features on images. They are given by the linear functionals

$$f \mapsto I_{\Omega}(f) = \int_{\partial\Omega} \frac{\partial f}{\partial n}\, \mathrm{d}\sigma, \qquad f \in \mathbb{H}^{2,2}_{\gamma}(\mathbb{R}^2).$$

where Ω is a bounded region in $\mathbb{R}^2$, with surface measure $\mu(\Omega) < \infty$ with an orientable piecewise smooth boundary $\partial\Omega$ with outward normal $\mathbf{n}$. These linear functionals are continuous on $\mathbb{H}^{k,2}_{\gamma}(\mathbb{R}^2)$ if $k \geq 2$, which directly follows by Gauss divergence theorem and Cauchy-Schwarz: $|I_{\Omega}(f)| \leq \left|\int_{\Omega} \Delta f \mathrm{d}\mathbf{x}\right| \leq \mu(\Omega)\|f\|_{\mathbb{H}^{2,2}_{\gamma}(\mathbb{R}^2)}$. As a result there exist flux-kernels $\phi_{\Omega,k,\gamma}$ in $\mathbb{H}^{k,2}_{\gamma}(\mathbb{R}^2)$, $k \geq 2$, such that

$$I_{\Omega}(f) = (\phi_{\Omega,k,\gamma}, f)_{\mathbb{H}^{k,2}_{\gamma}(\mathbb{R}^2)}.$$

Figure 3.11: Reconstruction (right) ($k = 1$, $\gamma = 10$, up to 2ndorder features in 1500 top-points) from the second order structure at stable top-points of Lena's face(left, 300×300 pixels).

The Motivation for using Flux Features:
In the previous chapters we improved top-point reconstruction by introducing spaces of Sobolev-type. The idea was to pick a smooth element within the metameric class of images with top-points at the same locations as those of the original image f, where a positive parameter controls the smoothness of this reconstruction. By increasing this parameter ($\gamma > 0$ in Corollary 1 or $s > 0$ in Corollary 2) this representative becomes smoother and thereby the number of extra top points of the scale space of this representant is reduced. Nevertheless, in practice there exists an upper bound to the parameter γ, since if the representant becomes too smooth, contrasting areas (such as corners/edges) tend to vanish, which results in so-called "edge-leaking", cf.[78]. Therefore, we propose to reduce the number of extra top-points in the representative by means of additional features. Flux-features obtained by surfaces around critical paths in scale space are highly suitable for this purpose, as they describe how grey-value particles flow between extremal paths.

3.4.6.1 Definition and Implementation of Flux Features in Scale Space

Definition 15 *Let $s > 0$, $f \in \mathbb{L}_2(\mathbb{R}^2)$, with α scale space representation $u_f^\alpha = K_s^\alpha * f$. Let Ω_s be a bounded region in $\mathbb{R}^2$, with an orientable piecewise smooth boundary $\partial\Omega_s$ with outward normal $\boldsymbol{n}$. Then we define the flux feature $I_{\Omega_s}^\alpha(f,s) = \frac{\partial}{\partial t} \int_{\Omega_s} u_f^\alpha(\boldsymbol{x},t)\mathrm{d}\boldsymbol{x}\Big|_{t=s}$.*

We notice that by means of Gauss' divergence theorem and changing the order of differentiation with respect to $s > 0$ and integration over Ω_s we can relate flow-vector fields $\mathbf{F}_\alpha u_f^\alpha(\cdot,s)$, recall

(3.2), to flux-features

$$\begin{aligned} I^{\alpha}_{\Omega_s}(f,s) &= \int_{\Omega_s} \frac{\partial}{\partial s} u^{\alpha}_f(\mathbf{x},s)\,\mathrm{d}\mathbf{x} = \int_{\Omega_s} -(-\Delta)^{\alpha} u^{\alpha}_f(\mathbf{x},s)\,\mathrm{d}\mathbf{x} = \int_{\Omega_s} \operatorname{div}\mathbf{F}_{\alpha}\, u^{\alpha}_f(\mathbf{x},s)\,\mathrm{d}\mathbf{x} \\ &= \int_{\partial\Omega_s} \mathbf{F}_{\alpha}\, u^{\alpha}_f(\mathbf{x},s)\cdot\mathbf{n}(\mathbf{x})\,\mathrm{d}\sigma(\mathbf{x}), \end{aligned} \tag{3.31}$$

Recall that $\mathbf{F}_1$ equals the gradient operator $\mathbf{F}_1 = \nabla$ and $\mathbf{F}_{\frac{1}{2}}$ equals the Riesz transform $\mathbf{F}_{\frac{1}{2}} = \mathbf{R}$. So, in case $\alpha = 1$ and in case $\alpha = 1/2$ we have, respectively,

$$I^1_{\Omega}(f,s) = \int_{\partial\Omega_s} \frac{\partial u^1_f(\cdot,s)}{\partial n}\,\mathrm{d}\sigma(\mathbf{x}) \qquad I^{1/2}_{\Omega}(f,s) = \int_{\partial\Omega_s} \mathbf{q}(\mathbf{x},s)\cdot\mathbf{n}(\mathbf{x})\,\mathrm{d}\sigma(\mathbf{x}), \tag{3.32}$$

where $\mathbf{q} = \mathbf{f}_s^{\frac{1}{2}} * f$ denotes the conjugate Poisson scale space, where we recall (3.2).

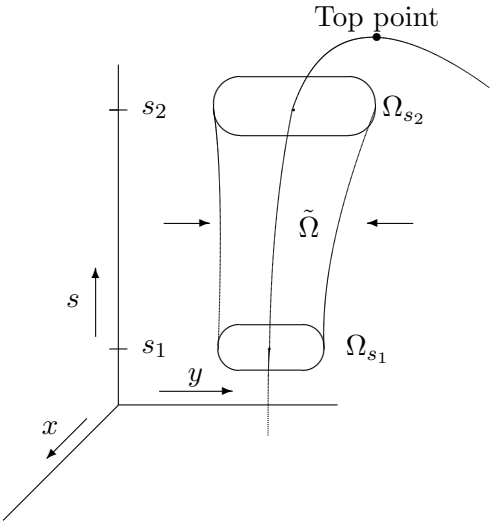

Grey-value flow of grey-value particles through surface $\partial\tilde{\Omega}$ around an extremal path in scale space

Definition 16 *Let $\tilde{\Omega} = \{(\boldsymbol{x},s) \in \mathbb{R}^2 \rtimes [0,\infty) \mid 0 \le s_1 \le s \le s_2, \boldsymbol{x} \in \Omega_s \subset \mathbb{R}^2\}$, where for all $s > 0$, Ω_s is a bounded region in $\mathbb{R}^2$, with an orientable piecewise smooth boundary $\partial\Omega_s$ with outward normal $\boldsymbol{n}$. Suppose the lifetime of a grey-value particle through scale space is negatively exponentially distributed with expectation μ^{-1}. Then the grey-value flow trough $\tilde{\Omega}$ is given by*[14]

$$I^{\alpha,\mu}_{\tilde{\Omega}}(f) = \frac{1}{\mu}\int_{s_1}^{s_2} I^{\alpha}_{\Omega_s}(f,s)\, e^{-\mu s}\,\mathrm{ds}. \tag{3.33}$$

Notice that $\tilde{\Omega}$ need not be equal to $\Omega \times (s_1, s_2)$ as Ω_s may vary in $s > 0$. By straightforward computation and the Plancherel Theorem we have

$$\begin{aligned} I^{\alpha}_{\Omega_s}(f,s) &= -((-\Delta)^{\alpha} u^{\alpha}_f(\cdot,s), 1_{\Omega_s})_{\mathbb{L}_2(\mathbb{R}^2)} = -(\boldsymbol{\omega} \mapsto -\|\boldsymbol{\omega}\|^{2\alpha}\hat{u}^{\alpha}_f(\boldsymbol{\omega},s), \widehat{1_{\Omega_s}})_{\mathbb{L}_2(\mathbb{R}^2)} \\ &= (\boldsymbol{\omega} \mapsto \tfrac{1}{\sqrt{1+(\gamma\|\boldsymbol{\omega}\|)^{2k}}}\hat{f}(\boldsymbol{\omega}), \boldsymbol{\omega} \mapsto \tfrac{-\|\boldsymbol{\omega}\|^{2\alpha}e^{-s\|\boldsymbol{\omega}\|^{2\alpha}}}{\sqrt{1+(\gamma\|\boldsymbol{\omega}\|)^{2k}}}\widehat{1_{\Omega_s}}(\boldsymbol{\omega}))_{\mathbb{L}_2(\mathbb{R}^2\,;\,(1+\gamma\|\boldsymbol{\omega}\|^{2k})\,\mathrm{d}\boldsymbol{\omega})} \\ &= (\phi^{\alpha,s}_{\Omega_s,k,\gamma}, f)_{\mathbb{H}^{k,2}_{\gamma}(\mathbb{R}^2)} \end{aligned} \tag{3.34}$$

[14] In case $\Omega_s = \Omega$, i.e. Ω_s does not change over scale, and $s_0 = 0$ and $s_1 \to \infty$ we obtain $\psi^{\alpha,\mu}_{\Omega,k} = \frac{1}{\mu}\mathcal{L}[s \mapsto \phi^{\alpha,s}_{\Omega_s,k}](\mu)$, where $\mathcal{L}$ denotes the well-known Laplace transform.

with $f \in \mathbb{L}_2(\mathbb{R}^2)$, $\alpha \in (0,1]$ and flux-kernel

$$\phi^{\alpha,s}_{\Omega_s,k,\gamma} = \mathcal{F}^{-1}[\hat{\phi}^{\alpha,s}_{\Omega_s,k,\gamma}] = \mathcal{F}^{-1}[\boldsymbol{\omega} \mapsto \frac{-\|\boldsymbol{\omega}\|^{2\alpha} e^{-s\|\boldsymbol{\omega}\|^{2\alpha}}}{\sqrt{1+(\gamma\|\boldsymbol{\omega}\|)^{2k}}} \widehat{1_{\Omega_s}}(\boldsymbol{\omega})]. \tag{3.35}$$

Notice that the substitution $k=0$ in equality (3.34) yields $I^{\alpha}_{\Omega_s}(f,s) = (\phi^{\alpha,s}_{\Omega_s,0}, f)_{\mathbb{L}_2(\mathbb{R}^2)}$ only for $s>0$. In case $s=0$, where $u^{\alpha}_f(\cdot,0)=f$, we may write $I^{\alpha}_{\Omega_s}(f,0) = (\phi^{\alpha,0}_{\Omega_s,k,\gamma}, f)_{\mathbb{H}^{k,2}_{\gamma}(\mathbb{R}^2)}$ for $k \geq 2$. For $k=0$ the inner product is not defined. It now follows that

$$I^{\alpha,\mu}_{\tilde{\Omega}}(f) = (\psi^{\alpha,\mu}_{\tilde{\Omega},k}, f)_{\mathbb{H}^{k,2}_{\gamma}(\mathbb{R}^2)},$$

where the netto flux kernel needed to compute $I^{\alpha,\mu}_{\tilde{\Omega}}(f)$ is simply given by

$$\psi^{\alpha,\mu}_{\tilde{\Omega},k} = \frac{1}{\mu} \int_{s_0}^{s_1} \phi^{\alpha,s}_{\Omega_s,k} e^{-\mu\, s} \mathrm{ds}.$$

Finally we notice that $\phi^{\alpha,s}_{\Omega,k,\gamma} = \kappa_k * \phi^{\alpha,s}_{\Omega,k=0}$, $\qquad s>0, k>0$, where the flux-kernel $\phi^{\alpha,s}_{\Omega,0}$ is given by

$$\phi^{\alpha,s}_{\Omega,0} = \frac{\partial}{\partial s} K^{\alpha}_s * 1_{\Omega} = -(-\Delta)^{\alpha} K^{\alpha}_s * 1_{\Omega} = (\mathrm{div}\mathbf{F}_{\alpha} K^{\alpha}_s) * 1_{\Omega}, \tag{3.36}$$

which is easily numerically evaluated in practice, see figures 3.12 and 3.13.

The case where Ω_s equals an ellips:
In case of the disk $\Omega_s = B_{\mathbf{0},a}$, where a may depend on s, there are two reasonable options, either the flux kernel is evaluated via the Fourier domain, which yields:

$$\phi^{\alpha,s}_{\Omega,0}(\mathbf{x}) = -a \int_0^{\infty} \rho^{2\alpha} J_1\left(\frac{\rho}{a}\right) J_0(\rho\, r) e^{-s\rho^{2\alpha}}\, \mathrm{d}\rho, \qquad r = \|\mathbf{x}\|,$$

where we notice that $\mathcal{F}1_{\Omega}(\boldsymbol{\omega}) = \frac{a\, J_1\left(\frac{\rho}{a}\right)}{\rho}$, $\|\boldsymbol{\omega}\| = \rho$, or by means of (3.31), (3.32). In case $\alpha = 1$ we get

$$\phi^{1,s}_{\Omega,0}(\mathbf{y}) = \int_{\partial\Omega} \frac{\partial G_s(\mathbf{x}-\mathbf{y})}{\partial r} \mathrm{d}\sigma_{\mathbf{x}} = a \int_0^{2\pi} \left\{ \cos\phi \left(\frac{y_1 - a\cos\phi}{8\pi s^2} \right) + \sin\phi \left(\frac{y_2 - a\sin\phi}{8\pi s^2} \right) \right\} e^{\frac{-(a\cos\phi - y_1)^2 - (a\sin\phi - y_2)^2}{4s}} \mathrm{d}\phi,$$

with $r = \sqrt{(y_1)^2 + (y_2)^2}$, which is easily numerically approximated. Finally, we notice that the ellips-case

$$\Omega = E_{\theta,\lambda,a} = \{\mathbf{x} \in \mathbb{R}^2 \mid \|L^{-1}_{\lambda} R^{-1}_{\theta} \mathbf{x}\|^2 = a^2\}$$

where $\theta \in [0, 2\pi), \lambda > 0$ may depend on $s>0$, recall (3.9), directly follows from the disk case by means of

$$\phi^{\alpha,s}_{\Omega = E_{\theta,\lambda,a},k}(\mathbf{x}) = \phi^{\alpha,s}_{\Omega = B_{\mathbf{0},a},k}(L^{-1}_{\lambda} R^{-1}_{\theta} \mathbf{x}), \qquad \mathbf{x} \in \mathbb{R}^d, a, s > 0, \theta \in [0, 2\pi), \alpha \in (0,1], \lambda > 0, k \in \mathbb{N}.$$

The case where Ω_s equals a rectangle:

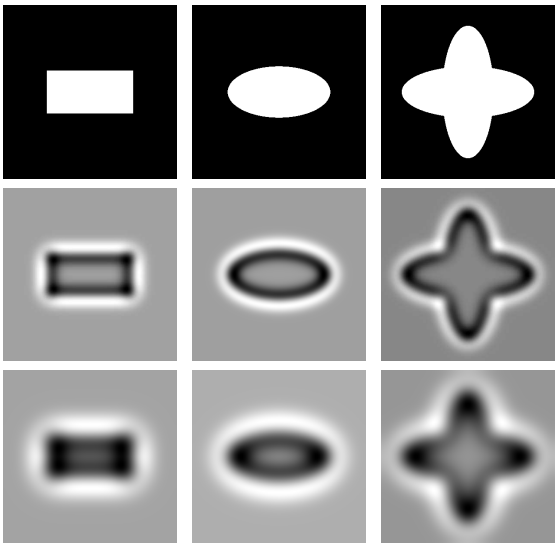

Figure 3.12: Computation of flux-kernels $\phi_{\Omega}^{\alpha,s}$ is very simple, for example in a Gaussian scale space ($\alpha = 1/2$) we have by (3.36) that we only need to compute the Gaussian Laplacian of 1_Ω. In the above figure, we illustrated the cases where Ω equals a rectangle, ellips and star, for two different scales $s > 0$.

In case of the rectangle $\Omega_s = [-a, a] \times [-b, b]$, with a and b depending on $s > 0$, and $\alpha = 1$, we have

$$\begin{aligned}\phi^{1,s}_{\Omega=[-a,a]\times[-b,b],0}(x,y) &= \int_{x-a}^{x+a}\int_{y-b}^{y+b} G_s^{(2)}(u)G_s(v) + G_s^{(2)}(v)G_s(u)\ \mathrm{dv}\ \mathrm{du} \\ &= \tfrac{1}{2}[G_s^{(1)}(x+a) - G_s^{(1)}(x-a)]\left[\mathrm{Erf}\left(\tfrac{y+b}{2\sqrt{s}}\right) - \mathrm{Erf}\left(\tfrac{y-b}{2\sqrt{s}}\right)\right] \\ &\quad +\tfrac{1}{2}[G_s^{(1)}(y+b) - G_s^{(1)}(y-b)]\left[\mathrm{Erf}\left(\tfrac{x+a}{2\sqrt{s}}\right) - \mathrm{Erf}\left(\tfrac{x-a}{2\sqrt{s}}\right)\right]\end{aligned}$$

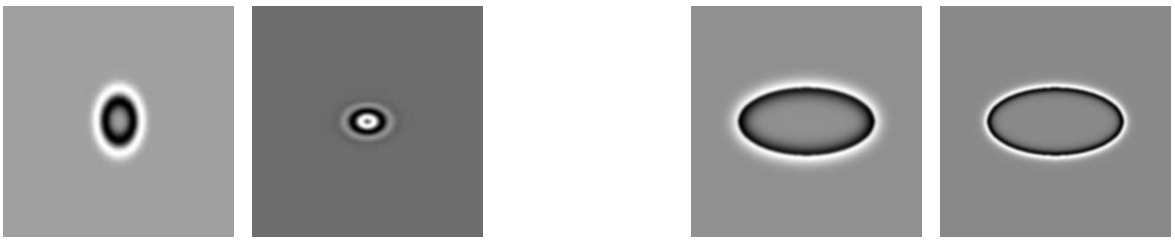

Figure 3.13: **Left:** Example of an ellips flux-kernel computed by means of an inverse DFT after sampling in the Fourier domain **Right:** Density Plots ($-2<x<2$, $-2<y<2$) of the integrated flux-kernels $\tilde{\psi}_{\tilde{\Omega}}^{\alpha,\mu}, k = 0$, for the simple case $\tilde{\Omega} = \Omega \times [0, 100]$, $\Omega = E_{0,2,\sqrt{0.7}}$ for $\mu = 0$ and $\mu = 0.05$. For comparison to single scale flux kernel see $\phi_{\Omega}^{\alpha,s=100}$ in the middle of figure 3.12

3.5 Conclusion

1. There exists a simple and strong connection between α scale spaces and the corresponding vector scale spaces (and their flow fields). In particular between the case of Poisson scale space ($\alpha = 1/2$), where this vector scale space is the well-known monogenic scale space, and the case of Gaussian scale space ($\alpha = 1$), where this vector scale space extension equals the first order jet, which is somewhat surprising concerning the different physical interpretations (respectively potential physics and heat physics). This raises the question whether these α scale spaces are essentially different for multi-scale image analysis, as methods in one framework are easily translated to methods in the other framework. From a topological point of view, however, we conclude that the deep structures of α scale spaces, although continuously deformed by α are rather different:

- Experiments on daily life images often show that different extrema and saddles annihilate in α scale spaces. Moreover, creation events that take place in one scale space need not take place in the other.
- By applying Morse theory on Poisson scale space and Gaussian scale space we deduce that creations are generic events in 1D-Poisson scale space (illustrated by both analytic and numerical examples), whereas they cannot occur in Gaussian scale space.
- Isophotes through critical points do behave differently in Gaussian scale space compared to those in the other α scale spaces, where they behave similarly.

2. The common (non)-linear reconstruction frameworks follow an Euler Lagrange minimization. If the Lagrangian (prior) is a norm induced by an inner product of a Hilbert space this Euler Lagrange minimization boils down to a simple orthogonal projection within the corresponding Hilbert space. This basic observation has been overlooked in image analysis for the cases where the Lagrangian equals a norm of Sobolev type resulting in iterative (non-linear) numerical methods, where we provide exact solutions. By means of Gelfand triples we consider two extreme cases: Standard isotropic Sobolev spaces and trajectory spaces. Although the reconstruction algorithm is slightly simpler for the trajectory space case, best results seem to be obtained by minimizing isotropic Sobolev norms of low order, taking into account that in both cases smoothness of the reconstruction is tuned by a positive parameter. In our opinion a linear reconstruction should at least capture the topology (deep structure) of the scale space of the original image. Therefore we only consider linear features inspired by the deep structure of images. Besides top-points, the well-known scale space singularities, we introduce the concept of flux-features. They describe the transport of grey-value particles between extremal paths that lead to singular points in scale space. By including these features we provide another tool to minimize spurious top-points in the reconstruction image. In future work we will include these flux-features in our algorithms and we will consider how to choose the surfaces $\tilde{\Omega}$ around the extremal paths.

Part II

Orientation

Chapter 4

Invertible Orientation Scores as an Application of Generalized Wavelet Theory

Inspired by the human visual system we consider the construction of—and reconstruction from—an orientation score of an image, via a wavelet transform corresponding to the left-regular representation of the Euclidean motion group in $\mathbb{L}_2(\mathbb{R}^2)$ and oriented wavelet $\psi \in \mathbb{L}_2(\mathbb{R}^2)$. Because this representation is reducible the general wavelet reconstruction theorem does not apply. By means of reproducing kernel theory we formulate a new and more general wavelet theory, which is applied to our specific case. As a result we can quantify the well-posedness of the reconstruction given the wavelet ψ and deal with the question of which oriented wavelet ψ is practically desirable in the sense that it both allows a stable reconstruction and a proper detection of local elongated structures. This enables image enhancement by means of left-invariant operators on orientation scores.

4.1 Introduction

In many medical image applications it is desirable to construct a local orientation-score of a grey-value image. In the case of 2D images $f : \mathbb{R}^2 \to \mathbb{R}$ such an orientation score $U_f : \mathbb{R}^2 \rtimes \mathbb{T} \to \mathbb{C}$ depends on 3 variables $(b_1, b_2, e^{i\theta})$, where $(b_1, b_2) \in \mathbb{R}^2$ denote position and $e^{i\theta} \in \mathbb{T} \leftrightarrow (\cos\theta, \sin\theta) \in S^1$ is a local orientation variable.

Such an **orientation score** is obtained by means of a convolution with some anisotropic

Figure 4.1: Example of an orientation score(right, where the vertical axis is the orientation axis and the horizontal axes are the b_1-axis and b_2-axis) and its corresponding image(left, where the horizontal axis is the x-axis and the vertical axis is the y-axis).

wavelet[1] $\psi \in \mathbb{L}_2(\mathbb{R}^2)$, cf.[79]:

$$U_f(\mathbf{b}, e^{i\theta}) = \int_{\mathbb{R}^2} \overline{\psi(R_\theta^{-1}(\mathbf{x}' - \mathbf{b}))} f(\mathbf{x}') \, \mathrm{d}\mathbf{x}' \ , \qquad \text{with } R_\theta = \begin{pmatrix} \cos\theta & -\sin\theta \\ \sin\theta & \cos\theta \end{pmatrix} . \tag{4.1}$$

Definition 17 *Let $f \in \mathbb{L}_2(\mathbb{R}^2)$ and $\psi \in \mathbb{L}_2(\mathbb{R}^2) \cap \mathbb{L}_1(\mathbb{R}^2)$. Then the function $U_f : \mathbb{R}^2 \rtimes \mathbb{T} \to \mathbb{C}$ given by (4.1) is called the orientation score of image f.*

This idea is inspired by our own visual system, in which receptive fields exist that are tuned to various locations and orientations. A simple cell receptive field can be parameterized by its position and orientation. Assemblies of oriented receptive fields are grouped together on the surface of the primary visual cortex in a pinwheel like structure, cf.figure 4.2. Perceptual organization on the basis of orientation similarity on images f can be done via their orientation scores U_f, as long as there exists a linear *well-posed invertible* transformation $\mathcal{W}_\psi$ from the image f to the orientation score U_f and vice versa. The domain of U_f is the well-known Euclidean motion group $G = \mathbb{R}^2 \rtimes \mathbb{T}$ and the mapping $f \mapsto U_f$ is a wavelet transformation

$$U_f(\mathbf{b}, e^{i\theta}) = (\mathcal{W}_\psi[f])(g) = (\mathcal{U}_g\psi, f)_{\mathbb{L}_2(\mathbb{R}^2)} = (\mathcal{T}_{\mathbf{b}}\mathcal{R}_{e^{i\theta}}\psi, f)_{\mathbb{L}_2(\mathbb{R}^2)} \ , \qquad g = (\mathbf{b}, e^{i\theta}) \ , \tag{4.2}$$

where $\mathcal{T}_{\mathbf{b}}\mathcal{R}_{e^{i\theta}}\psi$ is the translated and rotated wavelet and $g \mapsto \mathcal{U}_g$ is the left-regular action of G onto $\mathbb{L}_2(\mathbb{R}^2)$. The definitions and conventions are explained in the preliminaries.

In section 4.3 we give a brief overview of the standard wavelet theory. Although this theory guarantees a perfectly well-posed reconstruction of f from its wavelet transform $\mathcal{W}_\psi[f]$, in the sense that the quadratic norm is preserved, it does not apply to our case.

Therefore in section 4.4 we give a brief overview of a more general approach to wavelet theory (by means of reproducing kernel theory), leading to a wavelet reconstruction theorem and apply it to our case. For more detailed in-depth mathematical treatment of this recently developed theory we refer to earlier work [22]. In section 4.5 we consider the practical consequences of

[1] We follow the convention in physics and mathematics to call the kernel corresponding to a wavelet transformation a wavelet. However, in 1D-signal analysis people consider wavelet transformations with respect to representations of the $ax + b$-group (scaling and translation) onto $\mathbb{L}_2(\mathbb{R})$. We stress that the interpretation of a wavelet as a localized wave in signal processing does not apply to our case.

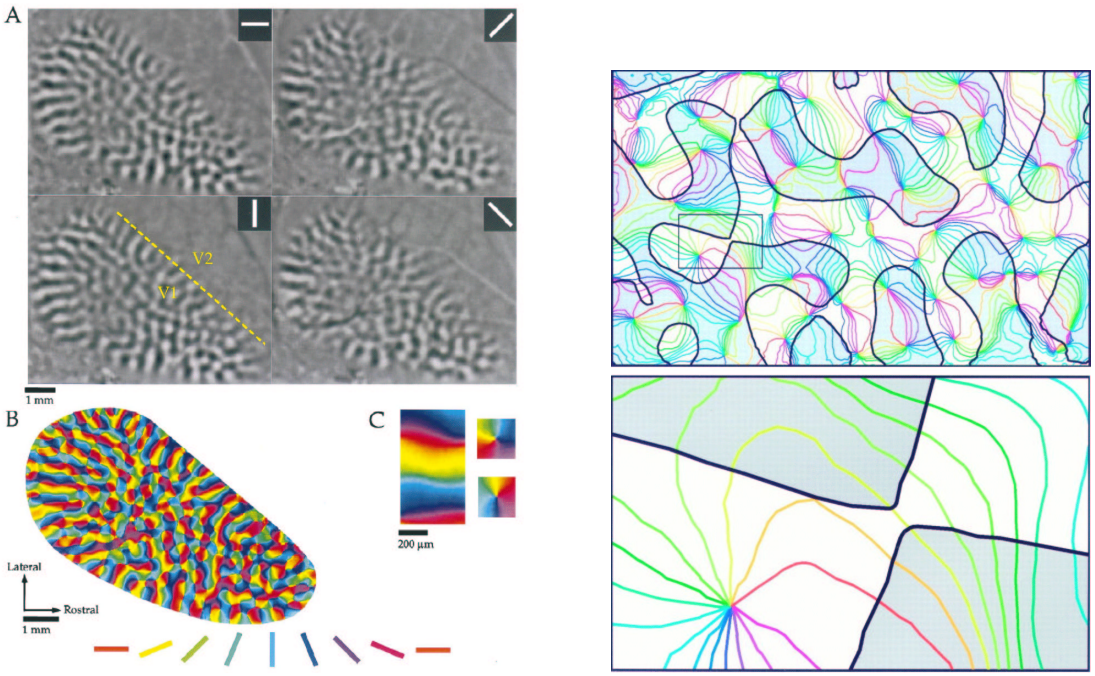

Figure 4.2: Left: A:Parts of visual cortex active under different orientation stimuli. B: Orientation preference map obtained by vector summation of data obtained for each angle. Orientation preference is color coded according to the key shown below, replicated with permission from cf.[13], Copyright 1997 Society of Neuroscience. Right:enlarged section of the rectangular area in the upper figure. Shaded and unshaded areas denote the left and right eye resp. Colored lines connect cells with equal orientation sensitivity, replicated with permission from cf.[120].

this reconstruction theorem and quantify the well-posed ness of reconstruction by a condition number that explicitly depends on the wavelet ψ. We follow two different approaches to parameterize classes of wavelets which allow a stable/well posed reconstruction give some explicit examples. These examples show that it is possible to derive wavelets that both allow a well-posed reconstruction and which are also good line detectors. We compare these wavelets with the usual line detectors used in image analysis, which do not allow a stable reconstruction. In section 4.7 we generalize our results to orientation scores of $3D$-images.

In section 4.8 we give explicit practical examples of perceptual organization by means of left-invariant operations on orientation scores. In these examples we first construct an orientation score $U_f = \mathcal{W}_\psi[f]$, then apply an operation Φ on the orientation score $\Phi[U_f]$ after which we reconstruct to obtain an enhanced image $\Upsilon_\psi[f] = [\mathcal{W}_\psi^* \circ \Phi \circ \mathcal{W}_\psi](f)$. We show that the concatenation

$$\Upsilon_\psi = \mathcal{W}_\psi^* \circ \Phi \circ \mathcal{W}_\psi \tag{4.3}$$

is Euclidean invariant if and only if Φ is left invariant.

4.2 Preliminaries and Notation

Here we make a selection of the general preliminaries in the very beginning of this thesis, to stress those conventions that are relevant for the second part of the thesis. Moreover, we add some conventions that only play a specific role in the second part of this thesis.

- The Fourier transform $\mathcal{F} : \mathbb{L}_2(\mathbb{R}^d) \to \mathbb{L}_2(\mathbb{R}^d)$, is almost everywhere defined by

$$[\mathcal{F}(f)](\boldsymbol{\omega}) = \hat{f}(\boldsymbol{\omega}) = \frac{1}{(2\pi)^{d/2}} \int_{\mathbb{R}^d} f(\mathbf{x})\, e^{-i\boldsymbol{\omega}\cdot\mathbf{x}}\, \mathrm{d}\mathbf{x}\ .$$

  Notice that $\|\mathcal{F}[f]\|^2 = \|f\|^2$ for all $f \in \mathbb{L}_2(\mathbb{R}^d)$ and that $\mathcal{F}[f * g] = (2\pi)^{d/2}\mathcal{F}[f]\mathcal{F}[g]$, for all $f, g \in \mathbb{L}_2(\mathbb{R}^d)$.

- We use the following notation for Euclidean/polar coordinates in spatial and Fourier domain, respectively: $\mathbf{x} = (x, y) = (r\cos\phi, r\sin\phi)$, $\boldsymbol{\omega} = (\omega_x, \omega_y) = (\rho\cos\varphi, \rho\sin\varphi)$, with $\phi, \varphi \in [0, 2\pi), r, \rho > 0$. The corresponding complex variables, will be denoted by $z = x + iy = re^{i\phi}$ and $w = \omega_x + i\omega_y = \rho e^{i\varphi}$.

- We will use short notation for the following groups:
  - $\mathrm{Aut}(\mathbb{R}^d) = \{A : \mathbb{R}^d \to \mathbb{R}^d \mid A \text{ linear and } A^{-1} \text{ exists}\}$
  - dilation group $D(d) = \{A \in \mathrm{Aut}(\mathbb{R}^d) \mid A = aI, a > 0\}$.
  - orthogonal group $O(d) = \{X \in \mathrm{Aut}(\mathbb{R}^d) \mid X^T = X^{-1}\}$
  - rotation group $SO(d) = \{R \in O(d) \mid \det(R) = 1\}$.
  - circle group $\mathbb{T} = \{z \in \mathbb{C} \mid |z| = 1\}$, $z = e^{i\theta}$, $\theta = \arg z$ with group homomorphism $\tau : \mathbb{T} \to SO(2) \subset \mathrm{Aut}(\mathbb{R}^2)$:

$$\tau(z) = R_\theta = \begin{pmatrix} \cos\theta & -\sin\theta \\ \sin\theta & \cos\theta \end{pmatrix}\ . \tag{4.4}$$

- Let T and S be locally compact groups and let $\tau : T \to \mathrm{Aut}(S)$ be a group homomorphism. The **semi-direct product** $S \rtimes_\tau T$ is defined to be the group (which is again locally compact) with underlying set $\{(s,t) \mid s \in S,\ t \in T\}$ and group operation

$$(s,t)(s',t') = (s\tau(t)s', tt') \ . \tag{4.5}$$

  In this part we mainly consider the group $\mathbb{R}^2 \rtimes \mathbb{T}$, where τ is given by (4.4).The group product (4.5) is now given by

$$g\,g' = (\mathbf{b}, e^{i\theta})(\mathbf{b}', e^{i\theta'}) = (\mathbf{b} + R_\theta \mathbf{b}', e^{i(\theta+\theta')}) \ , g = (\mathbf{b}, e^{i\theta}), g' = (\mathbf{b}', e^{i\theta'}) \in \mathbb{R}^2 \rtimes \mathbb{T}.$$

  This non-commutative group is the **Euclidean motion group**.

- A representation $\mathcal{R}$ of a group G into a Hilbert space H is a homomorphism $\mathcal{R}$ between G and $\mathcal{B}(H)$, the space of bounded linear operators on H. It satisfies $\mathcal{R}_{gh} = \mathcal{R}_g \mathcal{R}_h$ for all $g \in G, h \in G$ and $\mathcal{R}_e = I$. A representation $\mathcal{R}$ is irreducible if the only invariant closed subspaces of H are H and $\{\mathbf{0}\}$ and otherwise reducible. We mainly consider unitary representations (i.e. $\|\mathcal{U}_g\psi\|_H = \|\psi\|_H$ for all $g \in G$ and $\psi \in H$), which will be denoted by $\mathcal{U}$ rather than $\mathcal{R}$. Within the class of unitary representations we mainly consider the representations of $\mathbb{R}^d \rtimes T$ into $\mathbb{L}_2(\mathbb{R}^d)$ which are given by

$$(\mathcal{U}_g\psi)(\mathbf{x}) = \frac{1}{\sqrt{\det(\tau(t))}}\psi((\tau^{-1}(t))(\mathbf{x}-\mathbf{b})), \text{ with } g = (\mathbf{b}, \tau(t)) \in \mathbb{R}^d \rtimes T. \tag{4.6}$$

  We will call these representations **left-regular actions** of $G = \mathbb{R}^d \rtimes T$ in $\mathbb{L}_2(\mathbb{R}^d)$.

- Let $\mathbf{b} \in \mathbb{R}^d$, $a > 0$ and $g \in G$ with corresponding $\tau(g) \in \mathrm{Aut}(\mathbb{R}^d)$. Then the unitary operators $f \mapsto \check{f}$, $\mathcal{T}_\mathbf{b}$, $\mathcal{D}_a$ and $\mathcal{R}_g$ on $\mathbb{L}_2(\mathbb{R}^d)$ are defined by

$$\begin{array}{ll} \check{f}(\mathbf{x}) = f(-\mathbf{x}) & \mathcal{T}_\mathbf{b}\psi(\mathbf{x}) = \psi(\mathbf{x}-\mathbf{b}) \\ \mathcal{D}_a\psi(\mathbf{x}) = \frac{1}{a^{\frac{d}{2}}}\psi(\frac{\mathbf{x}}{a}) & \mathcal{R}_g\psi(\mathbf{x}) = \frac{1}{\sqrt{\det\tau(g)}}\psi((\tau(g))^{-1}\mathbf{x}) \ . \end{array} \tag{4.7}$$

  The mappings $\mathbf{b} \mapsto \mathcal{T}_\mathbf{b}$, $g \mapsto \mathcal{R}_g$, $a \mapsto \mathcal{D}_a$ are respectively left regular actions of $\mathbb{R}^d, D(d), G$ into $\mathbb{L}_2(\mathbb{R}^d)$.

- A functional Hilbert space[2] is a Hilbert space consisting of complex valued functions on an index set $\mathbb{I}$ on which the point evaluation $\delta_\mathbf{a}$, is a continuous/bounded linear functional for all $\mathbf{a} \in \mathbb{I}$. Consequently, it has a Riesz representant $K_\mathbf{a} \in H$

$$f(\mathbf{a}) = \langle \delta_\mathbf{a}, f\rangle = (K_\mathbf{a}, f)_H.$$

  The function $K : \mathbb{I} \times \mathbb{I} \to \mathbb{C}$ given by $K(\mathbf{a},\mathbf{b}) = (K_\mathbf{a}, K_\mathbf{b})_H = K_\mathbf{b}(\mathbf{a})$ is called reproducing kernel. Notice that the spaces $\mathbb{L}_2(\mathbb{R}^d)$ are *not* functional Hilbert spaces.

- For a given wavelet $\psi \in \mathbb{L}_1(\mathbb{R}^d) \cap \mathbb{L}_2(\mathbb{R}^d)$ we define $\tilde{\psi}$ and M_ψ almost everywhere by

$$\begin{array}{l} \tilde{\psi}(\mathbf{x}) = \int\limits_{SO(d)} (\overline{\mathcal{R}_t\check{\psi}} * \mathcal{R}_t\psi)(\mathbf{x})\mathrm{d}\mu_\mathrm{T}(\mathrm{t}) \\ M_\psi(\boldsymbol{\omega}) = (2\pi)^{d/2} \int\limits_{SO(d)} |\mathcal{F}(\mathcal{R}_t\psi)(\boldsymbol{\omega})|^2 \mathrm{d}\mu_\mathrm{T}(\mathrm{t}) \ , \end{array} \tag{4.8}$$

[2]Also known as reproducing kernel Hilbert space.

where $d\mu_T(t)$ is the normalized left-invariant Haar-measure of $SO(d)$. It directly follows by compactness of $SO(d)$ and Fubini that $M_\psi \in \mathbb{L}_1(\mathbb{R}^d)$ and

$$\begin{aligned} \|M_\psi\|_{\mathbb{L}_1(\mathbb{R}^d)} &= (2\pi)^{d/2}\|\mathcal{F}[\psi]\|^2_{\mathbb{L}_2(\mathbb{R}^d)} \int\limits_{SO(d)} \mathrm{d}\mu_{\mathrm{T}}(\mathrm{t}) \\ &= (2\pi)^{d/2}\|\psi\|^2_{\mathbb{L}_2(\mathbb{R}^d)} < \infty \end{aligned} \tag{4.9}$$

Consequently the kernel $\tilde{\psi}$, which is the inverse Fourier transform of M_ψ, is a continous function vanishing at infinity. Moreover M_ψ and $\tilde{\psi}$ are rotationally symmetric since $\mathcal{R}_t M_\psi = M_\psi$ for all $t \in SO(d)$ and $\mathcal{F}\mathcal{R}_t = \mathcal{R}_t\mathcal{F}$. Conversely, by compactness of $SO(d)$ and since a convolution of two $\mathbb{L}_1(\mathbb{R}^d)$ elements is again within $\mathbb{L}_1(\mathbb{R}^d)$, we have that $\tilde{\psi} \in \mathbb{L}_1(\mathbb{R}^d)$, so M_ψ is also a continuous function vanishing at infinity.

4.3 Wavelet Theory

In this section we will give a condensed treatment of continuous wavelet theory. For the sake of illustration we will first consider the well-known signal case, i.e. $d = 1$ with $G = \mathbb{R} \rtimes D(1)$ known as the $ax + b$-group. Then we give the group theoretic generalization first formulated by Grossmann et al.[67]. This theorem and other generalizations of this theorem, such as [121], [40] are not applicable to the *reducible* left regular action of the Euclidean motion group onto $\mathbb{L}_2(\mathbb{R}^2)$ given by (4.6), which is needed for our orientation score application in image analysis. Therefore we give a true generalization to the wavelet theorem, where irreducibility is neither a requirement nor replaced by another requirement.

4.3.1 Continuous Wavelet Theory on 1D-Signals

The continuous wavelet transform $\mathcal{W}_\psi[f] : \mathbb{R}^+ \times \mathbb{R} \to \mathbb{C}$ of a signal $f \in \mathbb{L}_2(\mathbb{R})$ with respect to wavelet $\psi \in \mathbb{L}_2(\mathbb{R})$ is defined by $\mathcal{W}_\psi[f](a,b) = (\mathcal{T}_b\mathcal{D}_a\psi, f)_{\mathbb{L}_2(\mathbb{R})}$. An alternative expression of the continuous wavelet transform is given by: $\mathcal{W}_\psi[f](a,b) = (f * \overline{\mathcal{D}_a\check{\psi}})(b)$. We say $\psi \in \mathbb{L}_2(\mathbb{R})$ is an admissible wavelet if it satisfies the condition

$$0 < C_\psi = (2\pi) \int\limits_{\mathbb{R}^+} \frac{|\mathcal{F}[\psi](a\omega)|^2}{a} \mathrm{d}a < \infty \quad \text{for almost all } \omega \in \mathbb{R}. \tag{4.10}$$

So in particular for $\omega = 0$ we find $\mathcal{F}[\psi](0) = \int\limits_{\mathbb{R}} \psi(x)\ dx = 0$. If (and only if) ψ satisfies $\psi(-\mathbf{x}) = e^{i\alpha}\psi(\mathbf{x})$ for almost every $x \in \mathbb{R}$ and some $\alpha \in [0, 2\pi)$, in particular when ψ is almost everywhere odd or even, then (4.10) is independent of ω, which can easily be verified by substitution $(a \to a/|\omega|)$.

Notice that $\mathcal{T}_b\mathcal{D}_a \circ \mathcal{T}_{b'}D_{a'} = \mathcal{T}_{ab'+b}\mathcal{D}_{aa'}$ and that $(\mathcal{T}_b\mathcal{D}_a)^{-1} = (\mathcal{T}_{-b/a}\mathcal{D}_{1/a})$ and therefore $\{\mathcal{T}_b\mathcal{D}_a\}$ forms a 2-parameter Lie group G^+, known as the $ax+b$-group, isomorphic to the matrix group

$$\left\{ \begin{pmatrix} a & b \\ 0 & 1 \end{pmatrix} | a > 0, b \in \mathbb{R} \right\} .$$

Let $\mathcal{U}$ be the representation of G^+, given by

$$\left[\mathcal{U}_{(a,b)}f\right](x) = \frac{1}{\sqrt{a}} f\left(\frac{x-b}{a}\right) \ , \tag{4.11}$$

then $\mathcal{U}$ is unitary, i.e. $(\mathcal{U}_{(a,b)}f, \mathcal{U}_{(a,b)}g) = (f,g)$ for all $a > 0$ and $b \in \mathbb{R}$, and $\mathcal{W}_\psi[f](a,b) = (\mathcal{U}_{(a,b)}\psi, f)_{\mathbb{L}_2(\mathbb{R}^d)}$. By Parseval's equality, the wavelet constant C_ψ (independent of ω!) can be rewritten:

$$\begin{aligned}
C_\psi &= (2\pi) \int_0^\infty \left|\left(\mathcal{D}_{1/a}\mathcal{F}[\psi]\right)(\omega)\right|^2 \ \tfrac{\mathrm{d}a}{a^2} \\
&= (2\pi) \int_0^\infty |\mathcal{F}[\mathcal{D}_a\psi](\omega)|^2 \ \tfrac{\mathrm{d}a}{a^2} \\
&= \tfrac{2\pi}{(\psi,\psi)} \int_{\mathbb{R}} \int_0^\infty |\mathcal{F}[\mathcal{D}_a\psi](\omega)|^2 \, |\mathcal{F}[\psi](-\omega)|^2 \ \tfrac{\mathrm{d}a}{a^2} \, \mathrm{d}\omega \\
&= \tfrac{1}{(\psi,\psi)} \int_0^\infty \int_{\mathbb{R}} \left|\sqrt{2\pi}\mathcal{F}[\mathcal{D}_a\psi](\omega)\, \mathcal{F}[\psi](-\omega)\right|^2 \ \mathrm{d}\omega \ \tfrac{\mathrm{d}a}{a^2} \\
&= \tfrac{1}{(\psi,\psi)} \int_0^\infty \int_{\mathbb{R}} \left| \int_{\mathbb{R}} \tfrac{\overline{\psi(\frac{x-b}{a})}}{\sqrt{a}} \psi(x) \, \mathrm{d}x \right|^2 \ \tfrac{\mathrm{d}b\,\mathrm{d}a}{a^2} \\
&= \tfrac{1}{(\psi,\psi)} \int_{G^+} |(\mathcal{U}_{(a,b)}\psi, \psi)|^2 \ \tfrac{\mathrm{d}a}{a^2} \, \mathrm{d}b \ .
\end{aligned} \tag{4.12}$$

The measure $\mathrm{d}\mu_{\mathrm{G}^+}(\mathrm{g}) = \frac{\mathrm{da}}{\mathrm{a}^2}\,\mathrm{db}$ is the left-invariant Haar measure of G^+:

$$\int_{G^+} f(a',b') \frac{\mathrm{d}a'}{(a')^2} \, \mathrm{d}b' = \int_{G^+} f(aa', ab'+b) \frac{\mathrm{d}a'}{(a')^2} \, \mathrm{d}b' \ , \tag{4.13}$$

which easily follows by substitution $u = aa'$ and $v = ab'$.

Theorem 16 (Wavelet Reconstruction Theorem For Signals)
Let $\psi \in \mathbb{L}_2(\mathbb{R})$ be an admissible wavelet, with wavelet constant[3] $C_\psi = (2\pi) \int_{\mathbb{R}^+} \frac{\left|\hat{\psi}(a\omega)\right|^2}{a} \mathrm{d}a < \infty$ *for almost all $\omega \in \mathbb{R}$. Then the mapping Φ which maps f onto $\frac{1}{\sqrt{C_\psi}} \mathcal{W}_\psi[f]$ is an isometry from $\mathbb{L}_2(\mathbb{R})$ into $\mathbb{L}_2(\mathbb{R} \rtimes \mathbb{R}^+)$, i.e.*

$$\begin{aligned}
&\|\mathcal{W}_\psi[f]\|^2_{\mathbb{L}_2(\mathbb{R}\times\mathbb{R}^+\,;\, db\frac{da}{a^2})} = C_\psi \|f\|^2_{\mathbb{L}_2(\mathbb{R})} \\
&\tfrac{1}{C_\psi} \mathcal{W}_\psi[f] = \Phi(f) \Leftrightarrow f = \tfrac{1}{C_\psi} \Phi^*(\mathcal{W}_\psi[f]) \Leftrightarrow \\
&f(x) = \tfrac{1}{\sqrt{C_\psi}} \int_{\mathbb{R}^+} \int_{\mathbb{R}} \mathcal{W}_\psi[f](a,b) \, \psi\left(\tfrac{x-b}{a}\right) \, \mathrm{d}b \tfrac{\mathrm{d}a}{a^2\sqrt{a}} = \tfrac{1}{\sqrt{C_\psi}} \int_{\mathbb{R}^+} ((f * \overline{\mathcal{D}_a\check{\psi}}) * \mathcal{D}_a\psi)(x) \ \tfrac{\mathrm{d}a}{a^2} \\
&\textit{for almost every } x \in \mathbb{R}.
\end{aligned}$$

Proof
This follows by the general result in the next subsection, Theorem 17: Take $H = \mathbb{L}_2(\mathbb{R})$, $G = G^+ = \mathbb{R} \rtimes D(1) \rtimes O(1)$ and the unitary representation $\mathcal{V}$ of G on $\mathbb{L}_2(\mathbb{R})$ by

$$\left[\mathcal{V}_{(a,b,c)}f\right](x) = \frac{1}{\sqrt{a}} f\left(\frac{c^{-1}(x-b)}{a}\right) \ , c \in \{-1,1\}, a > 0, b \in \mathbb{R} \ , f \in \mathbb{L}_2(\mathbb{R}).$$

[3] This is a constant iff $\psi(-\mathbf{x}) = e^{i\alpha}\psi(\mathbf{x})$, for some $\alpha \in [0, 2\pi)$ and almost every $x \in \mathbb{R}$.

Notice to this end that in contrast to the representation $\mathcal{U}$ given by (4.11), representation $\mathcal{V}$ is irreducible: Suppose there exists a subspace S of H which is invariant under $\mathcal{V}$. In particular, since $\mathcal{V}_{(a,b,1)} = \mathcal{U}_{(a,b)}$, it is also invariant under $\mathcal{U}$. Now we notice that $\mathbb{L}_2(\mathbb{R}^d) = H_+ \oplus H_-$ is an orthogonal decomposition into $\mathcal{U}$-irreducible subspaces, [4]. So either $S = \{0\}$ or $S = H$ or $S = H_+ = \{f \in \mathbb{L}_2(\mathbb{R}^d) \mid \hat{f}(\omega) = 0 \text{ for } \omega > 0\}$ or $S = H_- = \{f \in \mathbb{L}_2(\mathbb{R}^d) \mid \hat{f}(\omega) = 0 \text{ for } \omega < 0\}$. But $\mathcal{V}_{a,b,-1}H_+ = H_-$ and $\mathcal{V}_{a,b,-1}H_- = H_+$ and therefore $S = \{0\}$ or $S = H$.

As a result by Theorem 17 we have

$$\int_{\mathbb{R}}\int_{\mathbb{R}^+} \frac{1}{2} \sum_{c\in\{-1,1\}} |(\mathcal{V}_{(a,b,c)}\psi, f)|^2 \, \mathrm{db}\frac{\mathrm{da}}{\mathrm{a}^2} = \frac{\|\mathrm{f}\|^2}{(\psi,\psi)} \int_{\mathbb{R}}\int_{\mathbb{R}^+} \frac{1}{2} \sum_{\mathrm{c}\in\{-1,1\}} |(\mathcal{V}_{(\mathrm{a,b,c})}\psi, \psi)|^2 \, \mathrm{db}\frac{\mathrm{da}}{\mathrm{a}^2} \tag{4.14}$$

and since ψ is assumed to be admissible with wavelet constant C_ψ, the left hand side of equality (4.14) equals $\|\mathcal{W}_\psi[f]\|^2$ and the right hand side equals $C_\psi\|f\|^2$. □

4.3.2 Wavelet Transformations constructed by Unitary Irreducible Representations of Locally Compact Groups

Rather than restricting ourselves to the particular case of left regular action of the $ax+b$ group representation on $\mathbb{L}_2(\mathbb{R})$ we will generalize by defining a wavelet transform given a Hilbert space H and any unitary irreducible representation $g \mapsto \mathcal{U}_g$ of any locally compact group G in H. It is well-known that every locally compact group G has a left invariant Haar measure, which we denote by μ_G. A left invariant Haar measure on G is a Radon measure on G such that $\mu_G(gE) = \mu_G(E)$ for all $g \in G$ and Borel sets E. It is uniquely determined up to a constant multiplicative factor,[112]. A nonzero vector ψ in H is said to be an admissible vector (or wavelet) if

$$C_\psi = \int_G \frac{|(\mathcal{U}_g\psi, \psi)|^2}{(\psi,\psi)} \, \mathrm{d}\mu_{\mathrm{G}}(\mathrm{g}) < \infty$$

Given an admissible vector ψ and a unitary irreducible representation $\mathcal{U}$ of a locally compact group G in a Hilbert space H, the wavelet transform $\mathcal{W}_\psi : H \to \mathbb{L}_2(G)$ is defined by

$$\mathcal{W}_\psi[f](g) = (\mathcal{U}_g\psi, f)_H \ .$$

The next theorem is well-known in mathematical physics, [121] and is first formulated and proven in Grossmann et al. [67]. For a simple alternative and self-contained proof, see [22] p.20, where we use a topological version of Schur's lemma, for proof see [21] p.86.

Theorem 17 (The Wavelet Reconstruction Theorem) *The wavelet transform is a linear isometry (up to a constant) from the Hilbert space H onto a closed subspace $\mathbb{C}^G_{K_\psi}$ of $\mathbb{L}_2(G, \mathrm{d}\mu)$:*

$$\|\mathcal{W}_\psi[f]\|^2_{\mathbb{L}_2(G)} = C_\psi\|f\|^2 \tag{4.15}$$

The space $\mathbb{C}^G_{K_\psi}$ is the unique functional Hilbert space with reproducing kernel

$$K_\psi(g, g') = \frac{1}{C_\psi}(\mathcal{U}_g\psi, \mathcal{U}_{g'}\psi) \ .$$

The corresponding orthogonal projection $\mathbb{P}_\psi : \mathbb{L}_2(G, \mathrm{d}\mu) \to \mathbb{C}^{\mathrm{G}}_{\mathrm{K}_\psi}$ *is given by*

$$(\mathbb{P}_\psi \Phi)(g) = \int_G K_\psi(g, g')\Phi(g')\, \mathrm{d}\mu_{\mathrm{G}}(\mathrm{g}') \qquad \Phi \in \mathbb{L}_2(\mathrm{G}, \mathrm{d}\mu)\ . \tag{4.16}$$

Furthermore, $\mathcal{W}_\psi$ *intertwins* $\mathcal{U}$ *and the left regular representation* $\mathcal{L}$ *(i.e.* $\mathcal{L}_g$ *is given by* $\mathcal{L}_g(\Phi) = (h \mapsto \Phi(g^{-1}h))$*) on* $\mathbb{L}_2(G)$

$$\mathcal{W}_\psi \mathcal{U}_g = \mathcal{L}_g \mathcal{W}_\psi \tag{4.17}$$

Remarks/Consequences:

- The Inverse wavelet transform is the adjoint of the wavelet transform: $\mathcal{W}_\psi^{-1} = (\mathcal{W}_\psi)^*$, which is explicitly given by

$$\mathcal{W}_\psi^*(\Phi) = \int_G (\mathcal{U}_g \psi)\, \Phi(g)\, \mathrm{d}\mu_{\mathrm{G}}(\mathrm{g})\ . \tag{4.18}$$

  The condition number $c_\psi = \|\mathcal{W}_\psi^{-1}\|\|\mathcal{W}_\psi\| = 1$, so wavelet transform and its inverse are optimally well-posed.

- By polarization it follows from (4.15) that $(\mathcal{W}_\psi[f_1], \mathcal{W}_\psi[f_2])_{\mathbb{L}_2(G)} = C_\psi(f_1, f_2)$ for all $f_1, f_2 \in H$.

- Define $\widetilde{\mathcal{W}}_\psi = (1/\sqrt{C_\psi})\mathcal{W}_\psi$ then the operator (which indeed coincides with the projection operator given in (4.16)) $\mathbb{P}_\psi = \widetilde{\mathcal{W}}_\psi \widetilde{\mathcal{W}}_\psi^*$ is the orthogonal projection onto the range $\mathcal{R}(\mathcal{W}_\psi)$ of $\mathcal{W}_\psi$, since $\mathbb{P}_\psi^2 = \mathbb{P}_\psi$, $\mathbb{P}_\psi^* = \mathbb{P}_\psi$ and Obviously $\mathcal{R}(\mathbb{P}_\psi) \subset \mathcal{R}(\widetilde{\mathcal{W}}_\psi)$. Moreover,

$$\begin{array}{l} \mathcal{R}^\perp(\mathbb{P}_\psi) = \mathcal{R}^\perp(\mathbb{P}_\psi^*) = \mathcal{N}(\mathbb{P}_\psi) = \mathcal{N}(\widetilde{\mathcal{W}}_\psi^*) \Rightarrow \\ \mathcal{R}(\mathbb{P}_\psi)^{\perp\perp} = \mathcal{R}(\widetilde{\mathcal{W}}_\psi)^{\perp\perp} \Rightarrow \overline{\mathcal{R}(\mathbb{P}_\psi)} = \mathcal{R}(\widetilde{\mathcal{W}}_\psi) \end{array}$$

  and by $\mathcal{R}(\mathbb{P}_\psi) = \mathcal{N}(I - \mathbb{P}_\psi)$ the range of $\mathbb{P}_\psi$ is closed, so $\mathcal{R}(\mathbb{P}_\psi) = \mathcal{R}(\mathcal{W}_\psi)$.

- The set of admissible vectors $\mathcal{A} = \{\psi \in H \mid C_\psi < \infty\}$ is a $\mathcal{U}$ invariant vector space. Irreducibility of $\mathcal{U}$ implies that $\overline{\mathcal{A}} = H$ or $\overline{A} = \{0\}$. If G is unimodular (i.e. left and right Haar-measures coincide) then $\overline{\mathcal{A}} = \mathcal{A} = H$, cf. Grossmann etal.[67]. They also show that the mapping $\psi \mapsto C_\psi$ is a closed symmetric positive form, therefore there exists a unique positive operator $\mathcal{C}$, with $\mathcal{D}(\mathcal{C}) = \mathcal{A}$ such that $C_\psi = (\mathcal{C}\psi, \mathcal{C}\psi)$, so by polarization we have $(\mathcal{W}_\psi[f], \mathcal{W}_{\psi'}[g]) = (\mathcal{C}\psi, \mathcal{C}\psi')(f, g)$. If G is uni-modular then they show that $\mathcal{C} = \mathcal{I}$. From this one can clearly see that Theorem 17 is in fact a generalization of the famous Peter-Weyl Theorem for irreducible representations of compact groups. Since the Peter-Weyl Theorem also applies to reducible representations the assumption of irreducibility may not be necessary. In section 4.4 we deal with the case where the assumption of irreducibility is dropped for locally compact groups of the form $G = \mathbb{R}^d \rtimes_\tau T$, with T locally compact.

- In the special case where $G = \mathbb{R}^d \rtimes_\tau T$ and $\mathcal{U}$ a left regular action of G in $\mathbb{L}_2(\mathbb{R}^d)$, given by (4.6), which is unitary and *if* it is also irreducible one has the reconstruction formula:

$$\begin{array}{rl} f(\mathbf{x}) & = \frac{1}{C_\psi} \int\limits_{\tau(T)} \int\limits_{\mathbb{R}^d} \mathcal{W}_\psi[f](t, \mathbf{b})\, \psi((\tau(t))^{-1}(\mathbf{x} - \mathbf{b}))\, \mathrm{d}\mathbf{b}\, \mathrm{dt} \\ & = \frac{1}{C_\psi} \int\limits_{\tau(T)} ((f * \overline{\mathcal{R}_t \check{\psi}}) * \mathcal{R}_t \psi)(\mathbf{x})\, \mathrm{dt} \end{array} \tag{4.19}$$

for almost every $\mathbf{x} \in \mathbb{R}^d$, which is clearly a generalization of the reconstruction in Theorem 16, where $d = 1$, $T = D(1)$ and $\tau(t) = tI$. The reproducing kernel in the wavelet domain is then given by:

$$\begin{aligned} K_g(g') &= \tfrac{1}{C_\psi} \int_{\mathbb{R}^d} \tfrac{\psi((\tau(t'))^{-1}(\mathbf{x}-\mathbf{b}'))}{\sqrt{\det \tau(t')}} \overline{\tfrac{\psi(\tau(t)^{-1}(\mathbf{x}-\mathbf{b}))}{\sqrt{\det \tau(t)}}}\, \mathrm{d}\mathbf{x} = \\ &\tfrac{1}{C_\psi} \int_{\mathbb{R}^d} e^{-i\boldsymbol{\omega}\cdot(\mathbf{b}'-\mathbf{b})} \int_{\mathbb{R}^d} \tfrac{\psi((\tau(t'))^{-1}\boldsymbol{\omega})}{\sqrt{\det \tau(t')}} \overline{\tfrac{\psi(\tau(t)^{-1}\boldsymbol{\omega})}{\sqrt{\det \tau(t)}}}\, \mathrm{d}\mathbf{x}\mathrm{d}\boldsymbol{\omega} = \\ &\tfrac{(2\pi)^{d/2}}{C_\psi} [\mathcal{F}^{-1}(\boldsymbol{\omega} \mapsto \tfrac{\overline{\hat{\psi}(\tau(t^{-1})\boldsymbol{\omega})}\hat{\psi}(\tau((t')^{-1})\boldsymbol{\omega}))}{\sqrt{\det \tau(t)\, \det \tau(t')}}](\mathbf{b}-\mathbf{b}') \end{aligned} \tag{4.20}$$

Notice that $\mathcal{W}_\psi[f](g) = (K_g, \mathcal{W}_\psi[f])_{\mathbb{L}_2(G)}$.

Of course, we would like to apply Theorem 17 to the wavelet transformation that maps an image to its orientation score, see (4.2), since it would imply that reconstruction of an image from its orientation score is perfectly well-posed in the sense that (just like Fourier transform) the quadratic norm is preserved. It follows by the next lemma that we are not allowed to apply Theorem 17 to our case. Therefore in section 4.4 we generalize the standard wavelet theory where irreducibility is neither a requirement nor replaced by a requirement.

Lemma 5 *The left-regular action $\mathcal{U}$ of the Euclidean motion group in $\mathbb{L}_2(\mathbb{R}^2)$, given by (4.6), is a reducible representation.*

Proof
Consider the set of $\mathbb{L}_2$-functions whose Fourier transform have a support inside a given disk around the origin with radius, say $\rho > 0$, i.e. $\mathbb{L}_2^\rho(\mathbb{R}^2) := \{f \in \mathbb{L}_2(\mathbb{R}^2) \mid \mathrm{supp}(\mathcal{F}[f]) \subset B_{0,\rho}\}$, then obviously this is a non-trivial vector space unequal $\mathbb{L}_2(\mathbb{R}^2)$ which is invariant under $\mathcal{U}$, which directly follows by $\mathcal{F}[\mathcal{U}_g\psi] = e^{i\boldsymbol{\omega}\cdot\mathbf{b}}\mathcal{R}_\theta\mathcal{F}[\psi]$, for all $\psi \in \mathbb{L}_2^\rho(\mathbb{R}^2)$ □.

Analogue to the example in section 4.3.1, where we had to take an extra semi-direct product with $O(1)$, we could consider the similitude group $SIM(2) = \mathbb{R}^2 \rtimes \mathbb{T} \times D(1)$ with representation

$$\mathcal{V}_{\mathbf{b},e^{i\theta},a}\psi(\mathbf{x}) = \frac{1}{a}\psi\left(\frac{R_\theta^{-1}(\mathbf{x}-\mathbf{b})}{a}\right) \ , a > 0, \theta \in [0, 2\pi), \mathbf{b} \in \mathbb{R}^2 \ ,$$

which is irreducible, for proof see [93]p.51-52. This brings us within the standard wavelet framework of (and in particular to 2D Gabor wavelets, [88], or Cauchy-wavelets [6]) in 2D-image analysis.

We want to be able to reconstruct from a single scale layer in a robust manner. Therefore, for the moment we restrict ourselves to a single scale. This coincides with *Euclidean coherent states* from mathematical physics, [77], which are not to be confused with the more familiar Euclidean coherent states constructed from the irreducible[4] representations of the Euclidean motion group onto $\mathbb{L}_2(S^1)$ given by

$$(\mathcal{V}^p_{e^{i\theta},\mathbf{b}}\psi)(e^{i\alpha}) = e^{ip(b^1\cos\alpha + b^2\sin\alpha)}\psi(e^{i(\alpha-\theta)}), \qquad p > 0, \psi \in \mathbb{L}_2(S^1) \ ,$$

[4]They are in fact, up to equivalence, the only irreducible representations of the Euclidean Motion group, cf. [117].

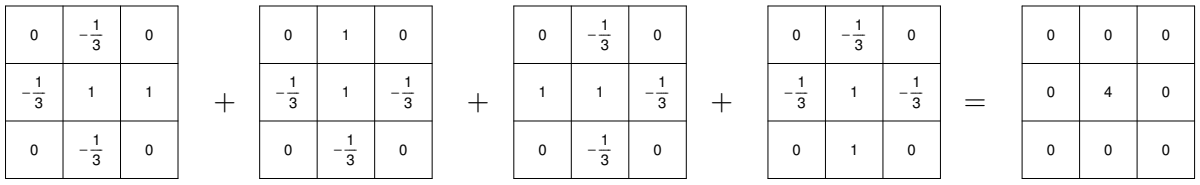

Figure 4.3: Integrating the rotated kernel ψ (left) over 4 discrete orientations gives a discrete spike δ.

see [4] p.219-220. Further we notice that the generalization of the wavelet reconstruction theorem to reducible representations of quotient groups, [121], inducing vector coherent states, rather than coherent states, is also too restrictive to be applied to our case as there is no (finite dimensional) dilation invariant subspace in $\mathbb{L}_2(\mathbb{R}^2)$.

From an image analysis point of view omitting the dilation group poses an important question. For example in scale space theory, [30], it is a well-known problem that reconstruction of a sharp image f, from its (say Gaussian) blurred version $f * G_s$ is extremely ill-posed: Is it possible to get around this ill-posedness by considering all rotated versions of linear combinations of Gaussian derivatives $f * (\partial_x)^p(\partial_y)^q G_s$? Before we give an affirmative answer to this question and deal with the issue of well-posed reconstruction of images from orientation scores, we give an illustration by means of an extremely simplified discrete example, where reconstruction is done by integration over discrete orientations, rather than inverse convolution.
Example: Suppose we construct a discrete orientation score with only 4 orientations, up, down left and right, constructed with the following discrete oriented wavelet $\psi : \mathbb{Z} \times \mathbb{Z} \to \mathbb{R}$, given by

$$\psi[x^1, x^2] = \begin{cases} 1 & \text{if } (x^1, x^2) \in \{(0,0),(0,1)\} \\ -1/3 & \text{if } (x^1, x^2) \in \{(0,1),(0,-1),(-1,0)\} \\ 0 & \text{else.} \end{cases}$$

which detects a direction at a width of 2 pixels. Then reconstruction of the original discrete image $f : \mathbb{Z} \times \mathbb{Z} \to \mathbb{R}$ from its orientation score is done by integration over all directions

$$f[x^1, x^2] = \frac{1}{4} \sum_{k=1}^{4} U_f^4[x^1, x^2, e^{ik\pi/2}] \quad ,$$

since the righthandside is in fact a convolution with a discrete δ-spike, see Figure 4.3.

4.4 A Functional Hilbert Space Approach to Wavelet Theory

In this section we will put the theory of wavelets in a more generic framework. First we construct unitary maps from a Hilbert space H into a functional Hilbert space $\mathbb{C}_K^{\mathbb{I}}$, which is a vector subspace of $\mathbb{C}^I$, the vector space of all complex valued functions on a set $\mathbb{I}$ (not necessarily a group). In subsection 4.4.2 we consider a special case and obtain a generalization of the standard wavelet theory for affine groups. The main strength of this generalization is

that we will not assume the representation to be irreducible, which by Lemma 5 is necessary for our application.

Recall from section 4.2 that a functional Hilbert space is a Hilbert space such that point evaluation is continuous, so by the Riesz representation theorem there exists a set $\{K_m \mid m \in \mathbb{I}\}$ with

$$(K_m, f)_H = f(m) \ , \text{ for all } m \in \mathbb{I} \text{ and } f \in H \ .$$

The span of the set $\{K_m \mid m \in \mathbb{I}\}$ is dense in the functional Hilbert space. Indeed if $f \in H$ is orthogonal to all K_m then $f = 0$ on $\mathbb{I}$.

Then define $K(m, m') = K_{m'}(m) = (K_m, K_{m'})_H$, for $m, m' \in \mathbb{I}$. K is called reproducing kernel and it is a function of positive type on $\mathbb{I}$, i.e.

$$\sum_{i=1}^{n}\sum_{j=1}^{n} K(m_i, m_j)\overline{c_i}c_j \geq 0 \ , \text{ for all } n \in \mathbb{N},\ c_1, ..., c_n \in \mathbb{C},\ m_1, ..., m_n \in \mathbb{I}.$$

So to every functional Hilbert space there belongs a reproducing kernel, which is a function of positive type. Conversely, as Aronszajn pointed out in his paper, cf. [7], a function K of positive type on a set $\mathbb{I}$ uniquely induces a functional Hilbert space consisting of functions on $\mathbb{I}$ with reproducing kernel K. We denote this space by $\mathbb{C}_K^{\mathbb{I}}$. Before we will briefly discuss the construction of this space we give an illustrative example.

Example: Consider the first order Sobolev space $\mathbb{H}^1(\mathbb{R})$, $\mathbb{I} = \mathbb{R}$, with

$$(f, g)_{\mathbb{H}^1(\mathbb{R})} = (f, g)_{\mathbb{L}_2(\mathbb{R})} + (f', g')_{\mathbb{L}_2(\mathbb{R})}, \tag{4.21}$$

where f' and g' are the generalized first order derivatives of resp. f and g. Then δ_a is a bounded (i.e. continuous) linear functional on $\mathbb{H}^1(\mathbb{R})$. This follows by the estimate

$$\begin{aligned}
|f(a)|^2 &= \int_{a-1}^{a} \{(x-(a-1))\overline{f(x)}f(x)\}'\mathrm{dx} \\
&= \int_{a-1}^{a} \{|f(x)|^2 + (x-(a-1))[\overline{f'(x)}f(x) + \overline{f(x)}f'(x)]\}\mathrm{dx} \\
&\leq \int_{a-1}^{a} \{|f(x)|^2 + 2|f'(x)||f(x)|\}\mathrm{dx} \\
&\leq \int_{a-1}^{a} \{2|f(x)|^2 + |f'(x)|^2\}\mathrm{dx} \leq 2\|f\|^2_{\mathbb{H}^1(\mathbb{R})}.
\end{aligned}$$

So by the Riesz representation theorem the reproducing kernel exists and by Fourier transformation it follows that the reproducing kernel is given by

$$K(a, x) = \mathcal{F}^{-1}[e^{i\omega a}\frac{1}{1+|\omega|^2}](x) = (1/2)e^{-|x-a|} \ , a, x \in \mathbb{R} \tag{4.22}$$

and $\|\delta_a\|_{\mathbb{H}^{-1}(\mathbb{R})} = \|K_a\|_{\mathbb{H}^1(\mathbb{R})} = (1/2)\sqrt{2}$. So we conclude that in case K is given by (4.22), then $\mathbb{C}_K^{\mathbb{I}=\mathbb{R}} = \mathbb{H}^1(\mathbb{R})$.

Next we give a brief overview of how to construct $\mathbb{C}_K^{\mathbb{I}}$, given the index set $\mathbb{I}$ and the function of positive type $K : \mathbb{I} \times \mathbb{I} \to \mathbb{C}$. The span $\langle \{K_m \mid m \in \mathbb{I}\} \rangle$ is a pre-Hilbert space with respect to inner product

$$(\sum_{i=1}^{l} \alpha^i K_{m_i}, \sum_{j=1}^{n} \beta^j K_{m_j}) = \sum_{i=1}^{l} \sum_{j=1}^{n} \overline{\alpha^i} \beta^j K(m_i, m_j) \ .$$

By taking the completion we get $\mathbb{C}_K^{\mathbb{I}}$. The norm $\|\Phi\| = \sqrt{(\Phi, \Phi)}$ on the space $\mathbb{C}_K^{\mathbb{I}}$, is given by

$$\begin{aligned} \|\Phi\|^2_{\mathbb{C}_K^{\mathbb{I}}} &= \sup \left\{ \frac{|(\Phi, G)_{\mathbb{C}_K^{\mathbb{I}}}|^2}{\|G\|^2_{\mathbb{C}_K^{\mathbb{I}}}} \ \mid \ G \in \langle \{K_m \mid m \in \mathbb{I}\} \rangle \right\} \\ &= \sup \left\{ \left| \sum_{j=1}^{l} \alpha_j \overline{\Phi(m_j)} \right|^2 \left(\sum_{k,j=1}^{l} \overline{\alpha_k} \alpha_j K(m_k, m_j) \right)^{-1} \right. \\ &\quad \left. \left| l \in \mathbb{N}, \alpha_j \in \mathbb{C}, m_j \in \mathbb{I}, \sum_{k,j=1}^{l} \overline{\alpha_k} \alpha_j K(m_k, m_j) \neq 0 \right. \right\} \ , \end{aligned} \tag{4.23}$$

see [94] Lemma 1.7, p.31. We highly stress that this abstract construction of $\mathbb{C}_K^I$ may not be satisfactory in many cases. Recall the example of the first order Sobolev space $\mathbb{H}^1(\mathbb{R})$. In this case the norm is both given by (4.21) and by (4.23), but clearly (4.21) is a much more tangible characterization of the norm than (4.23).

4.4.1 The Construction of a Unitary Map from H to $\mathbb{C}_K^{\mathbb{I}}$

Let $V = \{\phi_m \mid m \in \mathbb{I}\}$ be a subset of H such that its linear span is dense in H. Define the function $K : \mathbb{I} \times \mathbb{I} \to \mathbb{C}$ by $K(m, m') = (\phi_m, \phi'_m)_H$. Given such a function, we define the function $K_m : \mathbb{I} \to \mathbb{C}$ as $K_m(m') = K(m, m')$. In earlier work, cf. [22], we obtained the following fundamental result:

Theorem 18 *If the span of $V = \{\phi_m \mid m \in \mathbb{I}\}$ is dense in H, then the transform $\mathcal{W} : H \mapsto \mathbb{C}_K^{\mathbb{I}}$ defined by*

$$(\mathcal{W}[f])(m) = (\phi_m, f)_H \tag{4.24}$$

is a unitary mapping, i.e. $\|\mathcal{W}[f]\|_{\mathbb{C}_K^{\mathbb{I}}} = \|f\|_H$.

Proof see Appendix 7.2

From the applied mathematical point of view this result in itself may not be satisfactory, since the norm on $\mathbb{C}_K^{\mathbb{I}}$ given by (4.23), is rather intangible. Nevertheless, in some special cases this norm has a simpler explicit form.

Special Cases:

- **Wavelet transforms:** Let $\mathbb{I} = G$, for some locally compact group G. Let $\psi \in H$ (the wavelet). Let $g \mapsto \mathcal{R}_g$ be a representation of G onto H such that

$$V_\psi = \{\mathcal{R}_g\psi \mid g \in G\} \tag{4.25}$$

is dense in H and $K(g, g') = (\mathcal{R}_g\psi, R_{g'}\psi)_H$, then by Theorem 18 the generalized Wavelet Transform given by

$$(\mathcal{W}_\psi[f])(g) = (\mathcal{R}_g\psi, f)_H \tag{4.26}$$

is a unitary mapping from H onto $\mathbb{C}_K^G$. Notice that it immediately follows by the Cauchy-Schwarz inequality that indeed δ_g is continuous on $\mathbb{C}_K^G$:

$$\langle \delta_g, \mathcal{W}_\psi[f] \rangle = |\mathcal{W}_\psi[f](g)| \leq \|\mathcal{R}_g\psi\|_H \|f\|_H \ , \text{ for all } g \in G, f \in H.$$

- **Sampling Theorems:** The following sampling Theorem, which is a generalization of a theorem by Kramer, cf. [72], where H is forced to be $\mathbb{L}_2((a, b))$, $0 < a < b$ directly (the proof is almost trivial) follows by Theorem 18. Also, the well-known Nyquist Theorem is a special case. We shall return to this in section 4.5.

  Corollary 3 *Let H be a separable Hilbert space. Let $V = \{\phi_m \mid m \in \mathbb{I}\}$ be a frame in H. Let $\{m_n\}_{n\in\mathbb{N}}$ be a sequence in $\mathbb{I}$ such that $\{\phi_{m_n} \mid n \in \mathbb{N}\}$ is an orthogonal basis in H. Then*

$$f(m) = \sum_{n\in\mathbb{N}} f(m_n) \frac{K(m, m_n)}{K(m_n, m_n)}$$

for all $m \in \mathbb{I}$ and $f \in \mathbb{C}_K^{\mathbb{I}}$. Moreover,

$$\|f\|^2 = \sum_{n\in\mathbb{N}} \frac{|f(m_n)|^2}{K(m_n, m_n)}, \text{ for all } f \in \mathbb{C}_K^{\mathbb{I}}.$$

  Proof
  By Theorem 18, the corresponding map W is unitary, therefore the set $\{K_{m_n} \mid n \in \mathbb{N}\}$ is an orthogonal basis for $\mathbb{C}_K^{\mathbb{I}}$. Let $f \in \mathbb{C}_K^{\mathbb{I}}$, then

$$f = \sum_{n\in\mathbb{N}} \beta_n K_{m_n} = \sum_{n\in\mathbb{N}} \frac{(K_{m_n}, f)_{\mathbb{C}_K^{\mathbb{I}}}}{\sqrt{K(m_n, m_n)}} \frac{K_{m_n}}{\sqrt{K(m_n, m_n)}} = \sum_{n\in\mathbb{N}} f(m_n) \frac{K_{m_n}}{K(m_n, m_n)}$$

  Therefore the second statement follows. For the first statement take the inner product with K_m for all $m \in \mathbb{I}$. □

- **Discrete frames:** Let $\{\psi_i \mid i \in \mathbb{N}\}$ be a frame within some Hilbert space $\hat{H}$ with frame bounds $m > 0$ and $M > 0$, i.e.

$$m\|f\|^2 \leq \sum_{i=1}^{\infty} |(\psi_i, f)|^2 \leq M\|f\|^2 \ , \tag{4.27}$$

  for all $f \in H = \overline{\text{span}\{\psi_i\}}$. The orthogonal projection onto H is given by

$$\mathbb{P}_H f = \sum_{j=1}^{\infty} (\psi_j, f)\tilde{\psi}_j = \sum_{j=1}^{\infty} (\tilde{\psi}_j, f)\psi_j, \qquad f \in \hat{H},$$

  in which $\tilde{\psi}_j = \mathcal{A}^{-1}\psi_j$ is the reciprocal frame, where $\mathcal{A}^{-1}$ is the bounded inverse[5] of the bounded operator[6] $\mathcal{A}\psi = \sum_{i\in\mathbb{N}} (\psi_i, \psi)_H \psi_i$. Now set $\mathbb{I} = \mathbb{N}$, $V = \{\psi_i\}$, $K(i, j) = (\psi_i, \psi_j)$

[5] This directly follows by the frame-bound $m > 0$ in (4.27) and the Lax-Milgram theorem.
[6] This directly follows by the frame bound $M > 0$ in (4.27).

and $H = \overline{\text{span}\{\psi_i\}}$, then from Theorem 18 we deduce that $\mathcal{W} : H \to \mathbb{C}_K^{\mathbb{I}}$ given by $(\mathcal{W}f)(i) = (\psi_i, f)_H$ is a unitary mapping.

If $\{\psi_i\}$ are linear independent, the Gram-matrix g_{ij} is invertible and it follows that $\tilde{\psi}_i$ equals the reciprocal basis $\tilde{\psi}^j = \sum_k g^{jk}\psi_k$, where g^{jk} are the matrix elements of the inverse of the Gram-matrix. In this case $\mathbb{C}_K^{\mathbb{I}}$ is a subspace of $\ell_2(\mathbb{N}) = \{\mathbf{a} = (a_k)_{k\in\mathbb{N}} \in \mathbb{C}^{\mathbb{N}} \mid \sum_{k\in\mathbb{N}} |a_k|^2 < \infty\}$ equipped with inner product

$$(\mathbf{a}, \mathbf{b}) = \sum_{n\in\mathbb{N}} \left\{ \sum_{k\in\mathbb{N}} \overline{g^{kn} a_k} \right\} b_n, \qquad \mathbf{a} = \{a_k\}_{k\in\mathbb{N}}, \mathbf{b} = \{b_n\}_{n\in\mathbb{N}} \in l_2(\mathbb{N}).$$

The reproducing kernel is given by $K_m(k) = K(m,k) = g_{mk} = (\psi_m, \psi_k)$:

$$(K_m, \mathbf{b}) = \sum_{n\in\mathbb{N}} \left\{ \sum_{k\in\mathbb{N}} \overline{g^{kn} g_{mk}} \right\} b_n = \sum_n \delta_m^n b_n = b_m, \text{ for all } \mathbf{b} \in \ell_2(\mathbb{N}), m \in \mathbb{N}.$$

If $m = M = 1$ then $\{\psi_i\}_{i=1}^{\infty}$ is an orthogonal base, cf. [19] p.57 and $\mathcal{A} = \mathcal{A}^{-1} = I$ and thereby $\mathbb{C}_K^{\mathbb{I}} = \ell_2(\mathbb{N})$ equipped with standard ℓ_2-inner product.

If $\{\psi_i\}_{i=1}^{\infty}$ is a Riesz basis in H, i.e. there exist $c, C > 0$ such that

$$c\|\mathbf{a}\|_{\ell_2} \leq \| \sum_{n\in\mathbb{N}} a_n \psi_n \|^2 \leq C\|\mathbf{a}\|_{\ell_2}, \text{ for all } \mathbf{a} \in \ell_2(\mathbb{N}) \ ,$$

then there exists a bounded invertible linear operator $\mathcal{U}$ on H such that $\{\mathcal{U}\psi_n\}$ is an orthonormal basis in H. Then it follows by $(\psi_i, f) = (\mathcal{U}\psi_i, (\mathcal{U}^*)^{-1} f)$ and the previous case, that $\mathbb{C}_K^{\mathbb{I}} = \ell_2(\mathbb{N})$ equipped with inner product: $(\mathbf{a}, \mathbf{b})_{\mathbb{C}_K^{\mathbb{I}}} = \sum_{k\in\mathbb{N}} \sum_{l\in\mathbb{N}} \sum_{n\in\mathbb{N}} \overline{u_n^k a_k} u_n^l b_l$, where $u_n^k = (\psi^k, \mathcal{U}^*\psi_n)$.

Next, we give an explicit characterization of $\mathbb{C}_K^G$, in the case $G = \mathbb{R}^d \rtimes T$ and $\mathcal{U}$ the left-regular action of G onto $H = \mathbb{L}_2(\mathbb{R}^d)$ and thereby formulate a generalization of the wavelet reconstruction theorem for affine groups.

4.4.2 Generalization of Wavelet Reconstruction Theorem for Affine Groups

Inspired by section 4.3.2, we call $\psi \in \mathbb{L}_2(\mathbb{R}^d)$ an admissible wavelet if

$$0 < M_\psi := (2\pi)^{d/2} \int_T \left| \frac{\mathcal{F}[\mathcal{R}_t \psi]}{\sqrt{\det \tau(t)}} \right|^2 \mathrm{d}\mu_{\mathrm{T}}(\mathrm{t}) < \infty \text{ a.e. on } \mathbb{R}^d \tag{4.28}$$

where we recall that $\mathcal{R}_t$ is given by (4.7) and where we notice that the function M_ψ for the special case $G = \mathbb{R}^2 \rtimes \mathbb{T}$ indeed corresponds to definition (4.8) in section 4.2.

Lemma 6 *Let ψ be an admissible wavelet. Then the span of V_ψ, for definition see (4.25) is dense in $\mathbb{L}_2(\mathbb{R}^d)$, i.e. $\overline{\langle V_\psi \rangle} = \mathbb{L}_2(\mathbb{R}^d)$.*

Proof:

$$
\begin{aligned}
f \in \langle V_\psi \rangle^\perp &\Leftrightarrow \forall_{\mathbf{b}\in\mathbb{R}^d}\forall_{t\in T}(\mathcal{U}_{\mathbf{b},t}\psi, f)_{\mathbb{L}_2(\mathbb{R}^d)} = 0 \\
&\Leftrightarrow \forall_{\mathbf{b}\in\mathbb{R}^d}\forall_{t\in T}\left((\mathbf{b},t) \mapsto \mathcal{F}^{-1}[[\mathcal{F}\mathcal{R}_t\psi][\mathcal{F}f]](\mathbf{b})\right) = 0 \\
&\Rightarrow ((\boldsymbol{\omega},t) \mapsto \mathcal{F}\mathcal{R}_t\psi(\boldsymbol{\omega})\mathcal{F}f(\boldsymbol{\omega})) = 0 \qquad \text{a.e. on } \mathbb{R}^d \rtimes T \\
&\Rightarrow \left((\boldsymbol{\omega},t) \mapsto |\mathcal{F}\mathcal{R}_t\psi(\boldsymbol{\omega})\mathcal{F}f(\boldsymbol{\omega})|^2\right) = 0 \qquad \text{a.e. on } \mathbb{R}^d \rtimes T
\end{aligned}
$$

Let $f \in \langle V_\psi \rangle^\perp$. Then

$$
M_\psi(\boldsymbol{\omega})|(\mathcal{F}f)(\boldsymbol{\omega})|^2 = (2\pi)^{d/2} \int\limits_T \left| \frac{\mathcal{F}[\mathcal{R}_t\psi](\boldsymbol{\omega})\mathcal{F}f(\boldsymbol{\omega})}{\sqrt{\det \tau(t)}} \right|^2 \mathrm{d}\mu_{\mathrm{T}}(\mathrm{t}) = 0 \quad \text{a.e. on } \mathbb{R}^d \ .
$$

Because ψ is an admissible wavelet $M_\psi > 0$ a.e. $\Rightarrow |\mathcal{F}f|^2 = 0 \Rightarrow f = 0$. □

Corollary 4 *If the wavelet ψ is admissible, then the corresponding wavelet transform $\mathcal{W}_\psi : \mathbb{L}_2(\mathbb{R}^d) \to \mathbb{C}_K^G$ is unitary.*

Proof: This follows by Lemma 6 and Theorem 18. □

Define the linear operator $\mathcal{T}_{M_\psi}$ on $\mathbb{C}_K^G$ by

$$
[\mathcal{T}_{M_\psi}[\Phi]](\mathbf{b},t) = \mathcal{F}^{-1}\left[\boldsymbol{\omega} \mapsto (2\pi)^{-d/4} M_\psi^{-\frac{1}{2}}(\boldsymbol{\omega})\ \mathcal{F}[\Phi(\cdot,t)](\boldsymbol{\omega})\right](\mathbf{b}) \ .
$$

Operator $\mathcal{T}_{M_\psi}$ is well defined since $M_\psi > 0$ a.e. on $\mathbb{R}^d$ and $M_\psi^{-\frac{1}{2}}\mathcal{F}[\Phi(\cdot,t)] \in \mathbb{L}_2(\mathbb{R}^d)$ for all $t \in T$.

Theorem 19 *Let $G = \mathbb{R}^d \rtimes T$. Let ψ be an admissible wavelet. Then $\mathcal{T}_{M_\psi}\Phi \in \mathbb{L}_2(G, \mathrm{d}\mu_{\mathrm{G}}(\mathrm{g}))$ for all $\Phi \in \mathbb{C}_K^G$. Therefore $(\cdot,\cdot)_{\mathcal{T}_{M_\psi}} : (\mathbb{C}_K^G)^2 \to \mathbb{C}$ defined by*

$$
(\Phi, \Psi)_{M_\psi} = (\mathcal{T}_{M_\psi}[\Phi], \mathcal{T}_{M_\psi}[\Psi])_{\mathbb{L}_2(G)}, \tag{4.29}
$$

is an explicit characterization of the inner product on $\mathbb{C}_K^G$, which is the unique functional Hilbert space with reproducing kernel $K : G \times G \to \mathbb{C}$ given by

$$
K(g,h) = (\mathcal{U}_g\psi, \mathcal{U}_h\psi)_{\mathbb{L}_2(\mathbb{R}^2)} = (\mathcal{U}_{h^{-1}g}\psi, \psi)_{\mathbb{L}_2(\mathbb{R}^d)}, g, h \in G \ . \tag{4.30}
$$

The Wavelet transformation $\mathcal{W}_\psi$ defined by

$$
\mathcal{W}_\psi[f](\boldsymbol{b},t) = (\mathcal{U}_g\psi, f)_{\mathbb{L}_2(\mathbb{R}^2)}, \quad f \in \mathbb{L}_2(\mathbb{R}^d), \ \ g = (\boldsymbol{b},t) \in \mathbb{R}^d \rtimes T, \tag{4.31}
$$

is a unitary mapping from $\mathbb{L}_2(\mathbb{R}^d)$ to $\mathbb{C}_K^G$.

The space $\mathbb{C}_K^G$ *is a closed subspace of the Hilbert space* $\mathbb{H}_\psi \otimes \mathbb{L}_2(T\ ;\ \frac{\mathrm{d}\mu_{\mathrm{T}}(\mathrm{t})}{\det(\tau(t))})$*, where* $\mathbb{H}_\psi = \{f \in \mathbb{L}_2(\mathbb{R}^d) \mid M_\psi^{-\frac{1}{2}}\mathcal{F}[f] \in \mathbb{L}_2(\mathbb{R}^d)\}$ *is equipped with inner product*

$$(f,g) = (M_\psi^{-\frac{1}{2}}\mathcal{F}f, M_\psi^{-\frac{1}{2}}\mathcal{F}g)_{\mathbb{L}_2(\mathbb{R}^d\ ;\ (2\pi)^{-d/2}\mathrm{d}\boldsymbol{x})}.$$

The orthogonal projection $\mathbb{P}_\psi$ *of* $\mathbb{H}_\psi \otimes \mathbb{L}_2(T\ ;\ \frac{\mathrm{d}\mu_{\mathrm{T}}(\mathrm{t})}{\det(\tau(t))})$ *onto* $\mathbb{C}_K^G$ *is given by* $(\mathbb{P}_\psi[\Phi])(g) = (K(\cdot,g),\Phi)_{M_\psi}$.

Proof See[7] [22] p.27-30.
Remarks:

1. Since $\mathcal{W}_\psi : \mathbb{L}_2(\mathbb{R}^d) \to \mathbb{C}_K^G$ is unitary, the inverse equals the adjoint and as a result image f can be reconstructed from its orientation score $\mathcal{W}_\psi[f]$ by

$$\begin{aligned} f &= \mathcal{W}_\psi^*[\mathcal{W}_\psi[f]] \\ &= \mathcal{F}^{-1}\left[\boldsymbol{\omega} \mapsto \int_T \mathcal{F}[\mathcal{W}_\psi[f](\cdot,t)](\boldsymbol{\omega})\ \mathcal{F}[\mathcal{R}_t\psi](\boldsymbol{\omega})\ \tfrac{\mathrm{d}\mu_T(t)}{|\det(\tau(t))|}\ M_\psi^{-1}(\boldsymbol{\omega})\right]\ . \end{aligned} \tag{4.32}$$

2. If $M_\psi = (2\pi)^{d/2}$, then $\mathbb{C}_K^{\mathbb{R}^d \rtimes T}$ is a closed subspace of $\mathbb{L}_2(G) = \mathbb{L}_2(\mathbb{R}^d \rtimes T)$. Then similar to the irreducible case, Theorem 17, the quadratic norm is preserved.

3. It is easily verified that $\mathcal{F}(R_t\psi)(\boldsymbol{\omega}) = \sqrt{\det\tau(t)}[\mathcal{F}\psi](\tau(t)^T\boldsymbol{\omega})$, for all $\boldsymbol{\omega} \in \mathbb{R}^d$ and $t \in T$. As a result M_ψ can be rewritten

$$M_\psi(\boldsymbol{\omega}) = (2\pi)^{\frac{d}{2}} \int_T |[\mathcal{F}\psi]((\tau(t))^T\boldsymbol{\omega})|^2 \mathrm{d}\mu_{\mathrm{T}}(\mathrm{t})\ , \boldsymbol{\omega} \in \mathbb{R}^d\ .$$

   From this expression (and by left invariance of the Haar measure) we conclude that

$$M_\psi((\tau(t))^T\boldsymbol{\omega}) = M_\psi(\boldsymbol{\omega})\ ,\ \text{for all } \boldsymbol{\omega} \in \mathbb{R}^d \text{ and } t \in T. \tag{4.33}$$

   Now assume that $t \mapsto (\tau(t))^T\boldsymbol{\omega}$ acts transitively on $\mathbb{R}^d$, then it follows by (4.33) that M_ψ is constant and the space $\mathbb{C}_K^G$, $G = \mathbb{R}^d \rtimes_\tau T$, is a closed subspace of $\mathbb{L}_2(G)$.

   Example: in the case of $T = \mathcal{D}(1) \times SO(2)$, which acts transitively on $\mathbb{R}^2$, we get the similitude group $G = \mathbb{R}^2 \rtimes T = \mathcal{D}(1) \times SO(2) \rtimes \mathbb{R}^2$. So indeed the functional Hilbert space $\mathbb{C}_K^G$ is a closed subspace of $\mathbb{L}_2(G)$ and the corresponding wavelet transform preserves the quadratic norm.

4. If T is a compact group (for example $\mathbb{T}$) then it follows by interchanging the order of summation and integration (Fubini) that $M_\psi \in \mathbb{L}_1(\mathbb{R}^d)$. As a result the desirable case $M_\psi = (2\pi)^{d/2}$ cannot be achieved.

[7] Here the result is generalized to semi-direct products of a locally compact group T and *any* commutative group S. Here we only consider $S = \mathbb{R}^d$.

Definition 18 *The inner product on* $\mathbb{H}_\psi \otimes \mathbb{L}_2(T\,;\,\frac{\mu_T}{\det(\tau(t))})$ *induces a norm* $\|\cdot\|_{M_\psi} : \mathbb{H}_\psi \otimes \mathbb{L}_2(T\,;\,\frac{\mu_T}{\det(\tau(t))}) \to \mathbb{R}^+$*, which is given by*

$$\|\Phi\|_{M_\psi} = \sqrt{(\Phi,\Phi)_{M_\psi}} = \int_{\mathbb{R}^2}\int_T |\mathcal{F}[\Phi(\cdot,t)](\boldsymbol{\omega})|^2 (2\pi)^{-d/2} M_\psi^{-1}(\boldsymbol{\omega})\, \frac{\mathrm{d}\mu_\mathrm{T}(\mathrm{t})}{\det\tau(\mathrm{t})}\, \mathrm{d}\boldsymbol{\omega}\ ,$$

which we will call M_ψ*-norm.*

Theorem 19 has the following important consequence for our application of orientation scores in image analysis:

Corollary 5 *The space of orientation scores is a reproducing kernel Hilbert space* $\mathbb{C}_K^{\mathbb{R}^2\rtimes\mathbb{T}}$ *which is a closed subspace of* $\mathbb{H}_\psi \otimes \mathbb{L}_2(\mathbb{T};\,\frac{\mu_T}{\det(\tau(t))})$ *which is a vector subspace*[8] *of* $\mathbb{L}_2(G)$*. The inner product on* $\mathbb{C}_K^{\mathbb{R}^2\rtimes\mathbb{T}}$ *is given by (4.29) and is explicitly characterized by means of the function* M_ψ *given in (4.8). The wavelet transformation which maps an image* $f \in \mathbb{L}_2(\mathbb{R}^2)$ *onto its orientation score* $U_f \in \mathbb{C}_K^{\mathbb{R}^2\rtimes\mathbb{T}}$ *is a unitary mapping:* $\|f\|^2_{\mathbb{L}_2(\mathbb{R}^2)} = \|U_f\|^2_{M_\psi}$*.*
As a result the image f *can be reconstructed from its orientation score* $U_f = \mathcal{W}_\psi[f]$ *by means of the adjoint wavelet transformation* $\mathcal{W}_\psi^*$*:*

$$f = \mathcal{W}_\psi^*\mathcal{W}_\psi[f] = \mathcal{F}^{-1}\left[\boldsymbol{\omega} \mapsto \int_0^{2\pi} \mathcal{F}[U_f(\cdot,e^{i\theta})](\boldsymbol{\omega})\, \mathcal{F}[\mathcal{R}_{e^{i\theta}}\psi](\boldsymbol{\omega})\, \mathrm{d}\theta\, M_\psi^{-1}(\boldsymbol{\omega})\right] \tag{4.34}$$

Proof
Take $d = 2$, $T = \mathbb{T}$ and $\tau : \mathbb{T} \to \mathrm{Aut}(\mathbb{R}^2)$ given by $\tau(e^{i\theta})\mathbf{x} = R_\theta\mathbf{x}$ in Theorem 19. □.

4.4.2.1 The Discrete Analogue

Since the general theory deals with $G = T \rtimes \mathbb{R}^d$, with T locally compact, we may as well choose T a finite rotation group (equipped with discrete topology) which is locally compact. So consider $G = \mathbb{T}_N \rtimes \mathbb{R}^2$, where

$$\mathbb{T}_N = \{e^{ik\Delta}\,|k \in \{0,1,\dots N-1\}, \Delta = \frac{2\pi}{N}\},\ \text{for } N \in \mathbb{N}. \tag{4.35}$$

The discrete version of Corollary 5 is then straightforward, where we notice that the discrete orientation score $U_f^N(\mathbf{b}, e^{ik\Delta})$ of an image $f \in \mathbb{L}_2(\mathbb{R}^2)$ is given by

$$U_f^N(\mathbf{b}, e^{ik\Delta}) = (\mathcal{T}_\mathbf{b}\mathcal{R}_{k\Delta}\psi, f)_{\mathbb{L}_2(\mathbb{R}^2)}\ , k \in \{0,1,\dots N-1\}, \Delta = \frac{2\pi}{N}.$$

and the discrete version of the function M_ψ is

$$M_\psi(\boldsymbol{\omega}) = \frac{1}{N}\sum_{k=0}^{N-1} |\mathcal{F}(\mathcal{R}_{k\Delta}\psi)(\boldsymbol{\omega})|^2\ . \tag{4.36}$$

[8] i.e. is a subspace as a vector space, but is equipped with a different norm.

4.5 Stability reconstruction of image f from its orientation score U_f

The usual way to quantify the well-posedness/stability of an invertible linear transformation $A : V \to W$ from a normed space $(V, \|\cdot\|_V)$ to a normed space $(W, \|\cdot\|_W)$ is by means of the condition number

$$\mathrm{cond}(A) = \|A^{-1}\|\|A\| = \left(\sup_{\mathbf{x}\in V} \frac{\|\mathbf{x}\|_V}{\|A\mathbf{x}\|_W}\right)\left(\sup_{\mathbf{x}\in V} \frac{\|A\mathbf{x}\|_W}{\|\mathbf{x}\|_V}\right) \geq 1 \tag{4.37}$$

The closer it approximates 1, the more stable the operator and its inverse is. Notice that the condition number depends on the norms imposed on V and W. We want to apply this general concept to the wavelet transformation which maps image f to its orientation score[9] U_f. In the previous section we considered the wavelet transform as a unitary mapping from the space $\mathbb{L}_2(\mathbb{R}^2)$ to the space $\mathbb{C}_K^G$ respectively equipped with $\mathbb{L}_2$-norm and M_ψ-norm. Consequently, by choosing these norms the condition number becomes 1. However, from a practical point and numerical point of view it is much more reasonable to impose the $\mathbb{L}_2(G)$-norm on the orientation score, since this norm does not depend on the wavelet ψ and is in general robust under noise. Moreover it seems consistent, with the $\mathbb{L}_2$-norm imposed on the space of images.[10]

Furthermore, we assume that our images f are bandlimited[11], i.e. the support of their Fourier transform is bounded, by say a sphere with radius ϱ. The space of these images is given by

$$\mathbb{L}_2^\varrho(\mathbb{R}^2) = \{f \in \mathbb{L}_2(\mathbb{R}^2) \mid \mathrm{supp}(\mathcal{F}[f]) \subset B_{0,\varrho}\} \ , \varrho > 0 \ . \tag{4.38}$$

The reason for this assumption is the well-known Nyquist theorem, which states that *every band-limited function is determined by its values on a discrete grid.* For example if $u_B : \mathbb{R}^2 \to \mathbb{C}$ is bandlimited on a square: $\mathrm{supp}(\mathcal{F}[u_B]) \subset [-l/2, l/2] \times [-l/2, l/2]$, then

$$u_B(x,y) = \sum_{(k_1,k_2)\in\mathbb{Z}^2} u_B\left(\frac{2\pi k_1}{l}, \frac{2\pi k_2}{l}\right) \mathrm{sinc}\left(\frac{lx}{2} - k_1\pi\right) \mathrm{sinc}\left(\frac{ly}{2} - k_2\pi\right) \ ,$$

where the cutoff frequency $\varrho = l/2$ is called the Nyquist frequency.

Actually, the Nyquist Theorem theorem is a direct consequence of Theorem 18 (and Corollary 3): Take $H = \mathbb{L}_2([-\varrho, \varrho] \times [-\varrho, \varrho])$, take $\mathbb{I} = \mathbb{R}^2$ and take $\psi_{\mathbf{x}} = \frac{1}{2\pi} e^{-i\boldsymbol{\omega}\cdot\mathbf{x}}$, $\mathbf{x} = (x, y) \in \mathbb{I}$ then $\mathcal{W}_\psi$ is the inverse Fourier transform restricted to $\mathbb{L}_2([-\varrho, \varrho] \times [-\varrho, \varrho])$ and thereby its range is the space $\{f \in \mathbb{L}_2 \mid \mathrm{supp}\mathcal{F}[f] \subset [-\varrho, \varrho] \times [-\varrho, \varrho]\}$, which is the subspace of $\mathbb{L}_2(\mathbb{R}^2)$ consisting of bandlimited images, which indeed is a reproducing kernel Hilbert space with reproducing

[9] In image analysis, orientation scores are sometimes called orientation bundles, but that name seems rather unappropriate. It is rather the domain of an orientation score, which is the Euclidean motion group, that can be considered as a principal fiber bundle over structure group $\mathbb{T}$, with respect to resp. left or right action of $\mathbb{T}$ on G. In these fibrations, the fibers are resp. the right cosets and left cosets, which are resp. the spirals $[g] = [(\mathbf{b}, e^{i\theta})] = \{(R_{\theta'}\mathbf{b}, e^{i(\theta+\theta')}) \mid e^{i\theta'} \in \mathbb{T}\}$ and the straight lines $[g] = \{(\mathbf{b}, e^{i\theta-\theta'}) \mid e^{i\theta'} \in \mathbb{T}\}$.

[10] For example in the discrete framework the trivial case $\psi = \delta$ gives $\mathcal{W}_\psi[f](\cdot, e^{i\theta_k}) = f$ for $k = 1, \ldots, N$ with preservation of norm and thereby condition number 1.

[11] Notice that the left-regular action of G onto $\mathbb{L}_2^\varrho(\mathbb{R}^2)$ is well defined: If $f \in \mathbb{L}_2^\varrho(\mathbb{R}^2)$, then $\mathcal{U}_g f \in \mathbb{L}_2^\varrho(\mathbb{R}^2)$ for all $g \in G$.

kernel $(\psi_{\mathbf{x}}, \psi_{\mathbf{x}'})_{\mathbb{L}_2([-\varrho,\varrho]\times[-\varrho,\varrho])} = \frac{1}{4\varrho^2\pi^2}\text{sinc}(\varrho(x-x'))\text{sinc}(\varrho(y-y'))$. By Theorem 18 operator $\mathcal{W}_\psi$ is unitary, so it maps the orthonormal base $\{\mathbf{x} \mapsto e^{\frac{im\pi x}{\varrho}} e^{\frac{in\pi y}{\varrho}}\}_{m,n\in\mathbb{Z}}$ to the orthonormal base $\{\text{sinc}(\varrho x - m\pi)\text{sinc}(\varrho y - n\pi)\}$ in the functional Hilbert space $\{f \in \mathbb{L}_2 \mid \text{supp}(\mathcal{F}[f]) \subset [-\varrho,\varrho]\times[-\varrho,\varrho]\}$ and the result follows.

By (4.38) we consider images which are bandlimited on a disk rather than on a square, but this is just a subtlety as the reproducing kernel $\frac{1}{4\varrho^2\pi^2}\text{sinc}(\varrho(x-x'))\text{sinc}(\varrho(y-y')) = \mathcal{F}^{-1}[\boldsymbol{\omega} \mapsto e^{i\boldsymbol{\omega}\cdot(\mathbf{x}-\mathbf{x}')}1_{[-\varrho,\varrho]\times[-\varrho,\varrho]}]$ is replaced by the kernel

$$J_1\left(\frac{\sqrt{(x-x')^2+(y-y')^2}}{\varrho}\right)\frac{\varrho}{\sqrt{(x-x')^2+(y-y')^2}} = \mathcal{F}^{-1}[1_{B_{\mathbf{0},\varrho}}](\mathbf{x}-\mathbf{x}'). \tag{4.39}$$

Finally, we notice that from the practical point of view it does not make sense to store frequencies of order greater than $> l/2$ if the signal contains l samples, which is captured by the fact that a discrete Fourier transform of a discrete image $f : \{1,\ldots,n\}\times\{1,\ldots,n\} \to \mathbb{C}$ is again of the form $\mathcal{F}f : \{1,\ldots,n\}\times\{1,\ldots,n\} \to \mathbb{C}$. So a finite sample width puts an upper bound on the domain of the Fourier transform.

Definition 19 *Let ψ be an admissible wavelet. Then the wavelet transformation $\mathcal{W}_\psi^\varrho : \mathbb{L}_2^\varrho(\mathbb{R}^2) \to \mathbb{L}_2(G)$ is given by*

$$(\mathcal{W}_\psi^\varrho[f])(g) = (\mathcal{U}_g\psi, f)_{\mathbb{L}_2(\mathbb{R}^2)},\ f \in \mathbb{L}_2^\varrho(\mathbb{R}^2),$$

for almost every $g \in G$.

Theorem 20 *Let ψ be an admissible wavelet, with $M_\psi(\boldsymbol{\omega}) > 0$ for all $\boldsymbol{\omega} \in \mathbb{R}^2$. Then the condition number cond $(\mathcal{W}_\psi^\varrho)$ of the wavelet transformation $\mathcal{W}_\psi^\varrho : \mathbb{L}_2^\varrho(\mathbb{R}^2) \to \mathbb{L}_2(G)$ is defined by*

$$\text{cond}(\mathcal{W}_\psi^\varrho) = \|(\mathcal{W}_\psi^\varrho)^{-1}\|\|\mathcal{W}_\psi^\varrho\| = \left(\sup_{f\in\mathbb{L}_2^\varrho(\mathbb{R}^2)}\frac{\|f\|_{\mathbb{L}_2(\mathbb{R}^2)}}{\|U_f\|_{\mathbb{L}_2(G)}}\right)\left(\sup_{f\in\mathbb{L}_2^\varrho(\mathbb{R}^2)}\frac{\|U_f\|_{\mathbb{L}_2(G)}}{\|f\|_{\mathbb{L}_2(\mathbb{R}^2)}}\right)$$

and satisfies

$$1 \le (\text{cond}(\mathcal{W}_\psi^\varrho))^2 \le \left(\sup_{\|\boldsymbol{\omega}\|\le\varrho} M_\psi^{-1}(\boldsymbol{\omega})\right)\left(\sup_{\|\boldsymbol{\omega}\|\le\varrho} M_\psi(\boldsymbol{\omega})\right)\ .$$

Proof
First we notice that $\sup_{\|\boldsymbol{\omega}\|\le\varrho} M_\psi(\boldsymbol{\omega}) = \max_{\|\boldsymbol{\omega}\|\le\varrho} M_\psi(\boldsymbol{\omega})$ and $\sup_{\|\boldsymbol{\omega}\|\le\varrho} M_\psi^{-1}(\boldsymbol{\omega}) = \min_{\|\boldsymbol{\omega}\|\le\varrho} M_\psi(\boldsymbol{\omega})$ do exist. This directly follows by the assumption $M_\psi > 0$, the continuity of M_ψ (recall section 4.2) and the compactness of $\{\boldsymbol{\omega} \in \mathbb{R}^2 \mid \|\boldsymbol{\omega}\| \le \varrho\}$).

For all bandlimited images, the restrictions of their corresponding orientation scores to fixed orientations $e^{i\theta}$ are again bandlimited, i.e.

$$f \in \mathbb{L}_2^\varrho(\mathbb{R}^2) \Rightarrow U_f(\cdot, e^{i\theta}) \in \mathbb{L}_2^\varrho(\mathbb{R}^2),\ \text{for all } \theta \in [0, 2\pi)\ .$$

This directly follows by $\mathcal{F}[\mathcal{R}_{e^{i\theta}}\check{\psi} * f](\boldsymbol{\omega}) = 2\pi\mathcal{F}[\mathcal{R}_{e^{i\theta}}\check{\psi}](\boldsymbol{\omega})\mathcal{F}[f](\boldsymbol{\omega})$. As a result we have by Theorem 19 that

$$\begin{aligned}(\mathrm{cond}(\mathcal{W}_\psi^\varrho))^2 &= \left(\sup_{f\in\mathbb{L}_2^\varrho(\mathbb{R}^2)} \frac{\int_{B_{\mathbf{0},\varrho}} |\mathcal{R}_{e^{i\theta}}\mathcal{F}[\psi](\boldsymbol{\omega})|^2|\mathcal{F}[f](\boldsymbol{\omega})|^2 M_\psi^{-1}(\boldsymbol{\omega})\,\mathrm{d}\theta\,\mathrm{d}\boldsymbol{\omega}}{\int_{B_{\mathbf{0},\varrho}} |\mathcal{R}_{e^{i\theta}}\mathcal{F}[\psi](\boldsymbol{\omega})|^2|\mathcal{F}[f](\boldsymbol{\omega})|^2\,\mathrm{d}\theta\,\mathrm{d}\boldsymbol{\omega}}\right)\\ &\left(\sup_{f\in\mathbb{L}_2^\varrho(\mathbb{R}^2)} \frac{\int_{B_{\mathbf{0},\varrho}} |\mathcal{R}_{e^{i\theta}}\mathcal{F}[\psi](\boldsymbol{\omega})|^2|\mathcal{F}[f](\boldsymbol{\omega})|^2\,\mathrm{d}\theta\,\mathrm{d}\boldsymbol{\omega}}{\int_{B_{\mathbf{0},\varrho}} |\mathcal{R}_{e^{i\theta}}\mathcal{F}[\psi](\boldsymbol{\omega})|^2|\mathcal{F}[f](\boldsymbol{\omega})|^2 M_\psi^{-1}(\boldsymbol{\omega})\,\mathrm{d}\theta\,\mathrm{d}\boldsymbol{\omega}}\right)\\ &\leq \left(\sup_{\|\boldsymbol{\omega}\|\leq\varrho} M_\psi^{-1}(\boldsymbol{\omega})\right)\left(\sup_{\|\boldsymbol{\omega}\|\leq\varrho} M_\psi(\boldsymbol{\omega})\right)\ .\end{aligned}$$

Moreover we have $1 = \|(\mathcal{W}_\psi^\varrho)^{-1}\mathcal{W}_\psi^\varrho\| \leq \|(\mathcal{W}_\psi^\varrho)^{-1}\|\,\|\mathcal{W}_\psi^\varrho\|$. □

Corollary 6 *The stability of the (inverse) wavelet transformation $\mathcal{W}_\psi^\varrho : \mathbb{L}_2^\varrho(\mathbb{R}^2) \to \mathbb{L}_2(G)$ is optimal if $M_\psi^\varrho(\boldsymbol{\omega}) =$ constant for all $\boldsymbol{\omega} \in \mathbb{R}$, with $\|\boldsymbol{\omega}\| \leq \varrho$.*

So in general, the closer the function M_ψ approximates the constant function, say 1, on $B_{\mathbf{0},\varrho}$, the better the norm on $\mathbb{C}_K^G$ approximates the $\mathbb{L}_2(G)$-norm, the better the stability of reconstruction. In case of a good approximation one may use the following approximative reconstruction of the image

$$\tilde{\psi} * f = \mathcal{F}^{-1}\left[\boldsymbol{\omega} \mapsto \frac{1}{2\pi}\int_0^{2\pi} \mathcal{F}[U_f(\cdot, e^{i\theta})](\boldsymbol{\omega})\ \mathcal{F}[\mathcal{R}_{e^{i\theta}}\psi](\boldsymbol{\omega})\ \mathrm{d}\theta\right]\ , \tag{4.40}$$

where we recall that $\tilde{\psi}$ was given in (4.8), with the numerical benefit that in contrast to the true reconstruction (4.34), it does not use divisions in Fourier domain.

In the theoretic case where the pixel size of our image f converges to 0 and thereby the Nyquist frequency $\varrho \to \infty$, the *upper bound* for stability tends to infinity. Since by $\psi \in \mathbb{L}_1(\mathbb{R}^2) \cap \mathbb{L}_2(\mathbb{R}^2) \Rightarrow M_\psi \in \mathbb{L}_1(\mathbb{R}^2)$ the continuous function M_ψ^{-1} is unbounded on the whole $\mathbb{R}^2$. Relaxing the demand[12] that $\psi \in \mathbb{L}_2(\mathbb{R}^2)$, by constructing a Gelfand Triple $\mathbb{H}^{2k}(\mathbb{R}^2) \hookrightarrow \mathbb{L}_2(\mathbb{R}^2) \hookrightarrow \mathbb{H}^{-2k}(\mathbb{R}^2)$, $k \in \mathbb{N}$, for details see [23], leads to an isometric wavelet transform from $\mathbb{L}_2(\mathbb{R}^2)$ to $\mathbb{L}_2(\mathbb{R}^2 \rtimes \mathbb{T})$, with condition number equal to 1 .

4.6 Classes of Wavelets that allow Wellposed Reconstruction

By Corollary 6, wavelets ψ with $M_\psi = 1_{B_{0,\varrho}}$ induce optimal stability of the (inverse) wavelet transform. Because of the discontinuity at $\rho = \|\boldsymbol{\omega}\| = \varrho$ this choice may cause numerical problems with the discrete inverse Fourier transform in practice.

[12] Similar to Fourier transformation on $\mathbb{L}_2(\mathbb{R}^d)$.

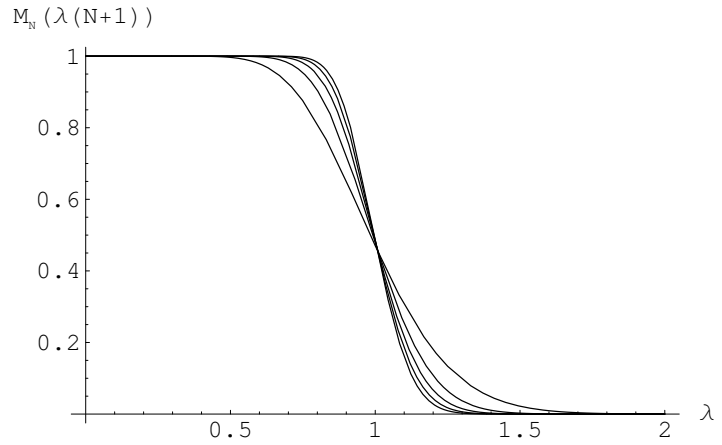

Figure 4.4: Plots of $\lambda \mapsto \mathcal{M}_N(\rho^2)$, with $\rho^2 = \lambda(N+1)$ for $N = 20, 40, 60, 80, 100$.

To avoid this practical problem we mainly focus on wavelets ψ, with either $M_\psi(\rho) = \mathcal{G}_\sigma(\|\boldsymbol{\omega}\|)$, a Gaussian kernel with standard deviation $\sigma \approx \varrho/2$ or $M_\psi(\rho) = \mathcal{M}_N(\sigma^2\rho^2)$, $N \in \mathbb{N}$, $\sigma > 0$, $\rho = \|\boldsymbol{\omega}\|$ where

$$\mathcal{M}_N(\rho^2) = e^{-\rho^2} \sum_{k=0}^{N} \frac{\rho^{2k}}{k!} \leq 1 \ . \tag{4.41}$$

In both cases the function M_ψ smoothly approximates $1_{B_{0,\varrho}}$ and thereby guarantee a stable reconstruction. In the sequel we will call a wavelet $\psi \in \mathbb{L}_2(\mathbb{R}^2) \cap \mathbb{L}_1(\mathbb{R}^2)$, with such a M_ψ, a **proper wavelet**.

For the first case this statement is obvious, for the second case, i.e. proper wavelets ψ with $M_\psi = \mathcal{M}_N(\rho^2)$, we give some explanation:

First of all we notice that

$$\begin{array}{l} \mathcal{M}'_N(v) = -\frac{v^N e^{-v}}{N!} < 0, \text{ for all } v > 0 \\ \mathcal{M}''_N(v) = 0 \Leftrightarrow v = N, \end{array} \tag{4.42}$$

so $\mathcal{M}_N(\rho^2)$ is monotonically decreasing with bending point $(N, \mathcal{M}_N(N))$ (with $\mathcal{M}'_N(N) = -e^{-N}\frac{N^N}{N!} = O(-\sqrt{N})$). Furthermore it follows by N-times partial integration that

$$\mathcal{M}_N(\rho^2) = 1 - \int_0^{\rho^2} \frac{e^{-t}t^N}{N!}\,\mathrm{dt} = 1 - \frac{\gamma[N+1,\rho^2]}{\Gamma[N+1]} = \frac{\Gamma(N+1,\rho^2)}{\Gamma[N+1]} \ ,$$

where the incomplete Gamma-functions are given by

$$\begin{aligned} \gamma(a,z) &= \int_0^z t^{a-1}e^{-t}\,\mathrm{dt}, \\ \Gamma(a,z) &= \int_z^\infty t^{a-1}e^{-t}\,\mathrm{dt}, \ |\arg(z)| < \pi, \Re(a) > 0 \ . \end{aligned}$$

The asymptotic expansion

$$\mathcal{M}_N(\lambda(N+1)) = \frac{1}{2}\mathrm{erfc}(\eta(\lambda)\sqrt{\frac{N+1}{2}}) + R_{N+1}(\eta(\lambda)) = \frac{1}{2}\mathrm{erfc}(\eta(\lambda)\sqrt{\frac{N+1}{2}}) + O\left(\frac{1}{\sqrt{N}}\right)$$

with $\eta(\lambda) = \mathrm{sgn}(\lambda-1)\sqrt{2(\lambda-1-\log\lambda)}$, and $R_{N+1}(\eta)$ analytic with respect to λ and λ close to 1, explains the nice behavior illustrated in Figure 4.4 , for details see [118]p.284-287. As a result, by Theorem 20 it follows that the condition number of wavelets ψ, with $M_\psi(\rho) = \mathcal{M}_N\left(\frac{\rho N}{\varrho}\right)$, satisfies

$$(\mathrm{cond}(\mathcal{W}_\psi^\varrho))^2 \leq 1 \cdot \mathcal{M}_N^{-1}(N+1) = 2 + O\left(\frac{1}{\sqrt{N}}\right) \ ,$$

which is indeed close to optimal stability.

4.6.1 A Simple Approach to Parameterization of Proper Wavelet classes

The following lemma shows us a simple but practical approach to obtain proper wavelets ψ with the same $M_\psi(\boldsymbol{\omega}) = \mathcal{M}(\rho)$, $\rho = \|\boldsymbol{\omega}\|$, $\boldsymbol{\omega} = (\rho\cos\phi, \rho\sin\phi)$, where $\mathcal{M}$ ensures a stable reconstruction.

Lemma 7 *Let $A : S^1 \to \mathbb{C} \setminus \mathbb{R}^-$ be such that*

$$\frac{1}{2\pi}\int_0^{2\pi} |A(\varphi)|\mathrm{d}\varphi = 1 \ , \tag{4.43}$$

then the wavelet $\psi = \mathcal{F}^{-1}[\boldsymbol{\omega} \mapsto \sqrt{A(\varphi)\mathcal{M}(\rho)}]$ has $M_\psi(\boldsymbol{\omega}) = \mathcal{M}(\rho)$ for all $\boldsymbol{\omega} \in \mathbb{R}^2$.

Proof: $M_\psi(\boldsymbol{\omega}) = \frac{1}{2\pi}\int_0^{2\pi} |\mathcal{F}(\mathcal{R}_\theta\psi)(\boldsymbol{\omega})|^2\mathrm{d}\theta = \frac{1}{2\pi}\int_0^{2\pi} |\sqrt{A(\varphi-\theta)\mathcal{M}(\rho)}|^2 \ \mathrm{d}\theta = \mathcal{M}(\rho)$, for all $\boldsymbol{\omega} \in \mathbb{R}^2$, $\|\boldsymbol{\omega}\| = \rho$. □

Lemma 7 is easily translated to the discrete framework $\mathbb{R}^2 \rtimes \mathbb{T}_N$, recall (4.35), where condition (4.43) must be replaced by

$$\frac{1}{N}\sum_{k=0}^{N} |A(\varphi - k\Delta)| = 1 \ . \tag{4.44}$$

If moreover $\frac{1}{2\pi}\int_0^{2\pi}\sqrt{A(\varphi)}\mathrm{d}\varphi \approx 1$ we have a fast/simple approximative reconstruction:

$$\begin{aligned} \tilde{f}(\mathbf{x}) \ &= \tfrac{1}{2\pi}\int_0^{2\pi} U_f(\mathbf{x},\theta)\ \mathrm{d}\theta \\ &\approx \mathcal{F}^{-1}[\boldsymbol{\omega} \mapsto \sqrt{\mathcal{M}(\rho)}\mathcal{F}[f](\boldsymbol{\omega})](\mathbf{x}) = (\sqrt{M_\psi} * f)(\mathbf{x}) \ , \text{for almost every } \mathbf{x} \in \mathbb{R}^2 \ . \\ &M_\psi \approx 1_{B_{0,\varrho}} \Rightarrow \tilde{f} \approx f \in \mathbb{L}_2^\varrho(\mathbb{R}^2) \ , \end{aligned} \tag{4.45}$$

which coincides with the exact reconstruction in the simple example of section 3, see figure 3.1.

For stability $M_\psi =$ constant is just as good as $M_\psi = 1$. Therefore (4.43) can be replaced by $\sqrt{A(\varphi)} \in \mathbb{L}_2(S^1)$. So, by expanding $\sqrt{A(\varphi)}$ in spherical harmonics: $\sqrt{A(\varphi)} = \sum_{m\in\mathbb{Z}} a_m e^{im\varphi}$ we get $\sum_{m\in\mathbb{Z}} |a_m|^2 < \infty$. Notice that $\frac{1}{2\pi}\int_0^{2\pi} \sqrt{A(\varphi)}\mathrm{d}\phi = 1 \Leftrightarrow c_0 = \sqrt{2\pi}$, which allows us to use the approximative reconstruction (4.45). However, in many applications one is interested in detection of symmetric elongated, in such case it is more suitable to expand in $\{e_m\}_{m\in\mathbb{N}\cup\{0\}} = \{\varphi \mapsto \cos^2\left(\frac{m\varphi}{2}\right)\} = \{\varphi \mapsto (1/2)(1+\cos(m\varphi))\}$, which is a complete base in the even subspace of $\mathbb{L}_2(S^1)$, which we denote by $\mathbb{L}_2^{\mathrm{EVEN}}(S^1)$, with the nice property that the basis elements are positive. The dual basis of $\{e_m\}_{m=0}^M$ is given by $\hat{e}^k(f) = (e^k, f)$, $f \in \mathbb{L}_2^{\mathrm{EVEN}}([-\pi,\pi))$, with $e^k = \sum_{m=0}^M g^{km} e_m$ and

$$g^{km} = \begin{cases} \frac{4}{\pi} & \text{if } k = m \neq 0\ , \\ \frac{2M+1}{2\pi} & \text{if } k = m = 0\ , \\ -\frac{2}{\pi} & \text{if } km = 0 \text{ and } k+m \neq 0 \\ 0 & \text{else.} \end{cases}$$

As a result the expansion of $B = \sqrt{A} \in \mathbb{L}_2^{\mathrm{EVEN}}([-\pi,\pi))$ in $\{e_m\}_{m\in\mathbb{Z}}$ takes the following simple form:

$$B = \sum_{m=0}^M B^m e_m = \frac{2M+1}{2\pi}(e_0, B)e_0 + \frac{4}{\pi}\sum_{k=1}^M (e_k, B)_{\mathbb{L}_2(S^1)}\left\{e_k - \frac{1}{2}e_0\right\} - \frac{2}{\pi}\sum_{k=1}^M (e_0, B)_{\mathbb{L}_2(S^1)} e_k\ .$$

Finally, we notice that $\frac{1}{2\pi}\int_0^{2\pi} \sqrt{A(\varphi)}\mathrm{d}\varphi = 1 \Leftrightarrow B_0 + (1/2)\sum_{m=0}^\infty B_m = 1$.

From Lemma 7 we deduce that every wavelet $\psi \in \mathbb{L}_2^\rho(\mathbb{R}^2)$, whose Fourier transform is separable in polar coordinates, $(\mathcal{F}[\psi])(\boldsymbol{\omega}) = \Phi(\varphi)R(\rho)$, with $\Phi \in \mathbb{L}_2([0,2\pi]) \cap \mathbb{L}_1([0,2\pi])$ and $R(\rho) = \sqrt{\mathcal{M}(\rho)}$, is a proper wavelet. On the one hand the class of proper wavelets induced by Lemma 7 is fairly wide, which allows us to select a proper wavelet that is a good detector of elongated structures (like blood vessels or catheters in medical images). On the other hand this class of wavelets seems rather restrictive as the Fourier transform of the wavelet, $\mathcal{F}[\psi]$, is assumed to be polar-separable, with a (more or less) fixed radial component R. The separability-restriction is not harmful in practice, since $\mathbb{L}_2^\varrho(\mathbb{R}^2) = \mathbb{L}_2(S^1) \bigotimes \mathbb{L}_2((0,\varrho), \rho\mathrm{d}\rho)$, so by choosing a basis in $\mathbb{L}_2(S^1)$ and $\mathbb{L}_2((0,\varrho),\rho\mathrm{d}\rho)$, the Fourier transform $\mathcal{F}[\psi]$ of a line detector wavelet is always a superposition of separable wavelets, $\mathcal{F}[\psi] = \sum_i c_i \mathcal{F}[\psi^i]$. Notice that $\mathcal{W}_\psi[f](g) = (\mathcal{U}_g\psi, f) = \sum_i c_i(\mathcal{U}_g\psi^i, f)$, so by the cost of extra storage this problem can be tackled.

The restriction on the radial component(s) is a more serious problem. Mostly, typical line detecting convolution kernels have a radial component with a much smaller width than $\mathcal{M}(\rho)$. Therefore, a replacement of the radial component R by $\mathcal{M}(\rho)$, will affect the radial shape of the wavelet, but preserves the angular part of the wavelet.

Example 1:

Consider $N = 18$ discrete orientations, so $\Delta = \frac{2\pi}{N} = \frac{\pi}{9}$. The idea is to "fill a cake by pieces of cake" in the Fourier domain. In order to avoid high frequencies in the spatial domain, these pieces must be smooth and thereby they must overlap.

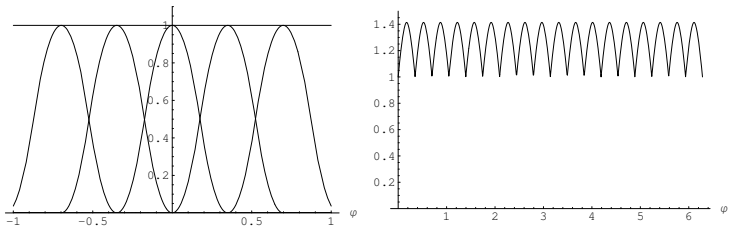

Figure 4.5: Left: Plots of $A(\phi - k\Delta)$, see (4.46), with $\Delta = \frac{2\pi}{18}$, $k = -2, -1, 0, 1, 2$. Notice that it follows by the point-symmetries at $\{k + (\frac{\Delta}{2}), \frac{1}{2}\}$ that $\frac{1}{N}\sum_{k=0}^{N-1} |A(\phi - k\Delta)| = 1$. Right: Graph of $\phi \mapsto \frac{1}{N}\sum_{k=0}^{N-1} \sqrt{A(\phi - k\Delta)} \approx 1$.

Let $\psi = \mathcal{F}^{-1}[\boldsymbol{\omega} \mapsto \sqrt{A(\varphi)\mathcal{M}(\rho)}]$ and let $A : S^1 \to \mathbb{R}^+$ be given by

$$A(\varphi) = \begin{cases} -\frac{2}{\Delta^2}\varphi^2 + 1 & \text{if } |\varphi| \leq \frac{\Delta}{2} \\ \frac{2}{\Delta^2}\varphi^2 - \frac{4}{\Delta}|\varphi| + 2 & \text{if } \frac{\Delta}{2} \leq |\varphi| \leq \Delta \\ 0 & \text{else} \end{cases} , \varphi \in [-\pi, \pi) \ , \tag{4.46}$$

then it is easily checked that $M_\psi(\boldsymbol{\omega}) = \mathcal{M}(\rho)$, $\rho = \|\boldsymbol{\omega}\|$, cf. (4.44) and Figure 4.5. Now we have $\frac{1}{N}\sum_{k=0}^{N} |\sqrt{A(\phi - k\Delta)}| \approx 1$, again see 4.5, which allows us to use the practical approximative reconstruction given by (4.45). Moreover, the real valued part of the wavelet is useful for line detection and the imaginary part of the kernel is appropriate for edge detection, see Figure 4.7 for plots and stability analysis, see Figure 4.6 for line detection with comparison to the usual line detection.

Notice that if $A_1 : S^1 \to \mathbb{R}^+$ and $A_2 : S^1 \to \mathbb{R}^+$, $A_i \in \mathbb{L}_1(S^1) \cap \mathbb{L}_2(S^1)$, satisfy condition (4.43) then so does the periodic convolution $A_1 \star A_2 : S^1 \to \mathbb{R}^+$ given by $(A_1 \star A_2)(\phi) = \int_0^{2\pi} A_1(\phi - \psi)A_2(\psi)\mathrm{d}\psi$. This enables us to generate explicit examples, which are similar to the wavelet in example 1 by the same token of splitting a cake into equal and smoothly overlapping pieces. For example take $A_i(\phi) = \sum_{k=0}^{N} \chi_k(\phi)$, $i = 1, 2$ where $\chi_k(\phi) = (\tau_{k\Delta}\,\chi_0)(\phi) = \chi_0(\phi - k\Delta)$, and $\chi(\phi) = 1_{-\Delta/2, \Delta/2}(\phi)$, then by $\chi_i \star \chi_j = \tau_{(i+j)\Delta}(\chi_0 \star \chi_0)$, we obtain a first order B-spline representation of 1_{S^1}. If we repeat this proces n times we obtain a $n+1$-th order B-spline representation of 1_{S^1}:

$$1_{S^1}(\phi) = \sum_{k=0}^{N-1} (\chi_0 \star^{(n)} \chi_0)(\phi - k\Delta) \ .$$

Although a base function in a second ($n = 2$) order B-spline representation looks very similar to (4.46), it is different in the sense that each value $\varphi \in [0, 2\pi)$ lies within the support of 3 base functions, whereas in our example (4.46) this value is 2.

Example 2:

The most common way of line detection in image analysis is by means of the largest eigenvalue

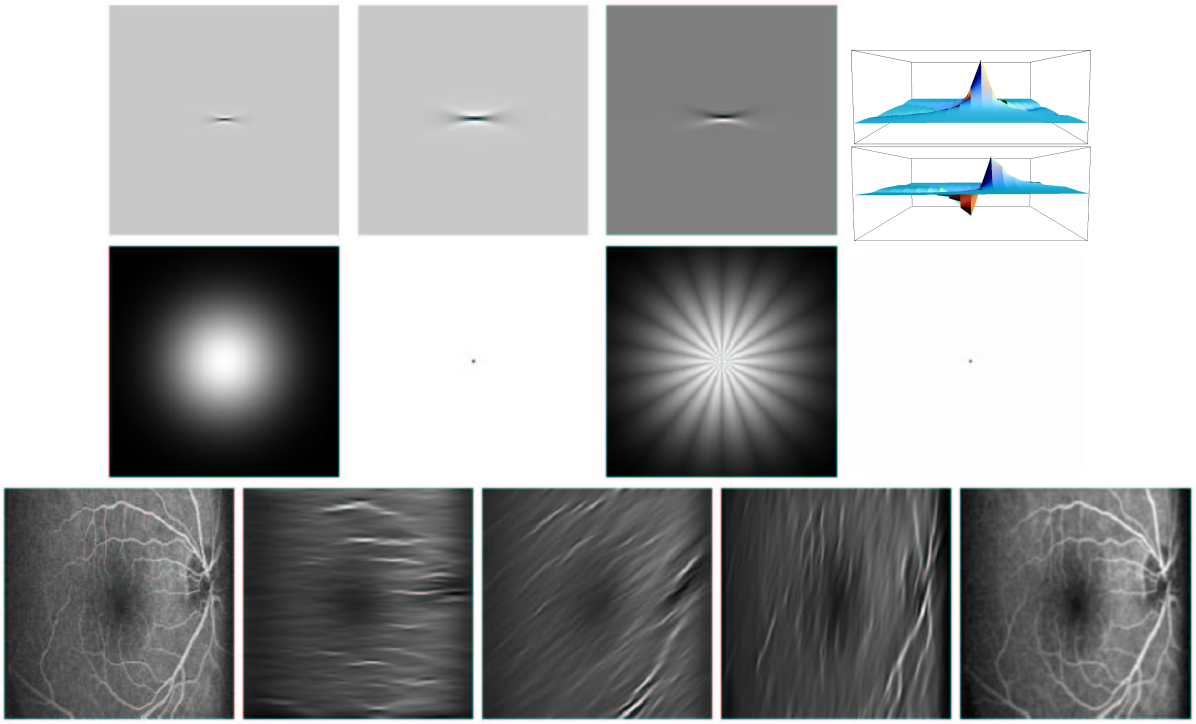

Figure 4.6: Upper row: Plots of the graph of the real and imaginary part of $\psi = \mathcal{F}^{-1}[\boldsymbol{\omega} \mapsto \sqrt{A(\varphi)\mathcal{M}(\rho)}]$, with $A(\varphi)$ given by (4.46) and $\mathcal{M}(\rho) = G_s(\rho)$, $s = 800$, determined by the discrete inverse Fourier transform of $\boldsymbol{\omega} \mapsto \sqrt{A(\varphi)\mathcal{M}(\rho)}$ sampled on a 256×256 equidistant grid. From left to right: Density plots (grey-values have been mapped to full range and inverted for the sake of clarity) of $\Re(\psi)$ at true size, $\Re(\psi)$ and $\Im(\psi)$ 2 times zoomed in and finally two 3D-plots of the graphs of $\Re(\psi)$ and $\Im(\psi)$. Second row: From left to right plots of M_ψ and Fourier inverse $\tilde{\psi} = \mathcal{F}^{-1}[M_\psi]$, sum of all rotated kernels in Fourier and spatial domain. Third row: MRI-image of the retina, three slices $U_f^N(e^{ik\Delta}, \cdot)$, $k = 0, 2, 4$ of the discrete orientation score U_f^N and fast approximative reconstruction,(4.45) which is close to exact reconstruction.

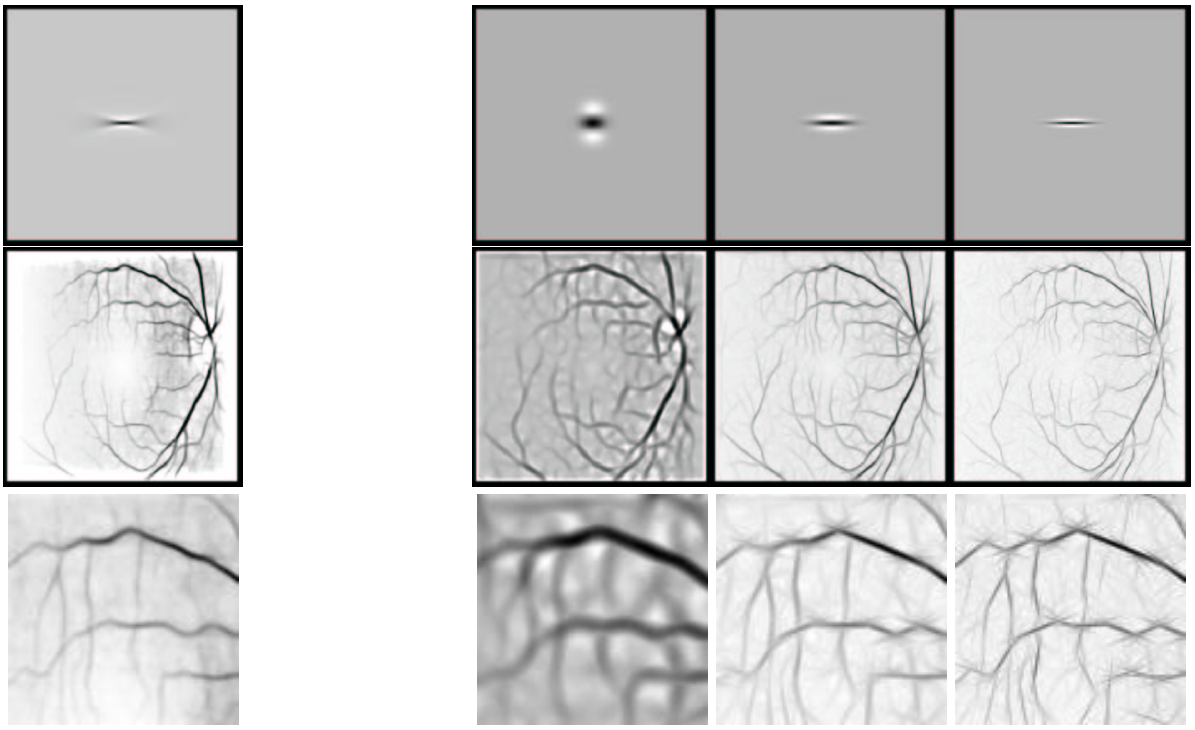

Figure 4.7: Top row, from left to right, a proper wavelet $\psi = \mathcal{F}^{-1}[\boldsymbol{\omega} \mapsto \sqrt{A(\varphi)\mathcal{M}(\rho)}]$ as shown in previous figure, second order derivatives of anisotropic Gaussian kernel $\gamma = 1$, $\gamma = 4$, $\gamma = 7$, see (4.48). For the sake illustration of we zoomed in by a factor of 2 in all cases. Middle row: Detection of elongated structures via orientation scores constructed by wavelet, $\mathcal{W}_{\psi}^{*}[\frac{|\Re(U_f)-\min\{\Re(U_f)\}|^2}{\max\{|\Re(U_f)-\min\{\Re(U_f)\}|}\}]$ and comparison with the usual line detection in image analysis with second order Gaussian kernel, for $\gamma = 1$, $\gamma = 4$ and $\gamma = 7$, see (4.47). Bottom row: enlarged small fragment of images. This figure shows us that there exist proper-wavelets (with the advantage of a stable reconstruction) that can be used for a line detection, which is as least as good as the usual approach. In fact, by demanding a stable reconstruction, the tail of a proper wavelet typically spreads out more naturally. Therefore proper wavelets, which look locally at the center like the usual line detectors, deal better with elongated lines which are slightly curved, which is usually the case in practical applications such as catheter, guide wire, blood vessel detection.

$\lambda_1(\mathbf{b})$ of the Hessian matrix $Hu(\mathbf{b})$ of second order Gaussian derivatives:

$$Hu(\mathbf{b}) = \begin{pmatrix} u_{xx}(\mathbf{b}) & u_{xy}(\mathbf{b}) \\ u_{xy}(\mathbf{b}) & u_{yy}(\mathbf{b}) \end{pmatrix} ,$$

where $u(\mathbf{b}, s) = (G_s * f)(\mathbf{b})$, $s = \frac{1}{2}\sigma^2 > 0$ is the so-called scale space representation of image $f \in \mathbb{L}_2(\mathbb{R}^2)$. We notice that

$$\begin{aligned} \lambda_1(\mathbf{b}) &= \max_{\theta\in[0,2\pi)} (R_\theta \mathbf{e}_x)^T Hu(\mathbf{b})(R_\theta \mathbf{e}_x) = \max_{\theta\in[0,2\pi)} \{u_{\xi\xi} \mid \xi = (\cos\theta)x + (\sin\theta)y\} \\ &= \max_{\theta\in[0,2\pi)} (f * \mathcal{R}_\theta(G_s)^{(2,0)})(\mathbf{b}) = \max_{\theta\in[0,2\pi)} \mathcal{W}_{G_s^{(2,0)}}[f](\mathbf{b}, e^{i\theta}) = \max_{\theta\in[0,2\pi)} U_f(\mathbf{b}, e^{i\theta}) , \end{aligned} \tag{4.47}$$

so the usual method in image analysis is in fact a maximum intensity projection of an orientation score with a second order derivative of the Gaussian kernel. Such a second order derivative of a Gaussian clearly distinguishes lines from edges and it can easily be stretched by replacing the Gaussian kernel by an anisotropic Gaussian kernel:

$$G_{s,\gamma}^{(2,0)}(x,y) = (G_{s/\gamma}^{(2)})_x (G_s)_y (x,y) = \frac{\gamma}{16\pi s^3}(\gamma x^2 - 2s) e^{-\frac{\gamma x^2}{4s}} e^{-\frac{y^2}{4s}}, \ s > 0, \gamma > 0. \tag{4.48}$$

Its Fourier transform is given by:

$$\mathcal{F}[G_{s,\gamma}^{(2,0)}](\boldsymbol{\omega}) = -\rho^2 (\cos\varphi)^2 e^{-\frac{1}{2}\left(\frac{\sigma\rho}{\kappa}\right)^2} e^{-\frac{1}{2}(\rho\sigma\sin\varphi)^2\left(1-\frac{1}{\kappa^2}\right)} , \boldsymbol{\omega} = (\rho\cos\varphi, \rho\sin\varphi) , \tag{4.49}$$

from which we immediately deduce that M_ψ, for $\psi = G_{s,\gamma}^{(2,0)}$ is not at all desirable; a well-posed reconstruction is not possible. Therefore we will construct new wavelets that are locally similar to $\psi = G_{s,\gamma}^{(2,0)}$ but that do allow a well-posed reconstruction. It directly follows by a Taylor expansion of the second exponent, $e^{-\frac{1}{2}(\rho\sigma\cos\varphi)^2\left(1-\frac{1}{\kappa^2}\right)}$ (and Fubini) in (4.49) that:

$$\mathcal{F}[G_{s,\gamma}^{(2,0)}] = \sum_{m=-\infty}^{\infty} \left(\sum_{n=0}^{\infty} \frac{A(m,n)}{n!} \left(\frac{-\rho\sigma}{2}\right)^{2n} \left(1 - \frac{1}{\kappa^2}\right)^n \right) \cos(m\varphi) , \tag{4.50}$$

where $A(m,n) = \int_0^{2\pi} (\cos\varphi)^2 (\sin\varphi)^{2n} \cos(m\varphi)\, \mathrm{d}\varphi$ can be computed by recursion

$$\begin{cases} A(m,n) = \frac{1}{2}A(m,n-1) - \frac{1}{4}A(m+2,n-1) - \frac{1}{4}A(m-2,n-1) \\ A(m,0) = \pi\delta_{m0} + (\pi/2)\delta_{|m|2} , \end{cases} \tag{4.51}$$

which directly follows from the fact that $2(\sin\varphi)^2 = 1 - \cos(2\varphi)$ and $2\cos(m\varphi)\cos(2\varphi) = \cos((m+2)\varphi) + \cos((m-2)\varphi)$. From this recursion we deduce that $A_{m,n} = 0$ iff n is odd and $\{|A_{m,2k}|\}_{k\in\mathbb{N}}$ is a bounded, monotonically decreasing sequence, so $A_{m,2k} \to 0$ as $k \to \infty$, for all $m \in \mathbb{N}$. So the series in (4.50) is convergent. Unfortunately the series converges slowly in n if $(\rho\sigma\cos\phi)^2 >> 1$. To this end we notice that the relative error

$$\frac{|e^{-v} - \sum_{n=N+1}^{\infty} (-1)^n \frac{v^n}{n!}|}{e^{-v}} \leq \frac{1}{\sqrt{2\pi N}} \quad \text{if } N = \alpha\, v\, e ,$$

where $v = (1/2)(\rho\sigma\sin\varphi)^2(1 - (1/\kappa^2))$ and $\alpha > \beta$, ($\alpha = 4/3$ will do) with $\beta\log\beta = (1/e)$, which follows by Leibnitz theorem [86] and Stirling's formula [86]. This estimate is sharp in the sense that if the cutoff N gets smaller than $\beta\, v\, e$, the relative error quickly explodes. However

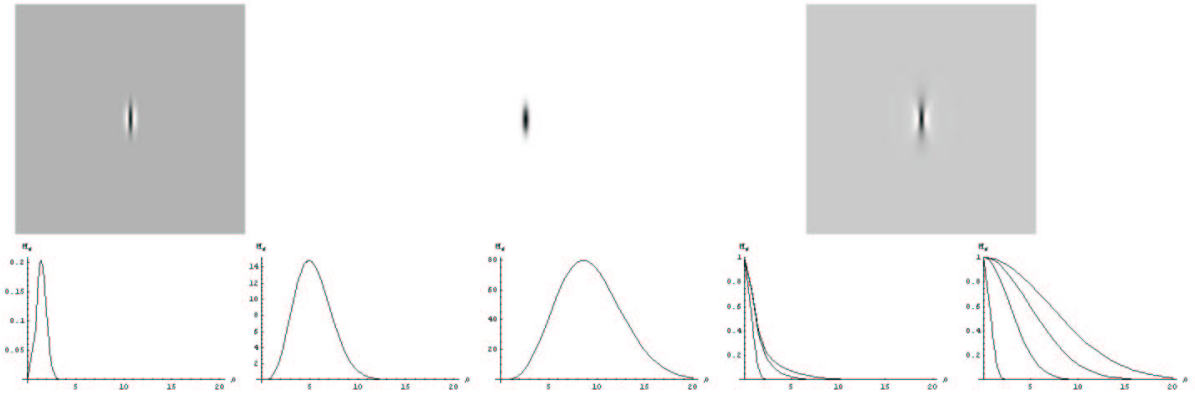

Figure 4.8: Plots of $G^{(2,0)}_{s,\gamma}$, $G_{s,\gamma}$ and $\psi_{\gamma,\beta=1/4}$, for $\gamma = 4$. Grey-values have been plotted to full range for the sake of illustration. Their corresponding functions M_ψ are respectively given by $\rho^4 e^{-\left(\frac{\sigma\rho}{\gamma}\right)^2} \frac{1}{2}\left(I_0(\frac{(\sigma\rho\mu)^2}{2}) + \left(\frac{-1+(\sigma\rho\mu)^2}{(\sigma\rho\mu)^2}\right) I_1(\frac{(\sigma\rho\mu)^2}{2})\right) e^{-\frac{(\sigma\rho\mu)^2}{2}}$, $e^{-\left(\frac{\rho\sigma}{\gamma}\right)^2} e^{-\frac{(\rho\sigma\mu)^2}{2}} I_0\left(\frac{(\rho\sigma\mu)^2}{2}\right)$ and $e^{-\left(\frac{\rho\sigma}{\gamma}\right)^2}$, where $\mu^2 = 1 - \frac{1}{\gamma^2}$ and I_0 and I_1 are modified Bessel functions of the first kind of order 0 resp. 1. They are plotted in the same order in the bottom row for respectively $\kappa = 4, 7, 10$. For $\psi = G^{(2,0)}_{s,\gamma}$, where the range fluctuates over κ, we plotted M_ψ separately for $\kappa = 1, 4, 7$.

an early truncation (say at $m = 16$, so only $m = 2k$, with $k = 0, 1, \ldots, 8$ are involved) of m in expansion (4.50) is harmless.

Instead of using $G^{(2,0)}_{s,\gamma}$ as a (line detector) wavelet we propose the wavelets $\psi_{\gamma,\beta}$ whose Fourier transform is given by

$$\mathcal{F}[\psi_{\gamma,\beta}](\boldsymbol{\omega}) = \cos^2\varphi \; e^{-\frac{1}{2}\frac{(\rho\sigma)^2}{\gamma^2}} \; e^{-\frac{\beta}{2}\sin^2(\phi)\sigma^2\left(1-\frac{1}{\gamma^2}\right)} \; , \beta \in [0, \frac{1}{2}) \; , \tag{4.52}$$

which is locally similar to $G^{(2,0)}_{s,\gamma}$, with the same angular components, but which has the following practical advantages over $G^{(2,0)}_{s,\gamma}$:

1. It has a much better M_ψ, especially for $\kappa > 1$, which allows a well-posed approximative reconstruction.
2. It is a simple steerable filter, in the sense that its expansion in $\{\cos m\varphi\}$ (in the Fourier domain) is simple and can be truncated at low m, ($m = 16$).
3. Its shape is more natural for line detection, since realistic objective elongated structures may have some curvature.

See figure 4.8. In the next subsection we consider a more general approach, but more difficult approach to parameterize proper wavelets.

4.6.2 A General Approach to Parameterization of Proper Wavelet Classes

In this subsection we will not make any assumptions on the wavelet ψ, besides the assumption $\psi \in \mathbb{L}_2(\mathbb{R}^2) \cap \mathbb{L}_2(\mathbb{R}^2)$ and derive ψ and M_ψ explicitly in a Fourier invariant orthonormal base. Some (classes of) proper wavelets pop up in a very natural way and they are essentially different from the ones in the previous section.

Notice that $\mathbb{L}_2(\mathbb{R}^2) = \mathbb{L}_2(S_1) \bigotimes \mathbb{L}_2((0,\infty), r\mathrm{d}r)$. Decompose the angular part $\mathbb{L}_2(S_1)$ into irreducible representations[13]:

$$\mathbb{L}_2(S_1) = \bigoplus_{m\in\mathbb{Z}} \mathcal{D}^{(m)} = \bigoplus_{m\in\mathbb{Z}} \langle Y_m \rangle = \bigoplus_{m\in\mathbb{Z}} \langle \phi \mapsto \frac{e^{-im\phi}}{\sqrt{2\pi}} \rangle$$

Let $\{\gamma_{mn}\}_{n\in\mathbb{N}}$ in $\mathbb{L}_2((0,\infty), r\mathrm{d}r)$ be an orthonormal base for each $m \in \mathbb{Z}$, then $(\gamma_{mn} \otimes Y_m)(r,\phi) = \gamma_{mn}(r)Y_m(\phi)$ is an orthonormal base in $\mathbb{L}_2(\mathbb{R}^2; r\mathrm{d}r)$. As a result we can expand any wavelet $\psi \in \mathbb{L}_2(\mathbb{R}^2)$ in terms of this basis:

$$\begin{aligned} \psi(r,\phi) &= \sum_{m\in\mathbb{Z}} \sum_{n=0}^{\infty} \gamma_{mn}(r)Y_m(\phi)(\gamma_{mn} \otimes Y_m, \psi)_{\mathbb{L}_2(\mathbb{R}^2)} \\ &= \sum_{m\in\mathbb{Z}} \psi_m(r,\phi) = \sum_{m\in\mathbb{Z}} g_m(r)Y_m(\phi) \end{aligned} \tag{4.53}$$

By the Bochner-Hecke Theorem, see Appendix 7.1, the Fourier Transform $\mathcal{F}[\psi]$ of the wavelet $\psi \in \mathbb{L}_2(\mathbb{R}^2)$ is given by

$$\mathcal{F}[\psi](\rho,\varphi) = \sum_{m\in\mathbb{Z}} \tilde{g}_m(\rho)Y_m(\varphi) \ ,$$

with $\tilde{g}_m \in \mathbb{L}_2(\mathbb{R}^2; r\mathrm{d}r)$ given by $\tilde{g}_m(\rho) = \rho^{1/2}\,\mathcal{H}_m[r^{1/2}g_m(r)](\rho)$, where the unitary Hankel Transform $\mathcal{H}_m : \mathbb{L}_2((0,\infty)) \to \mathbb{L}_2((0,\infty))$ is given by (7.1). Given such a wavelet $\psi \in \mathbb{L}_2(\mathbb{R}^d)$, the orientation score U_f can be written

$$U_f(\mathbf{b}, e^{i\theta}) = (\overline{\mathcal{R}_{e^{i\theta}}\check{\psi}} * f)(\mathbf{b}) = (\overline{\mathcal{R}_{e^{i(\theta+\pi)}}\psi} * f)(\mathbf{b}) = \sum_{m\in\mathbb{Z}} (-1)^m \frac{e^{-im\theta}}{\sqrt{2\pi}} (\overline{\psi_m} * f)(\mathbf{b}) \ .$$

If the radial functions do not depend wildly on m, the wavelet will be directed along $\phi = 0$ (and thereby the rotated kernel will be directed along $\phi = \theta$). The real part of the orientation score (constructed by a real valued wavelet which is even around $\phi = 0$) reveals elongated line structures, whereas the imaginary part (constructed by a real valued wavelet which is odd around $\phi = 0$) reveals elongated edge structures.

The angular variance of a wavelet ψ can be quantified by

$$\mathrm{Var}[\phi] = E[\phi^2] - (E[\phi])^2 = E[\phi^2] = \frac{1}{\|\psi\|^2_{\mathbb{L}_2(\mathbb{R}^d)}} \int_{-\pi}^{\pi} \int_{0}^{\infty} \phi^2 |\psi(r,\phi)|^2 \, r\mathrm{d}r\mathrm{d}\phi \ ,$$

in which substitution of (4.53) gives

$$\mathrm{Var}[\phi] = \frac{1}{\|\psi\|^2_{\mathbb{L}_2(\mathbb{R}^d)}} \sum_{m=0}^{\infty} \sum_{m'=0}^{\infty} \frac{(2-\delta_{m0})(2-\delta_{m'0})}{2\pi} (g_m, g_{m'})_{\mathbb{L}_2((0,\infty);r\mathrm{d}r)} \kappa_{mm'} \ , \tag{4.54}$$

[13] The irreducible representations of commutative groups are always defined on 1 dimensional subspaces.

with $\kappa_{mm'} = \int_{-\pi}^{\pi} \phi^2 \cos(m\phi)\ \cos(m'\phi)\,\mathrm{d}\phi$. The angular variance in the Fourier domain is the same as in the spatial domain, i.e. $\mathrm{Var}[\phi] = \mathrm{Var}[\,\overline{\varphi}\,]$, this immediately follows by the fact that $\rho^{-1/2}\mathcal{H}_m r^{1/2}$ is unitary on $\mathbb{L}_2((0,\infty); r\mathrm{dr})$ from which we indeed obtain

$$(\tilde{g}_m, \tilde{g}_{m'})_{\mathbb{L}_2((0,\infty);r\mathrm{dr})} = (\rho^{-1/2}\mathcal{H}_m r^{1/2} g_m, \rho^{-1/2}\mathcal{H}_m r^{1/2} g'_m)_{\mathbb{L}_2((0,\infty);r\mathrm{dr})} = (g_m, g_{m'})_{\mathbb{L}_2((0,\infty);r\mathrm{dr})}\ .$$

This can be easily be generalized to general n-th moments (beyond the above case where $n = 2$) in ϕ. So we conclude that a clearly directed kernel in Fourier domain corresponds to a similarly directed kernel in spatial domain.

The function $M_\psi : \mathbb{R}^2 \to \mathbb{R}$, which by theorem 20 completely determines the well-posedness of $f \leftrightarrow U_f$, is now given by

$$\begin{aligned} M_\psi(\boldsymbol{\omega}) &= \int_{SO(2)} |\mathcal{F}(\mathcal{R}_R\psi)(\boldsymbol{\omega})|^2 \mathrm{dR} \\ &= \sum_{m\in\mathbb{Z}} |\tilde{g}_m(\rho)|^2\ , \qquad \text{with } \rho = \|\boldsymbol{\omega}\|\ . \end{aligned} \tag{4.55}$$

This directly follows by Weyl's orthogonality Theorem for unitary group representations of the compact groups (in this case SO(2)) and changing the order of integration and summation:

$$(Y_m, Y_{m'})_{\mathbb{L}_2(S^1)} = \frac{1}{2\pi}\int_{-\pi}^{\pi} e^{+im\theta} e^{-im'\theta}\,\mathrm{d}\theta = \delta_{m,m'}\ .$$

4.6.2.1 Expansion of ψ and M_ψ in a Fourier Invariant Polar Base

Although equation (4.55) is of rather simple form, it still includes the non-trivial operator $\rho^{-1/2}\mathcal{H}_m r^{1/2}$. This unitary operator on $\mathbb{L}_2((0,\infty)\ ;\ r\,\mathrm{dr})$ has the following complete set of orthonormal eigenfunctions h_n^m, for details see Appendix section 7.1 and figure 4.9,

$$h_n^m(r) = \left(\frac{2\ n!}{(m+n)!}\right)^{1/2} r^m e^{-r^2/2} L_n^{(m)}(r^2), r > 0\ m \geq 0\ , \tag{4.56}$$

For $m < 0$ we *define* $h_n^m = h_n^{|m|}$. Therefore, we expand ψ and expres M_ψ in this angular-irreducible radially Fourierinvariant basis, which are also the eigen functions of the 2D-harmonic oscillator[14]:

$$\begin{aligned} \psi(\mathbf{x}) &= \sum_{m\in\mathbb{Z}}\sum_{n=0}^{\infty} \alpha_m^n\,(Y_m \otimes h_n^m)\,(\phi, r)\ , \\ \mathcal{F}[\psi](\boldsymbol{\omega}) &= \sum_{m\in\mathbb{Z}}\sum_{l=0}^{\infty} (i)^{|m|}(-1)^{n+m}\alpha_m^n\,(Y_m \otimes h_n^m)\,(\varphi, \rho)\ , \\ (\mathcal{R}_{e^{i\theta}}\psi)(\mathbf{x}) &= \sum_{m\in\mathbb{Z}}\sum_{n=0}^{\infty} \alpha_m^n\ e^{+im\theta}\,(Y_m \otimes h_n^m)\,(\phi, r) \\ M_\psi(\boldsymbol{\omega}) &= \sum_{m=-\infty}^{\infty}\left|\sum_{n=0}^{\infty}(-1)^n\alpha_m^n\ h_n^m(\rho))\right|^2 \\ &= \sum_{m=-\infty}^{\infty}\sum_{n=0}^{\infty}\sum_{n'=0}^{\infty}(-1)^{n+n'}\alpha_m^n\overline{\alpha_m^{n'}}h_n^m(\rho)h_{n'}^m(\rho)\ . \end{aligned} \tag{4.57}$$

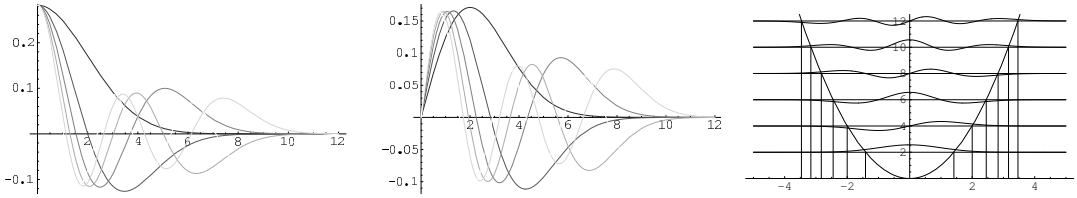

Figure 4.9: Radial basis functions h_n^m, left for $m = 0$ and middle for $m = 1$ and lighter gray for $n = 0, 1, 2, \ldots$. Right, the basis functions are effectively active on $[0, R_{mn})$, where $R_{mn} = \sqrt{2(2n + |m| + 1)}$, as this equals the radius where the total energy $E_{mn} = 2(2n + |m| + 1)$ equals the potential energy given by $V(\mathbf{x}) = r^2$. This is illustrated by joining the graphs of h_n^m, $m = 0, 1$, $n = 0, 1, 2$ together with their corresponding energy levels and the graph of the potential V.

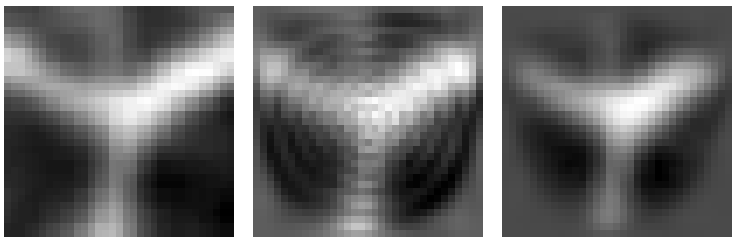

Figure 4.10: Local expansion of a 33×33 pixel patch of an MRI-image showing a bifurcating bloodvessel in the retina. The original image is left, the reconstruction with basis function up to $|m| = 32$ and $n = 12$ is in the middle, and the same reconstruction linearly dampening higher m and n components is depicted on the right.

Considering numerical expansions of local patches of elongated structures in to this basis (in order to see which components are important to detect) we notice that for each $|m|$ a soft (linear) cut-off in n is required, see Figure 4.10.

In the remainder of this section we will construct wavelets ψ_{N_1,N_2}, with coefficients $\alpha_m^n = 0$, for $|m| > N_1$ and $n > N_2$, for fixed N_1, $N_2 \in \mathbb{N}$, i.e.

$$\psi_{N_1,N_2} = \sum_{m=-N_1}^{N_1} \sum_{n=0}^{N_2} \alpha_m^n \, Y_m \otimes h_n^m$$

such that

$$M_{\psi_N}(\boldsymbol{\omega}) = \mathcal{M}_N(\rho^2), \quad \text{with } N = N_1 + 2N_2 \, , \rho = \|\boldsymbol{\omega}\| \tag{4.58}$$

where we recall that $\mathcal{M}_N(\rho^2)$ is given by (4.41). We consider (4.58) as an equation in variable ψ, determined by its coefficients $\{\boldsymbol{\alpha}_m\}_{|m|=0}^{N_1} = \{\{\alpha_m^n\}_{n=0}^{N_2}\}_{|m|=0}^{N_1}$ and thereby we obtain $M_{\psi_N}(\boldsymbol{\omega}) = \mathcal{M}_N(\rho^2)$ for almost every $\rho = \|\boldsymbol{\omega}\| > 0$, if and only if

$$\begin{aligned} &\sum_{|m|=0}^{N_1} \sum_{n=0}^{N_2} \sum_{n'=0}^{N_2} (-1)^{n+n'} \sqrt{\tfrac{2n!}{(n+|m|)!}} \sqrt{\tfrac{2n'!}{(n'+|m|)!}} \, \rho^{2|m|} \, L_n^{(m)}(\rho^2) L_{n'}^{(m)}(\rho^2) = \sum_{q=0}^{N} \tfrac{\rho^{2q}}{q!} \\ &\sum_{k=0}^{2N_2} \sum_{|m|=0}^{N_1} \boldsymbol{\alpha}_m^\dagger A_k^m \boldsymbol{\alpha}_m \, \rho^{2(k+|m|)} = \sum_{q=0}^{N} \tfrac{\rho^{2q}}{q!} \, , \end{aligned} \tag{4.59}$$

[14]The self-adjoint operators $\mathcal{F}$, $\mathcal{R}_R$ and the harmonic oscillator $\Delta - \|\mathbf{x}\|^2$ commute and thereby they have a common base of eigen functions which is indeed given by $Y_m \otimes h_n^m$.

where the $(N_2{+}1){\times}(N_2{+}1)$ positive symmetric matrices A_k^m are given by $[A_k^m]_{n'}^n = \sum_{j=0}^{k} (\mathbf{a}_j^m)_n \, (\mathbf{a}_{(k-j)}^m)_{n'}$, with

$$(\mathbf{a}_k^m)_n = \begin{cases} (-1)^n \sqrt{\frac{2(n!)}{(n+|m|)!}} d_k^{m,n} = (-1)^{n+k} \sqrt{\frac{2(n!)}{(n+|m|)!}} \frac{1}{k!} \binom{n+|m|}{n-k} \text{ if } k \leq n \ , \\ 0 \text{ else} \ , \end{cases}$$

where $d_k^{m,n} = \frac{(-1)^k}{k!} \binom{n+|m|}{n-k}$ equals the coefficient of ρ^{2k} in $L_n^{(|m|)}(\rho^2)$, cf. [2].

Now in the left hand side of (4.58) we introduce the summation index $q = |m| + k$ and assume $\boldsymbol{\alpha}_{-m} = \boldsymbol{\alpha}_m \in \mathbb{R}^{N_2+1}$ for all m, (i.e. the wavelet is symmetric around its direction) then we obtain

$$\begin{aligned} &\sum_{q=0}^{N} \sum_{k=\max\{0,q-N_1\}}^{2N_2} \boldsymbol{\alpha}_m^T A_k^{q-k} \boldsymbol{\alpha}_{q-k} \, \rho^{2q} = \sum_{q=0}^{N} \frac{\rho^{2q}}{q!} \qquad \Leftrightarrow \\ &\sum_{k=\max\{0,q-N_1\}}^{2N_2} \boldsymbol{\alpha}_{q-k}^T A_k^{q-k} \boldsymbol{\alpha}_{q-k} \, \rho^{2q} = \tfrac{1}{q!} \ , \text{ for } q = 0, \ldots, N \ , \end{aligned}$$

which are $N + 1 = N_1 + 2N_2 + 1$ equations for $(N_1 + 1)(N_2 + 1)$ variables $\{\boldsymbol{\alpha}_m\}_{m=0}^{N_1}$.

Example: The special case $\alpha_m^n = \alpha^m \delta_{n0}$

In this case $N = N_1$, $N_2 = 0$ and $A_0^q = \frac{1}{q!}$. The function M_ψ equals $\mathcal{M}_N$, recall (4.41),

$$M_\psi(\boldsymbol{\omega}) = \sum_{m=0}^{N} |\alpha^m|^2 (h_n^m(\rho))^2 = \mathcal{M}_N(\rho^2) \ , \rho = \|\boldsymbol{\omega}\| \ , \tag{4.60}$$

The (up to phase factors unique) solution ψ_N^0 of (4.58) is now given by ($\alpha_m = 1$ for all m)

$$\begin{aligned} \psi_N^0(\mathbf{x}) &= \sum_{m=0}^{N} \tfrac{1}{\sqrt{m!}} \rho^m e^{-\frac{\rho^2}{2}} \tfrac{e^{-im\phi}}{\sqrt{2\pi}} = \tfrac{1}{\sqrt{2\pi}} \sum_{m=0}^{N} \tfrac{(\overline{z})^m}{\sqrt{m!}} e^{-\frac{|z|^2}{2}} \\ &= \tfrac{1}{\sqrt{2\pi}} \sum_{m=0}^{N} (-\tfrac{1}{2})^m \tfrac{\left(\frac{\partial}{\partial z}\right)^m}{\sqrt{m!}} e^{-\frac{|z|^2}{2}} \qquad z = re^{i\phi} \ . \end{aligned} \tag{4.61}$$

This series converges uniformly on compacta, but not in $\mathbb{L}_2$-sense. The real part of this wavelet corresponds to the wavelet first proposed by Kalitzin cf.[79] as a line detector in medical images. The imaginary part is a good edge detector. For plots of the graph of wavelet ψ_N for several values of N, see figure 4.11. For more plots and a comparison of the corresponding M_ψ function to the M_ψ function of another wavelet used in practice (not designed for stable reconstruction) see Figure 4.13. The wavelets ψ_N^0 have minimal uncertainty in spatial and frequency domain, see Appendix 7.5 in the sense that the general uncertainty relation

$$\int_{\mathbb{R}^2} \|\mathbf{x}\|^2 \frac{|\psi_N^0|^2}{\|\psi_N^0\|^2_{\mathbb{L}_2(\mathbb{R}^2)}} \, \mathrm{d}\mathbf{x} \int_{\mathbb{R}^2} \|\boldsymbol{\omega}\|^2 \frac{|\mathcal{F}\psi_N^0(\boldsymbol{\omega})|^2}{\|\mathcal{F}(\psi_N^0)\|^2_{\mathbb{L}_2(\mathbb{R}^2)}} \, \mathrm{d}\boldsymbol{\omega} \geq \frac{1}{4} \quad \text{for all } \mathrm{N} \in \mathbb{N}$$

holds with equality. The basis functions $z \mapsto \frac{z^m}{\sqrt{m!}} e^{-\frac{|z|^2}{2}}$, are 2D-minimal uncertainty states with $E(\boldsymbol{\omega}) = 0$ analogue to the Gabor filters in 1D-signal analysis. The general reproducing

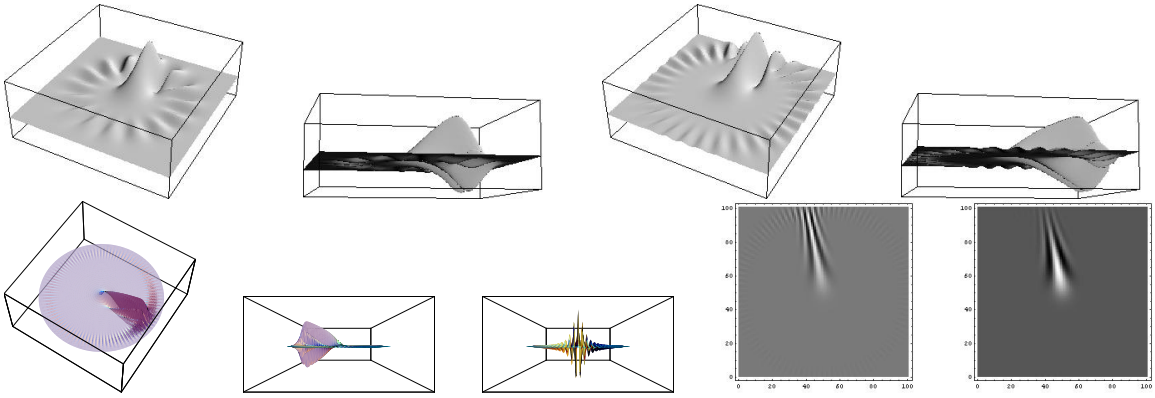

Figure 4.11: Top row: Left: 2 different viewpoint Plots of graphs $\psi^0_{N=15}$, Right: 2 different viewpoint Plots of graphs $\psi^0_{N=30}$. Bottom row: Left: 3 Plots of graph $\Re(\psi^0_{N=100})$. Right: 100×100-pixel grey-value plots of $\Re(\psi^0_{N=100})$ and Gaussian blurred (with $\sigma = 0.8$ pixels). Notice that the kernel becomes sharper and the wiggle-ring vanishes as N increases. The locally highly oscillatory behavior within $\Re(\psi^0_{N=100})$ which may seem akward, is not really harmful since it disappears immediately by convolution with Gaussian kernel with tiny scale, also see (4.62).

kernel (4.20) is now given by

$$\begin{aligned} K(g,g') &= 2\pi\mathcal{F}[\boldsymbol{\omega}\mapsto \sum_{m=0}^{N}\sum_{m'=0}^{N} e^{im'\theta'-im\theta}(i)^{m'-m}\frac{w^m}{\sqrt{m!}}\frac{\overline{w}^{m'}}{\sqrt{m'!}}e^{-|w|^2}](\mathbf{b}-\mathbf{b}') \\ &= 2\pi\sum_{m=0}^{N}\sum_{m'=0}^{N} e^{i(m'\theta'-m\theta)}\frac{(-1)^m}{2^{m+m'}\sqrt{m!}\sqrt{m'!}}\overline{\beta}^{m'}\beta^m e^{-\frac{|\beta|^2}{4}} \ , \end{aligned}$$

with $g=(\mathbf{b},e^{i\theta}), g'=(\mathbf{b}',e^{i\theta'})$, $\beta = b'_1-b_1+i(b'_2-b_2)$ and $\mathbf{b}=(b_1,b_2)^T$.

Practical Aspects:
The cutoff index N has a practical upper bound because of sampling. If N increases the reconstruction will become better, but if we choose N to large the wavelet behaves badly along $\phi = 0$, see Figure 4.12 and Appendix section 7.3.

We stress that ψ^0_N is essentially different than the proper wavelets constructed in the previous subsection: The wavelet ψ^0_N is clearly not an approximation of the identity as $N\to\infty$, whereas the wavelets constructed in the previous section are approximations of the identity as $\varrho\to\infty$. Therefore the simple approximative reconstruction from an orientation score U_f constructed by ψ^0_N to image f, by integration over the angles only, see (4.45), is not possible. So, we must use the exact inverse given by (4.34) or (4.40) as a close approximative reconstruction, where we notice that $\tilde{\psi}^N_0$ in contrast to ψ^N_0 is an approximation of the identity.

The size of the wavelet ψ^N_0 can be controlled by dilation, $\mathbf{x}\mapsto(\mathcal{D}_\sigma\psi^N_0)(\mathbf{x}) = \frac{1}{\sqrt{\sigma}}\psi^N_0(\mathbf{x}/\sigma)$. This does effect $\mathcal{M}_\psi$, since $\mathcal{D}_\sigma\mathcal{F}=\mathcal{D}_{1/\sigma}\mathcal{F}$, but, for N sufficiently large, the stability remains guaranteed. Moreover, for large N, the wavelet can be smoothed by convolving the wavelet with a relatively small Gaussian kernel:

$$\psi^0_{N,s}(\mathbf{x}) = (G_s * \psi^0_N)(\mathbf{x}) = e^{-(1/2)\left|\frac{z}{\varrho}\right|^2\beta(\varrho,s)}(\mathcal{D}_{\alpha(\varrho,s)}\psi^0_N)(z) \ , z=x+iy \tag{4.62}$$

where $\alpha(\varrho,s) = 1+\frac{s}{\varrho^2}\approx 1$ and $\beta(\varrho,s)=\frac{1}{\frac{\varrho^2}{s}+2+\frac{s}{\varrho^2}} = O\left(\frac{s}{\varrho^2}\right)$ and $\frac{s}{\varrho^2} << 1$. It is easily verified

that $\psi \mapsto G_s * \psi$ implies $\tilde{\psi} \mapsto G_{2s} * \tilde{\psi}$, so as long as the scale s is relatively small, the Gaussian convolution of the wavelet is harmless for the stability of the (re)construction.

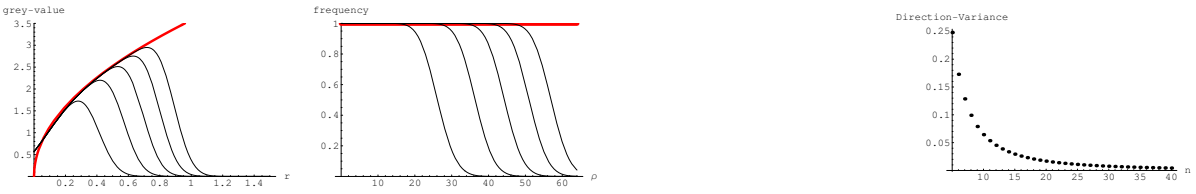

Figure 4.12: Left: The graphs of the kernel $\psi_N^0(\mathbf{x})$ cut off at $N = 10, 20, 30, 40, 50$ with $\sigma = 1/8$, restricted to its main direction $\phi = 0$. Notice that the peaks move out as m increases. Notice that the asymptotic formula derived for $\psi_\infty^0(r, \phi = 0) = (8\pi)^{1/4}\sqrt{r}(1 - \frac{1}{16r^2} + O\left(\frac{1}{r^4}\right)) = (8\pi)^{1/4}\sqrt{r} + O\left(r^{-\frac{3}{2}}\right)$ see Appendix 7.3, is a very good approximation (we included the graph of $r \mapsto (8\pi)^{1/4}\sqrt{r}$). Middle: The corresponding functions $\mathcal{M}_{\psi_N^0} = \mathcal{M}_N$ which indeed approximate 1 as $N \to \infty$. Right: Angular variance of ψ_N^0 plotted as a function in N.

Other Examples: See Appendix section 7.4 .

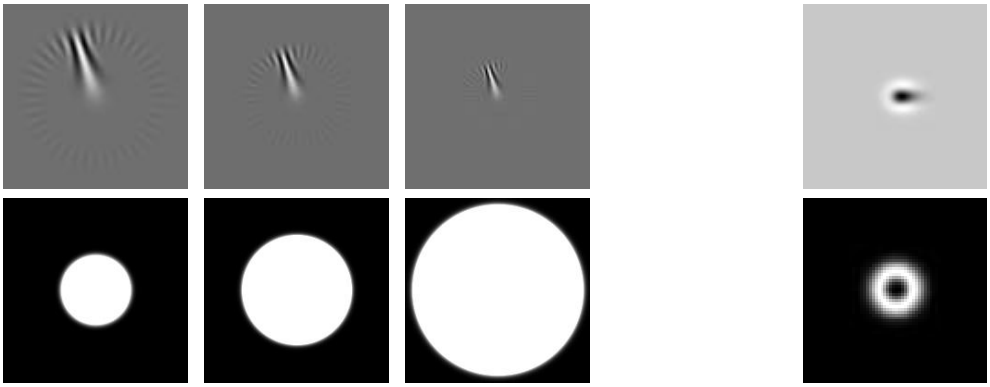

Figure 4.13: Top row: left three images; Example of line detector-wavelets ψ in practice (discrete impuls response at $\theta = (13/20)\pi$) at different scales. For the sake of illustration the plots of the kernels are zoomed in by a factor of 2. ; Right image Example of kernel developed for catheter endpoint detection. Bottom row: The corresponding functions M_ψ. Notice that the line detectors have better M_ψ and thereby induce a more stable exact reconstruction than the catheter endpoint detector (most right image).

4.7 Orientation Scores on 3D images

In this section we generalize our results on the construction of and reconstruction from orientation scores of 3D-images $f \in \mathbb{L}_2^\varrho(\mathbb{R}^3)$. Although some generalizations are straightforward, there arise some difficulties that did not arise in the 2D case. First of all $SO(3)$ is not commutative, so the $SO(3)$-irreducible representations are not one dimensional. Secondly, in practice one is mainly interested in constructing orientation scores by "sigar-shaped" wavelets, i.e. wavelets that are invariant under the stabilizer of the north pole, which brings us to the 2-sphere $S^2 = \frac{SO(3)}{SO(2)}$. Thirdly, it is not obvious which discrete subgroup of $SO(3)$ to take and thereby the question arises how to store the orientation score, since an equidistant sampling in spherical coordinates does not make sense.

Let $f \in \mathbb{L}_2^\varrho(\mathbb{R}^3)$ be a bandlimited 3D image, then we define its wavelet transform $\mathcal{W}_\psi[f] \in \mathbb{C}_K^G$ by

$$\mathcal{W}_\psi[f](g) = \int_{\mathbb{R}^3} \overline{\psi(R^{-1}(\mathbf{x}-\mathbf{b}))} f(\mathbf{x}) \mathrm{d}\mathbf{x} \ , g = (\mathbf{b}, R) \in G = \mathbb{R}^3 \rtimes SO(3) \ .$$

We restrict ourselves to the case where the wavelet ψ is invariant under under the stabilizer of the north-pole $\mathbf{e}_z$, which is the subgroup of $SO(3)$ consisting of all rotations around the z-axis. So we assume

$$\psi(R\mathbf{x}) = \psi(\mathbf{x}) \ , \text{ for all } R \in \mathrm{Stab}(\mathbf{e}_z) \ . \tag{4.63}$$

On $SO(3)$ we define the following equivalence relation:

$$R_1 \sim R_2 \Leftrightarrow (R_2)^{-1} R_1 \in \mathrm{Stab}(\mathbf{e}_z) \equiv SO(2) \ .$$

The equivalence classes are the left cosets $[R] = R\,\mathrm{Stab}(\mathbf{e}_z)$, $R \in SO(3)$. The partition of all equivalence classes will be denoted by $SO(3)/SO(2)$, which is isomorphic to S^2 and thereby not a group. Rather than using the canonical parameterization given by

$$R_{a,\phi}(\mathbf{x}) = (\cos\phi)\mathbf{x} + (1-\cos\phi)(\mathbf{a},\mathbf{x})\mathbf{a} + \sin\phi(\mathbf{a}\times\mathbf{x}) \ , \mathbf{x}, \mathbf{a} \in \mathbb{R}^3, \phi \in [0, 2\pi) \tag{4.64}$$

of $SO(3)$ we will use the well-known Euler angle parameterization $Y : B_{\mathbf{0},2\pi} \to SO(3)$:

$$Y(\mathbf{x}) = R_{\mathbf{e}_z,\gamma} R_{\mathbf{e}_y,\beta} R_{\mathbf{e}_z,\alpha} \ , \qquad \mathbf{x} = (\alpha \cos\gamma \sin\beta, \alpha \sin\gamma \sin\beta, \alpha \cos\beta)^T \ , \tag{4.65}$$

which gives us directly an explicit isomorphism between S^2 and $\frac{SO(3)}{SO(2)}$:

$$S^2 \ni \mathbf{n}(\beta,\gamma) = (\cos\gamma \sin\beta, \sin\gamma \sin\beta, \cos\beta)^T \leftrightarrow [R_{\mathbf{e}_z,\gamma} R_{\mathbf{e}_y,\beta}] \in \frac{SO(3)}{SO(2)}.$$

Because of our assumption (4.63) we can define the orientation score $U_f : \mathbb{R}^3 \times S^2 \to \mathbb{C}$ corresponding to image $f \in \mathbb{L}_2(\mathbb{R}^3)$ by means of

$$U_f(\mathbf{b}, \mathbf{n}(\beta,\gamma)) = \mathcal{W}_\psi[f](\mathbf{b}, R_{\mathbf{e}_z,\gamma} R_{\mathbf{e}_y,\beta}).$$

4.7.1 A Simple Approach for Constructing 3D Proper Wavelets

To generalize the idea of constructing proper wavelets by means of suitable decompositions of the unity as illustrated in Example 1 in section 4.6.1 to the 3D case, we must discretize S^2 in disjoint and equal pieces.

Consider an icosahedron I, which is the platonic solid with the largest[15] amount of faces $F = 20$. It is dual to the dodecahedron and has $V = 12$ vertices and $E = V + F - 2 = 30$ edges. Let SI be the discrete subgroup of $SO(3)$ consisting only of rotations that keep I invariant. Let $\mathbf{v}$ be a vertex of I, then $|SI * \mathbf{v}| = 12$ as SI acts transitively on I. Moreover, $\mathrm{Stab}_{SI}(\mathbf{v}) = \{R_{\mathbf{v},\beta_i} : \beta_k = \frac{2k\pi}{5}, k = 0, 1, \ldots, 4\}$, so we have $|SI| = |\mathrm{Stab}_{SI}(\mathbf{v})||SI * \mathbf{v}| = 5 * 12 = 60$. So all elements of SI are given by:

- The 24 non-trivial rotations by $\frac{2\pi k}{5}$, $k = 1, \ldots, 4$ about the line passing through a vertex and its opposite.
- The 20 non-trivial rotations by $\frac{2\pi k}{3}$, $k = 1, 2$ about the line passing through the center $\mathbf{c}_j$, $j = 1, \ldots, 12$ of a face and its opposite.
- The 15 non-trivial rotations by π about the line passing through the origin and the center of an edge.
- The identity.

Recall that by our assumption (4.63) we are more interested in a discretization of the two sphere $S^2 = \frac{SO(3)}{SO(2)}$ than in a discrete subgroup of $SO(3)$. Rather than taking all rotation axis of all elements in SI we consider all (normalized) center points $\tilde{\mathbf{c}}_i, i = 1, \ldots, 12 * 2^q$ of the triangles $\{P_{i_1}, P_{i_2}, P_{i_3}\}$ in a q-th order (in our example $q = 2$) regular tessellation of each face, which are more uniformly distributed over a sphere. For every $i \in \{1, \ldots, n\}$, we define V_i as the unique

[15] The platonic solids are the tetrahedron, cube, octahedron, dodecahedron and icosahedron. Notice to this end that in a convex regular solid in $\mathbb{R}^3$ with regular n-gon faces, we have $r(n-2)\pi/n < 2\pi$, where r is the amount of faces meeting at every vertex.

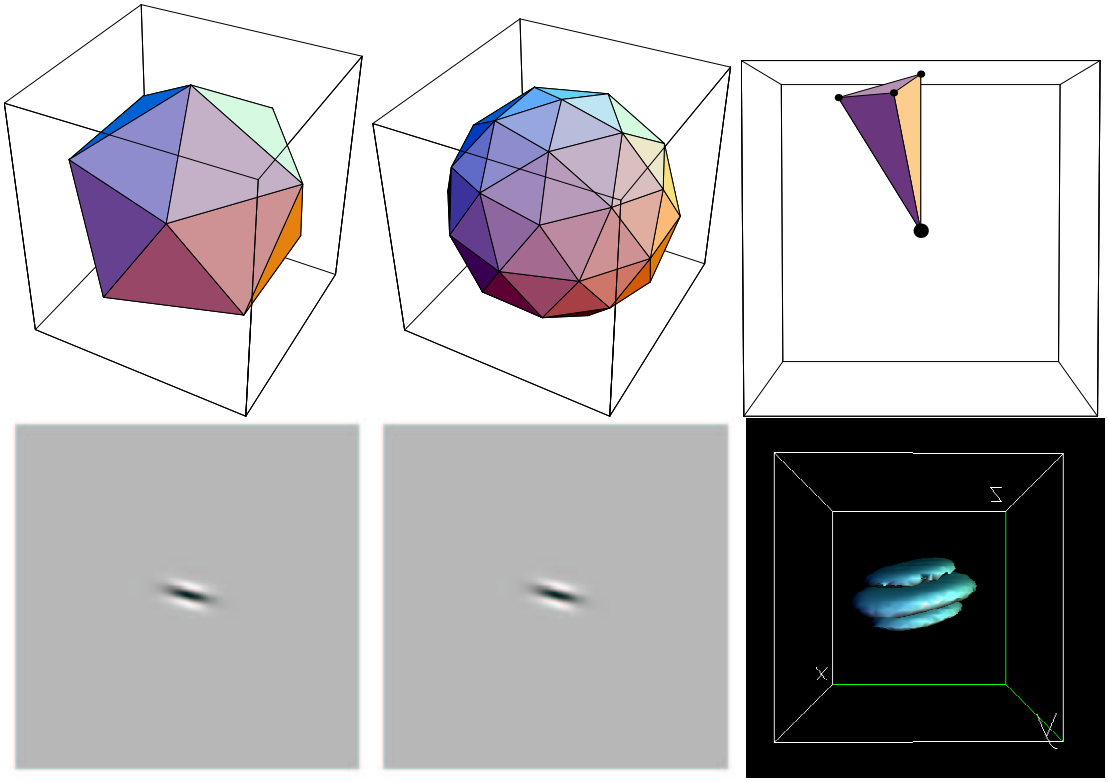

Figure 4.14: Top row: Icosahedron, spherical projection of second order tessellated icosahedron, volume V_i. Bottom row: density plots through XOZ-plane and YOZ-plane of the wavelet $\psi_i : \mathbb{R}^3 \to \mathbb{R}$ (ψ_i sampled at $128 \times 128 \times 128$ pixels, $s = (1/2)\sigma^2 = 6$, $2 * \varrho = 80$ pixels) given by (4.66), joint contour plot of iso-surphaces $\psi_i(\mathbf{x}) = +0.02$ and $\psi_i(\mathbf{x}) = -0.02$.

finite volume bounded by the polygons $\{O, P_{i_1}, P_{i_2}\}, \{O, P_{i_1}, P_{i_3}\}$ and $\{O, P_{i_2}, P_{i_3}\}$ and the unit sphere. Notice that the unit ball is the disjoint union of these volumes, so $\sum_{i=1}^{12*2^q} 1_{V_i} = 1_{B_{\mathbf{0},1}}$. We now define the smooth wavelets

$$\psi_i^{\varrho} = \mathcal{F}^{-1}[\boldsymbol{\omega} \mapsto (G_s * 1_{V_i})(\frac{1}{\varrho}\boldsymbol{\omega})] \ , \varrho > 0, s > 0, \tag{4.66}$$

which typically detect 2D-ridges/planes, see figure 4.14. They allow a stable (re)construction as $\mathcal{M}_\psi \simeq 1_{B_{\mathbf{0},1}}$ and a good approximative reconstruction

$$f(\mathbf{b}) \approx \sum_{i=1}^{12*2^q} U_f(\mathbf{b}, \tilde{\mathbf{c}}_i) \ ,$$

since we have $\sum_{i=1}^{12*2^q} \mathcal{F}[\psi_i^{\varrho}](\boldsymbol{\omega}) = (G_s * 1_{B_{\mathbf{0},\varrho}})(\boldsymbol{\omega})$, for all $\boldsymbol{\omega} \in \mathbb{R}^2$. Notice that for s sufficiently large the iso-surfaces of $G_s * V_i$ gets close to a circular cone, which implies that ψ_i is nearly symmetric around the z-axis, i.e. nearly satisfies (4.63). Clearly, the wavelet ψ_i is the 3D-analogue to the 2D wavelet in Example 1 in section 4.6.1. However, if one wants to obtain a line detector in $\mathbb{R}^3$, one must make a decomposition of the unit ball in the Fourier domain with planar structures rather than line-like structures.

4.7.2 General Approach of Constructing 3D proper wavelets

Notice that $\mathbb{L}_2(\mathbb{R}^3) = \mathbb{L}_2(S_2) \bigotimes \mathbb{L}_2((0,\infty), r^2 \mathrm{dr})$. Decompose the angular part $\mathbb{L}_2(S_2)$ into irreducible representations:

$$\mathbb{L}_2(S_2) = \bigoplus_{l \in \mathbb{N} \cup \{0\}} \mathcal{D}^{(l)} = \bigoplus_{l \in \mathbb{N} \cup \{0\}} \langle (\theta,\phi) \mapsto Y_l^m(\theta,\phi) \rangle_{m=-l,\ldots,l} \ ,$$

where the 3D spherical harmonics are $Y_l^m \in \mathbb{L}_2(S^2)$ are given by

$$Y_l^m(\theta,\phi) = (-1)^{m/2+|m/2|} \sqrt{\frac{(2l+1)(l-|m|)!}{4\pi(l+|m|)!}} P_l^m(\cos\theta) e^{im\phi} \qquad l \in \mathbb{N} \ , m = -l, \ldots, l. \quad (4.67)$$

The orthonormal base $Y_l^m \otimes g_n^l$, for definition g_n^l see (7.5) in Appendix 7.1, is Fourier invariant, see (7.6), so we have

$$\begin{aligned} \psi &= \sum_{n=0}^{\infty} \sum_{l=0}^{\infty} \sum_{m=-l}^{l} \alpha_{ml}^n \, Y_l^m \otimes g_n^l \ , \\ \mathcal{F}[\psi] &= \sum_{n=0}^{\infty} \sum_{l=0}^{\infty} \sum_{m=-l}^{l} \alpha_{ml}^n i^l (-1)^{n+l} \, Y_l^m \otimes g_n^l \ , \\ \mathcal{F}[\psi](R^{-1}\boldsymbol{\omega}) &= \sum_{n=0}^{\infty} \sum_{l=0}^{\infty} \sum_{m=-l}^{l} \sum_{m'=-l}^{l} \alpha_{ml}^n i^l (-1)^{n+l} \left(\mathcal{D}^{(l)}(R)\right)_{m'}^{m} \, Y_l^{m'} \otimes g_n^l \ , \end{aligned}$$

with $\alpha_{ml}^n = (\psi, Y_l^m \otimes g_n^l)_{\mathbb{L}_2(\mathbb{R}^3)}$.

Recall that M_ψ was given by (4.28), so for the $SO(3)$-case we have

$$M_\psi(\boldsymbol{\omega}) = \int_{SO(3)} |\mathcal{F}[\psi](R^{-1}\boldsymbol{\omega})|^2 \, \mathrm{dR}.$$

It then follows from Weyl's Theorem for compact groups (applied to the case $SO(3)$):

$$\int_{SO(3)} \overline{(\mathcal{D}^{(l)}(R))_{m'}^{m}} \, (\mathcal{D}^{(\tilde{l})}(R))_{\tilde{m}'}^{\tilde{m}} \, dR = \frac{1}{2l+1} \delta^{l\tilde{l}} \delta^{m\tilde{m}} \delta_{m'\tilde{m}'} \ \ 8\pi^2 \ .$$

and changing the order of integration and summation (Fubini) that

$$\mathcal{M}_\psi(\boldsymbol{\omega}) = 4\pi \sum_{n=0}^{\infty} \sum_{\tilde{n}=0}^{\infty} \sum_{l=0}^{\infty} \sum_{m=-l}^{l} \sum_{m'=-l}^{l} \frac{\overline{\alpha_{ml}^{\tilde{n}}} \alpha_{ml}^n}{2l+1} (-1)^{n+\tilde{n}} |Y_l^{m'}(\overline{\theta},\overline{\phi})|^2 g_n^l(\rho) g_{\tilde{n}}^l(\rho) \ , \quad (4.68)$$

now it follows by the fact that

$$\sum_{m=-l}^{l} |Y_l^m(\theta,\phi)|^2 = \frac{(2l+1)}{4\pi} \ ,$$

that (4.68) can be simplified to

$$\mathcal{M}_\psi(\boldsymbol{\omega}) = \sum_{n=0}^{\infty} \sum_{\tilde{n}=0}^{\infty} \sum_{l=0}^{\infty} \sum_{m=-l}^{l} \overline{\alpha_{ml}^{\tilde{n}}} \alpha_{ml}^n (-1)^{n+\tilde{n}} g_n^l(\rho) g_{\tilde{n}}^l(\rho).$$

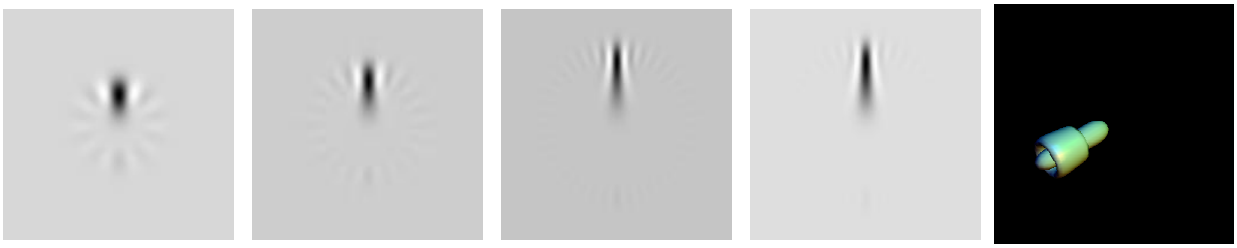

Figure 4.15: The wavelet $\psi_N^{0,3\mathrm{D}}$ given by (4.72). From left to right, plots of $\psi_N^{0,3\mathrm{D}}(x,0,z)$, for $N = 10, 20, 40$ and $G_s * \psi_{N=40}^{0,3\mathrm{D}}(x,0,z)$, for tiny scale s and finally a joined 3D plot of the iso-intensity contours of the rotated 3D kernel $\psi_i((R_{\mathbf{e}_z,\phi}R_{\mathbf{e}_x,\theta})^{-1}\mathbf{x}) = 0.5, -0.5$, ($\phi \approx -\frac{\pi}{4}$ and $\theta \approx \frac{3\pi}{4}$).

The only spherical harmonics Y_l^m which are invariant under $\mathrm{Stab}(\mathbf{e}_z)$ are the ones with $m = 0$, since $\mathcal{R}_{R_{\mathbf{e}_z,\beta}} Y_l^m = e^{\beta(\mathbf{e}_z \times \nabla)} Y_l^m = e^{\beta m i} Y_l^m$, so under the assumption (4.63) the expansion of ψ simplifies to

$$\begin{aligned} \psi(\mathbf{x}) &= \sum_{n=0}^{\infty}\sum_{l=0}^{\infty} \alpha_l^n g_n^l(r)\, Y_l^0(\theta,\phi)\ , \text{ where } \alpha_l^n = \alpha_{0l}^n, \\ \psi((R_{\mathbf{e}_z,\gamma}R_{\mathbf{e}_y,\beta})^{-1}\mathbf{x}) &= \sum_{n=0}^{\infty}\sum_{l=0}^{\infty}\sum_{m'=-l}^{l} \alpha_l^n \left[\mathcal{D}^{(l)}(R_{\mathbf{e}_z,\gamma}R_{\mathbf{e}_y,\beta})\right]_{m'}^{0} g_n^l(r)\, Y_l^{m'}(\theta,\phi)\ , \\ \mathcal{F}[\psi](\boldsymbol{\omega}) &= \sum_{n=0}^{\infty}\sum_{l=0}^{\infty} \alpha_l^n (-1)^{n+l} (i)^l g_n^l(\rho)\, Y_l^0(\vartheta,\varphi)\ , \end{aligned} \tag{4.69}$$

for almost every $\mathbf{x} \in \mathbb{R}^3$ and $\boldsymbol{\omega} \in \mathbb{R}^3$, where we notice that

$$\begin{aligned} \left[\mathcal{D}^{(l)}(R_{\mathbf{e}_z,\gamma}R_{\mathbf{e}_y,\beta})\right]_{m'}^{0} &= e^{-im'\gamma} \sum_{k=\max\{m',0\}}^{\min\{l,l+m'\}} \frac{(-1)^k (\cos\frac{\beta}{2})^{2l-2k+m'} (\sin\frac{\beta}{2})^{2k-m'}}{k!(l-k)!(l+m'-k)!(k-m')!} \\ &= \frac{(-1)^{m'} Y_l^{m'}(\beta,\gamma)}{\sqrt{\frac{(2l+1)}{4\pi}}}. \end{aligned} \tag{4.70}$$

The expansion of M_ψ now simplifies to

$$\mathcal{M}_\psi(\boldsymbol{\omega}) = \sum_{l=0}^{\infty}\sum_{n=0}^{\infty}\sum_{\tilde{n}=0}^{\infty} (-1)^{n+\tilde{n}} \overline{\alpha_l^n} \alpha_l^{\tilde{n}} g_n^l(\rho) g_{\tilde{n}}^l(\rho)\ , \text{ for all } \boldsymbol{\omega} \in \mathbb{R}^3\ . \tag{4.71}$$

which is the direct equivalent to the fourth equality of (4.57)! Again we consider the case $\alpha_l^n = \alpha_l \delta^{n0}$, and $\mathcal{M}_\psi(\boldsymbol{\omega})$ given by (4.41), then it follows by $(g_0^l(\varrho))^2 = \frac{1}{\Gamma(l+3/2)} e^{-\rho^2} \rho^{2l}$ and Taylor expansion of e^{ρ^2}, we find the solutions $|\alpha_l| = \sqrt{\frac{\Gamma(l+3/2)}{\Gamma(l+1)}}$. In particular $\alpha_l = \sqrt{\frac{\Gamma(l+3/2)}{\Gamma(l+1)}}$ gives the wavelet

$$\psi_N^{0,3\mathrm{D}}(\mathbf{x}) = \sum_{l=0}^{N} \frac{1}{\sqrt{l!}} r^l e^{-\frac{r^2}{2}} Y_l^0(\theta,\phi)\ , \tag{4.72}$$

where $Y_l^0(\theta,\phi) = P_l^0(\cos\theta)\sqrt{\frac{2l+1}{4\pi}}$, is independent of ϕ. So we found the 3D-analogue of the 2D-line detecting wavelet (4.61), compare Figure 4.15 to Figure 4.12 and Figure 4.13. We stress the practical advantage of the steerability property of our basis functions (4.69) for computing the orientation score:

$$\begin{aligned} U_f(\mathbf{b}, \mathbf{n}(\beta,\gamma)) &= (\mathcal{R}_{\gamma,\beta}\psi, \mathcal{T}_{\mathbf{b}} f)_{\mathbb{L}_2(\mathbb{R}^3)} \\ &= \sum_{n=0}^{\infty}\sum_{l=0}^{\infty}\sum_{m'=-l}^{l} \alpha_l^n \left[\mathcal{D}^{(l)}(R_{\mathbf{e}_z,\gamma}R_{\mathbf{e}_y,\beta})\right]_{m'}^{0} (g_n^l \otimes Y_l^{m'}, \mathcal{T}_{\mathbf{b}} f)_{\mathbb{L}_2(\mathbb{R}^3)}\ , \end{aligned} \tag{4.73}$$

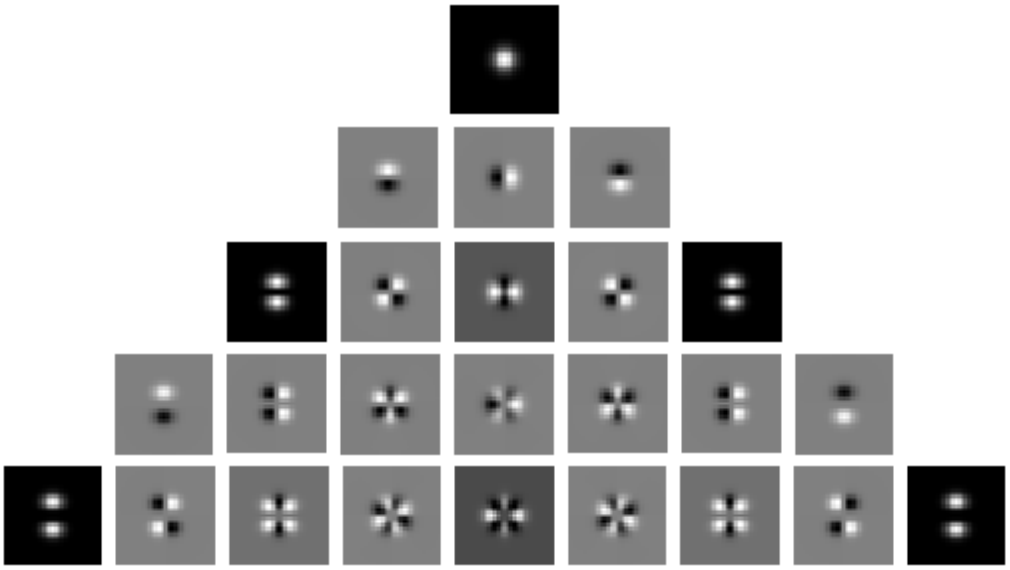

Figure 4.16: 2D density plots of the restrictions of the steerable basis functions $g_n^l \otimes Y_l^{m'}$, $l = 0, 1, 2, 3, 4$, $m = -l, l$, restricted to the plane $\theta = \frac{\pi}{2}$. These steerable basis functions allow us to rotate the wavelet (and thereby compute the score U_f, see (4.73)) in an exact manner by (4.69), which is a clear advantage over the numerical rotations using interpolation.

which is of course useful, since once coefficients $(g_n^l \otimes Y_l^{m'}, \mathcal{T}_{\mathbf{b}} f)_{\mathbb{L}_2(\mathbb{R}^3)}$ are computed it is easy to compute $U_f(\mathbf{b}, \mathbf{n}(\beta, \gamma))$ for a large amount of angles γ, β. For elongated structure detection via 3D orientation scores see Figures 4.17, 4.18, 4.19.

Another practical advantage of the decomposition in spherical harmonics is that it becomes fairly easy to compute the α scale spaces $W_f^\alpha(\mathbf{b}, \mathbf{n}(\beta, \gamma), s)$, cf.[30], of the spherical functions $U_f(\mathbf{b}, \cdot) : S^2 \to \mathbb{R}$, for all $\mathbf{b} \in \mathbb{R}^3$ fixed, i.e. $W_f^\alpha(\mathbf{b}, \mathbf{n}(\beta, \gamma), s)$ is the unique solution $W_f^\alpha(\mathbf{b}, \mathbf{n}(\beta, \gamma), s)$ of the evolution (diffusion iff $\alpha = 1$) system:

$$\begin{cases} \frac{\partial W^\alpha}{\partial s} = -(-\Delta_{LB})^\alpha W, \qquad \alpha \in [\frac{1}{2}, 1] \\ \lim\limits_{s \downarrow 0} W^\alpha(\mathbf{b}, \cdot, s) = U_f(\mathbf{b}, \cdot) \text{ in } \mathbb{L}_2(S^2)\text{-sense}, \end{cases}$$

where $\Delta_{LB} = \frac{\partial^2}{\partial \beta^2} + \frac{\cos \beta}{\sin \beta} \frac{\partial}{\partial \beta} + \frac{1}{(\sin \beta)^2} \frac{\partial^2}{\partial \gamma^2}$ is the Laplace-Beltrami operator on S^2. The unique solution (recall (4.70)) of this evolution problem is simply given by

$$W_f^\alpha(\mathbf{b}, \mathbf{n}(\beta, \gamma), s) = \sum_{n=0}^{\infty} \sum_{l=0}^{\infty} \sum_{m'=-l}^{l} \alpha_l^n \left[\mathcal{D}^{(l)}(R_{\mathbf{e}_z, \gamma} R_{\mathbf{e}_y, \beta}) \right]_{m'}^0 (g_n^l \otimes Y_l^{m'}, \mathcal{T}_{\mathbf{b}} f)_{\mathbb{L}_2(\mathbb{R}^3)} \, e^{-(l(l+1))^\alpha s}.$$

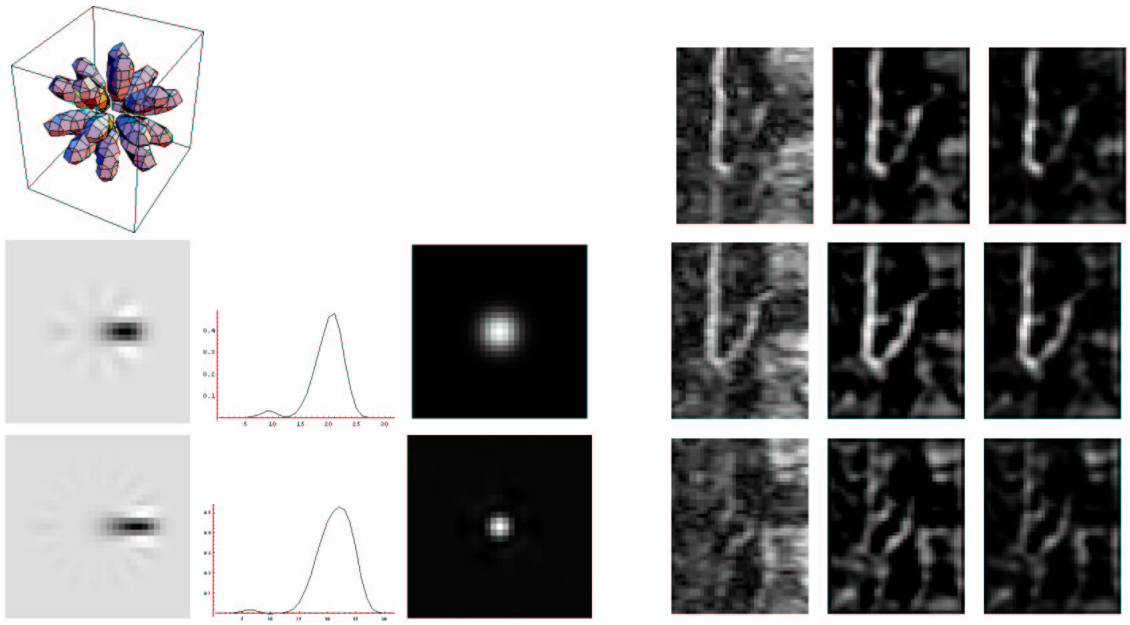

Figure 4.17: Left: First row $N = 8$, second row $N = 16$. From left to right plots of the wavelet restricted to $y = 0$: $\psi_N^{0,3D}(x, 0, z)$, the wavelet restricted to $y = 0$, $x = 0$: $\psi_N^{0,3D}(0, 0, z)$, the restriction of the corresponding $\mathcal{F}^{-1}(M_\psi) = \tilde{\psi}$ to $y = 0$, computed by only 20 sampling points, which are the centers $\mathbf{c}_i$ of the triangular faces of icosahedron. Right: Example of a medical application: Enhancement of Adam-Kiewicz vessel in 3D MRI-image by means of power enhancement on the orientation score (see (4.94)) constructed with wavelet, $N = 8$, illustrated in the left (upper row). For more details and evaluations on application of our theory to medical images (including 3D MRI-data of the Adam-Kiewicz vessel) we refer to the master thesis of van der Put [110]

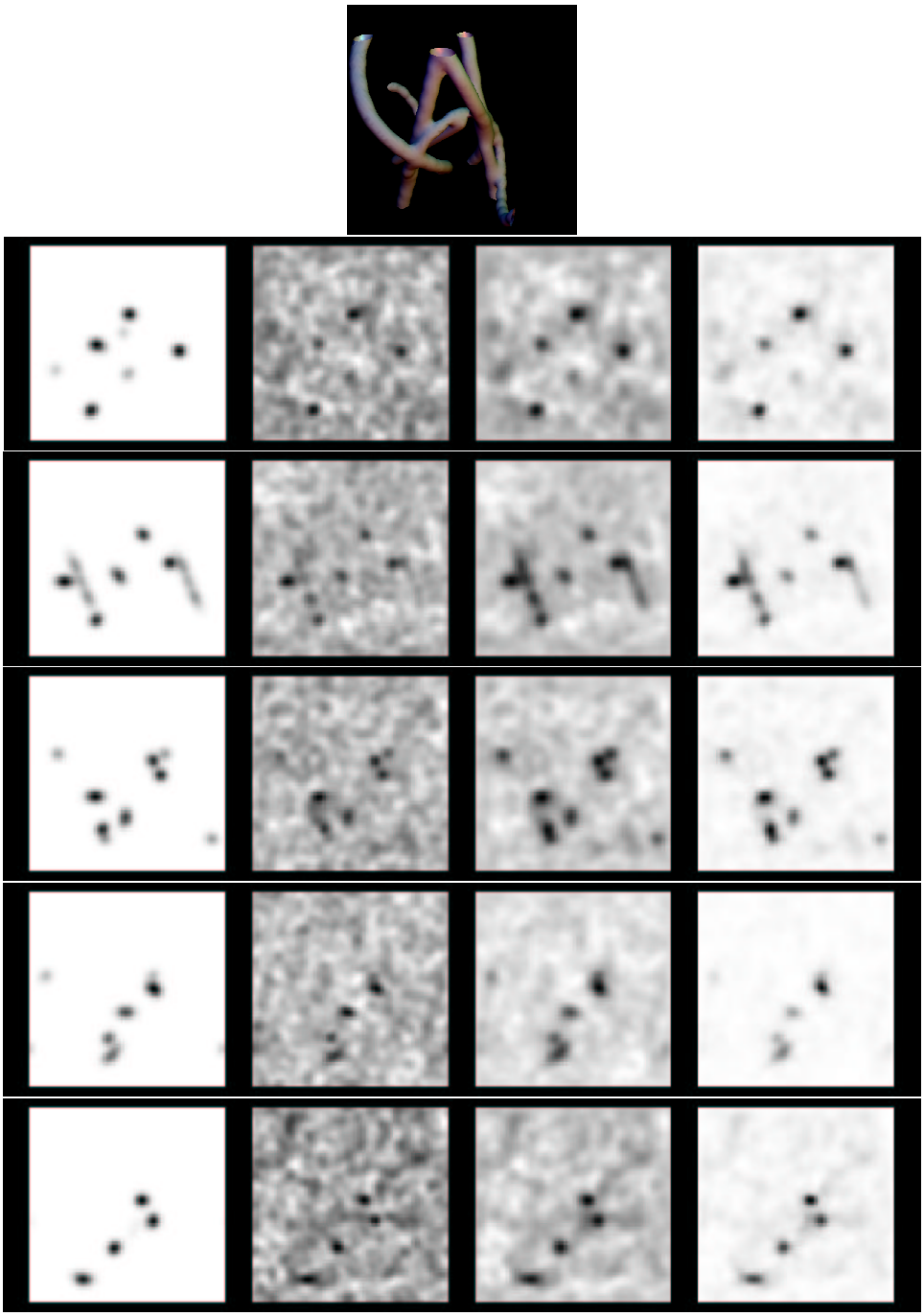

Figure 4.18: Illustration of robust line detection in 3D images via orientation scores constructed with wavelet $\psi^{3D}_{N=16}$. 3D-images ($64 \times 64 \times 64$) illustrated by 5 different 2D-cuts (along xy-plane, on $z = 5, 15, \ldots, 55$). From left to right: slices of ground truth 3D-image of several lines which are plotted in 3D in top of the figure, original image f obtained from ground truth and addition of correlated noise with high signal to noise ratio, approximative reconstruction $f * \tilde{\psi}$, processed image after simple power enhancement (see (4.94)) in the orientation score.

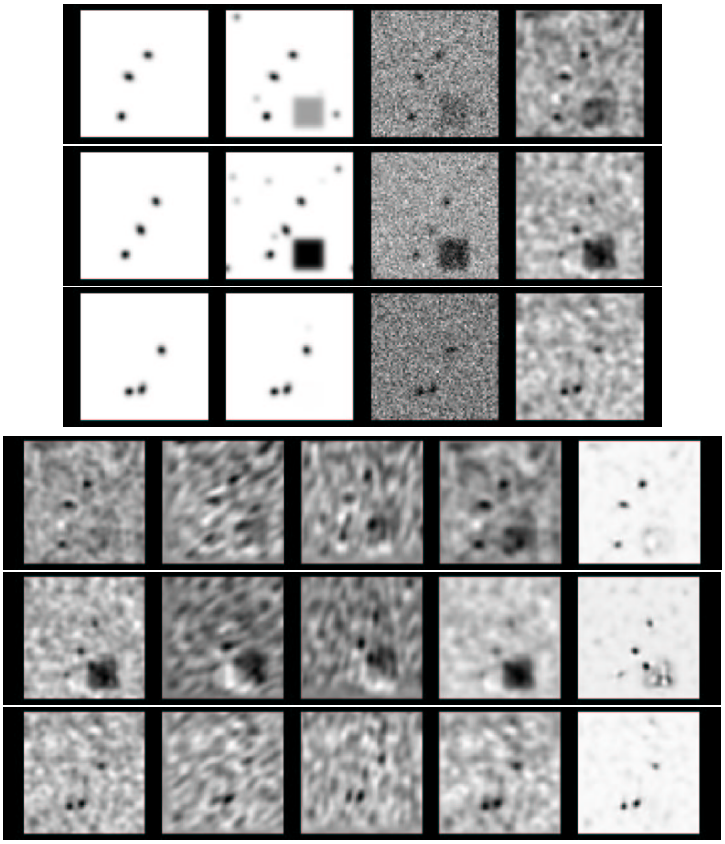

Figure 4.19: Illustration of robust line enhancement in 3D images via orientation scores. 3D-images ($64 \times 64 \times 64$) illustrated only by 3 different 2D-cuts (along xy-plane, on $z = 2, 12, 22$). Orientation scores are constructed with proper wavelet $\psi^{3D}_{N=16}$ illustrated in figures 4.15,4.17 . First 3 rows: First column original image of a straight line and 2 circular spirals. Parameterized by respectively $(10 + (0.2)t, 20 + (0.2)t, t)$, $\left(32 + 10\cos\left(\frac{2\pi t}{128}\right), 32 + 10\sin\left(\frac{2\pi t}{128}\right), t\right)$ and $\left(20 + 12\cos\left(\frac{2\pi t}{80}\right), 20 + 12\sin\left(\frac{2\pi t}{80}\right), t\right)$. In the second column we added other geometrical structures, some isolated spots and a cube. In the third column we obtained f_1 by adding Gaussian distributed noise on the grey-values and in the fourth column the approximative reconstruction. In the bottom three rows of this figure we added strongly correlated noise, with from left to right, 2D cuts of original 3D-image $f_2 = f_1 + \text{noise}$, two elements (which are 3D-images) in its orientation score $U_{f_2}(\cdot, \tilde{\mathbf{c}}_i) = \mathcal{W}_\psi[f_2](\cdot, \tilde{\mathbf{c}}_i)$, with $\tilde{\mathbf{c}}_2 \approx (-0.19, 0.58, 0.79)$, $\tilde{\mathbf{c}}_7 \approx (-0.30, 0.93, 0.19)$, the approximative reconstruction $f_2 * \tilde{\psi}$ and the processed image after simple power enhancement (see (4.94)) in score. We did **not** use any thresholding on the grey-values.

4.8 Image Enhancement by means of Left-Invariant Operations on Orientation Scores

Now that we have constructed a orientation score U_f from image f, such that it allows a well-posed reconstruction of f from orientation score U_f, one can think of suitable operations on the orientation scores.

Let ψ be a proper wavelet, then there exists a 1–to–1 correspondence between bounded operators $\Phi \in \mathcal{B}(\mathbb{C}_G^K)$ on orientation scores and bounded operators $\Upsilon \in \mathcal{B}(\mathbb{L}_2^{\varrho}(\mathbb{R}^d))$ on bandlimited images:

$$\Upsilon[f] = (\mathcal{W}_\psi^{\varrho})^*[\Phi[\mathcal{W}_\psi^{\varrho}[f]]], \quad f \in \mathbb{L}_2^{\varrho}(\mathbb{R}^d) \ , \tag{4.74}$$

which allows us to relate operations on orientation scores to operations on images in a robust manner.[16]

Recall (Theorem 19) and Corollary 5 that $\mathbb{C}_K^G$ is the space of orientation scores as a closed linear subspace of $\mathbb{H}_\psi$, which is a vector subspace of $\mathbb{L}_2(G)$. For proper wavelets we have (approximative) $\mathbb{L}_2$-norm preservation, so then we have $\mathbb{L}_2(G) \cong \mathbb{H}_\psi$. In this section we set $\mathbb{H}_\psi = \mathbb{L}_2(G)$, to avoid technical (irrelevant) subtleties concerning approximations.

Let $\Phi : \mathbb{L}_2(G) \to \mathbb{L}_2(G)$ be some bounded operator on $\mathbb{L}_2(G)$, then the range of the restriction of this operator to the subspace $\mathbb{C}_K^G$ of orientation scores need not be contained in $\mathbb{C}_K^G$, i.e. $\Phi(U_f)$ need not be the orientation score of an image. The adjoint mapping of $\mathcal{W}_\psi^{\varrho} : \mathbb{L}_2^{\varrho}(\mathbb{R}^d) \to \mathbb{L}_2(G)$, recall Definition 19 in section 4.5, is given by

$$(\mathcal{W}_\psi^{\varrho})^*(V) = \int_G \mathcal{U}_g\psi \; V(g) \; \mathrm{d}\mu_{\mathrm{G}}(\mathrm{g}) \ , V \in \mathbb{L}_2(G) \ .$$

The operator $\mathbb{P}_\psi = \mathcal{W}_\psi^{\varrho} \, (\mathcal{W}_\psi^{\varrho})^*$ is the orthogonal projection on the space of orientation scores $\mathbb{C}_K^G$. This projection can be used to decompose the manipulated orientation score:

$$\Phi(U_f) = \mathbb{P}_\psi(\Phi(U_f)) + (I - \mathbb{P}_\psi)(\Phi(U_f)) \ .$$

Notice that the orthogonal complement $(\mathbb{C}_K^G)^\perp$, which equals $\mathcal{R}(I - \mathbb{P}_\psi)$, is exactly the nil-space of $(\mathcal{W}_\psi^{\varrho})^*$, so

$$[(\mathcal{W}_\psi^{\varrho})^* \circ \Phi \circ \mathcal{W}_\psi^{\varrho}](f) = [(\mathcal{W}_\psi^{\varrho})^* \circ \mathbb{P}_\psi \circ \Phi \circ \mathcal{W}_\psi^{\varrho}](f) \text{ , for all } f \in \mathbb{L}_2^{\varrho}(\mathbb{R}^d) \text{ and all } \Phi \in \mathcal{B}(\mathbb{L}_2(G)) \ . \tag{4.75}$$

Definition 20 *An operator $\Phi : \mathbb{L}_2(G) \to \mathbb{L}_2(G)$ is left invariant iff*

$$\Phi[\mathcal{L}_h f] = \mathcal{L}_h[\Phi f] \ , \quad \textit{for all } h \in G, f \in \mathbb{L}_2(\mathbb{R}^2) \ , \tag{4.76}$$

[16] This can be compared with image processing via the Fourier domain. By the Plancherel Formula $\|f\|^2_{\mathbb{L}_2(\mathbb{R}^2)} = \|\mathcal{F}[f]\|^2_{\mathbb{L}_2(\mathbb{R}^2)}$ the Fourier transform $\mathcal{F} : \mathbb{L}_2(\mathbb{R}^2) \to \mathbb{L}_2(\mathbb{R}^2)$ has a stable inverse $\mathcal{F}^{-1} = \mathcal{F}^*$, allowing image processing via the Fourier domain.

where the left regular action $\mathcal{L}_g$ (also known as shift-twist transformation, cf.[130]) of $g \in G$ onto $\mathbb{L}_2(G)$ is given by

$$\mathcal{L}_g \psi(h) = \psi(g^{-1}h) = \psi(R_\theta^{-1}(\boldsymbol{b}' - \boldsymbol{b}), e^{i(\theta'-\theta)}) \ , \tag{4.77}$$

with $g = (\boldsymbol{b}, e^{i\theta}) \in G, h = (\boldsymbol{b}', e^{i\theta'}) \in G$.

Theorem 21 *Let Φ be a bounded operator on $\mathbb{C}_K^G$. Then the unique corresponding operator Υ on $\mathbb{L}_2^\varrho(\mathbb{R}^d)$, which is given by $\Upsilon[f] = (\mathcal{W}_\psi^\varrho)^* \circ \Phi \circ \mathcal{W}_\psi^\varrho[f]$ is Euclidean invariant, i.e. $\mathcal{U}_g \Upsilon = \Upsilon \mathcal{U}_g$ for all $g \in G$ if and only if Φ is left invariant, i.e. $\mathcal{L}_g \Phi = \Phi \mathcal{L}_g$ for all $g \in G$.*

Proof First we notice that

$$\mathcal{W}_\psi^\varrho \mathcal{U}_g = \mathcal{L}_g \mathcal{W}_\psi^\varrho \ , \text{ for all } g \in G, \tag{4.78}$$

since $\mathcal{W}_\psi^\varrho[\mathcal{U}_g[f]](h) = (\mathcal{U}_h \psi, \mathcal{U}_g f)_{\mathbb{L}_2(\mathbb{R}^d)} = (\mathcal{U}_{g^{-1}h}\psi, f)_{\mathbb{L}_2(\mathbb{R}^d)} = \mathcal{L}_g[\mathcal{W}_\psi^\varrho[f]](h)$. Moreover,

$$(\mathcal{W}_\psi^\varrho \mathcal{U}_g f, U)_{\mathbb{L}_2(G)} = (\mathcal{L}_g \mathcal{W}_\psi^\varrho f, U)_{\mathbb{L}_2(G)} \Leftrightarrow (f, \mathcal{U}_{g^{-1}} (\mathcal{W}_\psi^\varrho)^* U)_{\mathbb{L}_2(G)} = (f, (\mathcal{W}_\psi^\varrho)^* \mathcal{L}_{g^{-1}} U)_{\mathbb{L}_2(G)}$$

for all $U \in \mathbb{L}_2(G), f \in \mathbb{L}_2^\varrho(\mathbb{R}^d), g \in G$ and thereby we have

$$(\mathcal{W}_\psi^\varrho)^* \mathcal{U}_g = \mathcal{L}_g (\mathcal{W}_\psi^\varrho)^* \ , \text{ for all } g \in G. \tag{4.79}$$

Now suppose Φ is left invariant then it follows by (4.78) and (4.79) that

$$\begin{aligned} \Upsilon[\mathcal{U}_g f] &= (\mathcal{W}_\psi^\varrho)^* \circ \Phi \circ \mathcal{W}_\psi^\varrho \circ \mathcal{U}_g[f] \\ &= (\mathcal{W}_\psi^\varrho)^* \circ \Phi \circ \mathcal{L}_g \circ \mathcal{W}_\psi^\varrho[f] \\ &= (\mathcal{W}_\psi^\varrho)^* \circ \mathcal{L}_g \circ \Phi \circ \mathcal{W}_\psi^\varrho[f] \\ &= \mathcal{U}_g \circ (\mathcal{W}_\psi^\varrho)^* \circ \Phi \circ \mathcal{W}_\psi^\varrho[f] = \mathcal{U}_g[\Upsilon[f]] \end{aligned} \tag{4.80}$$

for all $f \in \mathbb{L}_2(\mathbb{R}^2)$ and $g \in G$. So we indeed obtain $\Upsilon \mathcal{U}_g = \mathcal{U}_g \Upsilon$ for all $g \in G$.
Now suppose Υ commutes with $\mathcal{U}_g$ for all $g \in G$. Then we again have by (4.78) and (4.79) that

$$(\mathcal{W}_\psi^\varrho)^* \circ \Phi \circ \mathcal{L}_g \circ \mathcal{W}_\psi^\varrho[f] = (\mathcal{W}_\psi^\varrho)^* \circ \mathcal{L}_g \circ \Phi \circ \mathcal{W}_\psi^\varrho[f] \ ,$$

for all $f \in \mathbb{L}_2(\mathbb{R}^2)$ and $g \in G$. Now since the range of $\mathcal{L}_g|_{\mathbb{C}_K^G}$ and the range of Φ are contained in $\mathbb{C}_K^G$ and since $(\mathcal{W}_\psi^\varrho)^*\Big|_{\mathbb{C}_K^G} = (\mathcal{W}_\psi^\varrho)^{-1}$ we obtain $\mathcal{L}_g \circ \Phi \circ \mathcal{W}_\psi^\varrho = \Phi \circ \mathcal{L}_g \circ \mathcal{W}_\psi^\varrho$. Now the final result follows by the fact that the range of $\mathcal{W}_\psi^\varrho$ equals $\mathbb{C}_K^G$: $\mathcal{L}_g \circ \Phi = \Phi \circ \mathcal{L}_g$ for all $g \in G$. □

Practical Consequences: Euclidean invariance of Υ is of great practical importance, since the result should not be different if the original image is rotated or translated. So by Theorem 21 the only reasonable operations on orientation scores are left invariant. Moreover by (4.75) it follows that is not a problem when the mapping $\Phi : \mathbb{C}_K^G \to \mathbb{L}_2(G)$ maps an orientation score to an element in $\mathbb{L}_2(G) \setminus \mathbb{C}_K^G$ as long one is aware of the effect that $\mathbb{P}_\psi \Phi : \mathbb{C}_K^G \to \mathbb{C}_K^G$ yields the same result. One can always compute the angle between $\Phi(U_f)$ and $\mathbb{C}_K^G$ to see how effective the operation Φ is (In most of our applications the angle was small).

All *linear* left invariant kernel operators $\Phi : \mathbb{L}_2(G) \to \mathbb{L}_2(G)$ are G-convolution operators. They are given by

$$\begin{aligned}[\Phi(U)](g) &= (K *_G U)(g) = \int_G K(h^{-1}g)U(h)\ \mathrm{dh} \quad , \mathrm{g} = (\mathbf{b}, \mathrm{e}^{\mathrm{i}\theta}) \\ &= \int_{\mathbb{R}^2} \int_0^{2\pi} K(e^{i(\theta-\theta')}, R_{\theta'}^{-1}(\mathbf{b}-\mathbf{b}'))\, U(\mathbf{b}', e^{i\theta'})\ \mathrm{d}\theta'\, \mathrm{db}_1' \mathrm{db}_2' \ ,\end{aligned} \tag{4.81}$$

for almost every $g = (\mathbf{b}, \theta) \in G$. From the practical point of view(speed) those can be implemented via impuls response and then taking the G-convolution. In practice it is conceptually easier to use G-correlations which are given by

$$K \star_G U = \check{K} *_G U, \tag{4.82}$$

where $\check{K}(g) = K(g^{-1})$, for all $g \in G$. For algorithms/practical implementation issues of (steerable !) G convolutions/G correlations we refer to section 7.8 on G-convolutions in the Appendix.

Before we propose left invariant operators on orientation scores, we give a brief overview of the interesting geometry within the domain G of orientation scores, which is the Euclidean Motion Group.

4.8.1 Geometry of the Euclidean Motion Group

For any Lie-group G the tangent space $T_e(G)$ at the unity element equipped with the product

$$[A, B] = \lim_{t \downarrow 0} \frac{a(t)b(t)(a(t))^{-1}(b(t))^{-1} - e}{t^2} \ ,$$

where $t \mapsto a(t)$ resp. $t \mapsto b(t)$ are *any* smooth curves in G with $a(0) = b(0) = e$ and $a'(0) = A$ and $b'(0) = B$, is isomorphic to $\mathcal{L}(G)$. $\mathcal{L}(G)$ is the Lie-Algebra of left invariant vector fields on G, i.e. all vector fields $\tilde{A}$ on G such that

$$\tilde{A}_g f = \tilde{A}_e(f \circ L_g) = \tilde{A}_e(h \mapsto f(g\ h)) \ ,$$

equipped with product

$$[\tilde{A}, \tilde{B}]_g f = \tilde{A}_g \tilde{B} f - \tilde{B}_g \tilde{A} f \ .$$

The isomorphism is given by $A \leftrightarrow \tilde{A} \Leftrightarrow \tilde{A}_g(\phi) = A(\phi \circ L_g) = A(h \mapsto \phi(g\ h))$ for all smooth $\phi : G \supset O_g \to \mathbb{R}$ and all g, h in G.

In our case of the Euclidean motion group we have that $T_e(G)$ is spanned by

$$\{A_1 = \mathbf{e}_\theta, A_2 = \mathbf{e}_\xi, A_3 = \mathbf{e}_\eta\} \tag{4.83}$$

with

$$\boxed{\begin{aligned}&\xi = b_1\ \cos\theta + b_2\ \sin\theta \\ &\mathbf{e}_\xi = \cos\theta\ \mathbf{e}_{b_1} + \sin\theta\ \mathbf{e}_{b_2}\end{aligned}} \tag{4.84}$$

(in the spatial plane along the measured orientation) and

$$\boxed{\begin{array}{l}\eta = -b_1\ \sin\theta + b_2\ \cos\theta \\ \mathbf{e}_\eta = -\sin\theta \mathbf{e}_{b_1} + \cos\theta \mathbf{e}_{b_2}\end{array}} \tag{4.85}$$

(in the spatial plane orthogonal to the measured orientation). The corresponding left(or shift-twist) invariant vector fields are given by

$$\{\tilde{A}_1 = \partial_\theta, \tilde{A}_2 = \partial_\xi = \cos\theta\,\partial_{b_1} + \sin\theta\,\partial_{b_2}, \tilde{A}_3 = \partial_\eta = -\sin\theta\,\partial_{b_1} + \cos\theta\,\partial_{b_2}\}\ . \tag{4.86}$$

It is easily verified that

$$\left\{\begin{array}{r} \tilde{A}_3 = [\tilde{A}_1, \tilde{A}_2] \\ -\tilde{A}_2 = [\tilde{A}_1, \tilde{A}_3] \\ 0 = [\tilde{A}_2, \tilde{A}_3] \end{array}\right. \quad \text{and} \quad \left\{\begin{array}{r} A_3 = [A_1, A_2] \\ -A_2 = [A_1, A_3] \\ 0 = [A_2, A_3]\ , \end{array}\right.$$

which coincides with $A \longleftrightarrow \tilde{A}$. For dimensional consistency define $X_1 = (\frac{2\pi}{Z})A_1, X_2 = A_2$ and $X_3 = A_3$, where Z is the width of the image domain (so $b_1, b_2 \in [0, Z]$).

We obtained the left-invariant vector fields (4.86) by means of the derivative of the *right* regular representation $\mathcal{R} : G \to \mathcal{B}(\mathbb{L}_2(G))$ given by $(\mathcal{R}_g\Phi)(h) = \Phi(hg)$, for all $\Phi \in \mathbb{L}_2(G)$ and almost every $h \in G$. The right regular representation (in contrast to the left regular representation) is left-invariant and its derivative $\mathrm{d}\mathcal{R}$, which maps $T_e(G)$ onto $\mathcal{L}(G)$, is given by

$$(\mathrm{d}\mathcal{R}(A)\Phi)(g) = \lim_{t\to 0} \frac{(\mathcal{R}_{\exp(tA)}\Phi)(g) - \Phi(g)}{t}\ , \qquad A \in T_e(G), \Phi \in \mathbb{L}_2(G), g \in G. \tag{4.87}$$

For example we have

$$(\mathrm{d}\mathcal{R}(\mathbf{e}_{b_1})\Phi)(g) = \lim_{t\downarrow 0} \frac{\Phi(\mathbf{b} + t\,R_\theta \mathbf{e}_{b_1}, e^{i\theta})}{t} = (\partial_\xi \Phi)(\mathbf{b}, e^{i\theta}), \qquad g = (\mathbf{b}, e^{i\theta}).$$

In a similar way one obtains

$$\begin{array}{ll} \partial_\theta & = \mathrm{d}\mathcal{R}(\mathbf{e}_\theta), \\ \partial_\xi & = \mathrm{d}\mathcal{R}(\mathbf{e}_{b_1}), \\ \partial_\eta & = \mathrm{d}\mathcal{R}(\mathbf{e}_{b_2}). \end{array} \tag{4.88}$$

The exponent map $\exp : T_e(G) \to G$, which is explicitly determined in Appendix 7.6, is surjective. Moreover, it follows by a more general result for solvable Lie-groups cf.[125]Theorem 3.18.11,p.243 that the mapping

$$(t_1, t_2, t_3) \mapsto \exp(t_2 X_2)\exp(t_3 X_3)\exp(t_1 X_1)\ ,$$

is an analytic homeomorphism of $\mathbb{R}^3$ *onto* G. In our case this mapping takes a trivial form, since $\exp(t_2X_2)\exp(t_3X_3)\exp(t_1X_1) = (t_2, 0, 1)(0, t_3, 1)(0, 0, e^{i\frac{2\pi t_1}{Z}}) = (t_2, t_3, e^{i\frac{2\pi t_1}{Z}})$. However, in our case, the mapping

$$(\beta_1, \beta_2, \beta_3) \mapsto \exp(\beta_1 X_1)\exp(\beta_2 X_2)\exp(\beta_3 X_3)$$

is also an analytic homeomorphism of $\mathbb{R}^3$ *onto* G, yielding much more relevant coordinates of the second kind.

So we conclude that any group element $g = (\mathbf{b}, \theta)$ can be parameterized using either coordinates of the first kind $\{\alpha_i\}_{i=1,2,3}$, see Appendix 7.6, or coordinates of the second kind $\{\beta_i\}_{i=1,2,3}$:

$$\begin{aligned} g &= \exp(\sum_{i=1}^{3} \alpha_i X_i) \\ &= \left(\tfrac{Z\alpha_3}{2\pi\alpha_1} \left(\cos\left(\tfrac{2\pi\alpha_1}{Z}\right) - 1 \right) + \tfrac{Z\alpha_2}{2\pi\alpha_1} \sin\left(\tfrac{2\pi\alpha_1}{Z}\right), \tfrac{Z\alpha_3}{2\pi\alpha_1} \sin\left(\tfrac{2\pi\alpha_1}{Z}\right) - \tfrac{Z\alpha_2}{2\pi\alpha_1} \left(\cos\left(\tfrac{2\pi\alpha_1}{Z}\right) - 1 \right), e^{i\frac{2\pi\alpha_1}{Z}} \right), \\ g &= \prod_{i=1}^{3} \exp(\beta_i X_i) = \\ &= \left(\beta_2 \cos\left(\tfrac{2\pi\beta_1}{Z}\right) - \beta_3 \sin\left(\tfrac{2\pi\beta_1}{Z}\right), \beta_2 \sin\left(\tfrac{2\pi\beta_1}{Z}\right) + \beta_3 \cos\left(\tfrac{2\pi\beta_1}{Z}\right), e^{i\frac{2\pi\beta_1}{Z}} \right) , \end{aligned} \tag{4.89}$$

where the coordinates of the second kind correspond to (θ, ξ, η), since by (4.89):

$$(\frac{2\pi\beta^1}{Z}, \beta^2, \beta^3) = (\theta, R_{-\theta}\mathbf{b}) = (\theta, \xi, \eta).$$

4.8.1.1 Metrics on the Euclidean Motion Group

Suppose we have two oriented particles in the orientation score at $g = (\mathbf{b}, e^{i\theta})$ and $g' = (\mathbf{b}', e^{i\theta'})$ then we would like to quantify the " connectivity " between them. So for the sake of perceptual organization, we want to introduce a metric[17] on the Euclidean motion group.

First of all we choose a metric must to be left invariant:

$$d_p(g, h) = d_p(g^{-1}h, e) = \|g^{-1}h\|_p \text{ for all } g, h \in G \, . \tag{4.90}$$

where $\|g\|_p = d_p(g, e)$.

We propose the following shift-twist invariant metrics:

- The logarithmic metric

$$d(g, g') = |g^{-1}g'| = \min_{k\in\mathbb{Z}} \sqrt{\left((\theta - \theta' + 2k\pi) \frac{X}{2\pi} \right)^2 + \frac{(\theta - \theta' + 2k\pi)^2}{2} \left(\frac{1}{1 - \cos(\theta - \theta')} \right) (b_1^2 + b_2^2)}, \tag{4.91}$$

  and corresponding norm $\|g\|^2 = \sum_{i=1}^{3} |\alpha_i|^2$, where $\{\alpha_i\}$ are the coordinates of the first kind. The balls $B_{g,\delta} = \{g' \in G \, | d(g', g) \leq \delta\}$ are "double-onions". The upper-parts of these " onion " balls are illustrated in Figure 4.20.

- The *Riemannian 2-norm* is defined by

$$\begin{aligned} \|g\| \quad = \inf \Bigg\{ & \left(\int_0^1 \sum_{i=1}^{3} |\gamma_i(t)|^2 \mathrm{dt} \right)^{\frac{1}{2}} \quad : \quad \text{with} \\ & \gamma \in C^1([0,1], G), \gamma(0) = e, \gamma(1) = g \text{ such that } \dot{\gamma}(t) = \sum_{i=1}^{3} \gamma_i(t) \, A_i|_{\gamma(t)} \Bigg\} \end{aligned}$$

[17] Formally it is incorrect to put a norm on G, since its components have different physical dimension. This can easily be solved for when using $\tilde{\theta} = \frac{Z\theta}{2\pi}$, which just like b_1 and b_2 has physical dimension length and where Z denotes the length of a (square) image.

and can be expressed in the coordinates of the second kind $\{\beta_i\}$:

$$\|g\| = \sqrt{\sum_{i=1}^{3} |\beta_i|^2} = \sqrt{\left(\frac{Z\theta}{2\pi}\right)^2 + \xi^2 + \eta^2} \quad , \theta \in [0, \pi] \ . \tag{4.92}$$

The corresponding metric is given by

$$\sum_{i,j=1}^{3} \delta_{ij} \ \mathrm{d}\beta^{\mathrm{i}} \otimes \mathrm{d}\beta^{\mathrm{j}} = \sum_{\mathrm{i}=1}^{3} \mathrm{d}\beta^{\mathrm{i}} \otimes \mathrm{d}\beta^{\mathrm{i}} = \sum_{\mathrm{i,j}=1}^{3} \mathrm{m_{ij}}(\mathbf{b}) \ \mathrm{db}^{\mathrm{i}} \otimes \mathrm{db}^{\mathrm{j}} \ ,$$

where $b_3 = \theta$ and where the matrix $M(\mathbf{b}) = [m_{ij}(\mathbf{b})]$ is given by

$$\begin{pmatrix} 1 & 0 & b_2 \\ 0 & 1 & -b_1 \\ b_2 & -b_1 & b_1^2 + b_2^2 + \frac{Z^2}{4\pi} \ . \end{pmatrix}$$

The corresponding geodesics are straight lines in ξ, η, θ, so they are given by

$$\begin{pmatrix} b_1(t) \\ b_2(t) \\ b_3(t) \end{pmatrix} = \begin{pmatrix} (A_1 t + B_1)\cos(\theta(t)) - (A_2 t + B_2)\sin(\theta(t)) \\ (A_1 t + B_1)\sin(\theta(t)) + (A_2 t + B_2)\cos(\theta(t)) \\ \theta(t) = \frac{2\pi(A_1 t + B_1)}{Z} \end{pmatrix} \quad , A_1, A_2, A_3, B_1, B_2, B_3 \in \mathbb{R} \, .$$

where we notice that $B_1 = B_2 = B_3 = 0$ iff $\gamma(0) = e = (\mathbf{0}, 0)$. One can easily build in anisotropies by using the norm

$$\sum_{i=1}^{3} \lambda_i \mathrm{d}\beta^{\mathrm{i}} \otimes \mathrm{d}\beta^{\mathrm{i}} \ .$$

- If besides a distance an interpolation curve[18] is required than we propose the following alternative:

$$d(g, g') = |g^{-1}g'| = \int_0^1 \left\| \frac{\partial \mathbf{x}}{\partial t} \right\| \ \mathrm{dt} \quad , \mathrm{g} = (\mathbf{b}, \theta), \mathrm{g}' = (\mathbf{b}', \theta'), (\theta' - \theta) \in [0, \pi] \ . \tag{4.93}$$

with $\mathbf{x}(t) = (x(t), y(t))$ the unique 2D curve with $\mathbf{x}(0) = \mathbf{0}$, $\frac{dy}{dx}(0,0) = \frac{y'(0)}{x'(0)} = 0$ and $(\mathbf{x}(1)) = (x(1), y(1)) = (R_\theta^{-1}(\mathbf{b}' - \mathbf{b}))$,

$$\frac{dy}{dx}(R_\theta(\mathbf{b}' - \mathbf{b})) = \gamma_{(\theta' - \theta)} := \begin{cases} \tan(\theta' - \theta) & \text{if } \theta' - \theta \in [0, \pi/2] \ . \\ \pi - \tan(\theta - \theta') & \text{if } \theta' - \theta \in [\pi/2, \pi] \ , \end{cases}$$

that minimizes the total curvature energy $\mathcal{E}(\mathbf{x}) = \int_0^1 \|\ddot{\mathbf{x}}(t)\| \ \mathrm{dt}$. It follows from the Euler-Lagrange equations that such a curve satisfies $\frac{d^3x(t)}{dt^3} = \frac{d^3y(t)}{dt^3} = 0$ and therefore

$$\mathbf{x}(t) = (\varepsilon_1 t^2 + \varepsilon_2 t, \varepsilon_3 t^2) \ ,$$

[18] In subsection 4.9.1 we will follow a much more elegant way by computing modes of Green's functions, cf. (4.122).

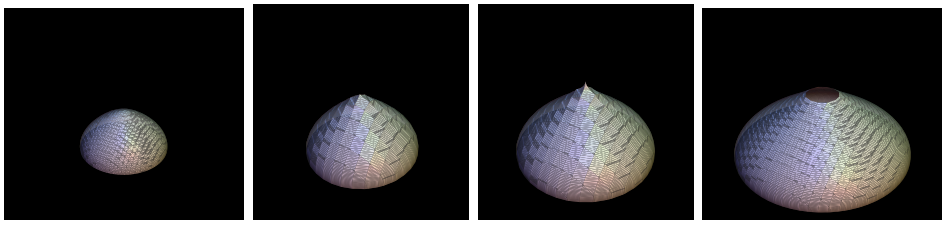

Figure 4.20: Plots of unit balls in bundle space, for increasing radii (from left to right). As the radius increases the ball becomes more and more onion shaped.

and where the boundary conditions uniquely give

$$\begin{cases} \varepsilon_1 &= 2\left\{x(1) - (1/\gamma_{(\theta'-\theta)})(y(1))\right\}, \\ \varepsilon_2 &= \left\{(2/\gamma_{(\theta'-\theta)})y(1) - (x(1))\right\}, \\ \varepsilon_3 &= y(1)\ , \end{cases}$$

so that (4.93) can be given explicitly by

$$d(g,g') = |g^{-1}g'| = \int_0^1 \sqrt{(2t\,\varepsilon_1 + \varepsilon_2)^2 + (2\,t\,\varepsilon_3)^2}\ \mathrm{dt},\ \mathrm{g} = (\mathbf{b}, \mathrm{e}^{\mathrm{i}\theta}), \mathrm{g}' = (\mathbf{b}', \mathrm{e}^{\mathrm{i}\theta'}).$$

Remark: It follows from the estimate $1 \leq \frac{\theta^2}{2}\left(\frac{1}{1-\cos\theta}\right) \leq \frac{\pi^2}{4}$, for all $\theta \in [0,\pi]$, that the logarithmic norm is equivalent to the Riemann 2-norm given by (4.92):

$$\|g\| \leq |g| \leq \frac{\pi^2}{4}\|g\| \text{ for all } g \in G.$$

4.8.2 Basic Left Invariant Operations on Orientation Scores

In image analysis it is well known that differential operators used for corner/line/edge/blob detection must be Euclidean invariant. Mostly, such differential invariants are easily expressed in a local coordinate system (gauge coordinates) where in 2D one coordinate axis (say v) is along the isoline/isophote and the other along the gradient direction (say w), cf. [52].

Rather than putting these gauge coordinates along isophotes we propose a local coordinate system along the measured orientation. Note to this end that in some medical image applications the elongated structures are not along isophotes. So in our orientation scores ξ and η play the role of v and w. Moreover we can differentiate along the direction θ and obtain directional frequencies.

Besides these local left invariant operators we can think of more global left-invariant operators, such as normalization or grey-value transformations to enhance certain elongated structures.
Overview of left invariant operations on orientation scores:

Figure 4.21: Illustration of image processing via elementary operation on orientation score. Visual illusion. Normalization of the orientation layers in the orientation scores reveals the most contrasting lines in the triangles.

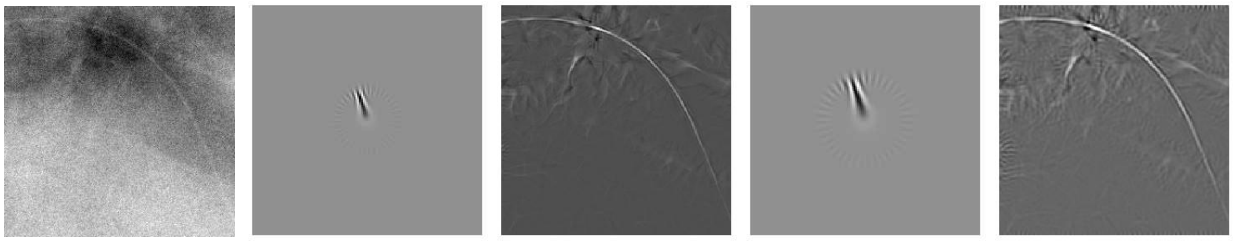

Figure 4.22: Illustration of image processing via elementary operation on orientation score. From left to right: 1:Noisy medical image with guide wire , 2-3: Small oriented wavelet ψ with corresponding processed image $\tilde{f} = \mathcal{W}_\psi^* \left[\tilde{U}_f\right]$, with $\tilde{U}_f = \left(\frac{\Re U_f - \min \Re(U_f)}{\max\{\Re(U_f) - \min(\Re(U_f))\}}\right)^2$. 4-5:Same as 2-3 with relatively larger kernel $\frac{1}{\sqrt{\sigma}}\psi_N^0(\frac{\mathbf{x}}{\sigma})$, where we recall that ψ_N^0 was given by (4.61). For the sake of clarity the wavelet plots (2,4) are zoomed in with a factor of 2.

- Monotonic Grey-value transformations. For example

$$\Phi(U_f) = (U_f - \min_g\{U_f(g)\})^q, q > 0. \tag{4.94}$$

  This can be used to enhance the strongly oriented spots in the score and reduce the noise/weakly oriented spots in the score, see figure 4.22. Note that it does *not* correspond to a simple grey-value transformation of the original image, since in general we have $(f)^q \neq (\mathcal{W}_\psi^\theta)^*[(\mathcal{W}_\psi[f])^q]$.

- Normalization. $[\Phi(U_f)](\mathbf{b}, e^{i\theta}) = U_f(\mathbf{b}, e^{i\theta}) / \left(\int_{\mathbb{R}^2} |U_f(\mathbf{x}, e^{i\theta})|^p \mathrm{d}\mathbf{x} \right)^{\frac{1}{p}}$, $p > 1$. See figure 4.21.

- Differential operators constructed from left invariant vector fields. For example enhancement of elongated structures via $\Phi(U_f) = \partial_{\eta\eta} U_f \; \partial_{\theta\theta} U_f \; U_f$.

- Left invariant evolution equations generated by left invariant vector fields. For examples see subsection 4.8.3.

4.8.3 Evolution Equations Corresponding to Left Invariant Stochastic Processes on the 2D Euclidean Motion Group

The linear 2nd-order left invariant evolutions on the Euclidean Motion Group are given by:

$$\begin{cases} \partial_s W = A\, W \ , \\ \lim\limits_{s\downarrow 0} W(\cdot, s) = U_f(\cdot) \ , \end{cases} \tag{4.95}$$

where the negative definite generator A acting on $\mathbb{L}_2(G)$ is given by (the closure of)

$$A \ = -\sum_{i=1}^{3} a_i \tilde{A}_i + \sum_{i,j=1}^{3} D_{ij} \tilde{A}_i \tilde{A}_j \qquad a_i, D_{ij} \in \mathbb{R}, i = 1, \ldots, 3. \tag{4.96}$$

We shall only consider the practically most relevant cases where the constant matrix D is positive and diagonal with respect to $\{\mathbf{e}_\theta, \mathbf{e}_\xi, \mathbf{e}_\eta\}$, in which case the generator simplifies to

$$A \ = \left[-\frac{a_1}{Z}\partial_\theta - a_2\partial_\xi - a_3\partial_\eta + \frac{D_{11}}{Z^2}(\partial_\theta)^2 + D_{22}(\partial_\xi)^2 + D_{33}(\partial_\eta)^2 \right] \ . \tag{4.97}$$

The first order derivatives take care of transport (convection) and the second order derivatives give diffusion.

We first consider the case where all D_{ii}'s are zero and the initial condition is a Dirac distribution $\delta_{\theta_0,\mathbf{b}_0}$ (i.e. one oriented particle). This spike will move over time along exponential curves, which are straight-lines in a spatial plane, spirals through G and straight lines along θ-direction. By introducing the variables, $t = s\frac{a_1}{Z}, \lambda_2 = \frac{a_2}{a_1}Z, \lambda_3 = \frac{a_3}{a_1}Z$ Equation (4.95) reduces to

$$\begin{cases} \partial_t W = [\partial_\theta + \lambda_2\partial_\xi + \lambda_3\partial_\eta]W \qquad \lambda_2, \lambda_3 \in \mathbb{C} \\ \lim\limits_{t\downarrow 0} W(\cdot, t) = \delta_{\theta_0,\mathbf{b}_0} \ . \end{cases}$$

Notice that indeed $[s] = 1 \leftrightarrow [t] = 1$ and $[a_1] = [a_2] = [a_3] = [\text{length}] \leftrightarrow [\lambda_2] = [\lambda_3] = [\text{length}]$. It follows by equality (4.89) that the orbit of the Dirac distribution at initial position $(\mathbf{b}_0, e^{i\theta_0})$ is given by

$$(b_0^1 + \lambda_3(\cos(t+\theta_0) - \cos(\theta_0)) \ + \lambda_2 \sin(t+\theta_0), b_0^2 + \lambda_3 \sin(t+\theta_0) \ - \lambda_2(\cos(t+\theta_0) - \cos(\theta_0)), e^{i(t+\theta_0)}) \ ,$$

which is a circular spiral with radius $\sqrt{\lambda_2^2 + \lambda_3^2}$ around central point

$$(-\lambda_3 \cos\theta_0 - \lambda_2 \sin\theta_0 + b_0^1, \lambda_2 \cos\theta_0 - \lambda_3 \sin\theta_0 + b_0^2),$$

which *exactly* corresponds to the results from our numerical implementation.

The solution of the diffusion problem i.e. $a_1 = a_2 = a_3 = 0$, $D_{11} > 0$, $D_{22} > 0$, $D_{33} > 0$ in (4.97) is a G-convolution kernel operator with some positive kernel $K_s \in \mathbb{L}_1(G)$, which can be sharply estimated from above and below by Gaussian kernels on G:

$$c'(V(s))^{-1/2} e^{-b'\frac{|g|^2}{s}} \leq K_s(g) \leq c(V(s))^{-1/2} e^{-b\frac{|g|^2}{s}} \ , \tag{4.98}$$

$c, c', b, b' > 0$, where $|g|$ denotes the Riemannian 2-norm given by (4.92), for details see [37]Theorem 3.3 and [34] Section II.5, specifically (II.25). In the degenerate case $a_1 = a_2 =$

$a_3 = D_{11} = 0$, the diffusion boils down to an ordinary spatial convolution for each fixed θ with an anisotropic Gaussian kernel where the fraction of D_{22} and D_{33} gives the anisotropy factor of Gaussian convolution along $\mathbf{e}_\xi$ and $\mathbf{e}_\eta$.

The evolution equations given by (4.95) correspond to stochastic processes. For example the case $a_1 = a_3 = 0$ and $D_{22} = D_{33} = 0$, $D_{11} = \frac{1}{2}\sigma^2$, is the Forward Kolmogorov equation corresponding to the stochastic process known as the direction process[19], cf.[97]:

$$\begin{cases} \overline{\kappa} = \frac{1}{L}\int_0^L k(s)\,\mathrm{ds} = \frac{1}{\mathrm{L}}\int_0^{\mathrm{L}} |\dot{\theta}(\mathrm{s})|\,\mathrm{ds} \sim \mathcal{N}(0,\sigma^2) \\ \mathbf{x}(s) = \int_0^s \begin{pmatrix} \cos\theta(\tau) \\ \sin\theta(\tau) \end{pmatrix} \mathrm{d}\tau + \mathbf{x}(0)\ , \\ L \sim NE(\alpha)\ . \end{cases}$$

which is the limit of the following *discrete* stochastic process

$$\begin{cases} e^{i\theta(s_k+\Delta s)} = e^{i(\theta(s_k)+\Delta s\,\varepsilon)}, \qquad \varepsilon \sim \mathcal{N}(0, N\sigma^2) \\ \mathbf{x}(s_k+\Delta s) = \mathbf{x}(s_k) + \Delta s \begin{pmatrix} \cos\theta(s_k) \\ \sin\theta(s_k) \end{pmatrix} \\ \Delta s = \frac{L}{N}, \text{ with } L \sim NE(\alpha), k = 0,\ldots,N-1. \end{cases} \tag{4.99}$$

A Gaussian scale space representation of an image $f \in \mathbb{L}_2(\mathbb{R}^2)$, given by $u(\mathbf{x},s) = (G_s * f)(\mathbf{x})$ can be considered as a rotation and translation invariant stochastic process, where the distribution of positions of grey-value particles/photons within $\mathbb{R}^2$ evolves over time[20] (the well-known Wiener process), as the forward Kolomogorov/Fokker-Plank equation of the Wiener proces is given by the heat equation. In exactly the same manner the left-invariant evolutions on orientation scores are forward Kolomogorov/Fokker Plank equations of left-invariant stochastic processes where the distribution of *oriented* photons within G evolves over time, see figure 4.23.

The life time T of a particle traveling with unit speed (so $T = L$) through G is assumed to be negative exponentially distributed, $T \sim NE(\alpha)$, i.e. $p(T=t) = \alpha e^{-\alpha t}$, with expected life time $E(T) = \frac{1}{\alpha}$, because it is memoryless

$$P(T > s+t | T > t) = \frac{P(T > s+t, T > t)}{P(T > t)} = P(T > s),$$

which must be the case in a Markov-process. The probability density of finding a $e^{i\theta}$-oriented particle at position $\mathbf{b}$ is given by

$$\boxed{\begin{aligned} p(g) &= p(\mathbf{b},\theta) = \int_0^\infty p(\mathbf{b},\theta|T=t)p(T=t)\,\mathrm{dt} \\ &= \alpha \int_0^\infty [e^{tA}U_f](\mathbf{b},\theta)e^{-t\alpha}\,\mathrm{dt} = -\alpha[(A-\alpha I)^{-1}U_f](\mathbf{b},\theta)\ . \end{aligned}} \tag{4.100}$$

Consider two independent stochastic processes generated by $A = A_{\mathrm{Conv}} + A_{\mathrm{Diff}}$, where A_{Conv},

[19] In many later work Mumford's final Fokker-Plank equation which is physically correct as long as σ^2 is the variance in *average* curvature $\overline{\kappa}$, is often mis-formulated in literature introducing dimensional inconsistencies. For example [130] and [9] where $\sigma^2/2$ must be σ.

[20] In a Gaussian scale space representation $u(\mathbf{x},s) = (G_s * f)(\mathbf{x})$ the evolution parameter $s = \frac{\sigma^2}{2}$ inherits the physical dimension of the generator Δ of the corresponding evolution equation $u_s = \Delta u$ and thereby in image analysis $s > 0$ is usually considered as the scale of observation of an image f. Scale is related to time a diffusion constant D: $Dt = s = \frac{1}{2}\sigma^2$.

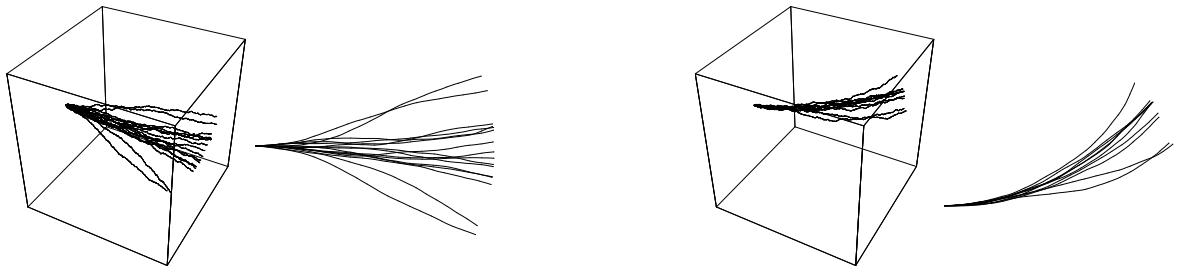

Figure 4.23: Illustration of random walks in the Euclidean Motion group $G = \mathbb{R}^2 \rtimes \mathbb{T}$ (together with their projections on the spatial plane $\mathbb{R}^2$): $(\mathbf{x}_{n+1}, \theta_{n+1}) = (\mathbf{x}_n, \theta_n) + \Delta t \left(\sum_{i=1}^{3} a_i A_i \right) + \sqrt{\Delta t} D_{11} \mathcal{N}(0,1) A_1$, where the $\{A_i\}_{i=1}^3$ are given by (4.83). Left: 10 random walks starting from the unit-element $(\mathbf{x}_0, \theta_0) = (\mathbf{0}, 0)$ of a direction process with parameter values $(a_1, a_2, a_3, D_{11}, \Delta t) = (0, 1, 0, \frac{1}{4}, 10^{-3})$. Right: 10 random walks of a curvature process with parameter values $(1, 1, 0, \frac{1}{4}, 10^{-3})$.

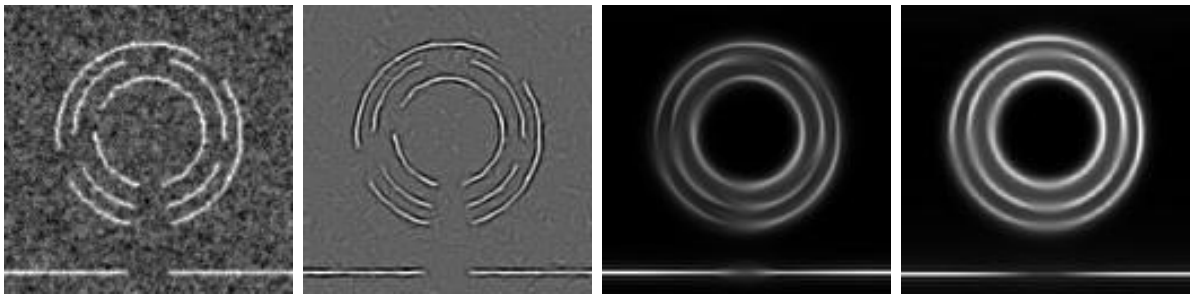

Figure 4.24: Example of perceptual organization. From left to right: 1. Original image; 2. detection of elongated structures via orientation scores U_f: $\tilde{f} = \mathcal{W}_\psi^*[\tilde{U}_f]$ with $\tilde{U}_f = \left(\frac{\Re U_f - \min \Re(U_f)}{\max\{\Re(U_f) - \min(\Re(U_f))\}} \right)^2$ 3. Inverse transformation of evolved orientation score $\mathcal{W}_\psi^*[\Phi[\tilde{U}_f]]$, where Φ denotes the shooting process by maintaining curvature and direction; 4. Inverse transformation of probability density of collision of forward and backward proces on orientation score, see (4.101). In contrast to related work[130] we do not put sources and sinks by hand, but use our orientation scores instead. The only parameters involved are, range of wavelet t, decay time α and the stochastic process parameters b^1, b^2, b^3 in (4.97).

resp. A_{Diff} stands for the convection respectively diffusion part of A, given by (4.97), and its adjoint $A^* = -A_{\text{Conv}} + A_{\text{Diff}}$. So the direction of shooting particles is opposite and the stochastic behavior is similar in the two processes. The probability-density of collision of particles from these 2 independent processes, yields a so-called **completion field** and is obtained by the following left invariant operation

$$\boxed{(\Phi[U_f])(g) = \alpha^2 [(A - \alpha I)^{-1} U_f](g) [(A^* - \alpha I)^{-1} U_f](g) \ .} \tag{4.101}$$

cf. figure 4.24.

4.9 Analytic Approximations of (the Green's functions of) the Left-invariant Evolutions on the Euclidean Motion Group

In this section we will compute analytic approximations of the Green's functions $S_{\alpha,\{a_i\},\{D_{ii}\}} : G \setminus e \to \mathbb{R}$, which are given by

$$S_{\alpha,\{a_i\},\{D_{ii}\}} = -\alpha(A-\alpha I)^{-1}\delta_e \Leftrightarrow \left(\sum_{i=1}^{3} a_i\tilde{A}_i - \sum_{i=1}^{3} D_{ii}(\tilde{A}_i)^2 + \alpha I\right) S_{\alpha,\{a_i\},\{D_{ii}\}} = \alpha\,\delta_e \quad (4.102)$$

and which are needed for computing the probability of collision of particles from 2 independent stochastic processes given by (4.101) as explained in (4.100). But first we will apply some general results of the field of pure mathematics, [73], [34], [70], to our specific case (4.102). From which we deduce that the Greens functions do exist in the sense that they are smooth outside the unity element e and such that the solution of

$$W = -\alpha(A-\alpha I)^{-1}U_f$$

is given by $W = S_{\alpha,\{a_i\},\{D_{ii}\}} *_G U_f$, where we make an important distinction between the cases where the generator A is a Hörmander operator of type 1 or of type 2.

If the generator $A = \sum_{i=1}^{3} -a_i\tilde{A}_i + \sum_{i=1}^{3} D_{ii}(\tilde{A}_i)^2$, $a_i \in \mathbb{R}, D_{ii} \geq 0$ is such that

$$\{\tilde{A}_i \mid D_{ii} > 0\} \cup \{\sum_{i=1}^{3} a_i\tilde{A}_i\}$$

are C^∞-vector fields and their commutators up to a fixed order $r \in \mathbb{N}$ span the whole tangent space in every point of G then it follows by the Hörmander Theorem, [73]Theorem 1.1, p.149 that the operator $A-\alpha I$ is *hypo-elliptic*, i.e. for all distributions F on G, F is a $\mathbb{C}^\infty$-function on every open set where $(A-\alpha I)F$ is a C^∞-function. As a result, if the initial orientation score U_f is within $C^\infty(G)$, (which is usually the case, if the orientation wavelet ψ with $U_f = \mathcal{W}_\psi[f]$ is smooth) then $W = (A-\alpha I)^{-1}U_f$ is also in $C^\infty(G)$.

If the generator A is such that it contains a diffusion part and has the additional property that the convection part of the generator is contained within the span of the generators active in the diffusion part (so in particular for the *linear* case, if $a_i \neq 0 \Rightarrow D_{ii} \neq 0$, for all $i = 1,\ldots,3$), the generator is by definition a Hörmander operator of the first type. If the convection part of the generator is not contained in the span of the generators active in the diffusion part, the generator is by definition a Hörmander operator of the second type.

With respect to the Hörmander operators of the first type we notice that if the generator is a strongly elliptic operator (for example if $D_{11} = D_{22} = D_{33} > 0$) then it generates after closure, a strongly continuous semi-group on $\mathbb{L}_2(G)$ with a smooth convolution kernel $t \mapsto K_t$ which can be estimated between two Gaussian kernels on the Euclidean motion group, for details see [37]Theorem 3.3, p16.

If A is a Hörmander operator of the second type then it generates a continuous semi-group

$\{e^{tA}\}_{t>0}$ on $\mathbb{L}_2(G)$, and they are given by[21]

$$e^{tA}f = \delta_{\exp(-tA_{\mathrm{Conv}})} * K_t * f, \tag{4.103}$$

where the kernels $K_t \in \mathbb{L}_2(H)$, with H the Lie group generated by the Lie algebra spanned by

$$Y_{j,k} = \{\mathrm{ad}^k(A_{Conv})A_j\}, \qquad j = 1, \ldots, 3,$$

can again be estimated by Gaussian kernels, for details see [70]Theorem 1.2, p.3.

Example: In the direction proces we have $A = \tilde{A}_2 + (\tilde{A}_1)^2$. Notice that the commutator $[\tilde{A}_1, \tilde{A}_2] = \tilde{A}_3$, so $\tilde{A}_1$,$\tilde{A}_2$ and their commutators span the whole tangent space and thereby operator $A - \alpha I$ is *hypo-elliptic* and as a result we have $U_f \in C^\infty(G) \Rightarrow W \in C^\infty(G)$. The generator A is a Hörmander operator of the second type and by (4.103) we have

$$(e^{tA}U)(\mathbf{b}, e^{i\theta}) = \int_{-\pi}^{\pi} \int_{\mathbb{R}} K_t(R_{\theta'}^{-1}(\mathbf{b} - (t\mathbf{e}_\xi + w\mathbf{e}_\eta)), e^{i(\theta-\theta')})\, U(t\mathbf{e}_\xi + w\mathbf{e}_\eta, e^{i\theta'})\, \mathrm{d}w\mathrm{d}\theta',$$

where $K_t : G \to \mathbb{R}$ satisfies the Gaussian estimate $|Y_J K_t| \leq C_J t^{-q+\deg(J)/2} e^{-c|g|^2}$, with $Y_J = Y_{j_1,k_1} \cdots Y_{j_l,k_l}$ and $\deg(J) = \sum_{\nu=1}^{l}(1+2k_\nu)$ for $t \leq 1$ and for some constants $c, C_J, q \in \mathbb{R}$, which can be considered as a G-convolution in distributional sense with the somewhat awkward singular kernel $\delta_{\exp(-t\tilde{A}_2)} * K_t$. The G-convolution kernel (or Green's-function) of the resolvent is only singular at the identity element e, since by

$$\begin{aligned} -\alpha(A - \alpha I)^{-1}U(g) &= -\alpha \int_{-\pi}^{\pi} \int_{\mathbb{R}} \int_0^\infty K_t(e^{i(\theta-\theta')}, R_{\theta'}^{-1}(\mathbf{b} - (t\mathbf{e}_\xi + w\mathbf{e}_\eta)))\, U(t\mathbf{e}_\xi + w\mathbf{e}_\eta, e^{i\theta'}) e^{-ts}\, \mathrm{d}s\mathrm{d}w\mathrm{d}\theta \\ &= (S_\alpha *_G U)(\mathbf{b}, e^{i\theta}), \quad g = (\mathbf{b}, e^{i\theta}) \neq e, \end{aligned}$$

we have that $S_\alpha(\mathbf{b}, e^{i\theta}) = \alpha\, K_{\xi_{\mathbf{b}}}(g) e^{-\alpha\xi_{\mathbf{b}} s}$ if $\xi_{\mathbf{b}} = b^1 \cos\theta + b^2 \sin\theta > 0$ and $S_\alpha(\mathbf{b}, e^{i\theta}) = 0$ if $\xi_{\mathbf{b}} < 0$.

Remark: From now on in this chapter we write $x = b_1$ and $y = b_2$ for the sake of simplicity.[22]

4.9.1 A Heisenberg Approximation of The Euclidean Motion Group

The main problem with finding the Green's functions of the resolvents of the evolution processes generated by

$$D_{11}(\tilde{A}_1)^2 + \sum_{i=1}^{3} a_i \tilde{A}_i \tag{4.104}$$

[21]Consider for example the case where $G = \mathbb{R}^2$ and $A = (\partial_x)^2 + \partial_y$, then $H = (\mathbb{R}, 0)$ and (4.103) reads $(e^{tA}f)(x,y) = \int_{\mathbb{R}} G_t(x - v)f(v, y - t)\mathrm{dv} = \delta_{\exp(-t\partial_y)} * G_t * f(x,y)$. Nevertheless, the Green's function of the resolvent is only singular at the origin and $-\lambda(A - \lambda I)^{-1}f = S_\lambda * f$, where $S_\lambda(x,y) = \mathcal{L}(t \mapsto \delta_{\exp(-t\partial_y)} * G_t(x,y))(\lambda) = \lambda\, G_y(x) e^{-\lambda y}$ for $y > 0$ and $S_\lambda(y) = 0$ for $y < 0$.

[22]In contrast to the previous chapters there is no need for a distinction between spatial variables in the image domain $\mathbb{R}^2$ and spatial variables in the wavelet domain, as from now on we shall only consider the wavelet domain $\mathbb{R}^2 \rtimes \mathbb{T}$.

(which are Hörmander operators of the second type) is that the operators

$$\{(\tilde{A}_1)^2, \tilde{A}_1, \tilde{A}_2, \tilde{A}_3\} = \{(\partial_\theta)^2, \partial_\theta, \partial_\xi, \partial_\eta\}, \tag{4.105}$$

generate a Lie-Algebra of infinite dimension (Unfortunately we have that $\mathrm{ad}^k(\partial_\theta^2)\partial_\xi \neq 0$, generates independent directions for each $k \in \mathbb{N}$, although $\mathrm{ad}^3(\partial_\xi)\partial_\theta^2 = 0$). This is due to the fact that the Lie-algebra (and thereby the group, see [103]Theorem B24,p.318) of $G = \mathbb{R}^2 \rtimes \mathbb{T}$ is not nilpotent, despite the fact it is solvable[23].

Therefore, for the moment, we approximate the Lie-algebra of left-invariant vector fields $\mathcal{L}(G)$ spanned by $\{\tilde{A}_1, \tilde{A}_2, \tilde{A}_3\}$, by the Lie-algebra $\mathcal{L}(\hat{G})$ generated by the vector fields,

$$\begin{aligned}\hat{A}_1 &= \tilde{A}_1 = \partial_\theta \\ \hat{A}_2 &= \partial_x + \theta\partial_y \\ \hat{A}_3 &= -\theta\partial_x + \partial_y\end{aligned}$$

which is spanned by $\{\hat{A}_i\}_{i=1}^5$, where $\hat{A}_4 = [\hat{A}_1, \hat{A}_2] = \partial_y$, $\hat{A}_5 = [\hat{A}_1, \hat{A}_3] = -\partial_x$ and which is isomorphic to a (simply connected) $5D$-Matrix Lie-Algebra $\mathfrak{g}$:

$$\mathcal{L}(\hat{G}) \ni \sum_{i=1}^5 a_i \hat{A}_i \leftrightarrow \sum_{i=1}^5 a_i \, \mathbf{E}_i := \begin{pmatrix} 0 & a_1 & a_4 & a_5 \\ 0 & 0 & a_2 & a_3 \\ 0 & 0 & 0 & 0 \\ 0 & 0 & 0 & 0 \end{pmatrix} \in \mathfrak{g}.$$

The exponent $\exp_{\hat{G}} : \mathfrak{g} \to \hat{G}$ is given by

$$\exp(t\,B) = 1 + t\,B + \frac{t^2}{2}B^2 = \begin{pmatrix} 1 & ta_1 & ta_4 + (1/2)t^2 a_1 a_2 & ta_5 + (1/2)t^2 a_1 a_2 \\ 0 & 1 & t\,a_2 & t\,a_3 \\ 0 & 0 & 1 & 0 \\ 0 & 0 & 0 & 1 \end{pmatrix} \tag{4.106}$$

with $B = \sum_{i=1}^5 a_i \, \mathbf{E}_i$.

Notice that $\hat{G}$ is a Lie-group of Heisenberg type and that the approximation $\hat{A}_2 \approx \tilde{A}_2$ and $\hat{A}_3 \approx \tilde{A}_3$ are only appropriate for a small environment around $\theta = 0$, as we have $\cos\theta = 1 + O(\theta^2)$ and $\sin\theta = \theta + O(\theta^3)$. Notice that the exponential trajectories $t \mapsto \exp(t(\sum_{i=1}^3 a_i \tilde{A}_i))$ and $t \mapsto \exp(t(\sum_{i=1}^3 a_i \hat{A}_i))$ are respectively circular spirals and parabolic spirals. This follows by (4.106) and (4.89).

Nevertheless, we notice that these results can also be directly obtained by computation of the characteristics of the first order PDE's:

$$\begin{cases} \dot{\theta} = a_1 \\ \dot{x} = a_2\cos\theta - a_3\sin\theta \\ \dot{y} = a_2\sin\theta + a_3\cos\theta \end{cases} \qquad \begin{cases} \dot{\theta} = a_1 \\ \dot{x} = a_2 - a_3\theta \\ \dot{y} = a_2\theta + a_3 \end{cases}$$

[23] A Lie-Algebra $\mathfrak{g}$ is solvable if there exists a $p \in \mathbb{N}$ such that $\mathcal{D}_{p+1}\mathfrak{g} = [\mathcal{D}_p\mathfrak{g}, \mathcal{D}_p\mathfrak{g}] = 0$, with $\mathcal{D}_1\mathfrak{g} = \mathfrak{g}$

from which we deduce that the respective characteristics through the origin are given by

$$\begin{cases} \theta(s) = a_1\, s \\ x(s) = \frac{a_2}{a_1}\sin(a_1 s) + \frac{a_3}{a_1}(\cos(a_1 s) - 1) \\ y(s) = -\frac{a_2}{a_1}(\cos(a_1 s) - 1) + \frac{a_3}{a_1}\sin(a_1 s) \end{cases} \qquad \begin{cases} \theta(s) = a_1\, s \\ x(s) = a_2\, s - a_3 a_1\, \frac{s^2}{2} \\ y(s) = a_3\, s + a_2 a_1\, \frac{s^2}{2} \end{cases} \tag{4.107}$$

Finally we notice that the approximative generators

$$\{(\hat{A}_1)^2, \hat{A}_1, \hat{A}_2, \hat{A}_3\} = \{(\partial_\theta)^2, \partial_\theta, \partial_x + \theta\partial_y, -\theta\partial_x + \partial_y, \}, \tag{4.108}$$

do generate a finite dimensional nil-potent Lie-Algebra, in contrast to the true generators (4.105), which is spanned by

$$\{\partial_x, \partial_\theta, \partial_y, -\theta\partial_y, -\theta\partial_x, \partial_x\partial_\theta, \partial_y\partial_\theta, (\partial_x)^2, (\partial_y)^2, (\partial_\theta)^2\}. \tag{4.109}$$

Remark: We are mostly interested in the case $a_3 = 0$, which allows only transport only along ξ (i.e. along the measured orientation). Therefore (and because of computational simplicity) we will restrict ourselves from now on to the case $a_1 = \kappa$, $a_2 = 1$ and $a_3 = 0$. Nevertheless we notice that all results in this section can straightforwardly be generalized to the cases $a_3 \neq 0$, $a_2 \in \mathbb{R}$.

Theorem 22 *Let $\hat{S}_{\alpha,\kappa_0,D_{11}} : G \to \mathbb{R}$ be the Green's function of the operator*

$$\alpha^{-1}(\alpha I - \hat{A}) := \alpha\left(\alpha I - D_{11}(\hat{A}_1)^2 + \sum_{i=1}^{3} a_i \hat{A}_i\right), \text{ with } a_1 = \kappa_0, a_2 = 1, a_3 = 0, \tag{4.110}$$

i.e. it is the unique solution of

$$\left(\alpha I - D_{11}(\hat{A}_1)^2 + \sum_{i=1}^{3} a_i \hat{A}_i\right)\hat{S}_{\alpha,\kappa_0,D_{11}} = \alpha\,\delta_e \tag{4.111}$$

which is infinitely differentiable on $G \setminus \{e\}$. It is a strictly positive function, with[24]

$$\|\hat{S}_{\alpha,\kappa_0,D_{11}}\| \approx \|\hat{S}_{\alpha,\kappa_0,D_{11}}\|_{\mathbb{L}_1(\mathbb{R}^2\times\mathbb{R})} = 1 \tag{4.112}$$

for all $\alpha, D_{11}, \kappa_0 > 0$, and is given by

$$\boxed{\hat{S}_{\alpha,\kappa_0,D_{11}}(x,y,\theta) = \alpha\,\frac{\sqrt{3}}{2\,D_{11}\pi x^2} e^{-\alpha x} e^{-\frac{3(x\theta-2y)^2 + x^2(\theta-\kappa_0 x)^2}{4x^3 D_{11}}}.} \tag{4.113}$$

Proof

First we notice that by means Hörmander's Theorem, [73]Theorem 1.1, p.149 that the operator given in (4.110) is hypo-elliptic and consequently S_α is infinitely differentiable on $G \setminus \{e\}$.

On $G \setminus \{e\}$ we have

$$\left(\alpha I - D_{11}(\hat{A}_1)^2 + \sum_{i=1}^{2} a_i \hat{A}_i\right)\hat{S}_{\alpha,\kappa_0,D_{11}} = 0 \tag{4.114}$$

[24]The approximation is very accurate for D_{11} is small, which is usually the case in our applications.

Or equivalently, again on $G \setminus \{e\}$

$$\partial_x \hat{S}_{\alpha,\kappa_0,D_{11}} = B\, \hat{S}_{\alpha,\kappa_0,D_{11}} \tag{4.115}$$

where the generator $B = \hat{A} + \partial_x - \alpha I$ is given by

$$B = \left(-\alpha I + D_{11}(\partial_\theta)^2 - \theta\partial_y - \kappa_0\partial_\theta\right). \tag{4.116}$$

Moreover we have by (4.111) that

$$\langle (\alpha I - \hat{A})\hat{S}_{\alpha,\kappa_0,D_{11}}, \phi\rangle = (\hat{S}_{\alpha,\kappa_0,D_{11}}, (\alpha I - \hat{A})\phi)_{\mathbb{L}_2(G)} = \alpha\,\phi(e), \tag{4.117}$$

for all test functions $\phi \in \mathcal{S}(G)$. In particularly for $\phi = \eta \otimes \tilde{\phi}$, with $\tilde{\phi} \in \mathcal{S}(S^1 \times \mathbb{R})$ arbitrary and $\eta(x) = C \int_{-\infty}^{x} G_\epsilon(z)\mathrm{d}z$, with $C \in \mathbb{R}^+$, such that $\eta(0) = 1$, which gives us by taking the limit $\epsilon \downarrow 0$ that

$$\lim_{x\downarrow 0}\langle \hat{S}_{\alpha,\kappa_0,D_{11}}(\cdot,x), \psi\rangle = \eta(0)\psi(0,0) = \psi(0,0), \tag{4.118}$$

for all $\phi \in \mathcal{S}(S^1 \times \mathbb{R})$. So we conclude that $\hat{S}_{\alpha,\kappa_0,D_{11}}$ satisfies the following evolution system

$$\begin{cases} \partial_x \hat{S}_{\alpha,\kappa_0,D_{11}} = B\hat{S}_{\alpha,\kappa_0,D_{11}} \\ \lim\limits_{x\downarrow 0} \hat{S}_{\alpha,\kappa_0,D_{11}}(x,\cdot) = \delta_{0,0}. \end{cases} \tag{4.119}$$

Moreover, B lies within the nil-potent Lie-algebra spanned by[25]

$$\{I, x\partial_\theta, x^2\partial_y, x\theta\partial y, x\partial_\theta^2, x^2\partial_\theta\partial_y, x^3\partial_y^2\}.$$

As a result by cf. [125]Theorem 3.18.11,p.243, or by the Campbell-Baker-Hausdorff formula, there exist a sequence of constants $\{c_i\}_{i=1}^6$ such that

$$e^{x\,B}\delta_e = e^{-\alpha x}e^{-c_6 x\partial_\theta}e^{-c_5 x^2\partial_y}e^{-c_1 x\theta\partial_y}e^{c_2 x\partial_\theta^2}e^{c_3 x^2\partial_\theta\partial_y}e^{c_4 x^3\partial_y^2}\delta_{(0,0)}$$

and thereby we have

$$\hat{S}_{\alpha,\kappa_0,D_{11}}(x,y,\theta) = \frac{1}{4\pi x\sqrt{c_2(c_4x^2) - \frac{(c_3x)^2}{2}}}e^{-\frac{1}{4\pi x}\begin{pmatrix} \theta - c_6x & y - c_1x(\theta - c_6x) - c_5x^2 \end{pmatrix}\begin{pmatrix} c_2 & \frac{c_3}{2}x \\ \frac{c_3}{2}x & c_4x^2 \end{pmatrix}\begin{pmatrix} \theta - c_6x \\ y - c_1x(\theta - c_6x) - c_5x^2 \end{pmatrix}}$$

Substitution of this expression in (4.115) yields

$$c_1 = \frac{1}{2}, c_2 = D_{11}, c_3 = 0, c_4 = \frac{D_{11}}{12}, c_5 = \frac{\kappa_0}{2}, c_6 = \kappa_0,$$

resulting into (4.113). □

Important Remarks:

- The Green's function $\hat{S}_{\alpha,\kappa_0,D_{11}}$ in Theorem 22 is the impuls response of δ_e, i.e. a δ-spike at the unity element $e = (\mathbf{0}, e^{i0} = 1)$. The impuls responses $\hat{S}_{\alpha,\kappa_0,D_{11};\,\mathbf{b}_0,\theta_0}$ of a general δ spike, $\delta_{\hat{g}_0}$ with $\hat{g}_0 = (\mathbf{b}_0, \theta_0) \in G$, which satisfies

$$\alpha\left(\alpha I - D_{11}(\hat{A}_1)^2 + \sum_{i=1}^{3} a_i\hat{A}_i\right)\hat{S}_{\alpha,\kappa_0,D_{11};\,\mathbf{b}_0,\theta_0} = \delta_{\hat{g}_0}\ ,$$

[25]The base elements have the same physical dimension: Length.

is easily deduced from $\hat{S}_{\alpha,\kappa_0,D_{11}}$, as we have:

$$\boxed{\begin{array}{ll}\hat{S}_{\alpha,\kappa_0,D_{11};\mathbf{b}_0,\theta_0}(x,y,\theta) & = \hat{S}_{\alpha,\kappa_0,D_{11}}(x-x_0,y-y_0-\theta_0(x-x_0),\theta-\theta_0) \\ & = \alpha\frac{\sqrt{3}}{2D_{11}\pi x^2}e^{-\alpha x}e^{-\frac{3y^2-3xy(\theta+\theta_0)+x^2(\theta^2+\theta\theta_0+\theta_0^2)}{x^3D_{11}}}.\end{array}} \tag{4.120}$$

This directly follows by the fact that the approximative generators are the left invariant vector fields of the Heisenberg-group $\hat{G}$, which indeed gives us

$$\begin{array}{ll}\hat{S}_{\alpha,\kappa_0,D_{11};\mathbf{b}_0,g_0}(x,y,\theta) & = \alpha(-\hat{A}+\alpha I)^{-1}\delta_{\hat{g}_0} = \alpha(-\hat{A}+\alpha I)^{-1}\mathcal{L}_{\hat{g}_0}\delta_e \\ & = \mathcal{L}_{\hat{g}_0}\alpha(-\hat{A}+\alpha I)^{-1}\delta_e = \mathcal{L}_{\hat{g}_0}\hat{S}_{\alpha,\kappa_0,D_{11}},\end{array} \tag{4.121}$$

where we notice that $\mathcal{L}_{\hat{g}_0}$ is the left invariant representation of the Heisenberg group $\hat{G}$ onto $\mathbb{L}_2(\hat{G})$ and

$$\mathcal{L}_{\hat{g}_0}\hat{S}_{\alpha,\kappa_0,D_{11}}(\hat{g}) = \hat{S}_{\alpha,\kappa_0,D_{11}}((\hat{g}_0)^{-1}\hat{g}) = \hat{S}_{\alpha,\kappa_0,D_{11}}((S_c)^{-1}(\mathbf{x}-\mathbf{x}_0),\theta-\theta_0),$$

with $\mathbf{x}_0 = (x_0,y_0)^T$ and the shearing matrix $S_c = \begin{pmatrix}1 & c\\ 0 & 1\end{pmatrix}$. Notice if the initial condition $\delta_e = \delta_{(\mathbf{0},0)}$ in (4.111) is replaced by $(\mathbf{x},\theta)\mapsto U_f(\mathbf{x},e^{i\theta})$ the solution is given by $\hat{G}$-convolution with $(x,y,\theta)\mapsto\hat{S}_{\alpha,\kappa_0,D_{11}}(x,y,\theta)$, rather than a G-convolution with $(x,y,e^{i\theta})\mapsto S_{\alpha,\kappa_0,D_{11}}(x,y,e^{i\theta})$.

- Notice that we dropped the periodic boundary condition $\hat{S}_{\alpha,\kappa_0,D_{11}}(\mathbf{b},\theta) = \hat{S}_\alpha(\mathbf{b},\theta+k(2\pi))$ for all $\mathbf{b}\in\mathbb{R}^2$ and all $k\in\mathbb{Z}$. In practice, however, this is harmless as typically the Green's functions can be truncated far before the range of 2π. Nevertheless, we notice that in practice it is better to apply the substitution $\theta\mapsto\tan\theta$, where the orientation is replaced by the slope. We return to this in much more detail in subsection 4.9.3.

- Notice that the completion field, recall (4.101), is now closely approximated by

$$\boxed{\begin{array}{l}\left(\alpha\,(\hat{A}-\alpha I)^{-1}\delta_{\mathbf{x}_0,\theta_0}\right)(x,y,\theta)\ \left(\alpha\,(\hat{A}^*-\alpha I)^{-1}\delta_{\mathbf{x}_1,\theta_1}\right)(x,y,\theta) \\ = \hat{S}_{\alpha,\kappa_0,D_{11}\,;\mathbf{x}_0,\theta_0}(x,y,\theta)\hat{S}_{\alpha,\kappa_1,D_{11}\,;-\mathbf{x}_1,\theta_1}(-x,y,-\theta),\end{array}}$$

with $\mathbf{x}_0,\mathbf{x}_1\in\mathbb{R}^2$, $e^{i\theta_0},e^{i\theta_1}\in\mathbb{T}$ where we notice that

$$\begin{array}{ll}\hat{A}^*\Phi(x,y,\theta) & = \left(\partial_x+\theta\partial_y+\kappa_0\partial_\theta+D_{11}(\partial_\theta)^2\right)\Phi(x,y,\theta) \\ & = \left(\hat{A}(x',y',\theta')\mapsto\Phi(-x',y,-\theta')\right)(-x,y,-\theta).\end{array}$$

For illustration of some of these completion fields, which are easily computed in practice, see figures 4.25 and 4.26. The modes of these completion fields, neither depend on D_{11}, nor on α and only depend on the difference $\kappa_0-\kappa_1$, are given by:

$$\begin{array}{ll}y(x) & = x\theta_0+\frac{x^3}{x_1^3}(-2y_1+x_1(\theta_0-\theta_1))+\frac{x^2}{x_1^2}(3y_1+x_1(\theta_1-2\theta_0)), \qquad x\in[0,x_1] \\ & +\frac{x(\kappa_0-\kappa_1)}{2x_1^3}\left(-2x^4+5x^3x_1-4x^2x_1^2+x_1^3x\right) \\ \theta(x) & = \theta_0+2\frac{x}{x_1^2}(3y_1+x_1(\theta_1-2\theta_0))-3\frac{x^2}{x_1^3}(2y_1+x_1(\theta_1-\theta_0)) \\ & +\frac{(\kappa_0-\kappa_1)}{x_1^3}\left(-3x^4+6x^3x_1+xx_1^3-4x_1^2x^2\right)\end{array} \tag{4.122}$$

Notice that $y(0) = 0$, $\theta(0) = 0$ and $y(x_1) = y_1$, $\theta(x_1) = -\theta_1$ and $\frac{dy}{dx}(x_1) = \theta_0$ and $\frac{dy}{dx}(0) = -\theta_1$. and thereby these completion fields can be used for vector graphics representations of medical images with elongated structures. However the choice of the *anchor points* (locations in the Euclidean motion group where the interpolation lines should pass) $(\mathbf{x}_i, \theta_i)$, $i = 1 \ldots, N, N \in \mathbb{N}$ and also how they are connected is still work in progress.

- Notice that $e^{-\kappa_0 x \partial_\theta} e^{-\frac{\kappa_0}{2} x^2 \partial_y} f(x, y, \theta) = f(x, y - \frac{\kappa_0\, x^2}{2}, \theta - \kappa_0\, x)$ for $f \in C^\infty(\mathbb{R}^3)$. The corresponding coordinate transformation

$$\left\{ \begin{array}{l} \tilde{x} = x \\ \tilde{y} = y - \frac{1}{2}\kappa_0\, x^2 \\ \tilde{\theta} = \theta - \kappa_0\, x\ , \end{array} \right.$$

is exactly the coordinate transformation that transform a direction proces without angular drift, i.e. $\kappa_0 = 0$, to a direction proces with angular drift, i.e. a stochastic proces with $\kappa_0 > 0$, which directly follows by

$$\left\{ \begin{array}{ll} \partial_x & = \partial_{\tilde{x}} + \kappa_0 x \partial_{\tilde{y}} + \kappa_0\, \partial_{\tilde{\theta}} \\ \partial_y & = \partial_{\tilde{y}} \\ \partial_\theta & = \partial_{\tilde{\theta}} \end{array} \right.$$

This coordinate transformation is area preserving as $\det(\frac{\partial \tilde{\mathbf{x}}}{\partial \mathbf{x}}) = 1$, thereby the $\mathbb{L}_1$-norm of the deformed anisotropic Gaussian remains 1 (as it should in a stochastic proces), from which (4.112) follows.

- The discrete stochastic proces corresponding to the approximative generator is given by

$$\left\{ \begin{array}{l} \theta(s_k + \Delta s) = \theta(s_k) + \Delta s\, (\kappa_0 + \varepsilon), \qquad \varepsilon \sim \mathcal{N}(0, N\sigma^2) \\ \mathbf{x}(s_k + \Delta s) = \mathbf{x}(s_k) + \Delta s\, \mathbf{e}_1 + \Delta s\, \theta(s_k)\, \mathbf{e}_2 \\ \Delta s = \frac{L}{N}, \text{ with } L \sim NE(\alpha),\ k = 0, \ldots, N-1. \end{array} \right. \tag{4.123}$$

is related to the original direction proces (4.99) (with angular drift $\kappa_0 = 0$):

$$\mathbf{x}(s_k + \Delta s) - \mathbf{x}(s_k) = \Delta s \begin{pmatrix} \cos\theta(s_k) \\ \sin\theta(s_k) \end{pmatrix} \approx \Delta s \begin{pmatrix} 1 \\ \theta(s_k) \end{pmatrix} = \Delta s\, \mathbf{e}_x + \Delta s\, \theta(s_k)\, \mathbf{e}_y. \tag{4.124}$$

This brings us to the point that a better analytic approximation of the Green's function(s) of the resolvents generated by the operator given in (4.104), would be obtained by computing the Green's function of the (forward) Kolmogorov equation belonging to the corresponding continuous stochastic proces (obtained by taking the limit $N \to \infty$) of the following discrete proces

$$\left\{ \begin{array}{l} e^{i\theta(s_k + \Delta s)} = e^{i(\theta(s_k) + \Delta s\, (\kappa_0 + \varepsilon))}, \qquad \varepsilon \sim \mathcal{N}(0, N\sigma^2) \\ \mathbf{x}(s_k + \Delta s) = \mathbf{x}(s_k) + \Delta s\, \mathbf{e}_{r(s_k)} + \Delta s\, \theta(s_k)\, \mathbf{e}_{\phi(s_k)} \\ \Delta s = \frac{L}{N}, \text{ with } L \sim NE(\alpha)\ . \end{array} \right. \tag{4.125}$$

with

$$\begin{array}{ll} r(s_k) & = \|\mathbf{x}(s_k) - \mathbf{x}(s_0)\|, \qquad s_k = s_0 + k * \Delta, \\ \phi(s_k) & = \angle(\mathbf{x}(s_k) - \mathbf{x}(s_0)), \\ \theta_0 & = \angle \mathbf{x}(s_0), \end{array}$$

and where we replaced the unit vectors $\{\mathbf{e}_{b_1}, \mathbf{e}_{b_2}, \mathbf{e}_\theta\}$ of the *global* cartesian coordinates b^1, b^2, in (4.123) and (4.124) by the *local* unit vectors $\mathbf{e}_\phi$ and $\mathbf{e}_r$ of the cylindrical coordinate system given by $(b_1, b_2, \theta) = (r\cos\phi, r\sin\phi, \theta)$. In the next subsection we shall derive the Green's function of the resolvent of the corresponding Kolmogorov-equation.

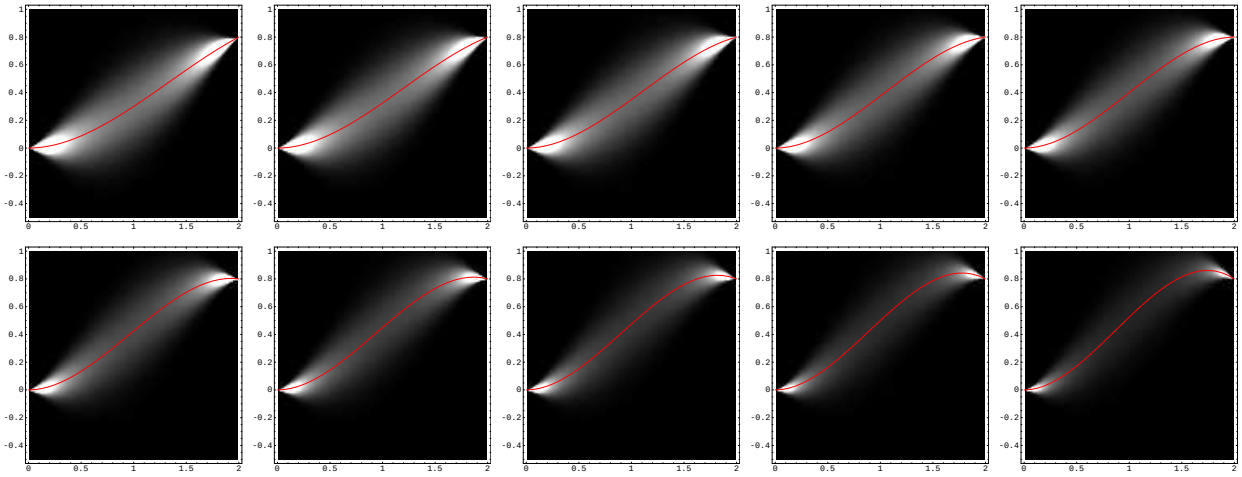

Figure 4.25: The fast analytic approximations of the completion field, projected on the spatial plane (plotted for $x \in (0,2)$, $y \in (-\frac{1}{2},1)$) by integration over θ i.e. $\int_{-\infty}^{\infty} \hat{S}_{D_{11}=0.5,\kappa_0=0,\alpha=0\,;\mathbf{x}_0=\mathbf{0},\theta_0=0}(x,y,e^{i\theta})\hat{S}_{D_{11}=0.5,\kappa_1=0,\alpha=0\,;x_1=-2,y_1=0.8,\theta_1}(-x,y,e^{-i\theta})\mathrm{d}\theta$ for respectively (from top-down bottom row) $\theta_1 = -0.4,-0.3,\ldots,0.3,0.4,0.5$. On top of these completion fields we plotted the corresponding modes (4.122) (projected on the spatial plane, i.e. we only plotted $x \mapsto y(x)$ in (4.122)).

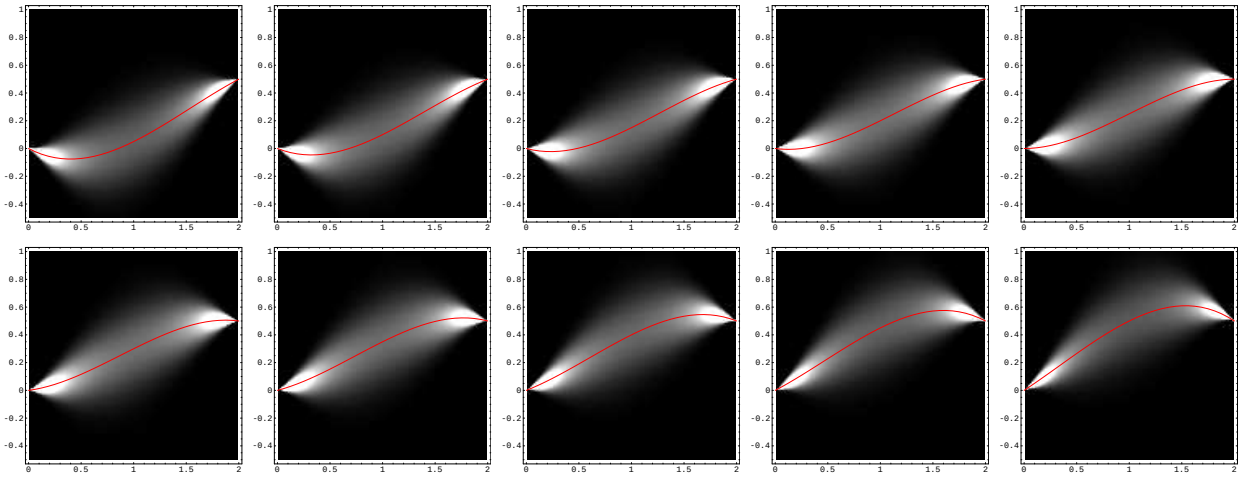

Figure 4.26: The fast analytic approximations of the completion field, projected on the spatial plane (plotted for $x \in (0,2)$, $y \in (-\frac{1}{2},1)$) by integration over θ i.e. $\int_{-\infty}^{\infty} \hat{S}_{D_{11}=0.5,\kappa_0=0,\alpha=0\,;\mathbf{x}_0=\mathbf{0},\theta_0}(x,y,e^{i\theta})\hat{S}_{D_{11}=0.5,\kappa_1=0,\alpha=0\,;x_1=-2,y_1=0.8,\theta_1=-\theta_0}(-x,y,e^{-i\theta})\mathrm{d}\theta$ for respectively (from top-down bottom row) $\theta_0 = -0.4,-0.3,\ldots,0.3,0.4,0.5$. On top of these completion fields we plotted the corresponding modes (4.122) (projected on the spatial plane, i.e. we only plotted $x \mapsto y(x)$ in (4.122)).

4.9.2 Better Analytic Approximations of The Green's function by means of Cylindrical Coordinates

First we express the left invariant vector fields on $\mathbb{R}^2 \rtimes \mathbb{T}$ in cylindrical coordinates:

$$\begin{cases} \tilde{A}_1 = \partial_\theta \\ \tilde{A}_2 = \cos(\theta-\phi)\partial_r + \frac{1}{r}\sin(\theta-\phi)\partial_\phi, \\ \tilde{A}_3 = -\sin(\theta-\phi)\partial_r + \frac{1}{r}\cos(\theta-\phi)\partial_\phi, \end{cases} \tag{4.126}$$

which enables us to write the objective equation

$$-(D_{11}(\tilde{A}_1)^2 - \sum_{i=1}^{3}\alpha_i \tilde{A}_i - \alpha I)S_{\alpha,\{a_i\},D_{11}} = \alpha\,\delta_e,$$

with $a_1 = \kappa_0$, $a_2 = 1, a_3 = 0$, in cylindrical coordinates:

$$\left(\cos(\theta-\phi)\partial_r + \frac{1}{r}\sin(\theta-\phi)\partial_\phi + \kappa_0\partial_\theta - D_{11}(\partial_\theta)^2 + \alpha I\right) S_{\alpha,\kappa_0,D_{11}} = \alpha\,\delta_e\ .$$

By approximating

$$\cos(\theta-\phi) \approx 1 \text{ and } \sin(\theta-\phi) \approx (\theta-\phi), \tag{4.127}$$

we get the following approximations of the left invariant generators (4.126):

$$\begin{aligned} &\breve{A}_1 = \partial_\theta \\ &\breve{A}_2 = \partial_r + (\theta-\phi)\tfrac{1}{r}\partial_\phi, \\ &\breve{A}_3 = -(\theta-\phi)\partial_r + \tfrac{1}{r}\partial_\phi, \end{aligned} \tag{4.128}$$

and we obtain the following equation for the Green's function of the resolvent of the (forward) Kolmogorov equation of the stochastic proces given by (4.125) (taking the limit $N \to \infty$):

$$\left(1\,\partial_r + \frac{1}{r}(\theta-\phi)\partial_\phi + \kappa_0\partial_\theta - D_{11}(\partial_\theta)^2 + \alpha I\right)\breve{S}_{\alpha,\kappa_0,D_{11}} = \alpha\,\delta_e\ , \tag{4.129}$$

with $D_{11} = \frac{1}{2}\sigma^2$. The function

$$(r,\phi,\theta) \mapsto \breve{S}_{\alpha,\kappa_0,D_{11}}(r,\phi,\theta)$$

which is smooth (on $\mathbb{R}^3 \setminus \{0,0,0\}$) is again an approximation (we again drop the boundary condition of 2π periodicity with respect to θ.) of the exact solution

$$(r,\phi,\theta) \mapsto S_{\alpha,\kappa_0,D_{11}}(r\cos\phi, r\sin\phi, e^{i\theta}).$$

See figure 4.28. Notice that the approximation $\breve{S}_{\alpha,\kappa_0,D_{11}} \approx S_{\alpha,\kappa_0,D_{11}}$ is much better than the approximation $\hat{S}_{\alpha,\kappa_0,D_{11}} \approx S_{\alpha,\kappa_0,D_{11}}$. Especially for high angular drifts, see figure 4.27 where the modes (which are independent of D_{11} and α) of $S_{\alpha,\kappa,D_{11}}$, $\hat{S}_{\alpha,\kappa,D_{11}}$ and $\breve{S}_{\alpha,\kappa,D_{11}}$ (projected on the spatial plane) are jointly plotted for increasing values of κ. Here we notice that these modes coincide with the characteristics of the convection part of the generator. With respect to the characteristics of $S_{\alpha,\kappa,D_{11}}$, $\hat{S}_{\alpha,\kappa,D_{11}}$ we recall (4.107). The characteristics of $\breve{S}_{\alpha,\kappa,D_{11}}$ can be similarly obtained:

$$\begin{cases} \dot{\theta} = \kappa_0 \\ \dot{\phi} = \frac{1}{r}(\theta-\phi) \\ \dot{r} = 1 \end{cases} \Rightarrow \begin{cases} x(s) = s\cos\left(\frac{\kappa_0 s}{2}\right) \\ y(s) = s\sin\left(\frac{\kappa_0 s}{2}\right) \\ \theta(s) = \kappa_0 s \end{cases} \tag{4.130}$$

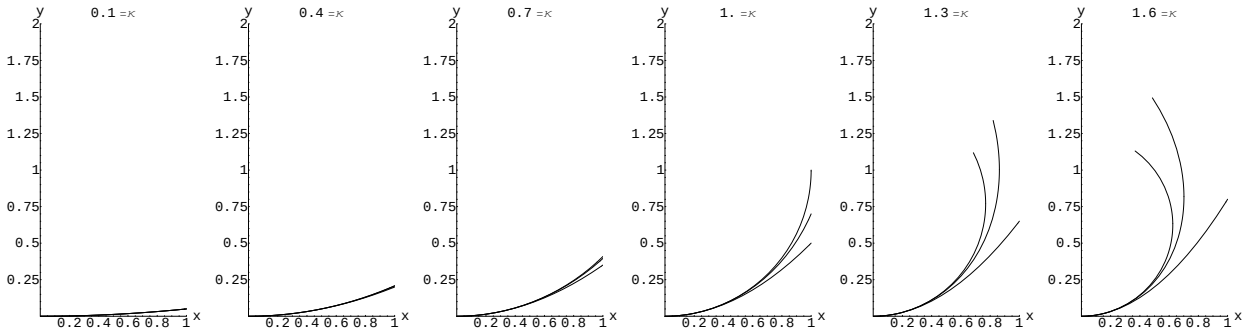

Figure 4.27: Joint plots of the projections of the modes of $S_{\alpha,\kappa,D_{11}}$, $\hat{S}_{\alpha,\kappa_0,D_{11}}$ and $\breve{S}_{\alpha,\kappa_0,D_{11}}$, which are given by (4.107), $(a_1 = \kappa_0, a_2 = 1, a_3 = 0)$, and (4.130) onto the spatial xy-plane, for increasing values of $\kappa_0 > 0$, from left to right $\kappa_0 = 0.1, 0.4, 0.7, 1.0, 1.3, 1.6$. Notice that the modes of $S_{\alpha,\kappa_0,D_{11}}$, which are circular spirals, are better approximated by the modes of $\breve{S}_{\alpha,\kappa_0,D_{11}}$ than by the modes of $\hat{S}_{\alpha,\kappa_0,D_{11}}$.

The substitution

$$\begin{cases} v(r) = r \\ w(r) = r\phi \end{cases} \Rightarrow \begin{cases} \frac{d}{dr}\breve{S}_{\alpha,\kappa_0,D_{11}} = \left(1\frac{d}{dv} + \phi\frac{d}{dw}\right)\breve{T}_{\alpha,\kappa_0,D_{11}}(w,v,\theta)\Big|_{w=r\phi,v=r} \\ \frac{d}{d\phi}\breve{S}_{\alpha,\kappa_0,D_{11}} = r\ \frac{d}{dw}\breve{T}_{\alpha,\kappa_0,D_{11}}(w,v,\theta)\Big|_{w=r\phi,v=r} \end{cases}$$

with $\breve{T}_{\alpha,\kappa_0,D_{11}}(r, r\phi, \theta) = \breve{S}_{\alpha,\{a_i\},D_{11}}(r\cos\phi, r\sin\phi, \theta)$ gives

$$\left(\partial_v + \theta\partial_w + \kappa_0\partial_\theta - D_{11}\partial_\theta^2 + \alpha\right)\breve{T}_{\alpha,\kappa_0,D_{11}} = \alpha\delta_e$$

and thereby by means of Theorem 22 we obtain the solution:

$$\boxed{\begin{aligned} \breve{S}_{\alpha,\kappa_0,D_{11}}(r,\phi,\theta) &= \breve{T}_{\alpha,\kappa_0,D_{11}}(r, r\phi, \theta) = \hat{S}_{\alpha,\kappa_0,D_{11}}(r, r\phi, \theta) \\ &= \alpha\tfrac{\sqrt{3}}{2\pi D_{11}r^2}e^{-\alpha r}\, e^{-\frac{3(\theta-2\phi)^2+(\theta-\kappa_0 r)^2}{4rD_{11}}}, \end{aligned}} \tag{4.131}$$

which is a fairly good approximation of the exact Green's function, recall (4.102), $(\mathbf{x}, e^{i\theta}) \mapsto S_{\alpha,\kappa_0,D_{11}}(r\cos\phi, r\sin\phi, e^{i\theta})$ with $\mathbf{x} = (r\cos\phi, r\sin\phi)$. This solution was first found (without derivation) by van Almsick et al.[123] where the solution was inspired by the approximative solution (also without derivation or reference to derivation, for $\kappa_0 = 0$) found by Thornber et al.[119].

4.9.3 Using Slope rather than Orientation

Although the approximation (4.127) leads to a nice analytic solution which is appropriate as long as[26] $\theta - \phi < \frac{\pi}{6} < \frac{\pi}{2}$, it has some serious consequences. First of all $r > 0$ becomes the evolution parameter, recall (4.119) and the first line of (4.131) and transportation of oriented particles is always along the positive direction $+\mathbf{e}_r$. This means that oriented particles are not

[26]The relative error $\frac{|(\theta-\phi)-\sin(\theta-\phi)|}{|\theta-\phi|} < 0.045$ if $|\theta-\phi| < \frac{\pi}{6}$.

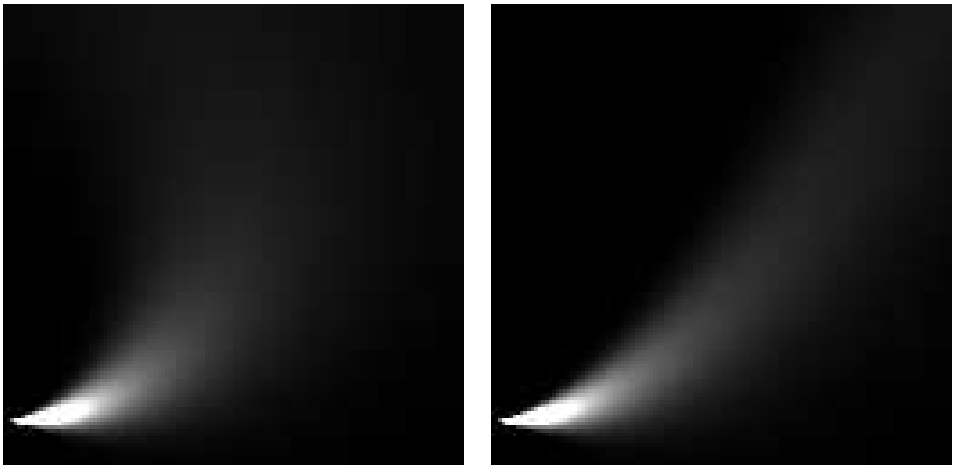

Figure 4.28: Left: density plot of the graph of $(x,y) \mapsto \int_{-\infty}^{\infty} \breve{S}_{\alpha=0.01,\kappa_0=1,D_{11}=0.5}(r,\phi,\theta)\ \mathrm{d}\theta = \frac{\sqrt{3\pi}\alpha}{2\sqrt{D_{11}}\pi r^{\frac{3}{2}}} e^{-\alpha r - \frac{3(r\kappa_0-2\phi)^2}{16 D_{11} r}}$. Right: density plot of the graph of $(x,y) \mapsto \int_{-\infty}^{\infty} \hat{S}_{\alpha=0.01,\kappa_0=1,D_{11}=0.5}(x,y,\theta)\ \mathrm{d}\theta = \int_{\mathbb{R}} T_{\alpha,\kappa_0,D_{11}}(x,y,\theta)\ \mathrm{d}\theta = \frac{1}{2}\alpha\, D_{11}\sqrt{\frac{3}{\pi}}\left(\frac{1}{D_{11}x}\right)^{3/2} e^{-x\alpha - \frac{3(-2y+\kappa_0 x^2)^2}{16 D_{11} x^3}}$, plotted for $0 < x < 2, -0.2 < y < 2$. See also figure 4.27 for a comparison between the modes.

allowed to travel in loops (which is possible, although very unlikely if D_{11} is small in the exact case). Suppose for instance that $(\theta - \phi)$ passes the boundaries $\pm\frac{\pi}{2}$, i.e. $|(\theta-\phi)| > \frac{\pi}{2}$, then in the exact solution an oriented particle with position $\mathbf{x} = (r\cos\phi, r\sin\phi)$ and orientation $e^{i\theta}$ is transported in a direction with negative radial component. However, in the approximative solution it would still be transported in a direction with positive radial component.

Secondly, because of the approximation we had to drop the periodic boundary conditions, which is somewhat unnatural.

To avoid these problems we consider the discrete stochastic proces with

$$\begin{cases} \tan\theta(s_i+\Delta s) = \tan\theta(s_i) + \Delta s\,(\kappa_0+\varepsilon), & \varepsilon \sim \mathcal{N}(0, N\sigma^2), \\ \mathbf{x}(s_i+\Delta s) = \mathbf{x}(s_i) + \Delta s\,\mathbf{e}_{r(s_i)} + \Delta s\,\tan\theta(s_i)\,\mathbf{e}_{\phi(s_i)} \\ \Delta s = \frac{L}{N}, \text{ with } L \sim NE(\alpha)\ . \end{cases} \tag{4.132}$$

with

$$\begin{array}{ll} r(s_k) & = \|\mathbf{x}(s_k) - \mathbf{x}(s_0)\|, \qquad s_k = s_0 + k*\Delta, k = 0,\ldots,N-1 \\ \phi(s_k) & = \angle(\mathbf{x}(s_k) - \mathbf{x}(s_0)), \\ \tan(\theta_0) & = \tan\left(\angle\mathbf{x}(s_0)\right), \end{array}$$

which is obtained from (4.125) by replacing the direction $e^{i\theta}$ by its corresponding slope $\beta = \tan\theta$. The Green's function of the resolvent $\bar{S}_{\alpha,\kappa_0,D_{11}} : [-\frac{\pi}{2},\frac{\pi}{2}] \times \mathbb{R}^2 \setminus \{0,0\} \to \mathbb{R}^+$ of the corresponding (forward) Kolmogorov equation (after taking the limit $N \to \infty$) satisfies the following equation

$$\left(1\,\partial_r + \frac{1}{r}(\beta-\phi)\partial_\phi + \kappa_0\partial_\beta - D_{11}(\partial_\beta)^2 + \alpha I\right)\bar{S}_{\alpha,\kappa_0,D_{11}} = \alpha\,\delta_e\ , \beta = \tan\theta, \tag{4.133}$$

where $D_{11} = \frac{1}{2}\sigma^2$ and therefore again by Theorem 22 we obtain

$$\boxed{\bar{S}_{\alpha,\kappa_0,D_{11}}(x,y,\theta) = \breve{S}(r,\phi,\tan\theta) = \alpha\frac{\sqrt{3}}{2\pi D_{11} r^2} e^{-\alpha r}\, e^{-\frac{3((\tan\theta)-2\phi)^2+((\tan\theta)-\kappa_0 r)^2}{4rD_{11}}},} \tag{4.134}$$

with $(x,y) = (r\cos\phi, r\sin\phi)$.
Remarks:

- The diffusion in $\beta = \tan\theta$ prevents that the oriented particle (starting at e), reaches the singular values $\theta = \pm\frac{\pi}{2}$, which coincides with the fact that $\bar{S}_{\alpha,\kappa_0,D_{11}}(x,y,\theta) \to 0$ uniformly on $\mathbb{R}^2$ as $\theta \to \pm\frac{\pi}{2}$.
- If the orientation score $U_f = \mathcal{W}_\psi[f]$ is constructed with an even wavelet, i.e. $\psi(\mathbf{x}) = \psi(-\mathbf{x})$ for all $\mathbf{x} \in \mathbb{R}^2$, from image $f \in \mathbb{L}_2(\mathbb{R}^2)$, then we may as well restrict θ to the interval of $(-\frac{\pi}{2}, \frac{\pi}{2})$. In this case $\beta = \tan\theta \in (-\infty, \infty)$, which solves the problem concerning the boundary conditions.
- Again one can set $v = r$, $w = r\phi$ and $\bar{T}(v,w,\theta) = \bar{S}_{\alpha,\kappa_0,D_{11}}(r\cos\phi, r\sin\phi, \theta)$ in this case we have by (4.133) that

$$\left(1\,\partial_v + \beta\,\partial_w + \kappa_0\partial_\beta - D_{11}(\partial_\beta)^2 + \alpha I\right)\bar{T}_{\alpha,\kappa_0,D_{11}} = \alpha\,\delta_e\ , \beta = \tan\theta. \tag{4.135}$$

- In stead of the Euclidean motion group $G = \mathbb{R}^2 \rtimes \mathbb{T}$ we consider the Lie-group of Heisenberg type, $H = \mathbb{R}^2 \rtimes \mathbb{R}$ (also of dimension 3) defined by

$$(\mathbf{v}_1,\beta_1)(\mathbf{v}_2,\beta_2) = (\mathbf{v}_1 + M_{\beta_1}\mathbf{v}_2, \beta_1+\beta_2), \text{ with } M_\beta = \begin{pmatrix} 1 & \beta \\ 0 & 1 \end{pmatrix},$$

with $\mathbf{v}_i = (v_i, w_i) = v^i\mathbf{e}_v + w^i\mathbf{e}_w, \in \mathbb{R}^2, i = 1,2$. Let $\mathcal{R}$ be the right-regular representation of H onto $\mathbb{L}_2(H)$, then the left invariant vector fields of H are given by

$$\begin{aligned} B_1 &= \mathrm{d}\mathcal{R}(0,0,1) = \partial_\beta. \\ B_2 &= \mathrm{d}\mathcal{R}(0,1,0) = \beta\partial_w + \partial_v, \\ B_3 &= \mathrm{d}\mathcal{R}(1,0,0) = \partial_v, \end{aligned}$$

The operator $-\kappa B_1 - B_2 + D_{11}(B_1)^2$ equals the generator of the forward Kolmogorov equation whose resolvent is given by (4.135). The exact solution of the resolvent equation

$$(\kappa B_1 + B_2 - D_{11}(B_1)^2 + \alpha I)W = B_f, \quad B_f \in C^\infty(H) \cap \mathbb{L}_2(H) \tag{4.136}$$

is given by a H-convolution with the Green's function, i.e. $W = \bar{S}_{\alpha,\kappa_0,D_{11}} *_H B_f$, rather than a G convolution.[27] Notice that

$$\tan(\theta_1+\theta_2) = \frac{\tan(\theta_1)+\tan(\theta_2)}{1-\tan(\theta_1)\tan(\theta_2)},$$

so if we set $\theta = \theta_1 + \theta_2$ we have $\beta = \tan\theta = (\beta_1+\beta_2)(1+O(\beta_1\beta_2))$, with $\beta_i = \tan\theta_i$, $i = 1,2$. Furthermore we notice that

$$(\cos\theta)^{-1}\partial_\xi = \partial_x + (\tan\theta)\partial_y.$$

[27] This is useful if in stead of an orientation score U_f, we construct a slope score B_f, i.e. it is given by $B_f(h) = \mathcal{W}_\psi[f](h) = (\mathcal{U}_h\psi, f), h \in H$, with $\mathcal{U}_h\psi(\mathbf{v}) = \psi(M_\beta^{-1}(\mathbf{v}-\mathbf{b}))$, $\mathbf{v} \in \mathbb{R}^2$.

So as long as U_f is smooth and supported in a small area around the origin (in particular an area with $|\theta| << 1$ and thereby $|\beta| << 1$) the H convolution can be used as an approximation of the G convolution.

- A different approach to deal with an analytic approximation of the solution of the objective by (4.102), with no angular drift (i.e. this approach one works if $a_1 = 0$) is to apply the substitution $\beta = \tan\theta$ directly from the beginning in which case (4.102) becomes (after dividing by $\cos\alpha$):

$$\left(\partial_x + \beta\partial_y - D_{11}2\beta(1+\beta^2)^{\frac{3}{2}}\partial_\beta - D_{11}(1+\beta^2)^{\frac{5}{2}} + \alpha(1+\beta^2)^{-\frac{1}{2}}\right) S_{\alpha,\{0,1,0\},\{D_{11},0,0\}} = \alpha\,\delta_e.$$

Again application of a first order Taylor approximation (but now in $\beta = \tan\theta$ rather than θ) of the coefficients of the generator, yields

$$(\partial_x + \beta\partial_y - 2D_{11}\beta\partial_\beta) - D_{11} + \alpha\hat{S}_{\alpha,\{a_i\},\{D_{ii}\}} = \alpha\,\delta_e. \tag{4.137}$$

Here again $z\partial_y$, $z\partial_z$, $\partial_z^2, \partial_y\partial_z, \partial_y^2$ form a 5 dimensional nil-potent Lie-algebra and again by [125]Theorem 3.18.11,p.243 (to relate coordinates of the first and second kind) one can solve for this equation following exactly the same line as in theorem 22, yielding

$$\hat{S}_{\alpha,\{0,1,0\},\{D_{11},0,0\}}(x,y,e^{i\theta}) = \alpha e^{-\alpha x}\,\frac{D_{11}\,e^{\frac{e^{-2xD_{11}}\left(-4e^{2xD_{11}}\theta(\theta+y2D_{11})+(\theta+2D_{11}y)^2-e^{4xD_{11}}(-3\theta^2+4\theta(-y+x\theta)D_{11}+4y^2D_{11}^2)\right)}{8\sinh(xD_{11})(2xD_{11}\cosh(xD_{11})-2\sinh(xD_{11}))}}}{\pi\sqrt{2e^{2xD_{11}}+e^{4xD_{11}}(-1+xD_{11})-(1+xD_{11})}}$$

The detailed derivation (using the adjoint representation of an extension of the involved 5 dimensional Lie-algebra to relate the coordinates of the first and second kind) will appear Appendix C in the thesis[28] by van Almsick[122], who used theorem 22 as a source of inspiration. Notice that the difference with respect to (4.136) is that the diffusion in $\beta = \tan\theta$ in (4.136) is replaced by diffusion in θ.

4.9.4 Evolution Equations Corresponding to Left Invariant Stochastic Processes on the 3D Euclidean Motion Group

In this subsection we consider all linear left invariant evolutions on $\mathbb{L}_2(G)$, $G = \mathbb{R}^3 \rtimes SO(3)$, (and in particular their restrictions to the linear subspace $\mathbb{C}_K^G$ of orientation scores of 3D images). Again we follow the same line as in the previous subsections where we considered all linear left invariant evolution equations on orientation scores of $2D$-images. Here we do not provide elegant analytic approximations of the corresponding Green's functions: We only **formulate** the resolvent equations, which (at first sight) seem to be much more difficult to deal with as the resolvent equations in the $2D$-case and are a challenge for future work.

The product on the 3D-Euclidean motion group $G = \mathbb{R}^3 \rtimes SO(3)$ is given by

$$gg' = (\mathbf{b}, R)(\mathbf{b}', R') = (\mathbf{b} + R\mathbf{b}', RR'), \qquad g, g' \in \mathbb{R}^3 \rtimes SO(3).$$

[28] Markus van Almsick and the author of this thesis closely cooperated on the subject of analytic approximations of left invariant processes on the Euclidean motion group. We certainly recommend his thesis, cf.[122], especially to (applied) physicists in the image analysis community.

Again we use the right invariant representation $\mathcal{R}$ of G onto $\mathbb{L}_2(G)$ to obtain a basis of the 6 dimensional Lie-Algebra $\mathcal{L}(G)$ of left invariant vector fields. To this end we first recall that the exponential maps $\exp_{SO(3)} : so(3) \to SO(3)$ and $\exp_{\mathbb{R}^3} : \mathbb{R}^3 \to \mathbb{R}^3$ are respectively given by $\exp_{SO(3)}(X_a) = I + \frac{\sin(\|\mathbf{a}\|)}{\|\mathbf{a}\|} X_a + \frac{1-\cos(\|\mathbf{a}\|)}{\|\mathbf{a}\|^2}(X_a)^2$, with $X_{\mathbf{a}}(\mathbf{x}) = \mathbf{a} \times \mathbf{x}$ and $\exp_{\mathbb{R}^3}(\mathbf{x}) = \mathbf{x}$ and then notice that

$$\exp_G(0, X) = (0, \exp_{SO(3)}(X)) \text{ for all } X \in so(3)$$
$$\exp_G(\mathbf{x}, 0) = (\mathbf{x}, I) \text{ for all } \mathbf{b} \in \mathbb{R}^3$$

Consequently, we have

$$\begin{aligned}(\mathrm{d}\mathcal{R}(0,X)\Phi)(\mathbf{b},R) &= \tfrac{d}{dt}\Phi((\mathbf{b},R)\exp_G(0,tX))\big|_{t=0} = \tfrac{d}{dt}\Phi((\mathbf{b},R)(\mathbf{0},tX))\big|_{t=0} \\ &= \tfrac{d}{dt}\Phi((\mathbf{b},RtX))\big|_{t=0} = \left[(I \otimes \mathrm{d}\mathcal{R}_{SO(3)}(X))\Phi\right](\mathbf{b},R),\end{aligned}$$

where $\mathcal{R}_{SO(3)}$ is the right regular representation of $SO(3)$ on $\mathbb{L}_2(SO(3))$. By choosing $X = X_{\mathbf{e}_i}$, $i = 1, 2, 3$ we obtain 3 independent left invariant vector fields,

$$\begin{aligned}\mathcal{A}_1 &= \cot\beta\,\cos\gamma\,\tfrac{\partial}{\partial\gamma} - \tfrac{\cos\gamma}{\sin\beta}\,\tfrac{\partial}{\partial\alpha} + \sin\gamma\,\tfrac{\partial}{\partial\beta} \\ \mathcal{A}_2 &= -\cot\beta\,\sin\gamma\,\tfrac{\partial}{\partial\gamma} + \tfrac{\sin\gamma}{\sin\beta}\,\tfrac{\partial}{\partial\alpha} + \cos\gamma\,\tfrac{\partial}{\partial\beta} \\ \mathcal{A}_3 &= \tfrac{\partial}{\partial\gamma}\end{aligned}$$

For more details see [15]Chapter 9.10. Moreover we have

$$(\mathrm{d}\mathcal{R}(\mathbf{x},0)\Phi)(\mathbf{b},R) = \frac{d}{dt}\Phi((\mathbf{b},R)(t\mathbf{x},I))\bigg|_{t=0} = \frac{d}{dt}\Phi((\mathbf{b}+t\mathbf{x},R))\bigg|_{t=0} = R^T\left[(\nabla \otimes I)\Phi(\mathbf{b},R)\right].$$

So by choosing $X = X_{\mathbf{e}_i}$, $i = 1, 2, 3$, we obtain 3 more independent left[29] invariant vector fields[30]

$$\begin{aligned}\tilde{A}_4 &= \tfrac{\partial}{\partial\xi} = \sin\beta\cos\gamma\,\partial_x + \sin\beta\sin\gamma\,\partial_y + \cos\beta\,\partial_z \\ \tilde{A}_5 &= \tfrac{\partial}{\partial\eta_1} = -\sin\gamma\,\partial_x + \cos\gamma\,\partial_y \\ \tilde{A}_6 &= \tfrac{\partial}{\partial\eta_2} = \cos\gamma\cos\beta\,\partial_x + \sin\gamma\cos\beta\,\partial_y - \sin\beta\,\partial_z\end{aligned}$$

where ξ is along the preferred direction $\mathbf{e}_\xi = R(\alpha,\beta,\gamma)\mathbf{e}_z$, with Euler angles α, β, γ, recall (4.65) and η_1 and η_2 are orthogonal to the preferred direction.

The linear left invariant 2nd order evolution equations (with constant coefficients) are generated by

$$\mathcal{A} = \sum_{i=1}^{6}(-a_i)\mathcal{A}_i + D_{ij}\mathcal{A}_i\mathcal{A}_j,$$

again we only consider the case $D_{ij} = D_{ii}\delta_{ij}$. The vector (a_1, a_2, a_3) denotes the direction of transport of an oriented particle, it seems most reasonable to set $a_2 = a_3 = 0$ and $a_1 = 1$, in which case the oriented particle moves with unit speed along the preferred direction $\mathbf{e}_\xi$. The vector (a_4, a_5, a_6) determines the (initial) 3D-curvature vector of the path of an oriented particle. For the sake of simplicity we set $a_4 = 0, a_5 = 0, a_6 = 0$. The vector (D_{11}, D_{22}, D_{33}) sets the diffusion in space, where we put $0 \leq D_{22} = D_{33} \leq D_{11}$ since this leads to (an)isotropic diffusion (along the preferred direction $\mathbf{e}_\xi$) and we do not want to make an a priori distinction between η_1 and η_2 (To this end we notice that a 3D orientation score, is constructed by a

[29] One may aspect the angular momentum operators $L_{\mathbf{a}} = \mathbf{a} \times \nabla$, but these are constructed by the left regular representation $\mathcal{L}$ and thereby they are **right** invariant, see [15]Chapter 10.5

[30] The 3D orientation scores do not depend on α, so we may omit the derivatives with respect to α

wavelet that is rotation invariant around the z-axis). The vector (D_{44}, D_{55}, D_{66}) determines the amount of diffusion in $SO(3)$. For the sake of simplicity we put $D_{44} = D_{55} = D_{66}$ which leads to the Laplace Beltrami-operator on the 2-sphere:

$$\sum_{i=4}^{6}(\mathcal{A}_i)^2 = (\partial_\beta)^2 + \frac{1}{\sin^2\beta}\,(\partial_\gamma)^2 + \cot\beta\frac{\partial}{\partial\beta} = \Delta_{LB}.$$

These observations lead to the following resolvent equation

$$(\partial_\xi - D_{44}\Delta_{LB} - D_{11}(\partial_\xi)^2 - D_{22}\Delta_{\eta_1,\eta_2} + \alpha I)W = \frac{1}{\alpha}\,U_f,$$

with $U_f \in \mathbb{L}_2(G)$, or more explicitly for the case $D_{11} = D_{22} = 0$:

$$\left(\sin\beta\cos\gamma\,\partial_x + \sin\beta\sin\gamma\,\partial_y + \cos\beta\,\partial_z - D_{44}\left((\partial_\beta)^2 + \frac{1}{\sin^2\beta}\,(\partial_\gamma)^2 + \frac{\cos\beta}{\sin\beta}\partial_\beta\right) + \alpha I\right)W = \frac{1}{\alpha}\,U_f.$$

Finding the Green's function (or analytic approximation of the Green's function) of this PDE is much more difficult than in the 2D-case.

4.10 Evolution Equations Corresponding to Left Invariant Stochastic Processes on the Similitude Group

In the current framework of image processing via left-invariant evolutions on orientation scores, the scale is fixed. The time parameter (or rather the lifetime α) in the evolution processes on the orientation scores does induce a notion of scale, but the orientation scores are constructed by a single scale oriented wavelet. In some applications (for example blood vessels in retinal images) the line-structures that are to be enhanced/completed have a varying thickness, see Figure 4.29. In such a case the wavelet ψ must be dilated to obtain good initial measurements (inducing a so-called initial scale) before the left invariant evolutions/stochastic processes can be used for perceptual organization purposes such as enhancement, completion and/or infilling.

Thereby we combine the concept of a scale space with the concept of an orientation score by using the left regular action of the similitude group $\tilde{G}$ (rather than the left regular action of the Euclidean motion group G) onto $\mathbb{L}_2(\mathbb{R}^2)$ and construct multi scale orientation scores. As mentioned before, in image analysis wavelet transforms are usually constructed by including the scaling group.

However, as we pointed out in Theorem 19 and Corollary 5, in contrast to the usual approaches we are able to get a stable reconstruction from each fixed scale layer (without using the lower scales) in the wavelet domain.

A multi-scale orientation score is constructed by means of

$$\mathcal{W}_\psi[f](\tilde{g}) = (\mathcal{U}_{\tilde{g}}\psi, f) = \frac{1}{\sqrt{a}}\int_{\mathbb{R}^2}\overline{\psi\left(a^{-1}\left(\mathbf{x}-\mathbf{b}\right)\right)}f(\mathbf{x})\,\mathrm{d}\mathbf{x}, \quad \tilde{g} = (\mathbf{b}, e^{i\theta}, a) \in \tilde{G} = \mathbb{R}^2 \rtimes \mathbb{T} \rtimes \mathbb{R}^+,$$

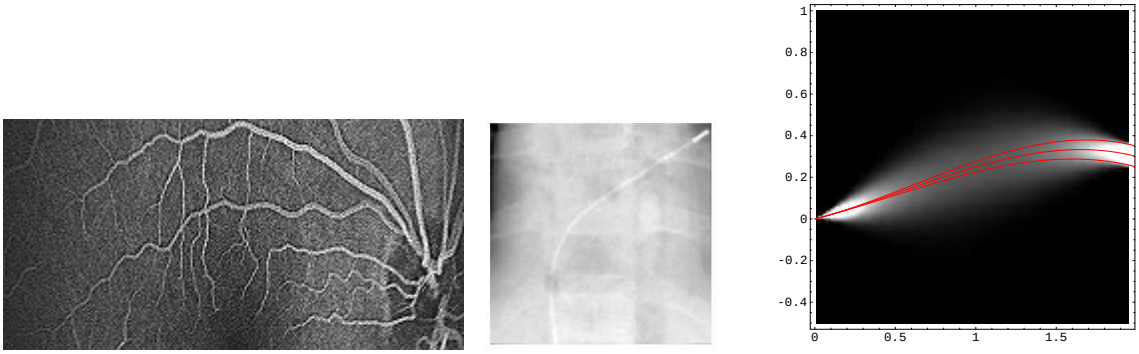

Figure 4.29: Left: Medical imaging example (bloodvessels in the retina), where the scale of the lines slightly varies. Middle: Medical image example (guidewire), where the scale of the lines is fixed. Right: A completion field between a thick and a thin oriented structure (naively obtained by $\hat{S}_{D,\alpha;x_0,y_0,\theta_0}(x,y,\theta)\frac{1}{2d}\int_{-d}^{d}\hat{S}_{D,\alpha;x_1,y+z,\theta_1}(-x,y,-\theta)\mathrm{d}z)$, plotted together with the modes of $(x,y,\theta)\mapsto \hat{S}_{D,\alpha;x_0,y_0,\theta_0}(x,y,\theta)\hat{S}_{D,\alpha;x_0,\tilde{y},\theta_0}(-x,y,-\theta)$, for $\tilde{y}=y_0$ and $\tilde{y}=y_0\pm d$, where $d>0$ represents the relative scale of thickness.

where the left regular action $\mathcal{U}:\tilde{G}\to\mathcal{B}(\mathbb{L}_2(\tilde{G}))$ of the similitude group $\tilde{G}=SIM(2)=\mathbb{R}^2\rtimes\mathbb{T}\times\mathbb{R}^+$ with group product

$$\tilde{g}\tilde{g}'=(\mathbf{b},e^{i\theta},a)(\mathbf{b}',e^{i\theta'},a')=(\mathbf{b}+a\,R_\theta\mathbf{b}',e^{i(\theta+\theta')},a\,a'),$$

is given by

$$(\mathcal{U}_{\tilde{g}}\psi)(\mathbf{x})=\psi\left(a^{-1}R_\theta^{-1}(\mathbf{x}-\mathbf{b})\right),$$

for almost every $\mathbf{x}\in\mathbb{R}^2$.

Let $\mathcal{R}:\tilde{G}\to\mathcal{B}(\mathbb{L}_2(\tilde{G}))$ be the right regular representation of the similitude group $\tilde{G}$ onto $\mathbb{L}_2(\tilde{G})$. Then we derive the following basis of left invariant vector fields on the similitude group:

$$\begin{aligned}\mathrm{d}\mathcal{R}(1,0,0,0)&=\partial_\theta\\ \mathrm{d}\mathcal{R}(0,1,0,0)&=a\,\partial_\xi\\ \mathrm{d}\mathcal{R}(0,0,1,0)&=a\,\partial_\eta\\ \mathrm{d}\mathcal{R}(0,0,0,1)&=a\,\partial_a=\partial_\tau,\end{aligned}$$

where the so-called log-scale $\tau=\log a,(\Leftrightarrow a=e^\tau)$ is the logarithm of scale. Notice the $a=e^\tau$ term in front of ∂_ξ and ∂_η, makes also sense from the physical point of view as oriented particles in a coarse scale orientation score are supposed to move faster than oriented particles in a fine scale orientation score.

We are interested in a profound mathematical approach to multi-scale completion fields, (i.e. $\tilde{G}$-convolution kernels) in the similitude group $\tilde{G}$, see Figure 4.29 to get a rough idea of how such a completion field (after an inverse wavelet transformation, or after integration over orientation and scale) is supposed to look like.

Therefore we consider (analogous to the previous subsections) the resolvents of linear left invariant evolution processes on the multi-scale orientation scores, i.e. evolution processes $\Phi:\mathbb{L}_2(\tilde{G})\to\mathbb{L}_2(\tilde{G})$ with the property that

$$\Phi\circ\mathcal{L}_{\tilde{g}}=\mathcal{L}_{\tilde{g}}\circ\Phi\ ,$$

for all $\tilde{g} \in \tilde{G}$, where

$$\mathcal{L}_{\tilde{g}}\Phi(\tilde{h}) = \Phi(\tilde{g}^{-1}\tilde{h}) \ , \text{ for almost every } \tilde{h} \in \tilde{G}.$$

These resolvent equations are given by

$$W = -\alpha(\tilde{A} - \alpha I)^{-1}U_f \ , \tag{4.138}$$

where $U_f(\tilde{g}) = \mathcal{W}_\psi[f](\tilde{g})$ for all $\tilde{g} \in \tilde{G}$ and where

$$\tilde{A} = -e^{\tau}\partial_\xi + D_{44}(\partial_\tau)^2 + D_{11}(\partial_\theta)^2 - \kappa_0\partial_\theta.$$

If $D_{44} = 0$ we end up in the situation of the direction process with angular drift κ_0, with which we dealt in the previous subsections. If $D_{44} > 0$, the extra term $D_{44}(\partial_\tau)^2$ takes care of a diffusion over log-scale.

Again we can compute completion fields, by considering the probability that grey-value particles (with identical position, orientation and scale) of a forward (generated by $\tilde{A}$) and backward process (generated by $\tilde{A}^*$) collide. Again this boils down to computation of

$$\Phi(U_f) = \alpha^2(\tilde{A} - \alpha I)^{-1}U_f(\tilde{A}^* - \alpha I)^{-1}U_f. \tag{4.139}$$

The marginal over scale and orientation of such a completion field is given by

$$\mathbf{b} \mapsto \alpha^2 \int_0^\infty \int_{-\pi}^{\pi} (\tilde{A} - \alpha I)^{-1}U_f(\mathbf{b}, e^{i\theta}, a)\ (\tilde{A}^* - \alpha I)^{-1}U_f(\mathbf{b}, e^{i\theta}, a)\ \mathrm{d}\theta \frac{\mathrm{d}a}{a}.$$

However, regarding the fact that blood vessels bifurcate (inducing abrupt changes in scale), see for example figure 4.29, it is reasonable to compute the probability of collision of particles of both processes where the position and orientations are identical, but where the scales may differ. To include this into our model we compute the left invariant completion field

$$\int_{\mathbb{R}} \alpha^2(\tilde{A} - \alpha I)^{-1}U_f(\mathbf{b}, e^{i\theta}, e^{\tau})(\tilde{A}^* - \alpha I)^{-1}U_f(\mathbf{b}, e^{i\theta}, e^{\tau'})q(\tau - \tau')\ \mathrm{d}\tau', \tag{4.140}$$

with marginal (over scale and orientation)

$$\mathbf{b} \mapsto \int_{\mathbb{R}} \int_{\mathbb{R}} \int_{-\pi}^{\pi} \alpha^2(\tilde{A} - \alpha I)^{-1}U_f(\mathbf{b}, e^{i\theta}, e^{\tau})(\tilde{A}^* - \alpha I)^{-1}U_f(\mathbf{b}, e^{i\theta}, e^{\tau'})q(\tau - \tau')\ \mathrm{d}\tau'\mathrm{d}\tau\mathrm{d}\theta, \tag{4.141}$$

where τ is log-scale, i.e. $a = e^{\tau}$, and where $q : \mathbb{R} \to \mathbb{R}^+$ is some probability function, i.e. $q \geq 0$ and $\|q\|_{\mathbb{L}_1(\mathbb{R})} = 1$ on $\mathbb{R}$. The probability density of collision of two particles (with different scales $a > 0$ and $a' > 0$) given the fact that they have the same position and orientation, is given by $q(\tau - \tau')$. Notice that in case the probability measure is a Dirac measure, i.e. $q(\tau - \tau') = \delta(\tau - \tau')$, (4.140) reduces to (4.139) and thereby end up in the old situation. On the other hand if q is uniformly distributed over some interval, particles have no preference of the scales within that interval. To model the cases in between q can (for example) be a 1D-Gaussian distribution or rather its Laplace-transform with respect to scale $s = \frac{1}{2}\sigma^2$ given by (4.144) below.

The Green's function of (4.138) is by the Hörmander Theorem smooth on $\tilde{G} \setminus \tilde{e}$, where $\tilde{e} = (0,0,1,1)$ equals the unity element and it is given by

$$\boxed{-(\tilde{A} - \alpha I)\tilde{S}_{\alpha,\kappa_0,D_{11},D_{44}} = \left(e^{\tau}\partial_\xi + \kappa_0\partial_\theta - D_{11}(\partial_\theta)^2 - D_{44}(\partial_\tau)^2\right)\tilde{S}_{\alpha,\kappa_0,D_{11},D_{44}} = \alpha\delta_{\tilde{e}}.}$$

As we will show in the next two subsections the Green's function can again be analytically approximated in case $D_{44} = 0$ and in the cases $\kappa_0 = 0$, $D_{11} = 0$ we derive the exact solutions.

4.10.1 Green's Functions for the Cases $D_{44} = 0$

In the case $D_{44} = 0$, we have no diffusion over scale, then by Theorem 22 and (4.134) we directly deduce after the substitution $x \mapsto \frac{x}{a}$, $y \mapsto \frac{y}{a}$ that a good analytic approximation of the Green's function is given by

$$\tilde{S}_{\alpha,\kappa_0,D_{11},D_{44}=0}(x,y,\theta,a) \approx \breve{S}(\frac{r}{a},\phi,\tan\theta) = \alpha\frac{\sqrt{3}a^2}{2\pi D_{11}r^2}e^{-\alpha\frac{r}{a}}\,e^{-\frac{3a\,((\tan\theta)-2\phi)^2+((\tan\theta)-\kappa_0\frac{r}{a})^2}{4rD_{11}}}, \tag{4.142}$$

with $(x,y) = (r\cos\phi, r\sin\phi)$.

It is interesting (but also difficult) to deal with the case $D_{11} > 0, D_{44} > 0$ as well, as $D_{44} > 0$ takes care of diffusion (over scale $a > 0$) between orientation scores at different scales $a > 0$. For practical purposes, however, it may be sufficient to put $D_{44} = 0$ and (if necessary) to apply the diffusion over log-scale, $\tau = \log a \in \mathbb{R}$, *afterwards*, i.e. solve for

$$\begin{aligned} W &= \beta\alpha\left(-D_{44}(a\partial_a)^2 + \beta\right)^{-1}\left(a\partial_\xi + \kappa_0\partial_\theta - D_{11}(\partial_\theta)^2 + \alpha\right)^{-1}U_f \\ &= (K_\beta *_{\mathbb{R}} (\tau' \mapsto (\tilde{S}_{\alpha,\kappa_0,D_{11},D_{44}=0} *_G U_f(\cdot,\cdot,e^{\tau'}))(\mathbf{b}, e^{i\theta})))(\tau), \end{aligned} \tag{4.143}$$

with convolution kernel $K_\beta : \mathbb{R}^+ \to \mathbb{R}$ is given by

$$K_\beta(\tau) = \frac{e^{-\sqrt{\beta}|\tau|}}{\beta}\sqrt{\frac{\pi}{2\,\beta}}, \tag{4.144}$$

and where we stress that the smoothing parameter $\beta > 0$ need not be equal to $\alpha > 0$. Furthermore we notice that if one is only interested in the completion field integrated over scale, the diffusion over log-scale *afterwards* does not make a difference, unless the 2 resolvent operators in (4.143) are iterated. In Figure 4.30 we use (4.142) to compute the completion field marginal (4.141) (with q is uniformly distributed) for artificial orientation scores consisting of two Dirac distributions on $\tilde{G}$.

4.10.2 Green's functions for the cases $\kappa_0 = 0$, $D_{11} = 0$.

The next theorem gives the exact analytic solution of the Green's functions for the case $\kappa_0 = 0$, $D_{11} = 0$. We note that the result also applies to left invariant evolutions on wavelet transforms constructed by left regular actions of the $ax + b$-group on $\mathbb{L}_2(\mathbb{R})$, recall Theorem 16.

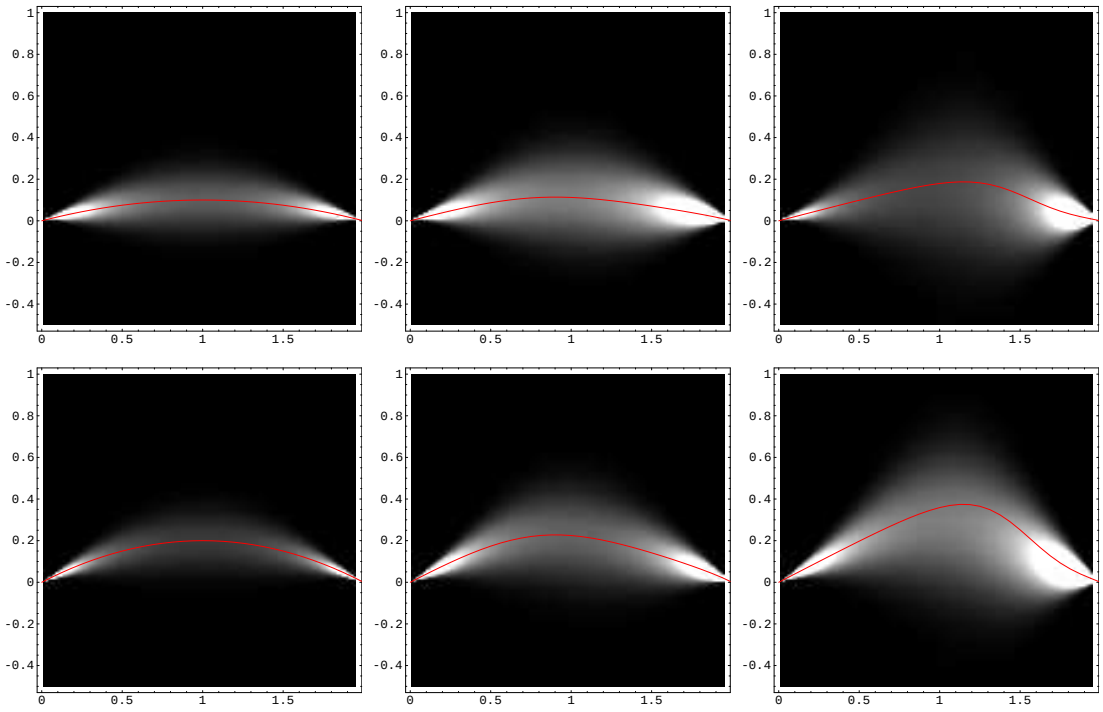

Figure 4.30: The completion field marginal (4.141) (with q is uniformly distributed) of the stochastic process generated by $-a\partial_\xi + D_{11}(\partial_\theta)^2$, so $D_{44} = 0$, applied on artificial orientation scores consisting of two Dirac distributions $\delta(x, y, \theta - \theta_0, 1) + \delta(x - 2, y, \theta + \theta_0 - \pi, a)$ for $\theta_0 = 0.2$ (top row) and $\theta_0 = 0.4$ (bottom row) and $a = 1$ (first column), $a = \frac{1}{4}$ (second column), $a = \frac{1}{16}$ (second column). Remark: The width of the tails of the completion field is inverse proportional to the scale of the oriented particles. The larger the scale of an oriented particle, the longer (and the narrower) the tail.

Theorem 23 *The solution (Green's function)* $\tilde{S}_{\alpha,D_{44}} : \mathbb{R}^+ \times \mathbb{R}^+ \to \mathbb{R}^+$ *of*

$$-\left(\tilde{A}\Big|_{\kappa=0,D_{11}=0} - \alpha I\right)\tilde{S}_{\alpha,D_{44};\,\xi_0,a_0} = \left(e^{\tau}\partial_\xi - D_{44}(\partial_\tau)^2 + \alpha I\right)\tilde{S}_{\alpha,D_{44};\,\xi_0,a_0} = \alpha\,\delta_{\tilde{g}_0}, \qquad (4.145)$$

with $\tau = \log a$*, is infinitely differentiable on* $\mathbb{R}^+ \times \mathbb{R}^+ \setminus \tilde{g}_0$*, with* $\tilde{g}_0 = \{\xi_0, a_0\}$*, and is given by*

$$\tilde{S}_{\alpha,D_{44};\,\xi_0,a_0}(\xi,a) = 2\alpha\, a_0 \left[\mathcal{H}_{\sqrt{\frac{2\alpha}{D_{44}}}}\left(\rho \mapsto e^{-\rho^2 D_{44}(\xi-\xi_0)} J_{\frac{2\alpha}{D_{44}}}(2\sqrt{a_0}\rho)\right)\right](\xi-\xi_0)$$

where the Hankel Transform is given by

$$[\mathcal{H}_{\sqrt{\frac{2\alpha}{D_{44}}}} f](\xi) = \int_0^\infty J_{\sqrt{\frac{2\alpha}{D_{44}}}}(\rho\,\xi)\, f(\rho)\, \rho \mathrm{d}\rho, \qquad \xi > 0. \qquad (4.146)$$

A more explicit form of the solution $\tilde{S}_{\alpha,D_{44};\,\xi_0,a_0}(\xi,a)$ *is given by*

$$\begin{aligned}\tilde{S}_{\alpha,D_{44};\,\xi_0,a_0}(\xi,a) = \quad & \alpha \sum_{m=0}^{\infty} \frac{(-1)^m}{m!\,\Gamma\left(1+\sqrt{\frac{2\alpha}{D_{44}}}\right)} \\ & (a_0)^{m+\sqrt{\frac{\alpha}{2D_{44}}}+1}\left(\frac{a}{D_{44}(\xi-\xi_0)}\right)^{\sqrt{\frac{\alpha}{2D_{44}}}} \frac{M(m+1+\sqrt{\frac{2\alpha}{D_{44}}},\sqrt{\frac{2\alpha}{D_{44}}}+1,-\frac{a}{D_{44}(\xi-\xi_0)})}{((\xi-\xi_0)D_{44})^{m+1+\sqrt{\frac{\alpha}{2\,D_{44}}}}},\end{aligned} \qquad (4.147)$$

where $(a,b,z) \mapsto M(a,b,z) = \sum_{m=0}^{\infty} \frac{(a)_n z^n}{(b)_n n!}$*, with* $(a)_n = \frac{\Gamma(a+n)}{\Gamma(a)}$*, is the Kummer function.*

Proof

Without loss of generality put $\xi_0 = 0$. The left invariant Haar measure on the similitude group $G = \mathrm{SIM}(2)$ is given by

$$\frac{1}{2\pi}\frac{\mathrm{d}a}{a^2}\mathrm{d}a\;\mathrm{d}\theta\;\mathrm{d}\mathbf{b}\,.$$

As a result the left invariant Haar measure on the subgroup $\mathbb{R}^+ \rtimes \mathbb{R}^+$ with product $(\xi_1,a_1)(\xi_2,a_2) = (\xi_1 + a_1\xi_2, a_1a_2)$, is given by $\frac{\mathrm{d}a}{a^2}\,\mathrm{d}\xi$, therefore (4.145) reads

$$(a\partial_\xi - D_{44}(a\partial_a)^2 + \alpha I)\tilde{S}_{\alpha,D_{44};\,\xi_0,a_0} = \left(e^{\tau}\partial_\xi - D_{44}(\partial_\tau)^2 + \alpha I\right)\tilde{S}_{\alpha,D_{44};\,\xi_0,a_0} = \alpha\,(a_0)^2\delta(\xi-0)\delta(a-a_0),$$

Following the same line as in the proof of theorem 22 (between (4.117) and (4.118)) we obtain the evolution system

$$\begin{cases} \partial_\xi \tilde{S}_{\alpha,D_{44};\,\xi_0,a_0} = \left(\frac{D_{44}}{a}(a\partial_a)^2 - \frac{\alpha}{a}I\right)\tilde{S}_{\alpha,D_{44};\,\xi_0,a_0} \\ \lim\limits_{\xi\downarrow 0} \tilde{S}_{\alpha,D_{44};\,\xi_0,a_0}(\xi,\cdot) = \alpha\, a_0 \delta_{a_0}, \end{cases}$$

in which we apply the substitution $b = 2\sqrt{a}$, $\tilde{T}_{\alpha,D_{44}}(\xi,2\sqrt{a}) = \tilde{S}_{\alpha,D_{44};\,\xi_0,a_0}(\xi,a)$, yielding

$$\begin{cases} \partial_\xi \tilde{T}_{\alpha,D_{44}} = D_{44}\left((\partial_b)^2 + \frac{1}{b}\,\partial_b - \frac{\alpha}{D_{44}}\left(\frac{2}{b}\right)^2\right)\tilde{T}_{\alpha,D_{44}} \\ \lim\limits_{\xi\downarrow 0} \tilde{T}_{\alpha,D_{44}}(\xi,\cdot) = \alpha\,\frac{b_0}{2}\delta_{b_0}, \end{cases}$$

with $b_0 = 2\sqrt{a_0}$. Next we notice that application of the Hankel transform (4.146) to the generator gives

$$\mathcal{H}_{\sqrt{\frac{2\alpha}{D_{44}}}}\left[b \mapsto D_{44}\left((\partial_b)^2 + \frac{1}{b}\,\partial_b - \frac{\alpha}{D_{44}}\left(\frac{2}{b}\right)^2\right) f\right](\rho) = -D_{44}\,\rho^2\,[\mathcal{H}_{\sqrt{\frac{2\alpha}{D_{44}}}} f](\rho),$$

for all $f \in \mathbb{H}_2((0,\infty);\mathrm{r}\,\mathrm{dr})$ and application to the initial condition gives

$$\mathcal{H}_{\sqrt{\frac{2\alpha}{D_{44}}}}\left[b \mapsto \frac{b_0}{2}\delta(b-b_0)\right](\rho) = 2\alpha\frac{b_0^2}{2}J_{\sqrt{\frac{2\alpha}{D_{44}}}}(\rho b_0)$$

and thereby we obtain

$$\begin{cases} \partial_\xi\,[\mathcal{H}_{\sqrt{\frac{2\alpha}{D_{44}}}}\tilde{T}_{\alpha,D_{44}}(\xi,\cdot)](\rho) = -D_{44}\rho^2\,[\mathcal{H}_{\sqrt{\frac{2\alpha}{D_{44}}}}\tilde{T}_{\alpha,D_{44}}(\xi,\cdot)](\rho) \\ \lim\limits_{\xi\downarrow 0}[\mathcal{H}_{\sqrt{\frac{2\alpha}{D_{44}}}}\tilde{T}_{\alpha,D_{44}}(\xi,\cdot)](\rho) = 2\alpha\frac{b_0^2}{2}J_{\sqrt{\frac{2\alpha}{D_{44}}}}(\rho b_0), \end{cases}$$

which is straightforward to solve, as the Hankel transform is its own inverse. As a result we have

$$\tilde{S}_{\alpha,D_{44};\xi_0,a_0}(\xi,a) = 2\alpha\,a_0\left[\mathcal{H}_{\sqrt{\frac{2\alpha}{D_{44}}}}\left(\rho \mapsto e^{-\rho^2 D_{44}\xi}J_{\frac{2\alpha}{D_{44}}}(2\sqrt{a_0}\rho)\right)\right](\xi), \quad \xi>0, a>0.$$

Now by means of the well-known series of the Bessel functions

$$J_{\frac{2\alpha}{D_{44}}}(z) = \sum_{m=0}^{\infty}\frac{(-1)^m}{m!\,\Gamma\left(\sqrt{\frac{2\alpha}{D_{44}}}+m+1\right)}\left(\frac{z}{2}\right)^{2m+\sqrt{\frac{2\alpha}{D_{44}}}},\ \text{for } z = 2\sqrt{a_0}\rho,$$

and interchanging summation and integration we obtain

$$\begin{aligned}\tilde{S}_{\alpha,D_{44};\xi_0,a_0}(\xi,a) &= 2\alpha\sum_{m=0}^{\infty}\frac{(-1)^m}{m!\,\Gamma\left(\sqrt{\frac{2\alpha}{D_{44}}}+m+1\right)}(a_0)^{m+1+\sqrt{\frac{\alpha}{2\,D_{44}}}} \\ &\quad \int_0^{\infty}\rho^{2m+1+\sqrt{\frac{2\alpha}{D_{44}}}}J_{\sqrt{\frac{2\alpha}{D_{44}}}}(2\sqrt{a}\rho)e^{-\rho^2 D_{44}\xi}\,\mathrm{d}\rho\,,\end{aligned}$$

which can be further simplified by means of [2]p.486, equality 11.4.29 to (4.147). □

Remarks:

1. Notice that if $\alpha>0$, then $\tilde{S}_{\alpha,D_{44};\xi_0,a_0}(\xi,a)\Big|_{a=0} = 0$. So the grey-value particles (traveling with the speed proportional to their present scale a) with a finite expected lifetime will not reach the boundary $a=0$. However, if their expected lifetime is infinite, i.e. $\alpha\downarrow 0$ they will reach the boundary scale $a=0$, as we have

$$\begin{aligned}&\tfrac{1}{\alpha}\,\tilde{S}_{\alpha=0,D_{44};\xi_0,a_0}(\xi,a)\Big|_{a=0} = \tfrac{a_0}{D_{44}r}e^{-\frac{a_0}{D_{00}r}} \\ &\tilde{S}_{\alpha>0,D_{44};\xi_0,a_0}(\xi,a)\Big|_{a=0} = 0.\end{aligned} \tag{4.148}$$

   Moreover, there is a critical value of $\alpha>0$ depending on a_0 where the mode of the distribution $\tilde{S}_{\alpha=0,D_{44};\xi_0,a_0}(\xi,a)$ initially increases (rather than decreasing) in scale. These observations are easily verified in Figure 4.31 and Figure 4.32 where the Green's functions are plotted for different $\alpha\geq 0$ and $D_{44}>0$.

2. Because the generator is left-invariant with respect to the similitude group (and in particularly with respect to translation and scaling subgroup) we have

$$\boxed{\tilde{S}_{\alpha,D_{44};\xi_0,a_0}(\xi,a) = \tilde{S}_{\alpha,D_{44};0,1}((a_0)^{-1}(\xi-\xi_0),(a_0)^{-1}a),}$$

since by the left invariance we have

$$(-(A-\alpha I))^{-1}\delta_{\tilde{g}_0} = (-(A-\alpha I))^{-1}\mathcal{L}_{\tilde{g}_0}\delta_{\tilde{e}} = \mathcal{L}_{\tilde{g}_0}(-(A-\alpha I))^{-1}\delta_{\tilde{e}}.$$

for all $\tilde{g}_0 = (\xi^0, a_0)(= \xi_0\mathbf{e}_\xi + a_0\mathbf{e}_a) \in \tilde{G}$.

3. Notice that $\tilde{S}_{\alpha,D_{44};\xi_0=0,a_0=1}$ takes the relatively simple form (for $\alpha > 0$)

$$\boxed{\tilde{S}_{\alpha,D_{44};\,0,1}(\xi,a) = \sum_{m=0}^{\infty} \frac{\alpha(-1)^m}{m!\,\Gamma\left(1+\sqrt{\frac{2\alpha}{D_{44}}}\right)} \left(\frac{a}{D_{44}\xi}\right)^{\sqrt{\frac{\alpha}{2D_{44}}}} \frac{M(m+1+\sqrt{\frac{2\alpha}{D_{44}}}, \sqrt{\frac{2\alpha}{D_{44}}}+1, -\frac{a}{D_{44}\xi})}{(\xi D_{44})^{m+1+\sqrt{\frac{\alpha}{2\,D_{44}}}}},} \tag{4.149}$$

and for $\alpha \downarrow 0$ we have

$$\frac{1}{\alpha}\tilde{S}_{\alpha=0,D_{44};\,0,a_0}(\xi,a) \to \sum_{m=0}^{\infty} \frac{(-a_0)^m}{m!} \frac{M(m+1,1,-\frac{a}{D_{44}\xi})}{(\xi D_{44})^{m+1}}, \tag{4.150}$$

with the additional property that

$$\lim_{a_0\downarrow 0} \frac{\tilde{S}_{0,D_{44};\,\xi_0,\alpha_0}(\xi,a)}{\alpha a_0} = \frac{1}{D_{44}} e^{-\frac{a}{D_{44}r}}.$$

4. The convergence of the series expansion of the solution (4.147) depends on the values $D_{44}(\xi-\xi_0)$ and a) . As soon as the relative error is small (say < 0.01) the approximation decreases extremely fast and can be neglected after a few steps. The closer (ξ, a) gets to (ξ_0, a_0) or to $(0,0)$ the higher the value of truncation of the series. As a rule of thumb the series for fixed value of (ξ, a), with $a/a_0 > 0.01$ can be truncated at $M = \lfloor 4 + (1.2)\frac{1}{(\xi-\xi_0)D_{44}} \rfloor$. Therefore an asymptotic expression at $0 < \xi - \xi_0 << 1$ is desirable for reduction of computation time.

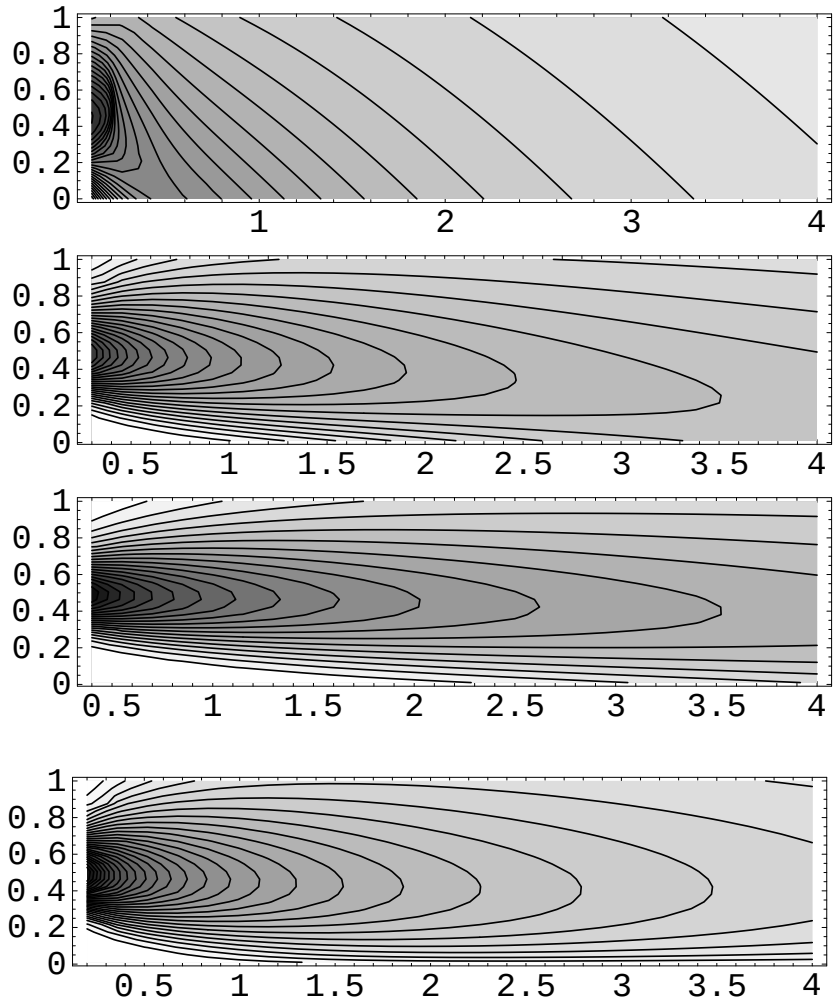

Figure 4.31: First three rows, contour plots of $\tilde{S}_{\alpha=0,D_{44};\,0,a_0=\frac{1}{2}}(\xi,a)$, cf. (4.150), for respectively (top-down) $D_{44}=1,0.1,0.05$, $0<\xi<4, 0<a<1$. Horizontal axis is a-axis, vertical axis is ξ-axis. Notice that $\tilde{S}_{\alpha=0,D_{44};\,0,a_0}(\xi,a)=\tilde{S}_{\alpha=0,D_{44}=1;\,0,a_0}(D_{44}\xi,a)$. Last row: Contour plot of $\tilde{S}_{\alpha=0.05,D_{44}=0.1;\,0,a_0=\frac{1}{2}}(\xi,a)$.

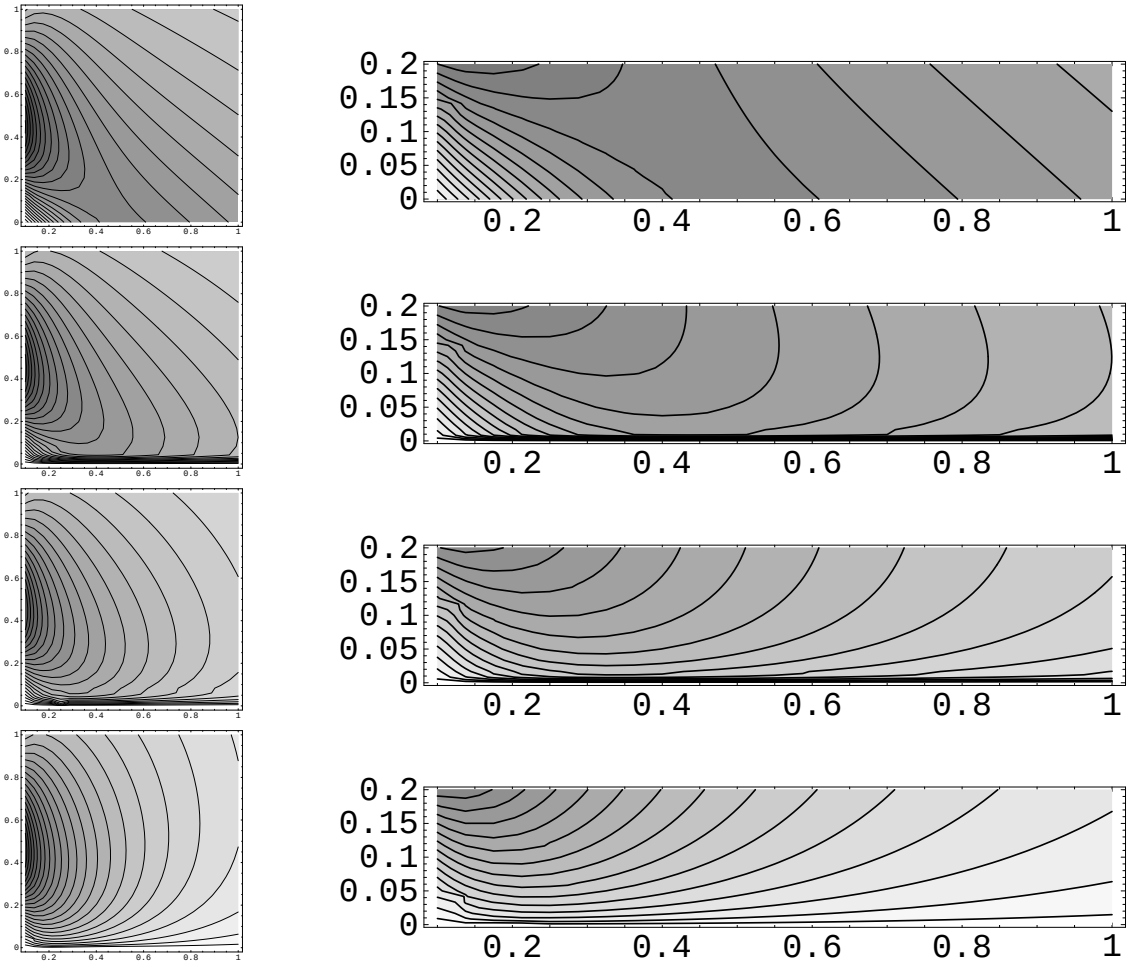

Figure 4.32: Contour plots of $\tilde{S}_{\alpha=0.1, D_{44}=1; 0, a_0=\frac{1}{2}}(\xi, a)$, cf. (4.150), for $\alpha = 0, 0.01, 0.1, 0.5$, $0 < \xi < 1, 0 < a < 1$ and corresponding close-ups, restrictions to $0 < a < 0.2$ on the right. Horizontal axis is a-axis, vertical axis is ξ-axis.

4.11 Conclusion

Given an image $f \in \mathbb{L}_2(\mathbb{R}^d)$, we construct a local orientation score U_f, which is a complex-valued function on the Euclidean motion group G. The corresponding transformation $f \mapsto U_f$ is a wavelet transform constructed from an oriented wavelet ψ and a representation of the Euclidean motion group onto $\mathbb{L}_2(\mathbb{R}^2)$. Since this representation $\mathcal{U}$ is *reducible* the well-known wavelet reconstruction theorem, which allows perfectly wellposed reconstruction, does not apply.

Therefore we generalized standard wavelet theory by means of reproducing kernel theory. From this generalization it followed that our wavelet transformation is a *unitary* mapping between the space of bandlimited images, modeled by $\mathbb{L}_2^o(\mathbb{R}^2)$ and the functional Hilbert space $\mathbb{C}_K^G$ of orientation scores which is explicitly characterized. The norm on $\mathbb{C}_K^G$ explicitly depends on the oriented wavelet ψ via a function M_ψ, which thereby characterizes the stability of the explicitly described inverse wavelet transformation. As a result, by proper choice of the wavelet ψ, the image f can be reconstructed from U_f in a robust way. We developed and implemented several approaches to obtain proper wavelets (which are also good line detectors in practice) in the 2 dimensional case, $d = 2$. These results are also explicitly generalized to (and implemented in) the 3 dimensional case, $d = 3$. These proper wavelets give rise to a stable transformation from image to orientation score and vice versa, which allows us to relate operations Φ on orientation scores to operations Υ on images in a robust way.

Then we show that operations Φ must be left invariant in order to obtain a Euclidean invariant transformation Υ on images. As an example we observe the probability of collision of particles from two left invariant stochastic processes (including curvature) on the Euclidean motion group, which is used to automatically detect elongated structures and to automatically close gaps between them.

This bring us to the framework of resolvents of linear left invariant second order evolution equations on the 2D Euclidean motion group, the solution of which is a G-convolution with the Green's function. We constructed analytic approximations for these Green's functions (which are simple and very useful for practical applications), and their modes, by replacing (both in cartesian and cylindrical coordinates) the generators of the Euclidean motion group by generators of a Heisenberg group. Furthermore we briefly consider the more difficult case of resolvents of linear left invariant second order evolution equations on the 3D Euclidean motion group.

Finally, we also apply scaling[31] to the wavelet ψ. Thereby the domain of the multiple scale orientation scores, becomes the similitude group, which is usually the case in wavelet based image processing. However, as we pointed out in Theorem 19 and Corollary 5, in contrast to the usual wavelet approaches in image analysis we are able to get a stable reconstruction from each fixed scale layer (without using the lower scale information !) in the wavelet domain. On these multi-scale orientation scores we apply the resolvents of second order left linear evolution equations on the *similitude group*. As a first step towards analytic approximations of the Green's functions of these resolvents, we restrict ourself to a subgroup isomorphic to the $ax + b$-group and obtain *exact* analytic formulas of the involved Green's functions.

[31] Notice that the lifetime α of oriented particles can also be considered as a scale parameter, but this issue of scale is relative to the initial scale of the wavelet

Chapter 5

Robust Orientation Estimation

5.1 Introduction

Orientation scores are a nice tool for *well-posed image enhancement* by means of left-invariant processing on the orientation scores. However, for many practical applications where detection of oriented structures is required it is more relevant to obtain a fast robust estimation for a *single* orientation per position, rather than image enhancement via orientation scores where the columns $U_f(\mathbf{x}, \cdot)$ represent a *distribution of local orientation* per position $\mathbf{x}$.

A simple way to get a first single orientation estimate $\hat{\theta}(\mathbf{x})$ from an orientation score would be by tracing the maximum (response)value in each orientation column of the score. To each orientation estimate $\hat{\theta}(\mathbf{x})$ we can attach a measure of reliability of the estimate $r(\mathbf{x})$. This could for example be obtained by comparing the maximum absolute value to the magnitudes in the orientation column $U_f(\mathbf{x}, \cdot)$. This would give a first rough estimate of the local orientation (with its corresponding confidence). For example, if the score is constructed by a second order directional derivative of the Gaussian kernel this boils down to an orientation estimate by means of the angle of the eigenvector $\mathbf{v}_1(\mathbf{x})$ in the Hessian matrix (consisting of Gaussian derivatives) with largest amplitude, so $\hat{\theta}(\mathbf{x}) = \angle \mathbf{v}_1(\mathbf{x})$ and we can attach the confidence $r(\mathbf{x}) = \frac{|\lambda_1(\mathbf{x})|-|\lambda_2(\mathbf{x})|}{|\lambda_1(\mathbf{x})|+|\lambda_2(\mathbf{x})|}$.

Another simple (and more common) way to get a rough orientation estimate is by convolving the image f with the gradient of a Gaussian kernel[1], $\mathbf{h}(\mathbf{x}) = (\nabla G_s * f)(\mathbf{x})$, $s = \frac{1}{2}\sigma^2$, $\mathbf{x} \in \mathbb{R}^2$. The orientation estimation $\hat{\theta}(\mathbf{x}) = \theta_h(\mathbf{x})$ is then given by

$$\theta_h(\mathbf{x}) = \angle h(\mathbf{x}) = \arccos\left(\frac{\mathbf{h}(\mathbf{x}) \cdot \mathbf{e}_x}{\|\mathbf{h}(\mathbf{x})\|}\right).$$

The corresponding confidence of this first orientation estimation is then given by $r(\mathbf{x}) = \|\mathbf{h}(\mathbf{x})\|$.

Typically these kind of first rough orientation estimates are rather sensitive to noise. Consequently, in medical image analysis these first estimates are unreliable. Therefore in this chapter

[1] Which is rather an edge than a line detector.

we consider 2 different methods to obtain new, more robust orientation estimations $\tilde{\mathbf{h}}$ from $\mathbf{h}$ by considering neighboring relations. First we discuss robust orientation estimation by means of so-called channel representations, cf. [65], and then we discuss robust orientation estimation by means of so-called tensor-voting, cf. [95],[60]. See the examples of Figure 5.6 and Figure 5.4, which clearly illustrate the idea of robust orientation estimation in a practical setting.

5.2 Channel Representations

Let $L > 0$, then the channel representation $\mathbf{u} : [0, L] \times \mathbb{R}^+ \to \mathbb{R}^L$ is an encoding of a *signal value* $f(\mathbf{x}) \in [0, L]$ obtained by a modular[2] *signal* $f : \mathbb{R}^2 \to \mathbb{R}$ at position $\mathbf{x}$, and an associated confidence $r(\mathbf{x}) > 0$, given by

$$\mathbf{u}(f(\mathbf{x}), r(\mathbf{x})) = r(\mathbf{x})(B^0(f(\mathbf{x})), \ldots, B^{L-1}(f(\mathbf{x})))^T,$$

where $B^n : [0, L] \to \mathbb{R}^+$, $n = 0, \ldots, L-1$ are continuous functions, such that the mapping $(y, r) \mapsto \mathbf{u}(y, r)$ is injective. The vector $\mathbf{u}(f(\mathbf{x}), r(\mathbf{x}))$ is usually called channel vector (at position $\mathbf{x} \in \mathbb{R}^2$) and its components are called channels. The injectivity assumption allows us to decode $(f(\mathbf{x}), r(\mathbf{x}))$ from the channel vector $\mathbf{u}(f(\mathbf{x}), r(\mathbf{x}))$.

Here we only consider the case where $f(\mathbf{x}) = \frac{L\hat{\theta}(\mathbf{x})}{2\pi}$, where $\hat{\theta}(\mathbf{x})$ is a first rough orientation estimation (for example by means of a gradient or a Riesz transform or Hessian of the original image). Thereby we have $f(\mathbf{x}) \in [0, L]$ for all $\mathbf{x} \in \mathbb{R}^2$ and the interval $[0, L]$ will be equipped with group product $f(\mathbf{x}) + g(\mathbf{x}) = f(\mathbf{x}) + g(\mathbf{x}) \text{mod } L$ and modular distance

$$d_L(f(\mathbf{x}), g(\mathbf{x})) = \min(\text{mod}(f(\mathbf{x}) - g(\mathbf{x}), L), \text{mod}(g(\mathbf{x}) - f(\mathbf{x}), L)),$$

which makes $[0, L)$ isomorphic to $\mathbb{T}$. Moreover, we will only consider the special case

$$B^n(f(\mathbf{x})) = B^0(d_L(f(\mathbf{x}), n)),$$

i.e. the basis functions B^n are obtained by a modular shift over n from smooth basis function B^0. The support of the symmetric function B_0 will be a connected bounded interval $[-\frac{W}{2}, \frac{W}{2}]$, where W is called the kernel width. As a result the support of B^n equals $[n - \frac{W}{2}, n + \frac{W}{2}]$. Consequently, we have a nice practical localized smooth basis. Further we notice that the number N_A of active (non-zero) channels in the channel representation is limited as it equals $1 + 2\lfloor \frac{W}{2} \rfloor$. This is a major practical advantage over for example the discrete Fourier basis where all discrete frequencies are needed to represent a discrete δ-spike.

Example: B-spline channels
The B-spline channel representation, [46], with parameter $K \in \mathbb{N}$ is obtained by setting

$$B^0_K(f(\mathbf{x})) = (\text{rect} *^{(K)} \text{rect})(f(\mathbf{x})), \tag{5.1}$$

where we used $K-$ fold periodic convolution (so that the channel width equals $K + 1$) and where $\text{rect}(y) = 1$ if if $|y| < \frac{1}{2}$ and $\text{rect}(y) = \frac{1}{2}$ if $|y| = \frac{1}{2}$ and $\text{rect}(y) = 0$ elsewhere.

[2] With modular, we mean periodic in its co-domain. For channel representations on non-modular signals, see [59].

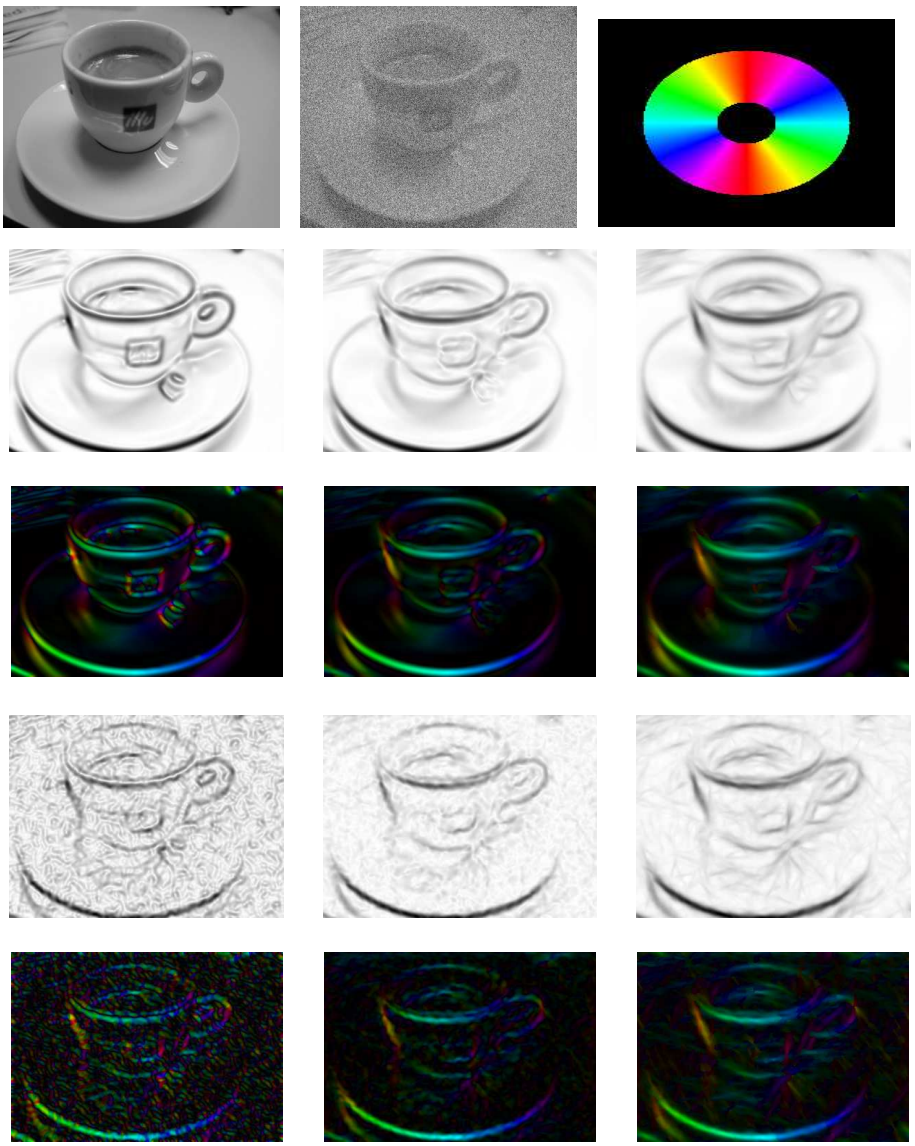

Figure 5.1: Illustration of robust orientation estimation by means of tensor voting and by means of channel representations. Top row from left to right, original image of teacup, with and without noise and legenda of color-coding of directions. Middle row, robust orientation of the very nice original image (without noise), from left to right: 1. Gaussian gradient field of original image (where length of the gradient is encoded by luminosity and direction of the gradient is encoded in color); 2. Output of tensor voting, the stickness of $\mathbf{H}_{NEW}$, $(x, y) \mapsto \tilde{s}(\mathbf{H}_{NEW}(x, y))$, see (5.13), is encoded in luminosity, the (double sided) orientation of the largest eigen vector of $\mathbf{H}_{NEW}(\mathbf{x})$ is illustrated in color. 3. Output of decoding (5.2) after channel smoothing (with smoothing kernel $\psi(\mathbf{x}) = \cos^{2n}(\phi)e^{-\frac{r^2}{2\sigma^2}}$, $n = 12$, $\sigma = 10$), where channels are encoded by means of quadratic B-splines, see (5.1), $K = 2$, $L = 12$. The confidence is encoded in luminosity, the orientation is encoded in color. Bottom row: Same settings as middle row but now applied on noisy image. (We used a first guess of the parameters, without pruning/optimization (and without thresholding/thinning) of the parameters, therefore the purpose of this figure is to show a practical proof of concept, rather than a profound comparison between the two methods).

The decoding is linear and is given by

$$(f(\mathbf{x}), r(\mathbf{x})) = \left(\frac{1}{r(\mathbf{x})} \sum_{n=0}^{L-1} n \; u_K^n(f(\mathbf{x}), r(\mathbf{x})), \sum_{n=0}^{L-1} u_K^n(f(\mathbf{x}), r(\mathbf{x})) \right), \tag{5.2}$$

where $u_K^n(f(\mathbf{x}), r(\mathbf{x})) = r(\mathbf{x}) B_K^0(f(\mathbf{x}) - n)$. It is not difficult to give a formal proof of (5.2):

1. The first part of (5.2) can easily be proved by induction: The case $K = 1$ is trivial, moreover if we assume that it holds for $K - 1$ then we have

$$\begin{aligned} \sum_{n=0}^{L-1} n \; B_K^n(y) &= \sum_{n=0}^{L-1} n \; B_K^0(y - n) \\ &= \sum_{n=0}^{L-1} n \int B_0^0(u) B_{K-1}^0(y - n - u) \, \mathrm{du} \\ &= \int B_0^0(u) \left(\sum_{n=0}^{L-1} n \; B_{K-1}^0(y - n - u) \right) \mathrm{du} \\ &= \int B_0^0(u)(y - u) \, \mathrm{du} = 1 \; y + 0 = y \end{aligned}$$

2. With respect to the second argument we notice that

$$\sum_{n=0}^{L-1} B_1^n(y) = 1 \text{ for all } y \in [0, L] \Rightarrow \sum_{n=0}^{L-1} B_K^n(y) = 1 \text{ for all } y \in [0, L] \; ,$$

from which we deduce that $\sum_{n=0}^{L-1} u^n(y, r) = r \sum_{n=0}^{L-1} B_K^n(y) = r$.

In practice one uses decoding after manipulation and then one would like to use a decoding window (of size say $2p + 1$) and obtain the following fast decoding estimate

$$\tilde{f}(\mathbf{x}) = \frac{\sum_{n=n_0-p}^{n_0+p} n \; u^n(f(\mathbf{x}), r(\mathbf{x}))}{\sum_{n=n_0-p}^{n_0+p} u^n(f(\mathbf{x}), r(\mathbf{x}))}. \tag{5.3}$$

In the experiments discussed in subsection 5.2.1 we set $p = 1$ and $K = 2$, i.e. we used quadratic B-splines with a decoding window size of 3, where the decoding estimate (5.3) is given by

$$\tilde{f}(\mathbf{x}) = \frac{u^{n_0+1}(f(\mathbf{x}), r(\mathbf{x})) - u^{n_0-1}(f(\mathbf{x}), r(\mathbf{x}))}{u^{n_0+1}(f(\mathbf{x}), r(\mathbf{x})) + u^{n_0}(f(\mathbf{x}), r(\mathbf{x})) + u^{n_0-1}(f(\mathbf{x}), r(\mathbf{x}))} + n_0, \tag{5.4}$$

the window center n_0 can be chosen in various (somewhat ad-hoc) ways. For example n_0 could be chosen such that $u^{n_0+1}(f(\mathbf{x}), r(\mathbf{x})) + u^{n_0}(f(\mathbf{x}), r(\mathbf{x})) + u^{n_0-1}(f(\mathbf{x}), r(\mathbf{x}))$ is maximal.

Example: Cosine Square Channels

The cosine square channel representation, cf.[58], with parameter $\omega > 0$ is obtained by setting

$$B^0(f(\mathbf{x})) = C_\omega^0(f(\mathbf{x})) := \begin{cases} \cos^2(\omega f(\mathbf{x})) & \text{If } \omega |f(\mathbf{x})| \leq \frac{\pi}{2} \; , \\ 0 & \text{else.} \end{cases} \tag{5.5}$$

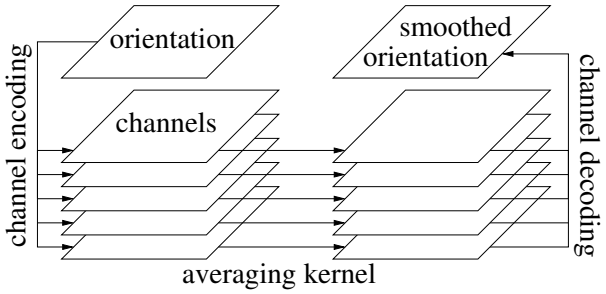

Figure 5.2: Illustration of robust orientation estimation by means of channel smoothing

where $\frac{\pi}{\omega} > 0$ equals the channel width.

The decoding algorithm is more complicated in this case compared to the B-spline case. It is nonlinear and involves $\mathbb{L}_2$-approximation for $\omega > \frac{\pi}{N}$, but it is possible to give an exact decoding for the case $\omega = \frac{\pi}{N}$ (i.e. channel width $W = N$), $N \geq 3$:

$$\begin{aligned} f(\mathbf{x}) &= l + \tfrac{N}{2\pi} \arg \left[\sum_{n=l}^{l+N-1} u^n_{\omega=\frac{\pi}{N}}(f(\mathbf{x}), r(\mathbf{x})) e^{i\frac{2(n-l)\pi}{N}} \right] , \\ &= l + \tfrac{N}{2\pi} \arg \left[\sum_{n=0}^{N-1} u^{n+l}_{\omega=\frac{\pi}{N}}(f(\mathbf{x}), 1) e^{i\frac{2n\pi}{N}} \right] , \end{aligned} \tag{5.6}$$

where l denotes the first index of the decoding window, see [59] p.17-19 for more details.

5.2.1 Channel Smoothing for Robust Orientation Estimation

In this section[3] we will consider robust orientation estimation by means of channel smoothing. The idea is to construct a channel representation, to smooth the channel representation and to decode from the smoothed channels to obtain an orientation estimate, see Figure 5.2.

If the decoding scheme $f(\mathbf{x}) = \Phi^{-1}[\mathbf{u}(f(\mathbf{x}), r(\mathbf{x}))]$ is linear we have that smoothing of f (by means of a continuous convolution kernel $K : \mathbb{R}^2 \to \mathbb{R}^+$, with $\int_{\mathbb{R}^2} K(\mathbf{x})\, \mathrm{d}\mathbf{x} = 1$) leads to the same result as decoding its smoothed channel representation $\tilde{\mathbf{u}}(f(\mathbf{x}), r(\mathbf{x})) = (K * \mathbf{u}(f(\cdot), r(\cdot)))(\mathbf{x})$. To this end we notice that

$$\begin{aligned} &(K * f)(\mathbf{x}) = \Phi^{-1}[\tilde{\mathbf{u}}(f(\mathbf{x}), r(\mathbf{x}))] \qquad \Leftrightarrow \\ &\int_{\mathbb{R}^d} f(\mathbf{y}) K(\mathbf{x}-\mathbf{y})\, \mathrm{d}\mathbf{y} = \int_{\mathbb{R}^d} \Phi^{-1}[\mathbf{u}(f(\mathbf{x}), r(\mathbf{x}))] K(\mathbf{x}-\mathbf{y})\, \mathrm{d}\mathbf{y} = \Phi^{-1} \left[\int_{\mathbb{R}^d} \mathbf{u}(f(\mathbf{x}), r) K(\mathbf{x}-\mathbf{y})\, \mathrm{d}\mathbf{y} \right] , \end{aligned} \tag{5.7}$$

for all $\mathbf{x} \in \mathbb{R}^d$. The windowed decoding in the B-spline case and the windowed decoding in the cosine square case (5.6), or similarly for general ω in [59]p.18 are non-linear (even in case $r(\mathbf{x}) = 1$). As a result, in general, the left hand side and right hand side (5.7) do not coincide. In fact, they only coincide if the orientation measurement $\mathbf{x} \mapsto f(\mathbf{x})$ is such that the decoding becomes linear. For example, in the B-spline case, it means that if $f(\mathbf{x})$ is such that the

[3] This section is part of a joint paper with Michael Felsberg submitted to IJCV, see [27].

active part of the smoothed channels is a subset of the decoding window, since then we have $\tilde{u}_{n_0-1}(f) + \tilde{u}_{n_0}(f) + \tilde{u}_{n_0+1}(f) = 1$ with the consequence that (5.4) and (5.2) coincide. This will only be the case if the image is locally 1D at $\mathbf{x}$. Also at discontinuities the channel will be smoothed, but here the contributions of the smoothing falls outside the decoding window, i.e. the smoothing contributions lie in the nil-space of the decoding operation. So, effectively the channel smoothing does not smooth over discontinuities, which is desirable in a robust orientation estimation.

In the cosine square channel case a similar observation can be made. Here we notice that if

$$\arg\left[\sum_{k=0}^{N-1} \tilde{u}^{k+l}(f(\mathbf{x}), r(\mathbf{x}))e^{\frac{2\pi ik}{N}}\right] = \frac{1}{N}\arg\left[\prod_{k=0}^{N-1} u^{k+l}e^{\frac{2\pi ik}{N}}\right] = \frac{1}{N}\sum_{k=0}^{N-1}\arg(u^{k+l}e^{\frac{2\pi ik}{N}}) = \frac{\pi(N-1)}{N},$$

which is the case[4] if $\tilde{\mathbf{u}}(f(\mathbf{x}), r(\mathbf{x}))$ is symmetric (for the sake of simplicity we assume N is odd):

$$\tilde{u}^{l+\frac{N-1}{2}+j}(f(\mathbf{x}), r(\mathbf{x})) = \tilde{u}^{l+\frac{N-1}{2}-j}(f(\mathbf{x}), r(\mathbf{x})), j = 1, \ldots \frac{N-1}{2},$$

which again will be the case if the image is locally 1D at $\mathbf{x}$. Moreover we again have that effectively the channel smoothing does not smooth over discontinuities.

5.2.1.1 Robust Estimation

In this section we will draw some parallels from channel smoothing to non-parametric methods in random variable estimation. Assume that $f : \mathbf{x} \mapsto f(\mathbf{x})$ is a realization of a stochastic process $\mathcal{P}$ that is ergodic for all $\mathbf{x} \in \Omega$. This implies that we can replace averaging realizations of $\mathcal{P}$ with averaging f in $f(\Omega) \subset [0, L]$. We denote the probability density function over f by pdf.

The orientation estimate due to decoding is robust in the sense that it minimizes the energy

$$\mathcal{E}(g) = \int_0^L \rho(f-g)\mathrm{pdf}(f)\ \mathrm{df} = (\rho * \mathrm{pdf})(g)\ .$$

If we use B-spline channels, it follows by (5.4) that the influence function is given by

$$\psi(f) = \rho'(f) = B_2(f-1) + B_2(f+1).$$

This influence function is smooth and compactly supported at $[-2.5, 2.5]$ and locally linear near the origin. The influence function tells us how much an outlier affects the orientation estimate. To this end we notice that $\left.\frac{\partial\mathcal{E}(f)}{\partial f}\right|_{f=f_0} = -(\psi * \mathrm{pdf})(f)$. For example, if the outlier is outside the compact support $[-2.5, 2.5]$ of the influence function it does not affect the estimate and if the outlier equals ± 1 then causes maximal damage to the estimate. Clearly, this influence function (see Figure 5.3) is highly preferable over the linear influence function in the non-robust case of a least square estimate $\rho(f) = f^2$. The channel vector $\mathbf{u}(\mathbf{x})$ at position $\mathbf{x}$ is related to the

[4] $\arg(e^{\frac{\pi i(N-1)}{N}}(1 + z + \overline{z})) = \arg(e^{\frac{\pi i(N-1)}{N}}) = \frac{\pi(N-1)}{N}$ for all $z \in \mathbb{C}$.

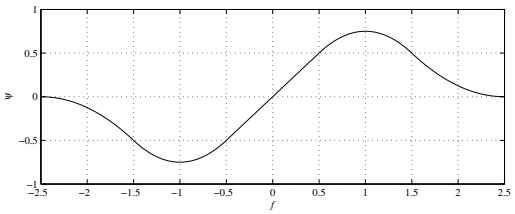

Figure 5.3: The influence function in case of robust orientation estimation by means of channel smoothing on B-splines

probability density function (pdf) of the generating stochastic process $\mathcal{P}$ at position $\mathbf{x}$. By definition a kernel density estimation with kernel B_0 is given by $\tilde{p}_{f_n}(f) = \frac{1}{N}\sum_{n=0}^{N} B_0(f - f_n)$, where $\{f_n\}$ is a set of N independent samples of the stochastic variable f.

By the ergodicity assumption averaging of the elements of the channel representation $\tilde{u}^n(f(\mathbf{x}),1) = \frac{1}{|\Omega|}\int_\Omega u^n(f(\mathbf{x}),1)\mathrm{d}\mathbf{x}$, is equivalent to sampling of a kernel density estimate with the symmetric positive kernel B^0. The expectation value of the kernel density estimate equals $(B^0 * \mathrm{pdf})(f)$ and thereby the expectation of the channel averaging is

$$E\left\{\frac{1}{|\Omega|}\int_\Omega u^n(f(\mathbf{x}),1)\mathrm{d}\mathbf{x}\right\} = (B^0 * \mathrm{pdf})(f)\big|_{f=n}\,. \tag{5.8}$$

5.2.1.2 Explicit Example of Channel Smoothing

To obtain adaptive channel smoothing we quadratically fitted the convolution kernels $K \geq 0$ of the type $\psi_{s,\omega}(\mathbf{x}) = e^{-rs}C^0_\omega(\phi)$, $\mathbf{x} = (r\cos\phi, r\sin\phi)$, where we recall that C^0_ω is given by (5.5), to the auto-correlations

$$A_n(\mathbf{x}) = \mathcal{F}^{-1}[\boldsymbol{\omega} \mapsto |\mathcal{F}(u^n(\cdot, r=1))(\boldsymbol{\omega})|^2](\mathbf{x})$$

of the channel vectors $u^n(\cdot, r=1)$. More precisely, we minimized

$$\min_{s,\omega}\sum_{n=0}^{N-1}\int_{\mathbb{R}^2} |\frac{\|A_n\|_{\mathbb{L}_1(\mathbb{R}^2)}}{\|\psi_{s,\omega}\|_{\mathbb{L}_1(\mathbb{R}^2)}}\psi_{s,\omega}(\mathbf{x}) - A_n(R_n^{-1}\mathbf{x})|^2 w(\mathbf{x})\mathrm{d}\mathbf{x},$$

where $\|A_n\|_{\mathbb{L}_1(\mathbb{R}^2)} = \int_{\mathbb{R}^2}|A_n(\mathbf{x})|\,\mathrm{d}\mathbf{x}$ and where $R_n \in SO(2)$ is a rotation such that the direction of the n-th channel is mapped to the direction of the 0-th channel, so that $\mathbf{x} \mapsto A_n(R_n^{-1}\mathbf{x})$ is aligned to $A_0(\mathbf{x})$. In the implementation we replaced the integral by a discrete summation and used a steepest descent algorithm. We took $w(\mathbf{x}) = \frac{1}{\|\mathbf{x}\|+\epsilon}$ ($1 >> \epsilon > 0$, to avoid singularity problems at the origin) to compensate for the Jacobian of a polar coordinate transformation. Notice to this end that local orientation means locally 1D signals, so we wanted to have a 1D subspace projection along the orientation.

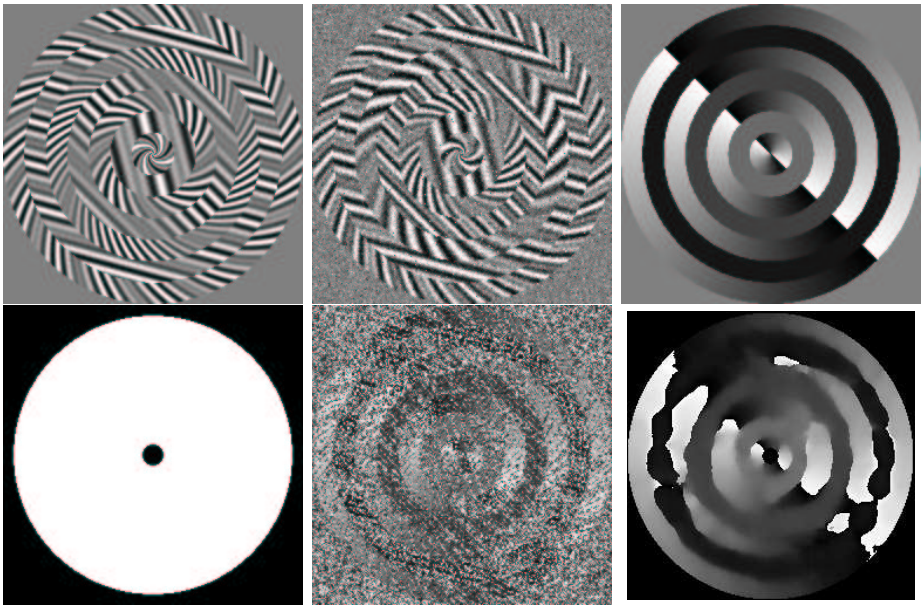

Figure 5.4: Robust orientation estimation by means of adaptive channel smoothing. Top row: from left to right, test pattern, t=test pattern with 1 percent salt and pepper noise and Gaussian noise of variance 0.01, ground truth of the orientation. Bottom row: from left to right, we considered orientation estimation only inside the white disk area, and the rough orientation estimation computed from gradient, the result after channel smoothing of $f(\mathbf{x}) = 2 * \arccos\left(\frac{\operatorname{grad} t(\mathbf{x}) \cdot \mathbf{e}}{\|\operatorname{grad} t(\mathbf{x})\|}\right)$, where $\mathbf{e} \in \mathbb{R}^2$ is a fixed normalized direction.

Some results are illustrated in Figure 5.4. This method showed very good results compared to other existing orientation estimation methods. For a detailed comparison to other orientation estimation methods, we refer to Felsberg [45]p.22-25.

5.2.1.3 The Number of Channels K and the Channel Width W

The shape of the B-spline and the cosine square channel representation are pretty similar if the corresponding channel widths coincide, i.e. $\frac{\pi}{\omega} = K + 1$. In practice there is not much difference between the two representations. It is rather the number of channels K and the channel width W that makes the difference. Both quantities lead to a trade-off situation.

On the one hand the channel width W should not be too narrow, since then the estimated pdf becomes to spiky, and consequently finding the maxima of the pdf is ill-posed. On the other hand W should not be too broad, as this leads to interference of the local maxima.

On the one hand the number of channels K should not be too large, as it requires a lot of samples of the pdf and there is only a limited number of samples of the measurement. On the other hand K should not be too small as the accuracy of the maxima of the pdf becomes better if there are more channels.

5.3 Tensor Voting

Tensor voting is a technique for robust extraction of curves of images. It was first introduced by Medioni, [95]. The technique consists of several subroutines and it seems to work rather well in practice. Nevertheless, a lot of choices in the algorithm are rather ad-hoc and the whole scheme certainly lacks mathematical description and underpinning.[5] Inspired by the more detailed and profound work of Franken et al.[60] on 2D-steerable tensor voting, we put (the robust estimation in) tensor voting in a more general mathematical framework and decompose the voting field into $SO(d)$-irreducible components. We will also deal with $3D$-steerable tensor voting. In this section upper indices do not indicate exponents, but serve as component labels, unless stated otherwise or evident from the context.

Let $\mathbf{H}_f = H_{f\,i_1,\ldots,i_n}\mathbf{e}_{i_1}\otimes\cdots\otimes\mathbf{e}_{i_n}$ be a rank N-tensor-field obtained from an image $f:\mathbb{R}^d\to\mathbb{R}$. For example by means of Gaussian derivatives on the image $f:\mathbb{R}^2\to\mathbb{R}$, i.e.

$$H_{f\,i_1,\ldots,i_n}(\mathbf{x}) = (D_{i_1,\ldots,i_n}G_s * f)(\mathbf{x}),\ s>0,\ \mathbf{x}\in\mathbb{R}^d.$$

In the rest of this section we will omit f and write $\mathbf{H}$ rather than $\mathbf{H}_f$. Such a tensor field $\mathbf{H}$ can be rotated by means of

$$\mathbf{H}_R(\mathbf{x}) = R^{i_1}_{i'_1}\cdots R^{i_1}_{i'_N}\,H_{i'_1\ldots i'_N}(R^{-1}\mathbf{x})\ \mathbf{e}_{i_1}\otimes\cdots\otimes\mathbf{e}_{i_N}, \tag{5.9}$$

where $H_{i_1\ldots i_N}$ are the components[6] of the tensor field with respect to the standard basis $\{\mathbf{e}_i\}_{i=1}^d$, where we identified each tangent space $T_{\mathbf{x}}(\mathbb{R}^d)$ with $\mathbb{R}^d$!

Suppose $\mathbf{H}(\mathbf{0})$ is a tensor on the tangent space at $\mathbf{0}$. Next we introduce a model of the expectation of $\mathbf{H}(\mathbf{x})$, for all $\mathbf{x}\neq\mathbf{0}$. This model is called the voting field $\mathbf{V}$ and it is also a rank N-tensor-field on $\mathbb{R}^d$. Such a voting field is mostly based on qualitative psychophysical Gestalt laws such as "proximity" and "good continuation".

Let $\mathcal{T}_N$ denote the vector space of rank N-tensors on $\mathbb{R}^d$. In the framework of tensor-voting one obtains a smoothed vector field $\mathbf{H}_{NEW}$ from $\mathbf{H}$ by such a voting field $\mathbf{V}$ by means of:

$$\mathbf{H}_{NEW}(\mathbf{x}) = \int_{\mathbb{R}^d}\tilde{s}(\mathbf{H}(\mathbf{x}))\mathbf{V}_{\tilde{R}(\mathbf{H}(\mathbf{x}))}(\mathbf{b}-\mathbf{x})\,\mathrm{d}\mathbf{x}, \tag{5.10}$$

where $\mathbf{V}_{\tilde{R}(\mathbf{H}(\mathbf{x}))}$ denotes the rotated voting field (rotated over $\tilde{R}(\mathbf{H}(\mathbf{x}))$, cf. (5.9)) and where $\tilde{s}:\mathcal{T}_N\to\mathbb{R}^+$ is such that

$$\tilde{s}(\mathbf{H}_R(\mathbf{x})) = \tilde{s}(\mathbf{H}(R^{-1}\mathbf{x})) \tag{5.11}$$

for all $R\in SO(d)$ and such that $\tilde{s}(\lambda\mathbf{H}) = |\lambda|\tilde{s}(\mathbf{H})$ for all $\lambda\in\mathbb{R}$. The function $\tilde{R}:\mathcal{T}_N\to SO(d)$ maps a tensor to a rotation in $SO(d)$, such that

$$\tilde{R}(\mathbf{H}_R(\mathbf{x})) = R\,\tilde{R}(\mathbf{H}(R^{-1}\mathbf{x})) \tag{5.12}$$

[5] For example, the approach in Medioni's book[95] contains a lot of practical issues and intuitive schemes, but no mathematical formulae nor precise algorithms.

[6] An inner product space of finite dimension can be identified with its dual, so here it is not necessary to make a distinction between contravariant and covariant vectors/components.

for all $R \in SO(d)$ and all $\mathbf{x} \in \mathbb{R}^2$. Notice that it follows from (5.11) and (5.12) that the tensor voting scheme is rotation invariant, i.e.

$$(\mathbf{H}_{NEW})_R = (\mathbf{H}_R)_{NEW}, \text{ for all } R \in SO(d).$$

In our examples we will specify $\tilde{s} : \mathcal{T}_N \to \mathbb{R}^+$ and $\tilde{R} : \mathcal{T}_N \to SO(d)$ more explicitly. For now we will assume that they are given.

Next we explain the general scheme of so-called **steerable tensor-voting**, which is obtained by expanding the voting field[7] into irreducible components, $\mathbf{V} = \sum_{m\in\mathbb{N}} \mathbf{V}^m$, we obtain

$$\mathbf{V}_R = \sum_{m\in\mathbb{N}} \Gamma^m(R)\mathbf{V}^m,$$

where $\Gamma^m(R)$ is the matrix obtained by restricting the rotation action to the m-th irreducible subspace of tensor fields, for more explanation and details concerning steerable tensor fields, see subsection 7.9.1 in the appendix.

The advantage (besides computation speed for $d = 2$) of this steerability is that tensor voting can be expressed in ordinary spatial convolutions:

$$\begin{aligned} \mathbf{H}_{NEW}(\mathbf{x}) &= \int_{\mathbb{R}^2} \tilde{s}(\mathbf{H}(\mathbf{x}))\mathbf{V}_{\tilde{R}(\mathbf{H}(\mathbf{x}))}(\mathbf{b}-\mathbf{x})\, \mathrm{d}\mathbf{x} \\ &= \int_{\mathbb{R}^2} \tilde{s}(\mathbf{H}(\mathbf{x})) \sum_{m\in\mathbb{N}} \Gamma^m(\tilde{R}(\mathbf{H}(\mathbf{x})))\mathbf{V}^m(\mathbf{b}-\mathbf{x})\, \mathrm{d}\mathbf{x} \\ &= \sum_{m\in\mathbb{N}} \int_{\mathbb{R}^2} \tilde{s}(\mathbf{H}(\mathbf{x}))\, \Gamma^m(\tilde{R}(\mathbf{H}(\mathbf{x})))\mathbf{V}^m(\mathbf{b}-\mathbf{x})\, \mathrm{d}\mathbf{x} \end{aligned} \tag{5.13}$$

Moreover, by expanding the whole framework into irreducible components, it is easier to tune the voting field for a given application.

5.3.1 The cases $d = 2$ and $N \leq 2$

The case $d = 2$ is by far the simplest case. The group $SO(2)$ is commutative and thereby all irreducible representations are 1-dimensional. Moreover we have $\Gamma^m(R_\theta) = e^{im\theta}$ and thereby $\Gamma^m \otimes \Gamma^n = \Gamma^{m+n}$. We shall consider the case $N = 1$ (vector-field) and $N = 2$ (2-tensor-field).

We will first focus on the latter case, where we notice that any 2-tensor $a \otimes b$ can be identified with the linear mapping $\mathbf{x} \mapsto \mathcal{R}(a \otimes b)(\mathbf{x}, \cdot)$, where $\mathcal{R}$ is the Riesz-mapping from the dual $(\mathbb{R}^2)^*$ of $\mathbb{R}^2$ to $\mathbb{R}^2$. In this section we identified $(\mathbb{R}^2)^*$ with $\mathbb{R}^2$ (by identifying the dual base with the reciprocal base) and the components of the 2-tensor $\mathbf{H}(\mathbf{x})$ correspond to the matrix elements of the corresponding linear mapping. The decomposition of a rank-2 tensor $\mathbf{A}$ into irreducible components, recall (7.26), now reads

$$\mathbf{A} = \sum_{m\in\mathbb{Z}} \mathbb{P}_m\mathbf{A} = \sum_{m\in\mathbb{Z}} \mathbf{A}^m = \mathbf{A}^0 + \mathbf{A}^{-2} + \mathbf{A}^2\ ,$$

[7] The irreducible components of the *field* $\mathbf{V}$ should not be mistaken with the irreducible components of the *tensor* $\mathbf{V}(\mathbf{x})$.

which is explicitly in components:

$$\begin{aligned}\mathbf{A} = \begin{pmatrix} A_1^1 & A_2^1 \\ A_1^2 & A_2^2 \end{pmatrix} &= (A_1^1 + A_2^2)\mathbf{E}^{0s} + (A_1^2 - A_2^1)\mathbf{E}^{0a} \\ &+((A_1^1 - A_2^2) - i(A_2^1 + A_1^2))\mathbf{E}^{-2} + ((A_2^2 - A_1^1) - i(A_2^1 + A_1^2))\mathbf{E}^{2}.\end{aligned}$$

with

$$\mathbf{E}^{0s} = \tfrac{1}{2}\begin{pmatrix} 1 & 0 \\ 0 & 1 \end{pmatrix} \quad \mathbf{E}^{0a} = \tfrac{1}{2}\begin{pmatrix} 0 & -1 \\ 1 & 0 \end{pmatrix} \quad \mathbf{E}^{-2} = \tfrac{1}{4}\begin{pmatrix} -1 & -i \\ -i & 1 \end{pmatrix} \quad \mathbf{E}^{2} = \tfrac{1}{4}\begin{pmatrix} -1 & i \\ i & 1 \end{pmatrix}$$

The irreducible components $\{\mathbf{A}^m\}$ are obtained by Weyl's orthogonal projection operator:

$$\mathbf{A}^m = \mathbb{P}_m\mathbf{A} = \frac{1}{2\pi}\int_0^{2\pi} e^{-im\phi} R_\phi \mathbf{A} R_\phi^{-1}\, \mathrm{d}\phi\ .$$

Now suppose that the voting field $\mathbf{V}$ is given by

$$\mathbf{V}(\mathbf{x}) = \sum_{q\in -2,2,0} (\mathbf{V}(\mathbf{x}))^q\ \mathbf{E}_q = \sum_{q\in -2,2,0}\left(\sum_{m\in\mathbb{Z}} e^{im\phi} g^{mq}(r)\right)\ \mathbf{E}^q, \mathbf{x} = (r\cos\phi, r\sin\phi),$$

where $g^{mq}; \mathbb{R}^+ \to \mathbb{R}$ are rapidly decaying (in r) such that $m \mapsto g^m(r) \in \ell_2(\mathbb{Z})$ for all $r > 0$ and all $q \in \{-2, 2, 0\}$. Then we define the tensor fields $\mathbf{V}^m$ by

$$\mathbf{V}^m(\mathbf{x}) = \sum_{q\in\{-2,2,0\}} e^{-i(m-q)\phi} g^{(m-q)q}(r)\ \mathbf{E}^q.$$

Note that $\mathbf{V}^m(\mathbf{x}) \neq (\mathbf{V}(\mathbf{x}))^m\mathbf{E}^m$. It now follows that the rotated vector field is given by

$$\mathbf{V}_R(\mathbf{x}) = R\mathbf{V}(R^{-1}\mathbf{x})R^{-1} = \sum_{m\in\mathbb{Z}} e^{im\theta}\mathbf{V}^m(\mathbf{x})\ , \qquad R = R_\theta,$$

Assume that the original tensor is symmetric (for example a Hessian matrix computed by means of Gaussian derivatives on the original image). Then the quantity $\tilde{s}(\mathbf{H}(\mathbf{x}))$ is usually the so-called *stickness* of the original tensor $s(\mathbf{H}(\mathbf{x}))$: $\tilde{s}(\mathbf{H}(\mathbf{x})) = s(\mathbf{H}(\mathbf{x}))$, with

$$s(\mathbf{H}(\mathbf{x})) = |(\mathbf{H}(\mathbf{x}))^{m=2}| = |\lambda_1(\mathbf{x})| - |\lambda_2(\mathbf{x})| > 0,$$

where $\lambda_1(\mathbf{x})$ and $\lambda_2(\mathbf{x})$ are the eigenvalues of $\mathbf{H}(\mathbf{x})$. Besides, *stick-ness* also the quantity *ball-ness* $\tilde{s}(\mathbf{H}(\mathbf{x})) = b(\mathbf{H}(\mathbf{x}))$, where

$$b(\mathbf{H}(\mathbf{x})) = \frac{1}{2}\left(|(\mathbf{H}(\mathbf{x}))^{m=0}| - |(\mathbf{H}(\mathbf{x}))^{m=2}|\right) = |\lambda_2(\mathbf{x})| > 0,$$

is used. For illustration of stickness and ball-ness, see Figure 5.5. The relation between these 2 quantities and the irreducible components of the original tensor $\mathbf{H}(\mathbf{x})$, is

$$\begin{aligned} s(\mathbf{H}(\mathbf{x})) = |\lambda_2(\mathbf{x})| &= \sqrt{4(H_2^1)^2 + (H_1^1 - H_2^2)^2} &&= |(\mathbf{H}(\mathbf{x}))^2| \\ b(\mathbf{H}(\mathbf{x})) = |\lambda_1(\mathbf{x})| - |\lambda_2(\mathbf{x})| &= \tfrac{1}{2}\left(H_1^1 + H_2^2 - \sqrt{4(H_2^1)^2 + (H_1^1 - H_2^2)^2}\right) &&= \tfrac{1}{2}\left(|(\mathbf{H}(\mathbf{x}))^0| - |(\mathbf{H}(\mathbf{x}))^2|\right). \end{aligned}$$

So in the case $d = 2$ this relation is rather straightforward. Such a relation also exists in the 3D-case, $d = 3$, although it is less straightforward. Note that the quantities $s(\mathbf{H}(\mathbf{x}))$ and $b(\mathbf{H}(\mathbf{x}))$ do not uniquely determine $\mathbf{H}(\mathbf{x})$, in contrast to the irreducible components $\{(\mathbf{H}(\mathbf{x}))^q\}_{q\in\{0,-2,2\}}$.

5.3.1.1 Example: 2D Steerable Voting Field based on Co-circularity

Suppose the voting field is given by

$$\mathbf{V} = p\,\mathbf{c}\otimes\mathbf{c},$$

where $\mathbf{c}(\mathbf{x})$ is the expected normalized vector(i.e. orientation) at position $\mathbf{x}$ given the fact that there is a vector pointing along $\theta = 0$ (say the x-axis) at $\mathbf{0}$ (reflecting the gestalt-law "good continuation") and where p is a rapidly decreasing function centered at the origin $\mathbf{0}$ and oriented along the x-axis (reflecting the Gestalt-law of "proximity"). For example Medioni[95] proposes good continuation by means of co-circularity.[8] (We consider this model for its simplicity, although we stress that the Green's functions of the evolution processes discussed in subsection 4.8.3 can be used to obtain much more sophisticated models for good continuation). If co-circularity is used, which means that $c(x,y)$ is the tangent vector at $\mathbf{x}$ of the unique circle[9] passing through $\mathbf{x}$ and tangentially through $\mathbf{0}$. So,

$$c(x,y) = (\cos 2\phi, \sin 2\phi), \qquad (x,y) = (r\cos\phi, r\sin\phi), \tag{5.14}$$

for $x > 0, y > 0$. For other quadrants the vectors are obtained by reflection in x and y-axis, see Figure 5.5. Consider the proximity function

$$p(\mathbf{x}) = 8\, e^{-\frac{r^2}{2\sigma^2}} \cos^4(\phi), \tag{5.15}$$

where $\sigma > 0$ reflects the scale of context that is taken into account, proposed by Franken et al.[60]. Then

$$\begin{aligned}
(\mathbf{V}(\mathbf{x}))^0 &= e^{-\frac{r^2}{2\sigma^2}}(e^{-4i\phi} + 4e^{-2i\phi} + 6 + 4e^{2i\phi} + e^{4i\phi})\\
(\mathbf{V}(\mathbf{x}))^2 &= e^{-\frac{r^2}{2\sigma^2}}(e^{-8i\phi} + 4e^{-6i\phi} + 6e^{-4i\phi} + 4e^{-2i\phi} + 1)\\
(\mathbf{V}(\mathbf{x}))^{-2} &= e^{-\frac{r^2}{2\sigma^2}}(1 + 4e^{2i\phi} + 6e^{4i\phi} + 4e^{6i\phi} + e^{8i\phi}),
\end{aligned}$$

and thereby the irreducible components $\mathbf{v}^m$ of the voting field are given by

$$\begin{aligned}
\mathbf{V}^0(\mathbf{x}) &= e^{-\frac{r^2}{2\sigma^2}}[6\,\mathbf{E}^0 + 4e^{-2i\phi}\,\mathbf{E}^{-2} + 4e^{2i\phi}\,\mathbf{E}^2]\\
\mathbf{V}^2(\mathbf{x}) &= \overline{\mathbf{V}^{-2}(\mathbf{x})} = e^{-\frac{r^2}{2\sigma^2}}[4e^{-2i\phi}\,\mathbf{E}^0 + 6e^{-4i\phi}\mathbf{E}^{-2} + \mathbf{E}^2]\\
\mathbf{V}^4(\mathbf{x}) &= \overline{\mathbf{V}^{-4}(\mathbf{x})} = e^{-\frac{r^2}{2\sigma^2}}[e^{-4i\phi}\,\mathbf{E}^0 + 4\,e^{-6i\phi}\mathbf{E}^{-2}]\\
\mathbf{V}^6(\mathbf{x}) &= \overline{\mathbf{V}^{-6}(\mathbf{x})} = e^{-\frac{r^2}{2\sigma^2}}[e^{-8i\phi}\,\mathbf{E}^{-2}],
\end{aligned}$$

and the other m-components are 0.

The case $N = 1$ is similar to the case $N = 2$. The only substantial difference is that the irreducible components of vectors are given by

$$\begin{pmatrix} a \\ b \end{pmatrix} = (a+ib)\mathbf{E}^1 + (a-ib)\mathbf{E}^{-1} \text{ with } \mathbf{E}^1 = \tfrac{1}{2}\begin{pmatrix} 1 \\ -i \end{pmatrix} \text{ and } \mathbf{E}^{-1} = \tfrac{1}{2}\begin{pmatrix} 1 \\ i \end{pmatrix}$$

[8] A lot of dubious claims has been written on the co-circularity model in image analysis. For example it is claimed to be "model-free".

[9] This transport along these circles is an orthogonal mapping between two tangent spaces (i.e. parallel transport). The circles involved are determined by 3 degrees of freedom and thereby they are not geodesics of some metric tensor on $\mathbb{R}^2$.

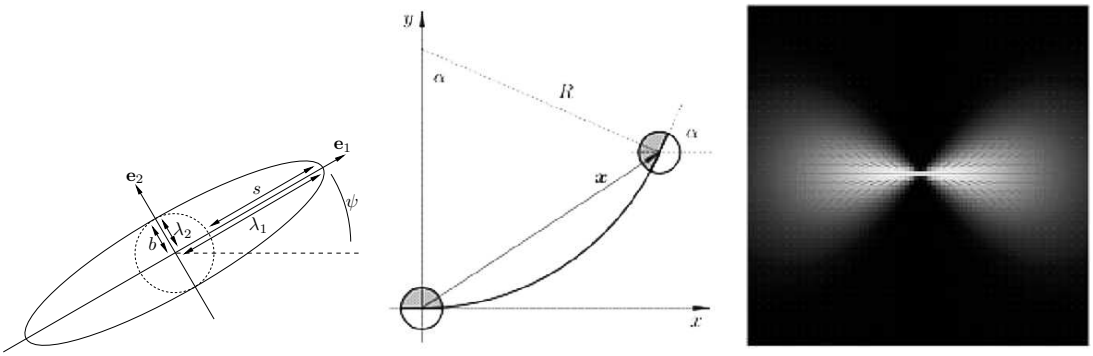

Figure 5.5: Left: Plot of the ellipsoids of the original symmetric tensors $\mathbf{H}(\mathbf{x})$ at $\mathbf{x}$, notice that the angle $\psi = R(H_f(\mathbf{x}))$ is a first rough estimate of the orientation at $\mathbf{x}$ in image f. Middle: Illustration of co-circularity, $\alpha = 2\phi$, where $\mathbf{x} = (r\cos\phi, r\sin\phi)$, as a model for good continuation. Right: The voting field $V = p\,\mathbf{c}\otimes\mathbf{c}$, where $\mathbf{c}(x,y) = (\cos 2\phi, \sin 2\phi)$ and p given by (5.15).

so we now obtain $\mathbf{V}^m(\mathbf{x}) = \sum_{q\in\{-1,1\}} e^{-i(m-q)\phi} g^{(m-q)q}(r)\ \mathbf{E}^q$. Notice that the voting field now becomes a vector field which is rotated by means of $\mathbf{V}_{R_\theta}(\mathbf{x}) = R_\theta \mathbf{V}(R_\theta^{-1}\mathbf{x}) = \sum_{m\in\mathbb{Z}} e^{im\theta}\mathbf{V}^m(\mathbf{x})$.

5.3.1.2 Explicit-Algorithm for 2D Steerable Tensor Voting

Let $\{(\mathbf{H}_{NEW}(\mathbf{b}))^m\}_{|m|\le N}$ be the irreducible components of the output tensor evaluated at position $\mathbf{b}\in\mathbb{R}^2$ (here we consider the case $d=2$ only). If for example[10] the tensor $\mathbf{H}(\mathbf{b})$ is of rank 2 (so the rank of $\mathbf{H}_{NEW}(\mathbf{b})$ is also 2) the only non-vanishing components are the ones with $m=-2$, $m=2$, $m=0$.

Let $(\mathbf{V}(\mathbf{y}))^m = (\tilde{V}(\mathbf{y}))^m\mathbf{E}^m$ be the irreducible components of the tensor $\mathbf{V}(\mathbf{y})$ for all $\mathbf{y}\in\mathbb{R}^2$ and define the vector functions $V_{mn}:\mathbb{R}^2\to\mathbb{R}^2$ by

$$V_{mn}(\mathbf{y}) = \int_0^{2\pi} \left(\tilde{V}(R_\theta^{-1}\mathbf{y})\right)^m e^{-in\theta}\,\mathrm{d}\theta,\ \text{for all } \mathbf{y}\in\mathbb{R}^2.$$

Let $\psi(\mathbf{x})$ be the angle of rotation of $\tilde{R}(\mathbf{H}_\mathbf{x})$, i.e.

$$\tilde{R}(\mathbf{H}_\mathbf{x}) = R_{\psi(\mathbf{x})}, \tag{5.16}$$

for all $\mathbf{x}\in\mathbb{R}^2$. Then $\{(\mathbf{H}_{NEW}(\mathbf{b}))^m\}_{|m|\le N}$ can be computed by means of

$$\begin{aligned}(\mathbf{H}_{NEW}(\mathbf{b}))^m &= \int_{\mathbb{R}^d} \tilde{s}(\mathbf{H}(\mathbf{x}))\left(\mathbf{V}_{\tilde{R}(\mathbf{H}(\mathbf{x}))}(\mathbf{b}-\mathbf{x})\right)^m\,\mathrm{d}\mathbf{x}\\ &= \mathbf{E}^m \int_{\mathbb{R}^d}\sum_{n\in\mathbb{Z}} \tilde{s}(\mathbf{H}(\mathbf{x}))\, e^{i(m+n)\psi(\mathbf{x})}\, V_{mn}(\mathbf{b}-\mathbf{x})\,\mathrm{d}\mathbf{x}\\ &= \mathbf{E}^m \sum_{n\in\mathbb{Z}} \left\{(e^{i(m+n)\psi}\ \tilde{s}\circ H) * V_{mn}\right\}(\mathbf{b}).\end{aligned}$$

[10] But if for example $N=4$, in which case the 4-tensor can be identified with a linear mapping on the vector space consisting of linear mappings on $\mathbb{R}^2$, the non-vanishing components are the ones with $m=-4,-2,0,2,4$.

5.3.2 The Case $d = 3$ and $N = 2$.

Again we use the identification of every tangent space with $\mathbb{R}^3$, equipped with standard inner product. Again we identify $\mathbb{R}^3 = (\mathbb{R}^3)^*$ and thereby any 2-tensor $a \otimes b$ can again be identified with a linear mapping from $\mathbb{R}^3$ to $\mathbb{R}^3$.

The decomposition (7.26) of a rank-2 tensor $\mathbf{A} : \mathbb{R}^3 \times \mathbb{R}^3 \to \mathbb{R}$ is now given by

$$\mathbf{A} = \sum_{l=0}^{\infty} \sum_{m=-l}^{l} \mathbb{P}^l_m \mathbf{A} = \sum_{l=0}^{\infty} \sum_{m=-l}^{l} \mathbf{A}^{l,m} = \mathbf{A}^{0,0} + \mathbf{A}^{1,-1} + \mathbf{A}^{1,0} + \mathbf{A}^{1,1} + \mathbf{A}^{2,-2} + \mathbf{A}^{2,-1} + \mathbf{A}^{2,0} + \mathbf{A}^{2,1} + \mathbf{A}^{2,2}.$$

In case $\mathbf{A}$ is symmetric then $\mathbf{A}^{1,-1} = \mathbf{A}^{1,0} = \mathbf{A}^{1,1} = \mathbf{0}$. The explicit expansion for a symmetric 2-tensor in components is given by

$$\begin{aligned} \mathbf{A} = \begin{pmatrix} A^1_1 & A^1_2 & A^1_3 \\ A^1_2 & A^2_2 & A^2_3 \\ A^1_3 & A^2_3 & A^3_3 \end{pmatrix} \quad &= \operatorname{trace}(A)\mathbf{E}^{0,0} - \tfrac{1}{2}(A^1_1 + A^2_2)\mathbf{E}^{2,0} + \tfrac{1}{2}(A^1_3 + i\, A^2_3)\mathbf{E}^{2,1} \\ &\tfrac{1}{2}(-A^1_3 + i\, A^2_3)\mathbf{E}^{2,-1} + \tfrac{1}{4}(A^1_1 + 2i\, A^1_2 - A^2_2)\mathbf{E}^{2,2} + \tfrac{1}{4}(A^1_1 - 2i\, A^1_2 - A^2_2)\mathbf{E}^{2,-2} \end{aligned}$$

with

$$\mathbf{E}^{0,0} = \begin{pmatrix} 0 & 0 & 0 \\ 0 & 0 & 0 \\ 0 & 0 & 1 \end{pmatrix} \qquad \mathbf{E}^{2,0} = \tfrac{1}{\sqrt{6}} \begin{pmatrix} -1 & 0 & 0 \\ 0 & -1 & 0 \\ 0 & 0 & 2 \end{pmatrix} \quad \mathbf{E}^{2,1} = \tfrac{1}{2} \begin{pmatrix} 0 & 0 & 1 \\ 0 & 0 & -i \\ 1 & -i & 0 \end{pmatrix}$$

$$\mathbf{E}^{2,-1} = \tfrac{1}{2} \begin{pmatrix} 0 & 0 & -1 \\ 0 & 0 & -i \\ -1 & -i & 0 \end{pmatrix} \quad \mathbf{E}^{2,2} = \tfrac{1}{2} \begin{pmatrix} 1 & -i & 0 \\ -i & -1 & 0 \\ 0 & 0 & 0 \end{pmatrix} \quad \mathbf{E}^{2,-2} = \tfrac{1}{2} \begin{pmatrix} 1 & i & 0 \\ i & -1 & 0 \\ 0 & 0 & 0 \end{pmatrix}$$

where the irreducible components $\{\mathbf{A}^m\}$ are obtained by Weyl's orthogonal projection operator:

$$\mathbf{A}^{l,m} = \mathbb{P}^{l,m}\mathbf{A} = \frac{(2l+1)}{8\pi^2} \int_{SO(3)} \overline{\Gamma^{(l)}_{mm}(R)} R\mathbf{A}R^{-1}\, \mathrm{d}\mu_{\mathrm{SO(3)}}(\mathrm{R}).$$

The space spanned by $\mathbf{A}^{l=2,m}$ consists of all symmetric matrices with zero trace (which is clearly invariant under rotations).

Notice that the $\mathbf{A}^{l,m}$ are isomorphic to the spherical harmonics Y^l_m under the rotation action:

$$\mathbf{A}^{l,m} \leftrightarrow Y^l_m \Rightarrow R\mathbf{A}^{l,m}R^{-1} \leftrightarrow (\mathbf{x} \mapsto Y^l_m(R^{-1}\mathbf{x})),$$

so we have

$$R\mathbf{A}^{l,m}R^{-1} = \sum_{m'=-l}^{l} \Gamma^{(l)}_{mm'}(R)\mathbf{A}^{l,m'} = \sum_{m'=-l}^{l} e^{-im'\alpha} e^{-im'\gamma} d^l_{mm'}(\beta),$$

where $R = D_{\mathbf{e}_z\gamma} D_{\mathbf{e}_y\beta} D_{\mathbf{e}_z\alpha}$ is the well-known Euler-angle parametrization and

$$\begin{aligned} \Gamma^{(l)}_{mm'}(R) \quad &= \Gamma^{(l)}_{mm'}(\alpha,\beta,\gamma) = e^{-im\alpha} e^{-im'\gamma} d^l_{mm'}(\beta) = \\ &e^{-im\alpha} e^{-im'\gamma} (-1)^{m-m'} \sqrt{(l+m)!(l-m)!(l+m')!(l-m')!} \\ &\sum_k (-1)^k \frac{\left(\cos\frac{\beta}{2}\right)^{2l-2k-m+m'} \left(\sin\frac{\beta}{2}\right)^{2k+m-m'}}{k!(l-m-k)!(l+m'-k)!(m-m'+k)!}. \end{aligned} \tag{5.17}$$

Now suppose that the voting field is given by

$$\mathbf{V}(\mathbf{x}) = \sum_{l\in 0,2} \sum_{m=-l}^{l} \sum_{l'=0}^{\infty} \sum_{m'=-l'}^{l'} R^{lml'm'}(r)\, Y^{l'}_{m'}(\theta,\phi)\mathbf{E}^{lm}$$

where $R^{lml'm'} : \mathbb{R}^+ \to \mathbb{R}$ are rapidly decaying (in r) such and $R^{lml'm'} = 0$ for $l > L \in \mathbb{N}$. Then the rotated voting field is given by

$$\mathbf{V}_{\alpha,\beta,\gamma}(\mathbf{x}) = \sum_{l\in 0,2} \sum_{m=-l}^{l} \sum_{l'=0}^{\infty} \sum_{m'=-l'}^{l'} R^{lml'm'}(r) \sum_{\tilde{m}=-l}^{l} \sum_{\tilde{m}'=-l'}^{l'} \Gamma^{l}_{m\tilde{m}}(\alpha,\beta,\gamma)\Gamma^{l'}_{m'\tilde{m}'}(\alpha,\beta,\gamma) Y^{l'}_{\tilde{m}'}(\theta,\phi)\mathbf{E}^{l\tilde{m}} \tag{5.18}$$

Further we notice that the computation of irreducible components of the voting field rather than the voting field evaluated at $\mathbf{x}$ itself, is much more complicated than in the 2D-case.[11]

The quantity $\tilde{s}(\mathbf{H}(\mathbf{x}))$ in the 3D-case in the non-steerable tensor voting schemes is usually the stickness $s(\mathbf{H}(\mathbf{x}))$, plateness $p(\mathbf{H}(\mathbf{x}))$ or ballness $b(\mathbf{H}(\mathbf{x}))$ of the original tensor $\mathbf{H}(\mathbf{x})$ (for example the tensor whose components coincide with a Hessian matrix computed from an image by means of Gaussian derivatives). They are given by

$$\begin{aligned} s(\mathbf{H}(\mathbf{x})) &= |\lambda_1(\mathbf{x})| - |\lambda_2(\mathbf{x})| > 0 \\ p(\mathbf{H}(\mathbf{x})) &= |\lambda_2(\mathbf{x})| - |\lambda_3(\mathbf{x})| > 0 \\ b(\mathbf{H}(\mathbf{x})) &= |\lambda_3(\mathbf{x})| > 0 \end{aligned}$$

where $\lambda_1(\mathbf{x}), \lambda_2(\mathbf{x}), \lambda_3(\mathbf{x})$, with $|\lambda_1(\mathbf{x})| \geq |\lambda_2(\mathbf{x})| \geq |\lambda_3(\mathbf{x})|$ are the eigenvalues of $\mathbf{H}(\mathbf{x})$. Again we notice that the quantities $\lambda_1(\mathbf{x}), \lambda_2(\mathbf{x}), \lambda_3(\mathbf{x})$ do not[12] uniquely determine the tensor $\mathbf{H}(\mathbf{x})$, in contrast to the 6-irreducible components $\{(\mathbf{H}(\mathbf{x}))^l_m \mid l = 0, 2, |m| \leq l\}$ of the tensor $\mathbf{H}(\mathbf{x})$. The precise relation between the irreducible components and the eigenvalues is somewhat complicated.

In the 3D-tensor voting scheme we usually consider voting fields which are invariant under rotations over the z-axis. So (similar as in the $3D$-invertible orientation score framework) we consider the quotient $SO(3)/SO(2) \equiv S^2$ rather than the whole rotation group, simply by setting the first Euler angle to zero, $\alpha = 0$.

As for the function R which maps a 2-tensor $\mathbf{H}(\mathbf{x})$ on $\mathbb{R}^3$ to a rotation element $R(\mathbf{H}(\mathbf{x}))$ (or rather an element within $SO(3)/SO(2)$), recall (5.13)), we propose the one that is given by the mapping $\mathbf{H}(\mathbf{x}) \mapsto (\beta(\mathbf{H}(\mathbf{x})), \gamma(\mathbf{H}(\mathbf{x})))$, where $\beta(\mathbf{H}(\mathbf{x}))$ and $\gamma(\mathbf{H}(\mathbf{x}))$ are the ball-coordinates of the eigen vector with largest eigen value of $\mathbf{H}(\mathbf{x})$.

[11] After identifying $\mathbf{E}^l_m$ with Y^l_m, the Clebsch-Gordan coefficients of $SO(3)$ are needed to express the direct products $Y^l_m Y^{l'}_{m'}$ in linear combinations of (single) spherical harmonics again.

[12] In comparison to the 2D-case we are even lacking 3 degrees of freedom rather than the single one in the 2D case.

5.3.2.1 Example: Steerable 3D-Voting Field based on Co-Circularity

In 3D we again use the principle of co-circularity to obtain a (stick) voting field $\mathbf{V} = p\ \mathbf{c} \otimes \mathbf{c}$, where the vector field

$$\mathbf{c}(\mathbf{x}) = \begin{pmatrix} \cos(\phi)\sin(2\theta) \\ \sin(\phi)\sin(2\theta) \\ \cos(2\theta) \end{pmatrix}, \quad \text{with } \mathbf{x} = (\cos(\phi)\sin(\theta), \sin(\phi)\sin(\theta), \cos(\theta))^T$$

reflects the expected direction at position $\mathbf{x}$ given the fact that the direction at the origin is along the z-axis $\mathbf{e}_z$. Notice that in each plane $\phi =$ constant this direction field coincides with the one earlier considered in the $2D$-case, recall (5.14). Analogous to the 2D case we propose the proximity function

$$p(\mathbf{x}) = (\cos\theta)^{2k} e^{-\frac{r^2}{2\sigma}}, \qquad r = \|\mathbf{x}\|,$$

where $\sigma > 0$ reflects the scale of context that is taken into account to get a robust orientation estimate at position $\mathbf{x}$, $\mathbf{H}_{New}(\mathbf{x})$ from the initial field $\mathbf{H}$ around $\mathbf{x}$. The parameter $k \in \mathbb{N}$ determines the directed-ness of the proximity function. Again we put $k = 2$. The voting field evaluated at $\mathbf{x} \in \mathbb{R}^3$ is now given by

$$\mathbf{V}(\mathbf{x}) = e^{-\frac{r^2}{2\sigma}} \begin{pmatrix} 4\cos^6(\theta)\,\cos^2(\phi)\,\sin^2(\theta) & 4\cos^6(\theta)\,\cos(\phi)\,\sin^2(\theta)\,\sin(\phi) & \frac{1}{2}\cos^4(\theta)\,\cos(\phi)\,\sin(4\theta) \\ 4\cos^6(\theta)\,\cos(\phi)\,\sin^2(\theta)\,\sin(\phi) & 4\cos^6(\theta)\,\sin^2(\theta)\,\sin^2(\phi) & \frac{1}{2}\cos^4(\theta)\,\sin(4\theta)\,\sin(\phi) \\ \frac{1}{2}\cos^4(\theta)\,\cos(\phi)\,\sin(4\phi) & \frac{1}{2}\cos^4(\theta)\,\sin(\phi)\,\sin(4\theta) & \cos^4(\theta)\cos^2(2\theta) \end{pmatrix}$$

Now expand $\mathbf{x} \mapsto \mathbf{V}(\mathbf{x})$ into spherical Harmonics:

$$\mathbf{V}(\mathbf{x}) = e^{-\frac{r^2}{2\sigma}}\, Y_m^l(\theta,\phi)\, \mathbf{V}_{l,m}\ ,$$

with

$$\mathbf{V}_{l,m} = \int_0^{\pi}\int_0^{2\pi} \begin{pmatrix} 4\cos^6(\theta)\,\cos^2(\phi)\,\sin^2(\theta) & 4\cos^6(\theta)\,\cos(\phi)\,\sin^2(\theta)\,\sin(\phi) & \frac{1}{2}\cos^4(\theta)\,\cos(\phi)\,\sin(4\theta) \\ 4\cos^6(\theta)\,\cos(\phi)\,\sin^2(\theta)\,\sin(\phi) & 4\cos^6(\theta)\,\sin^2(\theta)\,\sin^2(\phi) & \frac{1}{2}\cos^4(\theta)\,\sin(4\theta)\,\sin(\phi) \\ \frac{1}{2}\cos^4(\theta)\,\cos(\phi)\,\sin(4\phi) & \frac{1}{2}\cos^4(\theta)\,\sin(\phi)\,\sin(4\theta) & \cos^4(\theta)\cos^2(2\theta) \end{pmatrix} \overline{Y_m^l(\theta,\phi)}\, \mathrm{d}\phi \mathrm{d}\theta,$$

then it follows by some computation that

$$\begin{aligned} \mathbf{V}_{l,0} &= V_{l,0}^{2,0}\,\mathbf{E}^{2,0} + V_{l,0}^{0,0}\,\mathbf{E}^{0,0}, & l = 0,2,4,6,8, \\ \mathbf{V}_{l,\pm1} &= V_{l,\pm1}^{2,\pm1}\,\mathbf{E}^{2,\pm1}, & l = 2,4,6,8, \\ \mathbf{V}_{l,\pm2} &= V_{l,\pm2}^{2,\pm2}\,\mathbf{E}^{2,\pm2}, & l = 2,4,6,8, \end{aligned}$$

and all other components $V_{l,m}$ vanish. The fixed real numbers $V_{l,0}^{0,0}, V_{l,0}^{2,0}, V_{l,\pm1}^{2,\pm1}, V_{l,\pm2}^{2,\pm2}$ are easily computed in *Mathematica*. As a result we obtain the voting-field in steerable components

$$\begin{aligned} \mathbf{V}(\mathbf{x}) &= \sum_{l=0,2,4,6,8} \sum_{m=-2}^{2} \mathbf{V}_{lm}\, Y_m^l(\theta,\phi)\, e^{-\frac{r^2}{2\sigma^2}} \\ &= e^{-\frac{r^2}{2\sigma^2}} \sum_{l=0,2,4,6,8} \sum_{m=-2}^{2} V_{l,m}^{2,m} \left(Y_m^l(\theta,\phi)\,\mathbf{E}^{2,m}\right) + \delta_{m0} V_{l,0}^{0,0} \left(Y_0^l(\theta,\phi)\,\mathbf{E}^{0,0}\right). \end{aligned}$$

The rotated voting field is now given by

$$\begin{aligned} \mathbf{V}_{\alpha,\beta,\gamma}(\mathbf{x}) &= e^{-\frac{r^2}{2\sigma^2}} \sum_{l=0,2,4,6,8} \sum_{m=-2}^{2} \delta_{m0} V_{l,0}^{0,0} \left(\sum_{m''=-l}^{l} Y_{m''}^l(\theta,\phi)\, \Gamma_{0m''}^{(l)}(\alpha,\beta,\gamma) \right) \mathbf{E}^{0,0} \\ &\quad + V_{l,m}^{2,m} \left(\sum_{m'=-2}^{2} \Gamma_{mm'}^{(2)}(\alpha,\beta,\gamma) \left(\sum_{m''=-l}^{l} Y_{m''}^l(\theta,\phi)\, \Gamma_{mm''}^{(l)}(\alpha,\beta,\gamma) \right) \mathbf{E}^{2,m'} \right) \end{aligned}$$

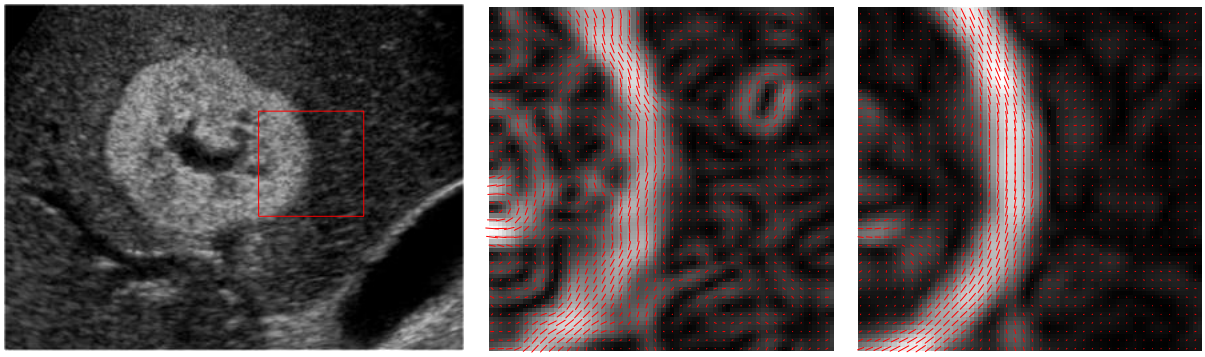

Figure 5.6: Left: Original ultrasound image of a kidney. Middle: gradient field on part of original image, Right: Resulting field after tensor voting, resulting in a more robust orientation estimation (and background noise is suppressed).

Here we notice that we may as well put $\alpha = 0$ because the voting-field is symmetric around the z-axis.

Unfortunately, the computation of $\mathbf{H}_{NEW}$ from $\mathbf{H}$ by means of voting field $\mathbf{V}$, recall (5.13), takes quite some $3D$-convolutions:

$$\begin{aligned}\mathbf{H}_{NEW}(\mathbf{b}) &= \int_{\mathbb{R}^3} \tilde{s}(H(\mathbf{x}))\, \mathbf{V}_{\beta(\mathbf{H}(\mathbf{x})),\gamma(\mathbf{H}(\mathbf{x}))}(\mathbf{b}-\mathbf{x})\, \mathrm{d}\mathbf{x} \\ &= \sum_{l=0,2,4,6,8} V^{0,0}_{l,0} (F_{l0} * (\tilde{s} \circ \mathbf{H}))(\mathbf{b})\, \mathbf{E}^{0,0} \\ &\quad + \sum_{m=-2}^{2} V^{2,m}_{l,m} \sum_{m'=-2}^{2} (G^{m'}_{lm} * (\tilde{s} \circ \mathbf{H}))(\mathbf{b})\, \mathbf{E}^{2,m'},\end{aligned} \tag{5.19}$$

where the functions $F_{lm} : \mathbb{R}^2 \to \mathbb{C}$ and $G^{m'}_{lm} : \mathbb{R}^2 \to \mathbb{C}$ are given by

$$\begin{aligned}F_{lm}(\mathbf{x}) &= e^{-\frac{r^2}{2\sigma^2}} \sum_{m''=-l}^{l} Y^l_{m''}(\theta,\phi) \\ G^{m'}_{lm}(\mathbf{x}) &= \Gamma^{(2)}_{mm'}(0, \beta(\mathbf{H}(\mathbf{x})), \gamma(\mathbf{H}(\mathbf{x})))\, F_{lm}(\mathbf{x}).\end{aligned}$$

Notice that by $\Gamma^{(l)}_{-m-m'}(\alpha,\beta,\gamma) = (-1)^{m+m'} \overline{\Gamma^{(l)}_{mm'}(\alpha,\beta,\gamma)}$ and $Y^l_{-m} = (-1)^m \overline{Y^l_m(\theta,\phi)}$ the number of convolutions can be reduced. Further reduction can be accomplished using recursion relations. But probably (this is a point for future investigation) the largest reduction is obtained by computing the irreducible components of the actual tensor field using the Wigner-Ekhart Theorem as sketched in section 7.9.1 in the appendix.

So we conclude by (5.19) that the algorithm for 3D-steerable tensor voting is established. Unfortunately, unlike the 2D-steerable tensor voting, the algorithm is still rather expensive.[13] In the next subsection we will further discus the analogy between the tensor voting framework and the orientation score framework.

[13] If the orientation parameters β and γ are not restricted to the special choice $\beta = \beta(\mathbf{H}(\mathbf{x}))$ and $\gamma = \gamma(\mathbf{H}(\mathbf{x}))$ the steerability is more useful for the computation speed purposes since then we have $\mathbf{H}_{NEW}(\mathbf{x}, \mathbf{n}(\beta,\gamma)) = \sum_{l\in\mathbb{N}} \Gamma^{(l)}(0,\beta,\gamma) \int_{\mathbb{R}^2} \tilde{s}(\mathbf{H}(\mathbf{x}))\, \mathbf{V}^l(\mathbf{b}-\mathbf{x})\, \mathrm{d}\mathbf{x}$.

5.4 Explicit Relation between 2D-Tensor Voting and G-Convolutions on Orientation Scores

Let $\mathbf{H}$ be the original N-tensor field computed from image $f : \mathbb{R}^2 \to \mathbb{R}$. Let $\mathbf{V}$ be the voting field, which is also a rank N-tensor field. Suppose that $\tilde{s} : \mathcal{T}_N \to \mathbb{R}^+$ and $R : \mathcal{T}_N \to SO(2)$ are given and let $\psi : \mathbb{R}^2 \to [0, 2\pi)$ be given by (5.16).

Define $U : G \to \mathbb{R}$, with $G = \mathbb{R}^2 \rtimes \mathbb{T}$, by

$$U(\mathbf{b}, e^{i\theta}) = \tilde{s}(\mathbf{H}(\mathbf{b}))\, \delta(\theta - \psi(\mathbf{b})),$$

and define $K : G \to \mathbb{R}$ by

$$K(\mathbf{b}, e^{i\theta}) = \sum_{m \in \mathbb{Z}} K^m(\mathbf{b}) e^{-im\theta},$$

where $K^m : \mathbb{R}^2 \to \mathbb{R}$, $m \in \mathbb{Z}$, are given by

$$K^m(\mathbf{b})\mathbf{E}^m = (\mathbf{V}(\mathbf{b}))^m,$$

then we have

$$\boxed{(\mathbf{H}_{NEW}(\mathbf{b}))^m = (K *_G U)^m(\mathbf{b})\, \mathbf{E}^m} \tag{5.20}$$

where $K *_G U$ is the G-convolution (Recall that a G-convolution is given by (4.81), for details on implementation issues see Section 7.8) of the score U with kernel K and where

$$(K *_G U)(\mathbf{b}, e^{i\theta}) = \frac{1}{2\pi} \sum_{m \in \mathbb{Z}} e^{-im\theta} (K *_G U)^m(\mathbf{b}). \tag{5.21}$$

Explicit verification of equality (5.20)

$$\begin{aligned}
(K *_G U)^m(\mathbf{b})\, \mathbf{E}^m &= \int_{-\pi}^{\pi} (K *_G U)(\mathbf{b}, e^{i\theta})\, e^{im\theta} \mathrm{d}\theta\, \mathbf{E}^m \\
&= \int_{\mathbb{R}^2} \int_{-\pi}^{\pi} \int_{-\pi}^{\pi} K(R_{\theta'}^{-1}(\mathbf{b} - \mathbf{b}'), e^{i(\theta - \theta')}) U(\mathbf{b}', e^{i\theta'}) \mathrm{d}\mathbf{b}' \mathrm{d}\theta' \mathrm{e}^{\mathrm{im}\theta} \mathrm{d}\theta\, \mathbf{E}^m \\
&= \int_{\mathbb{R}^2} \int_{-\pi}^{\pi} e^{im\theta'} K^m(R_{\theta'}^{-1}(\mathbf{b} - \mathbf{b}')) \mathbf{E}^m\, U(\mathbf{b}', e^{i\theta'})\, \mathrm{d}\mathbf{b}' \mathrm{d}\theta' \\
&= \int_{\mathbb{R}^2} e^{im\psi(\mathbf{b}')} K^m(R_{\psi(\mathbf{b}')}^{-1}(\mathbf{b} - \mathbf{b}')) \mathbf{E}^m\, \tilde{s}(\mathbf{H}(\mathbf{b}'))\, \mathrm{d}\mathbf{b}' \\
&= \int_{\mathbb{R}^2} \left(\mathbf{V}_{\psi(\mathbf{b}')}(\mathbf{b} - \mathbf{b}') \right)^m\, \tilde{s}(\mathbf{H}(\mathbf{b}'))\, \mathrm{d}\mathbf{b}' = (\mathbf{H}_{NEW}(\mathbf{b}))^m
\end{aligned} \tag{5.22}$$

We conclude from (5.20) that tensor voting can be expressed in G-convolutions by means of

$$\boxed{\mathbf{H}_{NEW}(\mathbf{b}) = \sum_{m \in \mathbb{Z}} (\mathbf{H}_{NEW}(\mathbf{b}))^m = \sum_{m \in \mathbb{Z}} (K *_G U)^m(\mathbf{b})\, \mathbf{E}^m.} \tag{5.23}$$

Note that the right hand side of equality (5.23) follows by equality (5.21) by replacing $\frac{1}{2\pi} e^{-im\theta}$ by $\mathbf{E}^m$.

5.5 Gauge Coordinates along Robust Orientation Fields and its Application to Curvature Estimation

It is common in image analysis, to algebraically combine Gaussian derivatives, recall (4), to obtain Euclidean invariant differential operators on images, cf.[84], [55], [51], [68]. To this end it is common and most useful to introduce localcoordinates, called gauge coordinates (w, v), along and orthogonal to the Gaussian gradient of an image, recall (3.7). For example, recall that a complete set of differential invariants up to second order given by (3.6) are simply given by $\{u, u_w, u_{vw}, u_{vv}, u_{ww}\}$, as we recall from (3.8), where $u = u_f(\cdot, s)$ is say the Gaussian scale space of image $f : \mathbb{R}^d \to \mathbb{R}$. Notice that the operators ∂_v (respectively ∂_w) are in fact Lie-derivatives of the scalar function $u : \mathbb{R}^d \to \mathbb{R}$ with respect to the field $\mathbf{v} = \frac{1}{\|\nabla u\|} R_{\pi/2} \nabla u$ (respectively $\mathbf{w} = \frac{1}{\|\nabla u\|} \nabla u$):

$$\begin{aligned} \partial_v u &= \mathcal{L}_{\mathbf{v}}[f] = \nabla f \cdot \mathbf{v} \\ \partial_w u &= \mathcal{L}_{\mathbf{w}}[f] = \nabla f \cdot \mathbf{w}. \end{aligned}$$

So they represent the change of $u = u_f(\cdot, s)$ along the flow-lines of $\mathbf{v}$, respectively $\mathbf{w}$. In case $d = 2$, the following algebraic combinations of these operators yield respectively the isophote and flowline curvature:

$$\begin{aligned} \kappa_1 &= \tfrac{-u_{vv}}{u_w} = -\tfrac{1}{((u_x)^2+(u_y)^2)^{3/2}}((u_y)^2 u_{xx} - 2u_y u_x u_{xy} + (u_x)^2 u_{yy}) \ , \\ \kappa_2 &= \tfrac{-u_{vw}}{u_w} = -\tfrac{1}{((u_x)^2+(u_y)^2)^{3/2}} \left(u_x u_{xx} u_y - (u_x)^2 u_{xy} + (u_y)^2 u_{xy} - u_x u_y u_{yy}\right) \ . \end{aligned} \tag{5.24}$$

Although this indeed puts curvature in a nice mathematical framework, in practice these curvatures (even if the curvatures are multiplied with the strength of an edge $u_w = \sqrt{(u_x)^2 + (u_y)^2}$) do not give good curvature indications or estimates at all. There are several reasons for this shortcoming. First of all the gauge-coordinates are based on the gradient field which is (especially at low scales) not a robust orientation estimation. Moreover in most applications one is interested in curvatures of lines, where the Gaussian gradient is a typical edge detector, not a line detector. Finally we notice that even if the lines in an image f at infinite resolution (i.e. at scale $s = 0$) are isophotes, these isophotes break apart in $u = u_f(\cdot, s)$ as soon as scale $s > 0$ is increased, yielding extreme magnitudes of curvatures at positions where the isophotes break, whereas in the original image f at these positions the magnitude of the curvature of the isophotes does not have these extreme values.

Therefore in the following section we will explain how to compute the curvatures along (and orthogonal to) the flow-lines of any robust orientation field $\mathbf{w}_f$. In Chapter 5 we explained several methods to obtain these robust orientation estimates from image f, so here we will assume that $\mathbf{w}_f$ is given.

5.5.1 Curvature in 2D-images

Next we shall derive a general formula for the curvature of the flow-lines along the robust vector field $\mathbf{w} = \mathbf{w}_f$, obtained from a 2D image $f \in \mathbb{L}_2(\mathbb{R}^2)$. Then through each $\mathbf{x}_0 \in \mathbb{R}^2$ there is a unique flow line $\mathbf{x} : \mathbb{R} \to \mathbb{R}^2$ which is given by

$$\begin{cases} \frac{d\mathbf{x}(t)}{dt} = \mathbf{w}(\mathbf{x}(t)) \\ \mathbf{x}(0) = \mathbf{x}_0 \end{cases} \tag{5.25}$$

The arc-length $s : \mathbb{R}^+ \to \mathbb{R}^+$ is given by $s(t) = \int_0^t \|\frac{\partial \mathbf{x}}{\partial \tau}\| \mathrm{d}\tau$. Note that $\frac{ds}{dt}(t) = \|\frac{\partial \mathbf{x}}{\partial t}(t)\|$, whence

$$\frac{dt}{ds}(s) = \|\frac{d\mathbf{x}}{dt}(t(s))\|^{-1}.$$

Then the curvature $\boldsymbol{\kappa}_1$ of the flow-line of $\mathbf{w}$ is by definition given by

$$\boldsymbol{\kappa}_1(\mathbf{x}(t(s))) = \ddot{\mathbf{x}}(s) = \frac{d^2}{ds^2}\mathbf{x}(t(s)) \ .$$

We notice that $\|\dot{\mathbf{x}}(s)\| = \|\frac{d}{ds}\mathbf{x}(t(s))\| = \|\frac{d\mathbf{x}}{dt}(t(s))\frac{dt}{ds}\| = \|\frac{d\mathbf{x}}{dt}(t(s))\|\|\frac{d\mathbf{x}}{dt}(t(s))\|^{-1} = 1$, and therefore

$$\frac{d}{ds}\|\dot{\mathbf{x}}(s)\|^2 = 2(\ddot{\mathbf{x}}, \dot{\mathbf{x}}) = 0,$$

from which we conclude that

$$\mathbf{w}(\mathbf{x}(s)) \equiv \dot{\mathbf{x}}(s) \perp \ddot{\mathbf{x}}(s) \text{ for all } s > 0. \tag{5.26}$$

Now we compute the curvature vector by means of the chain rule

$$\begin{aligned}
\ddot{\mathbf{x}}(s) &= \tfrac{d}{ds}\left(\tfrac{\mathbf{w}(\mathbf{x}(t(s)))}{\|\mathbf{w}(\mathbf{x}(t(s)))\|}\right) \\
&= \tfrac{d}{ds}\left\{\tfrac{1}{\|\mathbf{w}(\mathbf{x}(t(s)))\|}\right\}\mathbf{w}(\mathbf{x}(t(s)) + \tfrac{1}{\|\mathbf{w}(\mathbf{x}(t(s)))\|}\tfrac{dt}{ds}\ \tfrac{d}{dt}\mathbf{w}(\mathbf{x}(t))\big|_{t=t(s)} \ , \\
&= \tfrac{d}{ds}\left\{\tfrac{1}{\|\mathbf{w}(\mathbf{x}(t(s)))\|}\right\}\mathbf{w}(\mathbf{x}(t(s)) + \tfrac{1}{\|\mathbf{w}(\mathbf{x}(t(s)))\|^2}[\nabla\mathbf{w}(\mathbf{x}(t(s)))]\mathbf{w}(\mathbf{x}(t(s)))
\end{aligned}$$

Then it follows by the above computation and (5.26) that the curvature field along the flow lines is given by

$$\boldsymbol{\kappa}_1(\mathbf{x}(t(s))) = \ddot{\mathbf{x}}(s) = \left(\frac{1}{\|\mathbf{w}(\mathbf{x}(t(s)))\|^4}(\mathbf{w}^\perp(\mathbf{x}(t(s))))^T\ [\nabla\mathbf{w}]|_{\mathbf{x}=\mathbf{x}(t(s))}\,\mathbf{w}(\mathbf{x}(t(s)))\right)\mathbf{w}^\perp(\mathbf{x}(t(s))), \tag{5.27}$$

where $\mathbf{w}^\perp(\mathbf{x}) = R_{\frac{\pi}{2}}\mathbf{w}(\mathbf{x})$ for all $\mathbf{x} \in \mathbb{R}^2$. The magnitude of the curvature of a flow-line of $\mathbf{w}$ at position $\mathbf{x} \in \mathbb{R}^2$ is given by

$$\begin{aligned}
\kappa_1(\mathbf{x}) &= \|\boldsymbol{\kappa}_1(\mathbf{x})\| = |\boldsymbol{\kappa}_1(\mathbf{x}) \cdot \tfrac{1}{\|\mathbf{w}^\perp(\mathbf{x})\|}\mathbf{w}^\perp(\mathbf{x})| \\
&= \tfrac{1}{\|\mathbf{w}(\mathbf{x})\|^3}(\mathbf{w}^\perp(\mathbf{x}))^T[\nabla\mathbf{w}(\mathbf{x})]\mathbf{w}(\mathbf{x}).
\end{aligned} \tag{5.28}$$

Notice that the magnitude κ of the curvature also equals

$$\kappa^2(\mathbf{x}(s)) = \left(\frac{d\phi}{ds}(s)\right)^2 = \left(\lim_{\Delta s \to 0}\frac{\phi(s+\Delta s) - \phi(s)}{\Delta s}\right)^2,$$

where $\phi(s)$ is the angle between $\mathbf{w}(\mathbf{x}(s))$ and some axis $\mathbf{e}$, such that $\phi(\mathbf{x}(s+\Delta s)) - \phi(\mathbf{x}(s))$ is the angle between $\mathbf{w}(\mathbf{x}(s+\Delta s))$ and $\mathbf{w}(\mathbf{x}(s))$.

Similarly, the curvature $\boldsymbol{\kappa}_2$ of the flow-line of $\mathbf{w}^\perp$ at position $\mathbf{x} \in \mathbb{R}^2$ is given by

$$\boldsymbol{\kappa}_2(\mathbf{x}) = \frac{1}{\|\mathbf{w}(\mathbf{x})\|^4}\left((\mathbf{w}(\mathbf{x}))^T[\nabla\mathbf{w}^\perp(\mathbf{x})]\mathbf{w}^\perp(\mathbf{x})\right)\mathbf{w}(\mathbf{x}). \tag{5.29}$$

and

$$\kappa_2(\mathbf{x}) = \frac{1}{\|\mathbf{w}(\mathbf{x})\|^3}(\mathbf{w}(\mathbf{x}))^T[\nabla \mathbf{w}^\perp(\mathbf{x})]\mathbf{w}^\perp(\mathbf{x}).$$

Example:
Consider the case $\mathbf{w}(\mathbf{x}) = \mathbf{x} = (x, y)^T$. Then $\mathbf{w}^\perp(\mathbf{x}) = (-y, x)^T$ and obviously the integral curves of respectively $\mathbf{w}$ and $\mathbf{w}^\perp$ are respectively straight-lines through the origin and concentric circles around the origin and we have

$$\boldsymbol{\kappa}_1(\mathbf{x}) = \mathbf{0} \text{ and } \boldsymbol{\kappa}_2(\mathbf{x}) = \frac{1}{\|\mathbf{x}\|^2}\mathbf{x} \ .$$

A single integral curve of $\mathbf{w}^\perp$ through $\mathbf{x}$ is a positively oriented circle movement along a circle with constant radius $R = \|\mathbf{x}\|$. The curvature points outward and its magnitude equals $\kappa_2 = \frac{1}{\|\mathbf{x}\|} = \frac{1}{R}$.

Example: Suppose $\mathbf{w}_f = (\nabla f)^T$, then $\nabla \mathbf{w}_f = \nabla(\nabla f)^T$ equals the Hessian and by straightforward computation one easily obtains the special case of flowline curvature and isophote curvature (5.24).

So we conclude that we provided a much more general scheme of computing multi-scale curvatures. The input orientation field may be the eigenvectors (with smallest absolute eigenvalues) of the Gaussian Hessian matrix of f which is usually much better aligned with elongated structures/lines in images, see Figure 5.7, but it is of course much more interesting to first perform a robust orientation estimation technique like tensor voting or by means of the channel representations before computing the curvature, see Figure 5.8.

Remark:
A practical problem using the orientation field obtained by the eigenvectors of the Hessian is that there is a sign ambiguity. For the moment we solved this problem using ad-hoc approaches, but this certainly is a point for further investigation. Finally we notice that the curvatures along the flow-lines of $\mathbf{w}$ and along the flow-lines of $\mathbf{w}^\perp$ are related to the Lie-product of $\mathbf{w}$ and $\mathbf{w}^\perp$. This is not surprising as this Lieproduct tells us how the field $\mathbf{w}^\perp$ changes along the flow-lines of $\mathbf{w}$.

5.5.1.1 Lie-Derivatives and Curvature

The Lie-Derivative $\mathcal{L}_{\mathbf{v}}[\mathbf{w}]$ of a vector field $\mathbf{v} = v^i\partial_i$ with respect to vector field $\mathbf{w} = w^i\partial_i$ is given by

$$(\mathcal{L}_{\mathbf{v}}\mathbf{w})^j = v^i\partial_i w^j - w^i\partial_i v^j \tag{5.30}$$

Actually, there exist more general coordinate independent definitions of the Lie-derivative, cf. [1] p.211, p.220, p.221. The components of $\mathcal{L}_{\mathbf{v}}[\mathbf{w}]$, cf. [1] p.225 are indeed given by (5.30). As a result the components given by (5.30) are indeed components of a (contra-variant) vector field, so the components with respect to a different coordinate system $\{\partial_{i'}\}$ transform accordingly. If $x^{i'} = A^{i'}_j x^j$ then

$$(\mathcal{L}_{\mathbf{v}}\mathbf{w})^{j'} = v^{i'}\partial_{i'}w^{j'} - w^{j'}\partial_{i'}v^{j'} = A^{i'}_i v^i A^k_{i'}\partial_k(A^{j'}_j w^j) - A^{i'}_i w^i A^k_{i'}\partial_k(A^{j'}_j v^j) = A^{j'}_j(\mathcal{L}_{\mathbf{v}}\mathbf{w})^j \ .$$

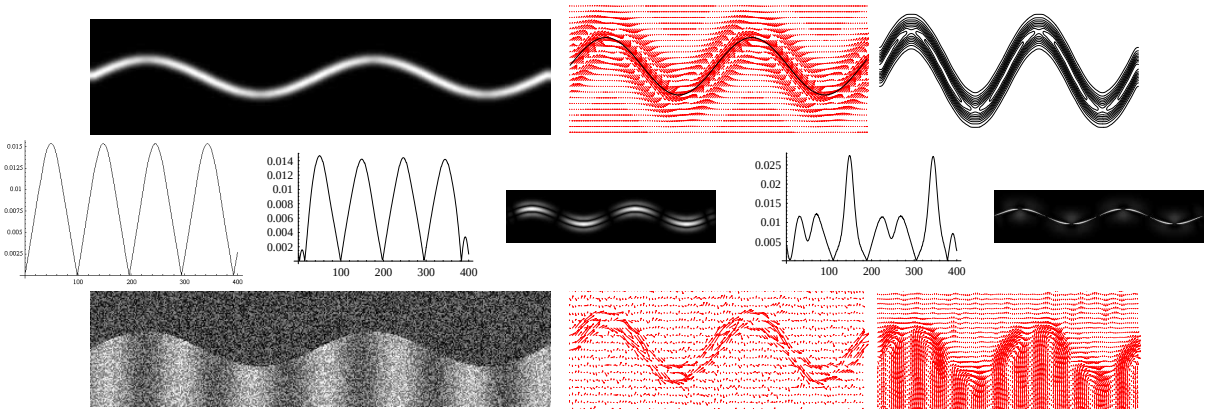

Figure 5.7: First two rows, a comparison between isophote curvature (third column) and the curvature of the flow-lines along the smallest eigen vector field of the Hessian 2-tensor field (second column) of an isophote on a sinusoid ridge. Notice that the isophotes break apart even with a small amount of blurring. As a result the isophote curvature does not work in these cases (moreover in medical imaging the elongated structures are usually not aligned with isophotes, as the intensity on elongated structures usually varies and thereby isophote curvature does not give a good curvature estimate of the curvature of these elongated structures). This is mainly due to the fact that the isophote lies on a ridge structure (which is of our most interest). If it would lie on a edge structure, isophotes get less curved and move away from the boundary. But even in those cases the vector field obtained by eigen vector with smallest absolute eigen value of the Hessian is usually favorable, as is illustrated in the last row of this figure.

Notice that $\mathcal{L}_{\mathbf{v}}\mathbf{w} = -\mathcal{L}_{\mathbf{w}}\mathbf{v}$. The Lie-derivative has the following geometrical interpretation: It can be shown that the Lie-derivative of $\mathbf{w}$ with respect to $\mathbf{v}$ is given by

$$\mathcal{L}_{\mathbf{v}}[\mathbf{w}](\mathbf{x}) = \left.\frac{d}{dt}\right|_{t=0} (F_t^*\mathbf{w})(\mathbf{x}) = \lim_{t\to 0}\frac{1}{t}[(f_{-t})^*\mathbf{w}(f_t(\mathbf{x})) - \mathbf{w}(\mathbf{x})], \text{ i.e.}$$

$$\mathcal{L}_{\mathbf{v}}[\mathbf{w}]_{\mathbf{x}}\phi = \left.\frac{d}{dt}\right|_{t=0} (F_t^*\mathbf{w})_{\mathbf{x}}\phi = \lim_{t\to 0}\frac{1}{t}[(f_{-t})^*\mathbf{w}_{f_t(\mathbf{x})}\phi - \mathbf{w}_{\mathbf{x}}\phi] = \lim_{t\to 0}\frac{1}{t}[\mathbf{w}_{f_t(\mathbf{x})}(\phi\circ f_{-t}) - \mathbf{w}_{\mathbf{x}}\phi] \ ,$$

for all locally smooth $\phi \in C^1(\Omega_{\mathbf{x}})$ and all $\mathbf{x} \in \mathbb{R}^2$. So $F_t^*\mathbf{w}$ is the pull-back of $\mathbf{w}$ with respect to the flow (union of trajectories) f_t of $\mathbf{v}$. Consequently, we have for all $t > 0$:

$$\frac{d}{dt}(F_t^*\mathbf{w}) = \left.\frac{d}{ds}\right|_{s=0} F_{t+s}^*\mathbf{w} = F_t^* \left.\frac{d}{ds}\right|_{s=0} F_s^*\mathbf{w} = F_t^*\mathcal{L}_{\mathbf{v}}[\mathbf{w}] \ .$$

So, geometrically the Lie-derivative $\mathcal{L}_{\mathbf{v}}[\mathbf{w}]$ tells us how vector field $\mathbf{w}$ changes along the flowlines of the vector field $\mathbf{v}$.

Again suppose $\mathbf{w} = w^1\partial_1 + w^2\partial_2$ is a given vector field obtained from image f, such that the flow-lines are supposed to lie along the elongated structures within image f. Then define the vector field $\mathbf{e}_v$ and $\mathbf{e}_w$ by

$$\begin{aligned}\mathbf{e}_w &= \frac{w^1}{\sqrt{(w^1)^2+(w^2)^2}}\partial_1 + \frac{w^2}{\sqrt{(w^1)^2+(w^2)^2}}\partial_2 \\ \mathbf{e}_v &= \frac{-w^2}{\sqrt{(w^1)^2+(w^2)^2}}\partial_1 + \frac{w^1}{\sqrt{(w^1)^2+(w^2)^2}}\partial_2\end{aligned}$$

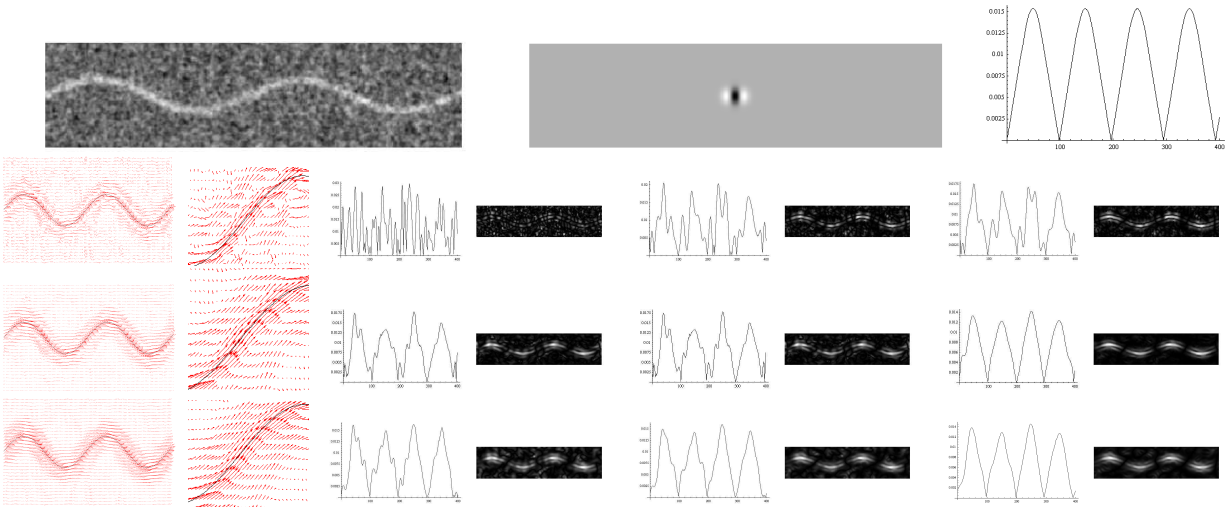

Figure 5.8: Computation of the curvature of the flow-lines with (left) and without (right) robust orientation techniques (in this case by means of channel representations) applied on the vector field obtained by taking the eigenvector with smallest absolute eigen value. Top Row: left, original noisy image with sinusoid $\mathbf{x}(t) = (t, b\sin(at))$ with correlated noise and fluctuating intensities on the line; middle plot of second order derivative of Gaussian at scale $\sigma = 5$, to illustrate the scale $\sigma = 5$ of the Gaussian-Hessian matrix whose eigen vectors with smallest absolute eigenvalues give us the *original flow field*; right, ground truth of the magnitude of the curvature $\|\ddot{\mathbf{x}}\| = \sqrt{\frac{a^4 b^2 \sin^2(at)}{(1+a^2 b^2 \cos^2(a*t))^3}}$, $t \in (0, 400), a = 0.032, b = 15$. Second row, curvature estimation by applying (5.28) on the *original flow field*, using respectively Gaussian derivatives for 3 fixed scales $\sigma = 1, 4, 8$. Third row, curvature estimation again by (5.28), but now after application of tensor voting on the original flow field, again with $\sigma = 1, 4, 8$. Fourth row, curvature estimation again by (5.28), but now after application of robust orientation estimation via channel representations on the original flow field, again with $\sigma = 1, 4, 8$.

Notice that $\{\mathbf{v}(\mathbf{x}), \mathbf{w}(\mathbf{x})\}$ form a orthonormal base at the tangent space $\mathbf{x}$ for each $\mathbf{x} \in \mathbb{R}^2$. It follows by some computation that:

$$\begin{array}{rl} \mathcal{L}_{\mathbf{e}_v}[\mathbf{e}_w](\mathbf{x}) & = \frac{1}{\|\mathbf{w}(\mathbf{x})\|^2} \left(w^2_x w^1 - w^2 w^1_x\right)\big|_{\mathbf{x}} \partial_1 + \left(w^2_y w^1 - w^2 w^1_y\right)\big|_{\mathbf{x}} \partial_2 \\ & \equiv \frac{1}{(w^1(\mathbf{x}))^2 + (w^2(\mathbf{x}))^2} \begin{pmatrix} w^2_x(\mathbf{x}) w^1(\mathbf{x}) - w^2(\mathbf{x}) w^1_x(\mathbf{x}) \\ w^2_y(\mathbf{x}) w^1(\mathbf{x}) - w^2(\mathbf{x}) w^1_y(\mathbf{x}) \end{pmatrix}. \end{array} \tag{5.31}$$

Notice that it directly follows by the geometric interpertation of the Lie-derivative that the curvature (with length κ_2) along the integral-curves of $\mathbf{v}$ is given by

$$\begin{array}{ll} \boldsymbol{\kappa}_2(\mathbf{x}) = \left(\mathcal{L}_{\mathbf{e}_w}[\mathbf{e}_v](\mathbf{x}) \cdot \mathbf{e}_v(\mathbf{x})\right) \mathbf{e}_w(\mathbf{x}) & = \kappa_1(\mathbf{x})\, \mathbf{e}_w(\mathbf{x}) \\ = -\left(\mathcal{L}_{\mathbf{e}_v}[\mathbf{e}_w](\mathbf{x}) \cdot \mathbf{e}_v(\mathbf{x})\right) \mathbf{e}_w(\mathbf{x}) & = -\frac{1}{\|\mathbf{w}(\mathbf{x})\|^3} \big((w^2(\mathbf{x}))^2\, w^1_x(\mathbf{x}) - w^2_x(\mathbf{x}) w^1(\mathbf{x}) w^2(\mathbf{x}) \\ & \quad + (w^1(\mathbf{x}))^2 w^2_y(\mathbf{x}) - w^1(\mathbf{x}) w^2(\mathbf{x}) w^1_y(\mathbf{x}) \big)\, \mathbf{e}_w(\mathbf{x}) \end{array} \tag{5.32}$$

whereas the curvature (with length κ_1) along the flow-lines of $\mathbf{w}$ is given by

$$\begin{array}{ll} \boldsymbol{\kappa}_1(\mathbf{x}) = \left(\mathcal{L}_{\mathbf{e}_v}[\mathbf{e}_w](\mathbf{x}) \cdot \mathbf{e}_w(\mathbf{x})\right) \mathbf{e}_v(\mathbf{x}) = \kappa_2(\mathbf{x})\, \mathbf{e}_v(\mathbf{x}) & = \frac{1}{\|\mathbf{w}(\mathbf{x})\|^3} \big((w^1(\mathbf{x}))^2 w^2_x(\mathbf{x}) - w^1(\mathbf{x}) w^2(\mathbf{x}) w^1_x(\mathbf{x}) \\ & \quad + w^2(\mathbf{x}) w^1(\mathbf{x}) w^2_y(\mathbf{x}) - (w^2(\mathbf{x}))^2 w^1_y(\mathbf{x}) \big)\, \mathbf{e}_v(\mathbf{x}). \end{array} \tag{5.33}$$

Notice that (5.33) and (5.32) indeed coincides with (5.28) and (5.29). Summarizing, in (v, w)-coordinates we have

$$\mathcal{L}_{\mathbf{e}_v}[\mathbf{e}_w] = -\kappa_1 \mathbf{e}_v + \kappa_2 \mathbf{e}_w = \begin{pmatrix} -\kappa_1 \\ \kappa_2 \end{pmatrix}_{vw}. \tag{5.34}$$

Now we return to the idea of computing curvature after applying a robust estimation technique like tensor voting or by means of channel representations as illustrated in Figure 5.8. A drawback of this approach is that we only use the direction field of the robust orientation field, as the strength (or confidence) of the robust orientation estimates does not influence the computation of curvature. Therefore (for visualizations) we multiply the curvature vector field with the confidence scalar field. Another way of including the confidence into the Lie-derivative framework (5.34), would be by substituting by $\phi \mathbf{e}_v$ and $\psi \mathbf{e}_w$, where ψ, ϕ depend on the strength of the robust orientation estimate(i.e. confidence). Notice that

$$\begin{array}{l} \mathcal{L}_{\mathbf{v}}[\psi \mathbf{w}] = \phi\, \mathcal{L}_{\mathbf{v}}[\mathbf{w}] + \mathbf{w} \mathcal{L}_{\mathbf{v}}[\psi] = \psi\, \mathcal{L}_{\mathbf{v}}[\mathbf{w}] + (\nabla \psi \cdot \mathbf{v}) \mathbf{w} \\ \mathcal{L}_{\phi \mathbf{v}}[\mathbf{w}] = -\mathcal{L}_{\mathbf{w}}[\phi \mathbf{v}] = \psi\, \mathcal{L}_{\mathbf{w}}[\mathbf{v}] - (\nabla \phi \cdot \mathbf{w}) \mathbf{v}. \end{array}$$

But if $\psi \neq 1$ or $\phi \neq 1$ the strict concept of curvature is lost.

5.6 Conclusion

In this section we analyzed two different approaches[14] for obtaining robust orientation estimation (based on the Gestalt laws proximity and good continuation):

[14]These 2 methods are easy to implement (for 2D images) and show quite similar results. Although the method of channel representations is less interesting from the mathematical point of view, it seems *slightly* favorable over tensor voting in practice. But at this point we stress that we did not do a decent comparison between these 2 methods.

1. By means of channel representations constructed by B-splines of arbitrary order.
2. By means of steerable tensor voting (also for the 3D-case).

In Section 5.4 we showed that tensor voting is in fact a G-convolution[15] on an orientation score, which puts the connection of Section 5.3 with the more general framework of section 4. Finally, in Section 5.5 we used robust vector fields (obtained by one of these methods) to obtain local gauge coordinate systems, that are much more reliable in practice than the local gauge coordinates based on the (Gaussian) gradient of an image as these fields are much better aligned with the local structures in the image. As a practical example we considered the computation of curvature of elongated structures in 2D-images[16]. We generalized the concept of isophote curvature to curvature along the flow-lines of any given vector-field, yielding better results if applied to robust orientation fields obtained from initial direction fields by means of either channel representations or by means of tensor voting.

[15] Where G stands for the Euclidean motion group, the domain of the orientation scores.

[16] The author also considered curvature estimation in 3D medical images (in cooperation with Richard van der Put, cf.[110]), but this is not included in this thesis.

Part III

Appendix

Chapter 6

Appendix Scale

6.1 The Reproducing kernels $R^2_{k,\gamma}$ of the Sobolev spaces $\mathbb{H}^{k,2}_\gamma(\mathbb{R}^2)$, $k > 1$.

In this section we compute the reproducing kernels $R^2_{k,\gamma}$ of the Sobolev spaces $\mathbb{H}^{k,2}_\gamma(\mathbb{R}^2)$, $k > 1$. They are needed in our reconstruction algorithms to relate $\mathbb{L}_2$-features to the Sobolev features on $\mathbb{H}^{k,2}_\gamma(\mathbb{R}^2)$, $k > 1$. Due to numerical limitations (sampling) the cases which are most practically relevant are $k \in [0, 4]$. The (isotropic) functions $\mathbf{x} \mapsto R^2_{k,\gamma}(\mathbf{x})$, which are illustrated in figure 6.1 , are bounded iff $k > 1$, which coincides with the fact that $\mathbb{H}^{k,2}_\gamma(\mathbb{R}^2)$ is a functional Hilbert space iff $k > 1$.

Lemma 8 *Let $k \in \mathbb{N}$. Define the integral*

$$I_{k,\beta}(r) = \int_0^\infty \frac{\rho J_0(\rho r)}{\beta^{2k} + \rho^{2k}} \mathrm{d}\rho \ .$$

Then $I_{1,\beta}(r) = K_0(\beta r), \Re(\beta) > 0$, where K_0 is the well-known BesselK-function of order 0. Moreover $I_{k,\beta}$ satisfies the recursion relation

$$I_{2k,\beta} = \frac{1}{2\beta^{2k}} \left(e^{-\frac{i\pi}{2k}} I_{k,\beta}(e^{-\frac{i\pi}{4k}} r) + e^{\frac{i\pi}{2k}} I_{k,\beta}(e^{\frac{i\pi}{4k}} r) \right).$$

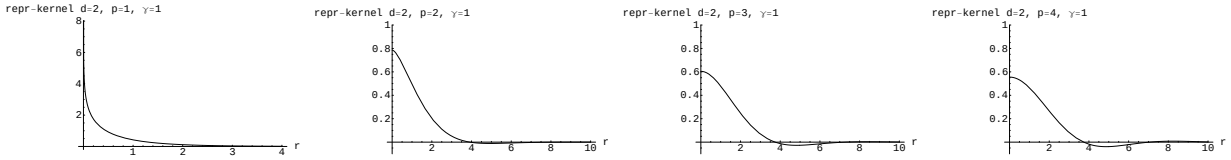

Figure 6.1: Plots of the graphs of the functions $\|\mathbf{x}\| \mapsto R^2_{k,\gamma}(\mathbf{x})$, for $k = 1, 2, 3, 4$ The functions

Proof
For $I_{1,\beta}(r)=K_0(\beta r), \Re(\beta)>0$, see [126]p.425. So it remains to show the recursion.

First we notice that

$$I_{k,\beta}(r)=\mathcal{F}^{-1}(\boldsymbol{\omega}\mapsto\frac{1}{\beta^{2k}+\|\boldsymbol{\omega}\|^{2k}})(\mathbf{x})\ ,\|\mathbf{x}\|=r,$$

and thereby it is readily verified that

$$I_{k,\beta}(r)=\frac{\beta^2}{\beta^{2k}}I_{k,1}(\beta r),\ \text{for all } \beta>0,k\in\mathbb{N}. \tag{6.1}$$

Then we notice that both sides in (6.1) are analytic for $\Re(\beta)>0$ and since an analytic functions is uniquely determined on a set with a point of density, equality (6.1) also holds for $\Re(\beta)>0$. Secondly we have

$$\frac{1}{2i}\left(\frac{1}{\rho^{2k}-i}-\frac{1}{\rho^{2k}+i}\right)=\frac{1}{\rho^{4k}+1}\ ,\text{for all } k\in\mathbb{N},\rho>0.$$

From these two observations, the result follows:

$$\begin{aligned}
I_{2k,\beta}(r) &= \tfrac{\beta^2}{\beta^{4k}}I_{2k,1}(\beta r)\\
&= \tfrac{\beta^2}{\beta^{4k}}\int_0^\infty\tfrac{\rho J_0(\rho r)}{1+\rho^{4k}}\,\mathrm{d}\rho\\
&= \tfrac{\beta^2}{\beta^{4k}}\int_0^\infty\tfrac{\rho J_0(\rho r)}{\rho^{2k}-i}-\tfrac{\rho J_0(\rho r)}{\rho^{2k}+i}\,\mathrm{d}\rho\\
&= \tfrac{\beta^2}{2i\beta^{4k}}\left(ie^{-\frac{i\pi}{2k}}I_{k,1}(e^{-\frac{i\pi}{4k}}r)+e^{\frac{i\pi}{2k}}I_{k,1}(e^{\frac{i\pi}{4k}}r)\right)\\
&= \tfrac{1}{2\beta^{2k}}\left(e^{-\frac{i\pi}{2k}}I_{k,\beta}(e^{-\frac{i\pi}{4k}}r)+e^{\frac{i\pi}{2k}}I_{k,\beta}(e^{\frac{i\pi}{4k}}r)\right)\qquad\square
\end{aligned}\tag{6.2}$$

In particular we have

$$\begin{aligned}
I_{1,\beta}(r) &= \tfrac{1}{2\pi}\ K_0(\beta r)\\
I_{2,\beta}(r) &= \tfrac{1}{2\pi}\ \tfrac{1}{2i\beta^2}(K_0(e^{-\frac{i\pi}{4}}\beta r)-K_0(e^{+\frac{i\pi}{4}}\beta r))=-\tfrac{1}{2\pi\beta^2}\mathrm{kei}_0(\beta r)\\
I_{4,\beta}(r) &= -\tfrac{1}{4\pi\ \beta^6}(e^{-i\pi/4}\mathrm{kei}_0(\beta re^{-i\pi/8})+e^{i\pi/4}\mathrm{kei}_0(\beta re^{i\pi/8}))\ .
\end{aligned}$$

and it can be shown by induction that

$$I_{2^k,\beta}(r)=\frac{\beta^2}{\beta^{2^{k+1}}}I_{2^k,1}(r)=\frac{\beta^2}{\beta^{2^{k+1}}}\sum_{l=0}^{2^{k-1}-1}K_0(e^{\frac{-i\pi(1+2l)}{2^{k+1}}}r)e^{-\frac{\pi i(1+2l)}{2^k}}+K_0(e^{\frac{i\pi(1+2l)}{2^{k+1}}}r)e^{\frac{\pi i(1+2l)}{2^k}}.$$

Mathematica expresses the more general integrals $I_{k,\beta}$ into Meyer-G functions

$$I_{k,\beta}=\frac{1}{2\pi}G^{k+1,0}_{0,2k}(\frac{\rho^{2k}}{k^k}|\mathbf{a}_k)\ ,$$

where $\mathbf{a}_k=\{a_{kj}\}_{j=1}^{2k}\in\mathbb{Q}^{2k}$ is given by

$$\begin{cases}
a_{kj}=\frac{j-1}{k} & \text{for } 1\le j\le k\\
a_{k(k+1)}=\frac{k-1}{k} & \\
a_{kj}=a_{k(j-k-1)} & \text{for } k+2\le j\le 2k.
\end{cases}$$

Theorem 24 *The space $\mathbb{H}^{k,2}_\gamma(\mathbb{R}^d)$ is a reproducing kernel space if and only if $k > d/2$. The reproducing kernel (i.e. the Riesz-representant of the continuous point evaluation, $F(\boldsymbol{a}) = (R^d_{\gamma,k,\boldsymbol{a}}, F)_{\mathbb{H}^{k,2}_\gamma(\mathbb{R}^d)}$) is then given by*

$$\begin{aligned} R^d_{\gamma,k,\boldsymbol{a}}(\boldsymbol{x}) &= \tfrac{1}{\gamma^{2k}}\mathcal{F}^{-1}(\boldsymbol{\omega}\mapsto e^{i\boldsymbol{\omega}\cdot\boldsymbol{a}}\tfrac{1}{\gamma^{-2k}+\|\boldsymbol{\omega}\|^{2k}})(\boldsymbol{x}) \\ &= \tfrac{1}{\gamma^{2k}}\mathcal{F}^{-1}(\boldsymbol{\omega}\mapsto \tfrac{1}{\gamma^{-2k}+\|\boldsymbol{\omega}\|^{2k}})(\boldsymbol{x}-\boldsymbol{a}) \\ &= r^{-\frac{d-2}{2}}\int_0^\infty \rho^{\frac{d}{2}} J_{\frac{d-2}{2}}(\rho r)\tfrac{1}{1+\gamma^{2k}\rho^{2k}}\mathrm{d}\rho\ , \end{aligned} \tag{6.3}$$

where $r = \|\boldsymbol{x}-\boldsymbol{a}\| > 0$ and $\rho = \|\boldsymbol{\omega}\|$. Moreover, these reproducing kernels satisfy the following recursion relation:

$$R^d_{\gamma,2k,\boldsymbol{a}} = \frac{1}{2}\left\{R^d_{\gamma\, e^{\frac{i\pi}{4k}},k,\boldsymbol{a}} + R^d_{\gamma\, e^{\frac{-i\pi}{4k}},k,\boldsymbol{a}}\right\},\ \textit{for all } k>0, d\in\mathbb{N}, \gamma>0, \boldsymbol{a}\in\mathbb{R}^d, \tag{6.4}$$

from which it follows that that

$$R^d_{\gamma,2^p,\boldsymbol{a}}(\boldsymbol{x}) = \frac{1}{2^p}\sum_{k=0}^{2^{p-1}-1}(R^d_{\gamma^+_{k,p},1,\boldsymbol{a}} + R^d_{\gamma^-_{k,p},1,\boldsymbol{a}}),\ \textit{with } \gamma^\pm_{k,p} = \gamma e^{\frac{\pm i\pi(1+2k)}{2^{p+1}}}, p\in\mathbb{N}, \tag{6.5}$$

In the case $d=2$ we have

$$R^{d=2}_{\gamma,k,\boldsymbol{a}}(\boldsymbol{x}) = \frac{1}{\gamma^{2k}} I_{k,\frac{1}{\gamma}}, \qquad r = \|\boldsymbol{x}-\boldsymbol{a}\|.$$

and in particular if $k = 1, 2, 4$ we have

$$\begin{aligned} R^{d=2}_{\gamma,k=1,\boldsymbol{a}}(\boldsymbol{x}) &= -\tfrac{1}{2\pi\gamma^2}K_0\left(\tfrac{r}{\gamma}\right) \\ R^{d=2}_{\gamma,k=2,\boldsymbol{a}}(\boldsymbol{x}) &= -\tfrac{1}{2\pi\gamma^2}kei_0(r/\gamma) = \tfrac{1}{4\pi\gamma^2 i}\left(K_0\left(\tfrac{r}{\gamma}e^{-\frac{i\pi}{4}}\right) - K_0\left(\tfrac{r}{\gamma}e^{\frac{i\pi}{4}}\right)\right), \\ R^{d=2}_{\gamma,k=4,\boldsymbol{a}}(\boldsymbol{x}) &= \tfrac{1}{8\pi\gamma^2}\left(e^{-\frac{3i\pi}{4}}K_0\left(\tfrac{r}{\gamma}e^{-\frac{3i\pi}{8}}\right) - e^{-\frac{3i\pi}{4}}K_0\left(\tfrac{r}{\gamma}e^{\frac{i\pi}{8}}\right) + e^{-\frac{\pi i}{4}}K_0\left(\tfrac{r}{\gamma}e^{\frac{-i\pi}{8}}\right) - e^{-\frac{i\pi}{4}}K_0\left(\tfrac{r}{\gamma}e^{\frac{3i\pi}{8}}\right)\right), \end{aligned}$$

with $r = \|\boldsymbol{x}-\boldsymbol{a}\|$.

Proof First we show that point-evaluation is a continuous/bounded linear functional on $\mathbb{H}^{k,2}_\gamma(\mathbb{R}^d)$ iff $k > \frac{d}{2}$. Without loss of generality we put $\gamma = 1$. Let $f\in\mathbb{H}^{k,2}_{\gamma=1}(\mathbb{R}^d)\cap\mathcal{D}(\mathbb{R}^d)$, then we have

$$\begin{aligned} f(\mathbf{a}) &= \tfrac{1}{(2\pi)^{\frac{d}{2}}}\int_{\mathbb{R}^d}\mathcal{F}[f](\boldsymbol{\omega})e^{i\boldsymbol{\omega}\cdot\mathbf{a}}\mathrm{d}\boldsymbol{\omega} \\ &= \tfrac{1}{(2\pi)^{\frac{d}{2}}}\int_{\mathbb{R}^d}\sqrt{1+\|\boldsymbol{\omega}\|^{2(1+\delta)}}\mathcal{F}[f](\boldsymbol{\omega})\tfrac{e^{i\boldsymbol{\omega}\cdot\mathbf{a}}}{\sqrt{1+\|\boldsymbol{\omega}\|^{2k}}}\mathrm{d}\boldsymbol{\omega} \text{ for all } \delta>0, \\ &\le \tfrac{1}{(2\pi)^{\frac{d}{2}}}\|\boldsymbol{\omega}\mapsto\sqrt{1+\|\boldsymbol{\omega}\|^{2(1+\delta)}}\mathcal{F}[f](\boldsymbol{\omega})\|_{\mathbb{L}_2(\mathbb{R}^d)}\|\boldsymbol{\omega}\mapsto\tfrac{1}{\sqrt{1+\|\boldsymbol{\omega}\|^{2(1+\delta)}}}\|_{\mathbb{L}_2(\mathbb{R}^d)} \\ &\le C\|f\|_{\mathbb{H}^{k,2}_{\gamma=1}(\mathbb{R}^d)}\ . \end{aligned}$$

An additional remark with respect to the constant $C>0$ above:
Iff $k > \frac{d}{2}$ then

$$\|\boldsymbol{\omega}\mapsto\frac{1}{\sqrt{1+\|\boldsymbol{\omega}\|^{2k}}}\|^2_{\mathbb{L}_2(\mathbb{R}^d)} = \int_{\mathbb{R}^d}\frac{1}{1+\|\boldsymbol{\omega}\|^{2k}}\mathrm{d}\boldsymbol{\omega} = \sigma_d\int_0^\infty\frac{\rho^{d-1}}{1+\rho^{2k}}\,\mathrm{d}\rho < \infty.$$

By the Riesz-representation theorem there exists a $K_{\mathbf{a}} \in \mathbb{H}^{k,2}_{\gamma=1}(\mathbb{R}^d)$ such that

$$\frac{1}{(2\pi)^{\frac{d}{2}}} \int_{\mathbb{R}^d} \mathcal{F}[f](\boldsymbol{\omega}) e^{i\boldsymbol{\omega}\cdot\mathbf{a}} \mathrm{d}\boldsymbol{\omega} = f(\mathbf{a}) = (K_{\mathbf{a}}, f)_{\mathbb{H}^{k,2}_{\gamma=1}(\mathbb{R}^d)} = \int_{\mathbb{R}^d} \frac{\mathcal{F}[f](\boldsymbol{\omega})\mathcal{F}[K_{\mathbf{a}}](\boldsymbol{\omega})}{1+\|\boldsymbol{\omega}\|^{2k}} \mathrm{d}\boldsymbol{\omega}$$

for all $f \in \mathbb{H}^{k,2}_{\gamma=1}(\mathbb{R}^d)$. Now $\mathbb{H}^{k,2}_{\gamma=1}(\mathbb{R}^d)$ is densely embedded in $\mathbb{L}_2(\mathbb{R}^2)$ so indeed

$$K_{\mathbf{a}} = \mathcal{F}^{-1}(\boldsymbol{\omega} \mapsto \frac{e^{i\boldsymbol{\omega}\cdot\mathbf{a}}}{1+\|\boldsymbol{\omega}\|^{2k}}).$$

Further we notice that the third equality in (6.3) is a special case of the Bochner-Hecke theorem, see Theorem 26. Now the rest follows by Lemma 8. □.

6.2 Holomorphic Semigroups and Generalized Functions

Florack[51] first mentioned the role that test-functions and distributions play in scale space theory. On the one hand there is a state space, i.e. the space of all possible scalar field configurations and on the other hand there is a device space consisting of all admissible detector devices. It seems reasonable, from a physical point of view to describe a model for the detector device and to prescribe the state space by duality. Since the Gaussian kernels lie in the (Fourier invariant) Schwartz space $\mathcal{S}$, one can take it as a device space. As a result the state space is the set of all tempered distributions $\mathcal{S}'$. In [64] De Graaf has derived a theory of generalized functions based on holomorphic semi-groups. In this appendix we will apply little of this theory onto the Poisson semigroup.

In a Hilbert Space X we consider the evolution equation

$$\frac{du}{ds} = \mathcal{A}u$$

with $\mathcal{A}$ a negative unbounded self-adjoint operator. $\mathcal{A}$ is the infinitesimal generator of a holomorphic semi-group. Solutions $u(\cdot) : (0,\infty) \to X$ of this equation are called trajectories. Such a trajectory may or may not correspond to an "initial condition at $s = 0$" in X. The set of trajectories is considered as a space of generalized functions. The test function space is defined to be

$$\mathcal{S}_{X,\mathcal{A}} = \bigcup_{s>0} e^{s\mathcal{A}}(X) \ .$$

Theorem 25 *Let X be a Banach space. Let Q be a strongly continuous, holomorphic semigroup, with infinitesimal generator $\mathcal{A} < 0$. Then $\mathcal{S}_{X,\mathcal{A}}$ consists exactly of those $f \in \mathcal{D}(\mathcal{A}^\infty)$ such that*

$$\sum_{k=1}^{\infty} \frac{s^k}{k!} \|\mathcal{A}^k f\| < \infty \qquad \textit{for a certain } s > 0 \ . \tag{6.6}$$

Proof
"$\subset$"

Let $x \in \mathcal{S}_{X,\mathcal{A}} \Rightarrow \exists_{s>0}\, \exists_{x_s \in X}\, x = Q_s x_s$. Now since Q is holomorphic, there exists a $M > 0$ that $\|\mathcal{A}Q_s\| \leq M\, s^{-1}$, see (1.21). Consequently,

$$\begin{aligned} \|\mathcal{A}^n x\| &= \|(\mathcal{A}Q_{s/n})^n x_s\| \\ &\leq M^n (n/s)^n \, \|x_s\| \\ &\leq (eM/s)^n n! \, \|x_s\| \end{aligned}$$

where we have used the elementary inequality $n^n \leq e^n n!$. With these bounds it is now obvious that $\sum\limits_{k=1}^{\infty} \frac{s^k}{k!} \|\mathcal{A}^k f\| < \infty$.

"$\supset$"

Let $x \in \mathcal{D}(\mathcal{A}^\infty)$, such that (6.6) is convergent. Choose $t > 0$ such that $\sum\limits_{n=1}^{\infty} \frac{s^n}{n!} \|\mathcal{A}^n x\| < \infty$ for all $s \leq 2t$. Since X is a Banach space, we have for $s \in (0, t)$

$$x_s = \sum_{k=1}^{\infty} \frac{s^k}{k!} (-\mathcal{A})^k x \qquad \text{exists in } X \ ,$$

(The sequence of partial sums is a Cauchy sequence). By differentiation we have $x = Q_s x_s = e^{s\mathcal{A}} x_s$. □

Remark:

Elements of $\mathcal{D}(\mathcal{A}^\infty)$ that satisfy (6.6) are often called analytic vectors. If (6.6) holds for any $s > 0$ then then they are called *entire* analytic vectors.

6.2.1 Example: The Test Space Corresponding to Poisson Filtering

In this paragraph we will only observe $d = 1$.

The test function space which belongs to the Dirichlet problem (1.25) is given by $\mathcal{S}_{\mathbb{L}_2(\mathbb{R}^d), -\sqrt{-\Delta}}$, which -as we shall next show- equals a Gelfand-Shilov space, namely

$$\mathcal{S}_{\mathbb{L}_2(\mathbb{R}^d), -\sqrt{-\Delta}} = \mathcal{S}_1. \tag{6.7}$$

If the reader is not familiar with Gelfand-Shilov spaces he/she is referred to Gelfand & Shilov [62] (2nd Edition, chapter 4) for a general and profound theory with regard to their spaces. For our purposes we will only need $\mathcal{S}_1$, $\mathcal{S}^1$, $\mathcal{S}_{1,A}$, $\mathcal{S}^{1,A}$. First we give the definitions of these spaces and then we give a short overview of main results with references, about these Gelfand-Shilov spaces and finally we will show (6.7). Recall that the Schwartz space $\mathcal{S}$ consists of all $\phi \in C^\infty(\mathbb{R})$ such that ,

$$\sup_{x \in \mathbb{R}} |x^k \phi^{(q)}(x)| \leq m_{qk} \qquad \text{for certain } m_{qk} < \infty$$

with $(k, q = 1, 2, \ldots)$. To obtain Gelfand-Shilov spaces, we have to impose conditions on m_{qk}. Below, a summary of conditions on m_{qk} and corresponding Gelfand-Shilov spaces:

- $\mathcal{S}_1$: $m_{kq} = C_q A^k k^k$, with $C_q, A > 0$ depending on ϕ.
- $\mathcal{S}^1$: $m_{kq} = C_q B^q k^k$, with $C_q, B > 0$ depending on ϕ.

- $\mathcal{S}_{1,A}$: $m_{kq} = C_q\overline{(A+\delta)}^k k^k$, with C_q depending on ϕ and *any* $\delta > 0$.
- $\mathcal{S}^{1,B}$: $m_{kq} = C_q\overline{(B+\delta)}^q k^k$, with C_q depending on ϕ and *any* $\delta > 0$.

The following relations hold:

- The test space $S_1 = \{\phi \in C^\infty(\mathbb{R}) : |\phi^{(q)}(x)| \leq C_q e^{-a|x|^{1/\alpha}}\}$, with $a = \frac{\alpha}{eA^{1/\alpha}}$ depending on ϕ. The idea behind this equality is that $\inf\limits_{\xi\in\mathbb{R}} \frac{k^k}{|\xi|^k} = O(e^{-\frac{1}{e}|\xi|})$.
- The test space S^1 consists of all functions ϕ in $C^\infty(\mathbb{R})$ which can be extended analytically onto a strip $\{z \in \mathbb{C} : |\Im(z)| \leq h(\phi)\}$, which width $h(\phi)$ depends on ϕ. All members of S^1 are analytic, since the remainder $|\frac{h^q}{q!}\phi^{(q)}(x+\theta h)|$ of a Taylor expansion smaller than $\frac{|h|^q}{q!}C_0 B^q q^q$.[1]
- Fourier Transform $\mathcal{F}$ maps $\mathcal{S}^1$ onto $\mathcal{S}_1$ and visa versa.[2] Note that $\mathcal{F}^2$ is an isometrical mapping from $\mathcal{S}^1$ ($\mathcal{S}_1$) onto itself, since it maps $x \mapsto \phi(x)$ onto $x \mapsto \phi(-x)$.
- The space $\mathcal{S}_{1,A}$ consists exactly of those infinitely differentiable functions that satisfy
$$|\phi^{(q)}(x)| \leq C_{q\delta} e^{-(a-\delta)|x|} \qquad \delta > 0$$
- The space $\mathcal{S}_1$ ($\mathcal{S}^1$) is the union of all $\mathcal{S}_{1,A}$ ($\mathcal{S}^{1,B}$), $A > 0$ ($B > 0$), i.e.
$$\mathcal{S}_1 = \bigcup_{A>0} \mathcal{S}_{1,A} \ , \text{ and } \mathcal{S}^1 = \bigcup_{B>0} \mathcal{S}^{1,B} \ .$$
A sequence $\{\phi_n\} \subset \mathcal{S}_1$ converges to zero, if all ϕ_n belong to some $\mathcal{S}_{1,A}$ in which they converge to zero.

Note that we assumed functions to be infinitely differentiable. We will use analytic vectors f. In the semi-groups, we are interested in (Poisson and Gaussian) we have (respectively) $\mathcal{D}(\mathcal{A}^\infty) = \bigcap\limits_{n=1}^{\infty} \mathbb{H}_n = \bigcap\limits_{n=1}^{\infty} \mathbb{H}_{2n} = \mathbb{H}_\infty$. This space consists of all functions, whose generalized derivatives have finite $\mathbb{L}_2$-norms. To this end we notice that by Sobolevs lemma (Yosida[132] p.174-175) states that such functions are indeed almost everywhere infintely differntiable functions in the usual sense. So, we then arive at a special case of the above. For instance the space $\mathcal{S}^1$ will now consists of all infinitely differentiable functions f which can be extended analytically on a strip with widht h along the real axis in the complex plane such that
$$\sup_{-h<y<h} \int_{-\infty}^{\infty} |f(x+iy)|^2 \, \mathrm{dx} < \infty \ .$$
This space equals the space $\mathcal{S}_{\mathbb{L}_2(\mathbb{R}^d),-\sqrt{-\Delta}}$, since
$$\begin{aligned}\mathcal{S}_{\mathbb{L}_2(\mathbb{R}^d),-\sqrt{-\Delta}} &= \mathcal{F}^{-1}\mathcal{F}\left(\bigcup_{s>0} e^{-s\mathcal{A}}(\mathbb{L}_2(\mathbb{R}^d))\right) = \mathcal{F}^{-1}\left(\bigcup_{s>0} e^{-s|\omega|}(\mathbb{L}_2(\mathbb{R}^d))\right) = \mathcal{F}^{-1}\left(\bigcup_{s>0}\mathcal{S}_{1,s}\right) \\ &= \mathcal{F}^{-1}\mathcal{S}_1 = \mathcal{S}^1 \ .\end{aligned}$$

[1] From Stirling's Formula $q! = q^{q+(1/2)}e^{-q}\sqrt{2\pi}E_q \quad (E_q \to 1)$ it follows that $h(q) = \frac{1}{B(\phi)e}$.

[2] In general we have $\mathcal{F}(\mathcal{S}^\beta_\alpha) = \mathcal{F}(\mathcal{S}^\alpha_\beta)$, so the Fourier invariant spaces are $\mathcal{S}^\alpha_\alpha$. For example the Schwarz-Space, $\alpha = \infty$.

Chapter 7

Appendix Orientation

7.1 The Bochner-Hecke Theorem and the Spectral Decomposition of the Hankel Transform

Theorem 26 *Let H be a harmonic homogeneous polynomial of degree m in d variables. Let F be an element of $\mathbb{L}_2((0,r);r^{d+2m-1}\mathrm{dr})$ then the Fourier transform of their direct product $(r,\boldsymbol{x})\mapsto F(r)H(\boldsymbol{x})$, which is in $\mathbb{L}_2(\mathbb{R}^d)$, is given by:*

$$(-i)^m H(\boldsymbol{\omega})\int_0^\infty (r\rho)^{\frac{d-2}{2}+m} J_{\frac{d-2}{2}+m}(\rho r)F(r)r^{d+2m-1}\mathrm{dr} =$$
$$(-i)^m H(\boldsymbol{\omega})\rho^{-(\frac{d-1}{2}+m)}\left[\mathcal{H}_{\frac{d-2}{2}+m} r^{\frac{d-1}{2}+m}F\right](\rho)\ ,$$

where $\rho=\|\boldsymbol{\omega}\|$ and the $\mathcal{H}_{\frac{d-2}{2}+m}$ the Hankel Transform given by:

$$(\mathcal{H}_{\frac{d-2}{2}+m}\phi)(\rho)=\int_0^\infty (\rho r)^{1/2}\phi(r)J_{\frac{d-2}{2}+m}(\rho r)\ \mathrm{dr}\ ,\phi\in\mathbb{L}_2((0,\infty))\ . \tag{7.1}$$

The proof can be found in [39]pp.24-25. The Hankel Transform $\mathcal{H}_\mu$, $\mu=\frac{d-2}{2}+m$, is a unitary map on $\mathbb{L}_2((0,\infty),\mathrm{dr})$ and has a complete set of orthonormal eigen functions $\{E_n^\mu\}$ given by

$$r\mapsto E_n^\mu(r)=\left(\frac{2n!}{\Gamma(n+\mu+1)}\right)^{\frac{1}{2}} r^{\mu+\frac{1}{2}}e^{-\frac{r^2}{2}}L_n^{(\mu)}(r^2), n=0,1,2,\ldots, r>0\ , \tag{7.2}$$

where $L_n^{(\mu)}(r)$ is the n-th generalized Laguerrre polynomial of type $\mu>-1$,

$$L_n^{(\mu)}(r)=\frac{r^{-\alpha}e^r}{n!}\left(\frac{d}{dr}\right)^n(e^{-r}r^{n+\mu}), r>0\ ,$$

with corresponding eigenvalues $(-1)^n$: $(\mathcal{H}_\mu \phi) = \sum_{n=0}^{\infty} (-1)^n (E_n^\mu, \phi)_{\mathbb{L}_2((0,\infty),\mathrm{dr})} E_n^\mu$. The functions E_n^μ are also eigen functions of the operator

$$-\frac{d^2}{dr^2} + r^2 + \frac{\mu^2 - \frac{1}{4}}{r^2} - 2\alpha \ ,$$

with eigen value $4n + 2$, cf.[36]p.79, which coincides with the fact that the Harmonic oscillator $\|\mathbf{x}\|^2 - \Delta$ commutes with Fourier transform.

These results gives us:

- For $d = 2$, we have $\mathbb{L}_2(\mathbb{R}^2) = \mathbb{L}_2(S^1) \bigotimes \mathbb{L}_2((0,\infty); \mathrm{rdr})$ and a Fourier invariant orthonormal base is given by $\{Y_m \otimes h_n^m\}_{m\in\mathbb{Z}, n\in\mathbb{N}\cup\{0\}}$, where

$$h_n^m = r^{-1/2} E_n^m(r) \ , \tag{7.3}$$

  and $Y_m(\phi) = \frac{1}{\sqrt{2\pi}} e^{im\phi}$. It now follows by the Bochner-Hecke Theorem that:

$$\begin{aligned} \mathcal{F}(Y_m \otimes h_n^m) &= \mathcal{F}(r^m Y_m \otimes \tfrac{h_n^m}{r^m}) \\ &= (-1)^n (-i)^{|m|} (Y_m \otimes h_n^m) \\ &= (-1)^{n+m} (i)^{|m|} (Y_m \otimes h_n^m) \ . \end{aligned} \tag{7.4}$$

- For $d = 3$, we have $\mathbb{L}_2(\mathbb{R}^2) = \mathbb{L}_2(S^1) \bigotimes \mathbb{L}_2((0,\infty); \mathrm{rdr})$. All l homogeneous harmonic polynomials are spanned by $\{\mathbf{x} \mapsto r^l Y_l^m(\theta,\phi)\}_{l=0\ldots\infty \ ; \ m=-l,\ldots,l}$. Define

$$g_n^l(r) = r^{-1} E_n^{l+\frac{1}{2}}(r) \ , r > 0 \tag{7.5}$$

  then $g_n^l \in \mathbb{L}_2((0,\infty); \mathrm{rdr})$ are eigen functions of $\rho^{-1}\mathcal{H}_{\frac{1}{2}+m} r^1$ with corresponding eigenvalues $(-1)^n$. Therefore it follows by the Bochner-Hecke Theorem that

$$\mathcal{F}(Y_l^m \otimes g_n^l) = (i)^l (-1)^{n+l} (Y_l^m \otimes g_n^l) \ . \tag{7.6}$$

7.2 Proof of Theorem 18

We will use the following lemma which gives a useful characterization of the elements of $\mathbb{C}_K^{\mathbb{I}}$:

Lemma 9 *Let K be a function of positive type on $\mathbb{I}$ and F a complex-valued function on $\mathbb{I}$. Then the function F belongs to $\mathbb{C}_K^{\mathbb{I}}$ if and only if there exists a constant $\gamma > 0$ such that*

$$\Big| \sum_{j=1}^{l} \alpha_j \overline{F(m_j)} \Big|^2 \leq \gamma \sum_{k,j=1}^{l} \overline{\alpha_k} \alpha_j K(m_k, m_j), \tag{7.7}$$

for all $l \in \mathbb{N}$ and $\alpha_j \in \mathbb{C}$, $m_j \in \mathbb{I}$, $1 \leq j \leq l$.

Proof: See [94, Lemma 1.7, pp.31].

From this lemma it indeed follows that the norm on $\mathbb{C}_K^{\mathbb{I}}$, is indeed given by (4.23).

Proof of Theorem 18:
First we show that $\mathcal{W}f \in \mathbb{C}_K^{\mathbb{I}}$ for any element $f \in H = \overline{\langle V \rangle}$ and that $\mathcal{W}$ is bounded (and therefore continuous). If $f \in H$ then

$$\Big|\sum_{j=1}^{l} \alpha_j \overline{(\mathcal{W}f)(m_j)}\Big|^2 = \Big|\sum_{j=1}^{l} \alpha_j \overline{(\phi_{m_j}, f)_H}\Big|^2 = \Big|\Big(\sum_{j=1}^{l} \alpha_j \phi_{m_j}, f\Big)_H\Big|^2$$

$$\leq \Big\|\sum_{j=1}^{l} \alpha_j \phi_{m_j}\Big\|_H^2 \|f\|_H^2 = \Big(\sum_{k,j=1}^{l} \overline{\alpha_k}\alpha_j K(m_k, m_j)\Big)\|f\|_H^2,$$

for all $l \in \mathbb{N}$, $\alpha_1, ..., \alpha_l \in \mathbb{C}$, and $m_1, ..., m_n \in \mathbb{I}$. So $\mathcal{W}f \in \mathbb{C}_K^{\mathbb{I}}$ by Lemma 9 and $\|\mathcal{W}f\|^2_{\mathbb{C}_K^{\mathbb{I}}} \leq \|f\|_H^2$, by (4.23). Next we prove that $\mathcal{W}$ is an isometry. Because $(\phi_m, \phi_{m'}) = K(m, m')$, $\mathcal{W}$ maps a linear combination $\sum_i \alpha_i \phi_{m_i}$ onto the linear combination $\sum_i \alpha_i K(\cdot, m_i)$. So $\mathcal{W}(\langle V \rangle) = \langle \{K(\cdot, m) | m \in \mathbb{I}\}\rangle$. Moreover, it maps $\langle V \rangle$ isometrically onto $\langle \{K(\cdot, m) | m \in \mathbb{I}\}\rangle$, because

$$\Big(\mathcal{W}\big(\sum_i \alpha_i \phi_{m_i}\big), \mathcal{W}\big(\sum_j \beta_j \phi_{m'_j}\big)\Big)_{\mathbb{C}_K^{\mathbb{I}}} = \Big(\sum_i \alpha_i K(\cdot, m_i), \sum_j \beta_j K(\cdot, m'_j)\Big)_{\mathbb{C}_K^{\mathbb{I}}}$$

$$= \sum_{i,j} \overline{\alpha}_i \beta_j K(m_i, m'_j) = \sum_{i,j} \overline{\alpha}_i \beta_j (\phi_{m_i}, \phi_{m'_j})_H.$$

Since $\langle V \rangle$ is dense in $\overline{\langle V \rangle}$ and $\mathcal{W}$ is bounded on $H = \overline{\langle V \rangle}$ it follows that $\mathcal{W}$ is an isometry. Furthermore, $\mathcal{W}[\langle V \rangle]$ is dense in $\mathbb{C}_K^{\mathbb{I}}$. So $\mathcal{W}$ is also surjective and therefore unitary. □

7.3 Asymptotic behavior of the wavelet $\psi^0\big|_{\phi=0}$

Let $\psi^0(r, 0)$ be the restriction of the point wise limit $\psi^0(\mathbf{x}) = \lim_{N\to\infty} \psi_N^0(\mathbf{x})$ to $\phi = 0$:

$$\psi^0(r, 0) = \sum_{m=0}^{\infty} \frac{r^m}{\sqrt{m!}} e^{-\frac{r^2}{2}} .$$

We will give a simple asymptotic formula for large r, which is also rather accurate for relatively small r. First we notice that the multiplicative factor between two successive terms equals $\frac{r}{\sqrt{m+1}}$, so the main contribution to the series comes from the term $r^2 = m + 1$. By Stirling's formulas for the Gamma-function we have

$$\Gamma(z) = \sqrt{2\pi} z^{z-1/2} e^{-z} \left(1 + \tfrac{1}{12\,z} + O\left(\tfrac{1}{z^2}\right)\right) ,$$
$$\tfrac{\Gamma(z+a)}{\Gamma(z+b)} \sim z^{a-b} \left(1 + \tfrac{(a-b)(a+b-1)}{2z}\right) ,$$

as long as $|\arg z| < \pi$, cf. [2]p.257. As a result

$$\begin{aligned} \tfrac{1}{\sqrt{m}} &= \tfrac{\pi^{(1/4)} 2^{-\frac{m}{2}}}{\Gamma(\frac{1}{2}m + \frac{3}{4})} \left[1 - \tfrac{1}{16m} + O\left(\tfrac{1}{m^2}\right)\right], (m \to \infty) \\ &\sim \tfrac{\pi^{(1/4)} 2^{-\frac{m}{2}}}{\Gamma(\frac{1}{2}m + \frac{3}{4})} - \tfrac{1}{32} \tfrac{\pi^{(1/4)} 2^{-\frac{m}{2}}}{\Gamma(\frac{1}{2}m + \frac{7}{4})} \end{aligned}$$

As a result we have that

$$\phi_0(r,0) \sim (\pi)^{1/4} e^{-r^2/2} \left[\mathcal{E}_{1/2,3/4}\left(\frac{r}{\sqrt{2}}\right) - \frac{1}{32}\mathcal{E}_{1/2,7/4}\left(\frac{r}{\sqrt{2}}\right)\right], (r \to \infty)$$

where the well-known Mittag-Leffler function is defined by

$$\mathcal{E}_{\alpha,\beta}(z) = \sum_{n=0}^{\infty} \frac{z^n}{\Gamma(\alpha n + \beta)} ,$$

with asymptotic expansion

$$\mathcal{E}_{\alpha,\beta}(z) = \frac{1}{\alpha} z^{(1-\beta)/\alpha} e^{z^{1/\alpha}} - \sum_{n=1}^{N-1} \frac{z^{-n}}{\Gamma(\beta - \alpha n)} + O(|z|^{-N}) , N \in \mathbb{N} ,$$

for $|\arg z| \leq \frac{1}{2}\alpha\pi$, [38]. Therefore we conclude that

$$\psi^0(r,0) = (8\pi)^{1/4}\sqrt{r}\left(1 - \frac{1}{16r^2}\right) , (r \to \infty).$$

This coincides with the following result by Olver, cf. [101]p.307-309: The entire function

$$F_p(x) = \sum_{m=0}^{\infty} \left(\frac{x^m}{m!}\right)^p ,$$

with fixed $p > 0$ has the asymptotic expansion

$$F_p(x) = \frac{e^{px}}{\sqrt{p}(2\pi x)^{(p-1)/2}} \left\{ 1 + \frac{p^2-1}{24px} + O\left(\frac{1}{x^2}\right)\right\}, (0 < p \leq 4, x \to \infty).$$

So we indeed obtain

$$\psi^0(r,0) = e^{-\frac{r^2}{2}} F_{1/2}(r^2) = (8\pi)^{1/4}\sqrt{r}\left(1 - \frac{1}{16r^2} + O\left(\frac{1}{r^4}\right)\right), (r \to \infty).$$

7.4 Examples of Proper Wavelets in General Approach

In this section we derive some solutions $\psi = \sum_{|m|=0}^{N_1} \sum_{n=0}^{N_2} \alpha_m^n (Y_m \otimes h_n^m)$ of equation (4.59). In all our examples we will impose a condition on the expansion coefficients α_m^n such that the solution becomes unique (up to phase factors; $|\alpha_m^n|^2$ are uniquely determined).

7.4.1 The cases $\alpha_m^n = \delta_m^{nl}$, $l \in \mathbb{N} \cup \{0\}$ fixed

By fixing the radial index to l equation (4.59) simplifies to

$$\sum_{|m|=0}^{N_1} \sum_{k=0}^{2l} |\alpha_m^l|^2 [A_k^m]_l^l \, \rho^{2(l+|m|)} = \sum_{q=0}^{N_1+l} \frac{\rho^{2q}}{q!} , \tag{7.8}$$

since $[A_k^m]_l^l = 0$ for $k > 2l$. By solving equation (7.8) for each power ρ^{2q} one obtains the following the $2l+1$-term recursion:

$$|\alpha_m^l|^2 = \frac{1}{m! A_0^m} - \sum_{j=1}^{\min\{m,2l\}} |\alpha_{m-j}^l|^2 \frac{[A_j^{m-j}]_l^l}{[A_0^m]_l^l} \ . \tag{7.9}$$

The cases $l = 0, 1, 2, 3$

In case $l = 0$ we arrive at ψ_N^0, see the example in subsection 4.6.2. In case $l = 1$, the recursion reads

$$\begin{cases} a_0 = 1/2 \\ a_1 = 3/4 \\ a_m = \frac{1}{2(m+1)} + 2\frac{m}{(m+1)} a_{m+1} - \frac{m}{(m+1)} a_{m-2} \ , \end{cases}$$

where $a_m = |\alpha_m^1|^2$. It is possible to solve this recursion, since its generating function is given by

$$\frac{1}{2x}\left(\sum_{n=0}^{\infty} x^n + \frac{e^{\frac{x}{x-1}}}{1-x}\right) = \frac{-1 + e^{1+\frac{1}{x-1}}}{2x(x-1)} = \sum_{n=0}^{\infty} a_n x^n \qquad x < 1.$$

This generating function is directly related to the generating function of the Laguerre polynomials:

$$\sum_{n=0}^{\infty} \mathcal{L}_n^{(m)}(w) x^n = (1-x)^{-m-1} e^{\frac{wx}{x-1}} \quad , |x| < 1 \ .$$

From which we deduce that

$$a_n = \frac{1}{2} - \frac{\mathcal{L}_{n+1}^{(0)}(1)}{2} \ ,$$

which leads to wavelet ψ_N^1, which can be dilated $\psi_N^{1,\sigma} = \mathcal{D}_\sigma \psi_N^1$:

$$\psi^{1,\sigma}(\mathbf{x}) = \frac{1}{\sqrt{2\pi}} \sum_{m=0}^{\infty} \frac{\sqrt{1 - \mathcal{L}_{m+1}^{(0)}}}{\sqrt{(m+1)!}} \left(\frac{\overline{z}}{\sigma}\right)^m e^{-\frac{|z|^2}{2\sigma^2}} \mathcal{L}_1^{(m)}\left(\left|\frac{z}{2}\right|^2\right) \ .$$

In case $l = 2$ the recursion (7.9) is given by

$$\begin{cases} a_0 = 1/2, a_1 = 15/18, a_2 = 11/12, a_3 = 17/20 \\ a_i = \frac{1}{i![A_0^i]_2^2} - \sum_{j=1}^{4} a_{i-j} \frac{[A_j^{(i-j)}]_2^2}{[A_0^i]_2^2} \ , \end{cases}$$

For plots of the coefficients $a_i = |\alpha_i^l|^2$, for $l = 2, 3, 4$, see figure C.1.

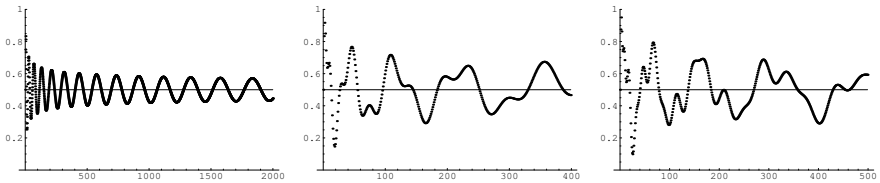

Figure 7.1: The coefficients $|\alpha_i^l|^2$ for $i = 0 \ldots 400$, left $l = 1$, middle $l = 2$ and right $l = 3$. .

The cases $\alpha_m^n = \begin{cases} \gamma^{m+n,n}\delta_{nk} & m \geq 0 \\ \gamma^{-m,n}\delta_{n,k+m} & m < 0 \end{cases}$ **, with** $k \in \mathbb{N} \cup \{0\}$ **fixed**

Then (4.59) boils down to

$$2\pi \sum_{m=0}^{\infty} |\gamma_k^m|^2 |\Psi_{k,m}(z)|^2 = 1 \ , \tag{7.10}$$

where

$$\Psi_{l,m}(z) = (\eta_{l-m} \otimes \mathrm{L}^{(l-m)}_{\min(l,m)})(\phi, r) = \frac{e^{-|z|^2/2}}{\sqrt{\pi}} \ \frac{1}{\sqrt{l!}\sqrt{m!}} \left(\left(\frac{\partial}{\partial z}\right)^*\right)^l \left(\left(\frac{\partial}{\partial \overline{z}}\right)^*\right)^m 1 \ ,$$

where the $\mathbb{L}_2(\mathbb{C}; \frac{e^{-|z|^2}}{\pi}; \mathrm{dz})$-adjoint of $\frac{\partial}{\partial z}$ and $\frac{\partial}{\partial \overline{z}}$ are respectively given by

$$\begin{array}{l} \left(\frac{\partial}{\partial z}\right)^* = z - \frac{\partial}{\partial \overline{z}} \\ \left(\frac{\partial}{\partial \overline{z}}\right)^* = \overline{z} - \frac{\partial}{\partial z} \ . \end{array} \tag{7.11}$$

The complete orthonormal basis Ψ_{lk} in $\mathbb{L}_2(\mathbb{C})$ has several interesting properties. For our purposes the two most important ones, [12], are:

$$\begin{array}{ll} 1.) & \sum\limits_{m=0}^{\infty} \overline{\Psi_{m,l}(z)} \Psi_{m,k}(z) = \sum\limits_{m=0}^{\infty} \Psi_{l,m}(z) \Psi_{m,k}(z) = \frac{1}{\pi}\delta_{lk} \\ 2.) & \Psi_{n+m,n}(z) = \overline{\Psi_{n,n+m}}(z) = (\eta_m \otimes \mathrm{L}_n^m)(\phi, r) \ , z = r\, e^{i\phi} \ . \end{array} \tag{7.12}$$

It follows from the second property that the unique solutions of equation (7.10) are given by $|\gamma_k^m|^2 = 1/2$, for all m. Choose $\gamma_k^m = \frac{\sqrt{2}}{2}$, then we find the proper wavelets

$$\begin{aligned} \psi^k(z) &= \sum_{m=0}^{N} \tfrac{\sqrt{2}}{2} \Psi_{k,m}(z) \\ &= \sum_{m=0}^{N} \tfrac{\sqrt{2}}{2} (\eta_{k-m} \otimes \mathrm{L}^{(k-m)}_{\min(k,m)})(\phi, r) \\ &= \sum_{m=0}^{k-1} \tfrac{\sqrt{2}}{2} (\eta_{k-m} \otimes \mathrm{L}_m^{(k-m)})(\phi, r) + \sum_{m=0}^{N} \tfrac{\sqrt{2}}{2} (\eta_{-m} \otimes \mathrm{L}_k^{(m)}) \ . \end{aligned}$$

These wavelets are quite similar to the cases $\alpha_m^n = \delta_m^{nl}$, $l \in \mathbb{N} \cup \{0\}$ fixed, but they have the advantage that they are explicitly characterized so that iteration or band-matrix inversion is involved. The case $k = 0$ again corresponds to the case $\alpha_m^n = \delta_m^{n0}$, see (4.61). See figure C.2.

7.5 Minimal Uncertainty States

Let $\psi \in \mathbb{L}_2(\mathbb{R}^d)$ such that $\|\psi\|_{\mathbb{L}_2(\mathbb{R}^d)} = 1$. Let A and B be self-adjoint operators on $\mathbb{L}_2(\mathbb{R}^d)$. Define corresponding expectation values and variances by

$$\begin{array}{l} E(X) = (\psi, X\psi) \\ \mathrm{Var}(X) = (X - E(X)\psi, X - E(X)\psi), \qquad X = A, B \ , \end{array}$$

then

$$\mathrm{Var}(A)\mathrm{Var}(B) \geq \left(\frac{1}{2i} E([A, B])\right)^2 \ , \tag{7.13}$$

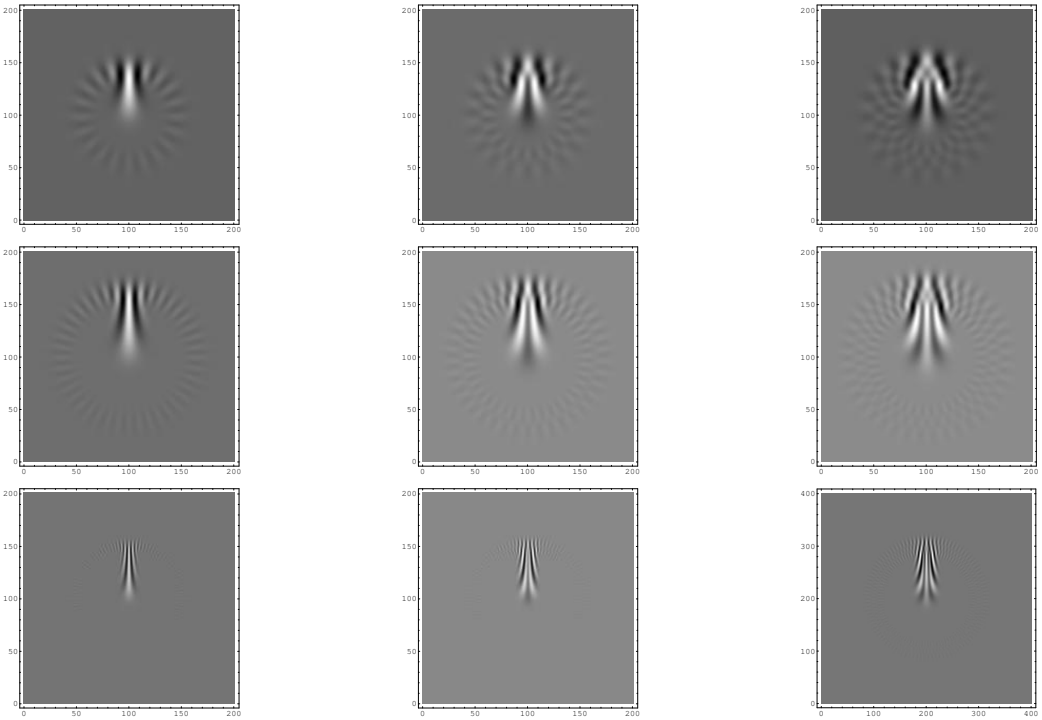

Figure 7.2: Density plots of $\psi_N^k(z)$, for $k = 0, 1, 2$ left to right and truncated at respectively $N = 20, 40, 100$ top down.

where the commutator of A and B is given by $[A, B] = AB - BA$. Notice that $A^* = A$ and $B^* = B \Rightarrow [A, B]^* = -[A, B]$, which explains why $E([A, B])$ is purely imaginary. The proof of (7.13) is simple, since by Cauchy-Schwarz and the fact that $|z|^2 \geq \Im(z)^2$, for every $z \in \mathbb{C}$ we have

$$\begin{aligned} \mathrm{Var}(A)\mathrm{Var}(B) &\geq |((A - E(A))\psi, (B - E(B))\psi)|^2 \\ &\geq (\mathrm{Im}\,((A - E(A))\psi, (B - E(B))\psi))^2 \\ &= \left(\tfrac{1}{2i}\left(((A - E(A))\psi, (B - E(B))\psi)\right.\right. \\ &\qquad \left.\left. -((B - E(B))\psi, (A - E(A))\psi)\right)^2 \\ &= \left(\tfrac{1}{2i}E([A, B])\right)^2 \ . \end{aligned} \tag{7.14}$$

Therefore equality holds if and only if

$$(A - < A >)\psi = \lambda i(B - < B >)\psi \ . \tag{7.15}$$

Examples:

1. The operator $\frac{1}{i}\partial_x : C^1(\mathbb{R}) \to C^0(\mathbb{R})$ corresponds to the multiplication operator $\boldsymbol{\omega}$ in the Fourier domain and $[x, \partial_x] = 1$. As a result it extends to a self-adjoint operator on $\mathbb{L}_2(\mathbb{R})$ and

$$\left(\int_{\mathbb{R}} x^2\psi(x)\ \mathrm{dx}\right)\left(\int_{\mathbb{R}} \omega^2[\mathcal{F}\psi](\omega)\ \mathrm{d}\omega\right) \geq \frac{1}{4}\|\psi\|^4 \geq \frac{1}{4}$$

   The independent solutions of (7.15) with $A = \frac{1}{i}\partial_x$ and $B = x$ are given by the Gabor

filters

$$\begin{aligned}\psi(x) &= C_1 e^{-\lambda\frac{(x-E(x))^2}{2}} e^{iE[\omega]x} \\ &= C_2 G_s(x)(\cos E[\omega] + i\sin E[\omega]) \qquad s=\tfrac{1}{2\lambda}, C_1, C_2 > 0.\end{aligned}$$

2. The above is easily generalized to $d=2$, where $\boldsymbol{\omega} \leftrightarrow \frac{2}{i}\partial_{\overline{z}}$ and $\|\boldsymbol{\omega}\| = -\Delta = -4\partial_z\partial_{\overline{z}}$. Notice that these operators are not self-adjoint on $\mathbb{L}_2(\mathbb{R}^2)$, because $(\partial_z)^* = \partial_{\overline{z}}$ and $z^* = \overline{z}$. Therefore (7.14) does not apply. Nevertheless, if one follows exactly the same scheme it is easily verified that

$$\begin{aligned}\mathrm{Var}(A)\mathrm{Var}(B) &\geq \left(\tfrac{1}{2i}E[A^*B - B^*A] - E[A^*]E[B] + E[A]E[B^*]\right)^2 \\ &= \left(\Im[E[A^*B] - \Im[E[A^*]E[B]]]\right)^2 \ .\end{aligned}$$

So for the case $A = z$ and $B = \frac{2}{i}\partial_{\overline{z}}$ and $\Im[E[\overline{z}]E[\frac{2}{i}\partial_{\overline{z}}]] = 0$ we have

$$\mathrm{Var}(A)\mathrm{Var}(B) = \int_{\mathbb{R}^2} \|\boldsymbol{\omega}\|^2[\mathcal{F}(\psi)](\boldsymbol{\omega})\, d\boldsymbol{\omega} \int_{\mathbb{R}^2} \|\mathbf{x}\|^2|\psi(\mathbf{x})|^2\, d\mathbf{x} \geq \left(\Im[[\overline{z}, \frac{1}{2i}\partial_{\overline{z}}]]\right)^2 \geq \frac{1}{4}.$$

The homogeneous PDE giving the minimal uncertainty states now becomes

$$i\lambda(z - E(z))f(z,\overline{z}) = \left(\frac{2}{i}\partial_{\overline{z}} - E(w)\right) f(z,\overline{z}) \ , \qquad w = \omega_1 + i\omega_2$$

which can be rewritten in $\frac{E(w)i - \lambda(z-\mu)}{2} = \frac{\partial}{\partial\overline{z}}\log f(z,\overline{z})$. Notice that $\partial_{\overline{z}} f(z) = 0$, for all complex analytic functions f, so the general solution is given by

$$f(z,\overline{z}) = A(z)e^{\frac{iE(w)\overline{z}}{2}} e^{-\frac{\lambda(z-E(z))\overline{z}}{2}} = B(z)e^{\frac{iE(w)\overline{z}}{2}} e^{-\lambda\frac{|z-E(z)|^2}{2}} \ ,$$

where $A(z)$, $B(z) = e^{-\lambda E(z)(z-E(z))}A(z)$, are arbitrary analytic. Now $B(z) = \sum_{n=0}^{\infty} \frac{B^{(n)}(0)}{n!} z^n$ and the PDE is homogeneous, so the solutions are linear combinations of the $\mathbb{L}_2$-normalized kernels

$$\frac{1}{\sqrt{\pi}\sqrt{\sigma}} \frac{\left(\frac{z}{\sigma}\right)^n}{\sqrt{n!}} e^{-\frac{|z-E(z)|^2}{2\sigma^2}} \qquad , \sigma > 0 \ . \tag{7.16}$$

3. Rather than considering the infinitesimal generators of the Schrödinger representation of the Heisenberg group on $\mathbb{L}_2(\mathbb{R}^d)$ (see previous examples) we consider the infinitesimal generators of the left regular action of the Euclidean motion group onto $\mathbb{L}_2(\mathbb{R}^2)$. We consider these generators in polar coordinates in the Fourier domain, $A = i\hat{A}_k$, $k = 1, 2$, $B = i\hat{A}_3$, where

$$\begin{aligned}(\hat{A}_k\hat{\psi})(\boldsymbol{\omega}) &= \tfrac{d}{db^k}(\mathcal{F}[\mathcal{U}_g\psi])(\boldsymbol{\omega})\big|_{(\mathbf{0},1)} = i\omega_k\hat{\psi}(\boldsymbol{\omega}),\ \boldsymbol{\omega} = (\omega_1,\omega_2) = (\rho\cos\varphi, \rho\sin\varphi), \\ (\hat{A}_3\hat{\psi})(\boldsymbol{\omega}) &= \tfrac{d}{d\theta}(\mathcal{F}[\mathcal{U}_g\psi])(\boldsymbol{\omega})\big|_{(\mathbf{0},1)} = -\partial_\varphi\hat{\psi}(\rho,\varphi), \quad g = (\mathbf{b}, e^{i\theta}).\end{aligned}$$

Notice that $[\hat{A}_3, \hat{A}_1] = \hat{A}_2, [\hat{A}_1, \hat{A}_2] = 0, [\hat{A}_3, \hat{A}_2] = -\hat{A}_1$. So in particular we obtain $\mathrm{Var}(\hat{A}_1)\mathrm{Var}(\hat{A}_3) \geq \frac{1}{4}|E[\hat{A}_2]|^2$ or more explicitly:

$$\int_{\mathbb{R}^2} (\omega_1)^2|\hat{\psi}|^2 \mathrm{d}\boldsymbol{\omega} \int_{\mathbb{R}^2} |\partial_\varphi\hat{\psi}|^2 \mathrm{d}\boldsymbol{\omega} \geq \frac{1}{4}\left(\int_{\mathbb{R}^2} \omega_2|\hat{\psi}|^2 \mathrm{d}\boldsymbol{\omega}\right)^2 \ .$$

The minimal uncertainty states $\hat{\psi} \in \mathbb{L}_2(\mathbb{R}^2)$ are now subject to

$$\partial_\varphi \hat{\psi} = \left(-(1/\lambda)(\rho \cos\varphi + iE[\hat{A}_1]) - E[\hat{A}_3] \right) \hat{\psi} \ , \lambda > 0.$$

By integration and the side condition that $\hat{\psi}$ is 2π periodic in φ one obtains the solution

$$\psi(\boldsymbol{\omega}) = \begin{cases} c(\rho) e^{im\varphi} e^{-\frac{\rho}{\lambda}\sin\varphi} & \text{if } |\varphi - \pi/2| < \pi/2 \\ 0 & \text{else} \end{cases}$$

and the equalities $E(\hat{A}_1) = 0$, $E(\hat{A}_3) = m \in \mathbb{Z}$. Notice that $\hat{\psi} \in \mathbb{L}_2(\mathbb{R}^2)$, implies that $\hat{\psi} \to 0$ as $\rho \to \infty$ and since $\lambda > 0$ we must have $\sin\varphi > 0 \Leftrightarrow \varphi \in (0, \pi)$. Therefore the support of $\hat{\psi}$ should be contained in the open upper plane $\omega_2 > 0$. If we moreover assume that $\hat{\psi}$ is real valued, then $m = 0$.

In [6] the authors consider the similitude group (so besides the generators $\hat{A}_k$, $k = 1, 2, 3$ also the infinitesimal generator of dilation: $\hat{A}_4\hat{\psi} = i(\rho\partial_\rho + 1)\hat{\psi}$ is included) where they obtain that $c(\rho)$ must be equal to $c(\rho) = \rho^\kappa$, $\kappa > 0$, which leads to the well-known Cauchy wavelets as minimal uncertainty wavelets. However, these wavelets are not suitable for our purposes, since they do not allow a stable reconstruction from a single scale orientation score (unless $\kappa \to 0$, $\lambda \to \infty$).

7.6 Derivation of the exponent mapping $\exp : T_e(G) \to G$

We follow the general scheme of relating an element in the Lie-algebra to the corresponding Lie-group element by the exponential mapping, described in [113]Chapter 5.

Define $A \in T_{\mathbf{e}}(G)$ by $A = A_1 + \lambda_1 A_2 + \lambda_2 A_3$. The uniquely determined left-invariant vector field corresponding to A, $\tilde{A}$ is given by

$$\tilde{A}_p \phi = A(\phi \circ L_p) = A(q \mapsto \phi(pq)) \ , p = (\mathbf{b}, e^{i\theta}) \in G, q = (\mathbf{b}', e^{i\theta'}) \in G \ ,$$

which can be written, by (4.77),

$$\begin{array}{rl} (\tilde{A}_p\phi) & = (1A_1 + \lambda_2 A_2 + \lambda_3 A_3)(\phi \circ L_p) \\ & = (D_1 + \lambda_2 D_2 + \lambda_3 D_3)|_e \, \phi(R_\theta(\mathbf{b}' - \mathbf{b}), e^{i(\theta' - \theta)}) \\ & = (D_1\phi)(\mathbf{b}, e^{i\theta}) + \lambda_2 \cos\theta (D_2\phi)(\mathbf{b}, e^{i\theta}) + \lambda_2 \sin\theta (D_3\phi)(\mathbf{b}, e^{i\theta}) \\ & -\lambda_3 \sin\theta (D_2\phi)(\mathbf{b}, e^{i\theta}) + \lambda_3 \cos\theta (D_3\phi)(\mathbf{b}, e^{i\theta}) \ , \end{array} \tag{7.17}$$

$p = (\mathbf{b}, e^{i\theta}) \in G$, so indeed $\mathcal{A} = 1\partial_\theta + \lambda_2\partial_\xi + \lambda_3\partial_\eta$. Now let $\boldsymbol{\gamma}(= \boldsymbol{\gamma}_{\tilde{Z}})$ be the unique integral curve through e, i.e.

$$\begin{cases} \frac{d}{dt}\boldsymbol{\gamma}(t) = \tilde{Z}(\boldsymbol{\gamma}(t)) \Leftrightarrow \forall_{\phi \in C^\infty(G,\mathbb{R})} \ \boldsymbol{\gamma}(t)\phi = \tilde{Z}(\boldsymbol{\gamma}(t))\phi \\ \boldsymbol{\gamma}(0) = (0, \mathbf{0}) \ , \end{cases}$$

where we notice that

$$\boldsymbol{\gamma}(t)\phi = \tfrac{d}{dt}(\phi \circ \boldsymbol{\gamma})(t) = (\partial_\theta\phi)(\boldsymbol{\gamma}(t)) + \lambda_2\dot{\gamma}_2(t)(\partial_\xi\phi)(\boldsymbol{\gamma}(t)) + \lambda_3\dot{\gamma}_3(t)(\partial_\eta\phi)(\boldsymbol{\gamma}(t)) \tag{7.18}$$

So it follows by equality (7.17) and (7.18) (by taking respectively $\phi(\mathbf{b}, e^{i\theta}) = \theta$, $\phi(\mathbf{b}, e^{i\theta}) = b_1$ and $\phi(\mathbf{b}, e^{i\theta}) = b_2$) that

$$\begin{cases} \gamma_1'(t) = 1 \\ \gamma_2'(t) = \lambda_2 \cos\gamma_1(t) - \lambda_3 \sin\gamma_1(t) \qquad \gamma(0) = (0, \mathbf{0}) \\ \gamma_3'(t) = \lambda_2 \sin\gamma_1(t) + \lambda_3 \cos\gamma_1(t) \end{cases}$$

the unique solution of which is given by

$$\boldsymbol{\gamma}(t) = (t, \lambda_3(\cos t - 1) \ + \lambda_2 \sin t, \lambda_3 \sin t \ - \lambda_2(\cos t - 1)) \ , \qquad \square$$

7.7 Numerical Scheme and Analysis for Computing Resolvent of Evolutions on Orientation Scores

We will first explain the numerical scheme for computing $W = -(A - \alpha I)^{-1} U_f$, with A given by (4.97). This scheme (which we used our experiments) is a generalization of the scheme proposed by Jonas August [8] for the directional process. This scheme is preferable over the more usual finite difference approach as we will argue at the end of this section.

For the sake of clarity in this appendix, we use the symbols $\mathbf{x} = (x, y)$ rather than $\mathbf{b} = (b_1, b_2)$ for the spatial variables in G in this Appendix section. Moreover for the sake of simplicity in this section we will write $U(\mathbf{b}, \theta)$ rather than $U(\mathbf{b}, e^{i\theta})$.

Consider the (discrete Fourier transform) basis functions

$$\eta_{jkl}(x, y, \theta) = e^{2\pi i \left(\frac{jx}{N_1} + \frac{ky}{N_2} + \frac{l\theta}{N_3} \right)} \ ,$$

$j \in \{0, N_1\}, k \in \{0, N_1\}, l \in \{0, N_3\}$. Since the spatial variables in our orientation bundles have the same dimensions as the spatial variables in the given $X \times Y$ image we have $N_1 = X$ and $N_2 = Y$.

Define the complex-valued constants $\hat{W}_{j,k,l}$ by

$$\hat{W}_{j,k,l} = (\eta_{jkl}, U_f)_{\mathbb{L}_2([0,X]\times[0,Y]\times S_1)} = \int_0^X \int_0^X \int_0^{2\pi} e^{-2\pi i \left(\frac{jx}{X} + \frac{ky}{Y} + \frac{l\theta}{2\pi} \right)} U_f(x, y, \theta) \ \mathrm{d}\theta \mathrm{dx} \mathrm{dy} \ ,$$

Notice that by integration by parts

$$(\eta_{jkl}, \cos\theta \frac{\partial W}{\partial x}) = \int_{X\times Y\times S_1} \cos\theta \ W(x, y, \theta) \left(\frac{2\pi i j}{X} \right) e^{-2\pi i \left(\frac{jx}{X} + \frac{ky}{Y} + \frac{l\theta}{2\pi} \right)} \ \mathrm{dx} \mathrm{dy} \mathrm{d}\theta \ , \tag{7.19}$$

now use the Euler formula $\cos\theta = \frac{e^{i\theta} + e^{-i\theta}}{2}$ and we see that

$$(\eta_{jkl}, \cos\theta \frac{\partial W}{\partial x}) = -\frac{\pi i \, j}{X} (\hat{W}_{jk(l-1)} + \hat{W}_{jk(l+1)}) \ . \tag{7.20}$$

In the same matter we find

$$(\eta_{jkl}, \sin\theta \frac{\partial W}{\partial y}) = -\frac{\pi k}{Y}(\hat{W}_{jk(l-1)} + \hat{W}_{jk(l+1)}) \ .$$

It now directly follows by (7.19) and (7.20) that

$$(\eta_{jkl}, \partial_\xi W) = \beta_{j,k}\hat{W}_{jk(l-1)} - \overline{\beta_{j,k}}\hat{W}_{jk(l+1)} = \left[\beta_{j,k}S_{001} - \overline{\beta_{j,k}}S_{00-1}\right]\hat{W}_{jkl} \ , \tag{7.21}$$

with $\beta_{j,k} = \pi\left(\frac{ij}{X} + \frac{k}{Y}\right)$, where the shift operator $S_{abc}, a, b, c \in \mathbb{Z}$ is given by $S_{abc}\hat{W}_{jkl} = \hat{W}_{j-a,k-b,l-c}$. Notice that the discrete operator in the right hand side of (7.21) is just like the first order operator ∂_ξ skew adjoint.

In an analogue matter one can verify that

$$(\eta_{jkl}, \partial_\eta W) = \gamma_{j,k}\hat{W}_{jk(l-1)} - \overline{\gamma_{j,k}}\hat{W}_{jk(l+1)} = \left[\gamma_{j,k}S_{001} - \overline{\gamma_{j,k}}S_{00-1}\right]\hat{W}_{jkl} \quad , \tag{7.22}$$

with $\gamma_{j,k} = \pi\left(\frac{ik}{Y} - \frac{j}{X}\right)$. By (7.22) respectively (7.21) it now follows that

$$\begin{aligned}
(\eta_{jkl}, \partial_\xi\partial_\xi W) &= \left[\beta_{j,k}S_{001} - \overline{\beta_{j,k}}S_{00-1}\right]^2\hat{W}_{jkl} \\
&= [(\beta_{j,k})^2 S_{002} + (\overline{\beta_{j,k}})^2 S_{00-2} - 2|\beta_{j,k}|^2]\hat{W}_{jkl} \\
(\eta_{jkl}, \partial_\eta\partial_\eta W) &= \left[\gamma_{j,k}S_{001} - \overline{\gamma_{j,k}}S_{00-1}\right]^2\hat{W}_{jkl} \\
&= [(\gamma_{j,k})^2 S_{002} + (\overline{\gamma_{j,k}})^2 S_{00-2} - 2|\gamma_{j,k}|^2]\hat{W}_{jkl} \ .
\end{aligned}$$

Moreover it follows by integration by parts that

$$\begin{aligned}
(\eta_{jkl}, \partial_\theta W) &= \tfrac{-il}{N_3}\hat{W}_{j,k,l} \\
(\eta_{jkl}, \partial_\theta\partial_\theta W) &= -\left(\tfrac{l}{N_3}\right)^2\hat{W}_{j,k,l} \ .
\end{aligned}$$

Notice that the operator A leaves the spaces $\{\eta_{j,k,l}\}_{l\in\mathbb{Z}}$ for fixed j, k invariant and thereby the corresponding matrix is a block-matrix:

$$A = \begin{pmatrix} A_{1,1} & 0 & 0 \\ 0 & \ddots & 0 \\ 0 & 0 & A_{N_1N_2} \end{pmatrix} \to (\alpha I - A)^{-1} = \begin{pmatrix} (\alpha I - A_{1,1})^{-1} & 0 & 0 \\ 0 & \ddots & 0 \\ 0 & 0 & (\alpha I - A_{N_1,N_2})^{-1} \end{pmatrix}$$

It easily follows by the preceding that the matrix $\alpha I - A_{j,k}$ with respect to basis $\{\eta_{j,k,l}\}_{l\in\{1,\ldots,N_1\}}$ is a 5-band sparse matrix given by

$$\begin{pmatrix}
\alpha+q_1 & \beta_{j,k}a_2+\gamma_{j,k}a_3 & \beta_{j,k}^2D_{22}+\gamma_{j,k}^2D_{33} & 0 & \cdots & \overline{\beta_{j,k}}^2D_{22}+\overline{\gamma_{j,k}}^2D_{33} & -\overline{\beta_{j,k}}a_2-\overline{\gamma_{j,k}}a_3 \\
-\overline{\beta_{j,k}}a_2-\overline{\gamma_{j,k}}a_3 & \alpha+q_2 & \beta_{j,k}a_2+\gamma_{j,k}a_3 & \beta_{j,k}^2D_{22}+\gamma_{j,k}^2D_{33} & 0 & 0 & \overline{\beta_{j,k}}^2D_{22}+\overline{\gamma_{j,k}}^2D_{33} \\
\overline{\beta_{j,k}}^2D_{22}+\overline{\gamma_{j,k}}^2D_{33} & -a_2\overline{\beta_{j,k}}-a_3\overline{\gamma_{j,k}} & \alpha+q_3 & \beta_{j,k}a_2+\gamma_{j,k}a_3 & \beta_{j,k}^2D_{22}+\gamma_{j,k}^2D_{33} & 0 & 0 \\
0 & \ddots & \ddots & \ddots & \ddots & \ddots & 0 \\
\beta_{j,k}^2D_{22}+\gamma_{j,k}^2D_{33} & 0 & 0 & \ddots & \ddots & \ddots & \ddots \\
\beta_{j,k}a_2+\gamma_{j,k}a_3 & \beta_{j,k}^2D_{22}+\gamma_{j,k}^2D_{33} & 0 & 0 & \overline{\beta_{j,k}}^2D_{22}+\overline{\gamma_{j,k}}^2D_{33} & -\overline{\beta_{j,k}}a_2-\overline{\gamma_{j,k}}a_3 & \alpha+q_{N_3}
\end{pmatrix}$$

where $q_l = D_{11}\frac{l^2}{N_3^2} + D_{22}|\beta_{j,k}|^2 + D_{33}|\gamma_{j,k}|^2 + \frac{il}{N_3}a_1$, for $l = 1, \ldots N_3$. This algorithm is implemented in *Mathematica* using fast fourier transform and it takes approximately 2 minutes to compute the output W from a $64 \times 64 \times 64$ initial orientation score U_f. The over-all time complexity of computing W from U_f is $O(n \log n)$, where $n = N_1N_2N_3$. So for larger orientation bundles it may be worth-wile to first compute the impuls response or Green's function and then compute the G-convolution (4.81). The order of this alternative approach (via a fast fourier transform and direct multiplication in Fourier domain) is also $n \log n$, *but* since our kernels are very narrow in practice they can be cut-off very quickly which makes the algorithm closer to $O(n)$ then $O(n \log n)$.

7.7.1 Explicit Finite Difference Scheme

Next we will deal with the simple alternative of an explicit finite difference scheme for the direction process and explain its drawback. As a finite difference scheme for

$$\begin{cases} u_s = -\cos\theta\ u_x - \sin\theta\ u_y + \sigma u_{\theta\theta} \\ \lim_{s\downarrow 0} u(\cdot,\cdot,s) = U_f(\cdot,\cdot), \end{cases}$$

it is natural to propose

$$\begin{aligned} \tfrac{u^{n+1}_{ijk}-u^n_{ijk}}{\Delta s} &= A_d u^n_{ijk} = \tfrac{\sigma}{(\Delta\theta)^2}(S_{00-1} - 2I + S_{001})u^n_{ijk} \\ &\quad -\tfrac{\cos\theta_k}{\Delta x}(S_{-100} - I)u^n_{ijk} - \tfrac{\sin\theta_k}{\Delta y}(S_{0-10} - I)u^n_{ijk}\ , \end{aligned}$$

where $u^0_{ijk} = U_f(i\Delta x, j\Delta y, k\Delta\theta)$. Then $W = -(A-\alpha I)^{-1}U_f$ which is also given by $W(\cdot,\cdot) = \alpha \int_0^\infty e^{-s\alpha}u(\cdot,\cdot,s)\mathrm{ds}$ can be numerically approximated by

$$W(i\Delta x, j\Delta y, k\Delta\theta) = \alpha \sum_n e^{-\alpha n\Delta s} u^n_{i,j,k}\Delta s\ .$$

To analyze stability of such a scheme we consider the error $e^n_{ijk} = u^n_{ijk} - u(i\Delta x, j\Delta y, k\theta_k, n\Delta s)$. We follow the theory in [96]p.11-16 and obtain

$$e^{n+1}_{ijk} = e^n_{ijk} + \Delta s\ A_d e^n_{ijk} - T^n_{ijk}\ \Delta s\ \ ,$$

where T^n_{ijk} equals the truncation error. We have

$$\begin{aligned} e^{n+1}_{ijk} &= (1 - 2\sigma\nu + \mu\cos\theta_k + \mu\sin\theta_k)\, e^n_{ijk} - \mu\cos\theta_k\, e^n_{(i+1)jk} - \mu\sin\theta_k\, e^n_{i(j+1)k} \\ &\quad +\nu\sigma\, e^n_{i,j,k-1} + \nu\sigma\, e^n_{i,j,k+1}\ , \end{aligned}$$

where $\nu = \frac{\Delta s}{(\Delta\theta)^2}$ and $\mu = \frac{\Delta s}{\Delta x}$. We set $\mu = 1$, to ensure that the convection part (which is our main interest) is well approximated.[1]

Now by the Gershgorin theorem, see [66], the eigenvalues are contained in the circles with center point $1 - 2\sigma\nu + \mu\cos\theta_k + \mu\sin\theta_k$ and radius $\mu|\cos\theta_k| + \mu|\sin\theta_k| + 2\nu\sigma$. To guarantee stability the length of the eigenvalues must be less or equal to one. For $\theta_k \in [\pi, \frac{3\pi}{4}]$, the Gershgorin circle contains an open set around -1. But for $\theta_k \in [0, 2\pi)\backslash[\pi, \frac{3\pi}{4}]$, we have that $+1$ is an interior point of the Gershgorin circle. So, there is no guarantee for stability in contrast to the explicit diffusion scheme where these considerations give $\sigma\nu \leq \frac{1}{2}$. A practical solution to this problem is to separate the diffusion and the convection part: At each time step s first do a diffusion iteration followed by a convection iteration, cf. [133]. In this work the authors put a lot of emphasis on the fact that they *approximatively*[2] include left invariance in their discrete framework. This may not be as spectaculair as it seems, since every good numerical algorithm converging to the left invariant continuous case, will have this property. For example the algorithm proposed by August for the direction process [8] and our generalization also have this property, see figures G.1, G.2 and G.3.

[1] For example in 1D $u_s = u_\xi$ and $u^{n+1}_i - u^n_i = \frac{\Delta s}{\Delta\xi}(u^n_{i+1} - u^n_i)$ we must set $\mu = \frac{\Delta s}{\Delta\xi} = 1$ in order to obtain $u^{n+1}_i = u^n_{i+1}$.

[2] in particular see page 152 last alinea in [133]

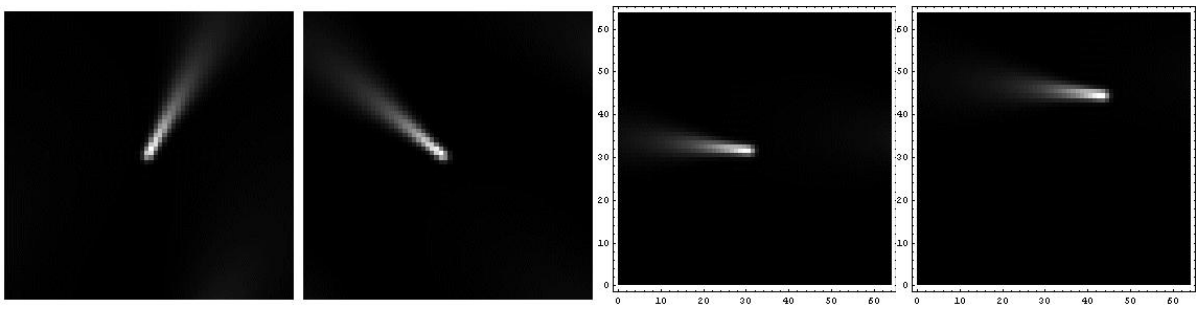

Figure 7.3: Illustrations of output W (equidistantly sampled over $64\times64\times64$ grid) of directional proces (i.e. $a_i = -\delta_{i2}, b_i = \sigma\delta_{i1}$), with $\alpha = 0.125$ (so expected life time $E[t] = (1/8) * 64 = 8$ pixels), $\sigma = 0.08$, applied on respectively from left to right (little bit blurred) initial $64 \times 64 \times 64$ score $\delta_{12}\delta_{32}\delta_{32}$, $\delta_{26}\delta_{32}\delta_{32}$, $\delta_{32}\delta_{32}\delta_{32}$, $\delta_{32}\delta_{45}\delta_{45}$. For the sake of illustration we integrated over the 64 orientations θ and plotted $\frac{2\pi}{64}\sum_{k=1}^{64} W(\mathbf{b},\theta_k) \approx \int_0^{2\pi} W(\mathbf{b},\theta)\mathrm{d}\theta$. Notice that these impuls responses are the numerical Green's functions of the evolution proces. So we see that shift-twist invariance of the transformation on the orientation score indeed corresponds to Euclidean invariance of the corresponding transformation on image and that this invariance is *not* seriously disrupted by the approximations in the numerical scheme. For the sake of clarity grey-values have been scaled to full range.

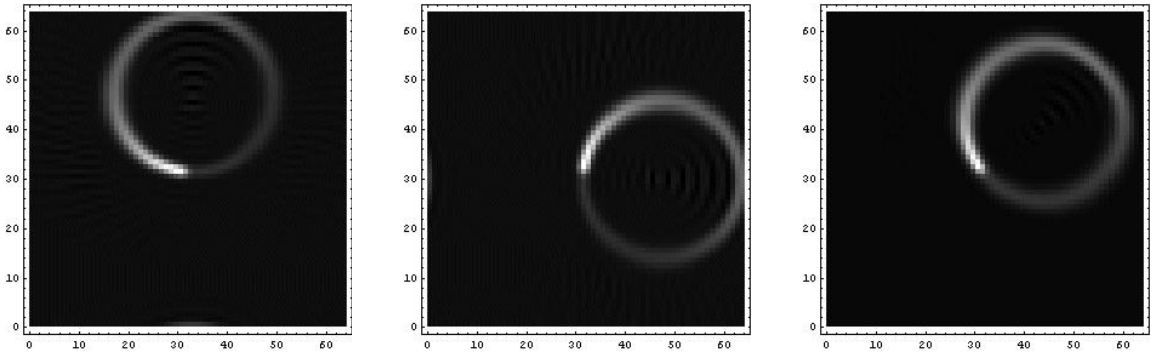

Figure 7.4: Output W of left invariant stochastic proces, with from left to right parameter values $\mathbf{a} = (a_1, a_2, a_3) = (4, 1, 0), (4, 0, 1), (4\sqrt{2}, 1, 1)$ and with $\alpha = 0.125$, so expected life time $E[t] = (1/8) * \frac{64}{a_1}$ pixels, applied on initial $64 \times 64 \times 64$ bundle $\delta_{32}\delta_{32}\delta_{32}$. For the sake of clarity grey-values have been scaled to full range. For the sake of illustration we integrated over the 64 orientations θ and plotted $\frac{2\pi}{64}\sum_{k=1}^{64} W(\mathbf{b},\theta_k) \approx \int_0^{2\pi} W(\mathbf{b},\theta)\mathrm{d}\theta$. The modes of these numerical Green's functions indeed correspond to the exponential curves of the Euclidean motion group, which we derived in Appendix F.

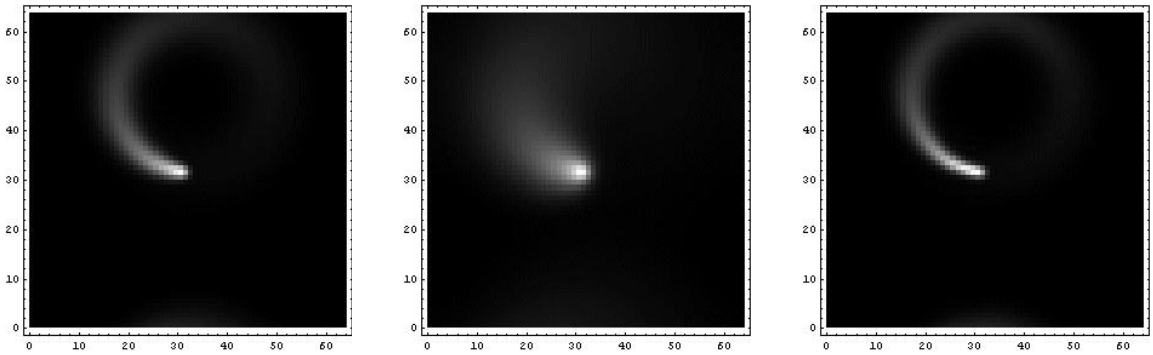

Figure 7.5: Output W of left invariant stochastic proces, with from left to right parameter values $(\mathbf{a};\mathbf{b}) = (a_1, a_2, a_3; b_1, b_2, b_3) = (4, 1, 0; 0, 0.02, 0.02), (4, 1, 0; 0, 0.2, 0.2), (4, 1, 0; 0, 0.2, 0.001)$ and with $\alpha = 0.125$, applied on initial $64 \times 64 \times 64$ bundle $\delta_{32}\delta_{32}\delta_{32}$. For the sake of clarity grey-values have been scaled to full range.

7.8 Numerical scheme of G-Convolutions, $G = \mathbb{R}^2 \rtimes \mathbb{T}$.

The input equals a function $U : G \to \mathbb{C}$ (for example an orientation score U_f of an image f) and a convolution kernel $K : G \to \mathbb{C}$. The output equals $W = K *_G U$, where the G-convolution is given by (4.81) and is related to the G-correlation by means of (4.82), i.e. $W = \check{K} \star_G U$, which are a lot easier to understand from the practical point of view, as a G-correlation is explicitly given by

$$\begin{aligned} W(\mathbf{b}, e^{i\theta}) &= (K *_G U)(\mathbf{b}, e^{i\theta}) = (\check{K} \star_G U)(\mathbf{b}, e^{i\theta}) \\ &= \int_{\mathbb{R}^2} \int_0^{2\pi} \check{K}(R_\theta^{-1}(\mathbf{b}' - \mathbf{b}), e^{i(\theta'-\theta)})\, U(\mathbf{b}', e^{i\theta'}) \mathrm{d}\theta' \mathrm{d}\mathbf{b}'. \end{aligned} \tag{7.23}$$

Now there are two reasonable options implementing this expression, either by means of discretization of (7.23), which means that (unless symbolic formulas are at hand for the kernel K) $\check{K}(R_\theta^{-1}(\mathbf{b}' - \mathbf{b}), e^{i\theta'})$ has to be computed by means of interpolation between a rectangular grid, or everything is expressed into steerable components. Concerning simplicity, speed and accuracy, the latter approach, which is explained below, is preferable.

Expand $\check{K}$ in steerable components [3] (with respect to both angle and position):

$$\check{K}(\mathbf{b}, e^{i\theta}) = \sum_{m\in\mathbb{Z}} \sum_{n\in\mathbb{Z}} \check{K}_{mn}(\mathbf{b})\, e^{im\theta} \ , \mathbf{b} = (r\cos\phi, r\sin\phi), \tag{7.24}$$

such that $\check{K}_{mn}(R_\theta^{-1}\mathbf{b}) = e^{in\theta}\check{K}_{mn}(\mathbf{b})$. Notice that

$$K_{mn}(\mathbf{b}) = \frac{1}{4\,\pi^2} \int_0^{2\pi} \int_0^{2\pi} K(R_{\theta'}^{-1}\mathbf{b}, e^{i\theta}) e^{im\theta} e^{in\theta'} \mathrm{d}\theta \mathrm{d}\theta'. \tag{7.25}$$

Expand U also into steerable components with respect to the angle only (in practice easily obtained by computing a discrete Fourier transform of the orientation columns $\theta \mapsto U_f(\cdot, e^{i\theta})$).

[3] If also a decomposition in radial functions is required we could expand K_m in terms of the eigen functions of the Harmonic oscillator $\{Y_m \otimes h_n^m\}$, see section 7.1.

Then we obtain

$$\begin{aligned} W(\mathbf{b}, e^{i\theta}) &= \int_{\mathbb{R}^2} \int_0^{2\pi} \check{K}(\mathbf{b}' - \mathbf{b}, e^{i\theta'}) \, \mathrm{d}\theta' \mathrm{d}\mathbf{b}' \\ &= \int_{\mathbb{R}^2} \int_0^{2\pi} \sum_{m\in\mathbb{Z}} \sum_{n\in\mathbb{Z}} \sum_{\tilde{m}\in\mathbb{Z}} \check{K}_{mn}(\mathbf{b}' - \mathbf{b}) U_{\tilde{m}}(\mathbf{b}') e^{i(n+m)\theta} e^{-i(m+\tilde{m})\theta'} \, \mathrm{d}\theta' \mathrm{d}\mathbf{b}' \\ &= \int_{\mathbb{R}^2} \sum_{m\in\mathbb{Z}} \sum_{n\in\mathbb{Z}} \sum_{\tilde{m}\in\mathbb{Z}} \check{K}_{mn}(\mathbf{b}' - \mathbf{b}) U_{\tilde{m}}(\mathbf{b}') e^{i(n+m)\theta} \left(\int_0^{2\pi} e^{-i(m+\tilde{m})\theta'} \, \mathrm{d}\theta' \right) \mathrm{d}\mathbf{b}' \\ &= 2\pi \sum_{m\in\mathbb{Z}} \sum_{n\in\mathbb{Z}} e^{i(n+m)\theta} (\check{K}_{mn} \star U_{-m})(\mathbf{b}) \ , \end{aligned}$$

where $(\check{K}_{mn} \star U_{-m})(\mathbf{b})$ are just ordinary $2D$-correlations in $\mathbb{R}^2$, i.e.

$$(\check{K}_{mn} \star U_{-m})(\mathbf{b}) = \int_{\mathbb{R}^2} \check{K}_{mn}(\mathbf{b}' - \mathbf{b}) U_{-m}(\mathbf{b}') \, \mathrm{d}\mathbf{b}'.$$

So in practice where the series is truncated at say $|m| \leq$ Mmax, a G-convolution can be implemented by means of only $(1 + 2 * \mathrm{Nmax})(1 + 2 * \mathrm{Mmax})$ 2D-convolutions prohibited that the convolution kernel is expanded according to (7.24). The evaluation of W can be sped up using a fast Fourier Transform (FFT) rather than a discrete Fourier Transform (DFT).

We stress that if in practice the convolution kernel K is very narrow in the angular component, $Mmax$ may become too large. In this case it may be better not to make a steerable decomposition in θ and thereby W can be computed by means of $Nmax$ 3D-correlations:

$$W(\mathbf{b}, e^{i\theta}) = \sum_{n=0}^{Nmax} \int_{\mathbb{R}^2} \int_0^{2\pi} \check{K}_n(\mathbf{b}' - \mathbf{b}, e^{i(\theta' - \theta)}) e^{in\theta'} U(\mathbf{b}', e^{i\theta'}) \, \mathrm{d}\theta' \mathrm{d}\mathbf{b}'.$$

7.9 Steerability

The issue of steerability is frequently use in image analysis, which is introduced by Freeman et al.[61]. The idea is that so-called steerable convolution kernels $\psi \in \mathbb{L}_1(\mathbb{R}^2) \cap C^1(\mathbb{R}^2, \mathbb{C})$, which by definition can be written

$$\psi(\mathbf{x}) = \sum_{m=-N}^{N} \psi_m(\mathbf{x}) = \sum_m f_m(r) e^{-im\phi} \ , N \in \mathbb{N},$$

for some $f_m \in C^1(\mathbb{R}, \mathbb{C})$, are easily rotated (without interpolation artifacts on a typically rectangular pixel-grid) by means of

$$\mathcal{R}_\theta \psi(\mathbf{x}) = \sum_{m=-N}^{N} \psi_m(r) e^{im\theta} e^{-im\phi} \ ,$$

with the additional advantage (regarding computation time, if multiple orientations are needed) that

$$(\mathcal{R}_\theta \psi * f)(\mathbf{x}) = \sum_m e^{im\theta} \ (\psi_m * f)(\mathbf{x}), \qquad \mathbf{x} \in \mathbb{R}^2, \theta \in [0, 2\pi).$$

At first sight the issue of steerability does not make any sense since of course any convolution kernel within $\mathbb{L}_2(\mathbb{R}^2)$ is steerable after expansion in the complete orthonormal base of eigen functions of the Harmonic oscillator. But we stress that $N < \infty$ and from the practical point of view only those convolution kernels with the property that their decomposition in $SO(2)$-irreducible components vanishes for $|m| > N$, with N small, are efficient in practical implementations.

7.9.1 Steerable Tensor fields

Let $\mathbf{V}$ be a tensor field on $\mathbb{R}^d$ given by

$$\mathbf{V}(\mathbf{x}) = V_{i_1 \cdots i_N}(\mathbf{x}) \mathbf{e}_{i_1} \otimes \cdots \otimes \mathbf{e}_{i_N}, \qquad \mathbf{x} \in \mathbb{R}^d,$$

with respect to standard base $\{\mathbf{e}_i\}_{i=1}^n$, where we identified each tangent space $T_{\mathbf{x}}(\mathbb{R}^d)$ with $\mathbb{R}^d$ and where we do not make a distinction between contravariant and covariant components as the dual base can also be identified with the standard base. Recall that such a tensor field is rotated by means of (5.9). Notice that the rotation action acts on both components as on the base vectors. In this subsection we explain how to compute the irreducible components of the tensor field $\mathbf{v}$ by means the Wigner-Eckhart Theorem, from both the irreducible-components of the components of the vector field and the irreducible components of the base vectors.

By the Peter-Weyl Theorem any rank N-tensor $\mathbf{A}$, in particular $\mathbf{A} = \mathbf{V}(\mathbf{x})$ (with $\mathbf{x} \in \mathbb{R}^d$ fixed), can be decomposed into a countable set of $SO(d)$-irreducible components $\mathbf{A}^m$:

$$\mathbf{A} = \sum_{m \in \mathbb{N}} \mathbf{A}^m, \text{ such that } \mathbf{A}_R = \sum_{m \in \mathbb{N}} \Gamma_m(R)\ \mathbf{A}^m, \tag{7.26}$$

where $\mathbf{A}_R$ denotes the rotated tensor, whose components are given by

$$\mathbf{A}_R = R^{i_1}_{i'_1} \cdots R^{i_1}_{i'_N} A_{i'_1 \cdots i'_N} \mathbf{e}_1 \otimes \cdots \otimes \mathbf{e}_N.$$

Secondly, again by the Peter-Weyl theorem, all components $\mathbf{x} \mapsto H_{i'_1 \cdots i'_N}(\mathbf{x})$ are rotated by

$$H_{i'_1 \cdots i'_N}(R^{-1}\mathbf{x}) = \sum_{n \in \mathbb{N}} \Gamma_n(R)\ g^n_{i'_1 \cdots i'_N}(r)\ H^n_{i'_1 \cdots i'_N}(\mathbf{u}), \quad \|\mathbf{x}\| = r, \mathbf{u} = (1/r)\mathbf{x} \in S_d.$$

where $H^n_{i'_1 \cdots i'_N}$ is the projection of $\mathbf{x} \mapsto H_{i'_1 \cdots i'_N}(\frac{\mathbf{x}}{\|\mathbf{x}\|})$ onto the subspace V_n within $\mathbb{L}_2(S^d)$ spanned by the of spherical harmonics (on S^d) of order n and where the radial functions $g^n_{i'_1 \cdots i'_N}(r)$ are obtained by projection (with r fixed) of $\mathbf{u} \mapsto H(r\mathbf{u})$ onto V_n. In this way we obtain direct products $\Gamma_n \bigotimes \Gamma_m$ of irreducible representations Γ_n and Γ_m, which can be reduced to direct sums (using the well-known Glebsch-Gordan coefficients, stored in matrix S):

$$\Gamma_n \otimes \Gamma_m = S^{-1} \bigoplus_{k \in \mathbb{N}} n_k\ \Gamma_k S,$$

which gives us the explicit expressions of the irreducible components of the tensor-field $\mathbf{V}$:

$$\mathbf{V}_R = \sum_m \Gamma_m(R) \mathbf{V}^m.$$

Bibliography

[1] R. Abraham, J.E. Marsden, and T. Ratiu. *Manifolds, Tensor Analysis, and Applications*. Addison-Wesley Publishing Company, London, Amsterdam, Ontario, Sydney, Tokio, 1983.

[2] M. Abramowitz and I. A. Stegun, editors. *Handbook of Mathematical Functions with Formulas, Graphs, and Mathematical Tables*. Dover Publications, Inc., New York, 1965. Originally published by the National Bureau of Standards in 1964.

[3] S. Agmon. *Lectures on Elliptic Boundary Value Problems*. D. VAN NOSTRAND Mathematical Studies, Princeton, New Yersey, New York, 1965.

[4] S.T. Ali, J.P. Antoine, and J.P. Gazeau. *Coherent States, Wavelets and Their Generalizations*. Springer Verlag, New York, Berlin, Heidelberg, 1999.

[5] L. Alvarez, F. Guichard, P. L. Lions, and J.-M. Morel. Axioms and fundamental equations of image processing. *Arch. Rat. Mech. Anal.*, 123:200–257, 1993.

[6] J.P. Antoine. Directional wavelets revisited: Cauchy wavelets and symmetry detection in patterns. *Applied and Computational Harmonic Analysis*, 6:314–345, 1999.

[7] N. Aronszajn. Theory of reproducing kernels. *Trans. A.M.S.*, 68:337–404, 1950.

[8] J. August. *The Curve Indicator Random Field*. PhD thesis, Yale University, 2001.

[9] J. August and S.W. Zucker. The curve indicator random field and markov processes. *IEEE-PAMI, Pattern Recognition and Machine Intelligence*, 25, 2003. Number 4.

[10] V. Balakrishnan. Fractional powers of closed operators and the semi-groups generated by them. *Pacific J. Math.*, 10:419–437, 1960.

[11] E. Balmachnova, L.M.J. Florack, B. Platel, F.M.W. Kanters, and B.M. ter Haar Romeny. Stability of top-points in scale space. In Weickert Kimmel, Sochen, editor, *Proc. on the 5th International Conference on Scale Space and PDE methods*, pages 62–72, Hofgeismar, Germany, April 2005. Springer.

[12] R. Beukema. *Positive Operator-Valued Measures and Phase-Space Representations*. PhD thesis, University of Technology Eindhoven, Department of Mathematics, Eindhoven, The Netherlands, 2003.

[13] W.H. Bosking, Y. Zhang, B. Schofield, and D. Fitzpatrick. Orientation selectivity and the arrangement of horizontal connections in tree shrew striate cortex. *The Journal of Neuroscience*, 17(6):2112–2127, March 1997.

[14] A.V. Bukhvalov and Arendt W. Integral representation of resolvent and semigroups. *Forum Math. 6*, 6(1):111–137, 1994.

[15] G. S. Chirikjian and A. B. Kyatkin. *Engineering applications of noncommutitative harmonic analysis: with emphasis on rotation and motion groups*. Boca Raton CRC Press, 2001.

[16] J. Damon. Local Morse theory for solutions to the heat equation and Gaussian blurring. *Journal of Differential Equations*, 115(2):368–401, January 1995.

[17] J. Damon. Generic properties of solutions to partial differential equations. *Arch. Rat. Mech. Anal.*, pages 353–403, 1997.

[18] J. Damon. Local Morse theory for Gaussian blurred functions. In Sporring et al. [116], chapter 11, pages 147–163.

[19] I. Daubechies. *Ten Lectures on Wavelets*. Number 61 in CBMS-NSF Series in Applied Mathematics. SIAM, Philadelphia, 1992.

[20] J. De Graaf. Evolution equations. Technical report, TUE, Potugal, March 1996. Course delivered at the Department of Mathematics of the University of Coimbra.

[21] M. Duits. A functional hilbert space approach to frame transforms and wavelet transforms. September 2004. Master thesis in Applied Analysis.

[22] M. Duits and R. Duits. A functional hilbert space approach to the theory of wavelets. Technical report, TUE, Eindhoven, March 2004. RANA/CASA Report RANA-7-2004, available on the web: ftp://ftp.win.tue.nl/pub/rana/rana04-07.pdf Department of Mathematics Eindhoven University of Technology.

[23] M. Duits and R. Duits. A functional hilbert space approach to frame transforms. In preparation for submission to a pure mathematics journal, 2005.

[24] R. Duits, M. Duits, and M. van Almsick. Invertible orientation scores as an application of generalized wavelet theory. Technical report, TUE, Eindhoven, March 2004. Technical Report 04-04, Biomedical Image and Analysis, Department of Biomedical Engineering, Eindhoven University of Technology.

[25] R. Duits, M. Felsberg, and L. Florack. α scale spaces on a bounded domain. Technical report, TUE, Eindhoven, March 2003. BMT-Report(Biomedical Image Analysis) 2003-01.

[26] R. Duits, M. Felsberg, and L.M.J. Florack. α scale spaces on a bounded domain. *Proceedings Scale Space Conference, Isle of Skye,UK.*, pages 494–510, June 2003.

[27] R. Duits, M. Felsberg, G. Granlund, and B.M. ter Haar Romeny. Image analysis and reconstruction using a wavelet transform constructed from a reducible representation of the euclidean motion group. Invited Submission to special issue on Early Cognitive Vision of IJCV, International Journal of Computer Vision.

[28] R. Duits, L. Florack, B. ter Haar Romeny, and J. de Graaf. Scale-space axioms critically revisited. In N.Younan, editor, *Signal and Image Processing*, pages 304–309, Kauai, August 2002. IASTED, ACTA Press. Proceedings of the Fourth IASTED international Conference.

[29] R. Duits, L. M. J. Florack, J. De Graaf, and B. M. ter Haar Romeny. On the axioms of scale space theory. Technical report, TUE, The Netherlands, Eindhoven, Januari 2002.

[30] R. Duits, L.M.J. Florack, J. de Graaf, and B. ter Haar Romeny. On the axioms of scale space theory. *Journal of Mathematical Imaging and Vision*, 20:267–298, May 2004.

[31] R. Duits, B. Janssen, F. Kanters, and L. M. J. Florack. Linear image reconstruction from a sparse set of alpha scale space features by means of inner products of sobolev type. *To appear in Proceedings DSSCV-Worskhop on Deep Structure, Singularities and Computer Vision, Springer-Verlag*, June 2005.

[32] R. Duits, F. Kanters, L.M.J. Florack, and B. M. ter Haar Romeny. A comparison of the deep structure of α-scale spaces. *To appear in Proceedings DSSCV-Worskhop on Deep Structure, Singularities and Computer Vision, Springer-Verlag*, June 2005.

[33] R. Duits, M. van Almsick, M. Duits, E. Franken, and L.M.J. Florack. Image processing via shift-twist invariant operations on orientation bundle functions. In Niemann Zhuralev et al. Geppener, Gurevich, editor, *7th International Conference on Pattern Recognition and Image Analysis: New Information Technologies*, pages 193–196, St.Petersburg, October 2004. Extended version is to appear in special issue of the International Journal for Pattern Recognition and Image Analysis MAIK.

[34] N. Dungey, A. F. M. ter Elst, and D. W. Robinson. *Analysis on Lie groups with polynomial growth*, volume 214. Birkhauser-Progress in Mathematics, Boston, 2003.

[35] Hille E. and R.S.Phillips. *Functional Analysis and semi-groups*. American Mathematical Society, 1957.

[36] S.J.L. Eijndhoven and J. de Graaf. Some results on hankel invariant distribution spaces. *Proceedings of the Koninklijke Akademie van Wetenschapppen, Series A*, 86(1):77–87, 1982.

[37] A. F. M. ter Elst and D. W. Robinson. Elliptic operators on lie groups. Technical report, Technische Universiteit Eindhoven (TUE), Eindhoven, August 1995. RANA-Report 95-11.

[38] A. Erdelyi, W. Magnus, F. Oberhettinger, and F.G. Tricomi. *Higher Transcedental Functions*, volume 3. McGraw-Hill, New York, 1955.

[39] J. Faraut and K. Harzallah. *Deux cours d'analyse harmonique*. Birkhaeuser, Tunis, 1984.

[40] M. Fashandi, R. A. Kamyabi Gol, A. Niknam, and M.A. Pourabdollah. Continuous wavelet transform on a special homogeneous space. *Journal of Mathematical Physics*, 44(9):4260–4266, 2003.

[41] W. Feller. *An Introduction to Probability Theory and its Applications*, volume 2. John Wiley and sons, Inc., New York, London, Sydney, 1966.

[42] M. Felsberg. *Low-Level Image Processing with the Structure Multivector*. PhD thesis, Institute of Computer Science and Applied Mathematics Christian-Albrechts-University of Kiel, 2002. TR no. 0203, available at http://www.informatik.uni-kiel. de/reports/2002/0203.html.

[43] M. Felsberg. Optical flow estimation from monogenic phase. In *1st International Workshop on Complex Motion*, volume 3417. Springer, 2004.

[44] M. Felsberg, R. Duits, and L.M.J. Florack. The monogenic scale space on a bounded domain and its applications. *Proceedings Scale Space Conference, Isle of Skye, UK.*, pages 209–224, June 2003.

[45] M. Felsberg, P.-E. Forssén, and H. Scharr. Efficient robust smoothing of low-level signal features. Technical Report LiTH-ISY-R-2619, SE-581 83 Linkoping, Sweden, August 2004.

[46] M. Felsberg, P.-E. Forssén, and H. Scharr. Channel smoothing: Efficient robust smoothing of low-level signal features. *IEEE Transactions on Pattern Analysis and Machine Intelligence*, 2005. accepted.

[47] M. Felsberg and G. Sommer. Scale adaptive filtering derived from the Laplace equation. In B. Radig and S. Florczyk, editors, *23. DAGM Symposium Mustererkennung, München*, volume 2191 of *Lecture Notes in Computer Science*, pages 124–131. Springer, Heidelberg, 2001.

[48] M. Felsberg and G. Sommer. The Poisson scale-space: A unified approach to phase-based image processing in scale-space. *Journal of Mathematical Imaging and Vision*, 21(1-2):5–26, 2004.

[49] L. Florack and A. Kuijper. The topological structure of scale-space images. *Journal of Mathematical Imaging and Vision*, 12(1):65–79, February 2000.

[50] L. M. J. Florack. *The Syntactical Structure of Scalar Images*. PhD thesis, University of Utrecht, Department of Medicine, Utrecht, The Netherlands, November 10 1993.

[51] L. M. J. Florack. *Image Structure*, volume 10 of *Computational Imaging and Vision Series*. Kluwer Academic Publishers, Dordrecht, The Netherlands, 1997.

[52] L. M. J. Florack. *Image Structure*. Kluwer Academic Publishers, Dordrecht, The Netherlands, 1997.

[53] L. M. J. Florack. A geometric model for cortical magnification. In S.-W. Lee, H. H. Bülthoff, and T. Poggio, editors, *Biologically Motivated Computer Vision: Proceedings of the First IEEE International Workshop, BMCV 2000 (Seoul, Korea, May 2000)*, volume 1811 of *Lecture Notes in Computer Science*, pages 574–583, Berlin, May 2000. Springer-Verlag.

[54] L. M. J. Florack, R. Duits, and J. Bierkens. Tikhonov regularization versus scale space: a new result. *Accepted for presentation at the ICIP conference, Singapore.*

[55] L. M. J. Florack, B. M. ter Haar Romeny, J. J. Koenderink, and M. A. Viergever. Cartesian differential invariants in scale-space. *Journal of Mathematical Imaging and Vision*, 3(4):327–348, November 1993.

[56] L. M. J. Florack, R. Maas, and W. J. Niessen. Pseudo-linear scale-space theory. *International Journal of Computer Vision*, 31(2/3):247–259, April 1999.

[57] L. M. J. Florack, A. H. Salden, B. M. ter Haar Romeny, J. J. Koenderink, and M. A. Viergever. Nonlinear scale-space. *Image and Vision Computing*, 13(4):279–294, May 1995.

[58] P.-E. Forssén and G. H. Granlund. Sparse feature maps in a scale hierarchy. In G. Sommer and Y.Y. Zeevi, editors, *Proc. Int. Workshop on Algebraic Frames for the Perception-Action Cycle*, volume 1888 of *Lecture Notes in Computer Science*, Kiel, Germany, September 2000. Springer, Heidelberg.

[59] P.E. Forssen. *Low and Medium Level Vision using Channel Representations*. PhD thesis, Linkoping University, Dept. EE, Linkoping, Sweden, March 2004.

[60] Erik Franken. Context-enhanced detection of electrophysiology catheters in noisy fluoroscopy images. Master's thesis, Eindhoven University of Technology, Department of Electrical Engineering, 2004.

[61] W. T. Freeman and E. H. Adelson. The design and use of steerable filters. *IEEE Transactions on Pattern Analysis and Machine Intelligence*, 13(9):891–906, September 1991.

[62] Gelfand and Shilov. *Generalized Functions*. Academic press inc., New York, 1968.

[63] J.E. Gilbert and M.A.M. Murray. *Clifford algebras and Dirac operators in harmonic analysis*. Cambridge University Press, Cambridge, 1991.

[64] J.de Graaf. A theory of generalized functions based on holomorphic semi-groups. *Koninklijke Nederlandse Akademie van Wetenschappen, Department of mathematics TUE, Series A*, 87(2):419–437, 1984.

[65] G.H. Granlund. An associative perception-action structure using a localized space variant information representation. In *Proceedings of Algebraic Frames for the Perception-Action Cycle (AFPAC)*, Kiel, Germany, September 2000. Also as Technical Report LiTH-ISY-R-2255.

[66] C.W. Groetsch. *Elements of Applicable Functional Analysis*. Marcel Dekker Inc., New York, Basel, 1980.

[67] A. Grossmann, J. Morlet, and T. Paul. Integral transforms associated to square integrable representations. *J.Math.Phys.*, 26:2473–2479, 1985.

[68] B. M. ter Haar Romeny. *Front-End Vision and Multi-Scale Image Analysis: Multi-Scale Computer Vision Theory and Applications, written in Mathematica*, volume 27. Kluwer Academic Publishers, Dordrecht, the Netherlands, 2003.

[69] B. M. ter Haar Romeny, L. M. J. Florack, J. J. Koenderink, and M. A. Viergever, editors. *Scale-Space Theory in Computer Vision: Proceedings of the First International Conference, Scale-Space'97, Utrecht, The Netherlands*, volume 1252 of *Lecture Notes in Computer Science*. Springer-Verlag, Berlin, July 1997.

[70] W. Hebisch. Estimates on the semigroups generated by left invariant operators on lie groups. *Journal fuer die reine und angewandte Mathematik*, 423:1–45, 1992.

[71] G. Hellwig. *Partial Differential Equations*. Blaisdell Publishing Company, 1964.

[72] J. R. Higgins. An interpolation series associated with the bessel-hankel transform. *J.London Math. Soc.*, 2:5–707–714, 1972.

[73] L. Hormander. Hypoellptic second order differential equations. *Acta Mathematica*, 119:147–171, 1968.

[74] R.A. Hummel, editor. *Proc. IEEE Comp. Soc. Conf. Computer Vision and Pattern Recognition*, Miami Beach, June 22-26 1986. IEEE.

[75] T. Iijima. Basic theory of pattern observation. Papers of Technical Group on Automata and Automatic Control, 1959. (in Japanese).

[76] T. Iijima. Basic theory on normalization of a pattern (in case of typical one-dimensional pattern). *Bulletin of Electrical Laboratory*, 26:368–388, 1962. (in Japanese).

[77] C. J. Isham and J. R. Klauder. Coherent states for n-dimensional euclidean groups $e(n)$ and their application. *Journal of Mathematical Physics*, 32(3):607–620, March 1991.

[78] B. Janssen, F. Kanters, R. Duits, L. M. J. Florack, and B. M. ter Haar Romeny. A linear image reconstruction framework based on sobolev type inner products. In Weickert Kimmel, Sochen, editor, *Proc. on the 5th International Conference on Scale Space and PDE methods*, pages 85–95, Hofgeismar, Germany, April 2005. Springer.

[79] S. N. Kalitzin, B. M. ter Haar Romeny, and M. A. Viergever. Invertible apertured orientation filters in image analysis. *International Journal of Computer Vision*, 31(2/3):145–158, April 1999.

[80] F. Kanters, M. Lillholm, R. Duits, B. Janssen, B. Platel, and L. M. J. Florack. On image reconstruction from multiscale top points. In Weickert Kimmel, Sochen, editor, *Proc. on the 5th International Conference on Scale Space and PDE methods*, pages 431–439, Hofgeismar, Germany, April 2005. Springer.

[81] F.M.W. Kanters, B. Platel, L.M.J. Florack and B.M. ter Haar Romeny. Image reconstruction from multiscale critical points. In Lewis Griffin and Martin Lillholm, editors, *Scale Space Methods in Computer Vision, 4th International Conference, Scale Space 2003*, pages 464–478, Isle of Skye, UK, June 2003. Springer.

[82] M. Kerckhove, editor. *Scale-Space and Morphology in Computer Vision: Proceedings of the Third International Conference, Scale-Space 2001, Vancouver, Canada*, volume 2106 of *Lecture Notes in Computer Science*. Springer-Verlag, Berlin, July 2001.

[83] J. J. Koenderink. The structure of images. *Biological Cybernetics*, 50:363–370, 1984.

[84] J. J. Koenderink and A. J. van Doorn. Operational significance of receptive field assemblies. *Biological Cybernetics*, 58:163–171, 1988.

[85] J. J. Koenderink and A. J. van Doorn. Receptive field families. *Biological Cybernetics*, 63:291–298, 1990.

[86] E. Kreyszig. *Advanced Engineering Mathematics*. Wiley, 1993.

[87] A. Kuijper and L. M. J. Florack. Hierarchical pre-segmentation without prior knowledge. In *Proceedings of the 8th International Conference on Computer Vision (Vancouver, Canada, July 9–12, 2001)*, pages 487–493. IEEE Computer Society Press, 2001.

[88] T. S. Lee. Image representation using 2d gabor wavelets. *IEEE-Transactions on Pattern Analysis and Machine Inteligence*, 18(10):959–971, 1996.

[89] M. Lillholm, M. Nielsen, and L. D. Griffin. Feature-based image analysis. *International Journal of Computer Vision*, 52(3):73–95, 2003.

[90] T. Lindeberg. Scale-space for discrete signals. *IEEE Transactions on Pattern Analysis and Machine Intelligence*, 12(3):234–245, 1990.

[91] T. Lindeberg. *Scale-Space Theory in Computer Vision.* The Kluwer International Series in Engineering and Computer Science. Kluwer Academic Publishers, Dordrecht, The Netherlands, 1994.

[92] M. Loog, J. J. Duistermaat, and L. M. J. Florack. On the behavior of spatial critical points under Gaussian blurring. a folklore theorem and scale-space constraints. In Kerckhove [82], pages 183–192.

[93] A.K. Louis, P. Maass, and A. Rieder. *Wavelets, Theory and Applications.* Wiley, New York, 1997.

[94] F.J.L. Martens. *Spaces of analytic functions on inductive/projective limits of Hilbert Spaces.* PhD thesis, University of Technology Eindhoven, Department of Mathematics and Computing Science, Eindhoven, The Netherlands, 1988. This PHD thesis is available on the webpages of the Technische Universiteit Eindhoven. Webpage in 2004: http://alexandria.tue.nl/extra3/proefschrift/PRF6A/8810117.pdf.

[95] Gérard Medioni, Mi-Suen Lee, and Chi-Keung Tang. *A Computational Framework for Segmentation and Grouping.* Elsevier, Amsterdam.

[96] K.W. Morton and D.F. Mayers. *Numerical Solution of Partial Differential Equations.* Cambridg University Press, Cambridge, 1994.

[97] D. Mumford. Elastica and computer vision. *Algebraic Geometry and Its Applications. Springer-Verlag*, pages 491–506, 1994.

[98] M. Nielsen, L. M. J. Florack, and R. Deriche. Regularization and scale space. Accepted for publication in the Journal of Mathematical Imaging and Vision, 1996.

[99] M. Nielsen, P. Johansen, O. F. Olsen, and J. Weickert, editors. *Scale-Space Theories in Computer Vision: Proceedings of the Second International Conference, Scale-Space'99, Corfu, Greece*, volume 1682 of *Lecture Notes in Computer Science.* Springer-Verlag, Berlin, September 1999.

[100] M. Nielsen and M. Lillholm. What do features tell about images? In Kerckhove [82], pages 39–50.

[101] F. W. J. Olver. *Asymptotics and Special Functions.* Academic Press, New York, 1974.

[102] N. Otsu. *Mathematical Studies on Feature Extraction in Pattern Recognition.* PhD thesis, Electrotechnical Laboratory, Ibaraki, Japan, 1981. (in Japanese).

[103] A. L. T. Paterson. *Amenability*, volume 29 of *Mathematical Surveys and Monographs.* American Mathematical Society, Providence, RI, 1988.

[104] E. J. Pauwels, L. J. Van Gool, P. Fiddelaers, and T. Moons. An extended class of scale-invariant and recursive scale space filters. *IEEE Transactions on Pattern Analysis and Machine Intelligence*, 17(7):691–701, July 1995.

[105] K. Pedersen, R. Duits, and M. Nielsen. On α-kernels, lévy processes, and natural image statistics. *Proc. 5th Scale Space Conference*, April 2005.

[106] B. Platel. Multiscale hierarchical segmentation. Master's thesis, Department of Biomedical Engineering Eindhoven University of Technology, December 2002. Technical Report BMIA-0204.

[107] B. Platel, F. M. W. Kanters, L. M. J. Florack, and E. G. Balmachnova. Using multiscale top points in image matching. *In Proc. of the 11th international conference on Image Processing*, October 2004.

[108] T. Poston and I. N. Stewart. *Catastrophe Theory and its Applications.* Pitman, London, 1978.

[109] M.H. Protter. *Maximum Principles in Differential Equations.* PRENTICE-HALL inc., New Jersey, 1967.

[110] R. W. van der Put. Methods for 3d orientation analysis and their application to the study of arterial remodelling. Master's thesis, Department of Biomedical Engineering Eindhoven University of Technology, June 2005. Technical Report BMIA-0502.

[111] D.W. Robinson. *Elliptic Operators and Lie groups*. Clarendon Press, Oxford, New York, Tokyo, 1991.

[112] W. Rudin. *Functional Analysis*. McGraw-Hill, New York, 1973.

[113] A.A. Sagle and R. E. Walde. *Introduction to Lie groups and Lie Algebras*, volume 51. Academic Press, New York and London, 1973.

[114] K. I. Sato. *Lévy processes and Infinitely Divisible Distributions*. Cambridge University Press, Cambridge, 1999.

[115] J. Sporring, M. Nielsen, L. Florack, and Johansen P. *Gaussian Scale-Space Theory*. KAP, Dordrecht, The Netherlands, 1997.

[116] J. Sporring, M. Nielsen, L. M. J. Florack, and P. Johansen, editors. *Gaussian Scale-Space Theory*, volume 8 of *Computational Imaging and Vision Series*. Kluwer Academic Publishers, Dordrecht, The Netherlands, 1997.

[117] M. Sugiura. *Unitary representations and harmonic analysis*. North-Holland Mathematical Library, 44., Amsterdam, Kodansha, Tokyo, second edition, 1990.

[118] M. Temme, N. *An Introduction to the Classical Functions of Mathematical Physics*. John Wiley and Sons, Inc., New York, 1996.

[119] K.K. Thornber and L.R. Williams. Analytic solution of stochastic completion fields. *Biological Cybernetics*, 75:141–151, 1996.

[120] D. Y. Ts'0, R. D. Frostig, E. E. Lieke, and A. Grinvald. Functional organization of primate visual cortex revealed by high resolution optical imaging. *Science*, 249:417–20, 1990.

[121] S. Twareque Ali. A general theorem on square-integrability: Vector coherent states. *Journal of Mathematical Physics*, 39, 1998. Number 8.

[122] M. A. van Almsick. *Context Models of Lines and Contours*. PhD thesis, Eindhoven University of Technology, Department of Biomedical Engineering, Eindhoven, The Netherlands, 2005. In Preparation.

[123] M. A. van Almsick, R. Duits, E. Franken, and B.M. ter Haar Romeny. From stochastic completion fields to tensor voting. In *Proceedings DSSCC-workshop on Deep Structure Singularities and Computer Vision*, pages –, Maastricht the Netherlands, June 9-10 2005. Springer-Verlag.

[124] Jan-Cees van der Meer. A note on local morse theory in state-scale space and gaussian deformations. In preparation: Technical CASA-report , Department of Mathematics, University of Technology Eindhoven, http://www.win.tue.nl/casa/research/casareports/2005.html, 2005.

[125] V.S. Varadarajan. *Lie Groups, Lie-Algebras and Their Representations*. Springer-Verlag, New York, Berlin, Heidelberg, Tokyo, 1984.

[126] J.N. Watson. *A Treatise on the Theory of Bessel Functions*. Cambridge University Press, Cambridge, 1996. Originally published by Cambridge University Press 1922.

[127] J. A. Weickert. *Anisotropic Diffusion in Image Processing*. ECMI Series. Teubner, Stuttgart, January 1998.

[128] J. A. Weickert, S. Ishikawa, and A. Imiya. On the history of Gaussian scale-space axiomatics. In Sporring et al. [116], chapter 4, pages 45–59.

[129] M. Westheimer. Untersuchungen zur lehre von der gestalt ii. *Psychologische Forschung*, 4:301–350, 1923.

[130] L. R. Williams and J.W. Zweck. A rotation and translation invariant saliency network. *Biological Cybernetics*, 88:2–10, 2003.

[131] J. Wloka. *Partial Differential Equations*. Cambridge University Press, Cambridge, 1987.

[132] K. Yosida. *Functional Analysis*. Springer Verlag, Berlin, Heidelberg, New York, 1980.

[133] J. Zweck and L. R. Williams. Euclidean group invariant computation of stochastic completion fields using shiftable-twistable functions. *Journal of Mathematical Imaging and Vision*, 21(2):135–154, 2004.

Nederlandse Samenvatting

Perceptuele organisatie is de organisatie van locale beeldfragmenten in de globale structuur van het beeld. Het is verbazingwekkend hoe goed ons eigen visueel systeem de locale responsies van de receptieve velden in de primaire cortex in een globale structuur weet te brengen. In de psychofysica zijn begin vorige eeuw de beroemde Gestalt wetten voor de perceptuele organisatie opgesteld. Deze wetten beschrijven de basis principes van de perceptuele organisatie van het visuele systeem van zoogdieren en zijn afgeleid aan de hand van een hele reeks psycho-fysische experimenten.

Het doel van dit proefschrift is het maken van mathematisch onderbouwde modellen en algoritmen voor perceptuele organisatie in de analyse van (bij voorkeur medische) digitale beelden. Hierbij dient het eigen visueel systeem als inspiratiebron en ligt de nadruk op low-level vision. Omdat de begrippen schaal en oriëntatie een dominante rol spelen bij de perceptuele organisatie in ons visueel systeem, leggen we sterk de nadruk op deze twee aspecten in onze theorie en algoritme ontwikkeling. In beide gevallen construeren we een nieuw object (respectievelijk een schaal ruimte representatie en een oriëntatie partituur) uit een beeld waar respectievelijk schaal en oriëntatie expliciet in gecodeerd zijn. Deze nieuwe objecten (sterk geïnspireerd door ons eigen visueel systeem) lenen zich vele malen beter om perceptuele organisatie operaties uit te voeren.

Allereerst beschouwen we de scale space (schaal ruimte) representaties waarin een plaatje op meerdere schalen tegelijkertijd wordt gerepresenteerd. In de beeldanalyse worden zulke representaties vrijwel altijd met een Gaussische convolutiekern gecreëerd, hetgeen neerkomt op een diffusie systeem op het boven half vlak $s > 0$, waarbij de schaal van observatie een half maal de variantie is, $s = \frac{1}{2}\sigma^2$. In de beeld analyse literatuur zijn er enkele artikelen die claimen dat de Gaussische scale space representatie uniek bepaald is door een per artikel variërende set van axioma's. Deze afleidingen zijn ofwel onjuist, ofwel (impliciet) gebaseerd op het coördinaat afhankelijke dogma van een te separeren convolutie kern. Hierbij heeft men een complete geparameteriseerde $0 < \alpha \leq 1$ klasse over het hoofd gezien, die we in dit proefschrift α scale spaces noemen. In deze klasse bevindt zich een zeer goed alternatief voor de Gaussische scale space representatie ($\alpha = 1$): De Poisson scale space representatie, die correspondeert met een potentiaal probleem op het boven halfvlak $s > 0$ en die gezien zijn Clifford analytische uitbreiding voordelen biedt als het gaat om op fase gebaseerde beeldanalyse technieken. In dit proefschrift wordt aangetoond dat slechts de α scale spaces aan alle[4] genoemde axioma's voldoen. De topologie in een scale space reflecteert de hiërarchische structuur van een beeld. Naarmate de schaal toeneemt verdwijnen (en soms verschijnen) er structuren. Er vinden annihilaties en creaties tussen extrema en zadels plaats. De punten waar dat gebeurt heten toppunten. Aan de hand van Morse-singulariteiten theorie worden de stabiele topologische veranderingen in de scale space representaties afgeleid. Mede hieruit en uit praktische experimenten komen we tot de conclusie dat de diepe structuur in de α scale spaces wezenlijk verschillend is. Tot slot tonen we aan dat het originele beeld behoorlijk goed kan worden benaderd gegeven de tweede orde structuur in deze punten. Daartoe is een nieuwe lineaire methode ontwikkeld aan de hand van de theorie van Gelfand triples, die het globale minimum levert van een bijbehorend optimalisatie probleem.

[4] behoudens het sterke causaliteit axioma dat door zwakke causaliteit moet worden vervangen.

Daarnaast beschouwen we oriëntatie partituren (de zogenoemde orientation scores[5]), gebaseerd op de oriëntatie kolommen in de primaire visuele cortex. De transformatie van een beeld in een oriëntatie partituur is een wat ongebruikelijke, inverteerbare wavelet transformatie en komt neer op convoluties met een aantal geroteerde versies van een wavelet op een vast gekozen schaal. Om de robuustheid van deze transformatie te garanderen hebben we de abstracte wavelet theorie zoals geformuleerd door Grossmann, Morlet en Paul, moeten generaliseren aan de hand van de theorie der reproducerende kernen. Uit deze generalisatie concluderen we onder andere dat de transformatie unitair is en dat de transformatie onder bepaalde condities op de wavelet van de transformatie robuust is. Oriëntatie wavelets die aan deze condities voldoen noemen we proper wavelets. We ontwikkelen diverse methoden om deze proper wavelets, die tevens nuttige lijn-detectoren zijn, te construeren. Hierbij maken we onder andere gebruik van de complete basis van eigen functies van de Harmonische oscillator gerepresenteerd in polaire coördinaten, die met het oog op Fourier transformatie, lokaliteit en stuurbaarheid uiterst geschikt is in de beeldanalyse. Het geheel is ook gegeneraliseerd en uitgevoerd tot het moeilijkere geval van inverteerbare oriëntatie scores van 3D-beelden.

Nadat we de stabiliteit van de transformaties tussen plaatje en oriëntatie score hebben gegarandeerd kunnen we de perceptuele organisatie via oriëntatie scores uitvoeren. Het netto resultaat op het plaatje is Euclidisch invariant dan en slechts dan als de operatie op de oriëntatie score links invariant is. Daarom beschouwen we lineaire links invariante evoluties op de oriëntatie scores behorende bij links invariante stochastische processen op de Euclidische bewegingsgroep, met als doel het versterken van langgerekte structuren in medische beelden en het automatisch opvullen van de onderbrekingen daarin. Deze links invariante evolutie vergelijkingen komen neer op een G-convolutie met de bijbehorende Greense functies die we aan de hand van gefundeerde Lie-groepen theorie benaderen met analytische expressies. Deze expressies in combinatie met een stuurbare implementatie van de G-convolutie, genieten praktisch gezien de voorkeur boven het numerieke schema voor de lineaire links invariante evoluties die ook zijn behandeld in dit proefschrift. Tot slot beschouwen we twee methoden (steerable tensor voting en channel representations) voor robuuste oriëntatie schattingen in een beeld, waarbij de nadruk wordt gelegd op de onderliggende wiskunde. Bij deze methoden wordt een initieel oriëntatie veld verkregen door de locale differentiaal structuur, gemanipuleerd tot een meer gestroomlijnd oriëntatie veld aan de hand van een model gebaseerd op eerder genoemde Gestalt wetten. De verkregen robuuste oriëntatie velden zijn niet alleen nuttig voor de detectie van langgerekte structuren in medische beelden, ze leveren ook een beter lokaal coördinatensysteem voor differentiaal invarianten. Dit laatste blijkt nuttig te zijn bij de bepaling van kromming van langgerekte structuren of randen in beelden.

[5]De initiators van dit idee, Stilian Kalitzin et al.[79], noemden deze objecten orientation bundles. Aangezien deze naam terecht verwarring veroorzaakt bij wiskundigen, hebben we ervoor gekozen om ze oriëntatie partituren te noemen.

Acknowledgements

The Technology Foundation STW, applied science division of NWO and the technology programme of the Ministry Economic Affairs is gratefully acknowledged for their financial support.

Large parts of this thesis have been produced in close cooperations with people from various fields of research. The most relevant cooperations with this respect were together with Markus van Almsick (physicist) from the biomedical engineering department of the Eindhoven University of Technology concerning the second part of Chapter 2 and Chapter 5 of this thesis, with Michael Felsberg (computer scientist) from the department of electro-technical engineering at the University of Linköping, on the Poisson (and Monogenic) scale space and the channel representations, with Frans Kanters and Bart Janssen (elektro-technical engineers[6]) regarding the practical aspects of top-point reconstructions, with Bram Platel (biomedical engineer) and Evguenia Balmachnova (applied mathematician) regarding the deep structure studies, with Erik Franken (elektro-technical engineer) regarding robust orientation estimation, with Richard van der Put (biomedical engineer) regarding the implementation of invertible scores of 3D images (Chapter 4.7.2 of this thesis) and last but certainly not least the cooperation with my brother Maurice Duits (mathematician) regarding the first part of chapter 2 and section 7.2.

Furthermore, I thank Prof. Joop Boersma (Department of Mathematics, Eindhoven University of Technology) for his help on classical analysis issues, and dr. Tom ter Elst (Department of Mathematics, Eindhoven University of Technology) for his strong explanations on Lie-groups.[7]

Thanks to the supervisors, Prof.dr.ir. Bart ter Haar Romeny, dr. Luc Florack and Prof.dr.ir. Jan de Graaf at the Eindhoven University of Technology, for their support. Thanks to Bart ter Haar Romeny for his enthousiast approach to his research group, his support regarding *Mathematica* and his inspiring ideas on perceptual organization. Thanks to Luc Florack for his support on deep structure and his efforts to combine the fields of mathematical physics and image analysis. Special thanks to Jan de Graaf for his few but rather crucial remarks regarding the "non-uniqueness" of the Gaussian scale space and his inspiring ideas regarding the role of reproducing kernels in the theory of wavelets.

Thanks to Tamara and my parents, for their patience and support.

[6] Most of their fundamental results are obtained from this work.

[7] Which was (and still is), surprisingly, not within the Mathematics curriculum at the TUE.

Curriculum Vitae

Remco Duits werd op 26 mei 1978 geboren in Weert. Van 1990 tot en met 1996 doorliep hij aldaar het VWO-programma aan de Philips van Horne Scholen gemeenschap. Na het behalen van zijn VWO-diploma begon hij in datzelfde jaar aan de studie technische wiskunde aan de Technische Universiteit Eindhoven. Hier ontving hij in 2001 zijn ingenieurs diploma cum laude. Zijn afstudeerscriptie onder begeleiding van professor Jan de Graaf betrof een nieuwe functionaal- analytische behandeling van het Stokes randwaarde probleem. Daarnaast, tevens onder de begeleiding van professor Jan de Graaf, liep hij stage bij ingenieursbureau Geodelta in Delft op het onderwerp toepassing van orthogonale matrix groepen in de geodesie. Tijdens zijn studie heeft hij diverse wiskunde zomer cursussen verzorgd aan de Technische Hogeschool Venlo. Aansluitend aan zijn afstuderen begon hij het in deze dissertatie beschreven onderzoek bij de vakgroep Biomedische Beeldanalyse (die op dat moment net opgestart was) in de faculteit Biomedische Technologie op de Technische Universiteit Eindhoven onder het toezicht van prof.dr.ir. Bart ter Haar Romeny, dr. Luc Florack en prof.dr.ir. Jan de Graaf. Dit onderzoek vond plaats in samenwerking met de vakgroep toegepaste analyse op de wiskunde faculteit van de Technische Universiteit Eindhoven. Naast dit onderzoek was hij actief in het onderwijs bij diverse vakken en projecten in het curriculum van de opleiding Biomedische Technologie.